

**Molecular Level Tuning of Redox-
active 2D-Covalent Organic
Frameworks for Energy Storage**

A Thesis

Submitted in Partial Fulfilment of the

Requirements

for the Degree of

Doctor of Philosophy

By

Sattwick Haldar

ID: 20153405

Thesis Supervisor: Dr. Ramanathan Vaidhyanathan



Indian Institute of Science Education and Research (IISER), Pune



भारतीय विज्ञान शिक्षा एवं अनुसंधान संस्थान, पुणे

INDIAN INSTITUTE OF SCIENCE EDUCATION AND RESEARCH (IISER), PUNE

(An Autonomous Institution, Ministry of Human Resource Development, Govt. of India)

Dr. Homi Bhabha Road, Pune – 411 008

Certificate

This is to certify that the work incorporated in the thesis entitled “*Molecular Level Tuning of Redox-active 2D-Covalent Organic Frameworks for Energy Storage*” submitted by **Sattwick Haldar** has been carried out by the candidate at the Indian Institute of Science Education and Research (IISER), Pune, under my supervision. The work presented here or any part of it has not been included in any other thesis submitted previously for the award of any degree or diploma from any other University or Institution.

Sattwick Haldar

Date:

Signature of Thesis Supervisor

Dr. R. Vaidhyanathan

Associate Professor



भारतीय विज्ञान शिक्षा एवं अनुसंधान संस्थान, पुणे

INDIAN INSTITUTE OF SCIENCE EDUCATION AND RESEARCH (IISER), PUNE

(An Autonomous Institution, Ministry of Human Resource Development, Govt. of India)

Dr. Homi Bhabha Road, Pune – 411 008

Declaration

I declare that this written submission represents my ideas in my own words and where others' ideas have been included; I have adequately cited and referenced the original sources. I also declare that I have adhered to all principles of academic honesty and integrity and have not misrepresented or fabricated or falsified any idea/data/fact/source in my submission. I understand that violation of the above will be cause for disciplinary action by the Institute and can also evoke penal action from the sources which have thus not been properly cited or from whom proper permission has not been taken when needed.

A handwritten signature in black ink, appearing to read "Sattwick Haldar".

Date: 27. 07. 2020

A handwritten signature in black ink, appearing to read "Sattwick Haldar".

Signature of Student

Sattwick Haldar

(Reg. No.:20153405)

Acknowledgement

I would like to thank to my PhD supervisor, Dr. Ramanathan Vaidhyanathan, for being supportive to me during this wonderful journey of my life. He has been given me the full-freedom to pursue various projects without any objection and also provided insightful discussions. I am also very thankful to him for his scientific guidance and many suggestions. He is my primary resource for getting my science questions answered and was instrumental in helping me crank out this thesis even in the time of COVID-19 pandemic. His devotion to the research career has inspired me to be brave to take on new challenges. I think my ability to interpret experimental results and provide novel research ideas has improved a lot – thanks to his supervision. He is an excellent scientist and approachable PhD supervisor, is really an invaluable asset to my PhD career at IISER Pune. I hope that I could be as lively, enthusiastic, and energetic as him and to someday be able to command an audience as well as he can.

This journey would never have been successful without the support of Emeritus Prof. Satishchandra B. Ogale and his helpful group members. The amazing instrumental facility in their lab and their thorough understanding of electrochemistry has encouraged me to penetrate in a completely new field of research. His experience and caring attitude had actually helped me to pursue this interdisciplinary research. I express my sincere gratitude towards his valuable guidance, scholarly inputs and consistent encouragement.

This feat was possible because of the positive disposition provided by my Research Advisory Committee (RAC) members Dr. Sreekumar Kurungot and Dr. Musthafa Muhammed. Their immense knowledge in the domain of electrochemistry and instantaneous advice truly guided me to overcome all the scientific difficulties arrived. I was very much privileged to get their help throughout my work and I owe a lot to them for this achievement.

Many thanks should go to my research collaborators Dr. Dinesh Kabra (IIT Bombay), Dr. Partha Hazra (IISER Pune), Prof. Ramaswamy Murugavel (IIT Bombay) and their students for their kind assistance and for allowing me to use their research facilities. Some of my projects would never have been fruitful without their valuable contributions and technical supports.

I thank Indian Institute of Science Education and Research (IISER), Pune and the director Prof. Jayant B. Udgaonkar and former Director Prof. K. N. Ganesh for providing excellent research facilities and an amazing and an outstanding research atmosphere. I am extremely thankful to DST-INSPIRE and SERB for providing me with the PhD fellowship for the last five years and for their travel support to attend international conferences.

Looking back to the MSc days my scientific research career has been started under the supervision of Dr. Amrita Saha (Jadavpur University). It was in her group where I got the first taste for experimental chemistry and that encouraged me to choose this career option. Her sincere guidance introduced me to this wonderful scientific world. Her words and suggestions motivated me always to be steady in every ups and downs in my research career. All my school and university teachers are unforgettable to me who had shown me the pathway to reach here up to and their lessons actually made me what I am now.

No research is possible without the help of academic staff, instrument-operators, library staff and IT-section. I take this time to express my gratitude to all of them for their dedicated services. I thank Dr. Umeshreddy Kacherki (deputy librarian) and Anuradha for library support and all other technical staff (Mr. Parveen Nasa, Ms. Archana, Mr. Yathish, Mr. Sandeep, Mrs. Megha Mr. Nilesh Dumbre, Ms. Nayana, Mr. Nitin, Mr. Anil, Mr. Mahesh, Mr. Neeraj Maheshwari, to name a few), as well as all the IISER Pune non-teaching staff members, especially Mr. Mayuresh, Mr. Tushar, Ms. Nayana, Ms. Vrushali, Mr. Suresh, Mr. Prabhas, Mr. Sandeep, Ms. Mariamma John, for their generous support at a number of times. I thank Ms. Neeta Deo, Mr. Suresh, Mr. Sachin and Mr. Sailesh for IT support. Special thanks to the housekeepers to keep research laboratories and institute neat and clean all the time.

I feel very happy to say during this tenure my lab-mates were like my second family members. Shyama, Shalini, Debanjan, Aparna, Rahul, Rinku, Himan and Pragalv have all extended their support in a very special way, and I gained a lot from them, through their personal and scholarly interactions, their suggestions at various points of my research programme.

I am very much indebted to my friends Anweshi, Anupam, Projwal, Banibrata, Sandip, Sumanta, Kingshuk, and Debashree. They actually didn't allow me to feel bore anytime and the quality time I have spent with them during my leisure and holidays truly used to provide me with a lot of enthusiasm to come-back in work.

No words are sufficient to convey my sense of gratefulness for my mother, father, and sister. Without their emotional support, it was never ever possible to fight with all the adversities. My hard-working parents have sacrificed their lives for myself and provided unconditional love and care. My sister has been my best friend all my life and I love her dearly and thank her for all her advice and support. I know I always have my family to count on when times are rough.

I am fortunate to have a wonderful person in my life who is my best friend, soul-mate, and girl-friend, Sniha. She has been non-judgmental of me and instrumental in implanting my confidence. She has complete belief on me and my intellect even when I felt like digging hole and crawling into hurdles. These past several years have not been an easy ride, both academically and personally. I truly thank

her for standing always by my side, even when I was irritable. This journey made us learnt a lot about real life and strengthened our commitment to each other and to live life to the fullest.

This beautiful journey in my career had not only given me experiences and courage but also has built up my self-confidence to fight with any adverse situation. Every moment of this learning period was though full of uncertainty but the success obtained after prolong patience gave me the inspiration to move on to conquer the next hurdle.

Sattwick Haldar

List of Acronyms

<i>Materials related</i>	<i>Units</i>
COF: Covalent Organic Frameworks	°C : Degree Celsius
CON: Covalent Organic Nanosheets	
MOF: Metal Organic Framework	mmol: Milli moles
CP: Coordination Polymer	μL : Micro liter
<i>Instrument and measurement related</i>	μm: micrometer
FE-SEM: Field Emission-Scanning Electron, HR-TEM: High Resolution Transmission electron Microscopy SAED: Selected Area Electron Diffraction	mL: Milliliter
TGA: Thermogravimetric analysis	nm : nanometer
PXRD: Powder X-Ray Diffraction SCXRD: Single Crystal X-ray diffraction	hrs: hours
AFM: Atomic Force Microscopy	min: Minutes
BET: Brunauer Emmett Teller	mol: moles
GCD: Galvanostatic charge-discharge	gm: Gram
EDLC: Electrical Double Layer Capacitance	Å : Angstrom
CE: Counter Electrode	C_{sp}: specific capacitance
WE: Working Electrode	MHz: Megahertz
RE: Reference Electrode	V: volts
CV: Cyclic Voltammogram	mV: Millivolts
<i>Chemicals related</i>	M: Molar
DMF: N, N-Dimethyl formamide	A: Ampere
DMSO: Dimethyl sulfoxide	mA: Milliampere
NMP: N-Methyl-2-pyrrolidone	
ACN: Acetonitrile	F: Farad
MeOH: Methanol	mg: Milligram
EtOH: Ethanol	K: Kelvin
H₂SO₄: Sulphuric Acid	THF: Tetrahydrofuran
H⁺: Hydrogen ion, Li⁺: Lithium ion, Na⁺: Sodium ion, K⁺: Potassium ion	mA/g: milliampere/gram
^tBu-NH₄PF₆: Tetrabutylammonium phosphate	mAh/g: milliampere hour/gram

Table of Contents

Thesis outline

Introduction

Strategies for COF design

- I.1. Choice of Schiff base chemistry; Cost-effective framework and multiple advantages*
- I.2. Stability under applied potential; Keto-enol tautomerism in the β -ketoenamine*
- I.3. C₂-C₃ / C₃-C₃ symmetry combination; Microporous to mesoporous structure*
- I.4. Importance of 2D layered structure over 3D network: Pivotal role of 1D-nanochannel*
- I.5. Surface area vs. surface accessibility; competition between stacking and exfoliation*
- I.6. Exfoliation of 2D-COF to CONs*

Fabrication of High performing electrodes for Battery and Supercapacitors

- I.7. Basic working principle of the energy storage system; battery and capacitor*
- I.8. Required features in electrode materials for metal-ion battery and supercapacitor*
- I.9. Redox-active polymers as electrodes for metal ion-battery and supercapacitors*
- I.10. Drawbacks associated with polymer-based electrode materials*
- I.11. Redox-active 2D-COF; A designer approach for high performing electrode*
- I.12. Recent literature of COF based electrodes for battery and supercapacitor*
- I.13. Glimpses of our works*

References

Chapter 1.

1.1. Introduction

1.2. Results and discussion

- 1.2.1. Synthesis of IISERP-CON1 and corresponding model compound*
- 1.2.2. Structure modeling of IISERP-CON1*
- 1.2.3. Characterization: Porosity and morphology*
- 1.2.4. Electrochemistry: Coin-cell- cyclic voltammetry and galvanostatic charge-discharge cycling*
- 1.2.5. 1.2.5. Stability of IISERP-CON1 under electrochemical potential*

1.3. Computational studies

- 1.3.1. Simulated structure of Li@CON: Li-framework interactions from model and XPS*
- 1.3.2. Bandgap and electrostatic potentials- electronic contributions*

1.4. Discussion

1.5. Conclusion

Acknowledgement

References

Chapter 2.

2.1. Introduction

2.2. Results and discussion

2.2.1. Synthesis, structure modeling and characterization of IISERP-COF7 and IISERP-COF8 IISERP-COF7

2.2.2. Chemical exfoliation of COFs to CONs (IISERP-CON2 and IISERP-CON3)

2.2.3. Electrochemical measurements in a half-cell LIB- Results and additional discussions

2.2.4. Calculation of Li concentration in the Li@CON and Li@COF from the specific capacity

2.2.5. Rapid Li-ion diffusion in exfoliated COF

2.2.6. Exfoliated-COFs performance under high potentials of a full-cell LIB

2.2.7. Structural and chemical reasons for the CON's superior performance

2.3. Conclusion

References

Chapter 3.

3.1. Introduction

3.2. Results and discussion

3.2.1. Synthesis and structural-modelling of IISERP-COF16, IISERP-COF17, IISERP-COF18

3.2.2. Electronic energy levels of the COFs

3.2.3. General principle of a SIB half-cell

3.2.4. Anodic reduction and concurrent sodiation process of a SIB half-cell

3.2.5. Lowered resistance to charge-transfer: Confirmed from AC-impedance and DC-measurements

3.2.6. Sodium-COF interactions from atomic modelling

3.3. Conclusion

Acknowledgement

References

Chapter 4.

4.1. Introduction

4.2. Results and discussion:

4.2.1. Synthesis and structure-modeling of IISERP-COF10, IISERP-COF11, IISERP-COF12

4.2.2. Redox activity at pyridine groups

4.2.3. Capacitance under acidic liquid-electrolyte

4.2.4. Contribution from EDLC and Faradaic Capacitance

4.2.5. Capacitance of the solid-state device

4.3. Conclusion

Acknowledgement

References

Appendix of all chapters

Molecular Level Tuning of Redox-active 2D-Covalent Organic Frameworks for Energy Storage

Synopsis

Covalent Organic Framework (COF) is an emerging class of crystalline polymers and are among the designable members of the porous organic materials. They can be constructed using modular chemistry, wherein the modules can be functionalized and connected via covalent bonds. Due to their fascinating properties such as periodic porous structures, large surface area, effortless surface/structural modification, and high thermal and chemical stability, COFs have been investigated as potential materials for various applications in energy storage, optoelectronic devices, gas separation, chemical catalysis, sensing and so on. Depending on the geometry of the monomeric modules the network of the COFs can propagate in 2D or 3D. In many 2D COFs, the strong interlayer π - π interaction generates honeycomb type 1D nanopores, which get decorated with multiple numbers of functional groups. This makes many of them resemble the stacked structure of Graphite. Thus 2D COFs are being regarded as a new source of layered materials. Interestingly, the relatively weaker π - π bonds of COF and the presence of pores within the layers, enable the exfoliation of the multilayers to few atom-thick layers, called as Covalent Organic Nanosheets (CONs). Such structure and property variation of 2D COFs facilitates the control of electrical properties via decorating this porous Nano channel of COF with various redox-active groups. Such redox-functionalized COF becomes potential candidates for energy storage applications.

Typically the storing of the charge both in metal ion batteries (LIB and SIB) and capacitors involves guest ions (Li^+ , Na^+ , and H^+ etc.) interaction with electronically-active electrode materials, for example, Graphite. The superiority of a battery or a capacitor is ranked by how long it can deliver the energy (battery) and how fast the burst of energy can be released (capacitor). These are termed as the 'energy density' and 'power density' parameters. The universal target is to achieve the maximum value for both these parameters in a single storage source. Of the various approaches, improving the performance of the battery by manipulating the chemistry around the electrode materials is an effective strategy, for example, incorporating electronegative heteroatoms in Graphite structure. COF can also be a suitable alternative for hetero-atoms doped Graphite when it comes to storing electrical

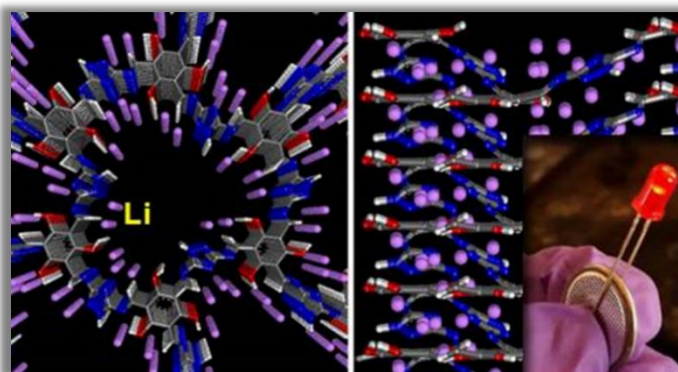
charges, particularly in metal-ion batteries. In this thesis, we have adopted a modular design approach to introduce electronically active segments into the backbone of porous COFs to make it suitable for high energy density anodes in LIB and SIBs. Two major features that impact the performance of this COF-based anodes in a metal-ion battery include, (i) The density, proximity and orientation of the redox-active functional groups (carbonyl, hydroxyl, pyridine, triazole, tetrazine etc) which decorate the walls of the pores and (ii) the electronic and pore-size driven diffusion of the guest ions like Li^+/Na^+ (from the electrolytes such as LiPF_6 or NaPF_6) towards the bulk of the framework structure. We implement an important methodology, namely the "Chemical Exfoliation" to improve the diffusion kinetics of the charges that flow in and out of the COF, this can deliver fast-charging batteries.

Alternatively, we have also periodically enriched the COFs with lightweight hetero-atoms such as N and O to enhance charge (H^+) accumulation both electrostatically and electrochemically under an applied potential in a capacitor configuration using easily dissociable acid electrolytes (H_2SO_4). The achieved high power density of the richly functionalized COFs have been successfully transferred into the all-solid-state supercapacitor device. Thus the work carried out in this thesis has contributed to COF-based energy storage from a molecular-level design to compatible device fabrication. Furthermore, via detailed experimental and theoretical investigations on the charge-storage ability of COF materials with benchmark capacities, we have brought out a multitude of insights which feeds to the attractive possibility of developing lightweight energy storage devices.

Chapter 1: High and Reversible Lithium-Ion Storage in Self- Exfoliated Triazole-Triformyl Phloroglucinol-Based Covalent Organic Nanosheets

Covalent organic framework (COF) can grow into self-exfoliated nanosheets. Their Graphene/Graphite resembling microtexture and nanostructure suits electrochemical applications. Here, covalent organic

nanosheets (CON) with nanopores lined with triazole and phloroglucinol units is presented, neither of these functional units binds to Lithium strongly. The CON's potential as an anode in Li-ion battery is investigated. Their fibrous



texture enables facile amalgamation as a coin-cell anode, which exhibits an exceptionally high specific capacity of $\approx 720 \text{ mAh/g}$ ($@100 \text{ mA/g}$). Its capacity is retained even after 1000 cycles. Increasing the current density from 100 mA/g to 1 A/g causes the specific capacity to drop only by 20%, which is the lowest among all high-performing anodic COFs. The majority of the Lithium insertion follows an

ultrafast diffusion-controlled intercalation (diffusion coefficient, $D_{Li^+} = 5.48 \times 10^{-11} \text{ cm}^2 \text{ s}^{-1}$). The absence of strong Li framework bonds in the density functional theory (DFT) optimized structure supports this reversible intercalation. The discrete monomer of the CON shows a specific capacity of only 140 mAh/g @50 mA/g and no sign of Lithium intercalation revealing the crucial role played by the polymeric structure of the CON in this intercalation-assisted conductivity. The potentials mapped using DFT suggest a substantial electronic driving-force for the Lithium intercalation. The findings underscore the potential of the designer CON as anode material for Li-ion batteries.

Chapter 2: Chemical Exfoliation as a Controlled Route to Enhance the Anodic Performance of COF in LIB

A covalent organic framework (COF), built from light atoms with a graphitic structure, could be an excellent anodic candidate for lightweight batteries, which can be of use in portable devices. But to replace the commercial Graphite anode, they need more Li-interactive sites/unit-cell and all such sites should be made to participate. The compromise made in the volumetric density to gain the gravimetric advantage should be minimal. Exfoliation enhances surface and functional group accessibility yielding high capacity and rapid charge storage. A chemical strategy for simultaneous exfoliation and increase of Li-loving active-pockets can

deliver a lightweight Li-ion battery (LIB). Here, anthracene-based COFs are chemically exfoliated into few-layer-thick nanosheets using

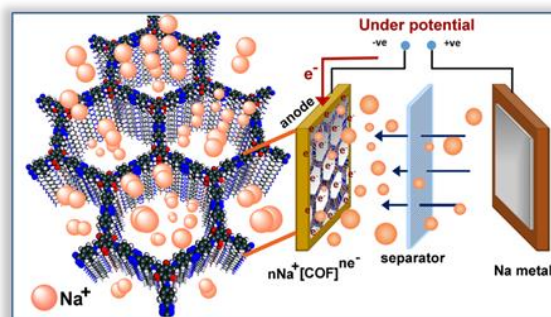


maleic anhydride as a functionalizing exfoliation agent (FEA). It not only exfoliates but also introduces multiple Li-interactive carbonyl groups, leading to a loading of 30 Li/unit-cell (vs one Li per C_6). The exfoliation enhances the specific capacity by ≈ 4 times (200–790 mAh/g @100 mA/g). A realistic full-cell, made using the exfoliated COF against a $LiCoO_2$ cathode, delivers a specific capacity of 220 mAh/g over 200 cycles. The observed capacity stands highest among all organic polymers.

Chapter 3: Tuning the Electronic Energy Level of Covalent Organic Framework for Crafting High-rate Na-ion Battery Anode

Crystalline Covalent Organic Frameworks (COFs) possess ordered accessible nano-channels. When these channels are decorated with redox-active functional groups, they can serve as the anode in metal ion battery (LIB and SIB etc). Though Sodium's superior relative abundance makes it a better choice over Lithium, its larger size and poor thermodynamic favourability with Graphite make it incompatible

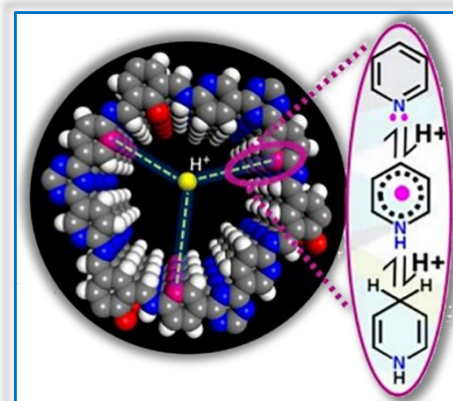
ion battery (LIB and SIB etc). Though Sodium's superior relative abundance makes it a better choice over Lithium, its larger size and poor thermodynamic favourability with Graphite make it incompatible with the commercial Graphite anodes used in Li-ion battery. Also, their sluggish movement inside the porous electrodes and electrolytes restricts the fast charging of SIB. Creating an electronic driving force at the electrodes via chemical manipulation can be a versatile approach to overcome this issue. Here we present anodes for



SIB drawn on three isostructural COFs with nearly the same Highest Occupied Molecular Orbitals (HOMO) levels but with varying Lowest Unoccupied Molecular Orbitals (LUMO) energy levels. This variation in LUMO levels has been deliberately performed by the inclusion of electron-deficient centres (phenyl vs. tetrazine vs. bispyridine-tetrazine) substituents into the modules that make up the COF. When connected to a source (electrical potential), electrons accumulate in the antibonding LUMO orbitals. Now, these electron-dosed LUMO levels become efficient anodes in attracting the otherwise sluggish Sodium ions from the electrolyte. While the intrinsic porosity of the COF favors the lodging and diffusion of the Na^+ ions. Cells made with these COFs achieve a high specific capacity (energy density) and rate-performance (rapid charging-discharging), something that is not as easy for a Na^+ compared to the much smaller sized Li^+ . The bispyridine-tetrazine COF with the lowest LUMO energy shows a specific capacity of 340 mAh/g at a current density of 1 A/g and 128 mAh/g at a high current density of 15 A/g. Only a 24% drop appears upon increasing the current density from 100 mA/g to 1 A/g, which is the lowest among all the top-performing COF derived Na-ion battery anodes.

Chapter 4: Pyridine-Rich Covalent Organic Frameworks as High-Performance Solid-State Supercapacitors

Covalent organic frameworks (COFs), because of their ordered pores and crystalline structure, become designable polymers for charge storage applications. Supercapacitors are critical in developing hybrid energy devices. Amalgamating these high-surface-area frameworks in the capacitor assembly can aid develop robust solid-state supercapacitors. Here, we present supercapacitors drawn on three closely related pyridine-hydroxyl functionalized COFs. The keto-enol tautomerism and the hydrogen bonding ability of the hydroxyl units promise added chemical stability in this potentially



hydrolysable Schiff-bonded COF. Meanwhile, the pyridine and triazine groups ensure rapid charge storage by reversibly interacting with protons from the acidic electrolyte. The COF with the highest surface area, as expected, yields an excellent specific capacitance of 546 F/g at 500 mA/g in acidic solution and ~ 92 mF/cm² at 0.5 mA/cm² in the solid-state device, which is the highest among all the COF-derived solid-state capacitors, which is reflected by a high power density of 98 μ W/cm² at 0.5 mA/cm², most of which is retained even after 10000 cycles. This high activity comes from a smooth electrical-double-layer-capacitance favored by an ordered-porous structure and some pseudo-capacitance assisted by the participation of redox-active functional groups. The study highlights the by-design development of COFs for superior energy/charge storage devices.

Introduction

Synthetic porous organic polymers decorated with the desired functional-group and constructed from the supramolecular assembly of monomeric building units exhibit diverse and advantageous properties that have been utilised for most aspects of modern life.^{1,2} Providing a systematic elucidation of structure-property correlation of the porous polymers needs better control over the topology, morphology and directional growth of the monomers.³ A practical experimental-computational approach could help in gaining such control which could lead to futuristic technological advantage. Achieving a high degree of polymerization with controlled directionality and protecting the structural periodicity requires precise integration of building units along with the topological evolution in a predictable manner. However, controlled growth of the polymeric skeleton maintaining a proper geometry, porosity and without losing the molecular-level properties is something very challenging to achieve. At that stage, the invention of Covalent Organic Frameworks (COFs) with full-fledged pre-designability made a breakthrough.⁴ The strategy of molecular-level design of COF is entirely different from those of linear polymers, cross-linked polymers and hyper-branched polymers, providing an opportunity to manipulate primary and high-order arrangements to an unprecedented level. This emerging class of polymeric materials shows reticular growth of organic subunits to configure two- or three-dimensional porous crystalline structures interlocked by strong covalent bonds with anticipation over composition and properties.⁵⁻⁸ The proper templated synthesis of COFs often generates confined void space and exposed surface to interplay with photons-excitons, electrons-holes, ions, and molecules. This creates a new molecular platform for developing materials for applications that interconnect materials chemistry, physics and technology. COFs have been exploited for a plethora of applications pertaining to gas separation,⁹ catalysis,¹⁰ chemical sensing,¹¹ optoelectronics,¹² energy conversion¹³ and very recently energy storage.¹⁴

To establish crystallinity and periodicity in the COFs' architecture, primary and essential criteria are to gain thermodynamic equilibria during reversible covalent bond formation between multivalent monomers. That allows self-correction and formation of stable long-range order to ensure practical applicability.¹⁵ So far, several linking chemistry (boronate ester, boraxine, borosilicate, imide, amide, hydrazine, thiazole, dithazole, oxazole etc.) are reported that trigger dynamic covalent bond formation to achieve highly crystalline framework (Figure I.1 and Figure I.2).⁸ In comparison with earlier reported boronate ester linkages, reversible imine bond formation shows improved structural stability towards

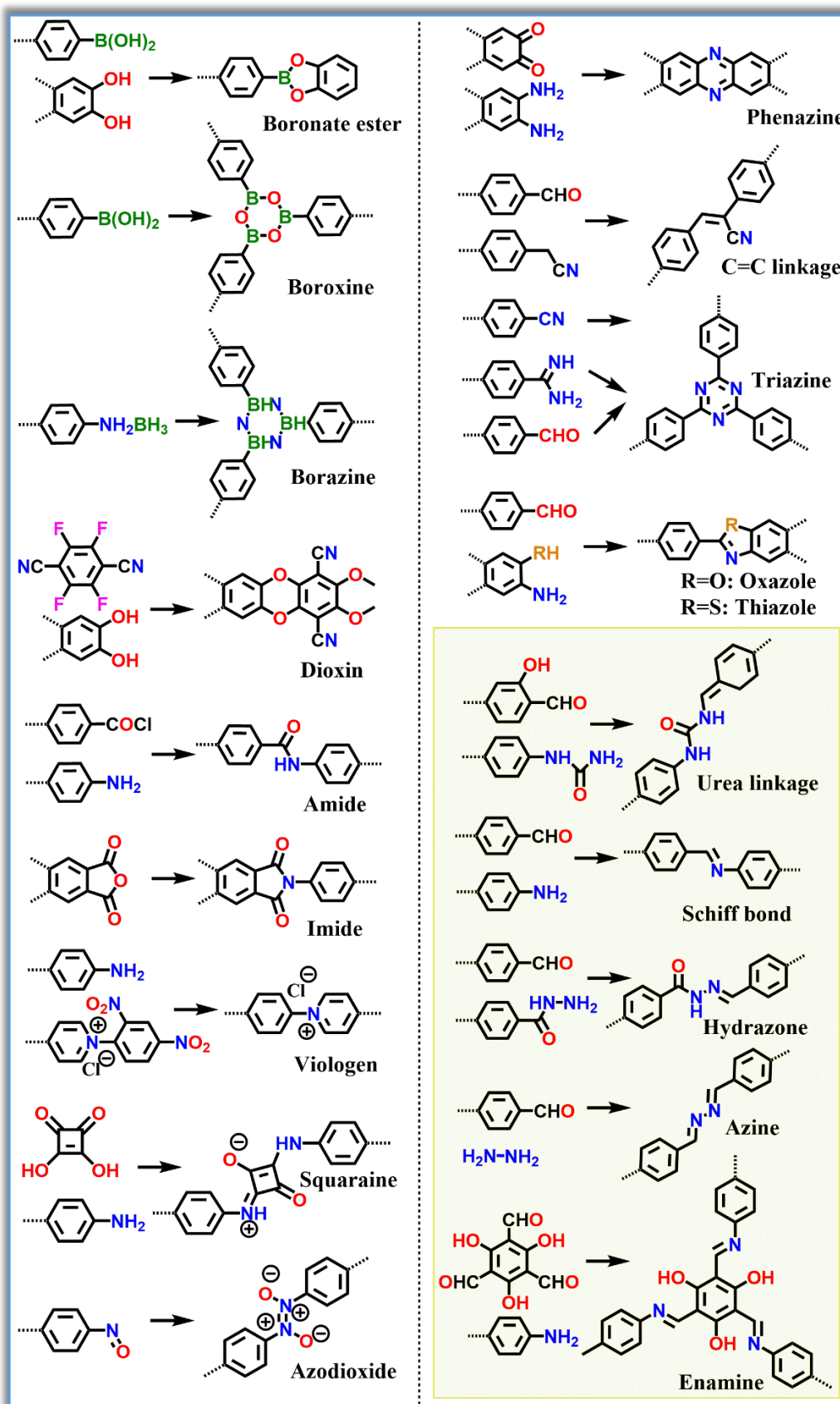


Figure I.1. Covalent linkages for COF formation. The shaded area shows *Schiff base* chemistry to develop frameworks.

solvents and chemicals.¹⁶ Additionally, the presence of interlayer hydrogen bonding stabilization in β -ketoenamine connected framework enables the fabrication of more chemically robust COFs.¹⁷ The sp^2 hybridized Schiff-bond formation guide the spatial orientation of the skeleton either in 2D or in 3D and confines the chain growth directions following a predesigned topology diagram (Figure I.3). The complementary geometry of aldehydes and amines and associated non-covalent interactions such as van der Waals and hydrogen bonding determine the topology of the COFs. Recently a single crystal structure of a 3D-COF connected via Schiff base linker has been reported by Yaghi and co-workers.¹⁸ (Figure I.2).

Generally, the combination of planar monomers controls the propagation of the polymer backbones in a polygon space on the 2D x-y planes leading to layered structure (Figure I.4). Also, the alignment of 2D covalent sheets along the z-direction is enabled by substantial π - π stacking interaction of the

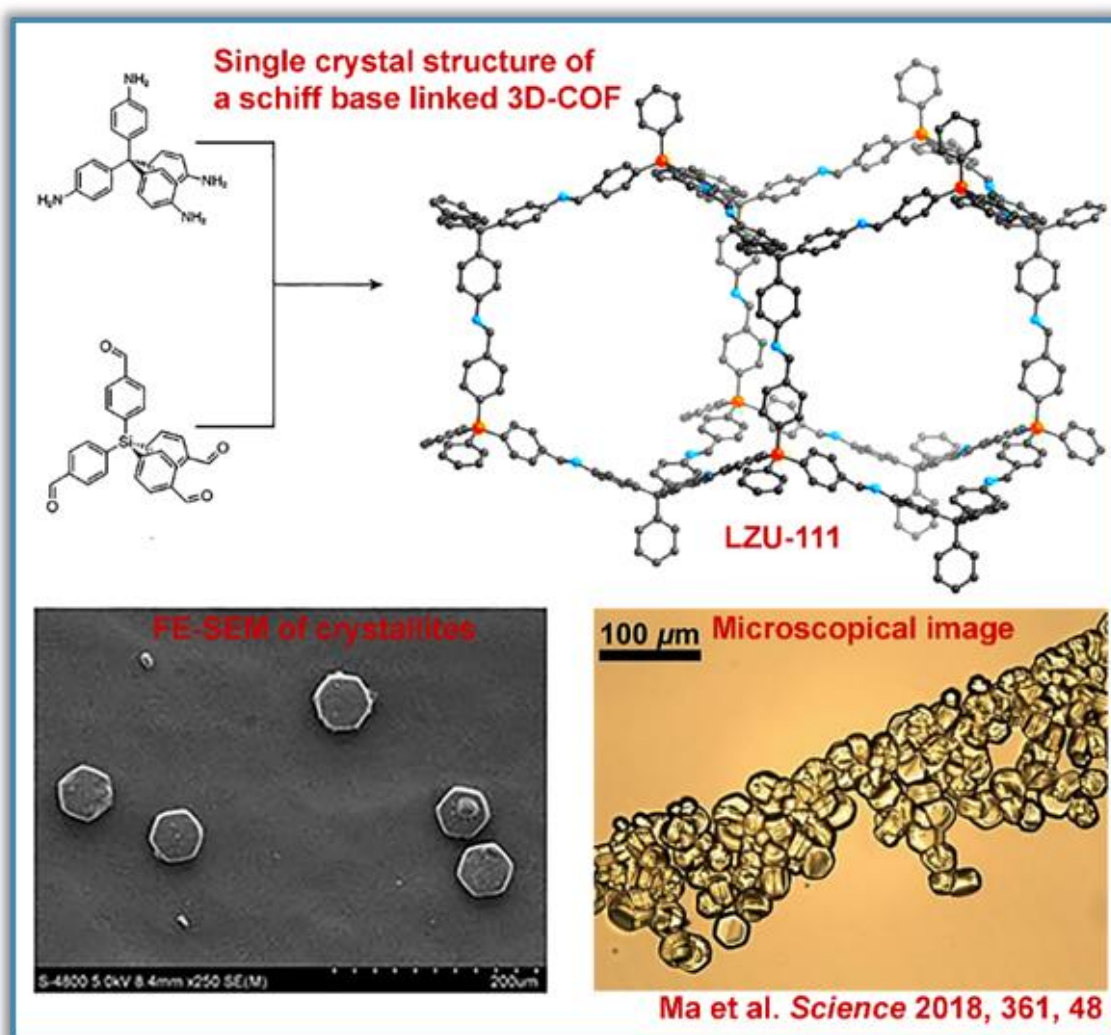


Figure I.2: Single crystal structure of a Schiff-bonded COF, microscopic view and SEM images of the single crystals.

constituent aromatic building blocks. Therefore, this 2D COFs not only create a fully ordered π -arrays but also 1D nano-porous channels (Figure I.4).⁵ They resemble a graphitic structure in addition to a honeycomb type porous morphology. The graphitic materials are widely used as electrodes in battery and capacitor, but their charge-storage capacity is limited owing to the lack of chemical designability. In contrast, the 2D-COFs with the graphitic network can be pre-designed with functionalized constituents (N, O, S and P), anchored with precise orientation. This offers an impeccable choice for next-generation electrode fabrication.

In recent times research on electrochemical energy storage utilising COF and COF-derived materials have emerged rapidly and broadened the horizons.^{19,20} This new class of materials are expected to address the challenge associated with a controllable degree of surface area and more stable frameworks (e.g., various organic solvents, and strong acid or base) for utilizing as organic electrode material. The achievement of higher performance would be possible by chemically tuning the electronic activity of the framework by increasing the number of electron-donating heteroatoms (N and O) per unit cell

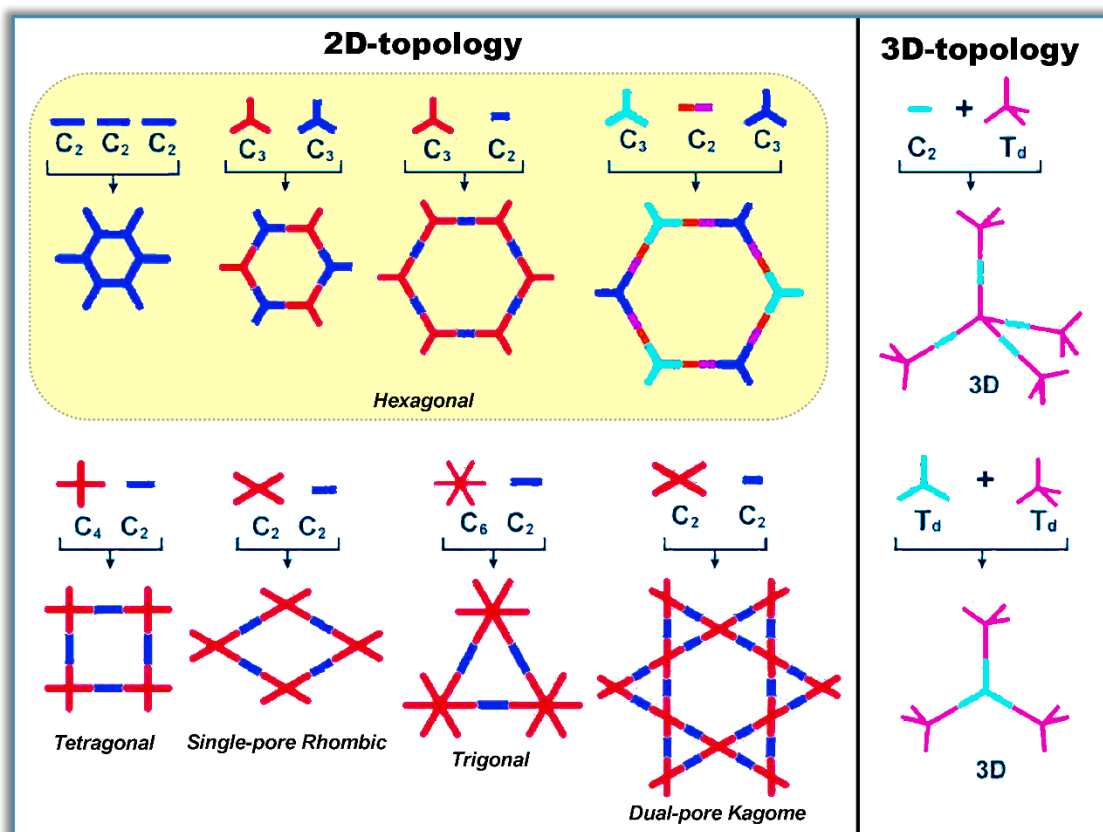


Figure I.3. A diagram showing the different 2D and 3D topologies of the COFs constructed from the particular choice of symmetry of the linkers.

of the periodic framework. Besides, COFs with their large micro and mesopores and conjugated skeletons could be well-suited for offering a facile charge carrier transport pathways for electron, hole, and ion. The diffused π electron cloud arrays among the stacked layers and confined nanochannels with a tuneable chemical environment of COF are noticeable active sites.²⁰

Even though 2D COFs are impending electro-functional materials, the stacked structure can bury the functional moieties in between their layers posing a serious obstacle for interacting with the guest charge carriers. This is in addition to the resistance to charge transportation developed due to the inherent defects of the framework and grain-boundaries between bigger particles.²¹ Thus the bulk COFs exhibit a higher mass transport resistance and reduced electronic conductivity, limiting their applicability as high performing electrode materials.¹⁴ Here we put forward the sheet-like COFs with a single- or few-atom layer thickness possess shortened transport length for the ions to reach the redox-active sites, and afford sufficient electron conduction pathways to access the more exposed heteroatoms, hence, as anodes, can elevate the rate performance of the Li-ion battery (LIB).²²⁻²⁶

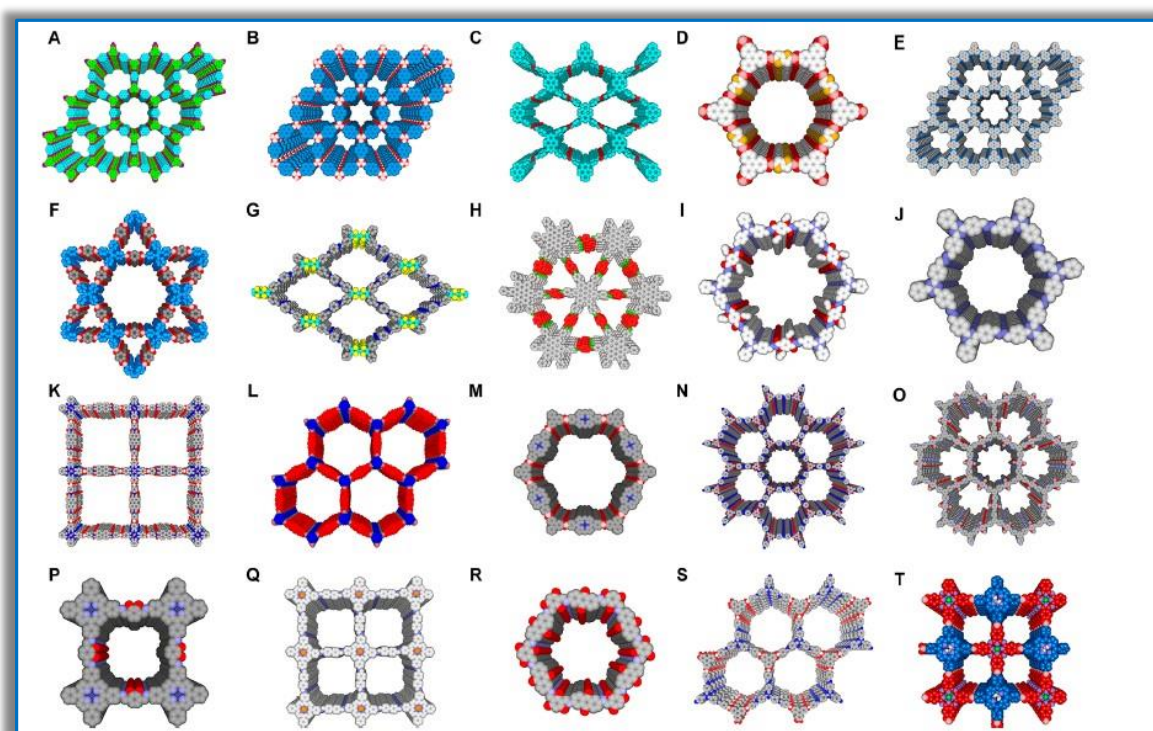


Figure I.4. Designable structure of 2D planer COFs of different pore dimension and tunability of the topologies. Copyright from reference number '7'.

For larger ions such as Na^+ , K^+ and Cs^+ , though the exfoliation or use of larger mesopores might certainly influence the storage, improving their diffusion kinetics require electronic modulation at the electrode surfaces. For this we have resorted to band structure engineering of the COFs to impart an additional driving force to overcome the thermodynamic barrier for the bigger sized Na^+ .²⁷⁻³¹ Such

electronically active COF surface can interact with the incoming ions through the electrostatic phenomena as well as through redox-assisted pseudo-activity to acquire high specific capacitances in supercapacitors.³²

Herein we employed the 2D-redox active COF for high performing electrode fabrication in metal ion battery and supercapacitor by the conceptual molecular-level design of the structure. Our approach validates the structural features and diversities, finds solutions for the bottleneck and challenging issues; and prophesies the future directions through experimental-computational elucidation.

Strategies for COF design:

1.1. Choice of Schiff base chemistry; Cost-effective framework and multiple advantages:

To date, the condensation reactions are mostly used to form COFs with various heteroatoms and with multiple functional groups. Following the combination of topology, symmetry and the linkage, COFs can be built with non-conjugated, partially conjugated and fully conjugated skeletons. The non-conjugated COFs can be constructed with boronate ester, boroxine, borazine, imide, amide, hydrazone, amine, and dioxin linkages. Whereas the partially π -conjugated skeletons are fashioned with triazine, imine, squaraine, azine, thiazole, oxazole, azodioxide, tetrazine and viologen linkages. But the fully π -conjugated skeletons can only be generated by phenazine and C=C linkages (Figure I.1).⁸ Among all these, the profuse use of Schiff-base condensation reaction or dynamic imine-bond connectivity for the construction of COFs has taken the attention of materials researchers owing to certain features. (i) Preparation is possible with variable reaction conditions including an easy scale-up even at room temperature; (ii) Availability of a vast library of the molecular precursors and diversity in the choice of functional groups (iii) Easy dispersity in the solution for depositing on the substrate and facile processibility to fabricate self-standing films (iv) Already established potential in physicochemical and electrochemical applications. (v) Substantial stability even under harsh environment and an applied potential (vi) Reversible polarizability and flexibility of the Schiff-bonds provide anchimeric assistance to the other framework moieties and the guest moiety without any structural degradation of the COFs. (vii) The free lone pair on Schiff-bond nitrogen also serves as a basic site to interact with Lewis acidic entities.¹⁶ this facilitates the adherence of Schiff-based COFs to many metallic substrates, a feature that is highly recommended for device fabrication.^{23,33,34} Though there is a compromise with the crystallinity of the 2D-COFs by choosing Schiff bond chemistry as building node, the versatile advantage of the Schiff-links provides a dynamic organization to implement the wonderful properties of this material for futuristic applications. Since electrochemical

applications require facile electrode fabrication with easily scalable materials Schiff-bonded COFs become an ideal choice.

1.2. Stability under applied potential; Keto-enol tautomerism in the β -ketoenamine:

Although most of those Schiff based COFs are thermally robust, they are susceptible to hydrolysis under prolonged exposure to an acidic or basic environment, and sometimes even by moisture present in ambient air.¹⁶ Therefore the formation of thermodynamically stable crystalline architectures does not always signify the inertness of the COFs. That requires an alternative strengthening of the framework via the introduction of resistive functionality. To achieve this a different protocol for the synthesis have been introduced by a combination of reversible Schiff base formation and irreversible keto tautomerization of the β -ketoenamine unit present in the backbone of the structure.^{17,35-37} This irreversible transformation of enolic bonds to corresponding keto form undoubtedly enhances the chemical stability of the COFs owing to conversion of Schiff base double bond (-C=N-) to single bond (=C-NH-) along with an extremely stable six-member interlayer hydrogen-bond formation (Figure I.5). This H-bond provides electronic shielding effect to protect the COF structure from collapse. Interestingly, this irreversible nature of the tautomerism does not alter the crystallinity of the COF, since the transformation comprises only shifting of electron cloud from enol group to the beta-positioned adjacent Schiff-base bond while keeping the atomic locations almost inviolate. So the COFs built up from the β -ketoenamine linkage is more suitable to use for electrochemical applications. Even under potential sweep through a wide range and in the presence of redox-active electrolytes these COFs exhibits excellent robustness over other COFs.

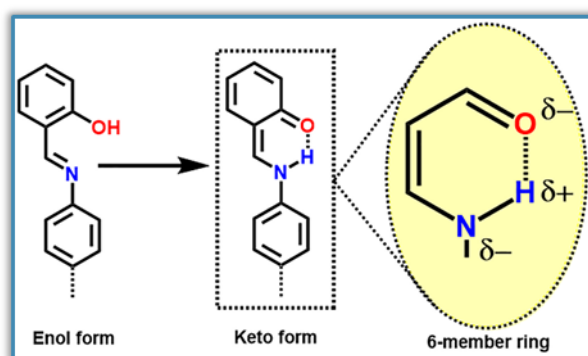


Figure I.5. Six membered ring formation due to H-bonding ability of keto form of the β -ketoenamine.

1.3. C_2 - C_3 / C_3 - C_3 symmetry combination; Microporous to mesoporous structure:

By coherent selection of the symmetry of the organic linkers, the pore dimension and pore geometry can be customized for desired electrochemical applications. Exploiting the numerous available symmetry options to tune the topology of the COFs, a systematic variation of pore diameters can be

engaged to improve the electrochemical activity. Considering that COFs comprise both linkages (bonding nodes) and struts (organic spacers) the innovations in COF design can be broadly categorised by choosing the desired symmetry and geometry of the monomeric units. The connection of monomers via poly-condensation can bring both the symmetric and asymmetric topology of the COFs. The combination of the C_3 - and C_2 -symmetric monomers yields a hexagonal topology (Figure I.3).^{7,8} Owing to the extensive diversity of C_3 and C_2 symmetric monomers, this hexagonal geometry is observed in an enormous number of 2D-COFs.^{19,20} Even with this simple hexagonal topology, the Schiff-based COFs enable engineering of pore-size from ultra-micropore to mesopore based on the length of the C_2/C_3 linkers and mode of the stacking interactions (AA, eclipsed and AB, staggered). Generally the ultra-microporous (4Å to 6Å) COFs arises from AB stacking of the C_3 - C_3 symmetry combinations whereas C_2 - C_3 combination provides a wide range of the pore-dimension, from micro (8Å-20Å) to mesoporous (20Å to 60Å) region (Figure I.6).³⁸ The proper matching of the solvated diameter of electrolytes with the dimension of the pores of the COFs is an important factor to decide the facile percolations of charge carriers.

1.4. Importance of 2D layered structure over 3D network: Pivotal role of 1D-nanochannel:

The periodic network present at the backbone of a COF can also propagate in both two dimensional (2D) as well as in three dimensional (3D) fashion determined by the directional nucleation of the covalent linking (Figure I.6 and Figure I.7). Networks extending in two dimensions are ultimately restricted to a linear or planar conformation of monomers with specific symmetry and generally have π - π stacking, H-bonding, van der Waals' forces to hold the consecutive layers strongly.¹⁹ The symmetry of the polygon lattices can provide both symmetric and asymmetric topologies; the symmetric topology constitutes regular polygon pores while the asymmetric one yields deformed polygon pores. Whereas a 3D network propagates in all three directions, ensuing a more isotropic morphology. In most cases, the most common tetrahedral geometry is implemented by the skeleton.^{7,8}

The beautiful Graphite resembling layered morphology of 2D-COF enable the predesign of 1D nano-channels (Figure I.7), while the pore of a 3D COF is much less predictable.³⁹ So proper investigation of the mechanism of foreign species circulation through the pores is much more convenient in 1D nano-space.⁴⁰ The 1D-nanospace of the 2D COF is entirely distinct from other porous materials such as zeolites, porous silica, porous carbons, amorphous porous organic polymers, and metal-organic frameworks (MOFs) in many aspects. (i) These microporous to mesoporous 1D-channels are exposed only on the (100) facet; So that external entities such as electrolytes can enter into these nano-spaces from either the top or the bottom of the 2D layers. (ii) This highly oriented 1D nano-channels affords a suitable pathway for selective molecular transport. (ii) Due to the tiny interlayer distance that is

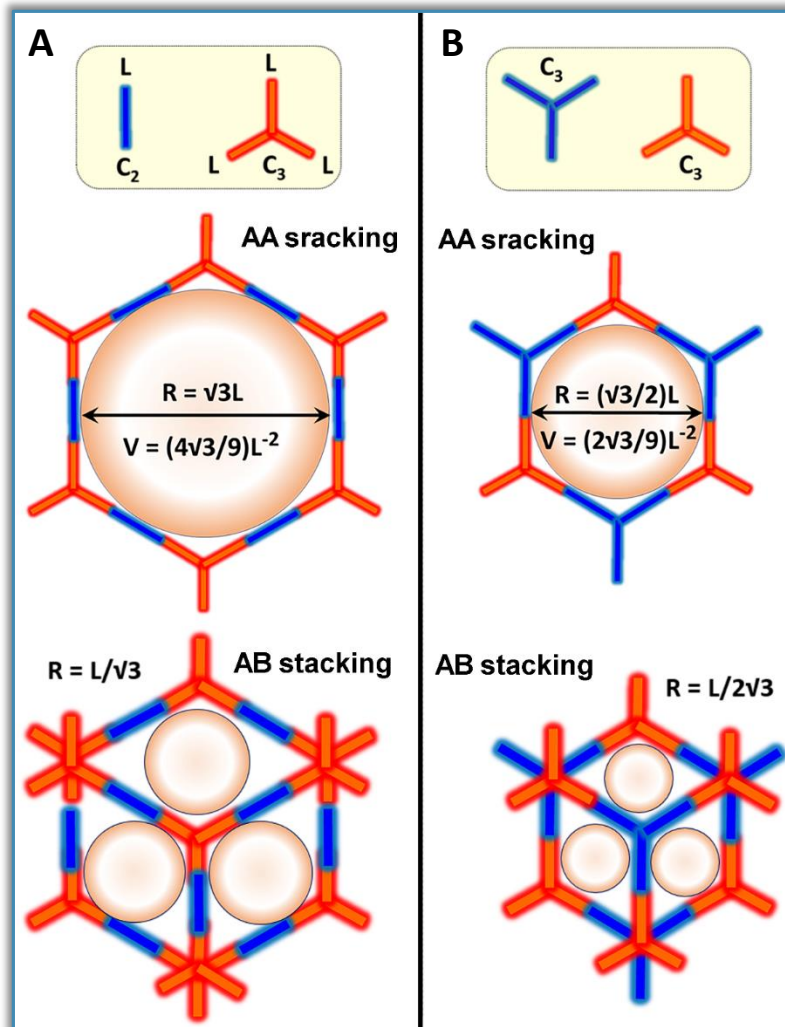


Figure 1.6. A schematic showing the tailor-made pore dimension of 2D-COFs built from **(A)** C_2 - C_3 symmetry monomers **(B)** C_3 - C_3 symmetry monomers. Variation of pore size and pore volume with AA and AB type stacking.

unapproachable to larger foreign molecules, each channel serves as isolated nano-pores. That restricts the propagation of any solvated ions in only unidirectional-manner. (ii) Interestingly, the walls of the 1D channels can be decorated with various heteroatoms and redox-active functional groups to build a tailor-made interface.³⁸ This interface provides the unique environment to trigger various interactions with the incoming guest-ions, which impacts the electrochemical activity of the 2D-COFs.

1.5. Surface area vs. surface accessibility; competition between stacking and exfoliation:

The extent of the surface area of 2D-COFs also depends on the degree of polymerization in 'xy' plane as well as elongation of the stacking interaction between layers in 'z' direction.⁴¹ With the increase of the pore diameter, there is an obvious scarcity of the periodicity in the poly-crystalline framework owing to the lack of stacking stability. Therefore the experimentally observed surface area of 2D isotropic COFs built from C_2/C_3 symmetric linkers reduces from microporous to mesoporous nature of the framework.⁴²

Analogous to Graphite, bulk 2D COFs can be converted into proper 2D-film only when reduced to the thickness of a single or a few unit cells.²² Presence of fused π -aromatic ring makes Graphite to Graphene exfoliation tricky owing to ultra-strong inter-layer stacking while the relatively weak π - π stacking of 2D-COFs along the z-axis allows the delamination into few-layer thin sheets with a definite compromise of the surface area (Figure I.7). Because the contribution of the surface area reflects mainly

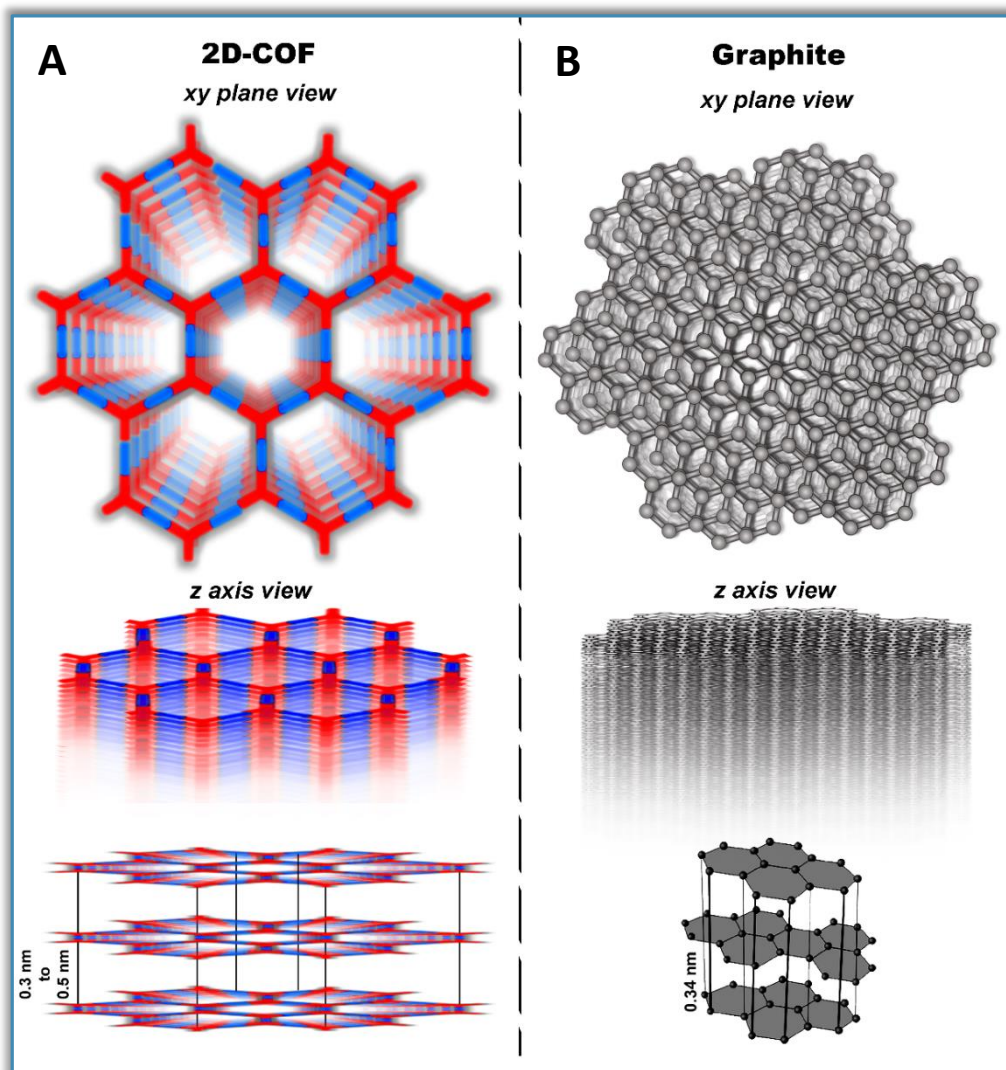


Figure I.7. The structural resemblance of 2D-COF with layered Graphite. **(A)** XY plane and Z-axis view of 2D-COF built from $C_2 - C_3$ symmetry monomers. **(B)** XY plane and Z-axis view of ABAB stacked Graphite.

in the oriental 1-D nano-pores which is being destroyed during this exfoliation. Moreover, the surface accessibility of the thin layer COFs called Covalent Organic Nanosheets (CONS) is remarkably higher than the pristine COFs. The functional groups, redox-active entities and the hetero-atoms used for the construction of the structure are mostly buried in between the layers of the highly stacked COFs structure. So the surface of each layer decorated with desired functionality hardly gets proper

exposure for the interaction with foreign molecules or ions. But the separated layers of the 2D-CONs offers greater surface approachability assisting the facile interaction of guest ions or molecules with the framework atoms. The path length for the diffusion of these external species through the nano-structure of the CONs is considerably shorter which improves the kinetics of electrochemical redox activity.²³ There are several advantages of CONs including (i) Enhanced surface activity (ii) More

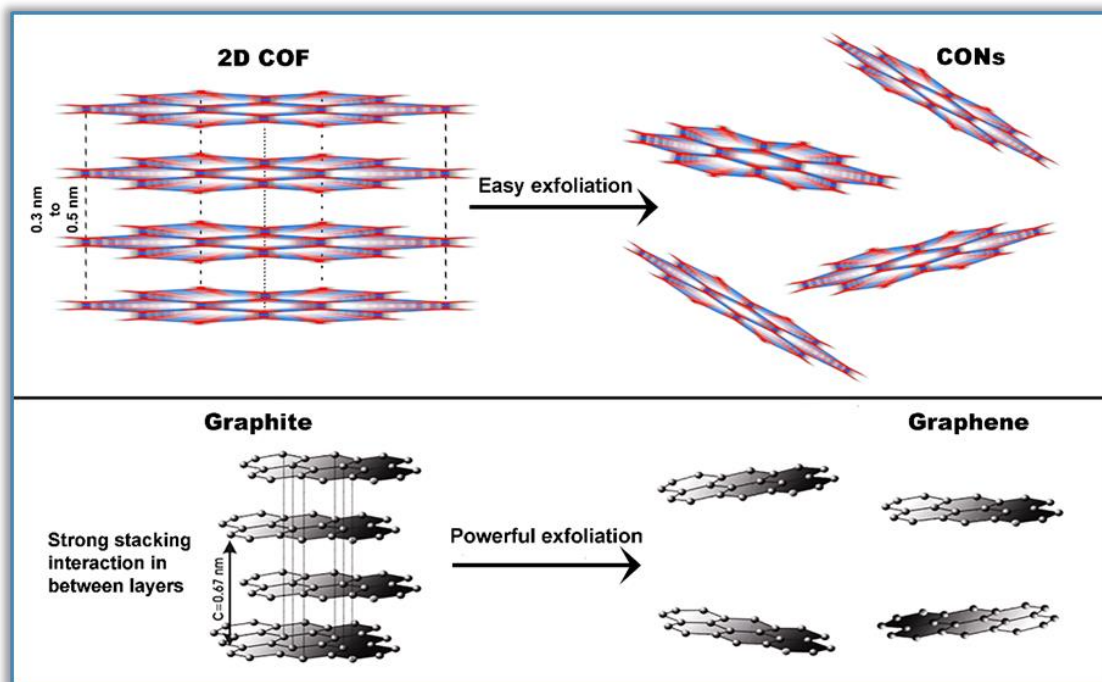


Figure I.8. Comparison of the exfoliation of COF with Graphite.

the flexibility of the thin layer organic-sheets (iii) Significant increment of in-plane electronic conjugation resulting from the reduction of the out of plane electron cloud distribution is attracting the attention of materials researchers. Inspired by advances in 2D materials, the exfoliation of 2D COF into ultrathin nano-sheets explores a new dimension of the research. Akin to Graphene⁴³ and MXenes,⁴⁴ the name 'COFene'⁴⁵⁻⁴⁸ has been already affiliated for single-layer 2D COF, which are believed to have assets distinct to layered 2D-COFs and conventional 2D-materials such as Graphene and transition metal dichalcogenides (TMDs).⁴⁹

I.6. Exfoliation of 2D-COF to CONs:

*"Unless we do open up the pages of a book, the valuable information remains undiscovered; the nanosheets of the COFs are the hidden treasure of numerous functional groups and atoms, which gets exposure only upon delamination of highly stacked 2D-COFs".*⁵⁰ In 2011 Zamora and co-workers firstly proposed exfoliation of 2D-COF8 similar to Graphene layer isolation using the mechanical forces of solvent assisted sonication to disrupt the noncovalent interactions between layers.⁵¹ The chemical

identity of the nano-layers was confirmed from IR, NMR and XPS spectra, that shows the structural integrity of Covalent Organic Nano-sheets (CONS) in comparison with the bulk COF. Though thickness distribution of the CONS obtained from the AFM had proved the presence of only few-layer thick COFs, isolation of true mono-layer with atomic level breadth yet to be achieved. Since then different essential concepts and strategies have been illustrated for the preparation of CONS following the two general approaches, top-down and bottom-up.^{22,52} Sonication induced and chemical delamination are the well-known top-down procedures to exfoliate COFs into thin layer nano-sheets (Figure I.9.1).^{52,53,54} Inclusion of the cavitation induced solvent bubbles in between the layers during mechanical sonication enhances the shearing force which suppresses the compressive and tensile forces of the π -stacked layers of the 2D COFs (Figure I.9.2). Thus the distance between each layers increases and stacking interaction fails to hold the layer together. As a result, the exfoliation of COFs happens, but with the compromise of a lot of defective hole formation on the layers owing to the solvent bubble explosion (Wedge effect).⁵⁵ However, chemical delamination is much convenient to form true nano-sheets by simply anchoring some chemical entity on the surface of the layer that grows along vertical direction.⁵⁶⁻⁵⁸ Sometimes appropriate designing of the monomeric unit assists the self-exfoliation of the COFs during synthesis itself. Decreasing the extent of π - π stacking or creating angle strain on the building linker at the time of polycondensation shows a novel pathway for self-exfoliation.⁵⁹⁻⁶¹ On the other hand, a true bottom-up approach configures the layer by layer growth of the 2D-COF on a particular substrate.^{24, 33, 62} Among all these methodologies chemically exfoliated CONS and self-exfoliated CONS are thermodynamically more stable owing to their inertness towards restacking of the layers. CONS produced in these manners persist for years without degradation and any change of chemical composition showing the aptness for electrochemical application, specifically for electrode fabrication.

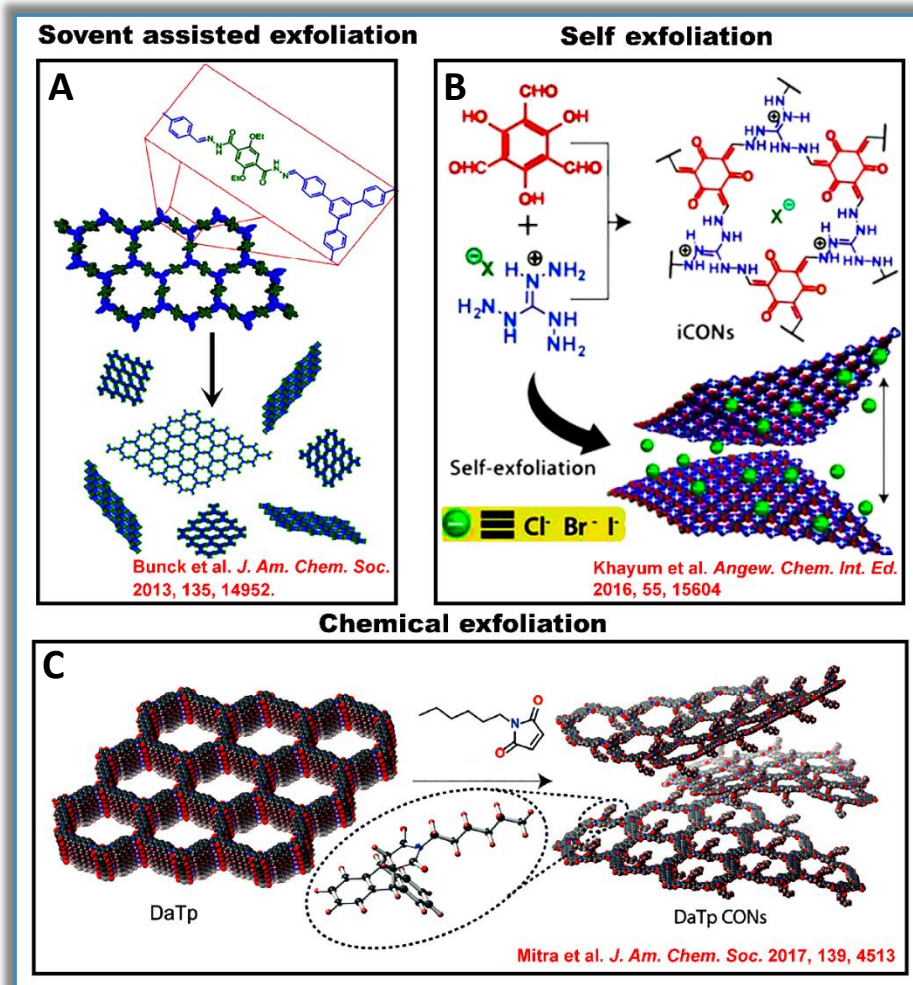


Figure I.9.1: Different exfoliation procedures of 2D-COFs. (A) Sonication-assisted exfoliation. (B) Self-exfoliation during solvothermal synthesis. (C) Chemical exfoliation. Copyright from reference number '53, 56, 59'.

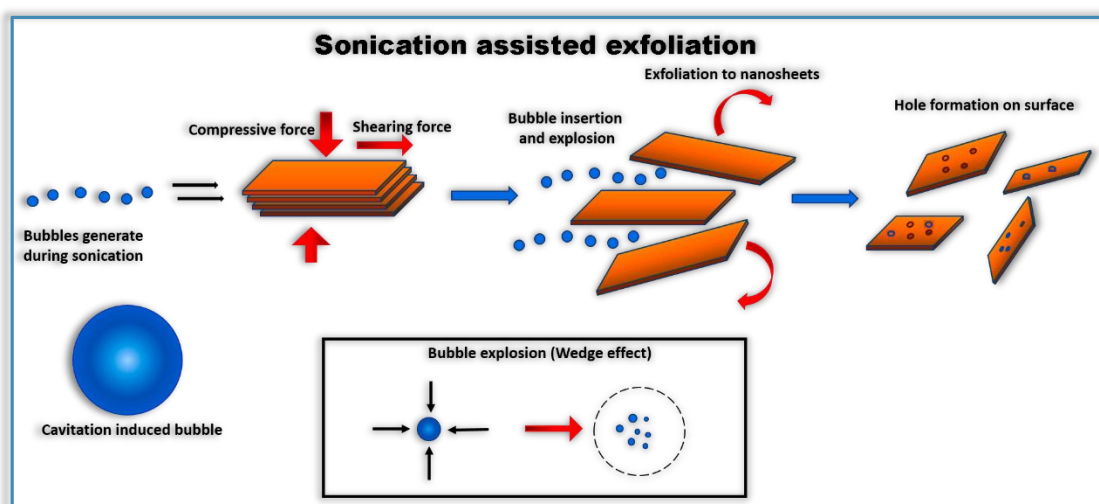


Figure I.9.2: Holes formation on the surface of the nanosheets during solvent assisted exfoliation.

Fabrication of High performing electrodes for Battery and Supercapacitors:

We have explored the aforementioned possibilities of redox-active 2D-COFs to enable futuristic energy storage applications.

I.7. Basic working principle of the energy storage system; battery and capacitor:

Electrical energy storage with rechargeable capability forms an integral part in human daily life, due to its wide application in telecommunication devices (cell phones, tabs), standby power systems (laptops, cameras, and iPads) and in electric hybrid vehicles. When it comes to circuit level of any electronic devices, energy is typically stored in one of two devices, battery or capacitor.⁶³ In either case, the stored energy generates an electric-potential that drives a unidirectional flow of electrons during charging or discharging, which generates an electric current. Thus produced current can be utilised to power electrical devices connected within a circuit. Classification of capacitors and batteries is based on an evaluation of the performance by two fundamental parameters (i) Energy density and (ii) Power density (Figure I.10). The energy density defines the extent of energy that can be stored in a certain volume or weight, while the power density describes the rapidity at which energy is stored or discharged from the device.⁶⁴ Batteries stores a large amount of electrical energy electrochemically, offering the highest energy density. When required, it converts chemical-energy into electrical-energy to deliver a static electrical charge for powering a device. In comparison, conventional capacitors possess high power density and deliver a burst of energy within a short period. It stores the electrostatic energy on the surface, under an applied electric field. Therefore, both of these electronic components are essential and concomitant with each other in powering a device (rapid supply of energy from capacitors) and to run the device for a long time (slow and sustained supply of energy from the battery). Though components (electrodes and electrolytes) to configure battery and capacitor have notable similarity, the working principle of each is significantly different.

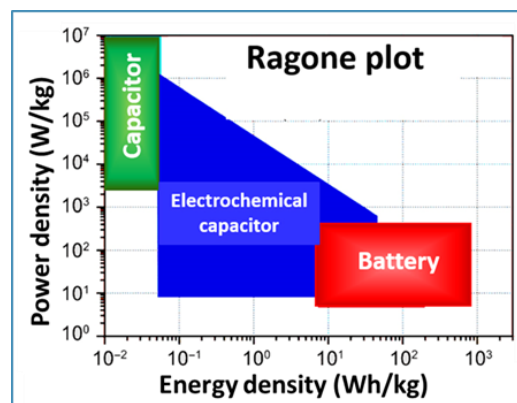


Figure I.10: The Ragone plot showing the position of battery and capacitor in terms of energy density and power density.

Difference between capacitor and battery:

Capacitor	Battery
The potential energy is stored under the electric field	The potential energy is stored in the form of chemical energy, later converts in electrical energy
Higher power density but lower energy density than a battery	It has a better energy density with a wide potential window
Charging and discharging rates are faster than a battery because it stores energy directly on to electrode surface.	Charging and discharging rates comparatively slower because of the conversion of chemical energy to electrical energy occurs via diffusion of charge carriers from and into the bulk of the electrode
Discharges instantaneously	Discharges over an extended period
Voltage decreases rapidly while discharging	Provides a constant voltage

Metal-ion Battery (LIB and SIB): Rechargeable, the battery can be made from a wide selection of chemistries (metal-ion battery,⁶⁵ metal-air battery,⁶⁶ metal-sulphur battery⁶⁷). But considering the advantages of high operating voltage, slow self-discharge, and nice reversibility, Lithium-ion batteries⁶⁸ and Sodium-ion batteries⁶⁹ have been targeted for the realization of high performing battery designs.

Alike the capacitor, a metal ion battery comprises of two electrodes anode and cathode where the charge gets stored; separated by an insulating but ion-permeable separator layer, all soaked in a metal-ion conductive electrolyte, which works as a charge carrier. Typically the source of metal ions i.e. layered metal oxides (LiCoO_2 for LIB, $\text{Na}_3\text{V}_2(\text{PO}_4)_3$ or NaTiO_2 for SIB) are well-known material for good cathode and layered graphitic carbon (specifically for LIB) or hard carbon skeleton (specifically for SIB) work nicely as an anode (Figure I.11). Under the potential bias, the weakly dissociable metal-salt electrolytes (LiPF_6 , LiClO_4 , NaPF_6 , NaClO_4) serves as a charge carrier and metal ions (Li^+ and Na^+) migrate from the cathode to the anode and intercalates into the inter-lamellar spaces of the layered structure of graphitic anode by accepting electron density. A device connected to the battery can be made to run with the current generated when the metal-ions moves back into the cathode materials from the anode creating a flow of the electron in the external circuit but in the opposition direction.

Half-cell and full-cell: The terminology of charging and discharging in metal ion battery alters depending on the conventions of cell-configuration.⁷⁰ Typically the configuration of a *half-cell* battery detects the applicability of any novel electrode material for storing the charge under potential in presence of corresponding metal plate reference. Since the metal plate acts as an uncountable source of the charge carriers (metal ions), the half-cell configuration assists to understand the maximum charge storage capacity of any novel electrode material and confirms whether it is compatible as an anode (metalation happens in lower potential) or cathode (metalation happens at higher potential).

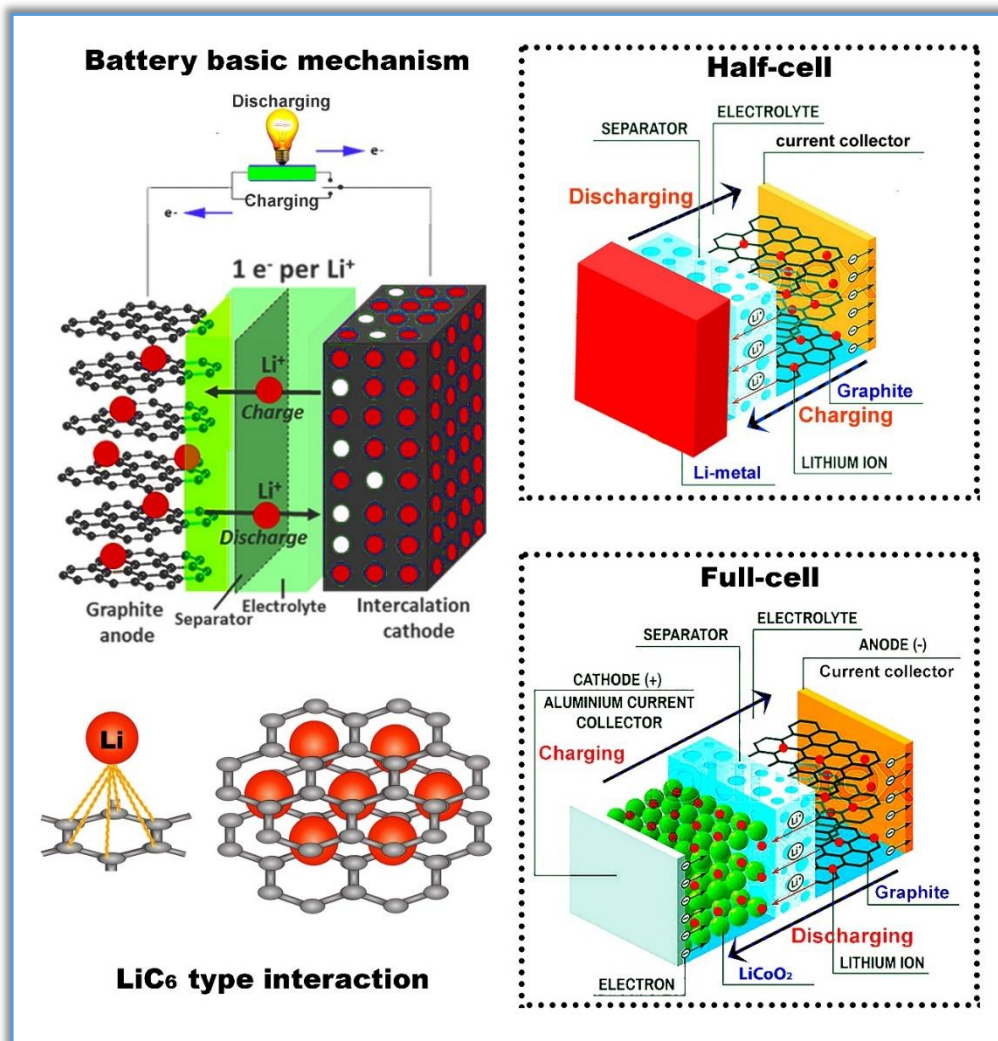


Figure I.11. The basic working mechanism of metal-ion battery during charging-discharging. Note the difference in the direction of charge flow in half-cell and full-cell metal-ion battery.

The Open Circuit Potential (OCP) of half-cell battery generated from metal/metal-ion interface needs to be reduced to perform the metalation of the electrode material. The decrease of OCP called as discharging of half-cell is a thermodynamically favourable process as oxidation of metals is a spontaneous process. While the OCP of a complete *full-cell* requires to be raised to execute the metalation process of the anode. This is something against the thermodynamic spontaneity, recognised as charging. So metalation of an anode in half-cell requires discharging whereas full-cell requires charging. There are several challenges to configure high performing and durable full-cell metal-ion batteries, particularly associated with the anodic electrodes that participate in the electrochemical redox reactions.⁷¹

Supercapacitor: The super-capacitor also known as ultra-capacitors is a specialised form of capacitor which stores the electrical charge much higher than other ordinary-capacitors within very lower

voltage limits, but undergoes frequent charge-discharge cycles even at high current.⁷² It bridges the gap between electrolytic capacitors and rechargeable batteries by slight push up of energy density. The supercapacitors have attracted significant research attention over the past decade attributed to higher power density, low maintenance cost, wide thermal operating range and more extended cycle life compared to electrolytic-capacitor.

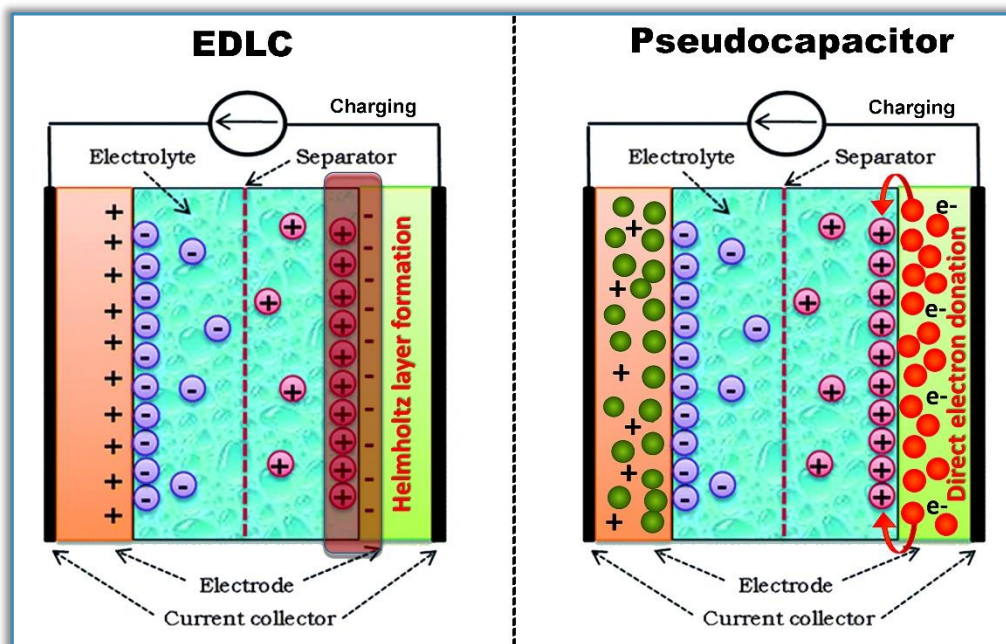


Figure I.12: Working mechanism of an EDLC and pseudocapacitor. The negatively charged electrode directly donates an electron to the electropositive electrolytes in a pseudocapacitor.

This energy storage system comprises a dielectric medium as an electrolyte and two electrodes of high surface area separated by an insulating material that transmits ions (Figure I.12). It stores electrical charge in the electric double layer formed at electrode-electrolyte interface via charge separation of easily dissociable electrolytes. Generally, this interface is a high surface-area carbonaceous material. The large surface area of the electrode, coupled with proximal double layer, provides the device one of the highest capacitance outputs. While charging, the accumulated charge at the inter-surface of the electrodes compensates for the potential biased produced at the electrode surface. A massive electrolyte accessible surface area for charge accumulation improves the capacitance value.⁷³ Based on the charge storage mechanism, supercapacitors can also be categorised, as electric **double-layer capacitors (EDLC)**⁷⁴ and **pseudo-capacitors**.⁷⁵ A perfect EDLC behaviour shows only static charge storage at the electrode-electrolyte interface using a high surface area electrode. However, pseudo-capacitance comes from the redox behaviour of the electrolytes at the surface of the electrode. Here near-surface faradaic reactions with by prominent electron donation from the electrode surface mainly contribute to the high capacitance.

1.8. Required features in electrode materials for metal-ion battery and supercapacitor:

The similarity lies in materials used as an anode for metal-ion battery and electrodes containing high surface area for supercapacitor fabrication, where carbonaceous graphitic materials have been extensively used in energy storage technology. An anode of a metal-ion battery, the inter-lamellar spaces in between layers of Graphite fits well for intercalation of the solvated metal ions; hence bulk diffusion of metal ions into the carbon skeleton becomes facile. While highly polarizable π -electron cloud of unsaturated graphitic materials offers a large electrochemical surface area for perfect electrostatic double-layer formation in supercapacitor. But restricted storage capacity of Graphite materials limits its applicability to developing high-performing energy storage system on demand. Simultaneous modification of the Graphite materials by hetero-atom (N, O, S) doping though assists to store more amount of charge carriers, the reproducibility in scaling up, destruction of the high surface area and a lot of energy consumptions during pyrolysis process to synthesis bring drawbacks towards bulk scale applicability.

1.9. Redox-active polymers as electrodes for metal ion-battery and supercapacitors:

Alternatively, organic polymers constructed from designed monomeric units can be chosen as working electrode materials for energy storage to enhance the charge storage ability. Atomically modified polymers with easily accessible redox-active functional groups bring higher storage capacity with prolonging stability under electrochemical condition. The synthetic availability, subjective design, high theoretical capacity, fast redox kinetics, flexibility, lightweight, low cost, and eco-friendliness are making them very promising in the application of energy-related devices.⁷⁶ Moreover, these polymers are very resistive towards the electrolyte dissolution called the shuttle effect and enhances the cycling stability of the battery.⁷⁷

Electro-active chemical moieties such as carbonyl, pyridine, imide, imine, quinone, nitroxyl, viologen, phenoxy anchored to the polymers bring exceptional high performance as electrode materials. The classification of electroactive polymers is possible according to their chemical construction. (i) Redox-active group-embedded polymers, including conjugated polymers (i.e., conductive polymers) and (2) Redox-active pendant-bearing polymers. Redox-active group-decorated polymers consist of an electrochemically active backbone of redox-active monomers. Whereas, redox-active pendant-bearing polymers possess redox-active groups anchored on their non-conductive polymeric backbone. Along with the difference in chemical structure, they have variation in chemical and physical

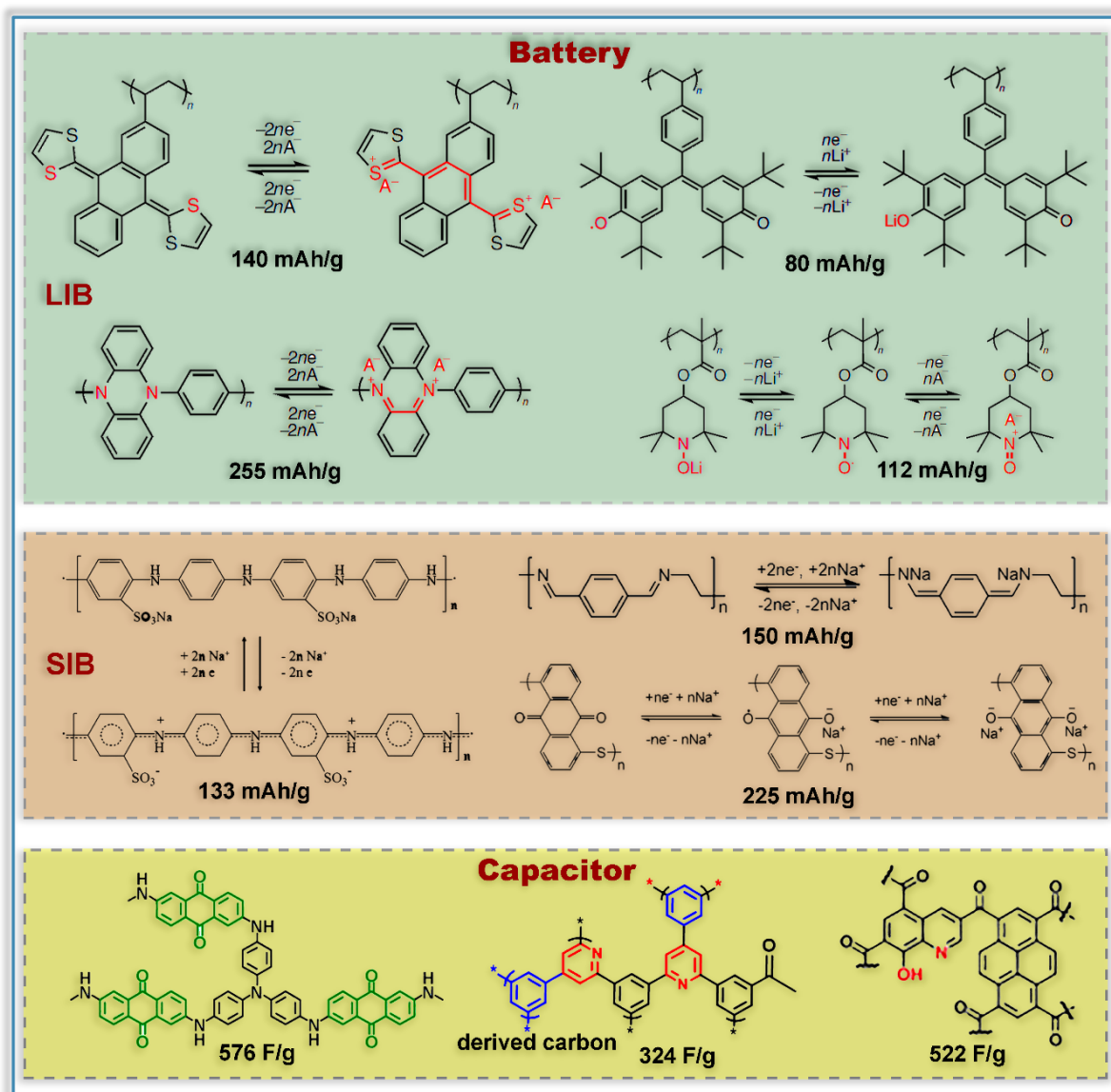


Figure I.13. The energy storage property of polymer-based electrode materials. *Copyright from reference 76-80.*

properties, redox reactions, and therefore in performances as an anode in metal ion battery (Figure I.13).^{77,78}

On the other hand, the high surface area is the primary criteria to have in the polymer-based electrode for supercapacitor application. Ultra-microporous or porous polymers are already proven as an excellent candidate to enhance the EDLC phenomena.⁷⁹ Although extremely poor conductivity and lack of orderliness of the pores restricts its activity in higher current density and therefore limits the power density. The development of novel porous organic polymers (POPs) with a high specific surface area which also provides reasonable conductivity and great stability is quite challenging.⁸⁰ Additionally, embedding the redox functional groups on the surface of the porous polymers enhances the pseudo activity. The microporous polymers enriched with functional groups like pyridine, pyrrole,

imide, keto shows electrochemical activity in the presence of strong acid electrolyte of supercapacitors (Figure I.13). Merging the electrostatic behaviour with electrochemical pseudo-activity brings extra advantage to enhance the performance of supercapacitors.

1.10. Drawbacks associated with polymer-based electrode materials:

Though electrodes fabricated with organic polymers delivers improved energy storage, many of the polymers have a 1D chain or branched cross-linked structure. The charge-carrier movement in such polymers is sluggish as the transport takes place via a hopping mechanism in between chains and across disordered fragments. Thus, the best solution would be to build planar-polymers which are conjugated in-plane. Such conjugated 2D structures will enhance the carrier mobility of the ions inside the structure. However, growth of the polymers in two independent directions without steric hindrance by reacting functionalized monomers and identification of an optimal template to trigger the formation of a continuous 2D network is not straightforward. So far, different approaches have been considered including the self-assembly of monolayers, Langmuir–Blodgett (LB) and layer-by-layer (LBL) elaboration of the polymer propagation and side-chain modification of 1D polymers through a supramolecular approach leads to the formation of the 2D-polymers.⁸¹ Nevertheless, the important issues associated with non-covalent nature that favours disorderliness, buckling and lack of uniformity causes low stability and low efficiency of energy storage devices. Thus, synthesis of proper 2D-polymers with controllable morphology but having sufficient robustness in nano-structure is essential for high-performance device fabrication.⁸²

Also unravelling the relationships between charge storage mechanism and chemical structures of disordered polymers is critical to shedding light on better understanding. The lack of periodicity of the electroactive moieties in the skeleton of the hyperbranched and 1D chain polymers restricts the theoretical investigation of the pathway for the charge carrier percolations inside it. Also, the determination of favourable interaction sites becomes difficult. Furthermore, the characterizations and the determination of the structural modulations brought about by the prolong charge-discharge cycling, etc. becomes near impossible for amorphous materials. This is exactly where the highly ordered structure of crystalline 2D-COFs carries the advantage.

1.11. Redox-active 2D-COF; A designer approach for high performing electrode:

The highly crystalline 2 dimensional (2D) Covalent Organic Frameworks (COFs) resemble a graphitic network, in which functionalized building blocks are precisely integrated to construct extended polymeric structures with periodic 1D- pores, could be no doubt a perfect choice for electrode

fabrication. In 2D-COFs, the well-defined alignment of atomic layers via π - π interactions of building units forms segregated arrays of 1D nano-porous channel (Figure I.7). In such arrays, the intra-layer covalent bonds form the 2D-sheets, whereas, interlayer non-covalent interactions bring the stability of the framework. Thus, from materials-design perspective, various COFs can be designed according to the sizes of the charge carrier (solvated ions) by controlling pore diameter and skeleton functionality. Something which is not possible in other existing electrode materials. Such atomic level-tunable features of 2D-COFs, with confined nano-spaces, offers the interaction sites for the electrolytes. Moreover, most of the easily synthesizable or commonly available and low-cost building units (like phenol, pyridine, imine, and enamine) consist of heteroatoms such as N and O. The COFs enriched with N and O are electron-rich which pushes up the HOMO energy level of the COFs. More electron density concentrated on the HOMO of the building units attracts the positive-charged metal ions in a better way. This can enhance the charge storage ability of 2D-COFs. While the more exposed redox-active functional groups in exfoliated COFs provides easily accessible interaction sites for incoming metal ions in metal ion battery (Figure I.8). *However, bringing the impact from a large surface area along with the contribution of redox-active groups present in each of the layers of the COFs is challenging which requires proper engineering of the band structure of the COFs to bring additional driving force for metal ion insertion even in highly stacked layers.* Such difficulties are not expected in supercapacitors. Because the inherent surface area of the highly stacked COFs with heteroatom rich 1D-nanochannels plays the key role to boost the capacitance of the supercapacitor by proper EDLC formation. Nevertheless, the crystalline and modular structure of COF enables a practical approach to comprehend the mechanism of ions insertion in COF derived electrode materials. The interaction sites and the type of contact of ions with the skeleton of the COFs (whether physical interaction or chemical bond formation) under potential can also be investigated by theoretical modelling. By this means, 2D-COFs exhibit unique advantage with outstanding potential as anodic material for battery and high surface area electrode for supercapacitor.

1.12. Recent literature of COF based electrodes for battery and supercapacitor:

The applicability of COF materials in the field of energy storage is a very recent finding references and since then became a rapidly emerging area. Few current pieces of literature which are parallel to our findings heralded the conjugated Covalent Organic framework as promising electrode materials for charge storage. *Some of them are briefly discussed below.*

Lei et al. integrated a few-layered 2D-COF trapped by carbon nanotubes as anode material for LIB. Upon prolonged activation, it delivers a specific capacity of 1021 mAh/g, which is governed by the 14-

electron redox chemistry (Figure I.14).⁸³ The theoretical investigation and electrochemical probing aided in revealing the step-by-step Lithium insertion. Chen et al. reported the chemical stripping of the layers of 2D-mesoporous COF by incorporation of MnO₂ nanoparticles. The few-layered COF nanosheets along with the redox behaviour of MnO₂ exhibited fast reversible kinetics for Lithium storage with a 968 mAh/g stabilized capacity.⁸⁴ Very recently, Shi et al. showed the reversible redox chemistry associated with the insertion of twelve Sodium ion into a pyrazine-COF, which was decorated with multiple carbonyls to achieve remarkably high sp. capacity of 452 mAh/g. Furthermore, practical life applicability of an assembled pouch-type battery displayed the gravimetric energy density of 101.1 Wh/kg cell.⁸⁵

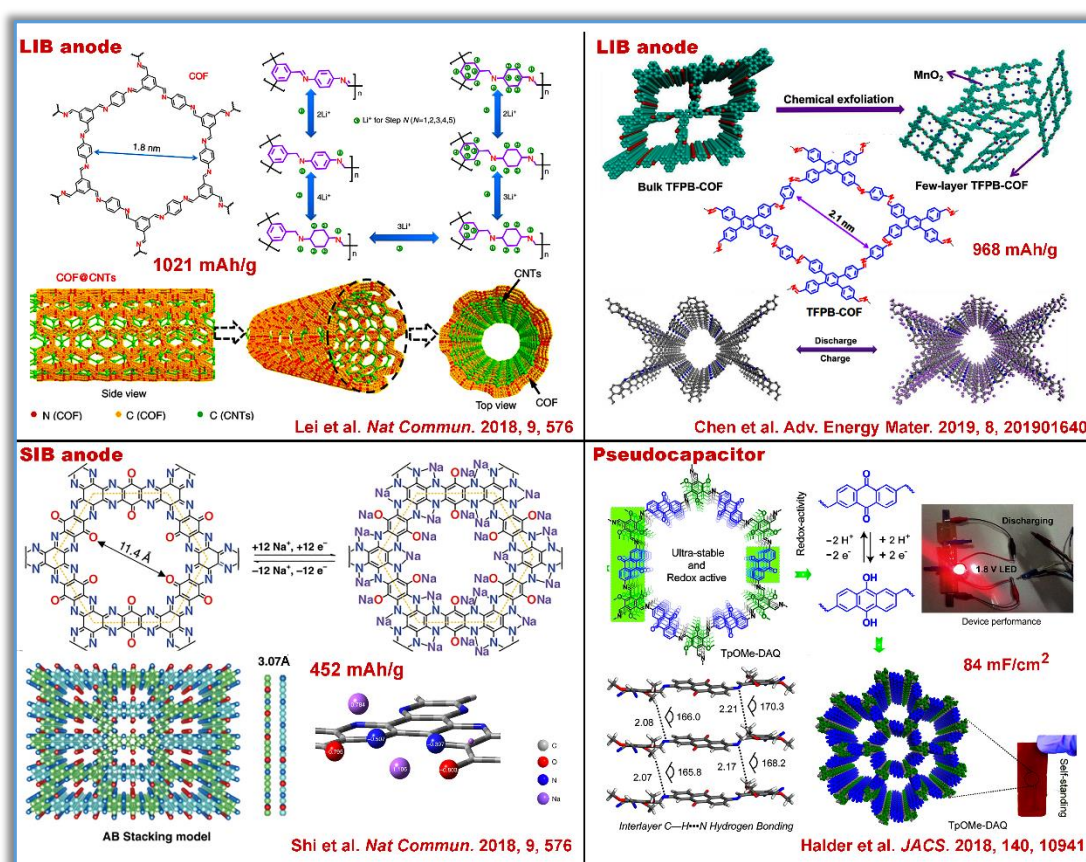


Figure I.14: Some recently published high-performing electrode materials for battery and supercapacitor. Copyright from reference 83 to 86.

The capacitive behaviour of COF materials are known for years, the insolubility of it in any kind of solvent restricts fabrication of the solid-state device. Halder et al. developed a free-standing supercapacitor electrode material out of an interlayer hydrogen bonding stabilized 2D-COF. A potential solid-state device configured with this COF film delivered a high capacitance value (84 mF/cm²) in strong acid medium.⁸⁶

Despite the high charge storage ability of 2D-COF, there are many open challenges to be addressed to bring the COF based electrode material to the practical ground. We kept our research focus on the investigation of electrochemical stability of COF for prolong period, faster diffusion of ions to improve reversible kinetics at high current and overall tuning of the storage performance by systematic variation of surface area and redox functionality.

I.13. Glimpses of our works:

Considering the aforesaid facts, herein, easily synthesizable and cost-effective Schiff base chemistry has been utilised following the C₂-C₃ or C₃-C₃ symmetry combinations of the monomeric aldehydes and amine to execute the pore structure engineering of the 2D-COFs with the incorporation of desired electroactive functional groups. We have systematically modified the pore dimension of the COFs from ultra-microporous (5Å) to highly mesoporous (40Å) region for the easy transportation of charge carriers (like Li⁺, Na⁺, H⁺ ions). Also, we strategically varied the electron-richness by manipulating the nitrogen and oxygen content along with the uniform 1D nano-channels of the COFs. The impact of such chemical manipulation on the structure-property relationship under an applied potential has been studied. The electronic driving force of the electron-donating (pyridine, phenol, resorcinol and phloroglucinol) and electron-accepting segments (triazine and tetrazine) have been employed to tune the redox behaviour of the COFs (Figure I.15). Significant stability of the COFs under electrochemical condition has been achieved by bringing intra-layer hydrogen bonding of β-ketoenamine linker and by conjugating electron-donating groups with the imine-bonds. The investigation of the mechanism has been carried out through experimental-computational approach to apprehend the guest ion insertion into the porous nano-channel and their interaction with heteroatoms, grafted to the nano-wall of the pores.

In chapter 1, we have shown an exceptional anodic capacity for Li-ion battery from covalent organic nanosheets. Considering it is the first time elucidation of Covalent Organic Nanosheets (CON) as anode materials, the observed high and stable performance is quite remarkable. CON can be considered as a disordered derivative of a Covalent Organic Framework (COF), which grow as few-layer thick 2D material with ample porosity. By functionalizing with ion binding groups they can be tailored for metal-ion battery applications. A key advantage arises from their ability to provide shortened path lengths for ion-diffusion, which makes developing new designer CON a very rewarding task, particularly, if it can bring newer insights.²⁶

Our structural design carries several unique and advantageous features, while the study brings some valuable insights. To highlight some,

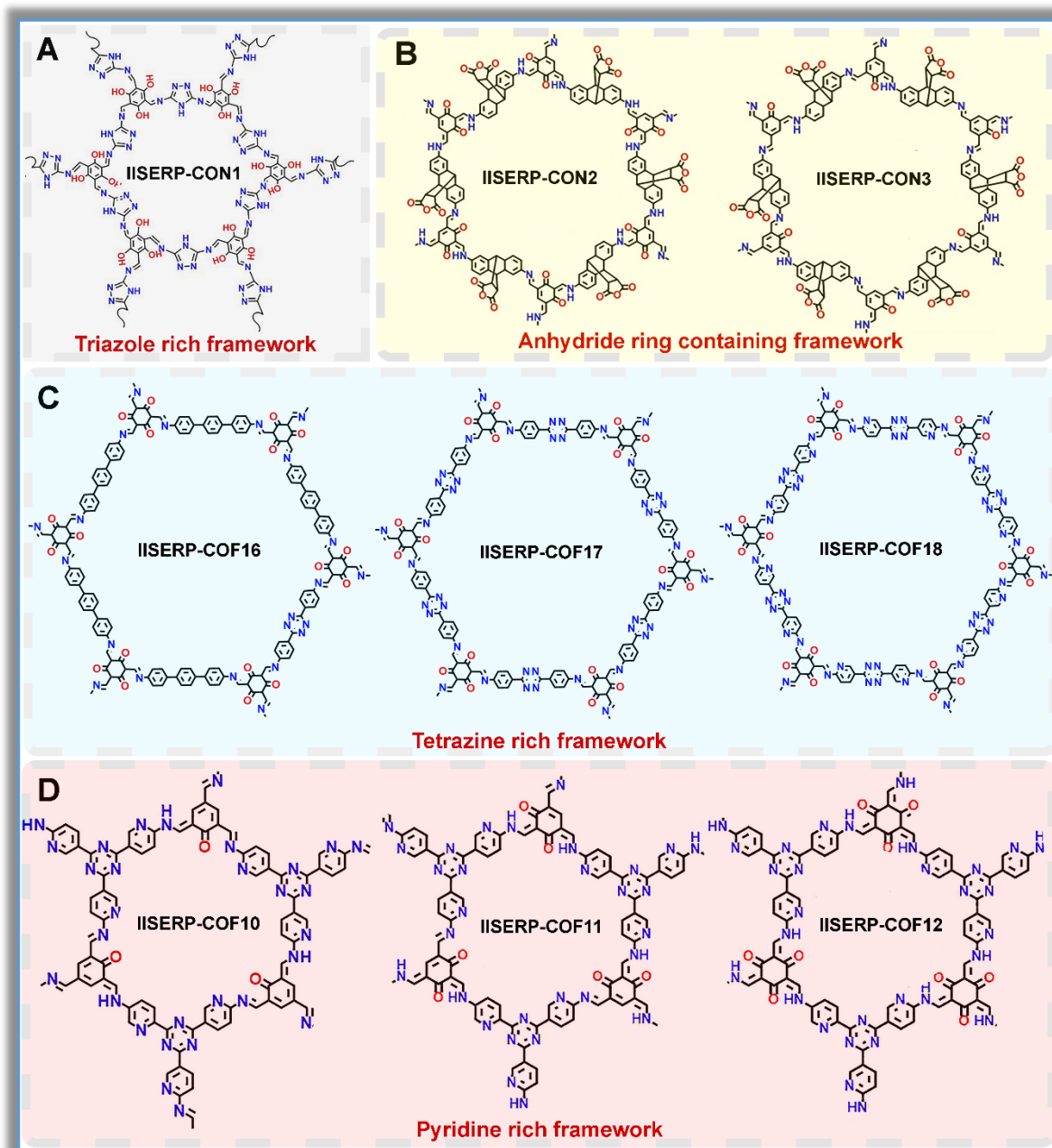


Figure I.15: (A) Triazole ring containing CON for half-cell LIB anode. (B) Anhydride ring containing CONs for full-cell-LIB. (C) Tetrazine ring containing COFs for half-cell LIB anode. (D) Pyridine ring containing COFs for supercapacitor electrode.

- For the first time, we have introduced a 1,2,4-triazole (a 120° linker) in the construction of a COF, which gives rise to flexibility resulting in a unique puckered N-rich framework.
- They grow as rare self-exfoliated nanosheets with highly functionalized micropores.
- ‘By design’ the functional groups (triazole and phloroglucinol) are chosen to be mildly binding Lewis acid/base to facilitate reversible binding of Li ions- aids in maintaining high specific capacities across a wide current density window.

- When integrated into a coin-cell, the material records an exceptional specific capacity of 720 mAh/g at 100 mA/g, with 100% retention of Coulombic Efficiency over 500 cycles.
- The capacity drops only by 20% upon increasing current density from 100 mA/g to 1 A/g, which is the lowest among all self-standing organic framework electrodes.
- We have synthesized the discrete monomer of the COF, which helps understand the key requirement of an extended covalent organic framework for the Li insertion-deinsertion.
- Using a combined experimental (Cyclic voltammetry, charge-discharge cycles, chemical analysis) and computational (GCMC, DFT, MD) approach we pinpoint the structure-property relationship, particularly the Li-CON interactions and the electronic synergy and stability.

We have adopted a crisp experimental-computational approach to gain coherent structure-property relation in this new class of material. Along the way, we have introduced several insights and few new concepts, which would certainly appeal to those working in this rapidly emerging area of research.

The work in **chapter 2**, identifies the critical disadvantage and advantage associated with the application of COF as an anode material in terms of its volumetric and gravimetric capacities. It brings about the simultaneous exfoliation and functionalization (for Li-interaction) of the COF to gain optimal capacities. We achieve this by using the concept of "Functionalizing Exfoliation Agent (FEA)." Wherein we use maleic anhydride as an FEA which exfoliates anthracene COFs and adds multiple-carbonyl groups to the framework as Li-interactive sites, this is on top of the already existing Li-interactive sites in the COF. This helps achieve a loading of 30 Li/unit-cell of the COF. This is much higher than the theoretical limit of Graphite (one Li per C_6). The exfoliation of the COF produces a ~ 4 times enhancement in the specific capacity. A full-cell, representing a practical battery, made using the exfoliated COF against $LiCoO_2$ cathode, delivers a stable specific capacity of 220 mAh/g with an energy density of 364 Wh/kg (vs. 320 Wh/kg for Graphite) over 200 cycles.²⁶ The observed full-cell capacity stands highest among all organic-polymers operating via Lithium insertion/intercalation. Another critical aspect is the high rate-performance even at 10C -rate, something where we see even the Graphite fails. This directly validates the superiority of the CON. Further, we vary the concentration of the Li-interactive hydroxyl groups in the COFs (phenol vs. resorcinol), which shows a systematic improvement in their specific capacities.

In **chapter 3**, we have shown how we can overcome the thermodynamic and kinetics barrier for Sodium intercalation in layered COF. In our work, atomic manipulation creates inverse electronic demand to

make highly uniform 1D nanochannel of COF as an apt candidate for facile Sodium insertion-intercalation mechanism. To take advantage of high surface area and uniform porous nano-channel present in the COF we utilized highly π -stacked instead of CONs. Here the strong electronic driving force created by band structure tuning enhances the surface accessibility of the COFs without any exfoliation strategy.

Compared to Li-ion, developing an anode material for Na-ions is a lot more challenging both due to its larger size and lowered diffusion tendency. Hence, developing an electrode for Sodium-ions requires viewing beyond Graphite. Covalent Organic Frameworks (COFs) are aptly suited for it. Advantage of the honeycomb type structure of the COFs where the pore-walls are grafted with electron-deficient centres has been properly exploited for bigger Na^+ ion insertion. Taking a different route, here we have proposed a novel concept of engineering the HOMO-LUMO levels of a family of COFs by exploiting the modular nature of the COF. The monomeric building units, in this case, a cross-linking trialdhehyde and a diamine, form the functionalizable modules of a COF. We have tinkered with the redox-active sites in such modules to gain systematic lowering of LUMO levels and show how it can impact the anodic performance of the COF to gain superior storage and rapid charge-discharge in Na-ion battery.

Unlike Lithium, the thermodynamics associated with the intercalation of the Sodium in layered structure is energetically unfavourable. Though the enthalpy of formation of LiC_6 and KC_8 were found to be -16.4 and -27.5 kJ/mol respectively. NaC_6 and NaC_8 are unstable with positive enthalpies of formation ($+20.8$ and $+19.9$ kJ/mol).⁸⁷ We tried to overcome this barrier by creating an inverse electronic demand by introducing low-lying LUMO energy level in the COF structure. That surely acts as a swift attractor for the incoming Sodium ion during the sodiation process by lowering the overall cell potential. Accumulation of profound electron density on the low-lying LUMO orbitals of the COFs (IISERP-COF17 and IISERP-COF18) concentrated on the tetrazine unit helps to overcome the thermodynamic limitation. A prompt comparison was made with another COF (COF16) deprived of tetrazine ring, hence the sluggish kinetics persists there.⁸⁸

We have tried to investigate the systems thoroughly to vindicate our approach. Some of the essential highlights of the work:

- To the best of our knowledge, for the first time, we have described the use of electron-deficient tetrazine/bipyridine-tetrazine centres to fabricate very high capacity (410 mAh/g @ 0.1 A/g) COF based anode for SIB. Realizing its role in creating an inverse electronic demand at the anode by providing a low-lying anti-bonding LUMO orbitals is original. This is crucial in establishing a rapid sodiation process at the anode.

- We arrive at the best working COF with the lowest LUMO level not by chance, but via a "by design" approach. For example, the side-on positioning of the β -ketoenamine, pyridine and tetrazine units to provide better chelation sites for Na^+ .
- Of the three COFs presented in this work, one of them is so far unreported. For all the COFs, we have furnished thorough structural modelling (periodic DFT optimizations and Pawley refinements) and all bulk characterizations.
- The push-pull electronics set-up by the redox-active modules knitted in the COF enables excellent rate-performance (even at 15 A/g shows 127 mA/g current density). Best among the COF based anode material.
- Substantial lowering of charge transfer resistance achieved by increasing the e-deficiency of the COF.
- Periodic DFT studies to identify the best sites for Na^+ ions in the COF and their most favourable reversible-interactions with the COF.

In a nutshell, we have tried our best to make the study comprehensive with experimental determination of electronic energy levels and related it to the electrochemical performance of the COF and also utilized computational modeling to bring valuable insights.

In **chapter 4**, the importance of the high surface area of the electron-rich COFs has been promptly investigated. The synergistic phenomena of the electrostatic double-layer formation along with reasonable electrochemical redox activity of the electron-donating substituents present in COFs have been properly employed to fabricate high performing solid-state supercapacitor.

In this work, three crystalline COFs built to form a tripyridine-triazine-triamine monomer with variable hydroxyl functionality in aldehyde (triformyl-phenol, triformyl-resorcinol and triformyl-phloroglucinol) sites has been used as an electrode for capacitor application.⁸⁹

The work explains the use of three new pyridine-rich COFs specifically designed to interact with protons. This feature, along with their high surface area manifests supercapacitor characteristics. We rationalized that COF can be functionalized with basic (Khattak et al. JMCA, 2016) and hydrogen-bonding groups to provide an enhanced driving force for interacting with protons. We chose pyridine groups to be the basic site, and incorporated intra- and inter-layer hydrogen-bond providing hydroxyl groups to gain chemical stability (Halder et al. JACS, 2018). Such decorated COF with their high surface area and porous structure would be anticipated to favor facile charge storage. But many capacitor applications utilize highly acidic electrolytes, with the small-sized H^+ serving as the charge carrier. For

superior capacitance, these H^+ needs to form an electrostatic double layer on the surface and if possible, some mild redox interactions with the framework, most importantly, they need to withstand multiple charge-discharge cycles. Electrochemical stability under such harsh chemical conditions is not guaranteed in Schiff-bonded frameworks.

Here we utilize the keto-enol tautomerism and hydrogen-bonding stabilization in the facile construction of a family of exceptionally acid-stable Schiff-base COF. And the presence of numerous ordered pyridine and triazine groups lining their pores ensures excellent H^+ interaction, and their ultra-microporous (pore size = $\sim 5.4 \text{ \AA}$) structure endows high surface area ($\sim 1300 \text{ m}^2/\text{g}$) favoring large ion-storage capacity. Importantly, despite these small-sized pores, their ordered nature still provides enormous room for the facile diffusion of H^+ and the counter-ions. Though, COFs having some of these features in isolation have been reported (see above for references), having all of them in one is quite advantageous. It helps achieve excellent solution phase and solid-state supercapacitance from the family of COFs reported in this chapter. The performance recorded are among the best reported for any class of framework solid-derived supercapacitor (546 F/g @ 500 mA/g in acidic solution and $\sim 92 \text{ mF/cm}^2$ at 0.5 mA/cm^2 in the solid-state device; Power density = 140 \mu W/cm^2 @ 0.5 mA/cm^2 , most of which is retained even after 10000 cycles). The structure and functional group participation and the underlying mechanism have been established to make the study comprehensive. Some of the essential highlights of the work:

- A systematic study has been carried out by tuning the microporosity and by enriching the high functionality in the framework.
- Thorough investigation on the co-operative effect of EDLC and faradaic pseudoactivity has been done by choosing structurally co-related and functionally tuneable COFs
- The highly ordered micropores of these COFs assists for channelized propagation of the H^+ ions under applied potential results high power density even at higher current.
- Solid-state COF derived capacitors with long cycle life delivers remarkable capacitance among all the stand-alone COF/MOF materials.

The comparison of the electrochemical activity of these three pyridine rich COFs provides an important understanding of futuristic high performing electrode assembly for capacitor application. The challenge associated with maintaining high power density with significant pseudo-activity has been properly addressed in a very logical way with various experimental techniques. Our achievement towards designer storage system fabrication with COF based electrodes fulfils by proper utilisation of all the unique properties of COFs materials.

References:

- [1] Wu, J.; Xu, F.; Li, S.; Ma, P.; Zhang, X.; Liu, Q.; Fu, R.; Wu, D., Porous Polymers as Multifunctional Material Platforms toward Task-Specific Applications. *Adv. Mater.* **2019**, *31*, 1802922.
- [2] Bandyopadhyay, S.; Anil, A. G.; James, A.; Patra, A., Multifunctional porous organic polymers: tuning of porosity, CO₂, and H₂ storage and visible-light-driven photocatalysis. *ACS Appl. Mater. Interfaces* **2016**, *8*, 27669-27678.
- [3] Das, S.; Heasman, P.; Ben, T.; Qiu, S., Porous organic materials: strategic design and structure-function correlation. *Chem. Rev.* **2017**, *117*, 1515-1563
- [4] Cote, A. P.; Benin, A. I.; Ockwig, N. W.; O'keeffe, M.; Matzger, A. J.; Yaghi, O. M., Porous, crystalline, covalent organic frameworks. *Science* **2005**, *310*, 1166-1170.
- [5] Alahakoon, S. B.; Diwakara, S. D.; Thompson, C. M.; Smaldone, R. A., Supramolecular design in 2D covalent organic frameworks. *Chem. Soc. Rev.* **2020**, *49*, 1344-1356.
- [6] Guan, X.; Chen, F.; Fang, Q.; Qiu, S., Design and applications of three dimensional covalent organic frameworks. *Chem. Soc. Rev.* **2020**, *49*, 1357-1384.
- [7] Geng, K.; He, T.; Liu, R.; Tan, K. T.; Li, Z.; Tao, S.; Gong, Y.; Jiang, Q.; Jiang, D., Covalent Organic Frameworks: Design, Synthesis, and Functions. *Chem. Rev.* **2020**.
- [8] Chen, X.; Geng, K.; Liu, R.; Tan, K. T.; Gong, Y.; Li, Z.; Tao, S.; Jiang, Q.; Jiang, D., Covalent Organic Frameworks: Chemical Approaches to Designer Structures and Built-In Functions. *Angew. Chem. Int. Ed.* **2020**, *59*, 5050-5091.
- [9] Zhu, L.; Zhang, Y.-B., Crystallization of covalent organic frameworks for gas storage applications. *Molecules* **2017**, *22*, 1149.
- [10] Sharma, R. K.; Yadav, P.; Yadav, M.; Gupta, R.; Rana, P.; Srivastava, A.; Zbořil, R.; Varma, R. S.; Antonietti, M.; Gawande, M. B., Recent development of covalent organic frameworks (COFs): synthesis and catalytic (organic-electro-photo) applications. *Materials Horizons* **2020**, *7*, 411-454.
- [11] Liu, X.; Huang, D.; Lai, C.; Zeng, G.; Qin, L.; Wang, H.; Yi, H.; Li, B.; Liu, S.; Zhang, M., Recent advances in covalent organic frameworks (COFs) as a smart sensing material. *Chem. Soc. Rev.* **2019**, *48*, 5266-5302.
- [12] Haug, W. K.; Moscarello, E. M.; Wolfson, E. R.; McGrier, P. L., The luminescent and photophysical properties of covalent organic frameworks. *Chem. Soc. Rev.* **2020**, *49*, 839-864.
- [13] Lin, C. Y.; Zhang, D.; Zhao, Z.; Xia, Z., Covalent organic framework electrocatalysts for clean energy conversion. *Adv. Mater.* **2018**, *30*, 1703646.
- [14] Alahakoon, S. B.; Thompson, C. M.; Occhialini, G.; Smaldone, R. A., Design principles for covalent organic frameworks in energy storage applications. *ChemSusChem* **2017**, *10*, 2116-2129

- [15] Wang, S.; Zhang, Z.; Zhang, H.; Rajan, A. G.; Xu, N.; Yang, Y.; Zeng, Y.; Liu, P.; Zhang, X.; Mao, Q., Reversible polycondensation-termination growth of covalent-organic-framework spheres, fibers, and films. *Matter* **2019**, *1*, 1592-1605
- [16] Segura, J. L.; Mancheño, M. J.; Zamora, F., Covalent organic frameworks based on Schiff-base chemistry: synthesis, properties and potential applications. *Chem. Soc. Rev.* **2016**, *45*, 5635-5671.
- [17] Kandambeth, S.; Mallick, A.; Lukose, B.; Mane, M. V.; Heine, T.; Banerjee, R., Construction of crystalline 2D covalent organic frameworks with remarkable chemical (acid/base) stability via a combined reversible and irreversible route. *J. Am. Chem. Soc.* **2012**, *134*, 19524-19527.
- [18] Ma, T.; Kapustin, E. A.; Yin, S. X.; Liang, L.; Zhou, Z.; Niu, J.; Li, L.-H.; Wang, Y.; Su, J.; Li, J., Single-crystal x-ray diffraction structures of covalent organic frameworks. *Science* **2018**, *361*, 48-52.
- [19] Li, X.; Yadav, P.; Loh, K. P., Function-oriented synthesis of two-dimensional (2D) covalent organic frameworks—from 3D solids to 2D sheets. *Chem. Soc. Rev.* **2020**.
- [20] Mandal, A. K.; Mahmood, J.; Baek, J. B., Two-Dimensional Covalent Organic Frameworks for Optoelectronics and Energy Storage. *ChemNanoMat* **2017**, *3*, 373-391
- [21] Dogru, M.; Bein, T., On the road towards electroactive covalent organic frameworks. *Chem. Commun.* **2014**, *50*, 5531-5546.
- [22] Rodríguez-San-Miguel, D.; Montoro, C.; Zamora, F., Covalent organic framework nanosheets: preparation, properties and applications. *Chem. Soc. Rev.* **2020**, *49*, 2291-2302.
- [23] Li, J.; Jing, X.; Li, Q.; Li, S.; Gao, X.; Feng, X.; Wang, B., Bulk COFs and COF nanosheets for electrochemical energy storage and conversion. *Chem. Soc. Rev.* **2020**.
- [24] Sun, J.; Klechikov, A.; Moise, C.; Prodana, M.; Enachescu, M.; Talyzin, A. V., A molecular pillar approach to grow vertical covalent organic framework nanosheets on Graphene: hybrid materials for energy storage. *Angew. Chem.* **2018**, *130*, 1046-1050.
- [25] Haldar, S.; Roy, K.; Nandi, S.; Chakraborty, D.; Puthusseri, D.; Gawli, Y.; Ogale, S.; Vaidhyanathan, R., High and Reversible Lithium Ion Storage in Self-Exfoliated Triazole-Triformyl Phloroglucinol-Based Covalent Organic Nanosheets. *Adv. Energy Mater.* **2018**, *8*, 1702170.
- [26] Haldar, S.; Roy, K.; Kushwaha, R.; Ogale, S.; Vaidhyanathan, R., Chemical Exfoliation as a Controlled Route to Enhance the Anodic Performance of COF in LIB. *Adv. Energy Mater.* **2019**, *9*, 1902428.
- [27] Eftekhari, A.; Kim, D.-W., Sodium-ion batteries: new opportunities beyond energy storage by Lithium. *J. Power Sources* **2018**, *395*, 336-348.
- [28] Lenchuk, O.; Adelhalm, P.; Mollenhauer, D., New insights into the origin of unstable Sodium Graphite intercalation compounds. *Phys. Chem. Chem. Phys.* **2019**, *21*, 19378-19390.
- [29] Wang, Z.; Selbach, S. M.; Grande, T., Van der Waals density functional study of the energetics of alkali metal intercalation in Graphite. *RSC Adv.* **2014**, *4*, 4069-4079.

- [30] Kim, H.; Hong, J.; Yoon, G.; Kim, H.; Park, K.-Y.; Park, M.-S.; Yoon, W.-S.; Kang, K., Sodium intercalation chemistry in Graphite. *Energy Environ. Sci.* **2015**, *8*, 2963-2969.
- [31] Haldar, S.; Kaleeswaran, D.; Rase, D.; Roy, K.; Ogale, S.; Vaidhyanathan, R., Tuning the Electronic Energy Level of Covalent Organic Framework for Crafting High-rate Na-ion Battery Anode. *Nanoscale Horizon*.
- [32] Wang, M.; Guo, H.; Xue, R.; Li, Q.; Liu, H.; Wu, N.; Yao, W.; Yang, W., Covalent organic frameworks: A new class of porous organic frameworks for supercapacitor electrodes. *ChemElectroChem* **2019**, *6*, 2984-2997.
- [33] Marele, A. C.; Mas-Balleste, R.; Terracciano, L.; Rodríguez-Fernández, J.; Berlanga, I.; Alexandre, S. S.; Otero, R.; Gallego, J. M.; Zamora, F.; Gómez-Rodríguez, J. M., Formation of a surface covalent organic framework based on polyester condensation. *Chem. Commun.* **2012**, *48*, 6779-6781.
- [34] Ourdjini, O.; Pawlak, R.; Abel, M.; Clair, S.; Chen, L.; Bergeon, N.; Sassi, M.; Oison, V.; Debierre, J.-M.; Coratger, R., Substrate-mediated ordering and defect analysis of a surface covalent organic framework. *Physical Review B* **2011**, *84*, 125421.
- [35] DeBlase, C. R.; Silberstein, K. E.; Truong, T.-T.; Abruña, H. D.; Dichtel, W. R., β -Ketoenamine-linked covalent organic frameworks capable of pseudocapacitive energy storage. *J. Am. Chem. Soc.* **2013**, *135*, 16821-16824.
- [36] Biswal, B. P.; Chandra, S.; Kandambeth, S.; Lukose, B.; Heine, T.; Banerjee, R., Mechanochemical synthesis of chemically stable isoreticular covalent organic frameworks. *J. Am. Chem. Soc.* **2013**, *135*, 5328-5331.
- [37] Chandra, S.; Kandambeth, S.; Biswal, B. P.; Lukose, B.; Kunjir, S. M.; Chaudhary, M.; Babarao, R.; Heine, T.; Banerjee, R., Chemically stable multilayered covalent organic nanosheets from covalent organic frameworks via mechanical delamination. *J. Am. Chem. Soc.* **2013**, *135*, 17853-17861.
- [38] Vardhan, H.; Nafady, A.; Al-Enizi, A. M.; Ma, S., Pore surface engineering of covalent organic frameworks: structural diversity and applications. *Nanoscale* **2019**, *11*, 21679-21708.
- [39] Babu, H. V.; Bai, M. M.; Rajeswara Rao, M., Functional π -conjugated two-dimensional covalent organic frameworks. *ACS Appl. Mater. Interfaces* **2019**, *11*, 11029-11060.
- [40] Xu, H.; Jiang, D., Covalent organic frameworks: crossing the channel. *Nat. Chem.* **2014**, *6*, 564
- [41] Baldwin, L. A.; Crowe, J. W.; Shannon, M. D.; Jaroniec, C. P.; McGrier, P. L., 2D covalent organic frameworks with alternating triangular and hexagonal pores. *Chem. Mater.* **2015**, *27*, 6169-6172.
- [42] Chen, X.; Addicoat, M.; Jin, E.; Xu, H.; Hayashi, T.; Xu, F.; Huang, N.; Irle, S.; Jiang, D., Designed synthesis of double-stage two-dimensional covalent organic frameworks. *Sci. Rep.* **2015**, *5*, 14650.

- [43] Xu, M.; Fujita, D.; Sagisaka, K.; Watanabe, E.; Hanagata, N., Production of extended single-layer Graphene. *Acs Nano* **2011**, *5*, 1522-1528.
- [44] Verger, L.; Natu, V.; Carey, M.; Barsoum, M. W., MXenes: an introduction of their synthesis, select properties, and applications. *Trends in Chemistry* **2019**, *1*, 656-669.
- [45] Kandambeth, S.; Dey, K.; Banerjee, R., Covalent organic frameworks: chemistry beyond the structure. *J. Am. Chem. Soc.* **2018**, *141*, 1807-1822.
- [46] Xu, L.; Zhou, X.; Tian, W. Q.; Gao, T.; Zhang, Y. F.; Lei, S.; Liu, Z. F., Surface-Confined Single-Layer Covalent Organic Framework on Single-Layer Graphene Grown on Copper Foil. *Angew. Chem. Int. Ed.* **2014**, *53*, 9564-9568.
- [47] Chen, C.; Joshi, T.; Li, H.; Chavez, A. D.; Pedramrazi, Z.; Liu, P.-N.; Li, H.; Dichtel, W. R.; Bredas, J.-L.; Crommie, M. F., Local electronic structure of a single-layer porphyrin-containing covalent organic framework. *ACS nano* **2018**, *12*, 385-391.
- [48] Dong, W.-l.; Wang, L.; Ding, H.-m.; Zhao, L.; Wang, D.; Wang, C.; Wan, L.-J., Substrate orientation effect in the on-surface synthesis of tetrathiafulvalene-integrated single-layer covalent organic frameworks. *Langmuir* **2015**, *31*, 11755-11759.
- [49] Chubarov, M.; Choudhury, T. H.; Zhang, X.; Redwing, J. M., In-plane x-ray diffraction for characterization of monolayer and few-layer transition metal dichalcogenide films. *Nanotechnology* **2018**, *29*, 055706.
- [50] Berlanga, I.; Mas-Ballesté, R.; Zamora, F., Tuning delamination of layered covalent organic frameworks through structural design. *Chem. Commun.* **2012**, *48*, 7976-7978.
- [51] Berlanga, I.; Ruiz-González, M. L.; González-Calbet, J. M.; Fierro, J. L. G.; Mas-Ballesté, R.; Zamora, F., Delamination of layered covalent organic frameworks. *Small* **2011**, *7*, 1207-1211.
- [52] Wang, H.; Zeng, Z.; Xu, P.; Li, L.; Zeng, G.; Xiao, R.; Tang, Z.; Huang, D.; Tang, L.; Lai, C., Recent progress in covalent organic framework thin films: fabrications, applications and perspectives. *Chem. Soc. Rev.* **2019**, *48*, 488-516.
- [53] Bunck, D. N.; Dichtel, W. R., Bulk synthesis of exfoliated two-dimensional polymers using hydrazone-linked covalent organic frameworks. *J. Am. Chem. Soc.* **2013**, *135*, 14952-14955.
- [54] Wang, S.; Wang, Q.; Shao, P.; Han, Y.; Gao, X.; Ma, L.; Yuan, S.; Ma, X.; Zhou, J.; Feng, X.; Wang, B., Exfoliation of Covalent Organic Frameworks into Few-Layer Redox-Active Nanosheets as Cathode Materials for Lithium-Ion Batteries. *J. Am. Chem. Soc.* **2017**, *139*, 4258-4261.
- [55] Xia, Z. Y.; Pezzini, S.; Treossi, E.; Giambastiani, G.; Corticelli, F.; Morandi, V.; Zanelli, A.; Bellani, V.; Palermo, V., The exfoliation of Graphene in liquids by electrochemical, chemical, and sonication-assisted techniques: A nanoscale study. *Adv. Funct. Mater.* **2013**, *23*, 4684-4693.

- [56] Khayum, M. A.; Kandambeth, S.; Mitra, S.; Nair, S. B.; Das, A.; Nagane, S. S.; Mukherjee, R.; Banerjee, R., Chemically delaminated free-standing ultrathin covalent organic nanosheets. *Angew. Chem. Int. Ed.* **2016**, *55*, 15604-15608.
- [57] Mitra, S.; Sasmal, H. S.; Kundu, T.; Kandambeth, S.; Illath, K.; Diaz Diaz, D.; Banerjee, R., Targeted drug delivery in covalent organic nanosheets (CONs) via sequential postsynthetic modification. *J. Am. Chem. Soc.* **2017**, *139*, 4513-4520.
- [58] Wang, S.; Wang, Q.; Shao, P.; Han, Y.; Gao, X.; Ma, L.; Yuan, S.; Ma, X.; Zhou, J.; Feng, X.; Wang, B., Exfoliation of Covalent Organic Frameworks into Few-Layer Redox-Active Nanosheets as Cathode Materials for Lithium-Ion Batteries. *J. Am. Chem. Soc.* **2017**, *139*, 4258-4261.
- [59] Mitra, S.; Kandambeth, S.; Biswal, B. P.; Khayum M, A.; Choudhury, C. K.; Mehta, M.; Kaur, G.; Banerjee, S.; Prabhune, A.; Verma, S., Self-exfoliated guanidinium-based ionic covalent organic nanosheets (iCONs). *J. Am. Chem. Soc.* **2016**, *138*, 2823-2828.
- [60] Singh, H.; Devi, M.; Jena, N.; Iqbal, M. M.; Nailwal, Y.; De Sarkar, A.; Pal, S. K., Proton-Triggered Fluorescence Switching in Self-Exfoliated Ionic Covalent Organic Nanosheets for Applications in Selective Detection of Anions. *ACS Appl. Mater. Interfaces* **2020**, *12*, 13248-13255.
- [61] Hang, N.; Wang, T.; Wu, X.; Jiang, C.; Chen, F.; Bai, W.; Bai, R., Self-exfoliation of 2D covalent organic frameworks: morphology transformation induced by solvent polarity. *RSC Adv.* **2018**, *8*, 3803-3808.
- [62] Xu, L.; Zhou, X.; Tian, W. Q.; Gao, T.; Zhang, Y. F.; Lei, S.; Liu, Z. F., Surface-Confined Single-Layer Covalent Organic Framework on Single-Layer Graphene Grown on Copper Foil. *Angew. Chem. Int. Ed.* **2014**, *53*, 9564-9568.
- [63] Dunn, B.; Kamath, H.; Tarascon, J.-M., Electrical energy storage for the grid: a battery of choices. *Science* **2011**, *334*, 928-935.
- [64] Choi, C.; Ashby, D. S.; Butts, D. M.; DeBlock, R. H.; Wei, Q.; Lau, J.; Dunn, B., Achieving high energy density and high power density with pseudocapacitive materials. *Nat. Rev. Mater.* **2019**, 1-15.
- [65] Yao, H.-R.; You, Y.; Yin, Y.-X.; Wan, L.-J.; Guo, Y.-G., Rechargeable dual-metal-ion batteries for advanced energy storage. *Phys. Chem. Chem. Phys.* **2016**, *18*, 9326-9333.
- [66] Li, Y.; Lu, J., Metal–Air Batteries: Will They Be the Future Electrochemical Energy Storage Device of Choice? *ACS Energy Letters* **2017**, *2*, 1370-1377.
- [67] Salama, M.; Rosy; Attias, R.; Yemini, R.; Gofer, Y.; Aurbach, D.; Noked, M., Metal–Sulfur Batteries: Overview and Research Methods. *ACS Energy Letters* **2019**, *4*, 436-446.
- [68] Goodenough, J. B.; Park, K.-S., The Li-Ion Rechargeable Battery: A Perspective. *J. Am. Chem. Soc.* **2013**, *135*, 1167-1176.

- [69] Eftekhari, A.; Kim, D.-W., Sodium-ion batteries: new opportunities beyond energy storage by Lithium. *J. Power Sources* **2018**, *395*, 336-348.
- [70] Andrews, D. H.; Richard J. K. "Electrochemistry". Fundamental Chemistry. New York: John Wiley & Sons, Inc. **1962**, 482.
- [71] Deng, D., Li-ion batteries: basics, progress, and challenges. *Energy Science & Engineering* **2015**, *3*, 385-418.
- [72] Poonam; Sharma, K.; Arora, A.; Tripathi, S. K., Review of supercapacitors: Materials and devices. *Journal of Energy Storage* **2019**, *21*, 801-825.
- [73] Wang, R.; Yao, M.; Niu, Z., Smart supercapacitors from materials to devices. *InfoMat* **2020**, *2*, 113-125.
- [74] Simon, P.; Brousse, T.; Favier, F. Electrochemical double-layer capacitors (EDLC). *Supercapacitors based on carbon or pseudocapacitive materials*. **2017**, 1-25.
- [75] Jiang, Y.; Liu, J., Definitions of Pseudocapacitive Materials: A Brief Review. *Energy & Environmental Materials* **2019**, *2*, 30-37.
- [76] Kim, J.; Kim, J. H.; Ariga, K., Redox-Active Polymers for Energy Storage Nanoarchitectonics. *Joule* **2017**, *1*, 739-768.
- [77] Bhosale, M. E.; Chae, S.; Kim, J. M.; Choi, J.-Y., Organic small molecules and polymers as an electrode material for rechargeable Lithium ion batteries. *J. Mater. Chem. A* **2018**, *6*, 19885-19911.
- [78] Rajagopalan, R.; Tang, Y.; Jia, C.; Ji, X.; Wang, H., Understanding the Sodium storage mechanisms of organic electrodes in Sodium ion batteries: issues and solutions. *Energy Environ. Sci.* **2020**, *13*, 1568-1592.
- [79] Liu, X.; Liu, C.-F.; Lai, W.-Y.; Huang, W., Porous Organic Polymers as Promising Electrode Materials for Energy Storage Devices. *Advanced Materials Technologies n/a*, 2000154.
- [80] ong, K. D.; Wang, T.; Smoukov, S. K., Multidimensional performance optimization of conducting polymer-based supercapacitor electrodes. *Sustainable Energy & Fuels* **2017**, *1*, 1857-1874.
- [81] ao, Y.; Dong, H.; Hu, W., Ordering of conjugated polymer molecules: recent advances and perspectives. *Polym. Chem.* **2013**, *4*, 5197-5205.
- [82] Vijayakumar, V.; Zhong, Y.; Untilova, V.; Bahri, M.; Herrmann, L.; Biniek, L.; Leclerc, N.; Brinkmann, M., Bringing Conducting Polymers to High Order: Toward Conductivities beyond 105 S cm⁻¹ and Thermoelectric Power Factors of 2 mW m⁻¹ K⁻². *Adv. Energy Mater.* **2019**, *9*, 1900266.
- [83] Lei, Z.; Yang, Q.; Xu, Y.; Guo, S.; Sun, W.; Liu, H.; Lv, L.-P.; Zhang, Y.; Wang, Y., Boosting Lithium storage in covalent organic framework via activation of 14-electron redox chemistry. *Nat. Commun.* **2018**, *9*, 576.

- [84] Chen, X.; Li, Y.; Wang, L.; Xu, Y.; Nie, A.; Li, Q.; Wu, F.; Sun, W.; Zhang, X.; Vajtai, R., High-Lithium-Affinity Chemically Exfoliated 2D Covalent Organic Frameworks. *Adv. Mater.* **2019**, *31*, 1901640.
- [85] Shi, R.; Liu, L.; Lu, Y.; Wang, C.; Li, Y.; Li, L.; Yan, Z.; Chen, J., Nitrogen-rich covalent organic frameworks with multiple carbonyls for high-performance Sodium batteries. *Nat. Commun.* **2020**, *11*, 1-10.
- [86] Halder, A.; Ghosh, M.; Khayum M, A.; Bera, S.; Addicoat, M.; Sasmal, H. S.; Karak, S.; Kurungot, S.; Banerjee, R., Interlayer Hydrogen-Bonded Covalent Organic Frameworks as High-Performance Supercapacitors. *J. Am. Chem. Soc.* **2018**, *140*, 10941-10945.
- [87] Wang, Z.; Selbach, S. M.; Grande, T., Van der Waals density functional study of the energetics of alkali metal intercalation in Graphite. *RSC Adv.* **2014**, *4*, 4069-4079.
- [88] Haldar, S.; Kaleeswaran, D.; Rase, D.; Roy, K.; Ogale, S.; Vaidhyanathan, R., Tuning the Electronic Energy Level of Covalent Organic Framework for Crafting High-rate Na-ion Battery Anode. *Nanoscale Horizon*.
- [89] Haldar, S.; Kushwaha, R.; Maity, R.; Vaidhyanathan, R., Pyridine-Rich Covalent Organic Frameworks as High-Performance Solid-State Supercapacitors. *ACS Materials Letters* **2019**, *1*, 490-497.

Chapters

Chapter 1:

High and Reversible Lithium Ion Storage in Self-Exfoliated Triazole-Triformyl Phloroglucinol based Covalent Organic Nanosheets

1.1. Introduction:

Covalent organic framework is a crystalline organic polymer. Many 2D COFs have layers built from cross-linking aromatic groups, which via columnar π - π stacking order into a periodic 3D structure (Scheme A.1.1). Their modular construct and ordered porosity makes them find use in diverse applications.^[1-27] Here we are seeking application of 2D COFs in metal-ion batteries, which are typically made of electrodes with layered structures. For example, Graphite as anode and LiCoO_2 as cathode. Owing to their Graphite resembling structure, COF can serve as anode. Since their initial discovery, many 2D materials with comparable layered structures have been explored as Lithium insertion-deinsertion materials.^[28-39] Some of the highly desirable characteristics of a superior anode material include moderate to high surface accessibility to ensure maximum charge storage per unit area, and the other is the hierarchical porosity for favorable kinetics. Exfoliation enhances surface accessibility and active site creation in such 2D materials.^[40-48] In this regard, COFs could have much more to offer.^[49-51]

Exfoliation in any 2D material is largely dependent on the interlayer forces holding them. Typically, the COF layers are held together by interlayer π - π interactions or in some cases via additional hydrogen bonding.^[52,53] However, unlike Graphite, the layers of COF are not built from fused aromatic rings. In their optimized structure, the layers are held together by relatively fewer π - π interactions at inter-layer separations of 3.4 to 4.5 Å (Scheme A.1.1), which can enable facile exfoliation into nanosheets without losing the overall structure.^[54-57] Nanosheets are known to perform well as ion storage materials because of their high active site access and shortened diffusion path length for the guests.^[41,58,59] The covalent organic nanosheets can be considered as a few-layers-thick disordered derivative of a COF. Many carbon-based materials with disordered structures exhibit much higher practical capacities for ion storage than the theoretical value of Graphite.^[60] This is because in their disordered form they possess more number of Li-C_6 rings interactions.^[60] Also, presence of electronegative atoms in such C_6 rings promote such interactions as the lone pairs from the heteroatom can stabilize the positive charge created on the ring during its interaction with the Lithium. The modular construction of a COF enables the stoichiometric introduction of such heteroatoms and also the chemical nature of the heteroatom can be tuned to control the interactions with the extra-framework species (e.g. Nitrogen: pyridine vs. triazine vs. Schiff- can be customized).^[2-6] Crucially, such electrochemically driven Lithium addition onto the heteroatom sites are reversible.^[60]

Compared to inorganic materials and Graphite,^[28-48] less is known about the utilization of COF for Li-ion storage.^[61-70] As an effective approach, Li et al.^[61] developed a thiophene-based conjugated COF as anode with high specific capacity (666 mAh/g), but this capacity drops significantly with increasing current density. Similarly, Fe_2O_3 supported on nanosheets of Graphene shows high anode

activity arising from the redox reactivity at the iron center (1355 and 982 mAh/g for charge and discharge cycles, respectively).^[71] However, over multiple cycles, these redox active systems tend to drop in performance owing to some irreversible reactions between the Lithium and the active material.^[71-73] At high current densities, such undesirable irreversible reactions become more frequent and lower the coulombic efficiency. This is true also for the other transition metal based anodic materials.^[72,73] So, use of relatively less reactive (milder Lewis base/acid) neutral groups or moieties as active sites could promise longer cycle life.

Here we report a new COF wherein, for the first time, we have incorporated triazole moiety as a means to introduce flexibility into the framework. This COF, even during synthesis, grows into self-exfoliated CON. The short triazole linkers (a 120° linker)^[74,75] generate uniform micropores with walls lined by optimally spaced -OH and N-atoms, giving rise to favorable Lithium interacting pockets. These groups, phenols and triazoles, being weak acids (pKa, phenol = 10.3; 1,2,4-triazole = 9.3) are expected to interact mildly with Lithium. A Li-ion coin-cell comprising this CON-derived anode exhibits high specific capacity ~720 mAh/g at 100 mA/g, which is among the highest reported capacities for self-standing non-graphenic organic materials. Importantly, the cell retains this high specific capacity even after 100 cycles and shows only a small drop (~150 mAh/g) in specific capacity even at a current density as high as 1 A/g. It retains a high specific capacity of 460 mAh/g even at 2 A/g. Simulations using DFT, coupled with analytical studies, help us identify the lowest energy configuration of the Lithium loaded CON (Li@CON), which has a structure with optimal Li-framework interactions. Plus, the electronic driving force for the insertion-deinsertion of Lithium is evident from the lowering of bandgap and from the difference in electron-density/potential maps.

1.2. Results:

1.2.1. Synthesis of IISERP-CON1 and corresponding model compound:

The IISERP-CON1, prepared from a reaction between a trialdehyde and 3,5-diaminotriazole under mild solvothermal conditions (Figure 1.1), grows as a homogeneous fluffy reddish-brown powder. For the preparation, 1,3,5-triformylphloroglucinol (90mg, 0.42mmol) and 3,5-diamino-1,2,4-triazole (45mg, 0.45mmol) were weighed into a Pyrex tube and were dissolved in dioxane (3.0 mL), to this solution, dimethylacetamide (1.0 mL) and mesitylene (3.0 mL) were added and stirred until a greenish yellow color was observed. Following this, 1.0 mL of 6M aqueous acetic acid was added. Then the Pyrex tube was flash frozen in a liquid nitrogen bath and sealed. The Pyrex tube along with its contents was placed in an oven at 120°C for 3 days. The mixture was cooled to room temperature and reddish brown precipitate was isolated by filtration. This yielded about 110mg of reddish brown coloured solid which was washed with hot DMF, dioxane, MeOH, acetone and THF (81%, isolated yield). This reddish brown solid was subjected to a Soxhlet extraction using DMF/methanol as solvent. Importantly, no color was found in the wash solution, suggesting lack of any unreacted materials or small oligomers, which was further confirmed from a solution NMR of the final wash solution. (Formula for IISERP-CON1: C₂₄N₁₅O₆H₁₅, M. Wt. 610g/mol, CHN Obsd. (Calculated within brackets) C = 46.89 (47.30); H = 2.68 (2.48); N = 34.15 (34.47)). Note: The slight deviation between the observed and the calculated CHN values for the IISERP-CON1 can be attributed to the presence of unreacted terminal aldehyde and amine functionalities. Note: The model compound is highly soluble in DMF, while the CON is totally insoluble even in hot DMF.

To prepare the model compound 3-amino-1, 2, 4-triazole (1.42 g, 0.017 mole) was dissolved in a hot mixture of ethanol (40 mL) and a solution of 1, 3, 5-Triformylphloroglucinol (1.26g, 0.006 mole) in ethanol was slowly added to it. The resulting mixture was refluxed and the off-white precipitate of the

model compound was collected. The precipitate of model compound was washed with copious amounts of hot ethanol and dried under reduced pressure. Finally the model compound was crystallized from a hot solution of DMF by slow evaporation. Crystals suitable for single crystal X-ray diffraction were found. The crystals were highly soluble in DMSO and DMF. (Formula for model compound: $C_{15}N_{12}O_3H_{12}$, M. Wt. 408.34g/mol, CHN Obsd. (Calculated within brackets) C = 44.30 (44.12); H = 3.11 (2.96); N = 40.80 (41.16)).

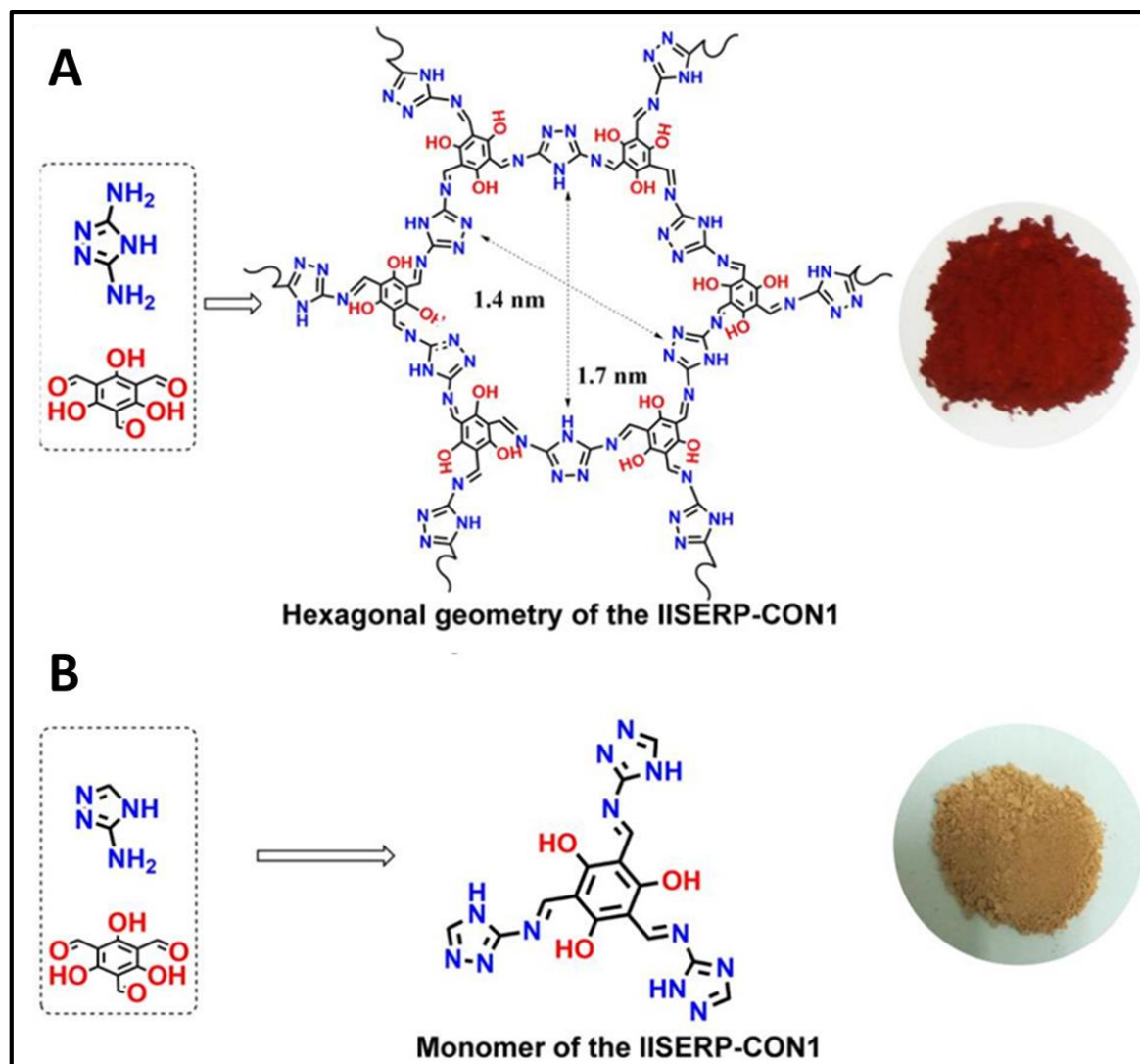


Figure 1.1. Schematic representation of the reaction procedure used for (A) the synthesis of the highly functionalised IISERP-CON1 and (B) its corresponding model compound. Inset shows the texture and colour of the products.

The ^{13}C -SSNMR and IR spectra of IISERP-CON1 are presented in Figure 1.2. In the SSNMR all the characteristic bands for the triazole (δ :151.47 ppm), the aldehyde (δ :172.62 ppm) and Schiff base (δ :157.54 ppm) units are seen. Importantly, there are extra peaks at (δ :185.75 ppm), which are due to the terminal aldehydes. These are the aldehydes from the partly unreacted trihydroxybenzaldehyde units. This indicates that the polycondensation is not too high in the CONs. This explains the deviation observed between the calculated and the observed CHN values. The model compound was soluble in high boiling solvents such as DMF and DMSO. So that it was characterized by liquid state NMR and solid state IR studies (Figure 1.2 and 1.3). 1H -NMR peaks due to the model compound are observed at triazole-NH (δ : 11-13.5 ppm), Schiff base -CH (δ :8.76, 8.73 ppm), triazolic -CH(δ :8.49 ppm), enolic -OH (δ :5.70

ppm). ^{13}C -NMR Chemical shifts (400MHz) at $\delta=157.6, 149.8, 145.0, 106.9$ and 107.3 ppm of the model compound is concurrent with CON. In the IR spectra we observe the characteristic carbonyl ($-\text{C}=\text{O}$) stretching frequency (1665 cm^{-1}) and the $\text{C}-\text{H}$ stretching frequency (2909 cm^{-1}) of the aldehyde in Tp and $\text{N}-\text{H}$ stretching frequency (3435 cm^{-1}) of the primary amine all disappear with the formation of the CON. This suggested complete utilization of the starting materials to form the product. FTIR spectra of IISERP-CON1 demonstrated similarity in peak pattern and positions with the model compound. See the $-\text{NH}$ str. ($\sim 3454\text{ cm}^{-1}$), $-\text{OH}$ str. (3250 cm^{-1}) $-\text{C}=\text{N}$ str. (1604 cm^{-1}), $-\text{C}=\text{N}$ (triazolic) str. ($\sim 1401\text{ cm}^{-1}$) and $\text{C}-\text{N}$ str. ($\sim 1256\text{ cm}^{-1}$) bands. Presence of the enol $-\text{OH}$ and imine $\text{C}-\text{H}$ stretching suggests that the COF adopts an enolic form and not the enamine form.

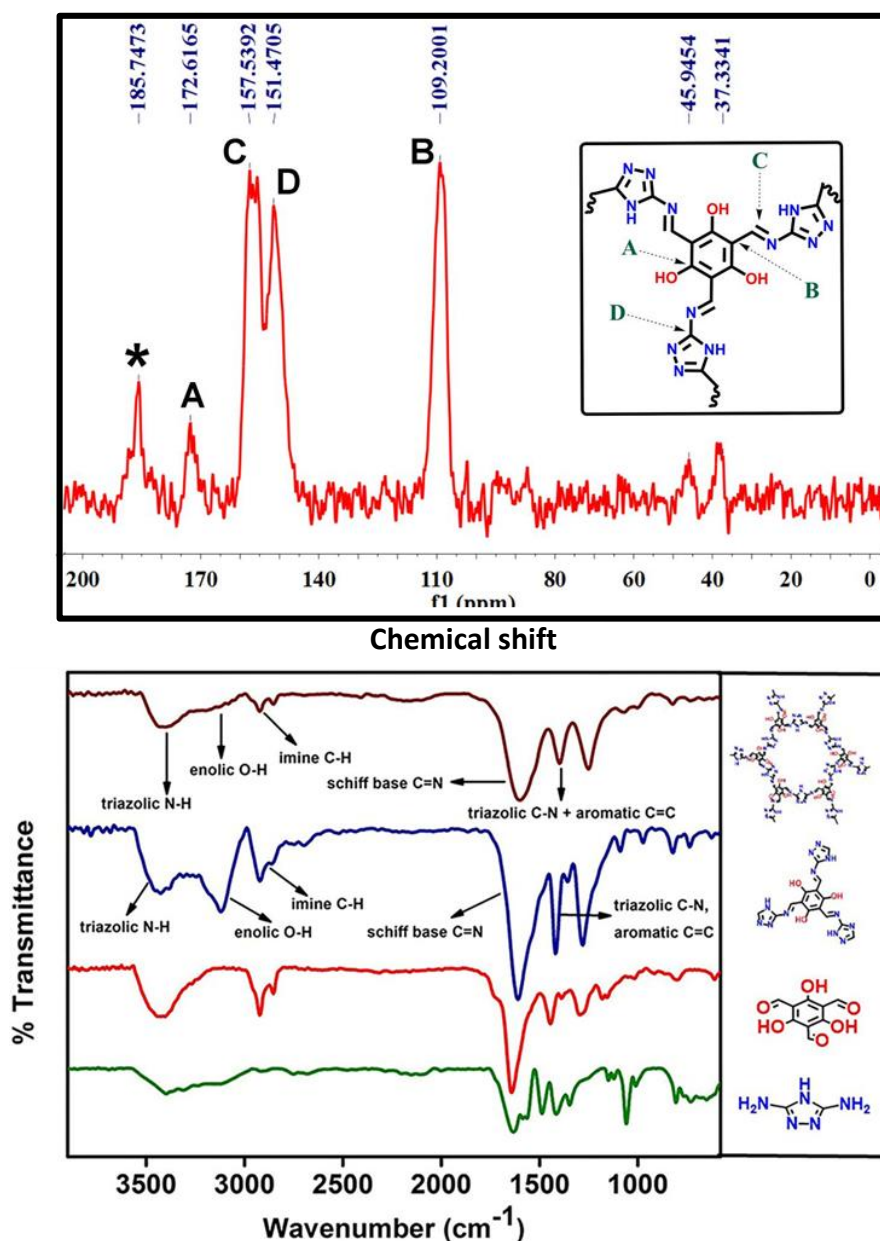


Figure 1.2. (Top) ^{13}C -Solid state NMR of IISERP-CON1. Chemical shift 400 MHz: $\delta= 109.2$ (B), 151.5 (C), 157.5 (D), 172.62 (A) ppm, * - corresponds to unreacted terminal aldehyde and the peaks at $37.33, 45.9$ ppm are due to DMF and methanol, respectively (solvents). **(Down)** Comparison of the FTIR spectra between Triformylphlorogucinol, diaminotriazole, model model compound and IISERP-CON1.

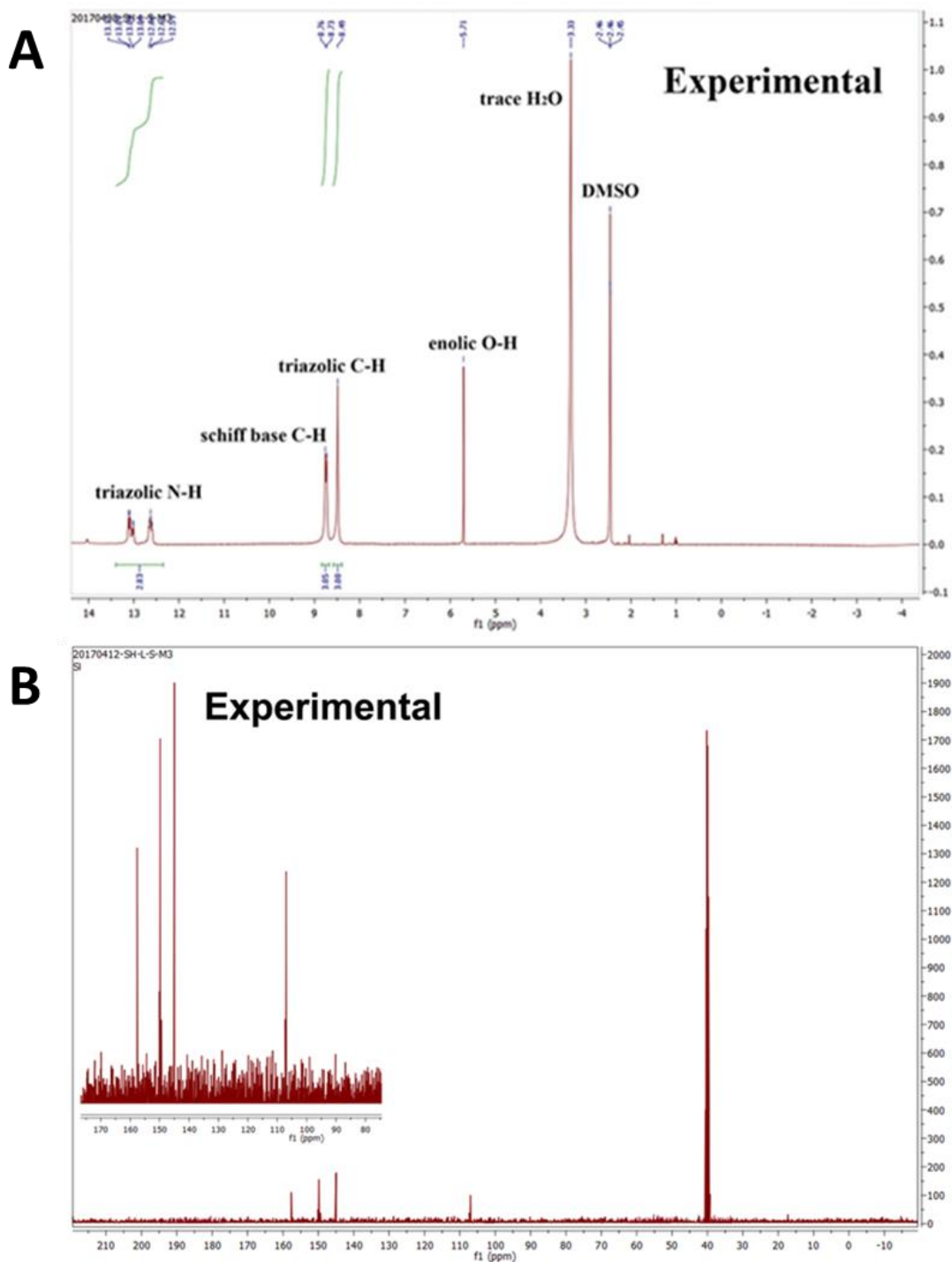


Figure 1.3. (A) ^1H NMR of model compound recorded in DMSO-d_6 at room temperature. Chemical shifts at $\delta = 2.45$ and 3.3 ppm are from DMSO-d_6 and trace amount of water, respectively. (B) ^{13}C NMR of the as-synthesized model compound recorded in DMSO-d_6 .

1.2.2. Structure modeling of IISERP-CON1:

The structure of IISERP-CON1 was modeled in both P3 and P6 symmetry. The experimental PXRD pattern of the powdered material was simulated with the modeled structure and then compared with calculated one (Figure 1.4). Typical reflection of 100 plane is missing here due to lack of exposure of

'*ab*' plane. But a sharp intense peak in the experimental pattern signifies the abundance of '*c*' plane because of exfoliated nature of the nanosheets.

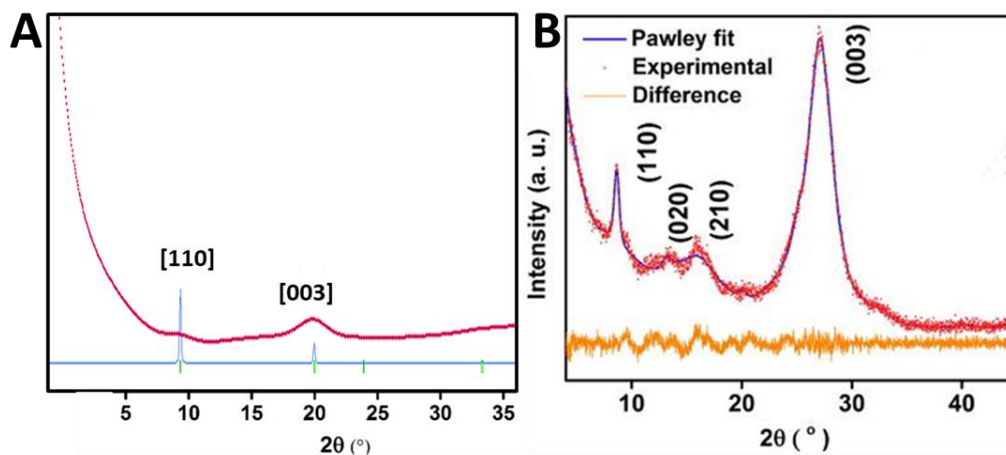


Figure 1.4. (A) A zoom-in on the refined pattern showing the presence of weak intensity at $\sim 2\theta = 9.1^\circ$ corresponding to the 110 reflection. The intensities are significantly lower for this peak owing to the nanosheet structure, which is expected to have significant preferred orientation and less number of atom contributing to this reflection. (B) Pawley fit to the experimental PXRD. Refinement parameters: $R_p = 4.45\%$; $wR_p = 5.80\%$. Remove the figures A and B.

From a Pawley refinement of the PXRD pattern, the structure was modeled in P-6 space group. This model has a 2D structure where hexagonal layers are held together in an eclipsed arrangement by π -stacking phloroglucinol and triazole rings (Figure 1.5 and Table A.1.1). To obtain the lowest energy configuration, we optimized the geometry of the 2D hexagonal model using periodic tight-binding Density Functional Theory (DFT-TB) method. A fully cell and motion group relaxed optimization resulted in a solution in P3 space group, which had 140kcal/mol lower relative energy (Figure 1.6). In this lowest energy structure, the layer flexes around the triazole ring '*pivot*' to form a wavy 2-D stack. The triazole rings now buckle *out-of-plane* and cross-link (120° linker) the phloroglucinol in the *ab*-plane.^[74] The phloroglucinols from the adjacent layers π -stack at distance of 3.47\AA , while the triazole units stack at a distance of 3.26\AA . The nanosheets in this self-exfoliated form do not contain sufficient layers to give rise to strong intensity peaks in the Powder X-ray Diffraction (PXRD) pattern (Figure 1.4 and Figure 1.6). This agrees well with the observations made by Banerjee and co-workers.^[76] Furthermore, the formation of the CON was confirmed from SSNMR and IR spectroscopy (Figure 1.2). Other experimental support for this covalent organic nanosheet structure as the most probable one come from the porosity measurements (Figure 1.7).

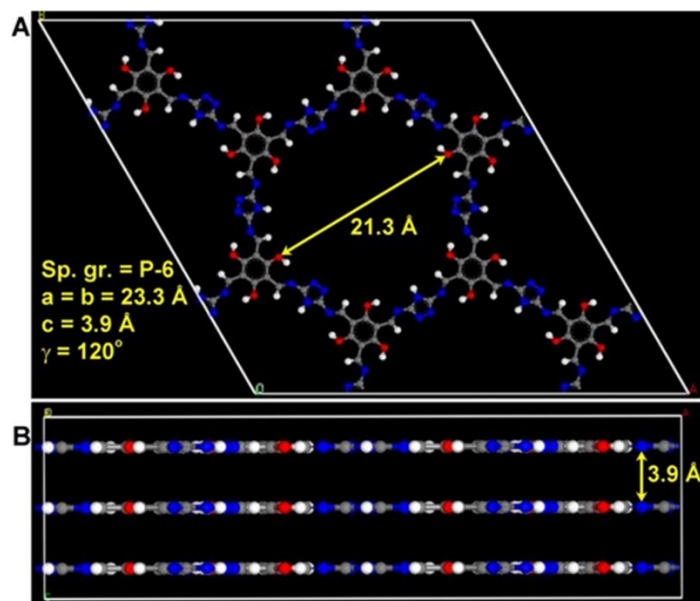


Figure 1.5. A model structure of the IISERP-CON1 obtained using Pawley refinement where a perfectly planar structure (Sp. gr. P-6) with interlayer separation of 3.9Å is shown. This has a energy 140kcal/mol higher than the actual structure proposed for the IISERP-CON1 with buckled layers (Sp.gr. P3).

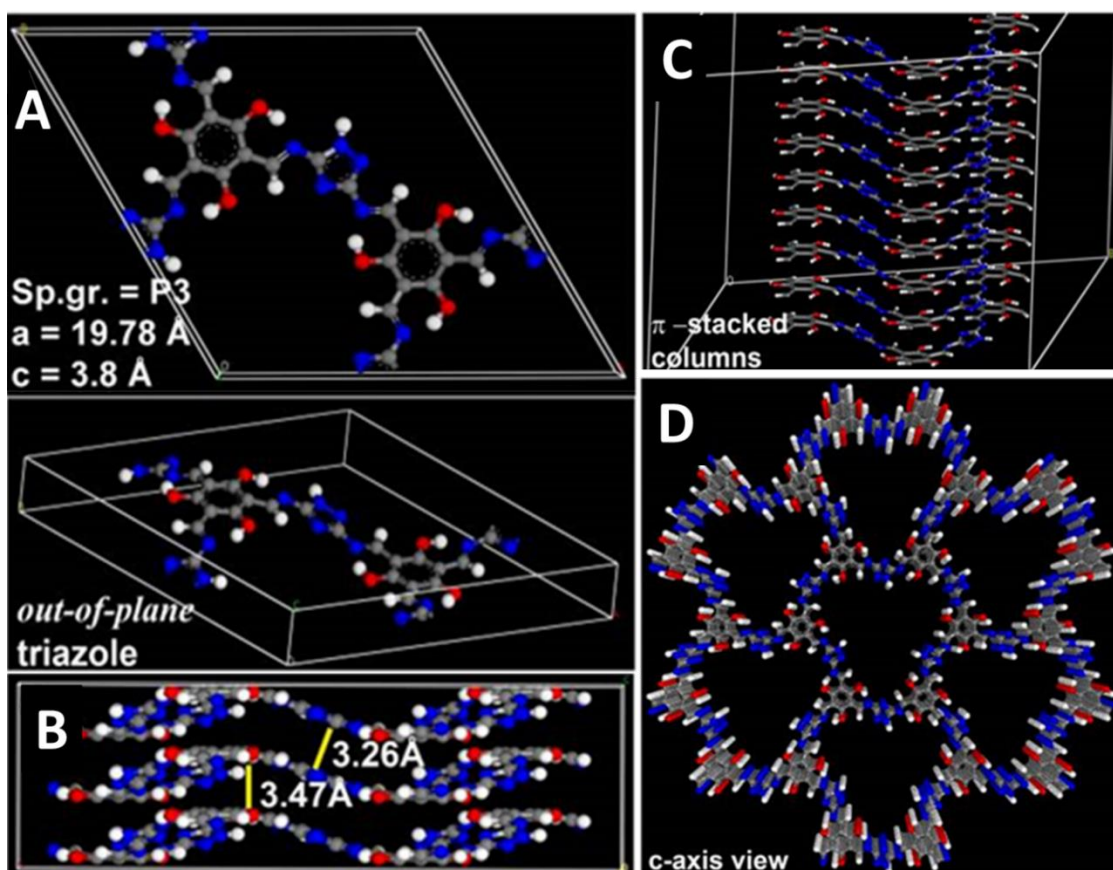


Figure 1.6. (A) Unit cell of IISERP-CON1 modeled in P3 symmetry showing the phloroglucinol units placed in different planes cross-linked by the triazole unit. C- Grey; N- Blue; O- Red; H- White. (B) Buckled layers of IISERP-CON1. (C) Uniform columnar π -stack of phloroglucinol units and the triazole units. (D) Framework structure showing the triangular pores along C-axis with dimensions of 13 (shortest non-covalent atom-to-atom distance) and 16Å (longest atom-to-atom).

1.2.3. Characterization: Porosity and morphology

The IISERP-CON1 shows good N_2 uptake at 77K (~ 220 cc/g in the P/P_0 range of 0-0.8 and a characteristic pore condensation at higher P/P_0 region). Such high uptakes confirm its behavior resembling COF-derived nanosheets.^[54-57,76] The pore size distribution was estimated from the 77K N_2 isotherms using a DFT fit. The majority of the micropores are concentrated around 13 and 17 Å (Figure 1.7A). Few hierarchical mesopores are also present (Figure 1.7B). If the material had adopted a perfectly planar hexagonal sheet structure, there should have been uniform 1-D channels of 21 Å (Figure 1.5), which was not the case. It exhibits a Brunauer–Emmett–Teller (BET) surface area of 507 m^2/g (Figure 1.7C) and a pore volume of 0.37 cc/g (from Non-localized Density Functional Theory (NLDFT), Carbon @ 77K, spherical model). The BET surface area of this CON is notably higher than what has been reported for other exfoliated COFs.^[55,56] However, it is much lower than the theoretically estimated Connolly surface area (2070 m^2/g ; pore volume = 0.57 cc/g; Figure 1.7D). This significant drop in surface area is most likely due to the exfoliated nature of the CON. Typically, exfoliation of COF is known to decrease its surface area to a large extent (Table A.1.2).

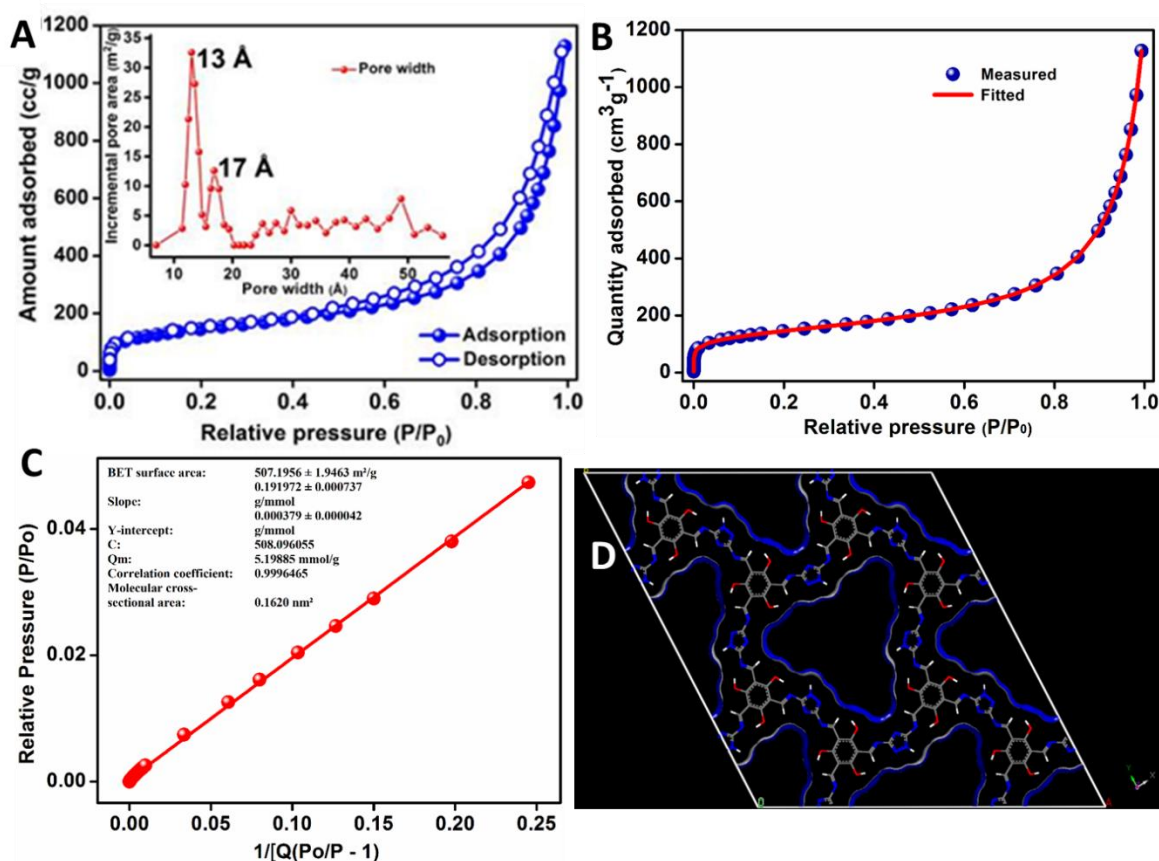


Figure 1.7. (A) Nitrogen adsorption isotherm at 77K. Inset shows the pore size distribution from a DFT fit. (B) A DFT fit obtained using 77 K N_2 adsorption data. (C) BET fits obtained using the 77K N_2 isotherm. Connolly surface representation of a single uni-dimensional channel of IISERP-CON1. (D) Connolly estimated surface area = 2070 m^2/g ; Connolly estimated pore volume = 0.57 cc/g. Probe radius: 1.4 Å; Grid size: 0.15.

The material is practically insoluble in any of the common organic solvents even under boiling conditions, which excludes it from being a mere organic cage or oligomer. The IISERP-CON1 shows good thermal up to 320°C. It is chemical stability towards different solvents, electrolytes and acidic media (Figure 1.8).

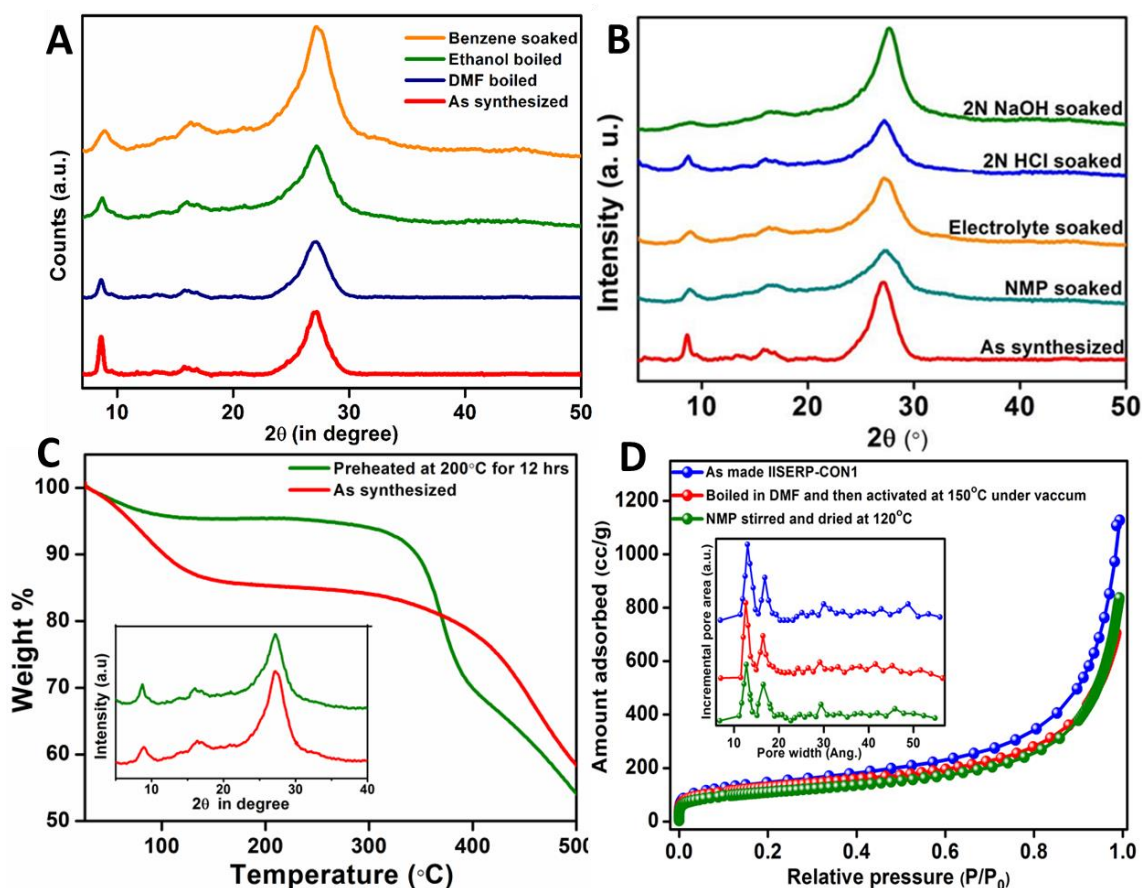


Figure 1.8. (A) PXRD pattern of IISERP-CON1 after boiling in DMF and ethanol, soaking in Benzene for 24 hrs. (B) Chemical stability of the CON from PXRD. No significant alterations in the PXRD patterns are noted which confirms the stability and structural integrity of the CON. (C) TGA profiles of as made and preheated IISERP-CON1, respectively. TGA were done under N_2 atmosphere at 5K/min. Inset: Comparison of PXRD pattern between as made and preheated condition. (D) Comparison of the porosity between the as-synthesized IISERP-CON1, DMF boiled IISERP-CON1 and N-methylpyrrolidone (NMP) soaked and dried at 120°C for 12hrs under vacuum (10^{-4} Torr) showing no change in the pore-structure. Pore size distribution (inset) shows no significant change of pore dimension in all cases. Note: NMP was used as solvent in the electrode making.

The particle size dispersion of the CON in solution was characterized using dynamic light scattering (DLS). Size differences were observed for different solvents due to the difference in the CON's agglomeration tendency. The activated IISERP-CON1 powder was suspended in different solvents and immediately sonicated for 2 min. Particle size in different solvents: DLS performed using the IPA suspension indicated dispersed polymers with a relatively narrow size distribution centered at 670 nm (Figure 1.9A). When this procedure was performed using MeOH, size distribution was centered at 720.2 nm. In contrast, larger sized particles were observed in THF. We note that the size distributions determined from these measurements are inconsistent with those measured by AFM. DLS measurements yield a diffusion coefficient, which is converted to a hydrodynamic diameter (D_h) using the Stokes Einstein equation. And, this is valid for spherical particles. The CON with its high aspect ratio markedly deviates from this spherical nature. Hence the diffusion coefficients carry larger errors. The presence of periodic porosity capable of occluding solvents might further complicate their behavior. However, the results from these DLS studies provide information on the relative sizes of dispersed CON in the solvents investigated, suggesting that exfoliating solvents disperse larger aggregates of 2D polymers. The DLS plot reveals that exfoliation stabilizes larger dispersions. PDIs:

DMF = 0.610; IPA = 0.751; MeOH = 0.867; THF = 0.541. Methanol having its high PDI makes homogeneous clear dispersion of IISERP-CON1. Hence, for all the morphology characterizations we used MeOH dispersion of the CON. The Tyndall effect was observed even after 24 hrs in CON dispersed MeOH solution and hardly any precipitate is observed at the bottom. But the agglomeration is slowly setting in giving rise to turbidity. Yet, being able to maintain the dispersion for several hours gives enormous advantage in electrode preparation and should be suited for other applications which involve formation of thin coatings.

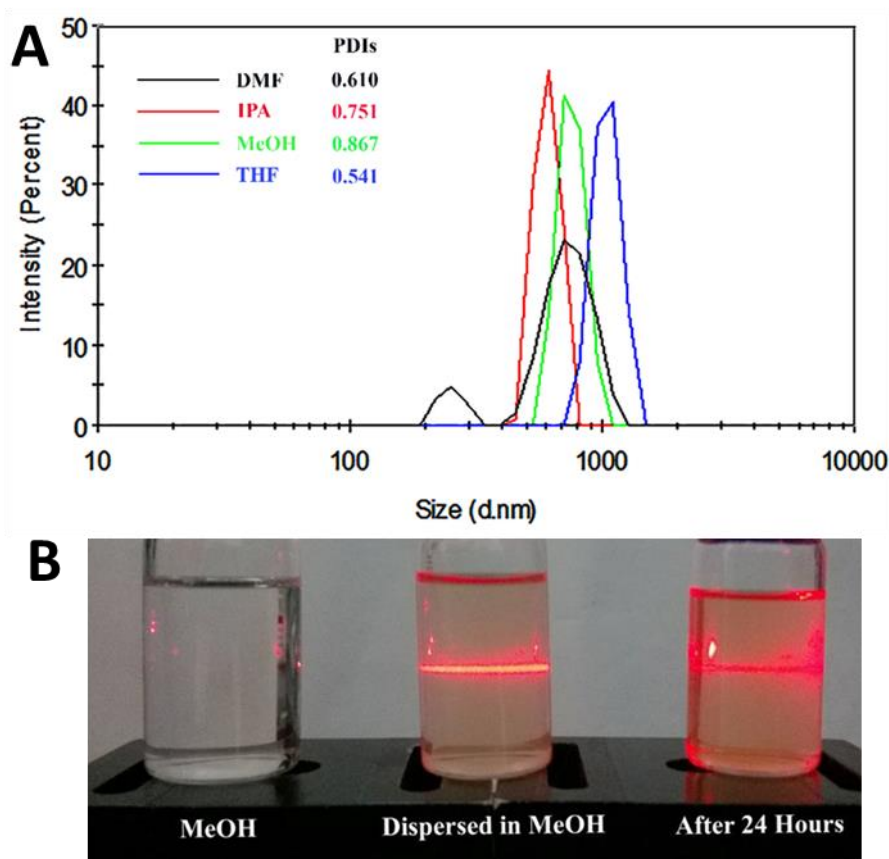


Figure 1.9. (A) A plot showing the DLS intensity trace of IISERP-CON1 obtained from dispersions across several solvents. (B) Tyndall tests using the methanolic dispersion of IISERP-CON1.

Under the FE-SEM, the CON shows a flaky morphology reminiscent of commercially available high surface area Graphenes (Figure 1.10A, Figure 1.10B, Figure A.1.1-A.1.3).^[77] Furthermore, the FE-TEM images of the CON shows a morphology archetypical of exfoliated COF- thin layers rolled up appearing as wavy flakes resembling HRTEM images of Graphenes (Figure 1.10C).^[78] In a higher resolution FE-TEM image (5nm), the fine porous surface of the nanosheets could be observed (Figure 1.10C). FE-TEM image of the CON under different magnifications showed the nanosheets occurring as very thin flakes formed by stacking of few sheets. Some of these sheets wrapped around the edges giving rise to the darker regions under the TEM. Other darker regions are from the inter-growing nanosheets.

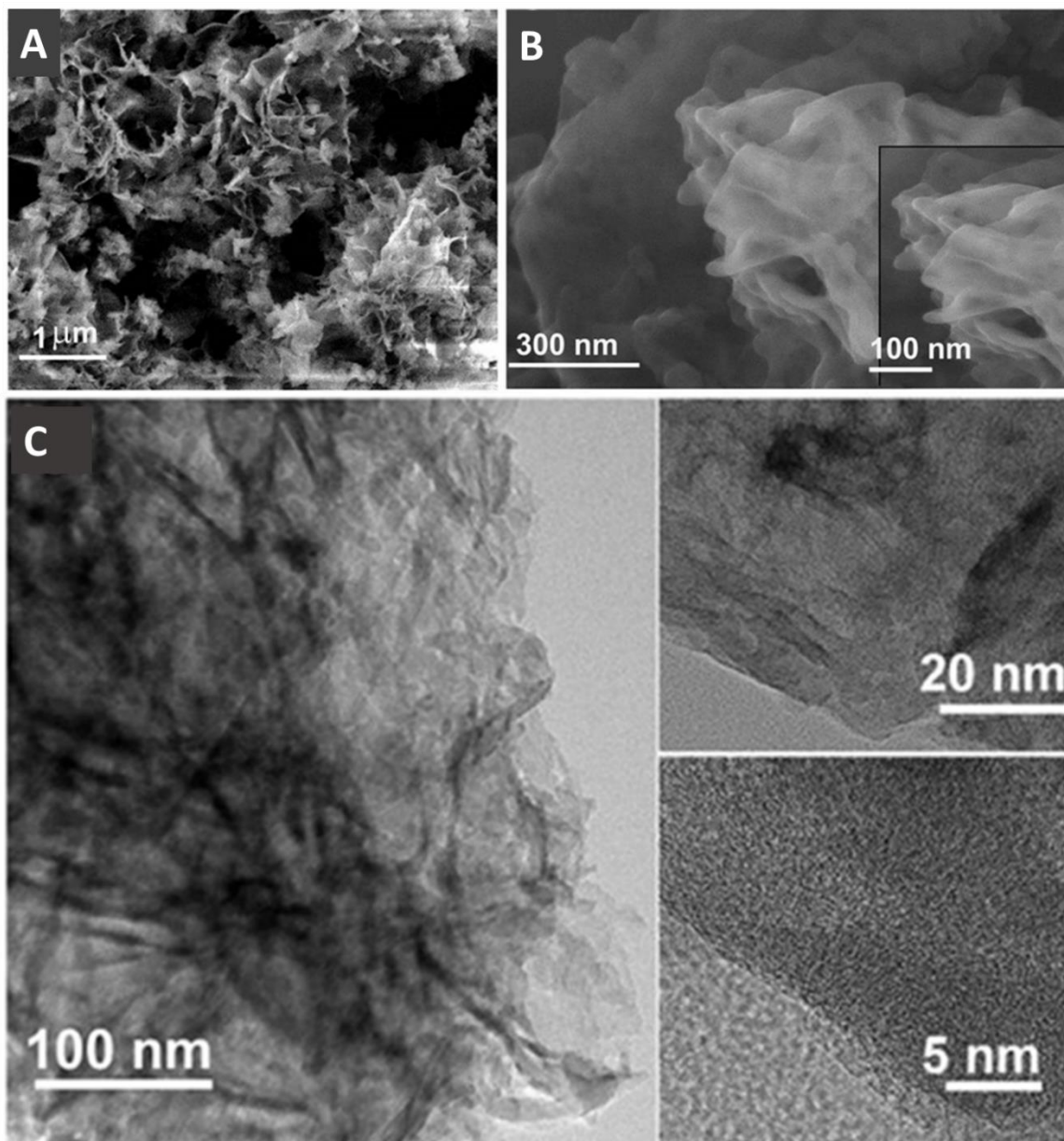


Figure 1.10. (A) FE-SEM image of IISERP-CON1 showing the flaky morphology. (B) Higher resolution FE-SEM showing stacking of very thin nanosheets. (C) FE-TEM image showing the thin layers of the nanosheets with inundated or wrinkled surface and at higher resolution the sub-nanopores on the surface of the nanosheets can be seen.

Another strong evidence for the presence of few-layers-thick nanosheets comes from the AFM. The height profile and the dimensions extracted from the AFM images of a drop-casted sample showed most of the nanosheet's have thickness in the range of 2 - 6nm, which correspond to about 5 - 15 layers of the COF and nanosheets' length falls within 1000 nm. So the nanosheets' aspect ratio (height/lateral length) ranges < 0.1 These are typical dimensions observed in exfoliated COF.(*Bunck et.al JACS. 2013, 135, 14952*). (Figure 1.11, 1.12, Figure A.1.4-A.1.5). Also, the contact angles between the nanosheets and the substrate fall in the range of $< 1^\circ$, suggesting that the surface of the nanosheets is almost flat having no curvature (Figure 1.13). These features are consistent with previous observations on exfoliated nanosheets.^[76,79,80]

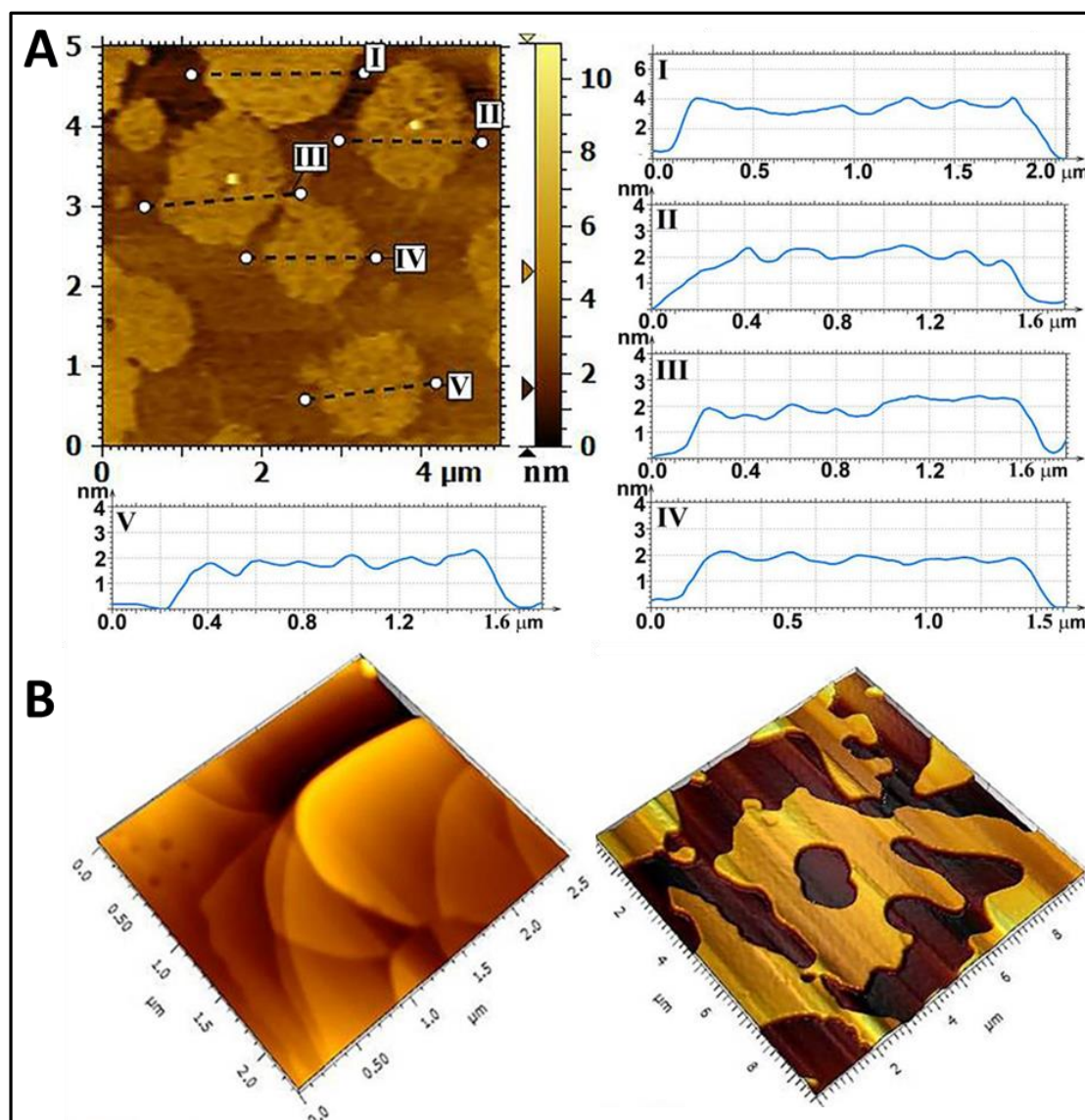


Figure 1.11. (A) The AFM image showing the thickness of the drop-casted sample. The height profile plot quantifies it to be in the range of ~ 2 -4nm. (B) 3D view from different regions of drop-casted sample prepared in MeOH.

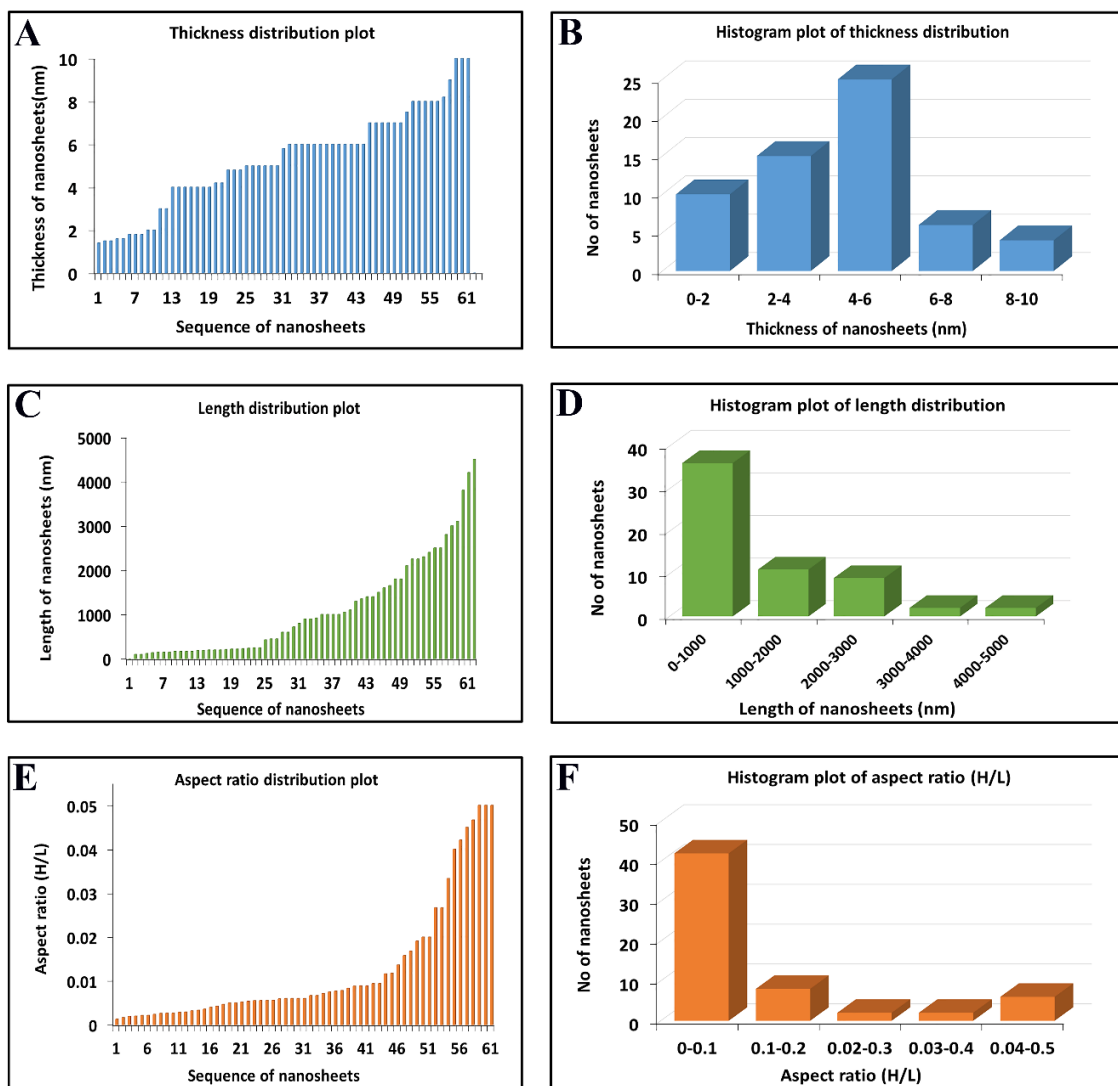


Figure 1.12. (A) Thickness distribution plot of self-exfoliated nanosheets. (B) Histograms of the thickness distribution. (C) Lateral length distribution plot of self-exfoliated nanosheets. (D) Histogram plot of lateral length distribution. (E) Aspect ratio (H/L) distribution plot of nanosheets. (F) Histogram plot of the aspect ratio distribution.

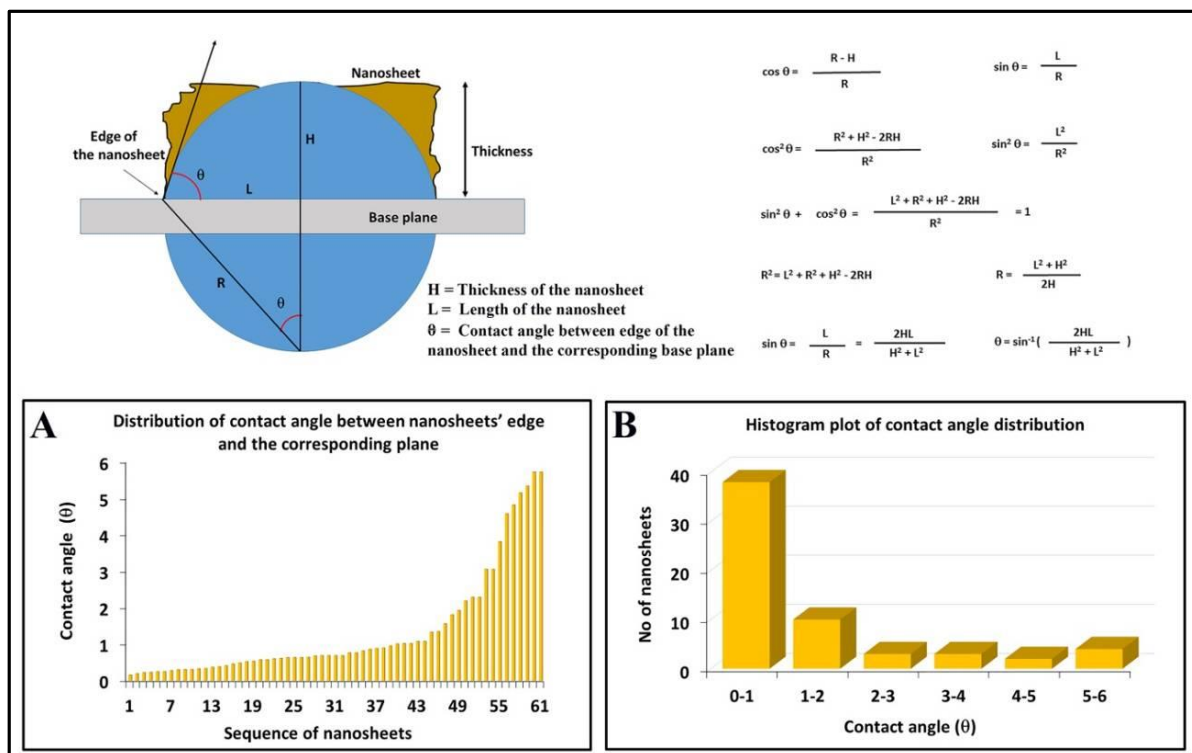


Figure 1.13. Calculation of contact angle between the nanosheet's edge and the substrate plane. **(A)** Distribution of contact angle of the nanosheets with the base plane. **(B)** Histogram plot of contact angle distribution. Most of the nanosheet's contact angle falls in the range of 0-1°, suggesting that the surface of the nanosheets is almost flat having no curvature. Note the dimensions have been extracted from the AFM images. (Xia *et al. Adv. Energy Mater* 2013, 23, 4684).

1.2.4. Electrochemistry: Coin-cell- cyclic voltammetry and galvanostatic charge-discharge cycling

Having obtained the porous structure with multiple organic functionalities (-OH, -C=N-, triazole rings and aromatic carbons) that can interact with inorganic cations and considering its exfoliated-carbon-like morphology, we investigated the potential of this material as an anode in Li-ion battery. For this purpose, IISERP-CON1 was activated by heating at 150°C under vacuum for 24 hrs. 75% of CON, 25% Super-P carbon & 10% PTFE binder were mixed by grinding thoroughly in a dry and clean mortar-pestle. N-methylpyrrolidone (NMP) was added drop by drop to make a highly viscous slurry. The slurry was coated on a copper foil to make an electrode containing the nanosheets. It was placed in a vacuum oven at 120°C for 24 hrs. The CON coating on the copper foil (electrode) remained non-leachable to this drying procedure and no visible cracks appeared (Figure 1.14). Thus coated electrodes were cut in accordance to the size of 2032 coin-cell. This aptly cut electrodes were again dried under vacuum at 80°C before taking into the glove box. Then coin-cells were prepared inside the glove-box. LiPF₆ dissolved in 1:1 ethylene carbonate and dimethyl carbonate was employed as the electrolyte and about 2% (v/v) of fluoro ethylene glycol solvent was added to prevent the formation of the solid electrolyte interphase after the 1st discharge cycle.

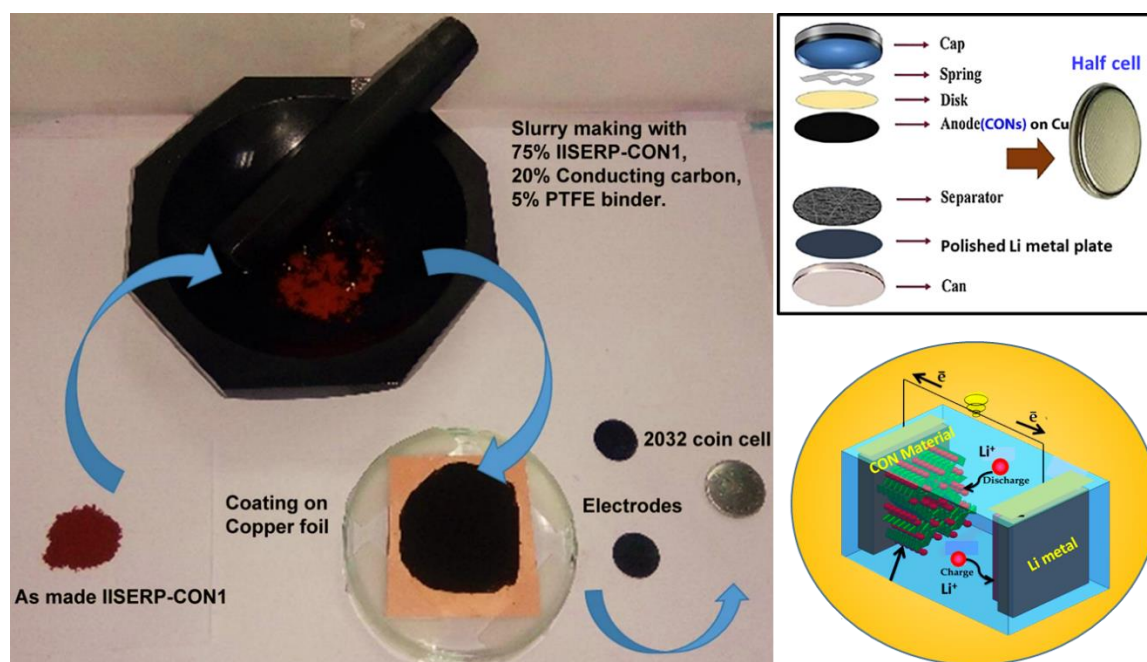


Figure 1.14. Schematic representation of coin-cell preparation for electrochemical measurements. (See experimental section for the preparation procedure). Note: From the charge-discharge set-up the Open Circuit Voltage of the coin-cells were determined to be $\sim 3\text{V}$. *In a half cell Li metal plate itself works as reference electrode. Discharging means lithiation of CONs. Charging means delithiation of CONs. In all electrochemical measurements the potential has been measured with respect to Li/Li⁺ half cell.*

To investigate the Lithium insertion-deinsertion characteristics of the CON, we engaged this coin-cell (2032) assembly connected to a charge-discharge unit. A cyclic voltammogram (CV) was measured using a 0.2mV/s sweep-rate in the potential window of 0.01 to 3V (Figure 1.15). In its 1st cycle, the CV showed a prominent peak at 0.48V corresponding to the formation of Solid Electrolyte Interphase (SEI) layer and the corresponding current is -0.36mA .^[81,82] The Li_2CO_3 , Li_2O formed from the decomposition of the electrolyte during this SEI layer formation, can react irreversibly with the unreacted aldehydes present in the CON (red shaded area). Importantly, the specific capacity, we report here, are from the higher cycles and this value is high and is stable over all the cycles (100 cycles). This means no undesirable irreversible Li-CON reactions are observed, except for the small amount in the first cycle (which is expected). From the 2nd cycle onwards, the peak due to the SEI layer formation diminished leaving a stable CV. The sharp peak at very low potential ($\sim 0.02\text{V}$) suggests effortless intercalation of Lithium into the nano-sheets. The second significant peak at 1.0V appears as a broad feature. Importantly, this peak arising from chemical interactions is notably weaker compared to what is reported for other COFs and organic materials which form true covalent bonds with Lithium.^[61,64,83]

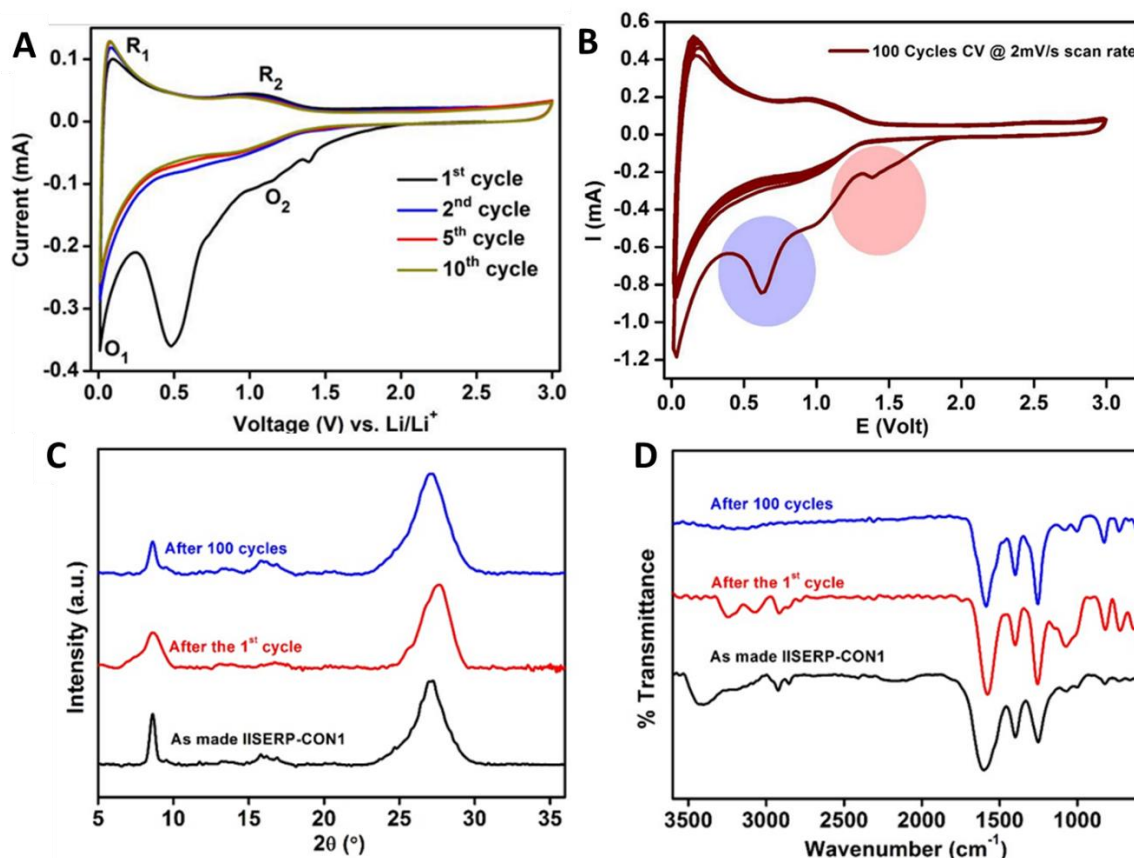


Figure 1.15. (A) CV curve showing the presence of two redox peaks due to the intercalation (0.02V) and weak binding ($\sim 1V$) of Lithium into the CON. (B) Cyclic voltammogram of IISERP-CON1 loaded coin-cell for 100 cycles. The first cycle looks significantly different from the subsequent ones because of the SEI layer formation (blue shaded area). Post CV stability of the CON from (C) PXRD and (D) IR. Note the 100 cycles represents samples subjected to 100 cycles of charge-discharging.

To verify, if there was any capacitive mechanism involved in the Lithium loading and to confirm that the broad peak at 1.0V is not merely due to a poor resolution from faster scan rate, a variable scan rate CV was performed (0.1- 10mV/s; potential window: 0.01 - 3V) (Figure 1.16A and 1.16B). The peak profiles remained the same. A fit to the power law, $i = av^b$ (i = current; v = scan rate), resulted in $b=0.5$ @0.02V which obeys Cottrell's equation suggesting that the Lithium loading operated mostly via a diffusion-controlled intercalation mechanism (Figure 1.16C).^[84,85] While the 'b' values (Table 1.1) of 0.93 @1V and 0.86 @2.5V suggest only a little contribution from the surface-controlled charge storage behavior (capacitive). Also, the anodic peak currents vary linearly with the square root of the scan rate suggesting that the process is mostly mass transfer controlled (Figure 1.16D).^[86] The mechanism of charge storage can be due to either charge transfer or mass transfer or both. Typically, the charge transfer process involve short time scales and rapid kinetics, on the other hand mass transfer processes happen at relatively longer time scales giving rise decreasing capacity with time. This can be established from a plot of the peak current vs. square root of the scan rate. The anodic peak current of IISERP-CON1 increases linearly with square root of scan rate demonstrating that the kinetics associated with the redox-reaction is dominated by Li-ion diffusion in the bulk materials (*Xing et al., Sci. Rep.* **2016**, 6, 26146).

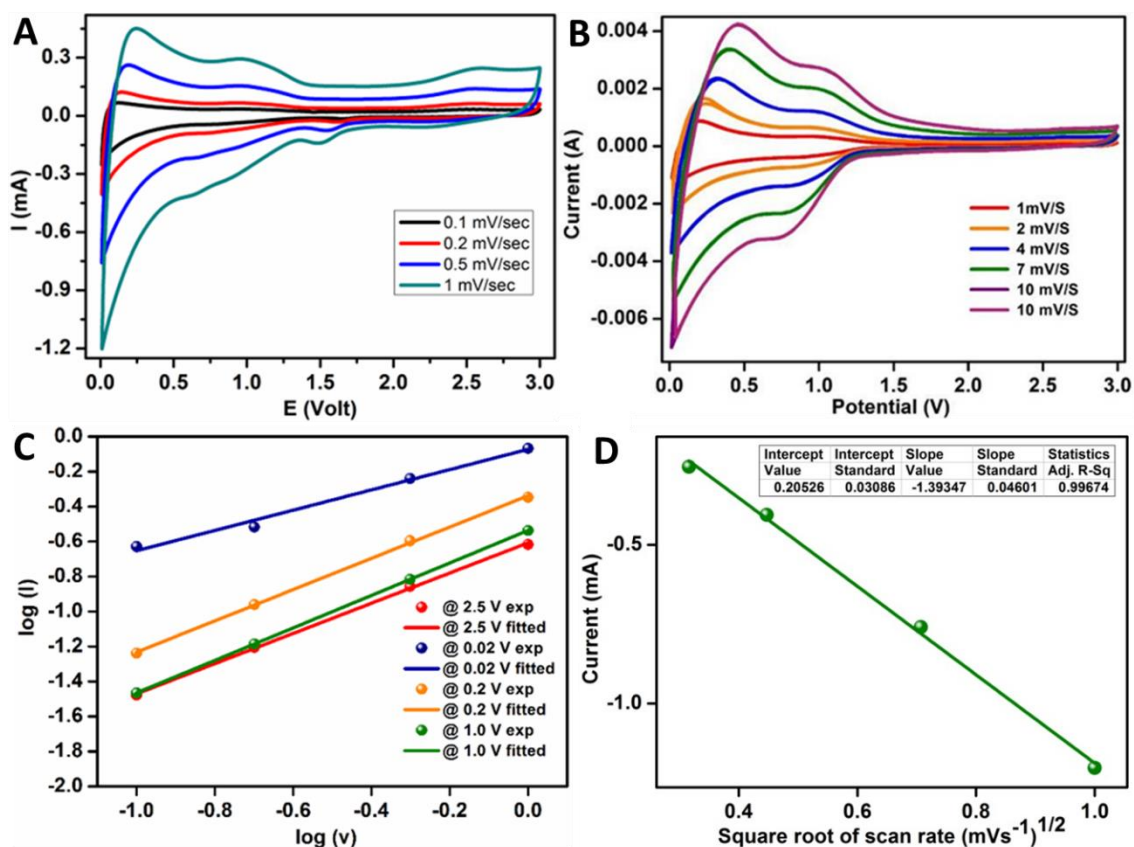


Figure 1.16. (A) and (B) Cyclic voltammogram plot of IISERP-CON1 loaded coin-cell measured at different scan rates. Increment of current density with the increment of scan rate indicates capacitive type behaviour. The first cycle involving the SEI layer formation has not been shown for clarity. (C) Logarithm of peak current intensity (anodic) vs. logarithm of scan rate at different potentials extracted from CV plots. Note the linear increment of peak current with the increase of current density. (D) The linear fit of anodic peak current vs. square root of scan rate of IISERP-CON1.

Table 1.1: Fitting parameters for the data from variable scan rate CV.

Potential (V)	Intercept value	Intercept standard error	Slope value	Slope standard error	Statistics adj. R-square
2.5	-0.60709	0.00968	0.86326	0.01541	0.99904
0.02	-0.07246	0.02739	0.57959	0.04359	0.98322
0.2	-0.33808	0.00923	0.89408	0.01468	0.99919
1.0	-0.53642	2.78641E-4	0.9286	4.43466E-4	1.00000

This would mean that the high specific capacity depends significantly on the mobility of the Lithium ions within the bulk of the CON. To establish this, the Warburg coefficient was calculated from the ac-impedance measurements and was fitted into the standard ionic diffusion expression (Figure 1.17). The notable less value of Warburg coefficient for IISERP-CON1 made coin-cell confirms the reduction of the hindrance of diffusion on the battery performance for these self-exfoliated nano sheets.

Li-ion diffusion coefficients were obtained by electrochemical impedance spectroscopy (EIS) and derived from Eq. (3):

$$D = 0.5(RT/AF^2\sigma C)^2 \dots\dots\dots \text{Equation (3)}$$

where R is the gas constant ($8.314 \text{ J mol}^{-1} \text{ K}^{-1}$), T is the temperature (298.5 K), A is the area of the electrode surface (1.14 cm^2), F is the Faraday's constant ($9.65 \times 10^4 \text{ C mol}^{-1}$), C is the molar concentration of Li^+ , and σ is the Warburg coefficient. The Warburg coefficient σ can be obtained from

$$Z_{re} = R_e + R_{ct} + \sigma \omega^{-0.5} \dots\dots\dots \text{Equation (4)}$$

where σ is the slope for the plot of Z_{re} vs. the reciprocal root square of the lower angular frequencies ($\omega^{-0.5}$). The obtained σ for IISERP-CON1 before cycling is 34.8. As a consequence, it gives a D^{Li^+} of $5.48 \times 10^{-11} \text{ cm}^2 \text{ s}^{-1}$. This is quite comparable to those found in other graphitic as well as 2D inorganic materials with large Lithium mobility.^[87-94]

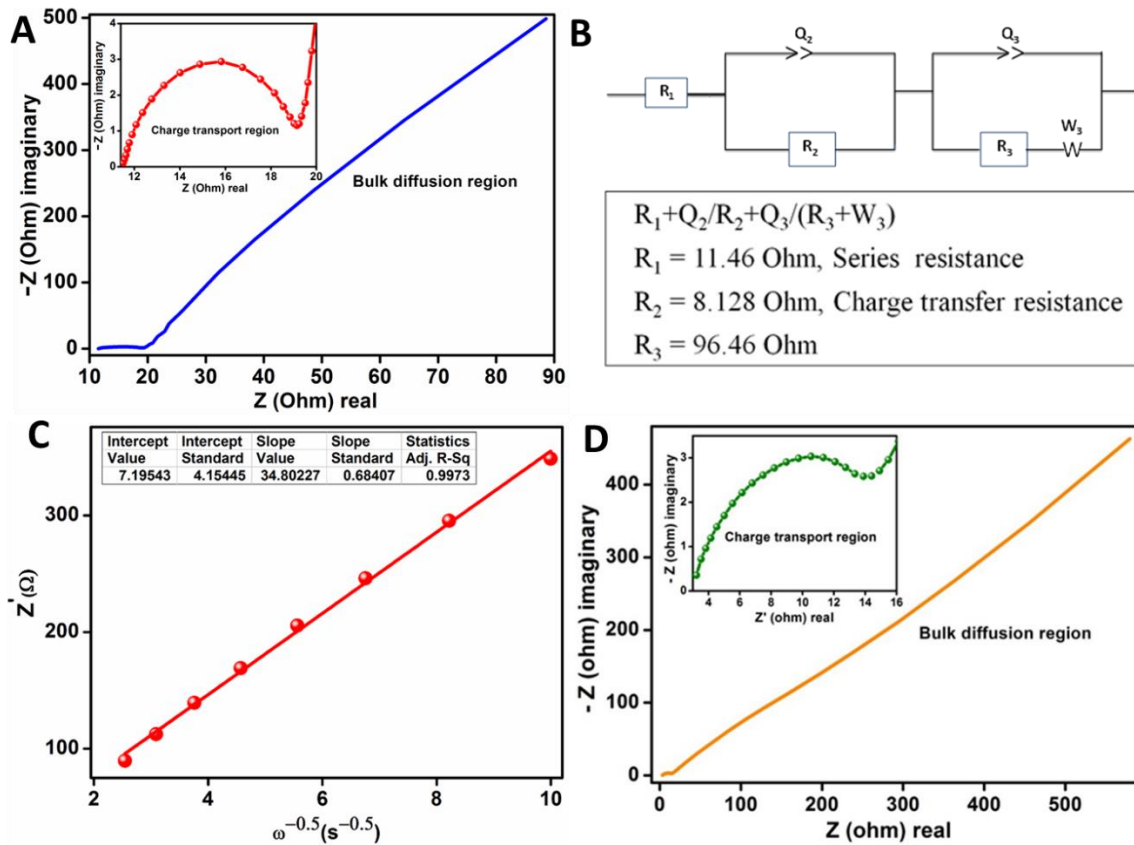


Figure 1.17. (A) Nyquist plots of IISERP-CON1 electrode after completion of SEI formation in first cycle (blue curve) . Inset: a zoom-in showing the intercepts. (B) The resistance of the IISERP-CON1 Li-ion coin-cell fabricated was simulated from the impedance measurements using an equivalent circuit of $R_s(Q_2(R_{ct}Z_w))$, where R_s is the ohmic resistance of solution and electrode, R_{ct} is the charge transfer resistance, Q is the double layer capacitance, and Z_w is the Warburg impedance. Note: The resistances extracted from the equivalent circuit model clearly displays the low resistive nature of the CON derived coin-cells. These resistances do not vary even after 100 cycles of charge-discharge suggesting that there is very less ohmic loss. (C) The plot of Z_{re} vs. the inverse square root of angular frequency (ω) for the IISERP-CON1 coin-cell. The slopes of the fitted lines represent the Warburg coefficient σ . (D) Nyquist plots of IISERP-CON1 electrode after completion of SEI formation after 100 cycles (orange curve).

Galvanostatic charge-discharge sweeps at a constant current density of 100 mA/g corroborate well with the I-V features in the CV curves (Figure 1.18). A peak centered at 0.48V in the CV (Figure 1.15A) denotes the formation of SEI layer in the first discharge cycle, which corresponds to the very high initial discharge capacity of 2060 mAh/g (Figure 1.18A). In the 2nd cycle, the capacity drops to 835 mAh/g as the SEI layer formation walks away. Following this, over 100 charge-discharge cycles were carried out. The cell maintains high and stable discharge capacity of 720 mAh/g (@100 mA/g) during this prolonged cycling, which essentially confirms the potential of our material to act as a stable Li-ion battery anode. Also, the CON-derived Li-ion cell desirably has a low resistivity. AC-impedance measurements revealed that the cell carries a series resistance as low as 11.46 Ω and a charge transfer resistance of 8.13 Ω (Figure 1.17A). Furthermore, only a small drop in specific capacity (150 mAh/g) is observed even at current density as high as 1 A/g (Figure 1.18B). The charging capacity in the corresponding cycles is compatible with the discharge capacities leaving a coulombic efficiency almost of 100% in every cycle (Figure 1.18C). In comparison, other nano-structured materials with high specific capacities for Li-ion battery show significant drop in capacity with both increasing current density and prolonged cycling.^[61,71,81,83,95-98] And, this has been explained by the formation of some highly energetic redox species which bind irreversibly with the Lithium during the battery cycling.^[71]

The exfoliated-COF structure and hierarchical pores most probably assist this faster Lithium diffusion into shortened paths compared to a highly stacked COF, where the slower kinetics would increase the contact time with the active sites leading to unwelcome irreversible chemical binding. However, it is essential to have the covalently bound extended framework structure to realize the observed intercalation assisted Lithium charge-discharge.

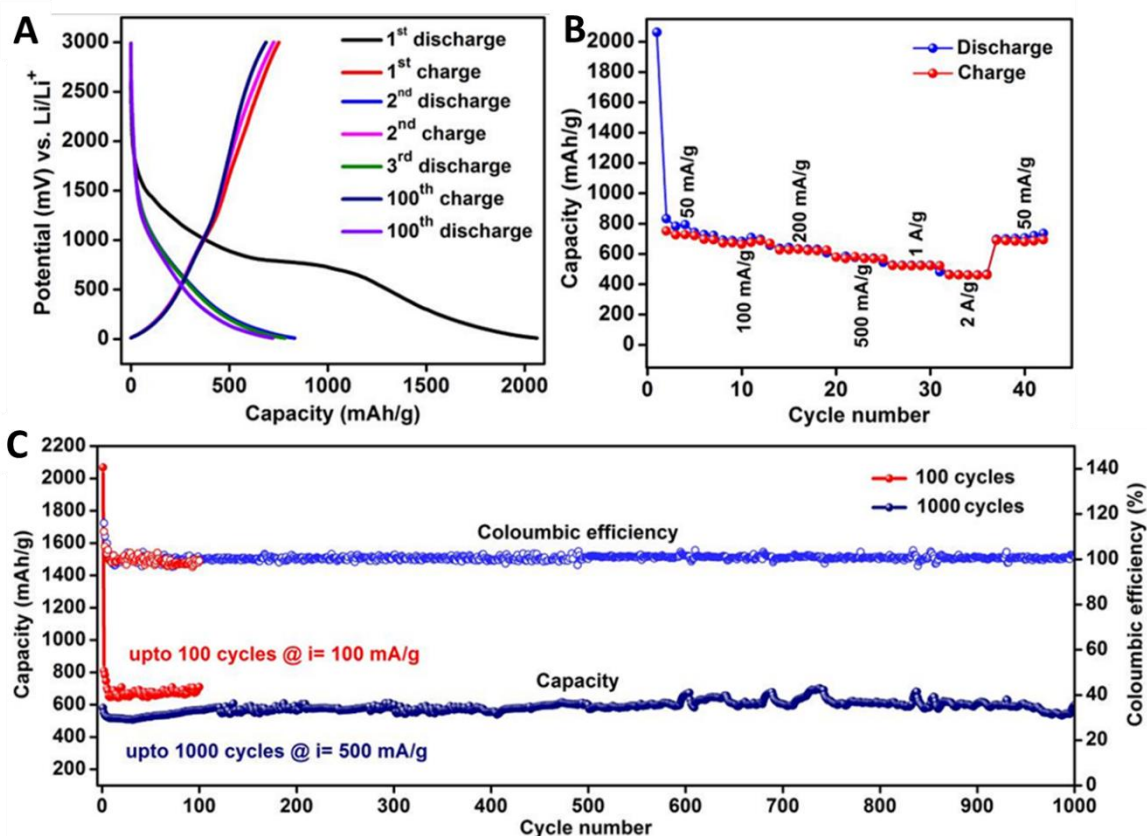


Figure 1.18. (A) Galvanostatic charge-discharge cycling measurements showing the high cyclability. (B) Rate performance plots for IISERP-CON1. (C) Capacity retention and 100% columbic efficiency over 100/1000 cycles.

For instance, when we carried out the charge-discharge cycles and the CV using the model compound formed by reacting the trialdehyde involved in the construction of IISERP-CON1 with 3-amino-1,2,4-triazole, the capacity was only 140 mAh/g (Figure 1.19). Moreover, in the CV, the intercalation peak expected at 0.02V was missing while the other peaks due to chemical interaction, observed for the IISERP-CON1, could be seen (Figure 1.19A). Unlike in the CON, here there is no significant intercalation peak at low potential due to the lack of a π - π stacked structure. While above 0.6V, peaks due to reversible chemical interactions can be observed. Just as in the CON, here too the first cycle is noticeably different than the subsequent cycles due to SEI layer formation (blue shaded area) and some chemical interactions between the Lithium and the model compound (red shaded area). In fact, the weak peaks at 2.2V occur only from the second cycle and this is clearly absent in the CON. Thus the model compound seems to have more interactions with Lithium at higher potentials. This could be due to the higher basicity of the triazole rings (formed from aminotriazole) in the model compound and its increased accessibility (being terminal groups). Interestingly, the Lithium insertion into the model compound is completely reversible with 100% columbic efficiency (Figure 1.19D). Meaning, the triazole units coupled with the phenolic triformyl units and its C₆ rings form modules capable of providing reversible chemical interactions with Lithium. This capability is retained in the CON

constructed from these modules. The presence of these weak interactions between the enolic model compound and the Lithium is confirmed from $^1\text{H-NMR}$ (Figure 1.19E).

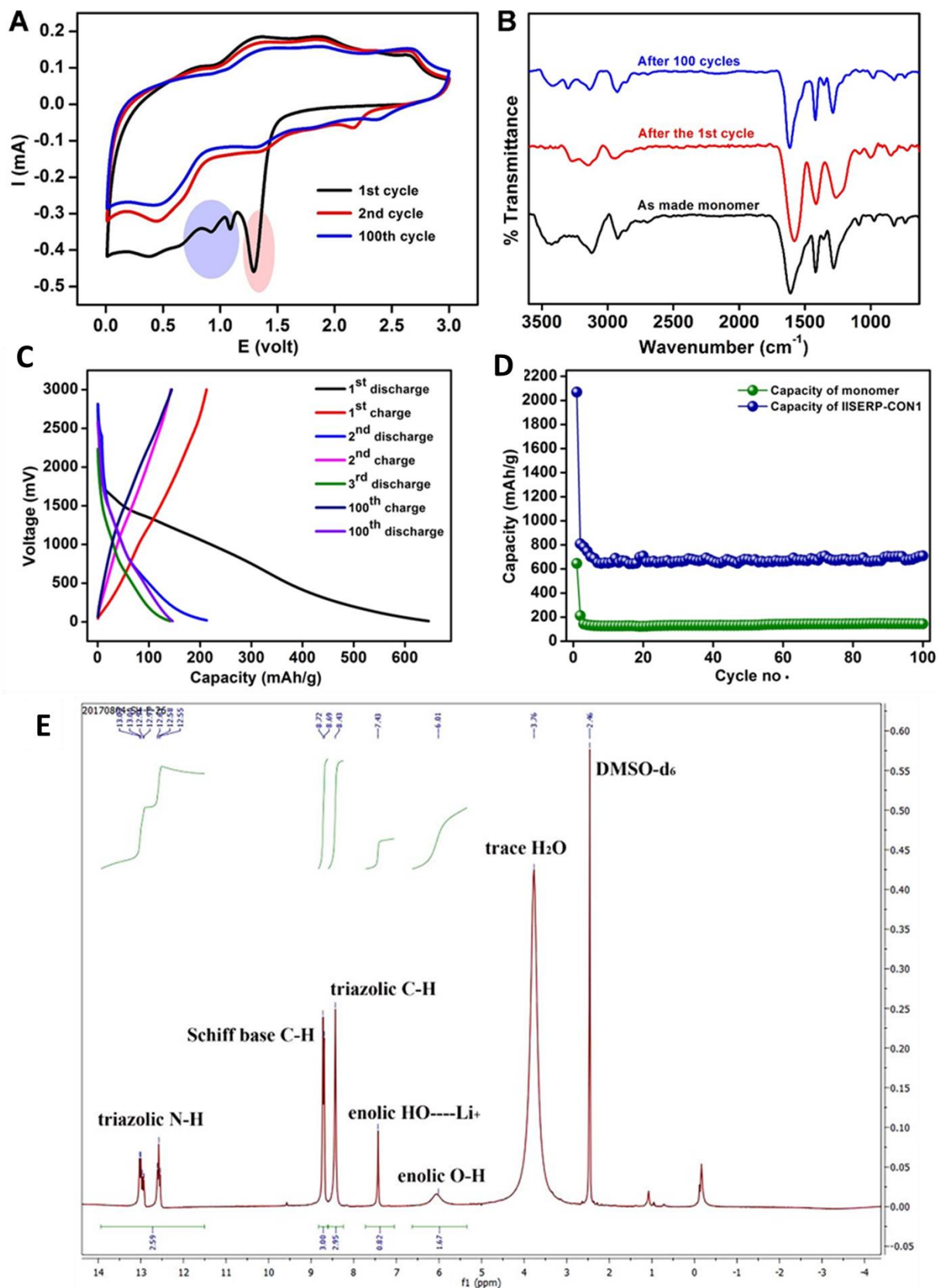


Figure 1.19. (A) Cyclic voltammogram of the model compound (model compound) loaded coin-cell, showing the 1st cycle, 2nd cycle and the 100th cycle (B) Post CV stability of the model compound from IR. Note the 100 cycles represents samples subjected to 100 cycles of charge-discharging. (C) Comparison of the cycle performance at a current density of 100 mA/g for IISERP-CON1 (blue curve) & model compound (green curve). (D) Galvanostatic charge-discharge curves for the model compound. (E) ¹H-NMR spectra of the model compound reacted with LiCl in DMSO-d₆. Clearly the Lithium interacts with the enol form of the compound.

1.2.5. Stability of IISERP-CON1 under electrochemical potential

The electrochemical cyclic stability of the CON was confirmed from complete retention of its redox activity (from CV) even after 100 charge-discharge cycles (@100 mA/g) (Figure 1.20A) and 98% retention of its capacity even after 1000 galvanostatic charge-discharge cycles (@500 mA/g). AC-impedance measurements indicated no change in resistance of the cycled cell (Bulk resistance: R = 19 Ω (before); 18.5 Ω (after)), which suggests the lack of any ohmic loss or material degradation (Figure 1.17D).^[87] To further substantiate the integrity of the CON under the applied electrochemical stress, an electrode with neat CON in NMP, without using any conducting carbon, was subjected to 100 charge-discharge cycles. From PXRD, IR and FE-SEM measurements (Figure 1.20B-1.20D), we confirmed that the post-cycling material retains crystallinity and its chemical structure. In the IR, a few new peaks appear at lower wave numbers, which can be attributed to the weak Li-framework interactions (Figure 1.20C). This stability is true for the model compound too.

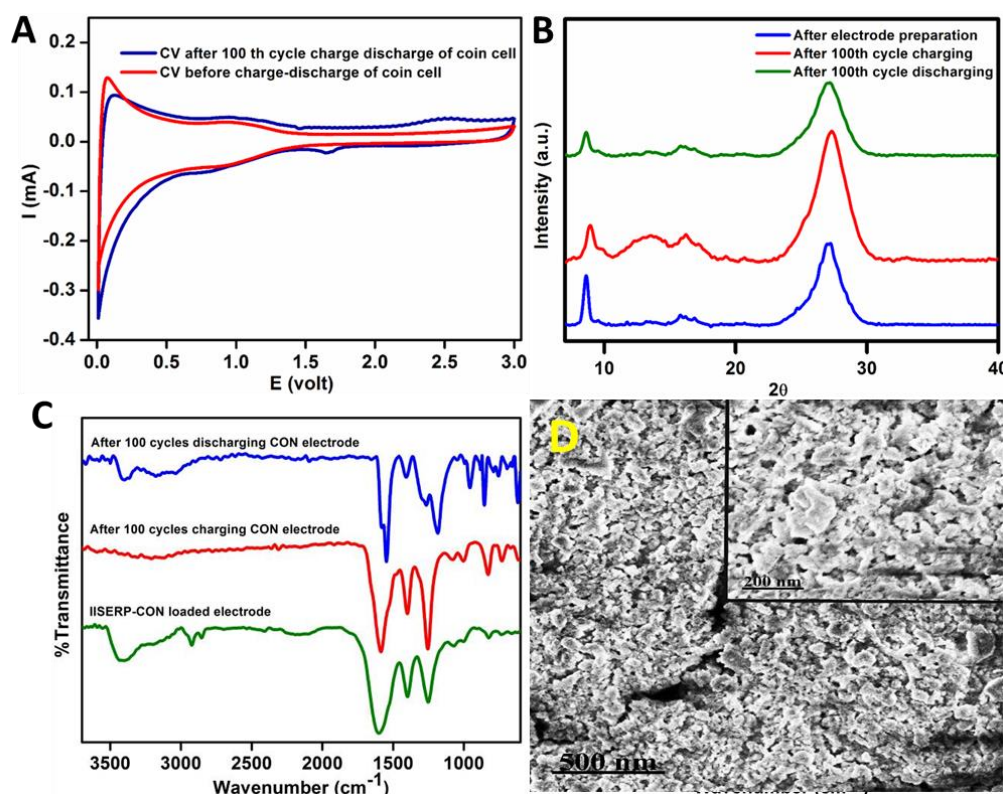


Figure 1.20. (A) Cyclic Voltammogram plot of IISERP-CON1 loaded coin-cell just after completion of SEI formation in first cycle and after 100cycles. Note: No significant change of CV profile peak position was obtained. That suggests no degradation of electrode was happened even after 100th cycle corresponding to no capacity loss. (B) PXRD pattern of IISERP-CON1 made electrode without any conducting carbon using before and after 100th cycle charge-discharge. The noticeable hump at $2\theta = 12-14^\circ$ is due to the Lithiation and as can be seen, it disappears upon discharging. (C) Comparison of the FT-IR spectra of IISERP-CON1, before charging-discharging and after 100 charging-discharging cycles. There was no significant change observed in the characteristic peaks (carbonyl (-C=O) at 1665 cm^{-1} ; -NH str. and -OH str. ($\sim 3454\text{ cm}^{-1}$); -C=N str. (1604 cm^{-1})).

¹); -C=N (triazolic) str. (~1401 cm⁻¹) and C-N str. (~1256 cm⁻¹) bands. **(D)** FE-SEM image in different magnification after 100th cycle discharging. There is no noticeable aggregation between particles or growth into larger particles via Ostwald ripening.

1.3. Computational studies:

1.3.1. Simulated structure of Li@CON: Li-framework interactions from model and XPS

To shed light into the CON's structural contributions towards this high and reversible Lithium storage capacity, we employed simulations.^[11,12,22,23,99] From the observed capacity 720 mAh/g, the number of Lithium ions stored per formula unit of the CON was calculated to be 16 (Figure 1.21A-1.21B).

Calculation of Lithium concentration in the Li@CON from the specific capacity:

1 mAh = 3.6C = 2.2×10^{19} number of electron or Li⁺.

Here, for the IISERP-CON1 based coin-cell we observed a specific capacity of 550 mAh/g in the potential region of 0.01- 0.5V (This potential window represents the intercalation region observed in the CV).

This would yield the number of Li⁺ ion = $2.2 \times 10^{19} \times 550 = 1210 \times 10^{19}$.

Thus, the specific capacity of 550 mAh/g is realized from 1210×10^{19} no of Li⁺ (assuming they are the sole charge carriers).

The calculated molecular weight of the IISERP-CON1 is 610 g/mol.

The weight for unit cell of the IISERP-CON1 is $610 / (6.023 \times 10^{23})$ g

Considering that for 1g of the CON, the number of Li⁺ ion calculated is $1210 \times 10^{19} \Rightarrow$ number of Li⁺ per unit cell = $1210 \times 10^{19} \times 610 / (6.023 \times 10^{23}) = 12$.

Similarly, the second oxidation peak in the CV occurs in the potential window of 0.5-1.54V, and the specific capacity in this region is observed to be 224 mAh/g. This now can be attributed to about 4 Li⁺ per unit cell.

So, in total there are 16 Li⁺ ions/unit cell of IISERP-CON1 involved in the insertion-deinsertion process giving rise to the overall specific capacity of 774 mAh/g.

The theoretical capacity of the material can be compartmentalized based on the number of Lithium interacting with the specific binding sites present within the COF framework. For establishing the different Lithium binding sites present within the COF, we have utilized the results from the XPS data and the short contact analysis carried out using the Li@IISERP-CON1 structure obtained from simulation. Typical theoretical capacity of a material is given by the equation: $C_t = n \cdot F / (3600 \cdot (MW/1000))$ Equation (5), where n is the number of Li-ions per molecule, F and MW are Faraday constant and molecular weight per active species, respectively.

Now theoretical calculation of Lithium insertion only possible when pure chemical interaction happens with the functional groups of the material. We can calculate the theoretical capacity considering the most reactive β -ketoenamine form of the IISERP-CON. If IISERP-CON1's molecular weight 610g/mol per unit cell; contains 6-quinone groups and 6 imine Schiff bases (C=N), all of which will serve as active sites in each unit cell. (See Figure 1.21C)

The molecular weight of the Quinone type active site per unit cell ($M_w = M_{\text{unit cell}}/6$) is =102g/mol. Thus, from Equation, the theoretical capacity for Quinone moiety per unit cell can be calculated to be 264 mAh/g. The molecular weight of imine type active site per unit cell ($MW = M_{\text{unit cell}}/6$) is = 102g/mol. Thus, from Equation, the theoretical capacity for imine moiety per unit cell can be calculated to be 264 mAh/g. So a total theoretical capacity due to the Quinone and the imine groups would be (264 + 264) = 528 mAh/g. But from the CV it is clear that the weak chemical interaction with the inserted Lithium is observed in the potential window of 0.5-1.5V and this is supported also by the XPS (Figure 1.22). But, typically, Quinone and Schiff base are known to react with Lithium (Nature Communications 7, Article number: 13318 (2016)).

In this potential window, the experimental specific capacity due to such chemical interactions is observed to be 224 mAh/g, which is much lower than the theoretical capacity (528 mAh/g, assuming a β -ketoenamine). This suggests that not all the functional groups are able to interact with the Li species under this potential window. However, when the overall specific capacity of the material is 720 mAh/g at 100 mA/g in overall anodic potential window of 0.01-1.55V. This is much higher than the calculated theoretical capacity (524 mAh/g). This suggests that majority of the charge discharge occurs via intercalation of Lithium ions between the π -stacked layers of the CON and or in the nanopores of the CON. This phenomenon is similar to few-layers-thick Graphene case where most of the capacity comes from such intercalation (Hui et al. ACS Nano 2016, 10, 4248–4257; Paronyan et al. Sci. Rep. 2017, 7, 39944).]

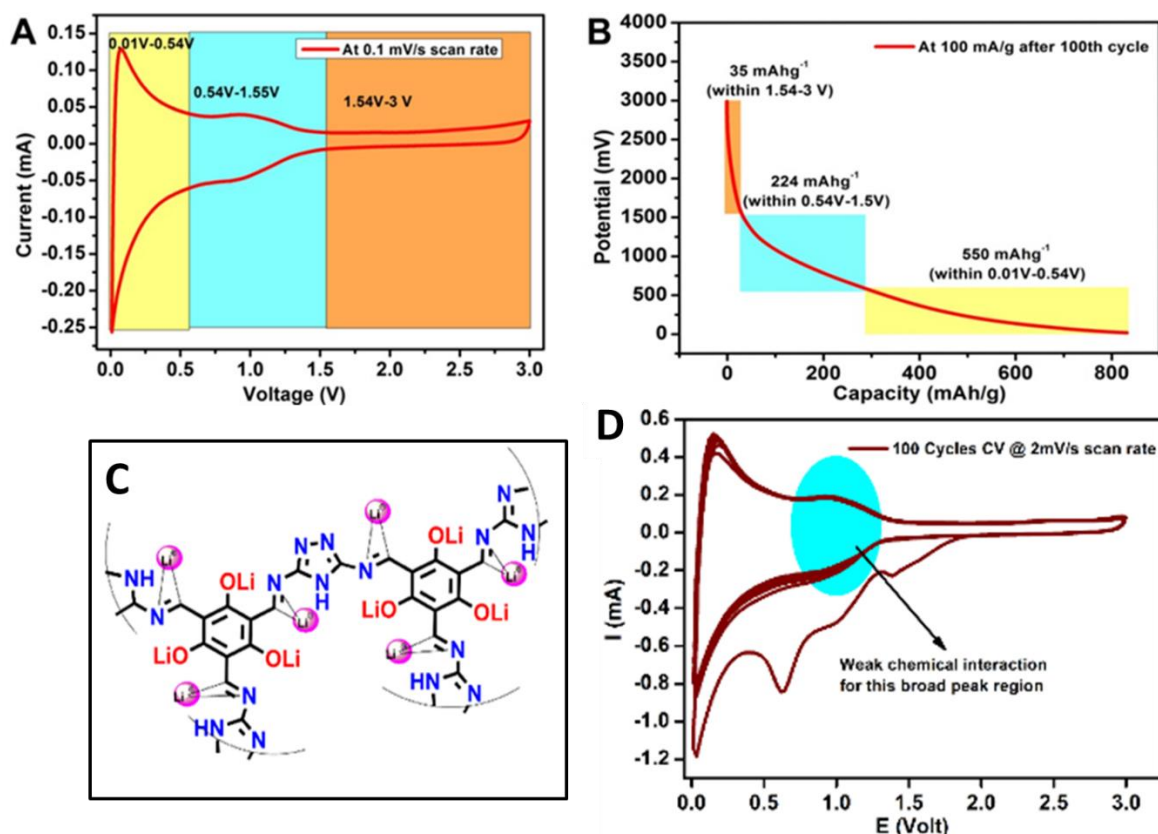


Figure 1.21. (A) Different potential region of CV for surface activity (chemical reaction) and diffusion activity (intercalation). 0.01-0.54 V mainly responsible for intercalation of Lithium and from 0.54- 1.55V for chemical reaction with functional group. (B) Potential vs capacity plot at 100 mA/g for 100th cycle. Same potential region obtained from CV and capacity contribution in each of those region was shown separately. Number of Lithium insertion contribution for capacity achievement in different

potential region was calculated from the following calculation. **(C)** Probable strong chemical interactions of Lithium with the polymeric IISERP-CON1 if it will be in β -ketoenamine form. **(D)** Green shaded area of CV profile indicates very broad peak due to weak chemical interaction with framework of IISERP-CON1. Importantly, other than the sharp peak at low potential ($\sim 0.02V$), which corresponds to the intercalation, there is no sharp peak at higher potentials. For the strong interactions between the β -ketoenamine and the Li a sharp peak is expected in the potential window of 0.5 to 1.5V, which is absent. Instead only a weak or shallow peak is observed (Nature Communications 7, Article number: 13318 (2016)). Neither a peak due to chemical interaction between Schiff bonds and Lithium is observed. (J. Mater. Chem. A, 2016,4, 14106-14110).

Using this as a starting composition, we generated a 2 x 2 x 2 cell of the IISERP-CON1, and the Lithium ions were allowed to find the best probable positions using simulated annealing methods (Materials Studio V6). The most probable positions were further DFT-optimized for geometry using the CASTEP package. The Monte-Carlo methods were used to obtain the most probable locations of the Li species within the low-energy configuration of the COF. These were carried out using the Simulated Annealing techniques available within the Materials Studio V.6.0. Default parameters were utilized. Automatic temperature control and 100000 cycles/cell was employed to optimize the structure. Universal force field (UFF) in conjugation with a Q_{Eq} charge equilibration method was employed for the geometry optimization, however, we noticed that applying the equilibration (Q_{Eq}) did not make much of a difference to the final configurations. No constraints were placed during the optimizations.

For the geometry optimization of the periodic COF structure, tight-binding Density Functional Theory was employed. The PBE exchange-correlation functional and parameters from the Slater-Koster library were used with a plane wave basis set cut-off of 340eV. All calculations were spin polarized and only the Γ -point was sampled. UFF-based Lennard-Jones dispersion corrections were included in Energy, Force and Displacement calculations and the cell was optimized. A smearing parameter of 0.005Ha was applied. In the final structure (relative energy: -127eV), the Lithium ions occupy positions close to the framework walls and reside in the interlayer space (Figure 1.22A and 1.22B). This is significantly different from their top-on positioning found in graphenic substrates.^[100,101] A short contact analysis reveals some meaningful findings vis-à-vis the Lithium positions around the ring nitrogens of the triazole and the hydroxyl oxygens of the phloroglucinol. Two different Lithium containing chains form, one is via the interaction of the Lithium with the -N and the -OH of these groups, respectively (Figure 1.22C and 1.22D), and the other from the interaction with only the nitrogens of the triazole. In these chains, the Li-N/Li-O separations are in the range of 2.69 to 2.80Å, which is much longer than the Li-N/Li-O distances found in the covalently bound Lithium ($\sim 1.8 - 2.0\text{\AA}$). Interestingly, owing to the geometry of these layers the more reactive Schiff bond nitrogens are not accessible for any interaction. This perhaps explains the lack of strong interactions which could lead to irreversible Lithium loading. To further verify this, we carried out an experiment wherein we reacted the CON with $\text{Li}(\text{OH})_2$ via both mechanical grinding and solution assisted process. The resulting products were analyzed using Inductively Coupled Plasma (ICP). The analysis revealed that there was only about < 2% loading of Lithium in both cases, which is considerably lower than the amount estimated from the measured specific capacity (16-18%). Thus, the bulk of the high specific capacity observed under the applied potential stems from intercalation involving weaker forces. However, since the Lithium loading was carried out without any electrochemical force, this cannot entirely exclude the formation of reactive species on the CON surface. In molecular compounds with fused aromatic rings, under an applied potential, Lithium is known to form strong interactions which are reversible.^[68-70] To establish this, we analyzed the post-discharge sample sealed under an argon atmosphere using X-ray Photoelectron Spectroscopy (XPS). XPS showed peaks corresponding to Li-N, Li-N_x and Li-O/Li-OH interactions. In addition, the peaks due to Li_2CO_3 , occurring from the electrolyte contributions, were also observed (Figure 1.23).

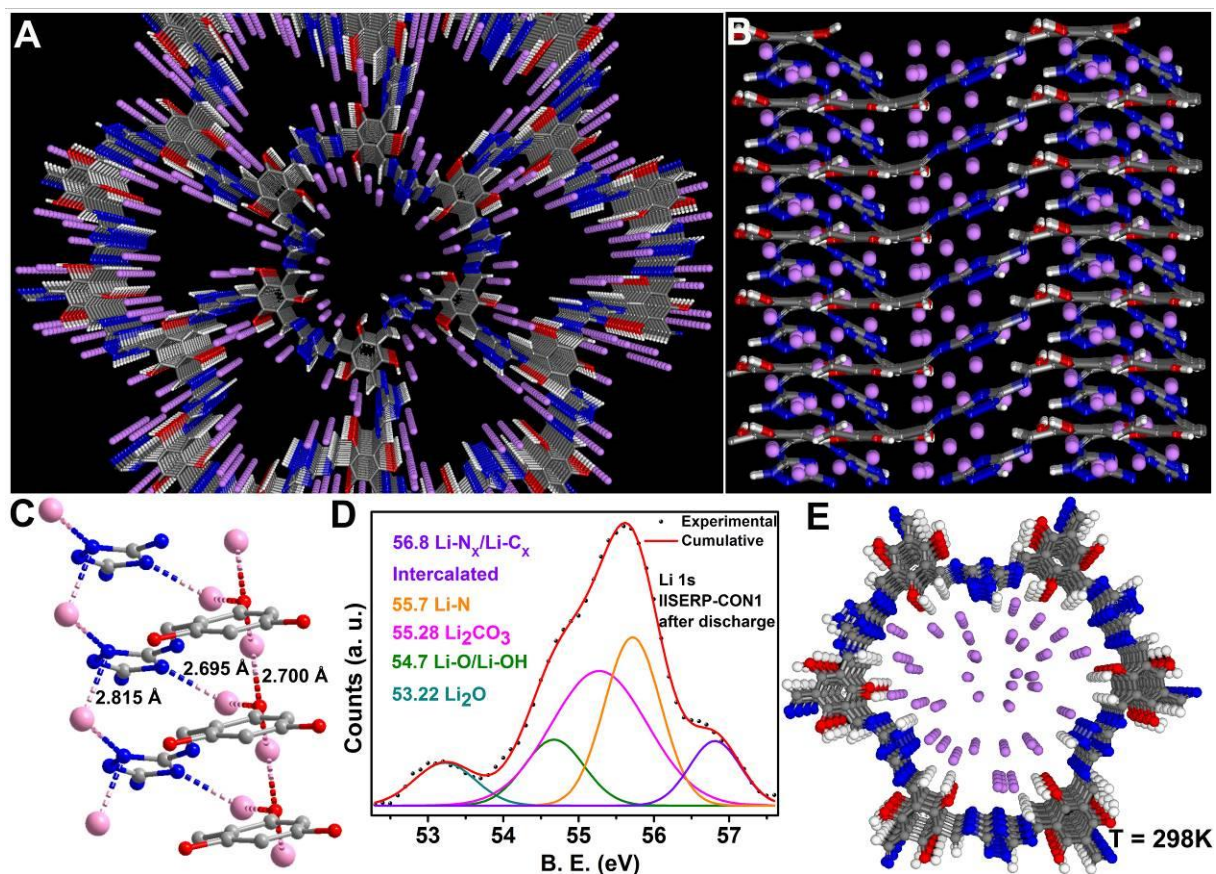


Figure 1.22. (A) A perspective view of the simulated 3D structure of the Lithiated CON. Li- Magenta; C- Grey; N- Blue; O- Red; H- White. (B) Shows the Li occupying the inter-lamellar spaces in the CON. (C) Shows the columns of Lithium that form via its interaction with phloroglucinol and triazole moieties. (D) Li 1s XPS spectra of the post-charge-discharge electrode (after 100 cycles). (E) Room temperature structure of the Li@CON from MD simulations. Note the Lithiums are more dispersed.

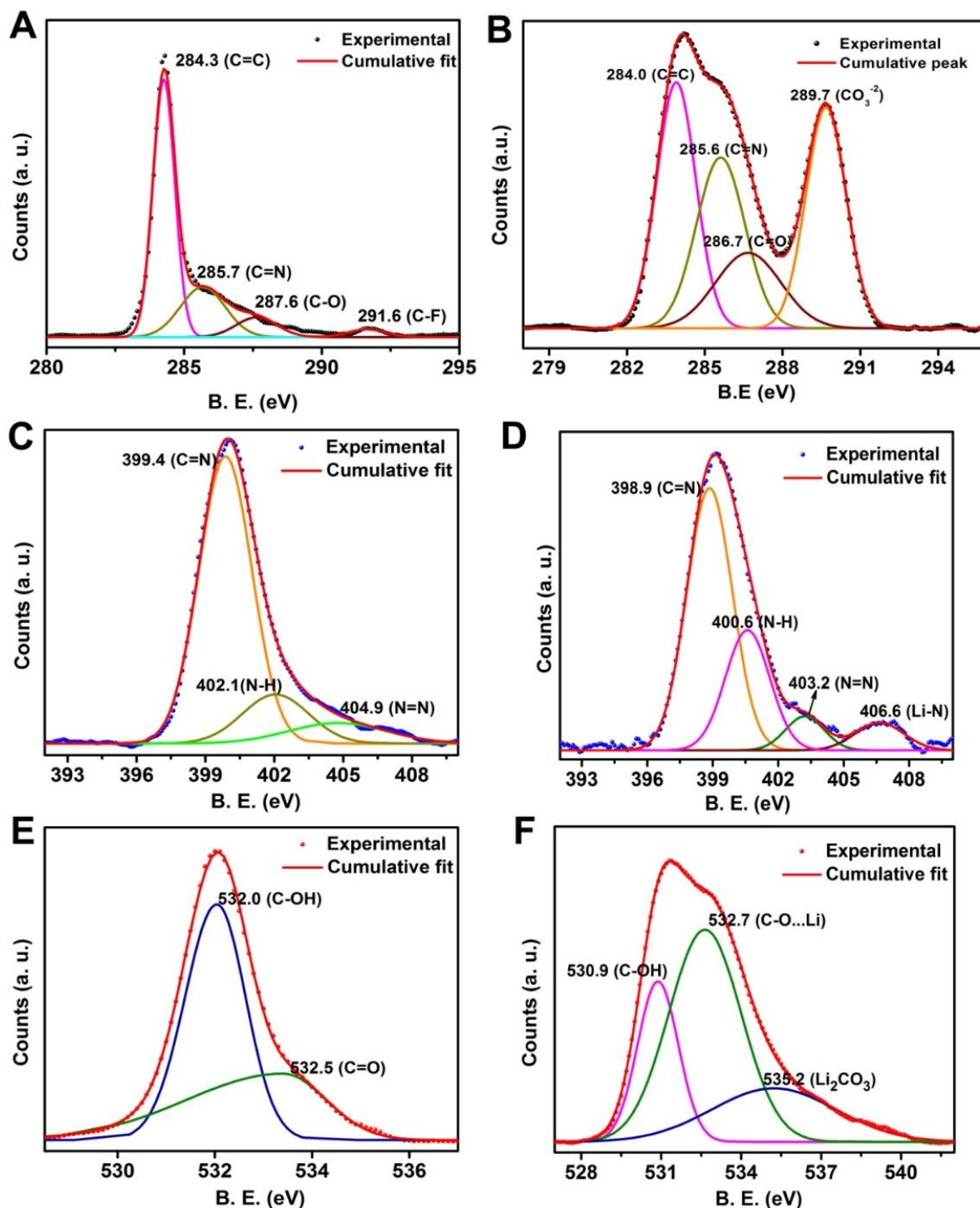


Figure 1.23. XPS spectra of IISERP-CON1 made electrode before and after completion of 100th discharge cycle (A) C1s before cycling (B) C1s after cycling (C) N1s before cycling (D) N1s after cycling (E) O1s before cycling (F) after cycling. Little change of binding energy of C=C, N=N/N-H, O-H and appearance of Li-N and Li-OC peaks after complete discharging of 100th cycle confirms weak chemical interaction of Lithium with the active sites of material.

A Molecular Dynamics (MD) simulation was carried out to establish the room temperature stability of the Li@CON. The relative total energy was higher by 459 kcal/mol compared to the 0K configuration. Importantly, the final averaged structure adopted a P1 symmetry and in this structure the framework was more buckled and the Lithium ions were randomly positioned, yet the framework maintains the overall symmetry (Figure 1.24). To establish the room temperature stability of the Lithiated CON, a Molecular Dynamics (MD) calculation employing a NPT ensemble was carried out. For the MD simulations, a 2 x 2 x 2 cell was used. The Newtonian equations of motions (NPT) were chosen for defining the ensemble considering its suitability in optimization of periodic 2D structure. The simulations were performed for a total time step of 50ps with a 0.1fs step (No. of steps = 500000) with a repulsive cut off at 6 Å. Pressure was controlled using Berendsen method, while the temperature was controlled using the Nose method. No constraints were applied and the cell was relaxed. Excellent convergence was achieved with no noticeable systematic shifts in energy. Final average temperature was 297.9 K. Importantly, the final averaged structure adopted a P1 symmetry with the unit cell parameters of $a = b = 20.4009$; $c = 3.9031$ Å; $\alpha = 90^\circ$; $\beta = 90^\circ$; $\gamma = 120^\circ$. The relative total energy was higher by 459 kcal/mol compared to the 0K configuration. Importantly, the framework was more buckled and the Li ions were more randomly positioned, yet the framework configuration maintains the overall symmetry.

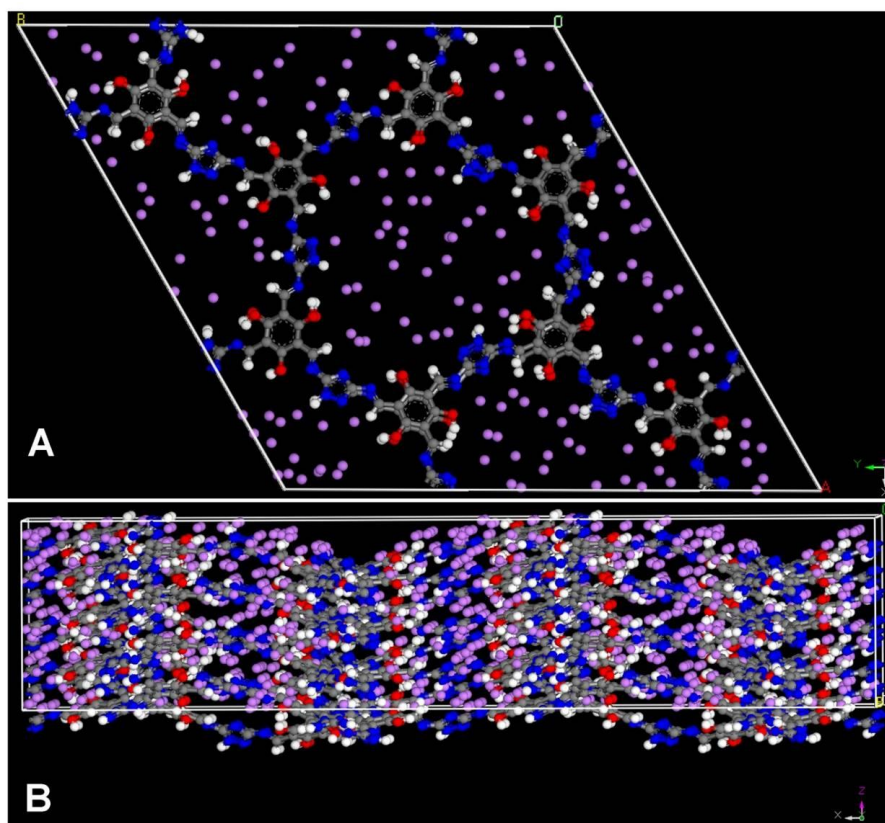


Figure 1.24. Averaged simulated structure of the Li@IISERP-CON1 obtained from the molecular dynamics calculation at 298K and 1bar. Unit cell parameters: $a = b = 20.4009$; $c = 3.9031$ Å; $\alpha = 90^\circ$; $\beta = 90^\circ$; $\gamma = 120^\circ$.

1.3.2. Bandgap and electrostatic potentials- electronic contributions

To gain evidence for the electronic driving force for the lithiation, we have calculated the bandgap changes between the pristine CON and its lithiated form. The dispersion corrected DFT calculation employing a plane wave basis cut-off of 500eV yielded a bandgap of 2.2eV for this non-conjugated

IISERP-CON1, which matches well with the experimentally determined optical bandgap (2.02eV, Figure 1.25A and 1.25B).^[12] This agrees well with the lack of appreciable electronic conductivity in the four-probe measurements.

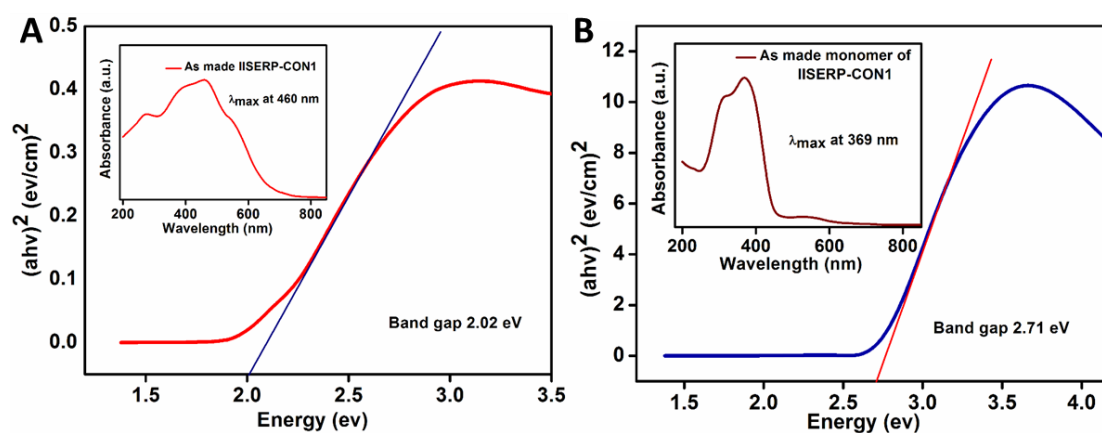


Figure 1.25. (A) Tauc plot of IISERP-CON1. The optical band gap was calculated to be 2.02eV. Inset: Solid state UV-visible spectra showing the λ_{max} at 460nm. (B) Tauc plot of model compound of IISERP-CON1. The optical band gap was calculated to be 2.71eV. Inset: solid state UV-visible spectra showing the λ_{max} at 369nm.

The band structures were calculated the geometry optimized configurations (lowest energy configuration from the DFTB) using the CASTEP built within the MS package. For these, a Norm-conserving pseudopotentials with a plane wave basis cut-off of 500eV was employed and the B3LYP functional was used. Electronic minimizations were achieved using an All Bands/EDFT algorithm. All calculations were performed on the unit cell and separately on a $2 \times 2 \times 2$ super cell. For the calculation of the electron density and the electrostatic potentials DMol³ implemented in the Materials Studio was employed. For the calculations a $2 \times 2 \times 2$ cell was used and the gradient-corrected exchange correlation were applied using the Generalized Gradient Approximation (GGA) and Perdew-Wang 91 (PW91) functional. A DFT-D correction was applied, a Global scheme was used for the orbital cut-off (5.1Å) with a SCF tolerance of 1×10^{-6} . A smearing parameter of 0.005Ha was applied.

Upon lithiation, the computed bandgap lowers to 0.144eV. Such lowering of the bandgap, in the minimized configuration of the Li@CON, suggests the likelihood of a strong electronic driving force.^[12] This is well substantiated by the observed electron density and potential map, calculated using DMol³ package of the Materials Studio. A comparison of the electrostatic potential of the pristine CON and the Lithium adsorbed CON shows a marked change in the electron distribution upon the Lithium insertion (Figure 1.26). Noticeably, due to the electrostatic interactions of the Lithium ions, the charge difference on the nearby carbon and nitrogen atoms has become less pronounced and the CON becomes highly activated and deplete of electrons. Clearly, the C₆ rings seem to participate by transferring significant electron density towards the Lithium ions.^[68-70] In our opinion, the calculation could be displaying the best case scenario by overestimating the electrostatics. Nonetheless, it is pointing in the right direction.

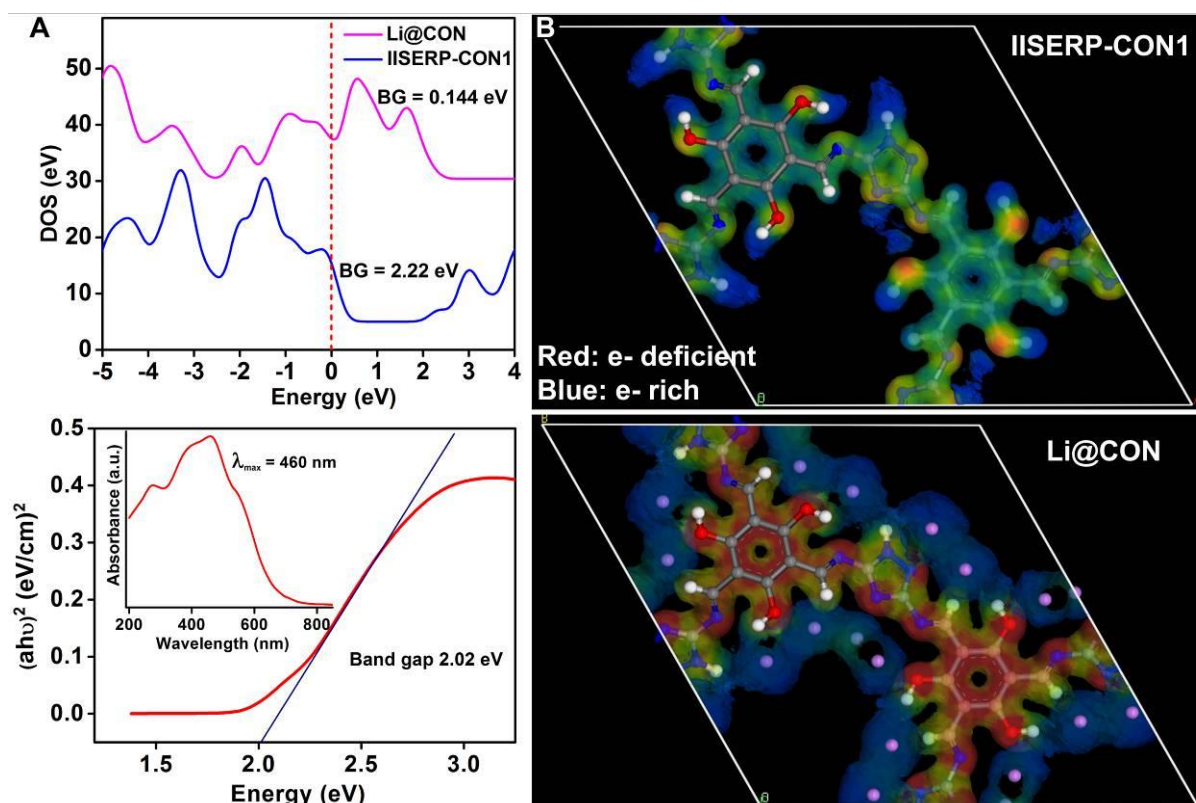


Figure 1.26. (A) Comparison of the band gaps of the as-made CON, the Li@CON calculated using DFT methods and the optical band gap of the as-made CON estimated from the solid-state UV-vis spectrum. (B) Comparison of the electron density and potential map of CON and the Li@CON. DOS- Density Of States.

1.4. Discussion:

Stable performance over a wide current density window is imperative for any competing anode material. In this regard, a worthy observation from our Lithium insertion-deinsertion study comes from a comparison of the specific capacities of IISERP-CON1 at the low (0.1 A/g) and the high (1 A/g) current densities with other organic materials.^[61,64,83,97,98] As can be seen from the bar chart in Figure 1.27, the drop in specific capacity with increasing the current density from 0.1 A/g to 1 A/g is about 20% in IISERP-CON1, which is the lowest among all the organic framework materials reported so far. We attribute this to the optimal interaction between the CON and the Lithium and more importantly to the lack of any undesirable irreversible redox activity. Figure 1.27 shows the structures of some of the recently reported self-standing organic frameworks with high capacities for Lithium storage. A comparison of their structures with that of the IISERP-CON1, evidently, brings some of its distinctive structural features. In IISERP-CON1 the electron-rich phloroglucinol nodes are linked by the short 120° linkers derived from 3,5-diaminotriazole. This short linker not only generates nanospaces with a high density of functional groups but favors cooperativity between the different functionalities in assembling the Lithium species. In comparison, the relatively longer linkers in the other frameworks (N2-COF, N3-COF and TThP) further far space the heteroatoms that serve as the active sites. On the other hand, in PDASA,^[83] the pores are large and the anhydride functionalities are even more proximal than the functional groups in IISERP-CON1 and this reflects in its higher specific capacity (1050 mAh/g @0.05 A/g). However, this high capacity drops by 73%, which is substantially higher in comparison to the 20% drop in the case of IISERP-CON1. This lowered stability of PDASA could be due to the presence of relatively stronger and potentially irreversible Li-COO bonds. Moreover, despite being short linkers, the triazoles generate large enough pores in the framework which are crucial to realizing smooth mass

and charge transport. Meanwhile, the flexibility at the triazole enables the buckling of the layers which assists the formation of π -stacking columnar motifs within its packing, which in turn ensures the necessary stability required under the electrolyte solutions and the applied potential.

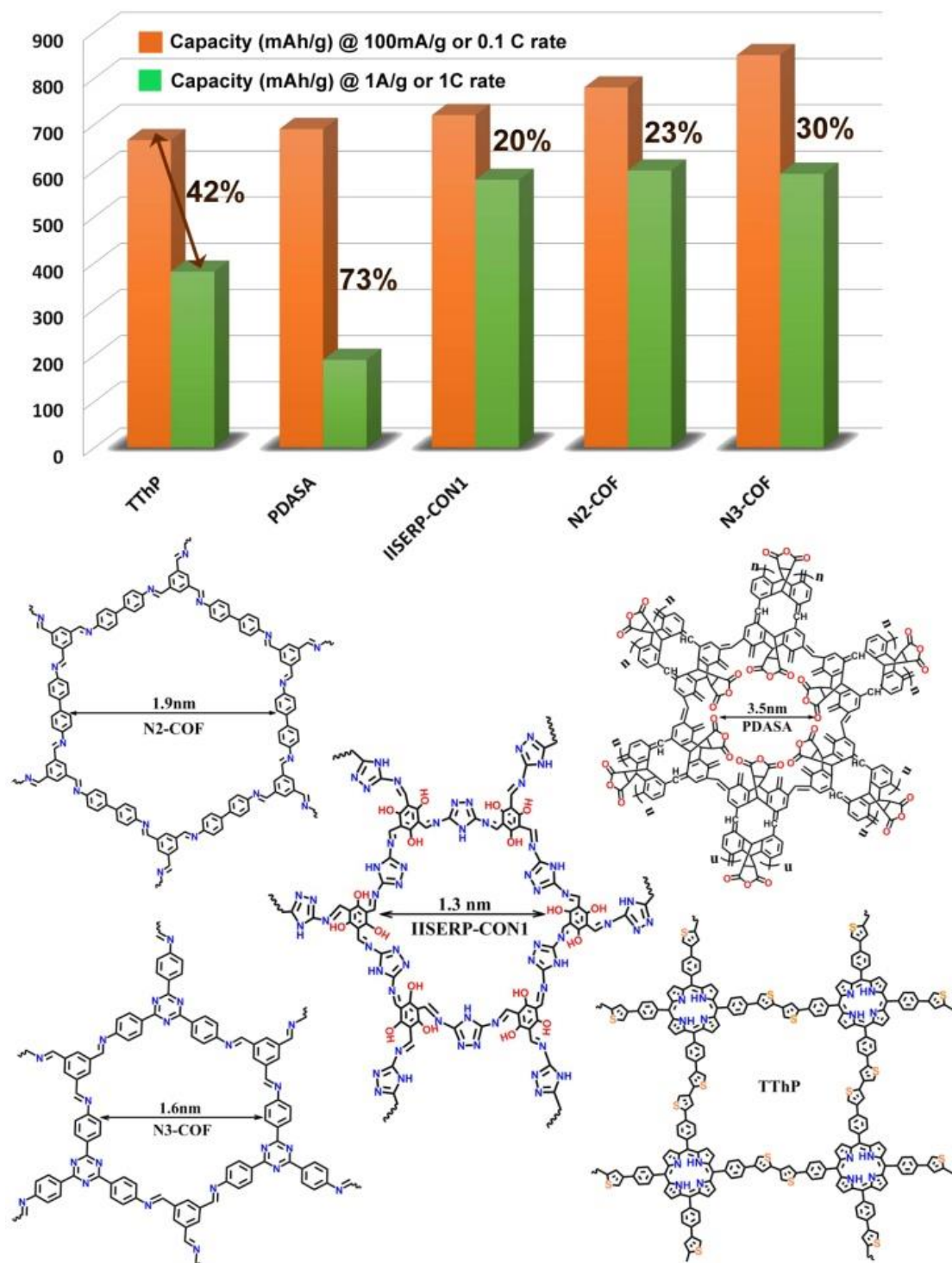


Figure 1.27. Top: A bar chart showing the drop in specific capacity when the current density is increased from 100 mA/g to 1 A/g in different organic framework materials with anodic character. **Bottom:** A schematic representation of the structure of these organic frameworks showing the high and compact packing of functional groups in IISERP-CON1 giving rise to highly favorable pockets for Li interaction. Note the compound codes have been adopted from the original literature.

1.5. Conclusions:

Here, we have developed 'by-design' a flexible covalent organic framework, which self-exfoliate into nanosheets under the solvothermal conditions. Presence of nanopores lined by mildly interacting triazole and phloroglucinol units in their framework enables these nanosheets to reversibly insert-deinsert Lithium ions. The short diffusion path lengths provided by the nanosheet structure favor ultra-fast kinetics for the Lithium insertion. DFT-optimized structure of the lithiated CON displays no strong Li-framework binding, which explains the reversibility and the cyclic stability. Importantly, the high capacity (720 mAh/g) and ability to maintain the capacity over a wide current density window is distinct to this material (< 20% drop with increase in current density from 100 mA/g to 1 A/g, lowest among all self-standing non-graphenic organic frameworks). Thus covalent organic frameworks functionalized with mildly binding groups can serve as highly active anodes in Li-ion battery. In their exfoliated form, they become highly suited for ion-intercalation. Our findings reveal the remarkable ability of these highly designable COF-derived nanostructures to act as electrode materials and prompt further studies.

Acknowledgements:

The authors thank Prof. Marimuthu Krishnan (International Institute of Information Technology (IIIT), Hyderabad) for the valuable discussions on the computational aspects. The authors acknowledge the IISER, Pune and the Ministry of Human Resource Development (MHRD), India for funding of our research through the Frontier Areas of Science and Technology (FAST) program. The authors thank "Funding by Department of Science and Technology (DST)-Nanomission under the Thematic Unit Program" and the Science and Engineering Research Board (SERB) (EMR/2016/003553) for the support. The authors thank Enovex Corp., Canada and DST-Clean Energy Research Initiative (CERI) for support. S.H. thanks DST-Inspire for financial support. The authors thank "Central Surface Analytical Facility of IIT Bombay" for the XPS and Centre for Materials for Electronics Technology (CMET), Pune for the TEM.

References

- [1] Cote, A. P.; Benin, A. I.; Ockwig, N. W.; O'keeffe, M.; Matzger, A. J.; Yaghi, O. M., Porous, crystalline, covalent organic frameworks. *Science* **2005**, *310*, 1166-1170.
- [2] Waller, P. J.; Gándara, F.; Yaghi, O. M., Chemistry of covalent organic frameworks. *Acc. Chem. Res.* **2015**, *48*, 3053-3063.
- [3] Feng, X.; Ding, X.; Jiang, D., Covalent organic frameworks. *Chem. Soc. Rev.* **2012**, *41*, 6010-6022.
- [4] Huang, N.; Zhai, L.; Coupry, D. E.; Addicoat, M. A.; Okushita, K.; Nishimura, K.; Heine, T.; Jiang, D., Multiple-component covalent organic frameworks. *Nat. Commun.* **2016**, *7*, 12325.
- [5] Huang, N.; Wang, P.; Jiang, D., Covalent organic frameworks: a materials platform for structural and functional designs. *Nat. Rev. Mater.* **2016**, *1*, 16068.
- [6] Rogge, S. M.; Bavykina, A.; Hajek, J.; Garcia, H.; Olivos-Suarez, A. I.; Sepúlveda-Escribano, A.; Vimont, A.; Clet, G.; Bazin, P.; Kapteijn, F., Metal-organic and covalent organic frameworks as single-site catalysts. *Chem. Soc. Rev.* **2017**, *46*, 3134-3184.
- [7] Colson, J. W.; Dichtel, W. R., Rationally synthesized two-dimensional polymers. *Nat. Chem.* **2013**, *5*, 453-465.

- [8] Alahakoon, S. B.; Thompson, C. M.; Occhialini, G.; Smaldone, R. A., Design principles for covalent organic frameworks in energy storage applications. *ChemSusChem* **2017**, *10*, 2116-2129.
- [9] Ding, S.-Y.; Wang, W., Covalent organic frameworks (COFs): from design to applications. *Chem. Soc. Rev.* **2013**, *42*, 548-568.
- [10] Xiang, Z.; Cao, D., Porous covalent–organic materials: synthesis, clean energy application and design. *J. Mater. Chem. A* **2013**, *1*, 2691-2718.
- [11] Mullangi, D.; Dhavale, V.; Shalini, S.; Nandi, S.; Collins, S.; Woo, T.; Kurungot, S.; Vaidhyanathan, R., Low-Overpotential Electrocatalytic Water Splitting with Noble-Metal-Free Nanoparticles Supported in a sp³ N-Rich Flexible COF. *Adv. Energy Mater.* **2016**, *6*, 1600110.
- [12] Nandi, S.; Singh, S. K.; Mullangi, D.; Illathvalappil, R.; George, L.; Vinod, C. P.; Kurungot, S.; Vaidhyanathan, R., Low Band Gap Benzimidazole COF Supported Ni₃N as Highly Active OER Catalyst. *Adv. Energy Mater.* **2016**, *6*, 1601189.
- [13] Furukawa, H.; Yaghi, O. M., Storage of hydrogen, methane, and carbon dioxide in highly porous covalent organic frameworks for clean energy applications. *J. Am. Chem. Soc.* **2009**, *131*, 8875-8883.
- [14] Li, Z.; Zhi, Y.; Feng, X.; Ding, X.; Zou, Y.; Liu, X.; Mu, Y., An Azine-Linked Covalent Organic Framework: Synthesis, Characterization and Efficient Gas Storage. *Chem. Eur. J.* **2015**, *21*, 12079-12084.
- [15] Vyas, V. S.; Haase, F.; Stegbauer, L.; Savasci, G.; Podjaski, F.; Ochsenfeld, C.; Lotsch, B. V., A tunable azine covalent organic framework platform for visible light-induced hydrogen generation. *Nat. Commun.* **2015**, *6*, 9508.
- [16] Xu, H.; Tao, S.; Jiang, D., Proton conduction in crystalline and porous covalent organic frameworks. *Nat. mater.* **2016**, *15*, 722-726.
- [17] Ma, H.; Liu, B.; Li, B.; Zhang, L.; Li, Y.-G.; Tan, H.-Q.; Zang, H.-Y.; Zhu, G., Cationic covalent organic frameworks: a simple platform of anionic exchange for porosity tuning and proton conduction. *J. Am. Chem. Soc.* **2016**, *138*, 5897-5903.
- [18] Peng, Y.; Xu, G.; Hu, Z.; Cheng, Y.; Chi, C.; Yuan, D.; Cheng, H.; Zhao, D., Mechano assisted Synthesis of Sulfonated Covalent Organic Frameworks with High Intrinsic Proton Conductivity. *ACS Appl. Mater. Interfaces* **2016**, *8*, 18505-18512.
- [19] Oh, H.; Kalidindi, S. B.; Um, Y.; Bureekaew, S.; Schmid, R.; Fischer, R. A.; Hirscher, M., A cryogenically flexible covalent organic framework for efficient hydrogen isotope separation by quantum sieving. *Angew. Chem. Int. Ed.* **2013**, *52*, 13219-13222.
- [20] Sprick, R. S.; Jiang, J.-X.; Bonillo, B.; Ren, S.; Ratvijitvech, T.; Guiglion, P.; Zwijnenburg, M. A.; Adams, D. J.; Cooper, A. I., Tunable organic photocatalysts for visible-light-driven hydrogen evolution. *J. Am. Chem. Soc.* **2015**, *137*, 3265-3270.
- [21] Ding, X.; Guo, J.; Feng, X.; Honsho, Y.; Guo, J.; Seki, S.; Maitarad, P.; Saeki, A.; Nagase, S.; Jiang, D., Synthesis of metallophthalocyanine covalent organic frameworks that exhibit high carrier mobility and photoconductivity. *Angew. Chem. Int. Ed.* **2011**, *50*, 1289-1293.
- [22] Ding, S.-Y.; Gao, J.; Wang, Q.; Zhang, Y.; Song, W.-G.; Su, C.-Y.; Wang, W., Construction of covalent organic framework for catalysis: Pd/COF-LZU1 in Suzuki–Miyaura coupling reaction. *J. Am. Chem. Soc.* **2011**, *133*, 19816-19822.
- [23] Mullangi, D.; Nandi, S.; Shalini, S.; Sreedhala, S.; Vinod, C. P.; Vaidhyanathan, R., Pd loaded amphiphilic COF as catalyst for multi-fold Heck reactions, CC couplings and CO oxidation. *Sci. Rep.* **2015**, *5*, 10876.

- [24] Mullangi, D.; Shalini, S.; Nandi, S.; Choksi, B.; Vaidhyanathan, R., Super-hydrophobic covalent organic frameworks for chemical resistant coatings and hydrophobic paper and textile composites. *J. Mater. Chem. A* **2017**, *5*, 8376-8384.
- [25] Guo, J.; Xu, Y.; Jin, S.; Chen, L.; Kaji, T.; Honsho, Y.; Addicoat, M. A.; Kim, J.; Saeki, A.; Ihee, H., Conjugated organic framework with three-dimensionally ordered stable structure and delocalized π clouds. *Nat. Commun.* **2013**, *4*, 3736.
- [26] Bertrand, G. H.; Michaelis, V. K.; Ong, T.-C.; Griffin, R. G.; Dincă, M., Thiophene-based covalent organic frameworks. *Proc. Natl. Acad. Sci. USA* **2013**, *110*, 4923-4928.
- [27] Wan, S.; Gándara, F.; Asano, A.; Furukawa, H.; Saeki, A.; Dey, S. K.; Liao, L.; Ambrogio, M. W.; Botros, Y. Y.; Duan, X., Covalent organic frameworks with high charge carrier mobility. *Chem. Mater.* **2011**, *23*, 4094-4097.
- [28] Coleman, J. N.; Lotya, M.; O'Neill, A.; Bergin, S. D.; King, P. J.; Khan, U.; Young, K.; Gaucher, A.; De, S.; Smith, R. J., Two-dimensional nanosheets produced by liquid exfoliation of layered materials. *Science* **2011**, *331*, 568-571.
- [29] Tan, C.; Cao, X.; Wu, X.-J.; He, Q.; Yang, J.; Zhang, X.; Chen, J.; Zhao, W.; Han, S.; Nam, G.-H., Recent advances in ultrathin two-dimensional nanomaterials. *Chem. Rev.* **2017**, *117*, 6225-6331.
- [30] Zhang, X.; Hou, L.; Ciesielski, A.; Samorì, P., 2D materials beyond Graphene for high-performance energy storage applications. *Adv. Energy Mater.* **2016**, *6*, 1600671.
- [31] Peng, L.; Zhu, Y.; Chen, D.; Ruoff, R. S.; Yu, G., Two-dimensional materials for beyond-Lithium-ion batteries. *Adv. Energy Mater.* **2016**, *6*, 1600025.
- [32] Shi, L.; Zhao, T., Recent advances in inorganic 2D materials and their applications in Lithium and Sodium batteries. *J. Mater. Chem. A* **2017**, *5*, 3735-3758.
- [33] Lukatskaya, M. R.; Mashtalir, O.; Ren, C. E.; Dall'Agnese, Y.; Rozier, P.; Taberna, P. L.; Naguib, M.; Simon, P.; Barsoum, M. W.; Gogotsi, Y., Cation intercalation and high volumetric capacitance of two-dimensional titanium carbide. *Science* **2013**, *341*, 1502-1505.
- [34] Peng, L.; Peng, X.; Liu, B.; Wu, C.; Xie, Y.; Yu, G., Ultrathin two-dimensional MnO₂/Graphene hybrid nanostructures for high-performance, flexible planar supercapacitors. *Nano Lett.* **2013**, *13*, 2151-2157.
- [35] Jin, S.; Yang, G.; Song, H.; Cui, H.; Wang, C., Ultrathin hexagonal 2D Co₂GeO₄ nanosheets: excellent Li-storage performance and ex situ investigation of electrochemical mechanism. *ACS Appl. Mater. Interfaces* **2015**, *7*, 24932-24943.
- [36] Li, Q.-F.; Duan, C.-G.; Wan, X.; Kuo, J.-L., Theoretical prediction of anode materials in Li-ion batteries on layered black and blue phosphorus. *J. Phys. Chem. C* **2015**, *119*, 8662-8670..
- [37] Sen, U. K.; Mitra, S., High-rate and high-energy-density Lithium-ion battery anode containing 2D MoS₂ nanowall and cellulose binder. *ACS Appl. Mater. Interfaces* **2013**, *5*, 1240-1247.
- [38] Huang, Y. F.; Ruan, W. H.; Lin, D. L.; Zhang, M. Q., Bridging Redox Species-Coated Graphene Oxide Sheets to Electrode for Extending Battery Life Using Nanocomposite Electrolyte. *ACS Appl. Mater. Interfaces* **2017**, *9*, 909-918.
- [39] Liu, C.; Li, F.; Ma, L. P.; Cheng, H. M., Advanced materials for energy storage. *Adv. Mater.* **2010**, *22*, E28-E62.
- [40] Sakaushi, K.; Antonietti, M., Carbon-and nitrogen-based organic frameworks. *Acc. Chem. Res.* **2015**, *48*, 1591-1600.
- [41] Agostini, M.; Brutti, S.; Hassoun, J., High voltage Li-ion battery using exfoliated Graphite/Graphene nanosheets anode. *ACS Appl. Mater. Interfaces* **2016**, *8*, 10850-10857.

- [42] S Stankovich, S.; Dikin, D. A.; Piner, R. D.; Kohlhaas, K. A.; Kleinhammes, A.; Jia, Y.; Wu, Y.; Nguyen, S. T.; Ruoff, R. S., Synthesis of Graphene-based nanosheets via chemical reduction of exfoliated Graphite oxide. *carbon* **2007**, *45*, 1558-1565.
- [43] Sahu, T. S.; Mitra, S., Exfoliated MoS₂ sheets and reduced Graphene oxide-an excellent and fast anode for Sodium-ion battery. *Sci. Rep.* **2015**, *5*, 12571.
- [44] Xiao, J.; Choi, D.; Cosimbescu, L.; Koech, P.; Liu, J.; Lemmon, J. P., Exfoliated MoS₂ nanocomposite as an anode material for Lithium ion batteries. *Chem. Mater.* **2010**, *22*, 4522-4524.
- [45] Luo, J.; Fan, F. R.; Jiang, T.; Wang, Z.; Tang, W.; Zhang, C.; Liu, M.; Cao, G.; Wang, Z. L., Integration of micro-supercapacitors with triboelectric nanogenerators for a flexible self-charging power unit. *Nano Research* **2015**, *8*, 3934-3943.
- [46] Ananya, G.; Raghu, S.; Ramaprabhu, S., Binary reaction ingrained high current density and long cycle life novel anode material for Lithium ion battery. *J. Mater. Chem. A* **2017**, *5*, 2784-2791.
- [47] Aravindan, V.; Lee, Y. S.; Madhavi, S., Research progress on negative electrodes for practical Li-ion batteries: beyond carbonaceous anodes. *Adv. Energy Mater.* **2015**, *5*, 1402225.
- [48] Qiu, B.; Zhang, M.; Xia, Y.; Liu, Z.; Meng, Y. S., Understanding and controlling anionic electrochemical activity in high-capacity oxides for next generation Li-ion batteries. *Chem. Mater.* **2017**, *29*, 908-915.
- [49] Bunck, D. N.; Dichtel, W. R., Bulk synthesis of exfoliated two-dimensional polymers using hydrazone-linked covalent organic frameworks. *J. Am. Chem. Soc.* **2013**, *135*, 14952-14955.
- [50] A. B. Marco, D. Cortizo-Lacalle, I. Perez-Miqueo, G. Valenti, A. Boni, J. Plas, K. Strutyński, S. D. Feyter, F. Paolucci, M. Montes, A. N, Khlobystov, M. Melle-Franco, A. Mateo-Alonso, *Angew. Chem. Int. Ed.* **2017**, *56*, 1.
- [51] Ishijima, Y.; Okaniwa, M.; Oaki, Y.; Imai, H., Two exfoliation approaches for organic layered compounds: hydrophilic and hydrophobic polydiacetylene nanosheets. *Chem. Sci.* **2017**, *8*, 647-653.
- [52] X. Chen, M. Addicoat, E. Jin, L. Zhai, H. Xu, N. Huang, Z. Guo, L. Liu, S. Irle, D. Jiang, *J. Am. Chem. Soc.* **2015**, *137*, 32417.
- [53] Mo, Y.-P.; Liu, X.-H.; Sun, B.; Yan, H.-J.; Wang, D.; Wan, L.-J., The intramolecular H-bonding effect on the growth and stability of Schiff-base surface covalent organic frameworks. *Phys. Chem. Chem. Phys.* **2017**, *19*, 539-543.
- [54] Khayum, M. A.; Kandambeth, S.; Mitra, S.; Nair, S. B.; Das, A.; Nagane, S. S.; Mukherjee, R.; Banerjee, R., Chemically delaminated free-standing ultrathin covalent organic nanosheets. *Angew. Chem. Int. Ed.* **2016**, *55*, 15604-15608.
- [55] Mitra, S.; Sasmal, H. S.; Kundu, T.; Kandambeth, S.; Illath, K.; Diaz Diaz, D.; Banerjee, R., Targeted drug delivery in covalent organic nanosheets (CONs) via sequential postsynthetic modification. *J. Am. Chem. Soc.* **2017**, *139*, 4513-4520.
- [56] Chandra, S.; Kandambeth, S.; Biswal, B. P.; Lukose, B.; Kunjir, S. M.; Chaudhary, M.; Babarao, R.; Heine, T.; Banerjee, R., Chemically stable multilayered covalent organic nanosheets from covalent organic frameworks via mechanical delamination. *J. Am. Chem. Soc.* **2013**, *135*, 17853-17861.
- [57] Smith, B. J.; Parent, L. R.; Overholts, A. C.; Beaucage, P. A.; Bisbey, R. P.; Chavez, A. D.; Hwang, N.; Park, C.; Evans, A. M.; Gianneschi, N. C., Colloidal covalent organic frameworks. *ACS Cent. Sci.* **2017**, *3*, 58-65.

- [58] Wang, S.; Wang, L.; Zhang, K.; Zhu, Z.; Tao, Z.; Chen, J., Organic $\text{Li}_4\text{C}_8\text{H}_2\text{O}_6$ nanosheets for Lithium-ion batteries. *Nano Lett.* **2013**, *13*, 4404-4409.
- [59] Caballero, Á.; Morales, J., Can the performance of Graphene nanosheets for Lithium storage in Li-ion batteries be predicted? *Nanoscale* **2012**, *4*, 2083-2092.
- [60] Han, X.; Qing, G.; Sun, J.; Sun, T., How many Lithium ions can be inserted onto fused C_6 aromatic ring systems? *Angew. Chem.* **2012**, *124*, 5237-5241.
- [61] Yang, H.; Zhang, S.; Han, L.; Zhang, Z.; Xue, Z.; Gao, J.; Li, Y.; Huang, C.; Yi, Y.; Liu, H., High conductive two-dimensional covalent organic framework for Lithium storage with large capacity. *ACS Appl. Mater. Interfaces* **2016**, *8*, 5366-5375.
- [62] Wang, S.; Wang, Q.; Shao, P.; Han, Y.; Gao, X.; Ma, L.; Yuan, S.; Ma, X.; Zhou, J.; Feng, X., Exfoliation of covalent organic frameworks into few-layer redox-active nanosheets as cathode materials for Lithium-ion batteries. *J. Am. Chem. Soc.* **2017**, *139*, 4258-4261.
- [63] Vazquez-Molina, D. A.; Mohammad-Pour, G. S.; Lee, C.; Logan, M. W.; Duan, X.; Harper, J. K.; Uribe-Romo, F. J., Mechanically shaped two-dimensional covalent organic frameworks reveal crystallographic alignment and fast Li-ion conductivity. *J. Am. Chem. Soc.* **2016**, *138*, 9767-9770.
- [64] Bai, L.; Gao, Q.; Zhao, Y., Two fully conjugated covalent organic frameworks as anode materials for Lithium ion batteries. *J. Mater. Chem. A* **2016**, *4*, 14106-14110.
- [65] Xu, F.; Jin, S.; Zhong, H.; Wu, D.; Yang, X.; Chen, X.; Wei, H.; Fu, R.; Jiang, D., Electrochemically active, crystalline, mesoporous covalent organic frameworks on carbon nanotubes for synergistic Lithium-ion battery energy storage. *Sci. Rep.* **2015**, *5*, 8225.
- [66] Mulzer, C. R.; Shen, L.; Bisbey, R. P.; McKone, J. R.; Zhang, N.; Abruña, H. c. D.; Dichtel, W. R., Superior charge storage and power density of a conducting polymer-modified covalent organic framework. *ACS Cent. Sci.* **2016**, *2*, 667-673.
- [67] Yang, D.-H.; Yao, Z.-Q.; Wu, D.; Zhang, Y.-H.; Zhou, Z.; Bu, X.-H., Structure-modulated crystalline covalent organic frameworks as high-rate cathodes for Li-ion batteries. *J. Mater. Chem. A* **2016**, *4*, 18621-18627.
- [68] Cao, D.; Lan, J.; Wang, W.; Smit, B., Lithium-doped 3D covalent organic frameworks: high-capacity hydrogen storage materials. *Angew. Chem.* **2009**, *121*, 4824-4827.
- [69] Tylianakis, E.; Klontzas, E.; Froudakis, G. E., Multi-scale theoretical investigation of hydrogen storage in covalent organic frameworks. *Nanoscale* **2011**, *3*, 856-869.
- [70] Kim, D. J.; Je, S. H.; Sampath, S.; Choi, J. W.; Coskun, A., Effect of N-substitution in naphthalenediimides on the electrochemical performance of organic rechargeable batteries. *RSC Adv.* **2012**, *2*, 7968-7970.
- [71] Zhu, X.; Zhu, Y.; Murali, S.; Stoller, M. D.; Ruoff, R. S., Nanostructured reduced Graphene oxide/ Fe_2O_3 composite as a high-performance anode material for Lithium ion batteries. *ACS nano* **2011**, *5*, 3333-3338.
- [72] Zhang, L.; Wu, H. B.; Lou, X. W., Iron-oxide-based advanced anode materials for Lithium-ion batteries. *Adv. Energy Mater.* **2014**, *4*, 1300958.
- [73] S. Goriparti, E. Miele, F. De Angelis, E. Di Fabrizio, R. P. Zaccaria, C. Capiglia, *J. Power Sources* **2014**, *257*, 421e443.
- [74] Beake, E.; Dove, M.; Phillips, A.; Keen, D.; Tucker, M.; Goodwin, A.; Bennett, T.; Cheetham, A., Flexibility of zeolitic imidazolate framework structures studied by neutron total scattering and the reverse Monte Carlo method. *J. Phys.: Condens. Matter* **2013**, *25*, 395403.
- [75] Yue, J.-Y.; Mo, Y.-P.; Li, S.-Y.; Dong, W.-L.; Chen, T.; Wang, D., Simultaneous construction of two linkages for the on-surface synthesis of imine-boroxine hybrid covalent organic frameworks. *Chem. Sci.* **2017**, *8*, 2169-2174.

- [76] Mitra, S.; Kandambeth, S.; Biswal, B. P.; Khayum M, A.; Choudhury, C. K.; Mehta, M.; Kaur, G.; Banerjee, S.; Prabhune, A.; Verma, S., Self-exfoliated guanidinium-based ionic covalent organic nanosheets (iCONs). *J. Am. Chem. Soc.* **2016**, *138*, 2823-2828
- [77] FE-SEM image of a commercially sold special Graphene sheet, <http://www.simbatt.com/en/XIE.html>.
- [78] Geng, D.; Chen, Y.; Chen, Y.; Li, Y.; Li, R.; Sun, X.; Ye, S.; Knights, S., High oxygen-reduction activity and durability of nitrogen-doped Graphene. *Energy Environ. Sci.* **2011**, *4*, 760-764.
- [79] Foster, J. A.; Henke, S.; Schneemann, A.; Fischer, R. A.; Cheetham, A. K., Liquid exfoliation of alkyl-ether functionalised layered metal–organic frameworks to nanosheets. *Chem. Commun.* **2016**, *52*, 10474-10477.
- [80] Berlanga, I.; Ruiz-González, M. L.; González-Calbet, J. M.; Fierro, J. L. G.; Mas-Ballesté, R.; Zamora, F., Delamination of Layered Covalent Organic Frameworks. *Small* **2011**, *7*, 1207-1211.
- [81] Xing, Z.; Ju, Z.; Zhao, Y.; Wan, J.; Zhu, Y.; Qiang, Y.; Qian, Y., One-pot hydrothermal synthesis of Nitrogen-doped Graphene as high-performance anode materials for Lithium ion batteries. *Sci. Rep.* **2016**, *6*, 26146.
- [82] Cohn, A. P.; Oakes, L.; Carter, R.; Chatterjee, S.; Westover, A. S.; Share, K.; Pint, C. L., Assessing the improved performance of freestanding, flexible Graphene and carbon nanotube hybrid foams for Lithium ion battery anodes. *Nanoscale* **2014**, *6*, 4669-4675.
- [83] Mukherjee, D.; Gowda Y. K, G.; Makri Nimbegondi Kotresh, H.; Sampath, S., Porous, hyper-cross-linked, three-dimensional polymer as stable, high rate capability electrode for Lithium-ion battery. *ACS Appl. Mater. Interfaces* **2017**, *9*, 19446-19454.
- [84] Augustyn, V.; Simon, P.; Dunn, B., Pseudocapacitive oxide materials for high-rate electrochemical energy storage. *Energy Environ. Sci.* **2014**, *7*, 1597-1614.
- [85] Simon, P.; Gogotsi, Y.; Dunn, B., Where do batteries end and supercapacitors begin? *Science* **2014**, *343*, 1210-1211.
- [86] Nokami, T.; Matsuo, T.; Inatomi, Y.; Hojo, N.; Tsukagoshi, T.; Yoshizawa, H.; Shimizu, A.; Kuramoto, H.; Komae, K.; Tsuyama, H., Polymer-bound pyrene-4, 5, 9, 10-tetraone for fast-charge and-discharge Lithium-ion batteries with high capacity. *J. Am. Chem. Soc.* **2012**, *134*, 19694-19700.
- [87] Liu, H.; Cao, Q.; Fu, L. J.; Li, C.; Wu, Y.; Wu, H., Doping effects of zinc on LiFePO₄ cathode material for Lithium ion batteries. *Electrochem. Commun.* **2006**, *8*, 1553-1557.
- [88] Rui, X.; Ding, N.; Liu, J.; Li, C.; Chen, C., Analysis of the chemical diffusion coefficient of Lithium ions in Li₃V₂(PO₄)₃ cathode material. *Electrochim. Acta* **2010**, *55*, 2384-2390.
- [89] Wang, Y.-Q.; Gu, L.; Guo, Y.-G.; Li, H.; He, X.-Q.; Tsukimoto, S.; Ikuhara, Y.; Wan, L.-J., Rutile-TiO₂ nanocoating for a high-rate Li₄Ti₅O₁₂ anode of a Lithium-ion battery. *J. Am. Chem. Soc.* **2012**, *134*, 7874-7879.
- [90] Wu, H.; Wang, K.; Meng, Y.; Lu, K.; Wei, Z., An organic cathode material based on a polyimide/CNT nanocomposite for Lithium ion batteries. *J. Mater. Chem. A* **2013**, *1*, 6366-6372.
- [91] Wang, G.; Yang, L.; Chen, Y.; Wang, J.; Bewlay, S.; Liu, H., An investigation of polypyrrole-LiFePO₄ composite cathode materials for Lithium-ion batteries. *Electrochim. Acta* **2005**, *50*, 4649-4654.
- [92] Ho, C.; Raistrick, I.; Huggins, R., Application of A-C techniques to the study of Lithium diffusion in tungsten trioxide thin films. *J. Electrochem. Soc.* **1980**, *127*, 343.
- [93] Cui, Y.; Zhao, X.; Guo, R., Improved electrochemical performance of La_{0.7}Sr_{0.3}MnO₃ and carbon co-coated LiFePO₄ synthesized by freeze-drying process. *Electrochim. Acta* **2010**, *55*, 922-926.

- [94] Ma, Z.; Peng, Y.; Wang, G.; Fan, Y.; Song, J.; Liu, T.; Qin, X.; Shao, G., Enhancement of electrochemical performance for LiFePO₄ cathodes via hybrid coating with electron conductor carbon and Lithium ion conductor LaPO₄. *Electrochim. Acta* **2015**, *156*, 77-85.
- [95] Luo, C.; Huang, R.; Kevorkyants, R.; Pavanello, M.; He, H.; Wang, C., Self-assembled organic nanowires for high power density Lithium ion batteries. *Nano Lett.* **2014**, *14*, 1596-1602.
- [96] Xie, J.; Rui, X.; Gu, P.; Wu, J.; Xu, Z. J.; Yan, Q.; Zhang, Q., Novel conjugated ladder-structured oligomer anode with high Lithium storage and long cycling capability. *ACS Appl. Mater. Interfaces* **2016**, *8*, 16932-16938
- [97] Wu, J.; Rui, X.; Wang, C.; Pei, W. B.; Lau, R.; Yan, Q.; Zhang, Q., Nanostructured conjugated ladder polymers for stable and fast Lithium storage anodes with high-capacity. *Adv. Energy Mater.* **2015**, *5*, 1402189.
- [98] Wu, J.; Rui, X.; Long, G.; Chen, W.; Yan, Q.; Zhang, Q., Pushing up Lithium storage through nanostructured polyazaacene analogues as anode. *Angew. Chem. Int. Ed.* **2015**, *54*, 7354-7358.
- [99] Meng, Y. S.; Arroyo-de Dompablo, M. E., First principles computational materials design for energy storage materials in Lithium ion batteries. *Energy Environ. Sci.* **2009**, *2*, 589-609.
- [100] Hankel, M.; Ye, D.; Wang, L.; Searles, D. J., Lithium and Sodium storage on graphitic carbon nitride. *J. Phys. Chem. C* **2015**, *119*, 21921-21927.
- [101] Chen, D.; Avestro, A. J.; Chen, Z.; Sun, J.; Wang, S.; Xiao, M.; Erno, Z.; Algaradah, M. M.; Nassar, M. S.; Amine, K., A Rigid Naphthalenediimide Triangle for Organic Rechargeable Lithium-Ion Batteries. *Adv. Mater.* **2015**, *27*, 2907-2912.

Chapter 2:

Chemical Exfoliation as a Controlled Route to Enhance the Anodic Performance of COF in Full-cell LIB

2.1. Introduction:

COF can be a potential anodic material in Lithium Ion Battery (LIB).^[1] Since they are built from lighter atoms and with a porous structure, they can be an excellent anodic candidate in developing lightweight batteries, which can be of use in portable devices such as solar lanterns, aviation systems and other auto-motives. However, to replace the volumetrically advantageous battery-grade Graphite as an anode, they need to have more number of Li-interactive sites per unit cell and all such sites should be made to participate. In short, the compromise made in the volumetric density to gain the gravimetric advantage should be minimal. COF's organic framework can be functionalized with Li-binding heteroatoms. Now, if a chemical strategy can be devised to achieve simultaneous exfoliation and increase of Li-loving active pockets, it could open up the possibility of an anodic material which is lightweight and yet can accomplish substantial Lithium loading when coupled with a practical cathode like LiCoO₂. Another structural advantage of COF as for exfoliation is the presence of in-layer pores, because of which their layers are held together by relatively less number of π - π interactions per specific area compared to Graphite. This makes COFs easily exfoliatable.^[2-8, 9-13] If it can be achieved via a chemical route, it can fetch high tunability.^[2-8]

Several new organic polymers with 2D structures are being considered as anodes in LIB. Some display substantial specific capacities; for example, the best-performing amorphous polymers have capacities in the range of ~ 400 - 670 mAh/g@100 mA/g.^[14-17] More specifically, the covalent organic frameworks, with a crystalline structure, exhibit capacities of 593, 600, 666 mAh/g.^[18-20] Lei et al. reported a COF@CNTs composite with a half-cell capacity of 952 mAh/g, but with moderate rate stability.^[19] In all these Graphite-resembling layered anodic COFs, the insertion/intercalation mechanism is dominant.^[21-24] In them, the concentration and the accessibility of the Li-interactive sites largely control the overall specific capacity of the anode, and the ion-diffusion rates control the charge-discharge speeds.^[25,26] Both can be positively impacted by exfoliation.

A common feature among all these studies is that most investigations have been on half-cell configuration wherein the anodic material is tested against Lithium metal (cathode). This presents the best-case scenario, as it is quite easy to pull the Lithium out of Li-metal at very low potentials (0.02-0.08V) and these Lithiums can occupy the anodes. Thus the electrochemical stability of the material being tested is not fully challenged. This is why the good performance of an anodic material in the half-cell does not necessarily translate to their full-cell.^[27-29] In contrast, in a full-cell, for example, one made using LiCoO₂, much higher potential is required to pull out the Li-ions from the cathode (~ 3.8 V).^[27] Which means the anode should withstand it. Also, the Li-insertion into the anode needs to continue as the potential drops and this typically yields a smooth and gradual curve in the

Galvanostatic charge-discharge measurements.^[30-33] To date, there are no reports of COF performing under such challenging full-cell conditions.

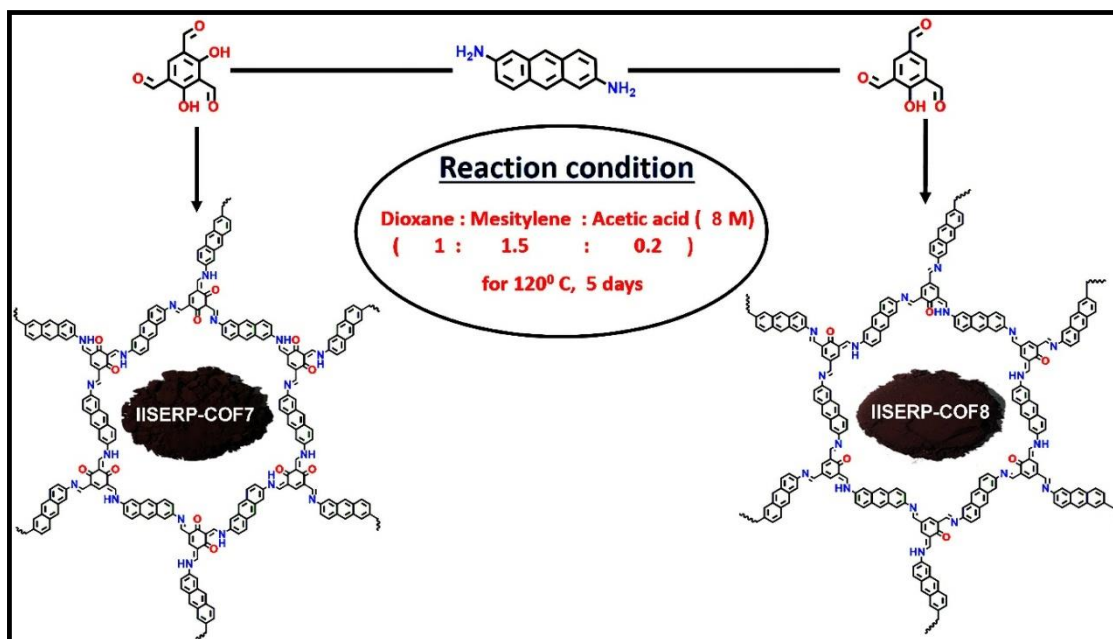
Recently, we demonstrated a COF, which forms as covalent organic nanosheets (CON) even during synthesis shows remarkable anodic performance in a LIB half-cell.^[25] Concomitantly, reports have appeared wherein COF (non-exfoliated) or its composite with highly conducting or anodic carbons have been shown to have appreciable performance in a Li-ion half-cell.^[18-20] However, a systematic study showing the enhancement of a COF's anodic performance upon exfoliation to CON is not available. Thus, our objective was to design a versatile exfoliation strategy involving a Functionalizing Exfoliation Agent (FEA) (Scheme A.2.1) and to see the performance of the COF vs. CON as an anode material in a LIB. Here, we describe two anthracene-rich COFs which are readily exfoliated into few-layer-thick nanosheets using maleic anhydride as the FEA. It provides a means to concentrate more Li-interactive carbonyl oxygens into the framework with improved active site access.^[14,34-36] These Covalent Organic Nanosheets (CONS) in a practical full-cell LIB, gives a stable specific capacity of 220 mAh/g@100 mA/g (vs. 184 mAh/g@100 mA/g for Graphite). It carries an energy density of 364Wh/kg (vs. 320Wh/kg for Graphite) over 200 cycles. The observed full-cell capacity is the highest among all organic-polymers operating with Lithium insertion or intercalation type phenomenon. For the first report of a full-cell performance of a COF-derived LIB, this is remarkable.

2.2. Results and discussion:

2.2.1. Synthesis, structure modeling and characterization of IISERP-COF7 and IISERP-COF8

IISERP-COF7: 2,4,6-triformylresorcinol (60mg, 0.3mmol) and 2,6-diaminoanthracene (98mg, 0.45mmol) were weighed into a Pyrex tube and were dissolved in dioxane (3.0 mL), to this solution, and mesitylene (4.5 mL) were added and stirred until a brownish blackcolor was observed. Following this, 1.0 mL of 6M aqueous acetic acid was added. Then the Pyrex tube was flash frozen in a liquid nitrogen bath and sealed. The Pyrex tube along with its contents was placed in an oven at 120°C for 5 days and gradually cooled for 12 hrs to room temperature. This yielded about 110mg of brownish black coloured solid which was washed with hot DMF, dioxane, MeOH, acetone and THF (85%, isolated yield). This product was also subjected to a Soxhlet extraction using DMF/methanol as solvent and filtered solid was characterized by CHN analysis (Table 2.1).

IISERP-COF8: 2,4,6-triformylphenol (55mg, 0.3mmol) and 2,6-diaminoanthracene (98mg, 0.45mmol) were weighed into a Pyrex tube and were dissolved in dioxane (3.0 mL), to this solution, and mesitylene (4.5 mL) were added and stirred until a brownish blackcolor was observed. Following this, 1.0 mL of 6M aqueous acetic acid was added. Then the Pyrex tube was flash frozen in a liquid nitrogen bath and sealed. The Pyrex tube along with its contents was placed in an oven at 120°C for 5 days and gradually cooled for 12 hrs to room temperature. This yielded about 110mg of brownish black coloured solid which was washed with hot DMF, dioxane, MeOH, acetone and THF (90%, isolated yield). This product was also subjected to a Soxhlet extraction using DMF/methanol as solvent and filtered solid was characterized by CHN analysis (Table 2.1).



Scheme 2.1. Synthetic scheme for the preparation of the COFs.

Table 2.1. CHN analysis of COFs

IISERP-COF7					
Mol. Weight (g/mol)	Formula		C	H	N
900.951	C ₆₀ N ₆ O ₄ H ₃₂	Calculated	79.99%	3.58%	9.33%
		Obtained	77.92%	4.02%	9.89%

IISERP-COF8					
Mol. Weight (g/mol)	Formula		C	H	N
872.983	C ₆₀ N ₆ O ₂ H ₃₆	Calculated	82.55%	3.58%	9.627%
		Obtained	81.92%	4.25%	8.26%

All the structure modeling were performed using the different modules implemented in the Materials Studio V8 (Figure 2.1). The Universal force field (UFF) in conjunction with a QEq charge equilibration method was employed for the geometry optimization, however, it was noticed that applying the equilibration (QEq) did not make much of a difference to the final configurations. No constraints were placed during the optimizations. For the geometry optimization of the periodic COF structure, tight-binding Density Functional Theory was employed. The Perdew-Burke-Ernzerhof (PBE) exchange-correlation functional and parameters from the Slater-Koster library were used. UFF-based Lennard-Jones dispersion corrections were included in Energy, Force and Displacement calculations and the cell was optimized. A smearing parameter of 0.005Ha was applied. For these periodic DFT optimizations, a 1x 1 x 2 cell was used. Ultrasoft pseudopotentials with a plane wave basis cut-off of 400 eV were employed. And, a DFT-D based semi-empirical dispersion correction was applied during

the optimization. Excellent convergence was achieved for all electronic levels and with no noticeable systematic shifts in energy. Tolerance used: 1×10^{-8} .

The experimentally obtained powder diffraction patterns were Pawley fitted to diffraction pattern came from the model structure. From the comparison data it is clear that eclipsed forms are energetically more favourable than staggered forms along with the better matching with the experimental PXRD patterns. (IISERP-COF8: R.E. for eclipsed = -100 kcal/mol; staggered = -199kcal/mol).

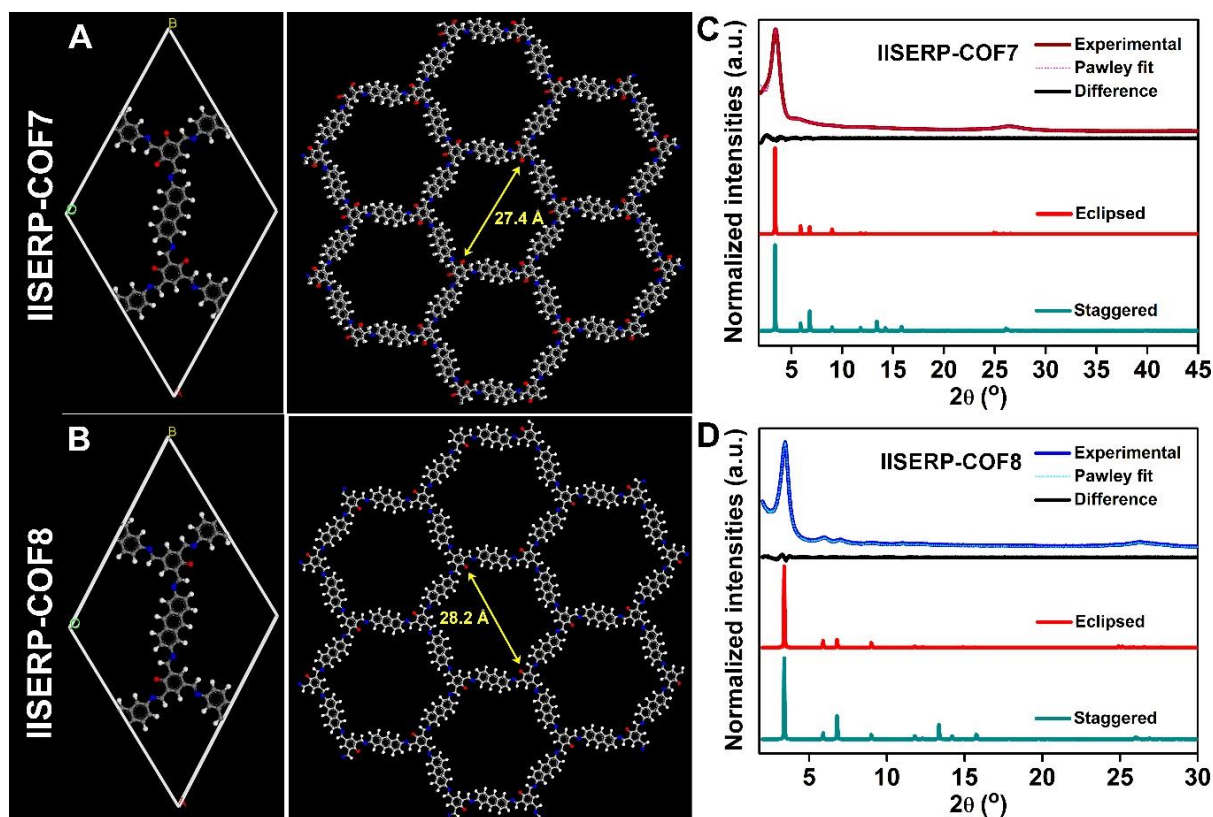


Figure 2.1. (A) and (B) unit cells and 2D view of the model structures of IISERP-COF7 and IISERP-COF8. (C) and (D) Comparison of experimental PXRDs with pawley fits and simulated PXRD patterns of corresponding eclipsed vs. staggered forms.

Adsorption-desorption isotherms of N_2 at 77 K, yielded a completely reversible type-1 isotherm for IISERP-COF7, and IISERP-COF8, which approves their expected microporous structure (Figure 2.2 and 2.3). A Barrett-Joyner-Halenda (BJH) fit to desorption branch reveals the presence of uniform ~ 28 Å pores. These COFs have a high Brunauer-Emmett-Teller (BET) surface area. All the powdered samples were subjected to Soxhlet washing using boiling THF/DMF mixture (48 hrs), to get rid of any soluble oligomers. The PXRD and porosity data reproduced well across different batches, confirming that the samples do not have any significant impurity phases.

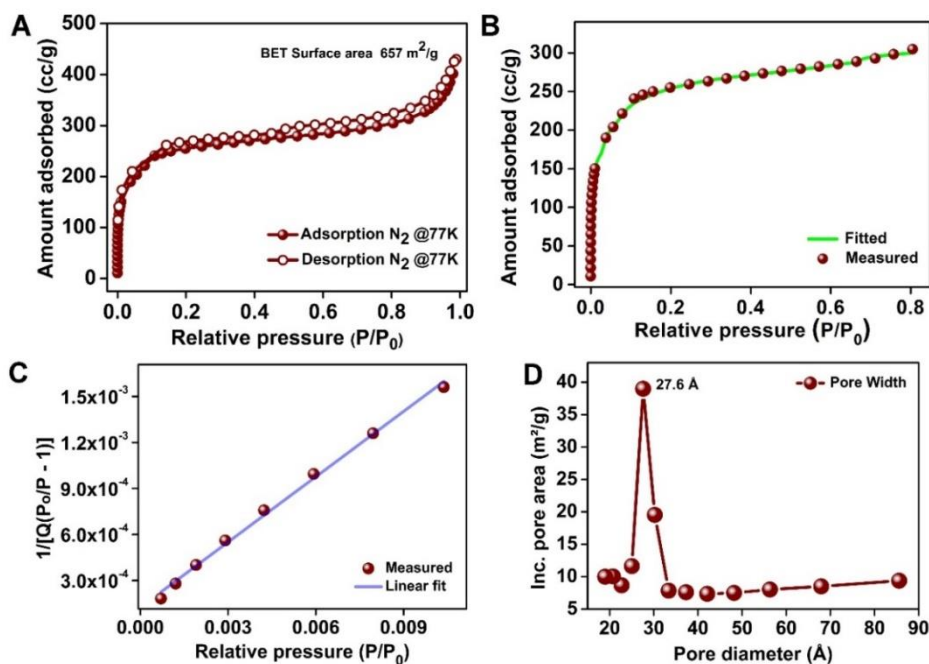


Figure 2.2. (A) N₂ adsorption-desorption isotherm of IISERP-COF7 at 77 K. (B) Goodness-of-fit plot of the adsorption isotherm plot from DFT model. (C) A BET fit obtained using the low pressure region data of the N₂ adsorption isotherm. (D) Pore width vs. incremental pore area plot of IISERP-COF7.

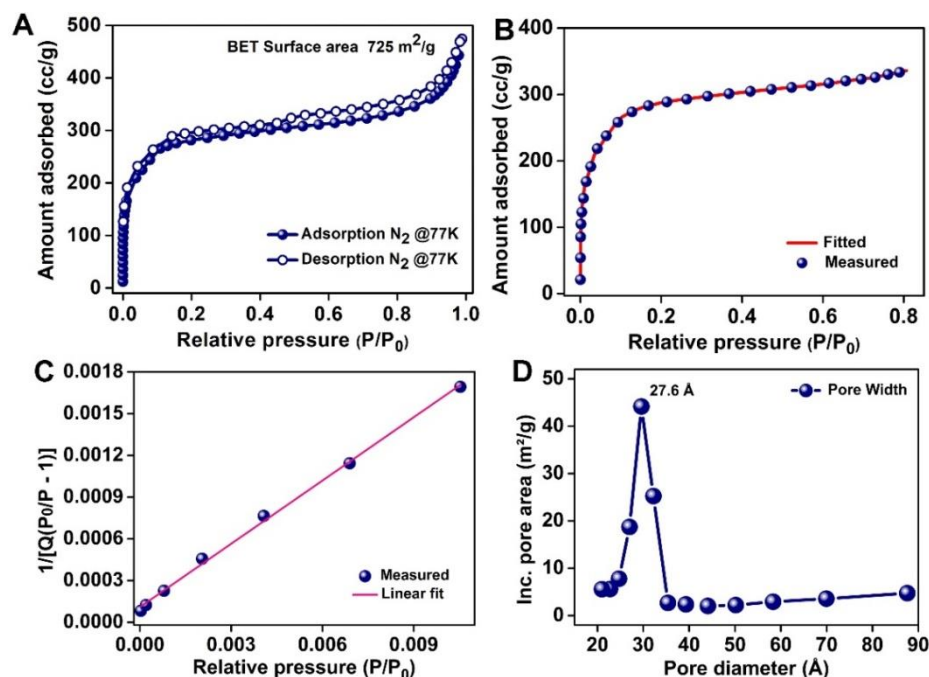


Figure 2.3. (A) N₂ adsorption-desorption isotherm of IISERP-COF8 at 77 K. (B) Goodness-of-fit plot of the adsorption isotherm plot from DFT model. (C) A BET fit obtained using the low pressure region data of the N₂ adsorption isotherm. (D) Pore width vs. incremental pore area plot of IISERP-COF8.

The high degree of crystallinity of these COFs was also confirmed from the HR-TEM imaging. At very higher magnification the lattice fringes were observed on the surface of the COF flakes. Throughout the region the detected d-spacing value was near 0.35 nm (Figure 2.4). Interestingly, this fringe value is comparable with interlayer separation distance obtained from the model structure.

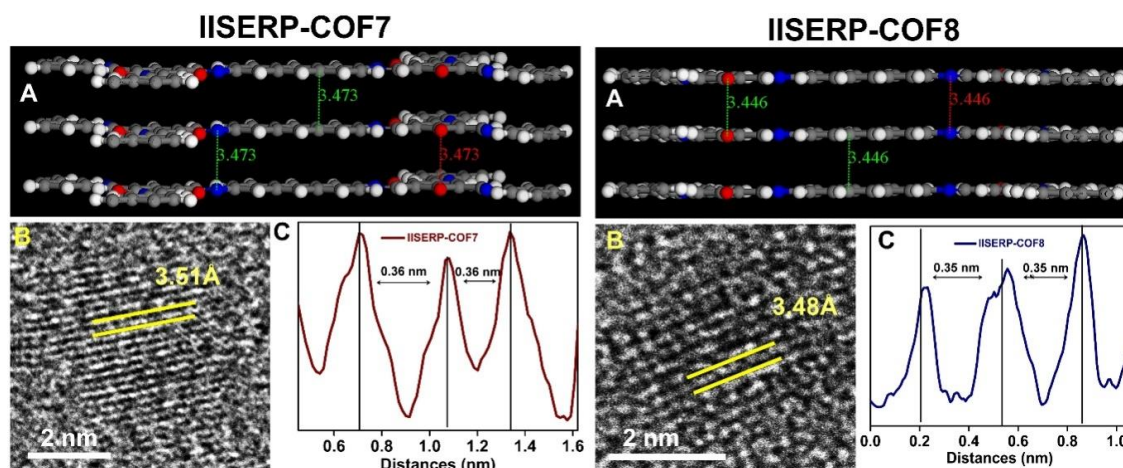


Figure 2.4. (A) Inter-layered spacing obtained from the c-axis view of the modeled structure. (B) d-spacing value obtained from the HR-TEM images. (C) A plot showing the average distances between the adjacent layers (Left: IISERP-COF7 Right: IISERP-COF8).

Both of these COFs are stable and able to sustain its crystallinity at temperature as high as 400 °C. The TGA and temperature swing PXRD confirms the structural integrity of the COF even in high temperature (Figure 2.5).

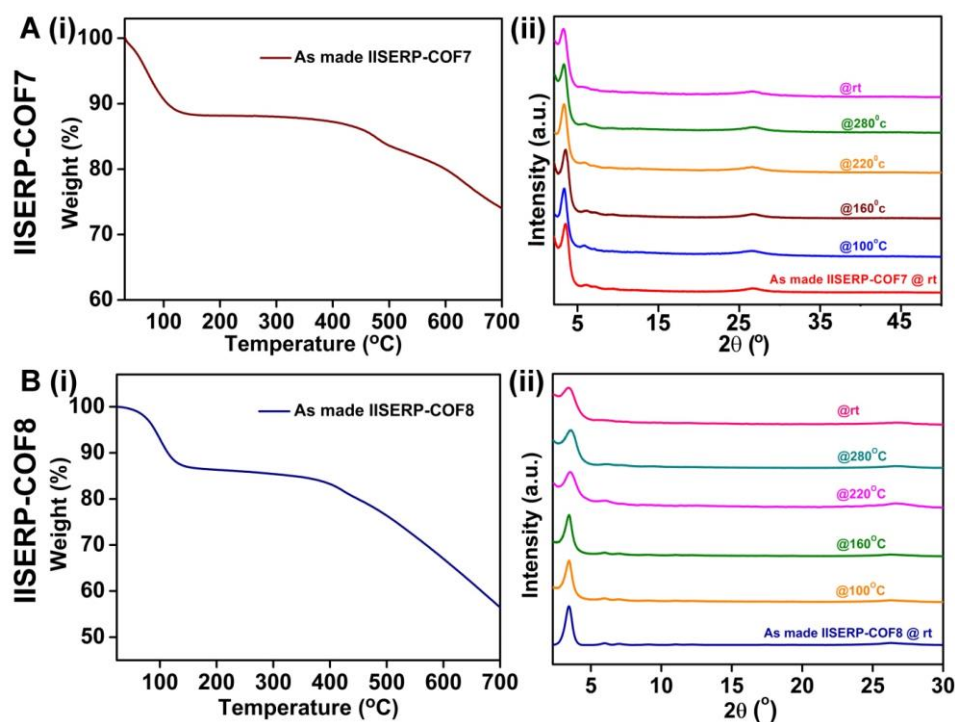


Figure 2.5. A(i) and B(i) Thermo gravimetric analysis of IISERP-COF7 and IISERP-COF8 under N₂ flow at 5K/min rate. A(ii) and B(ii) Variable temperature PXRDs of IISERP-COF7 and IISERP-COF8.

2.2.2. Chemical exfoliation of COFs to CONs (IISERP-CON2 and IISERP-CON3)

Anthracene moieties are known to react with anhydrides via an [4+2] addition mechanism.^[37-42] This breaks the conjugation at the anthracene sites, which can be monitored using UV-Vis and NMR studies.^[37-39] When this chemical reaction is carried out on systems containing stacks of anthracene, the associated structural changes can be followed.^[13] This prompted us to consider the anthracene

functionalized COFs for this exfoliation study. Here, we proposed the maleic anhydride to be a functionalizing exfoliation agent (FEA) (Figure 2.6 and Scheme A.2.1).

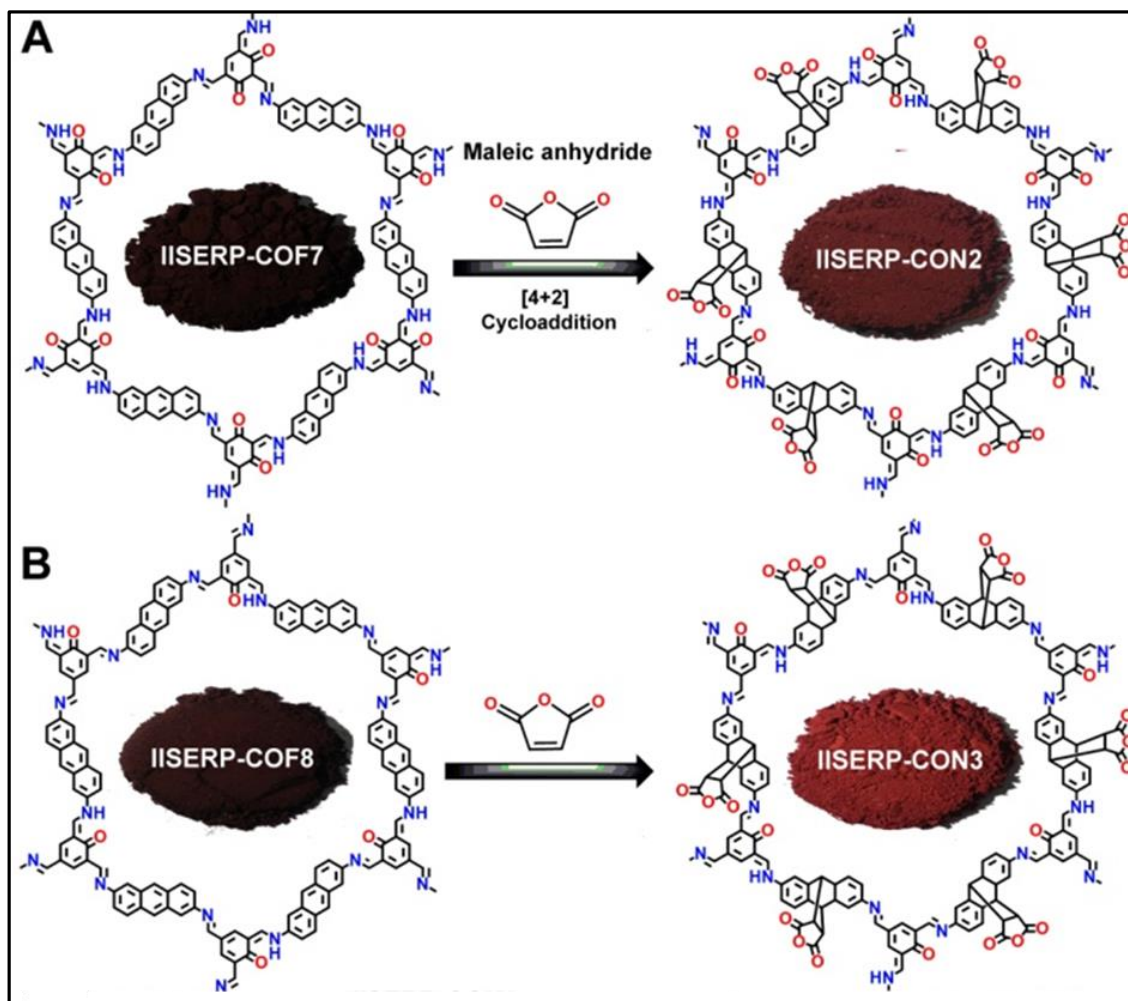


Figure 2.6. (A) and (B): Diels-Alder cycloaddition of maleic anhydride to the anthracene rings of the COFs. Inset shows the photographic images of the COF and the CONS.

IISERP COF7 and IISERP-COF8 were subjected to chemical exfoliation by Diels-Alder reaction using maleic anhydride. For that 1 M maleic anhydride solution was prepared in THF and COFs were dispersed in mesitylene. Then maleic anhydride solution transferred into COFs' dispersion and refluxed at 135°C under N₂ atmosphere. Which yielded 60% of reddish brown powders (IISERP-CON2 and IISERP-CON3).

Kinetics measurements of Diels-Alder reaction:

A homogenous mixture of anthracene and maleic anhydride, in solution, is known to follow second-order reaction kinetics during the thermal cycloaddition process. Adopting this and knowing that the D-A at the anthracene sites of the COF proceeds smoothly; we have attempted to monitor the reaction progress via the change of UV-Visible spectra during the reaction (Figure 2.7). Anthracene, the diene, shows a sharp absorption peak ~280 nm, which gradually decreases in intensity with the (4+2) cycloaddition of the dienophile, namely the maleic anhydride. The completion of the reaction is indicated by the disappearance of this absorption peak arising from the anthracene moiety of the framework.

After every three hours, a small aliquot of the reaction mixture was taken out from the reaction vessel and was quenched by freezing in liquid nitrogen. Then it was washed with tetrahydrofuran to remove the solvent mesitylene and any unreacted maleic anhydride. UV-measurements were carried out using this cleaned product dispersed in N-methyl pyrrolidone. We tracked the progress of the reaction with the change of the absorption intensity of the first peak (IA) vs. (IB) to the second peak. We plotted IB/IA vs. T (reaction time). Firstly up to 6hrs, the rate of the reaction was slow due to the higher activation energy of the Diels-Alder reaction in a heterogeneous phase compare to the homogenous phase. Then the reaction follows the second-order kinetics, and after 40 hrs, the rate again becomes slow, indicating the completion of the reaction. To confirm the completion of the reaction, we have added excess maleic anhydride after 48 hrs of reaction into the reaction vessel. Still, we did not find any change in the absorption spectra. This confirms the completion of the reaction after 48 hrs.

This besides aiding the exfoliation adds carbonyl groups into the polymeric framework through the anhydride functionality, such groups are known to interact with Lithium.^[15] The adduct formation causes a noticeable color change from black to brownish-red color. Visualizable morphological changes were also seen. Also, the Diels-Alder adduct formation between the COF's anthracene rings and the maleic anhydride follows second-order reaction kinetics as monitored from the disappearance of the anthracene's absorption peak in the UV-Vis spectra (Figure 2.7).^[43]

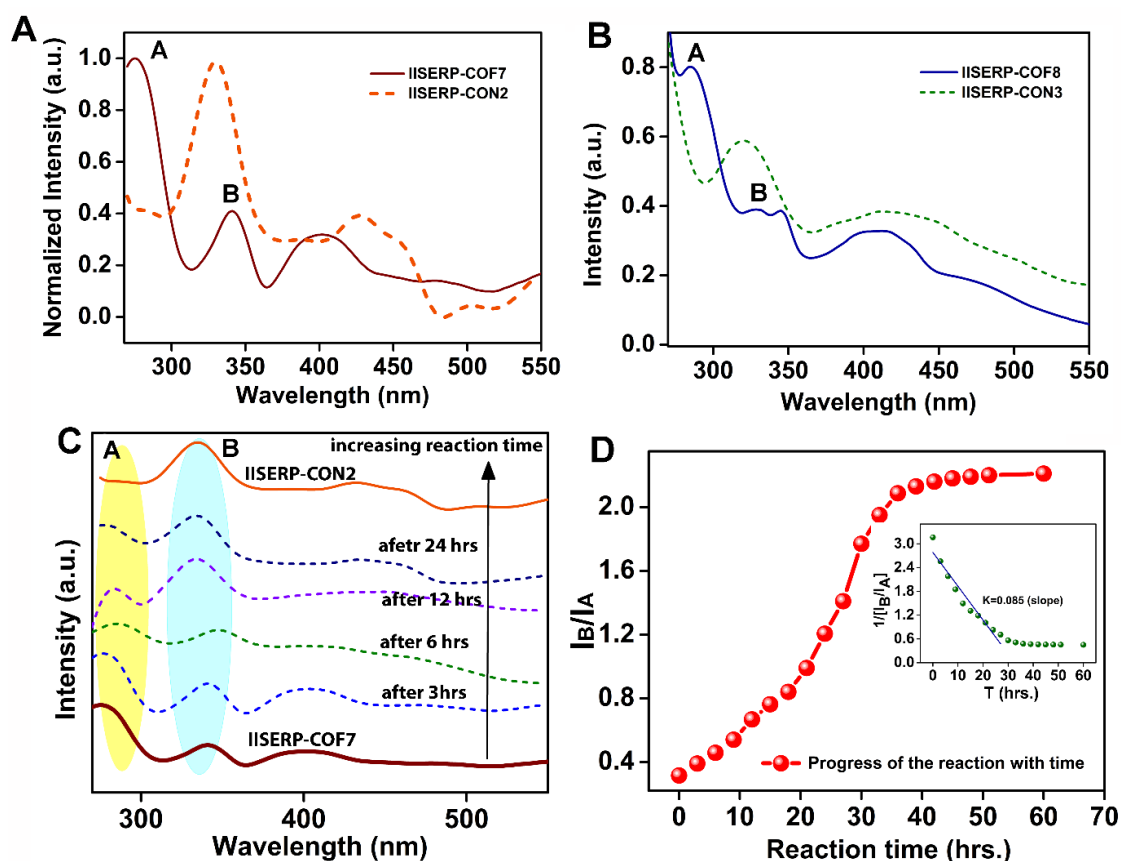


Figure 2.7. (A) UV-Visible spectra of IISERP-COF7 and IISERP-CON2 dispersed state in Dimethyl acetamide (DMA) (B) UV-Visible spectra of IISERP-COF8 and IISERP-CON3 dispersed state in Dimethyl acetamide (DMA) (C) Gradual change of the spectra of IISERP-COF7 in different time interval of the Diels-Alder cycloaddition reaction and diminishing of the first absorption peak. (D) Change of the intensity ratio of the first absorbance peak to the second one with the progress of the reaction time. (Inset) The fitting of the cycloaddition reaction rate to the second order reaction kinetics.

After completion of the Diels-alder reaction (observed from the UV-kinetics measurement), both the CONs were washed in boiled THF and DMF to remove all the unreacted anhydrides. We were unable to perform liquid state NMR analysis because of its insoluble nature in all laboratory solvents. So that the CONs were characterized by ^{13}C -SSNMR (Figure 2.8) and IR (Figure 2.9), CHN analysis (Table 2.2). The presence of anhydride C=O groups (δ :172 ppm) and appearance of a new C-C bond (δ :54 ppm) in the SSNMR confirms the formation of Diels-Alder adduct. Notably, in the COFs, the distinguishable peaks of its keto and enol forms were observed, whereas in the CONs only the keto form is prevalent. The IR peaks analysis of these plots indicate that there are no similarity in peak positions between COFs, CONs and the ingredients used to form the CONs (COFs and the maleic anhydride). So, a complete chemical addition of the anhydride groups with the COFs takes place via the Diels-Alder reaction.

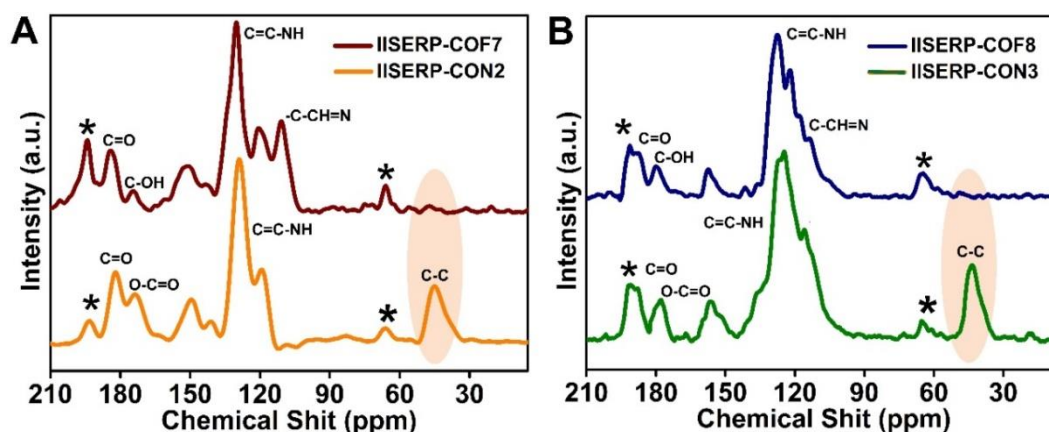


Figure 2.8. (A) A comparison of the ^{13}C solid state NMR between IISERP-COF7 and IISERP-CON2. (B) A comparison of the ^{13}C solid state NMR between IISERP-COF8 and IISERP-CON3.

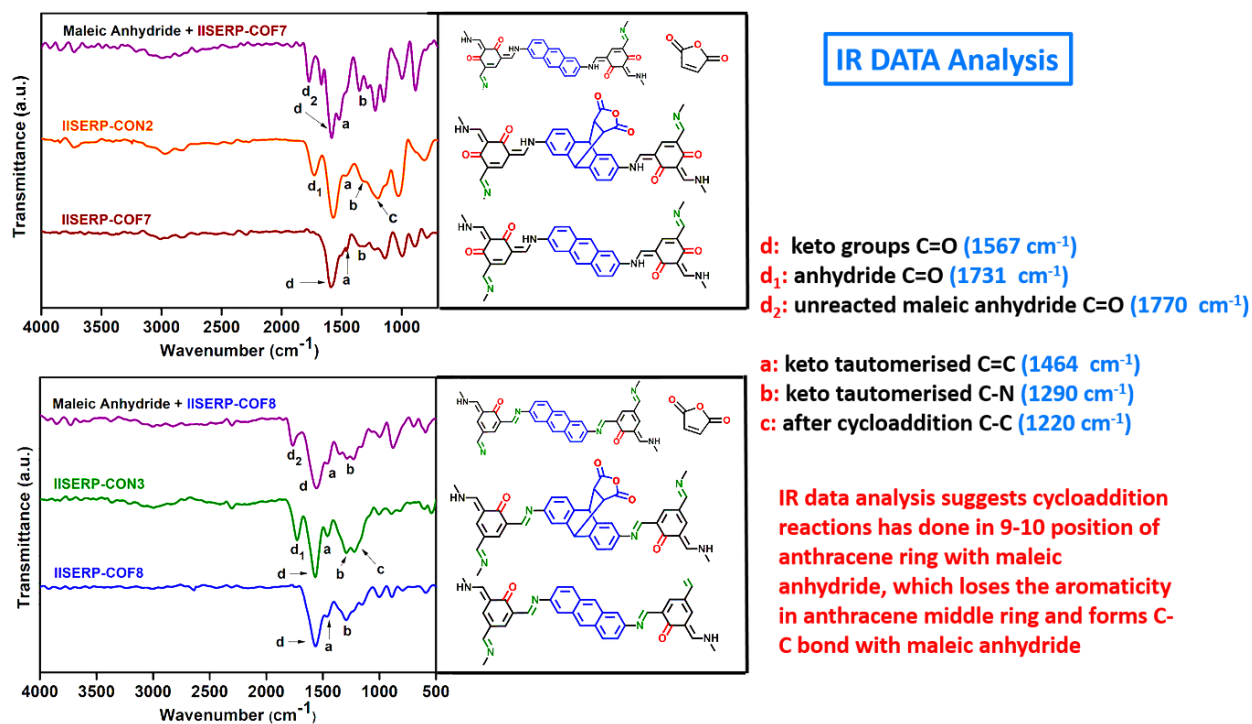


Figure 2.9. (Top) Comparison of the FTIR spectra between IISERP-COF7, IISERP-CON2 and the physical mixture of maleic anhydride and IISERP-COF7. (Bottom) Comparison of the FTIR spectra between IISERP-COF8, IISERP-CON3 and the physical mixture of maleic anhydride and IISERP-COF8.

Table 2.2. CHN analysis of CONs

IISERP-CON2					
Mol. Weight (g/mol)	Formula		C	H	N
1040.96	C ₆₄ N ₆ O ₁₀ H ₂₈	Calculated	73.85%	2.71%	8.07%
		Obtained	75.26%	3.64%	8.23%
IISERP-CON3					
Mol. Weight (g/mol)	Formula		C	H	N
1015.0075	C ₆₄ N ₆ O ₁₀ H ₂₈	Calculated	75.73%	3.38%	8.28%
		Obtained	72.26%	4.05%	7.75%

Note. This CHN analysis confirms ~60% enhancement of the oxygen content happened via chemical exfoliation process. This confirms ~65% enhancement of the oxygen content happened via chemical exfoliation process, which introduces the maleic anhydride units. Are the fonts same size for all the tables in the thesis? Maintain consistency.

A dispersion of this exfoliated COFs showed the characteristic Tyndall effect. The Tyndall effect is observed even after 24 hrs and in case of the CONs, hardly any precipitate is observed at the bottom. But the dispersion of pristine COFs even with very low concentration in solution shows turbidity. (Figure 2.10). In the case of the COFs, agglomeration slowly sets in giving rise to a turbid COF dispersion. This happens in few minutes.

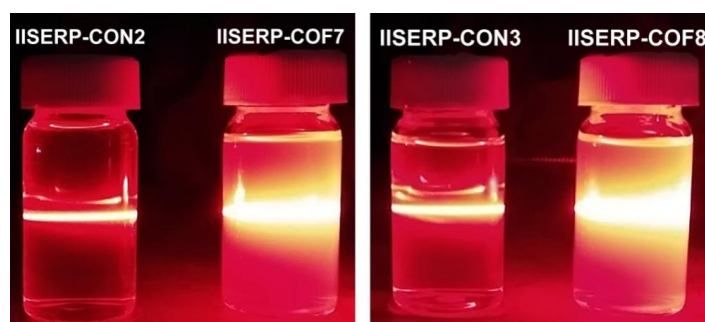


Figure 2.10. Tyndall tests using the methanolic dispersion of CONs and corresponding COFs.

Under the Field Emission Scanning Electron Microscope (FE-SEM) and Higher Resolution Transmission Electron Microscope (HR-TEM), the as-synthesized COFs appear as aggregated submicron-sized flaky crystallites (Figure 2.11). These crystallites have a hexagonal sheet morphology with prominent stacking and the lattice fringes could be observed and they correspond to a distance of 3.5 Å matching the interlayer distance expected from the modeled structure. Meanwhile, the C-C bond addition via the Diels-Alder reaction exfoliated the stacked COF into covalent organic nanosheets with substantially lowered aggregation and appeared with more exposed sheet-type structure as observed from the FE-SEM and HR-TEM images (Figure 2.12, Figure A.2.9 and Figure A.2.10). Such discrete sheets with flat surfaces distribute homogeneously.

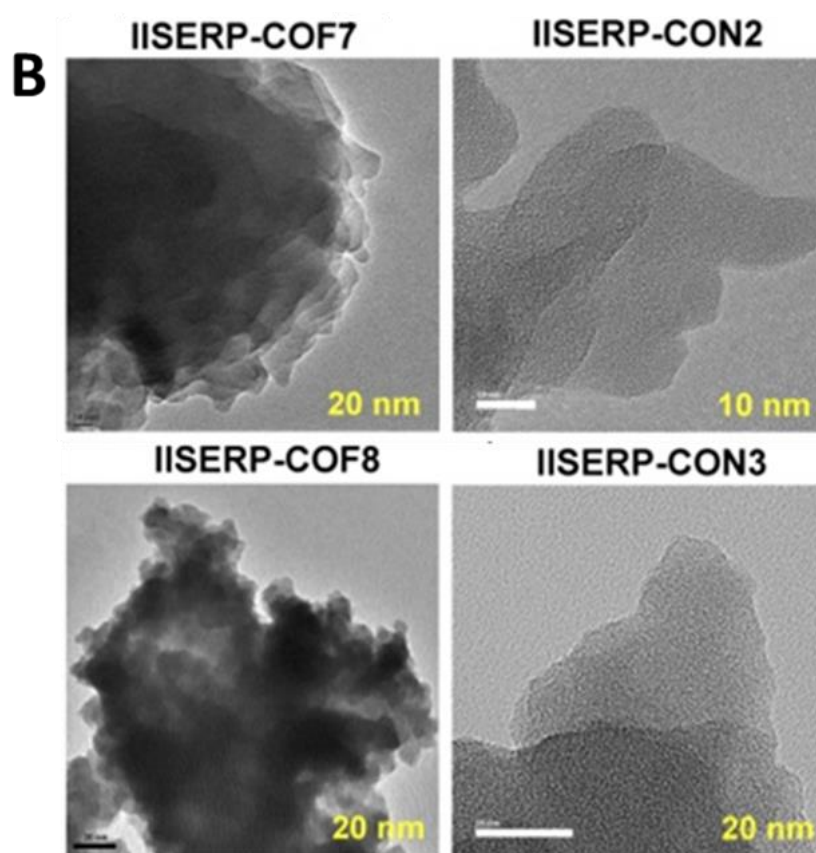
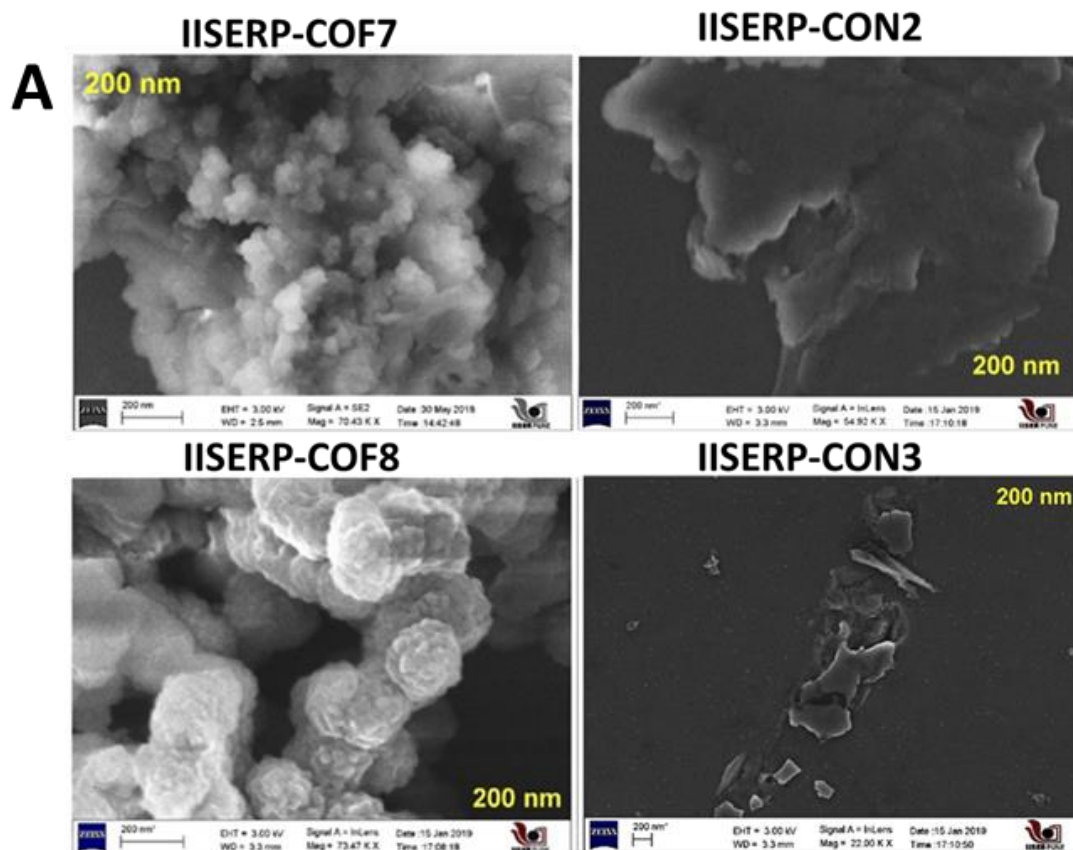


Figure 2.11. (A) Comparative FESEM images of the COFs and CONs. (B) Comparative HR-TEM images of the COFs and CONs. The chemical exfoliation of the COF to few-layer thick CON via the cycloaddition is evident. Presence of micro pores in the CONs can also be.

Now, there are two possibilities for the final structure of the CONs: (i) all the cycloaddition could have occurred on one face of the anthracene units of the COF layer (*all-up*); (ii) the cycloaddition could be happening at either faces of the anthracene units, giving rise to the anhydride group running above and below the plane of the layers (*up-down*) (Figure A.2.12). Though the structure with the up-down arrangement has lower relative energy (-29401 kcal/mol), the packing efficiency quantified by void volume turns out to be $\sim 26\%$ for both the configurations. The ordered packing is evident from the observation of lattice fringes for these CONs under the HR-TEM. Lattice fringes with two different separations, 3.4 and 5.4 Å, were observed, which agrees well with the modeled structure of the CON (Figure 2.13, Figure A.2.9 and Figure A.2.10). The larger inter-planar separation in the CON could also aid the facile insertion.

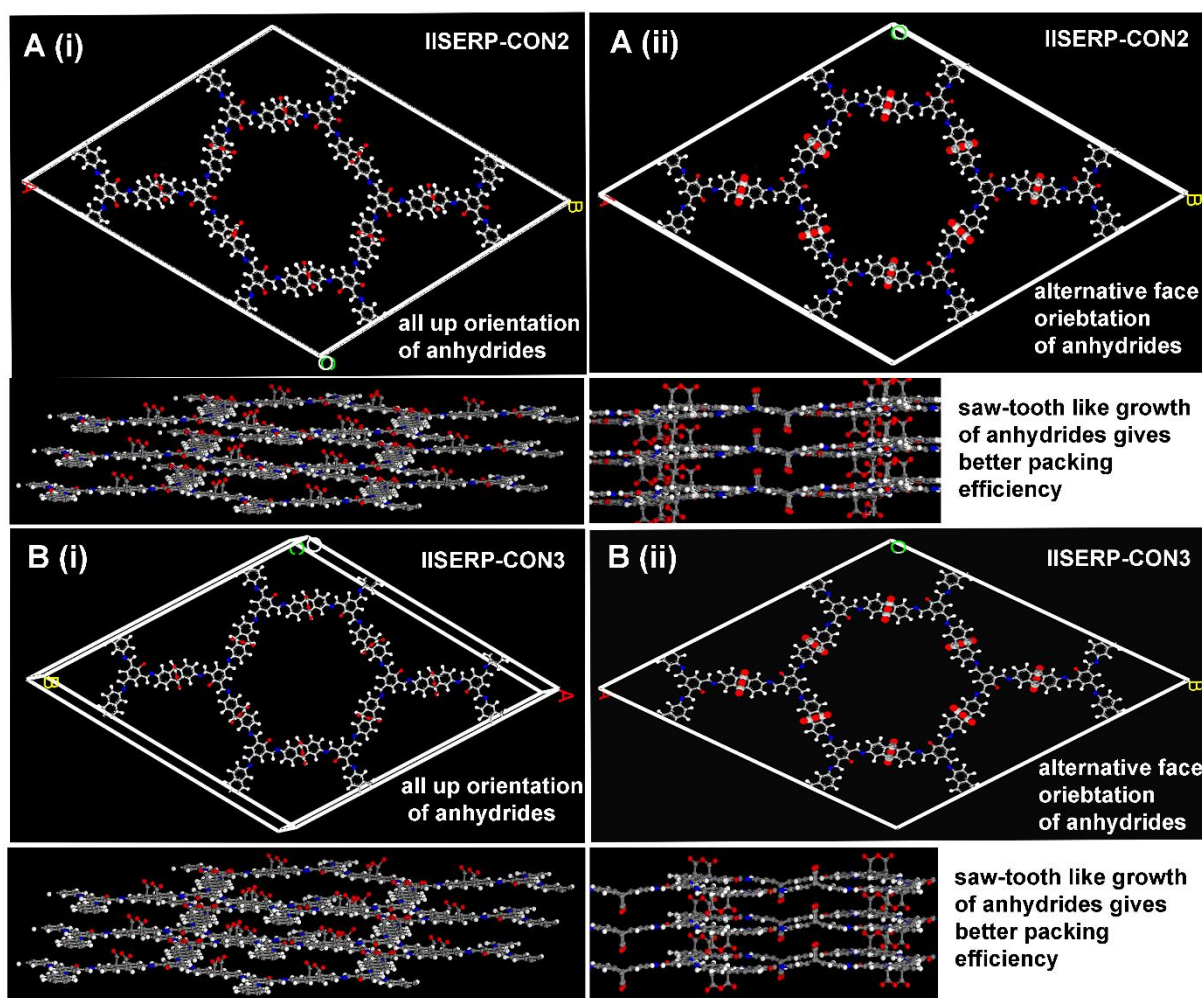


Figure 2.12. A(i) and B(i) DFTB energy-minimized model of IISERP-CON2 and IISERP-CON3, where all the anhydride groups are pointing vertically up from the plane of the COF layer (*all-up*). A(ii) and B(ii) DFTB energy-minimized model structure of IISERP-CON2 and IISERP-CON3, where the anhydride groups are in alternative up and down position in between the layers (*up-down*). The latter configuration with alternating up and down anhydride moieties provides better packing efficiency, with slightly better energy stabilization.

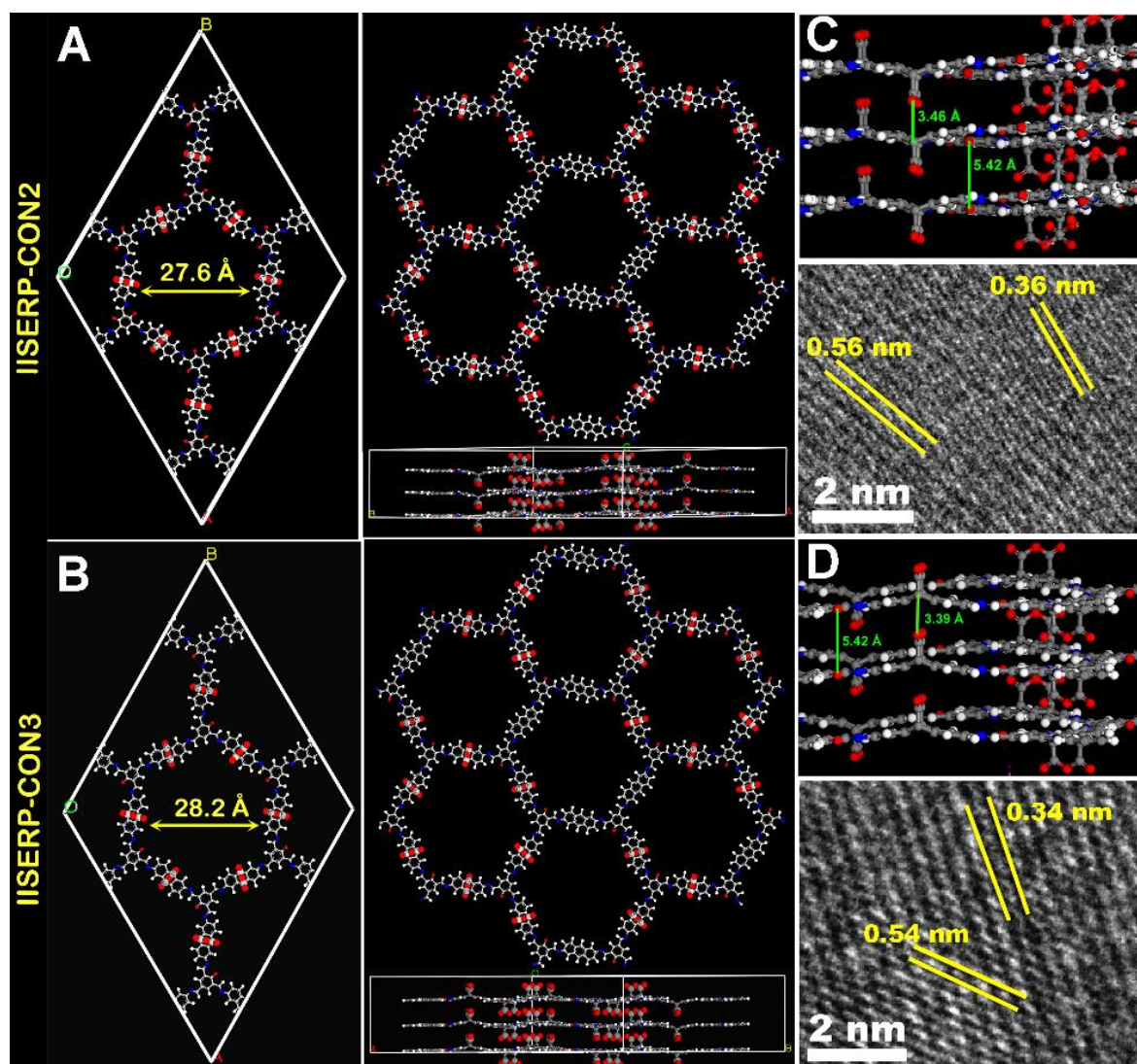


Figure 2.13. (A) and (B) Structure of the Diels-Alder cyclo-added CONs modeled using DFT methods (Relative energy for up-down anhydride con-figuration, IISERP-CON2= -100kcal/mol; IISERP-CON3= -95 kcal/mol). The lowest energy conformer having the maleic anhydride groups positioned up-and-down the COF layers is shown. C and D: Comparison of the interlayer separation of the model with those obtained from the HRTEM images.

Firm evidence for the exfoliation into CONs comes from the AFM. In comparison to the COFs (100 to 200 nm thick), these exfoliated nanosheets are very thin with only 1 nm and 1.5 nm thickness on average, which correspond to only 3-5 layers (Figure 2.14. and Figure A.2.11-A.2.15). Thickness and aspect-ratio were calculated with the help of AFM data analysis for both the products. From approximately, 65 images of each sample, the statistical distribution plots were made. Majority of the IISERP-CON2's flakes have a thickness in the range of 1-2 nm. The IISERP-CON3's thickness ranged from 2-3 nm. To our best knowledge, this is the lowest thickness values achieved for any exfoliated COFs. The lateral length of the nanosheets ranged from 1000 to 3000 nm. This yields extremely low aspect ratio (height/length) of $\sim 1 \times 10^{-6}$ - 2×10^{-6} (Figure A.2.15). Notably, the lateral dimensions of the flakes obtained from this chemical exfoliation route are much larger compared to the earlier reported self-exfoliated IISERP-CON1,^[25] but it is comparable to the dimensions observed in the solvent exfoliated COF reported by Dichtel and co-workers.^[2]

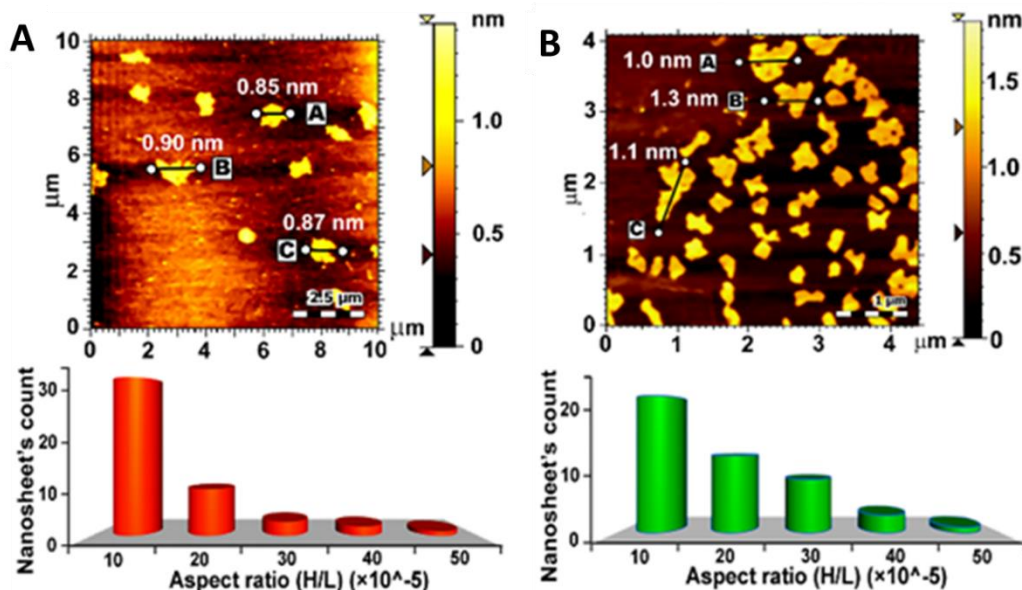


Figure 2.14. (A) and (B): Representative AFM images showing the thickness distribution (lateral width (L) and height (H)) of the IISERP-CON2 and IISERP-CON3 flakes respectively obtained from the chemical exfoliation. The statistical plots of the aspect ratio (H/L) are obtained from 65 independent AFM images.

The NMR comparisons also revealed the COFs co-existing in keto and enol tautomeric forms, but the CONs, in their solid-state, exist predominantly in the keto form (Figure 2.8). This has implications on the interactions with the incoming Lithium species during the cell operation. When the CONs were exposed to acidic (6N HCl) or basic (6N NaOH) environments they remained in their keto form which was confirmed from the lack of any phenolic -OH groups in the IR spectra, which is in contrast to the COFs (Figure 2.15).^[13] Thus the exfoliation alters the host's chemical structure. The CONs are stable up to 300 °C observed from TGA.

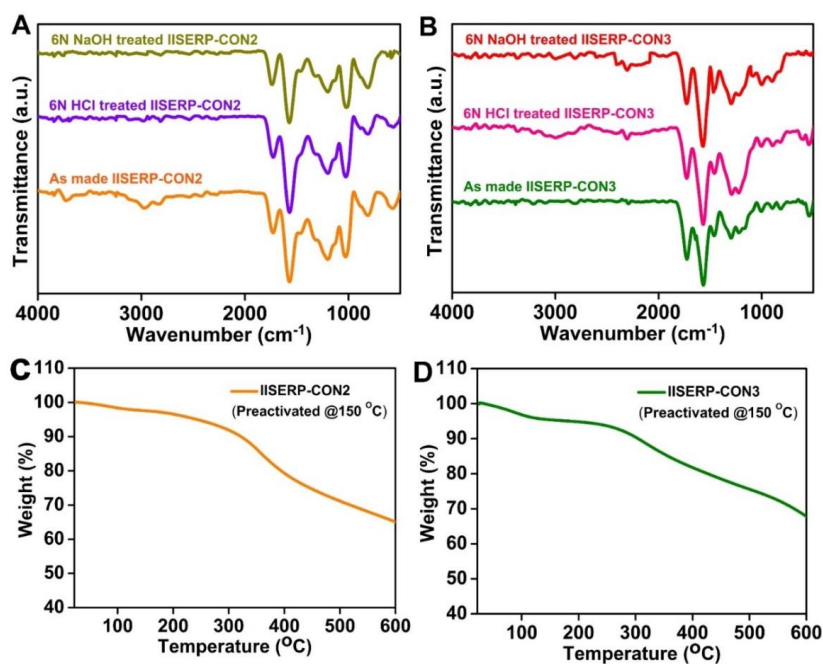


Figure 2.15. (A) and (B) Functional groups stability of CONs tested in 6N HCl and 6N NaOH by FT-IR. **Note.** No phenolic -OH peak was observed in CONs. (C) and (D) Thermal stability of pre-activated CONs.

The formation of the disordered nanosheets from the highly π -stacked COFs was monitored by comparing the Bragg reflections of the PXRD patterns and the adsorption data of the pre- and post-chemically exfoliated phases (Figure 2.16 and Figure 2.17). For this purpose, the reaction mixtures were quenched after 12 hrs and the insoluble solid products were isolated. In the PXRD, the intensity of the $(100/010)$ reflections appearing at the lowest 2θ drops significantly, while the intensity of the $00l$ reflections increases as the exfoliation is achieved (Figure 2.17). For both CONs, a prominent peak appears at 17.5° and the peak at 26.5° becomes more intense after the completion of the exfoliation (after 48hrs of reaction) (Figure 2.16 and 2.18). Importantly, the former peak indexes to the 001 reflection, while the higher angle peak to the 002 reflection from the optimized simulated structure. However, the peak at 17.5° is relatively sharper, and we suspect this could be due to some preferred orientation effects and not due to any oligomeric species forming as an impurity. This is because the powder pattern shown in Figure 2.18 was obtained very reproducibly from multiple batches of samples.

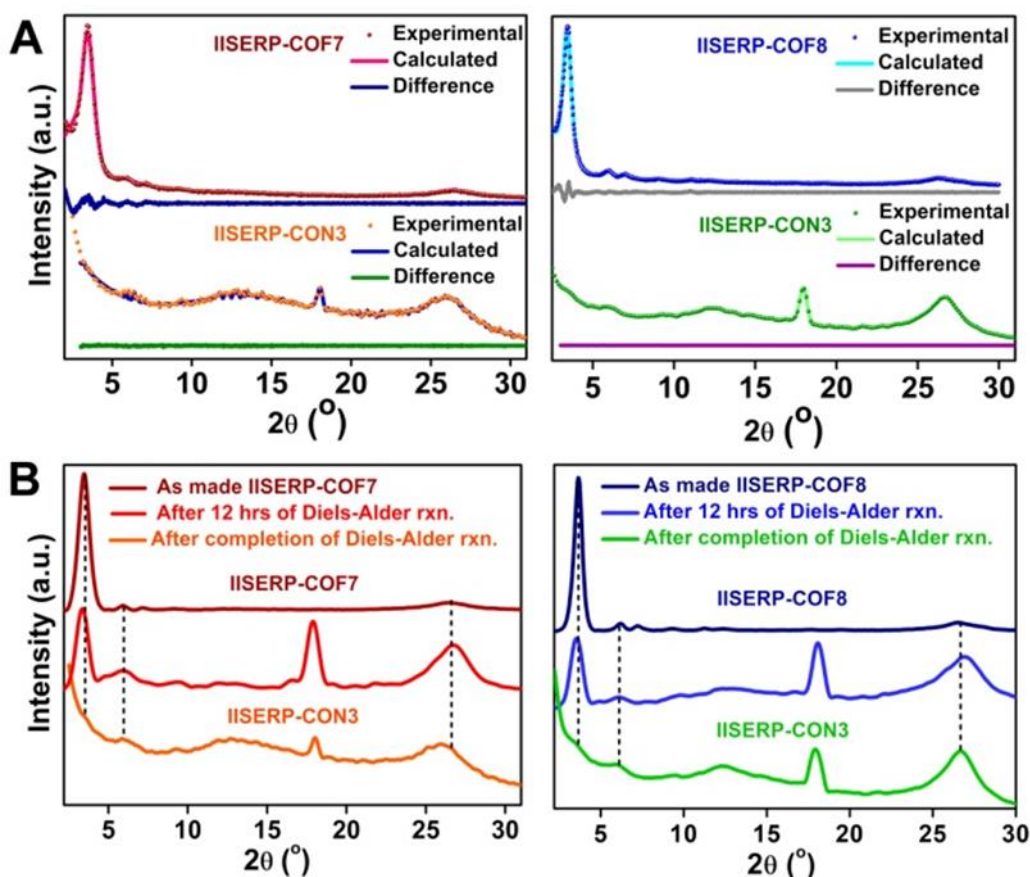


Figure 2.16. (A) Pawley fits of the COF and the CONs refined using Materials Studio. (B) The experimental PXRD of the COF compared with the PXRD of the extracts isolated at different time intervals during the cycloaddition reaction.

These changes in the PXRD pattern can be explained by considering the change in the ratio between the ab-plane atoms exposed to the X-ray to the c-direction planes that get exposed when the highly π -stacked COF converts to a few-layer thick disordered CON. Also, the appearance of the peak at $\sim 17.5^\circ$ in the PXRD pattern of the CONs is because of the introduction of the anhydride functionality (Dienophile), which orients along the c-direction. Hence the $00l$ reflections get altered. Notably, in the simulated PXRD pattern of the CONs, the peak at $\sim 17.5^\circ$ is prominent and this appears when we

introduce the maleic anhydride appendages into the modeled structure. This peak indexes to the 001 reflection in the tb-DFT optimized structure (Figure 2.18).

The appearance of this prominent peak at $2\theta = 17.5^\circ$ (001 reflection) in the CON is further supported by the presence of lattice fringes in the HRTEM images with a spacing of ~ 0.56 nm, which corresponds to a $2\theta = 17.5^\circ$ (from Bragg's Eqn.) (Figure 2.18). So, in the CON's PXRD, both the increase in the contribution from the atomic planes in the c-direction due to disorderliness as well as the increase of the number of atoms along the c-direction due to the insertion of the maleic anhydride units appears to increase the intensity of these $00l$ reflections.

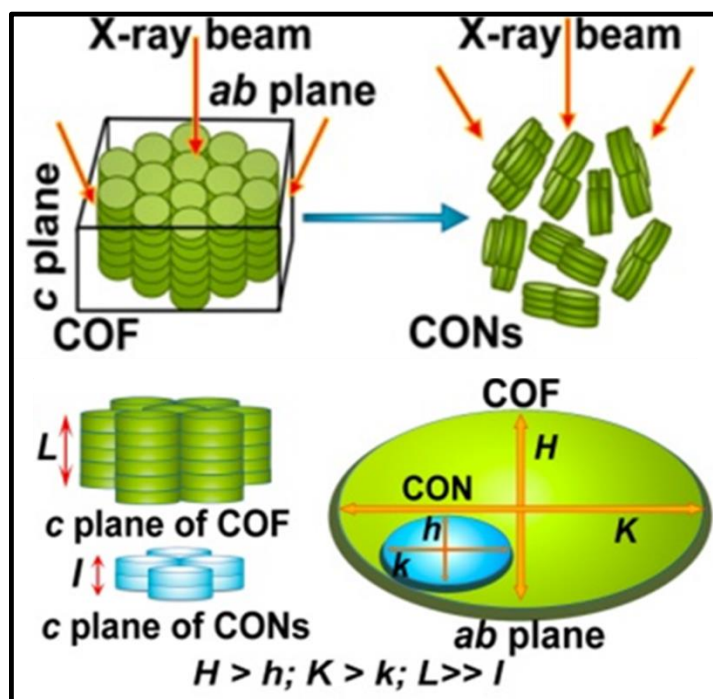


Figure 2.17. A schematic illustrating the reason for the relative intensity variations in the PXRD of the COF vs. CON. COF exposes more of *ab*-plane atoms, while the CON with increased height/lateral-length ratio exposes more atoms along the *c*-direction. COF planes are indicated with HKL; CON planes are indicated with hkl.

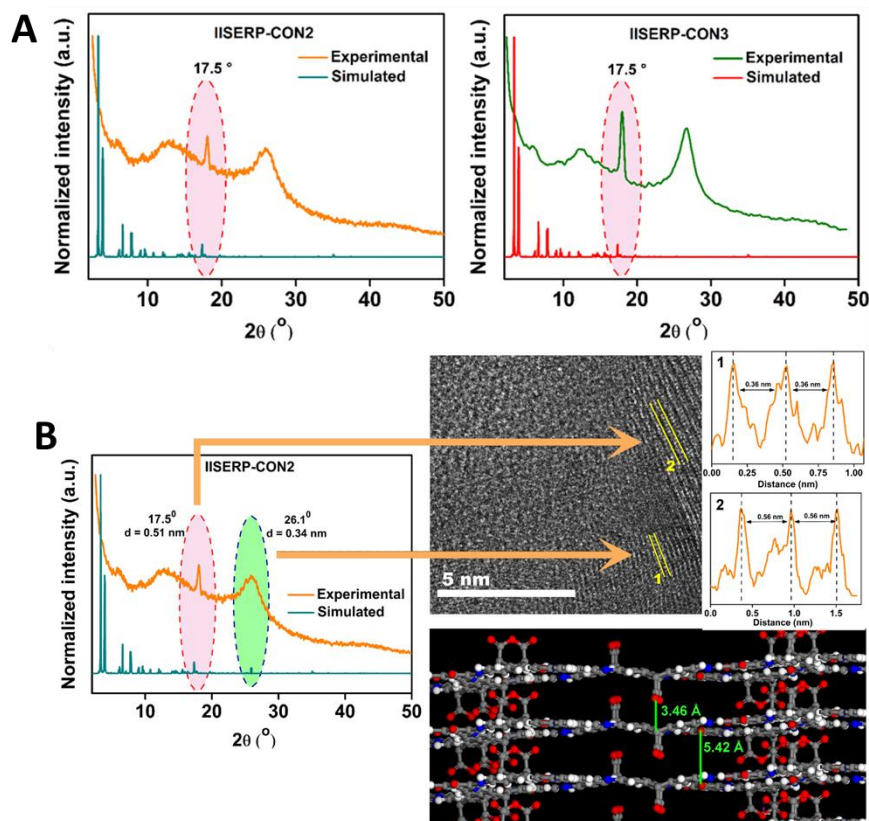


Figure 2.18. (A) Comparison of the experimental PXRDs with simulated PXRDs patterns of corresponding eclipsed form of the CONs. A peak at $2\theta \approx 17.5^\circ$ in the experimental pattern was assigned with the help of simulated pattern. Importantly, this peak was not present in the experimental PXRD of the as-synthesized COFs. **(B)** A well reflection of the crystallinity of IISERP-CON2 in PXRD and in lattice fringes observed under HRTEM. Theoretical modelling of IISERP-CON2 shows the increased interplaner distances along C axis view.

The porosity data further supports with a noticeable drop in BET surface area (from 657 to 164 m^2/g and 725 to 230 m^2/g) with the increase of the reaction time (Figures 2.19 and Figure A.2.16-2.17). This is because CONs do not form channels/tunnels as deep as COF in the c -direction. Nevertheless, the pore widths for IISERP-CON2 and IISERP-CON3 after 12 hrs and 48 hrs reaction remain almost the same compared to the pristine COFs. This advocates that the layer-by-layer exfoliation of the COF sheets did not destroy the orientation of the functional groups along the nanopores. Besides, in this exfoliated configuration, achieved by the insertion of the anhydride groups, many surface-exposed C=O groups become available for chemical interactions with Lithium as perceived from XPS and Raman studies (Figure A.2.19 –A.2.21 and Table A.2.3-A.2.4)

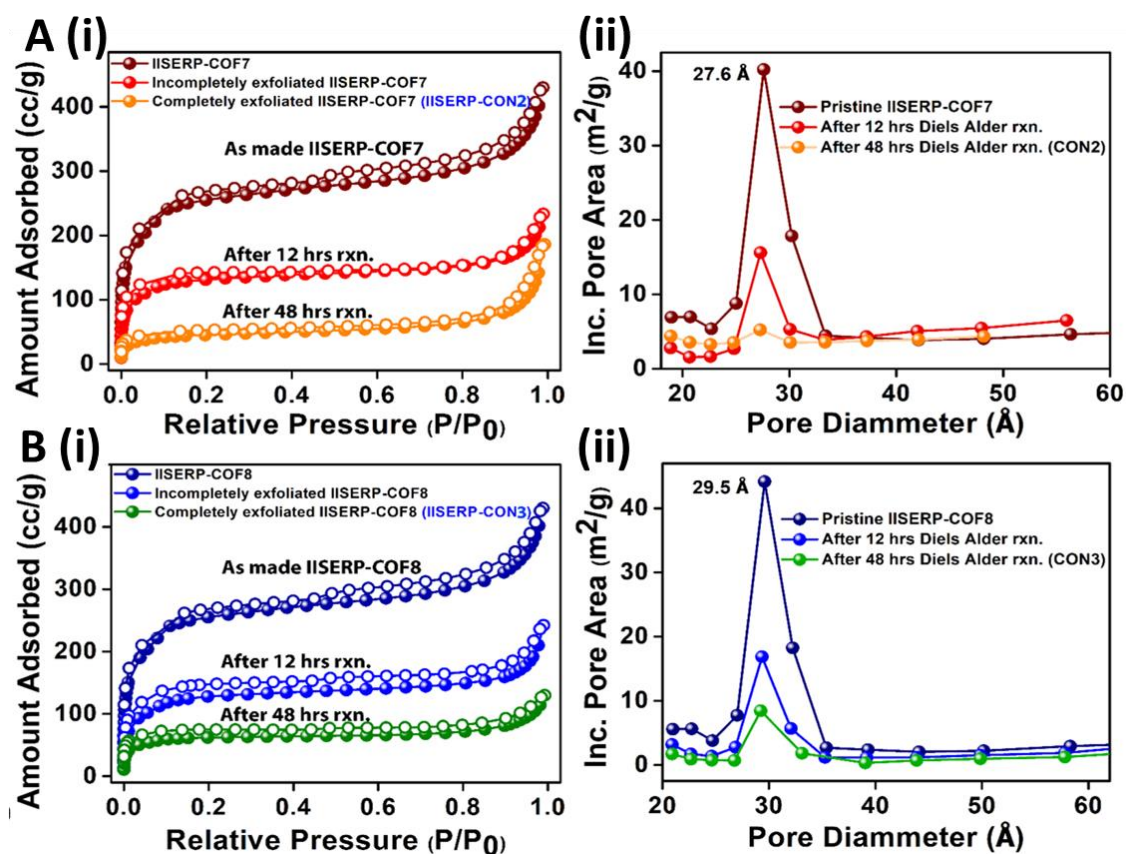


Figure 2.19. A(i) and B(i) N₂ adsorption-desorption isotherms of the COF and the CONs collected at 77K. The Diels-Alder adduct formation completes in 48 hrs. **A(ii) and B(ii)** Pore width vs. incremental pore area plot of COFs and CONs obtained from BET fit of the isotherm data.

2.2.3. Electrochemical measurements in a half-cell LIB- results and additional discussions

Taking advantage of the present case, where the COF could be chemically exfoliated to CON, we have compared the anodic performance between them. For this, four half-cell assemblies were fabricated in an argon filled glove-box using a slurry made by mixing 75% of the active material (IISERP-CON2/IISERP-CON3/IISERP-COF7/IISERP-COF8), 20% conducting carbon, 5% PTFE binder in N-methylpyrrolidone (NMP) solvent (Note: This composition was maintained in all cases). This slurry was coated on a copper foil, current collector) and dried in vacuum oven for 24 hrs and cut into electrodes in the size of 2032 coin cell. The electrodes of all the COFs and their corresponding CONs were assembled into individual coin-cells (2032) using Li metal as the counter electrode and 1M LiPF₆ in 1:1 ethylenecarbonate:dimethylcarbonate mixture as electrolyte. 2% Fluorethylene carbonate was added to the electrolyte solution to reinforce the near-complete formation of the SEI in the very first discharge process. The coin-cells with an Open Circuit Voltage (OCV) of around 2.85 V were connected to a charge-discharge cyler and cyclic voltammograms (CV) were recorded at a scan rate of 2mV/s. An anodic potential window of 0.01 to 3V was swept. Notably, the reversible peaks due to the insertion-deinsertion of Lithium were observed in both COF and CON with similar looking CV profiles (Figure 2.20). However, there are some differences: For IISERP-COF7 and IISERP-COF8, two reversible CV peaks appeared at 0.03 V and at 1.0 V; for IISERP-CON2 and IISERP-CON3, three reversible peaks appeared at 0.03 V, 1.0 V and at 1.6 V. The relatively sharper peak appearing at a very low potential of 0.03 V (R1/O1) in the CONs are not prominent in the COFs. This peak at such low-potential has been observed during the intercalation of Li-ions into graphitic materials ^[A.2.4, A.2.5] as well as for the facile

insertion Li-ions into the nanopores of the self-exfoliated COF.^[A.2.1] Also, by comparison of the CVs of the COF vs. CON, an extra peak (R3/O3) is observed at 1.6V ((R2/O2) for the CONs, which most likely is due to the chemical interaction of Li-ions with the anhydride units.^[S6, S7] The peak at 1.0 V (R2/O2) matches well with the earlier reported Lithium-ion-keto group interactions found in the COF/CON.^[A.2.1, A.2.6-A.2.9] These interactions are validated by the presence of discernible peaks in the XPS, Raman spectra (Figure 2.20A(ii) and Figure 2.20B(ii), Figure A.2.19–A.2.21 and Table A.2.3-A.2.4). The L1s XPS spectra exhibit peaks corresponding to Li-O interactions and the Li-O₂C-R, which are from the Li's interactions with the phenolic oxygens and the anhydride groups, respectively.^[A.2.13-A.2.15] Notably, no Li-N interactions could be found (Table A.2.3 and A.2.4). Also, the CV shows an increased current associated with the (R1/O1) and the (R2/O2) peaks of the CON as compared to the COF. We believe, this is due to the carbonyl oxygens being more exposed for interaction with the incoming Li-ions in the exfoliated structure of the CONs compared to the COFs, where they are more buried (Scheme 2.3).

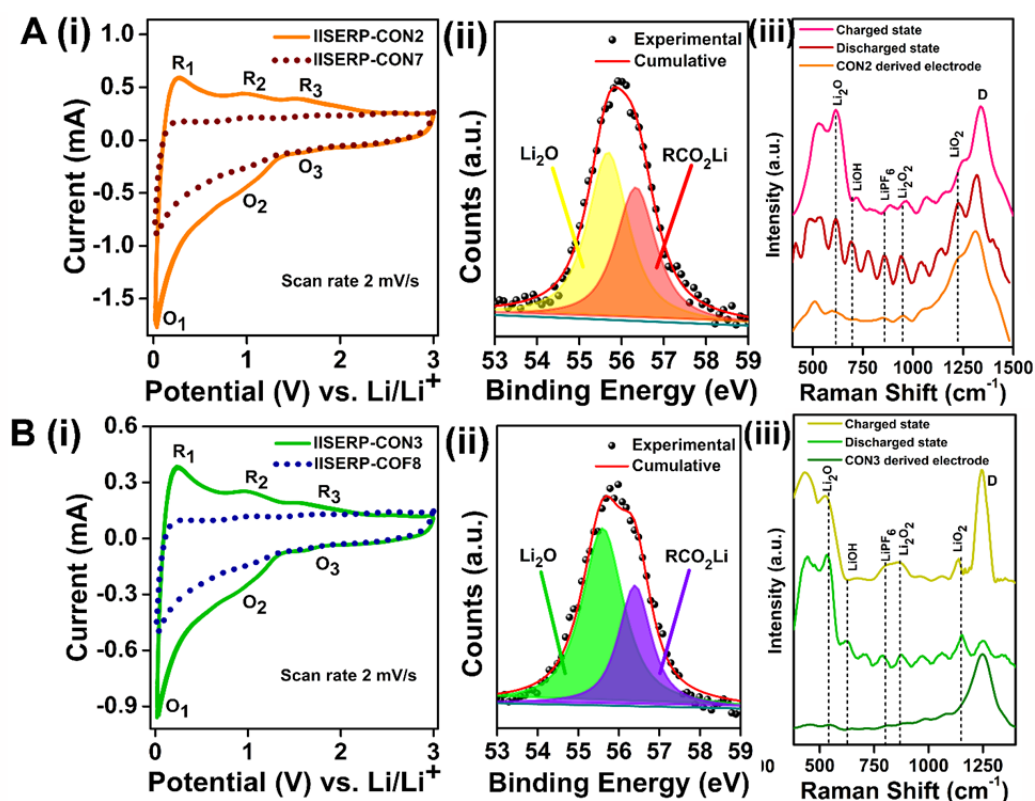


Figure 2.20. A(i) and B(i) Comparative CV-plots of IISERP-COF7 and IISERP-CON2 measured in a half-cell configuration with a 2 mV/s scan rate. A(ii) and B(ii) Li 1s XPS spectra showing the Li-O interactions, the oxygens are from the framework atoms. A(iii) and B(iii) Comparison of the Raman spectra of IISERP-CON2 and IISERP-CON3 derived electrodes with its completely discharged state and completely charged state.

Multiple CV cycles measured using the same CON-derived electrodes showed excellent reversibility (Figures A.2.21). With the increase of the number of cycles, the insertion of Lithium under very low potential (0.03V) enhances, which reflects in the higher current contribution in low potential with the cycling of the half-cell battery. Moreover, the reversible peak in higher potential (1.6V) becomes more prominent and contributes more amount of the current than the initial cycles.

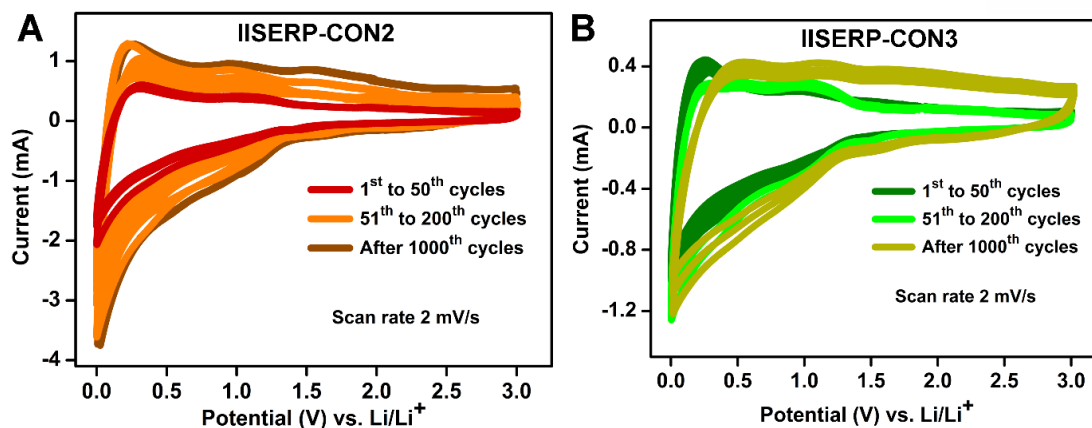


Figure 2.21. (A) and (B) CV measurements of the CON derived half-cell shows complete reversibility under lithiation-delithiation process. With increase of the cycle number the shape of the curve changes.

Concurrent with the observations from the CV, the I-V curves from the Galvanostatic charge-discharge experiments, carried out at a constant current density of 100 mA/g, showed superior performance by the CONs (Figure 2.22A and Figure 2.22B). In all cases, in the initial discharge mode, high capacities were evidenced due to the SEI formation, but the coulombic efficiency was very low. After the 2nd cycle, the capacities stabilize reaching values of 200 mAh/g and 130 mAh/g for the IISERP-COF7 and IISERP-COF8, respectively. These capacities were retained even after the 600th charge-discharge cycle (Figure 2.22C). In contrast, a different behavior was observed for the CONs. In the CONs, following a large capacity in the SEI layer forming 1st cycle (IISERP-CON2: 650 mAh/g and IISERP-CON3: 550 mAh/g), a drastic capacity drop was observed in the 2nd cycle (IISERP-CON2: 340 mAh/g and IISERP-CON3: 230 mAh/g). Following this, in both CONs, unlike the COFs, the capacity started to increase steadily up to ~300 cycles, stabilizing at 790 mAh/g for IISERP-CON2 and 580 mAh/g for IISERP-CON3. These high capacities remain intact even after 1000 cycles retaining their 100% coulombic efficiency (Figure 2.22.C). From the voltage plateau of the discharge profile of the CONs, it is seen that the marked jump in capacities occur in the low potential window of 0.5 to 0.01 V. This is in excellent agreement with the observations in the low-potential region of the CV, which was explained based on a facile insertion of Li-ions into the CONs.

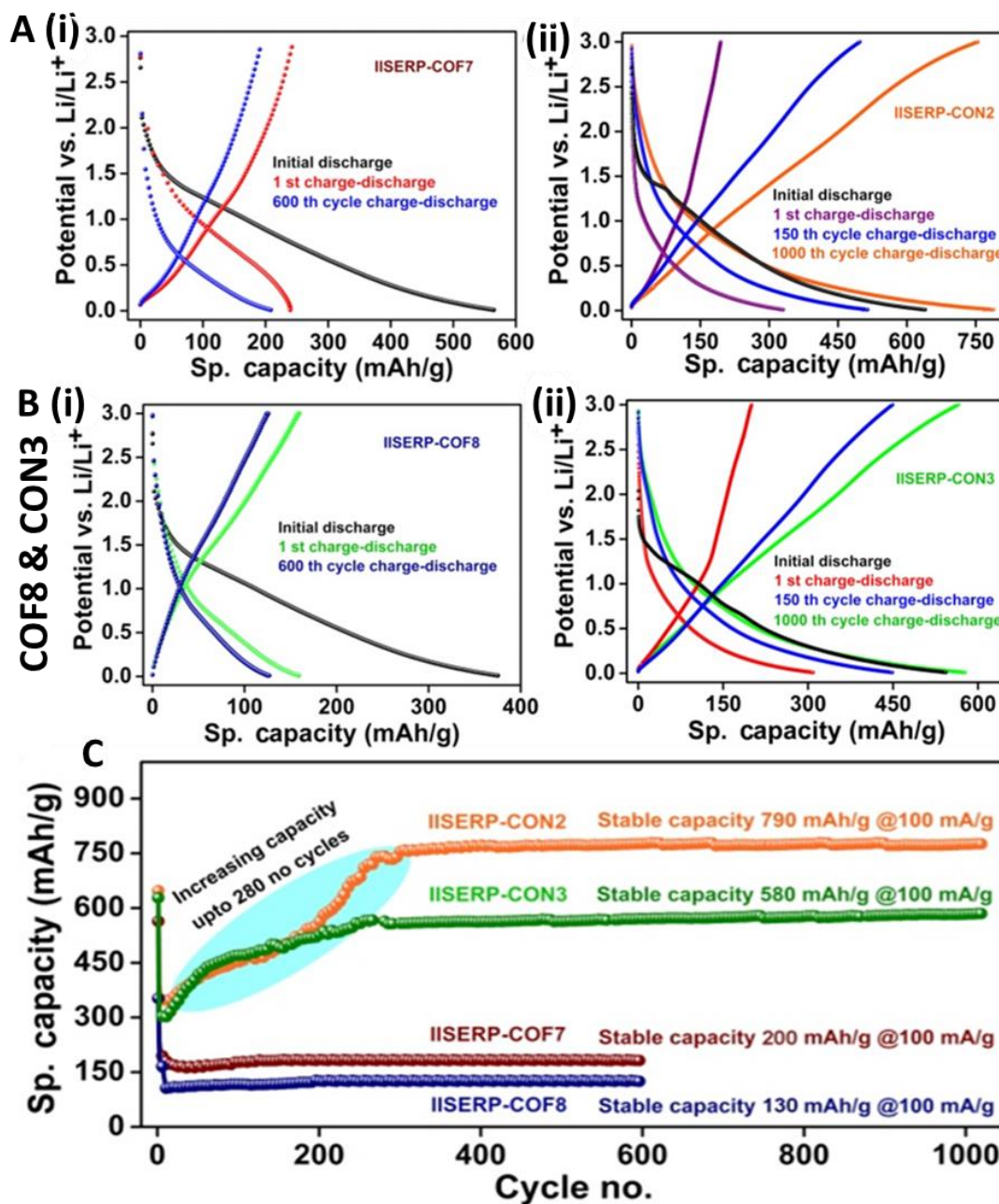


Figure 2.22. A(i) and (ii) and B(i) and (ii) Comparative galvanostatic charge-discharge curves of COFs and CONs measured in a half-cell configuration at a 100 mA/g current density. (C) Comparative cyclic stability for the COFs vs. CONs over 1000 cycles.

However, from these half-cell studies, a drop in specific capacity with increase of the current density from 0.1 to 1 A/g of about 34% for IISERP-CON2 and 42% for IISERP-CON3 could be observed (Figure 2.23). This drop is higher than what was observed in the case of the earlier reported IISERP-CON1,^[A.2.1] which probably is due to the relatively lowered chemical interactions between the Li-ions and the IISERP-CON1.^[A.2.1] However, the interactions in the IISERP-CON2 and IISERP-CON3, still appear to be mild enough to provide a reversible Li-insertion.

From the voltage plateau of the discharge profile of the CONs, it is seen that the marked jump in capacities occur in the low potential window of 0.5 to 0.01 V. This is in excellent agreement with the observations in the low-potential region of the CV, which was explained based on a facile insertion of Li-ions into the CONs. However, from these half-cell studies, a drop in specific capacity with increase

of the current density from 0.1 to 1 A/g of about 34% for IISERP-CON2 and 42% for IISERP-CON3 could be observed (Figure 2.23). This drop is higher than what was observed in the case of the earlier reported IISERP-CON1,^[A.2.1] which probably is due to the relatively lowered chemical interactions between the Li-ions and the IISERP-CON1. However, the interactions in the IISERP-CON2 and IISERP-CON3, still appear to be mild enough to provide a reversible Li-insertion.

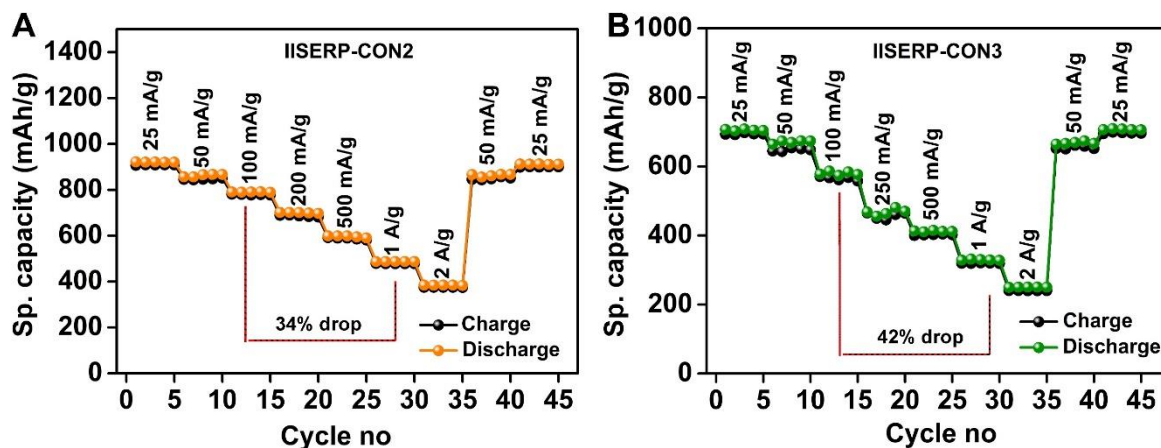


Figure 2.23. (A) and (B) Rate performance of CONs in a wide range of current densities (from 25 mA/g to 2 A/g). A 34% and 42% drop in specific capacity was observed when the current density increased from 100 mA/g to 1 A/g for the IISERP-CON2 and IISERP-CON3, respectively.

2.2.4. Calculation of Li concentration in the Li@CON and Li@COF from the specific capacity

The estimation of the number of Li inserts into the unit cell of CONs brings more insight for the Li-framework interaction studies. This can be easily correlated to the theoretical modelling in more reliable way. To do that, we have separated two different potential region in CV curves and in corresponding charge discharge curves on the basis of mechanism of Lithium insertion in the frameworks. i.e. 0.01 – 0.5 V (insertion region) and 0.5 V – 3.0 V (chemical interaction region). The result clearly shows the Li uptake of CONs enhance almost five times from COFs to corresponding CONs (Figure 2.24 and Figure 2.25). That means exfoliation actually assists for Li mobility inside the framework structure. But most interesting to see that in both COFs and CONs the theoretically estimated sp. capacity matches well with experimentally observed one. The indirectly conveys that the 1-D nano-channel of 2D COFs is good enough for the Li percolation. Exfoliation helps mainly for better interaction of Li with the framework and most of the functional groups gets exposure for Li interaction.

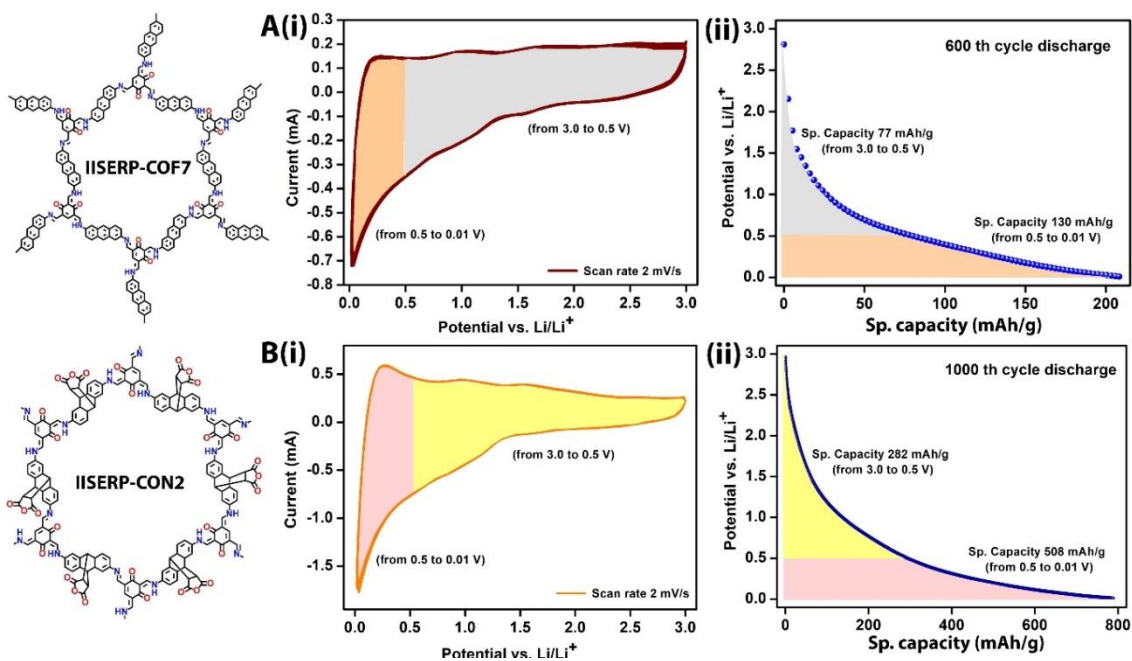


Figure 2.24. A(i) and B(i) Different potential region of the CV have been differently color coded, the diffusion activity (intercalation/insertion, 0.01-0.5V) and the surface activity (chemical reaction, 0.5-3V). Potential vs. capacity plot at 100 mA/g for A(ii) COF 600th cycle and B(ii) CON 1000th cycle. Note: The color codes have been kept consistent between the CV and the charge-discharge plots.

IISERP-CON2: (MW: 1041 g/mol)

1 mAh = $3.6C = 2.2 \times 10^{19}$ number of electron or Li^+ .

Here, for the IISERP-CON2 based coin-cell we observed a specific capacity of 508 mAh/g in the potential region of 0.01- 0.5V (This potential window represents the insertion region observed in the CV).

This would yield the number of Li^+ ion = $2.2 \times 10^{19} \times 508 = 1118 \times 10^{19}$.

Thus, the specific capacity of 508 mAh/g is realized from 1180×10^{19} no of Li^+ (assuming they are the sole charge carriers).

The calculated molecular weight of the IISERP-CON2 is 1041 g/mol. The weight for unit cell of the IISERP-CON2 is $1041 / (6.023 \times 10^{23})$ g. Considering that for 1g of the CON, the number of Li^+ ion calculated is $1180 \times 10^{19} \Rightarrow$ number of Li^+ per unit cell = $1118 \times 10^{19} \times 1041 / (6.023 \times 10^{23}) = 19$.

Similarly, the second oxidation peak in the CV occurs in the potential window of 0.5-3 V, and the specific capacity in this region is observed to be 282 mAh/g. This now can be attributed to about 11 Li^+ per unit cell.

So, in total there are 30 Li^+ ions/unit cell of IISERP-CON2 involved in the insertion-deinsertion process giving rise to the overall specific capacity of 790 mAh/g.

IISERP-COF7: (MW : 901 g/mol)

But the parent COF (IISERP-COF7) assists only 4 Lithiums/unit cell to insert in this same potential window of 0.01V – 0.5 V and only 3 Lithiums interact chemically with the functional groups of the COF in the potential window from 0.5 V – 3.0 V. Thus a total of 7 Lithiums per unit cell of the COF.]

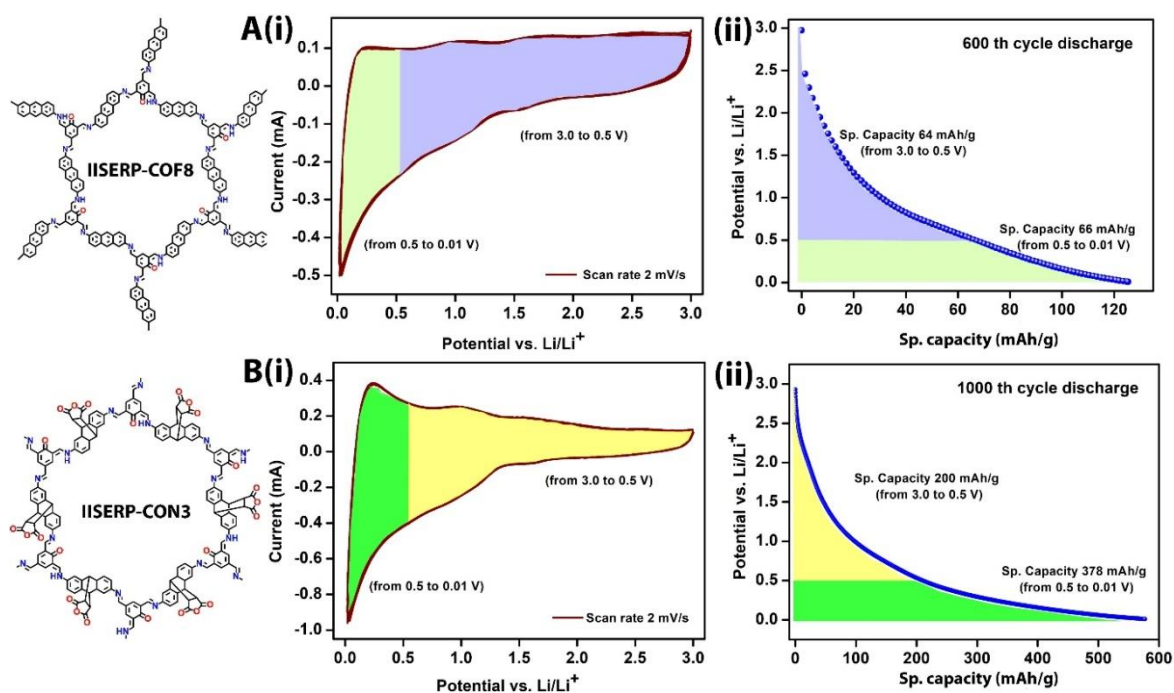


Figure 2.25. A(i) and B(i) Different potential region of the CV have been differently color coded, the diffusion activity (intercalation/insertion, 0.01-0.5V) and the surface activity (chemical reaction, 0.5-3V). Potential vs. capacity plot at 100 mA/g for A(ii) COF 600th cycle and B(ii) CON 1000th cycle. Note: The color codes have been kept consistent between the CV and the charge-discharge plots.

IISERP-CON3: (MW: 1015 g/mol)

From the IISERP-CON3 based coin-cell we obtained a specific capacity of 378 mAh/g in the potential region of 0.01- 0.5V (This potential window represents the insertion region observed in the CV).

This would yield the number of Li⁺ ion = $2.2 \times 10^{19} \times 378 = 832 \times 10^{19}$.

Thus, the specific capacity of 508 mAh/g is realized from 832×10^{19} no of Li⁺ (assuming they are the sole charge carriers).

The calculated molecular weight of the IISERP-CON3 is 1015 g/mol. The weight for unit cell of the IISERP-CON3 is $832 / (6.023 \times 10^{23})$ g. Considering that for 1g of the CON, the number of Li⁺ ion calculated is $1015 \times 10^{19} \Rightarrow$ number of Li⁺ per unit cell = $1015 \times 10^{19} \times 832 / (6.023 \times 10^{23}) = 14$.

Similarly, the second oxidation peak in the CV occurs in the potential window of 0.5-3V, and the specific capacity in this region is observed to be 200 mAh/g. This now can be attributed to about 8 Li⁺ per unit cell. So, in total there are 22 Li⁺ ions/unit cell of IISERP-CON3 involved in the insertion-deinsertion process giving rise to the overall specific capacity of 580 mAh/g.

IISERP-COF8: (MW: 873 g/mol)

But the parent COF (IISERP-COF8) assists the insertion of only 2 Lithiums/unit cell in the potential window of 0.01V – 0.5 V and allows 2 Lithiums/unit cell to chemically interact with the functional groups in the potential window of 0.5 V – 3.0 V.

Table 2.3. Classification of Lithium-framework interactions based on electrochemical studies

Sample Code	No of Li ⁺ follows insertion mechanism	No of Li ⁺ interacting with functional groups	Total no of Li ⁺ participating
IISERP-COF7	4	2	6
IISERP-CON2	19	11	30
IISERP-COF8	2	2	4
IISERP-CON3	14	8	22

The theoretical capacity of the material can be compartmentalized based on the number of Lithium interacting with the specific binding sites present within the COF/CON framework.

For establishing the different Lithium binding sites present within the COF/CON, we have utilized the reversible oxidation reduction peaks in higher potential region (0.5 V – 3.0 V) observed in CV and the results obtained from the XPS data. Typical theoretical capacity of a material is given by the equation: $C_t = n \cdot F / (3600 \cdot (MW/1000))$ Equation (1), where n is the number of Li-ions per molecule, F and MW are Faraday constant and molecular weight per active species, respectively.

Now, for the theoretical calculation of the number of Lithium inserting into the framework let us consider the most reactive β -ketoenamine forms of the IISERP-CON2 and IISERP-CON3.

IISERP-CON2: IISERP-CON2 has a molecular weight of 1041 g/mol; this unit of CON contains 4 quinone groups and 6 anhydride groups (O-C=O) all of which can serve as Li-interactive sites in each unit cell. The molecular weight of the quinone type active site per unit cell ($M_{wq} = M_{\text{unit cell}}/4$) is = 260.25 g/mol. Thus, from Equation (1), the theoretical capacity due to only quinone moiety within a unit cell can be calculated to be 103 mAh/g.

The molecular weight of anhydride type active site per unit cell ($M_{wanh} = M_{\text{unit cell}}/6$) is = 173.5 g/mol. Thus, from Equation (1), the theoretical capacity for anhydride moiety within the unit cell can be calculated to be 155 mAh/g. So a total theoretical capacity due to the quinone and the anhydride groups would be (103+154) = 257 mAh/g. Whereas galvanostatic charge-discharge measurements reveal that the functional groups deliver a specific capacity of 282 mAh/g. This excess specific capacity (25 mAh/g), most probably comes from the weak interactions of the Li with the imine nitrogens or the conducting carbon.

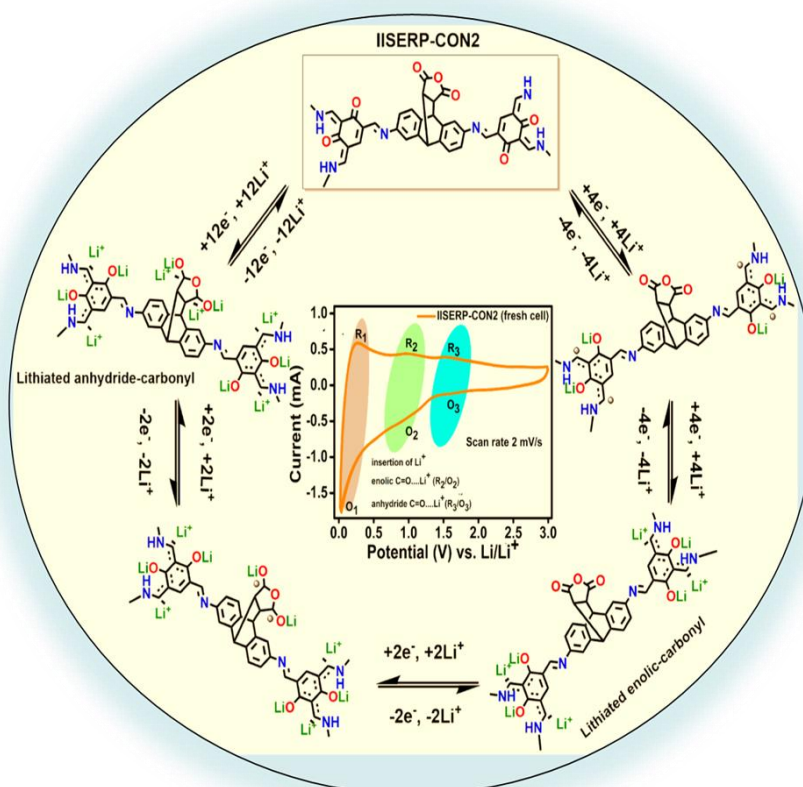
IISERP-COF7: IISERP-COF7's molecular weight is 901 g/mol. The molecular weight of the quinone type active site per unit cell ($M_{wq} = M_{\text{unit cell}}/4$) is = 225 g/mol. Thus, from Equation (1), the theoretical capacity for quinone moiety per unit cell can be calculated to be 119 mAh/g (Note there would be no anhydrides in the COF). But, from the galvanostatic charge-discharge measurements only a specific capacity of 77 mAh/g is observed (Figure A.2.33). Which is 35% lesser than the theoretical value. This could be due to the fact that in the highly stacked structure of the COF, significant proportion of the Li-interactive functional groups remain buried.

Similar calculation were performed for IISERP-CON3 and IISERP-COF8. The results are summarized in the below Table.

Table 2.4. Experimental vs. theoretical Sp.capacity

Sample Code	Experimental Sp. capacity (mAh/g)	Theoretical. Sp. capacity (mAh/g)
IISERP-CON2	282	257
IISERP-COF7	77	119
IISERP-CON3	200	211
IISERP-COF8	64	81

Herein, we propose a mechanism based on observations from CV, Raman and XPS and modeling studies (Scheme 2.2). We have represented the Lithium interaction sites in the framework using a schematic.^[A.2.16, A.2.17] The presence of weak redox active peaks in the CV and the contribution of the capacity calculated from the current obtained in different potential helps us identify the Lithium interacting functional site in the framework (Figure 2.24-2.25, Table 2.3-2.4). The facile Lithium interaction with the CON can happen in its tautomerizable site at ~ 1.0 V. The conversion of enolic form to keto form of the carbonyl groups itself helps for the Lithium uptake. In comparison, the anhydride groups which do not have such tautomerization need slightly higher potential (1.6 V). At the extremely low potential of ~ 0.03 V, the Lithium insertion happens inside pores quite swiftly. These are the three different peaks observed in the CV.



Scheme 2.2. Mechanistic pathway of Lithium interaction with the oxygen rich centre of IISERP-CON2. Similar way IISERP-CON3 can also participate in the redox reaction under applied potential.

2.2.5. Rapid Li-ion diffusion in exfoliated COF

The Lithium insertion into the CONs occurring at very low potential could be diffusion or surface controlled process.^[44-46] To verify this, the CVs were performed with a variable scan rate (from 1 mV to 50 mV) using fresh cells. A linear fit to the power-law $i = av^b$ (i = current; v = scan rate) resulted in $b=0.61$ @0.03V for IISERP-CON2 (Figure 2.26 and 2.27) obeys the Cottrell's equation and advocates a diffusion-controlled insertion mechanism as being the dominant process at the low potentials. At higher potentials, the 'b' values of 0.63 @1V and 0.80 @1.6V means surface-controlled charge storage arising from the chemical reactivity of CONs' functional groups with Li^+ . Also, with the increase of the cycle number, the functional groups become more activated towards the Lithium insertion, which is reflected again in the higher surface controlled behavior after 1000 cycle charge-discharge. This signifies the presence of mildly interacting oxygen-rich functional moiety in the skeleton of the CONs also contributes towards the Lithium affinity. For easy grasping, a diagram has been provided to denote the change of mechanism from diffusion-dominated kinetics to the surface-controlled kinetics of CON derived electrodes, which also results in the decreased resistance of ionic/charge-transfer and increased reversible capacities during the repetitive lithiation and delithiation process. However, this contribution to the overall specific capacity is much lesser compared to the contribution from the insertion occurring at the lower potentials. This suggests that the Lithium insertion into the pores of the nanosheets becomes more and more effortless with many cycling.

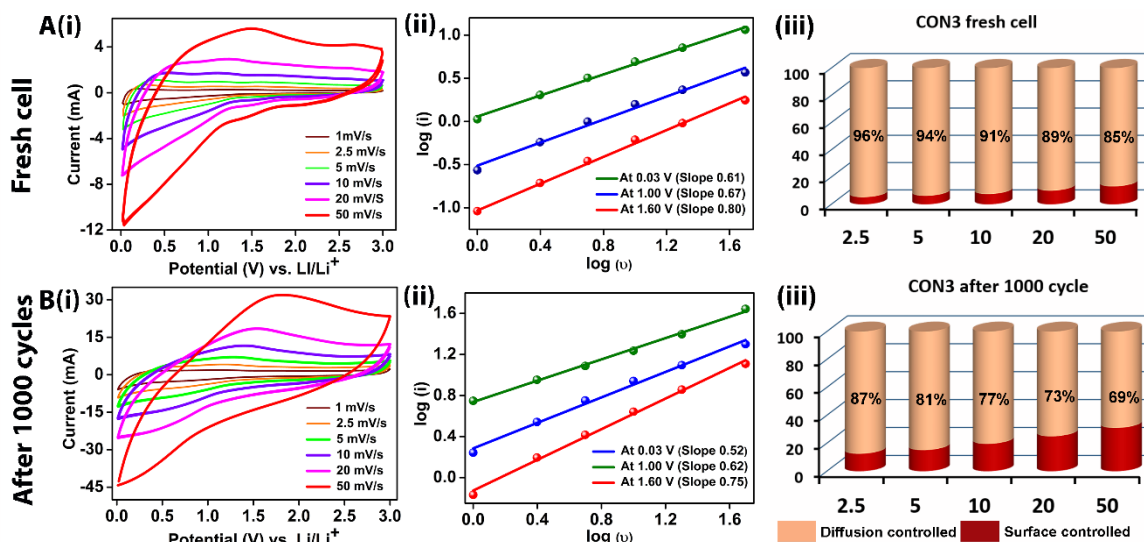


Figure 2.26. **A(i)** Cyclic voltammogram plot of IISERP-CON2 derived coin-cell (fresh cell) measured at different scan rates. **(ii)** Log. of peak current intensity (anodic) vs. log. of scan rate at different potentials extracted from the CV plots. Note the linear increment of the peak current with the increase of current density. **(iii)** Capacitive contribution of CON2 before cycling. **B(i)** Cyclic voltammogram plot of IISERP-CON2 derived coin-cell (after 1000 charge-discharge cycles) measured at different scan rates. **(ii)** Log. of peak current intensity (anodic) vs. log. of scan rate at different potentials extracted from the CV plots. Note the linear increment of peak current with the increase of current density. **(iii)** Capacitive contribution of CON2 after 1000 cycle.

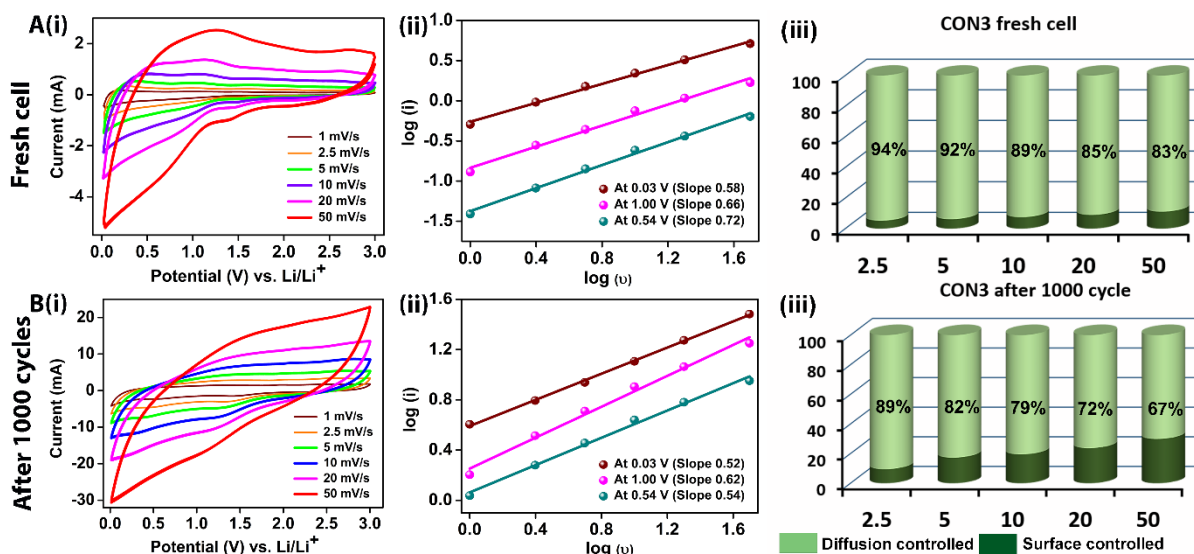


Figure 2.27. **A(i)** Cyclic voltammogram plot of IISERP-CON3 derived coin-cell (fresh cell) measured at different scan rates. **(ii)** Log. of peak current intensity (anodic) vs. log. of scan rate at different potentials extracted from the CV plots. Note the linear increment of the peak current with the increase of current density. **(iii)** Capacitive contribution of IISERP-CON2 before cycling. **B(i)** Cyclic voltammogram plot of IISERP-CON3 derived coin-cell (after 1000 charge-discharge cycles) measured at different scan rates. **(ii)** Log. of peak current intensity (anodic) vs. log. of scan rate at different potentials extracted from the CV plots. Note the linear increment of peak current with the increase of current density. **(iii)** Capacitive contribution of IISERP-CON2 after 1000 cycle.

Such capacity enhancement with cycling should typically reflect in improved Li-ion diffusion coefficient. Also, for structural reasons. It should be more prominent in the CON compared to the parent COF. To verify this, AC-impedance analyses were performed with the COF and CON derived half-cells. The diffusion coefficient calculated from the Warburg tail for the COF and the CON were compared using freshly-pressed coin-cells and the coin-cells, which had already been subjected to 1000 charge-discharge cycles (Figure 2.28). It yielded diffusion coefficients, D_{Li^+} of $\sim 3.69 \times 10^{-11} \text{ cm}^2/\text{s}$ for IISERP-CON2 and 3.62×10^{-11} for IISERP-CON3, which are almost three times higher than the D_{Li^+} values obtained for the COFs (i.e., 1.26×10^{-11} for IISERP-COF7 and 2.26×10^{-11} for IISERP-COF8, respectively, Table 2.5).^[25, 47,48] Combining the observations from the CV and the XPS and Raman, carried out on a completely discharged (Li-loaded CON) samples, we propose a mechanism for the Lithium loading, which displays the change from diffusion-dominated kinetics to surface-controlled kinetics at the CON-derived electrodes. This results in the decreased resistance for the ion/electron transfers and increases the reversible capacities during the repetitive lithiation and delithiation process.

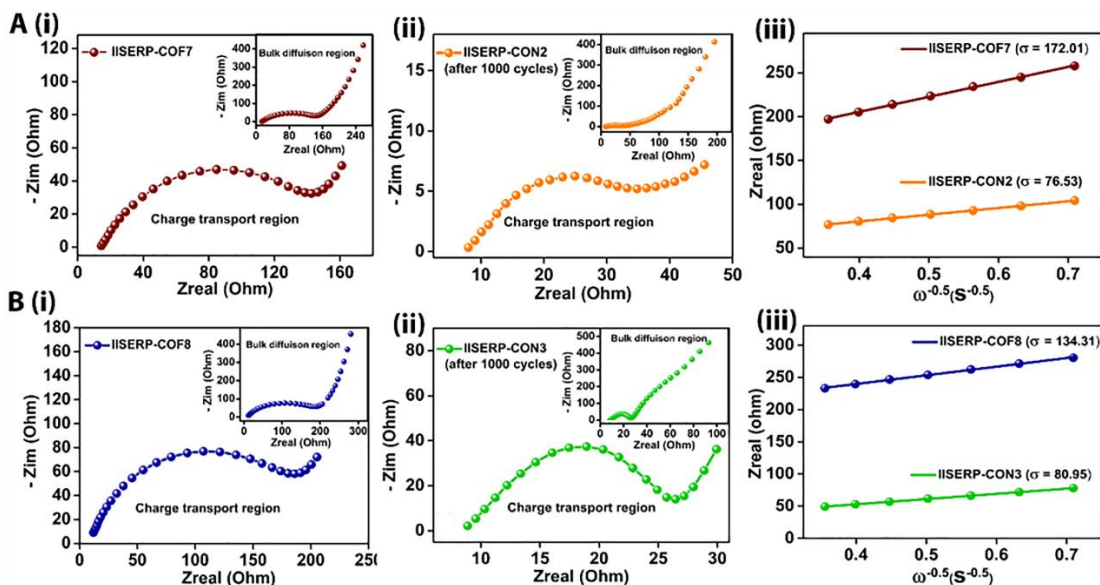


Figure 2.28. Nyquist plots from the AC-impedance measurements showing, **A(i) and (ii)**: Change of charge-transfer resistance with the conversion from IISERP-COF7 to IISERP-CON2 **(iii)** The plot of Z real vs. the inverse square root of angular frequency (ω) for the IISERP-COF7 and IISERP-CON2. The slopes of the fitted lines represent the Warburg coefficient, σ .

Li-ion diffusion coefficients were obtained by electrochemical impedance spectroscopy (EIS) and derived from Eq.:

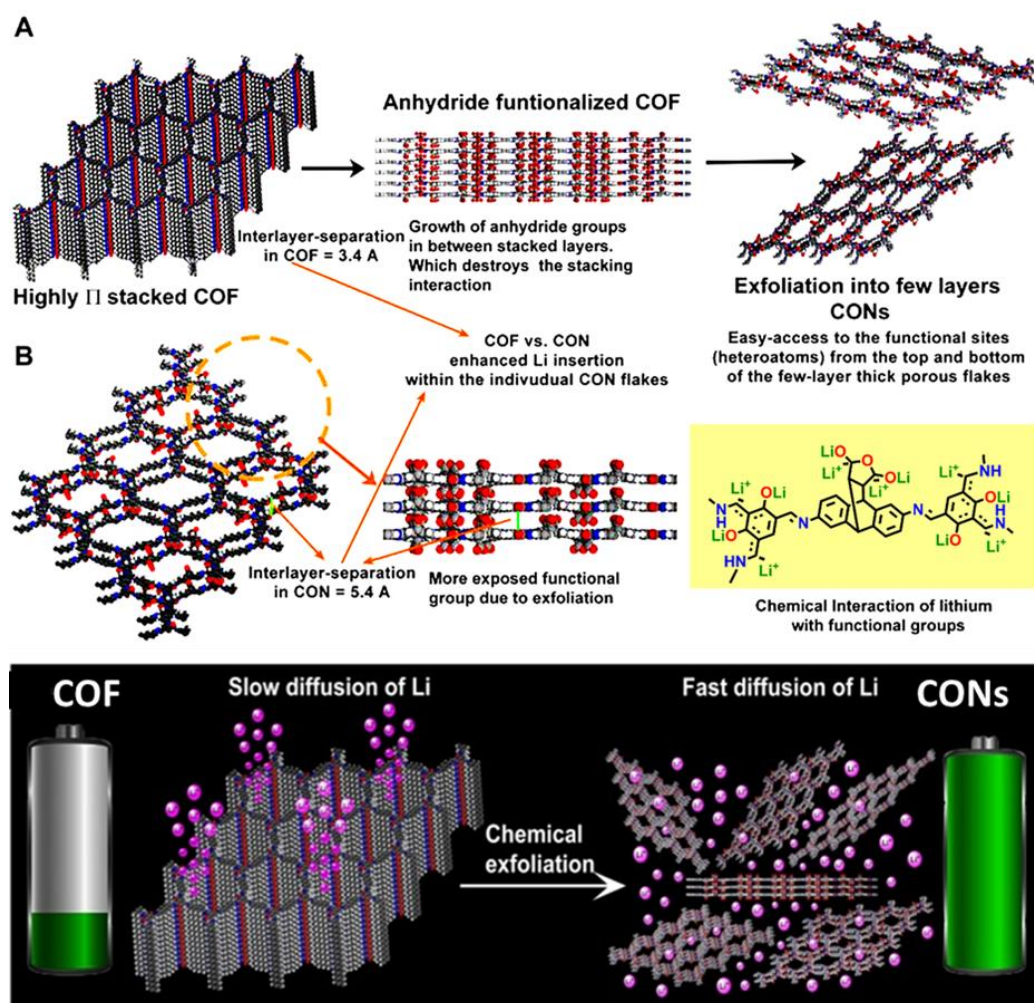
$$D = 0.5(RT/AF^2 \sigma C)^2 \dots \text{Eq}(2),$$

where R is the gas constant ($8.314 \text{ J mol}^{-1} \text{ K}^{-1}$), T is the temperature (298.5 K), A is the area of the electrode surface (1.14 cm^2), F is the Faraday's constant ($9.65 \times 10^4 \text{ C mol}^{-1}$), C is the molar concentration of Li^+ , and σ is the Warburg coefficient. The Warburg coefficient σ can be obtained from $Z_{re} = R_e + R_{ct} + \sigma \omega^{-0.5} \dots \text{Eq}(3)$, where σ is the slope for the plot of Z_{re} vs. the reciprocal root square of the lower angular frequencies ($\omega^{-0.5}$). The obtained σ values calculated diffusion coefficients has been represented in the below table.

Table 2.5. List of Lithium diffusion coefficients for the COFs and CONs

Sample Code	Warbug coefficient (σ)	Diffusion coefficient (D_{Li^+}) cm^2/s
IISERP-COF7	172.01	1.26×10^{-11}
IISERP-CON2	76.53	3.69×10^{-11}
IISERP-COF8	134.31	2.26×10^{-11}
IISERP-CON3	80.95	3.62×10^{-11}

Note. The observed high diffusivity of Li-ions inside the CONs is comparable to those of many commercial electrode materials.



Scheme 2.3. Pictorial representation of the exfoliation of COFs by post-synthetic modification. The covalent insertion of maleic anhydride opens up spaces within the individual flakes, while the exfoliation of the polymeric COF generates smaller flakes of CONs, which are better dispersed. Both these structural and morphological changes together enhance the diffusion of the Li-ions within them and thereby provides fast and easy access to the Li-interactive sites.

2.2.6. Exfoliated-COFs performance under high potentials of a full-cell LIB

The noticeable stable and high specific capacities of the CONs encouraged us to assess their actual performance as an anode in a practical LIB. A full-cell brings the maximum energy density that can be derived from a specific anode-electrolyte-cathode combination. Thus, measuring the anodic

performance of the IISRP-CON2 against well-standardized commercial cathode and electrolyte would explicitly display its practical capacity. Here, activated LiCoO_2 (LCO) was employed as the counter cathode and activated CON(s) as the anode to fabricate a full-cell. At first, a slurry of the cathode, LCO, and the anode, CON, was prepared using 70% of the active material, 30% Super-P carbon and 10% PVDF binder. The LCO and the CON(s) electrodes were electrochemically pre-activated by 200 charge-discharge cycles at 50 mA/g in a typical half-cell using Li metal as the counter. This is required to get an estimate of the truly available active sites in the CON to act as anode against LiCoO_2 , barring the sites lost to SEI layer formation. *It is essential to recognize that the CONs could retain their activity and structure even after this pre-treatment step.*

The half-cell having the LCO pressed against the Lithium electrode, after 200 cycles, stabilized to a specific capacity of 198 mAh/g at 50 mA/g current density (Figure 2.29). The impedance of LCO-half cell shows two semicircles. The charge transfer resistance of second one defines the actual resistivity of the LCO. But the first semi-circle appears due to incomplete SEI formation on the LCO electrode. It sometimes happens due to very fast self-discharging of the coin-cells.

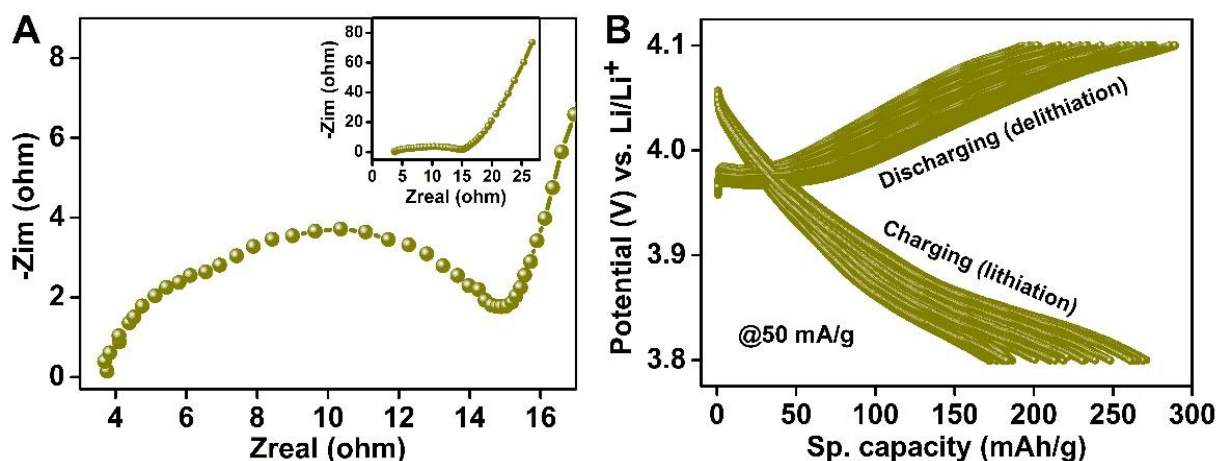


Figure 2.29. (A) Nyquist plots of LCO derived half-cell coin cells. Inset: a zoom-in showing the bulk diffusion region. (B) Charge-discharge curves of LCO derived half-cell @ 50 mA/g current density.

Meanwhile, the half-cells having the CON electrode pressed against the Lithium metal yielded three and four times higher specific capacities compared to the LiCoO_2 , respectively. Therefore, to achieve maximum capacity in the CON-LCO full-cell, a CON to LCO weight ratio of 1:4 was employed. A full-cell was fabricated integrating the completely charged CON(s) as anode and completely discharged LCO as the cathode. About 200 μL of 1M LiPF_6 dissolved in a 1:1 EC:DMC solvent mixture along with 5% FEC was used as the electrolyte (Figure 2.30A and Figure 2.30B). To ensure complete lithiation and delithiation in the full-cell, $E^0 \pm 0.5$ V i.e., 2.6 to 3.6 V was employed as the potential window (see the similar calculation for Graphite derived full-cell in supporting information). CVs were recorded for 5 cycles at 2 mV/s scan rate for both the full-cells in a working potential window of 2.6 V to 3.6 V (Figure 2.30C). Looking at the CV, one can see a large area under the curve in the potential window of 3.2 to 3.6 V, rendering a high current \times voltage value. This is the potential where the Li-ions are stripped-off from the LCO cathode and the same is spontaneously inserted into the CON anode. This larger current at this high potential is realized due to the facile insertion of Li into the CON. Impedance measurements on the full-cells show two distinct charge transfer resistances in the high-frequency region (Figure 2.30D). Such Nyquist plots with two semicircles are known. The higher frequency semicircle can be assigned as the surface film resistance (R_{sf}) which is due to the formation of

electrode-electrolyte inter-phase layer and the lower frequency semicircle can be assigned as the charge transfer resistance (R_{ct}).^[49]

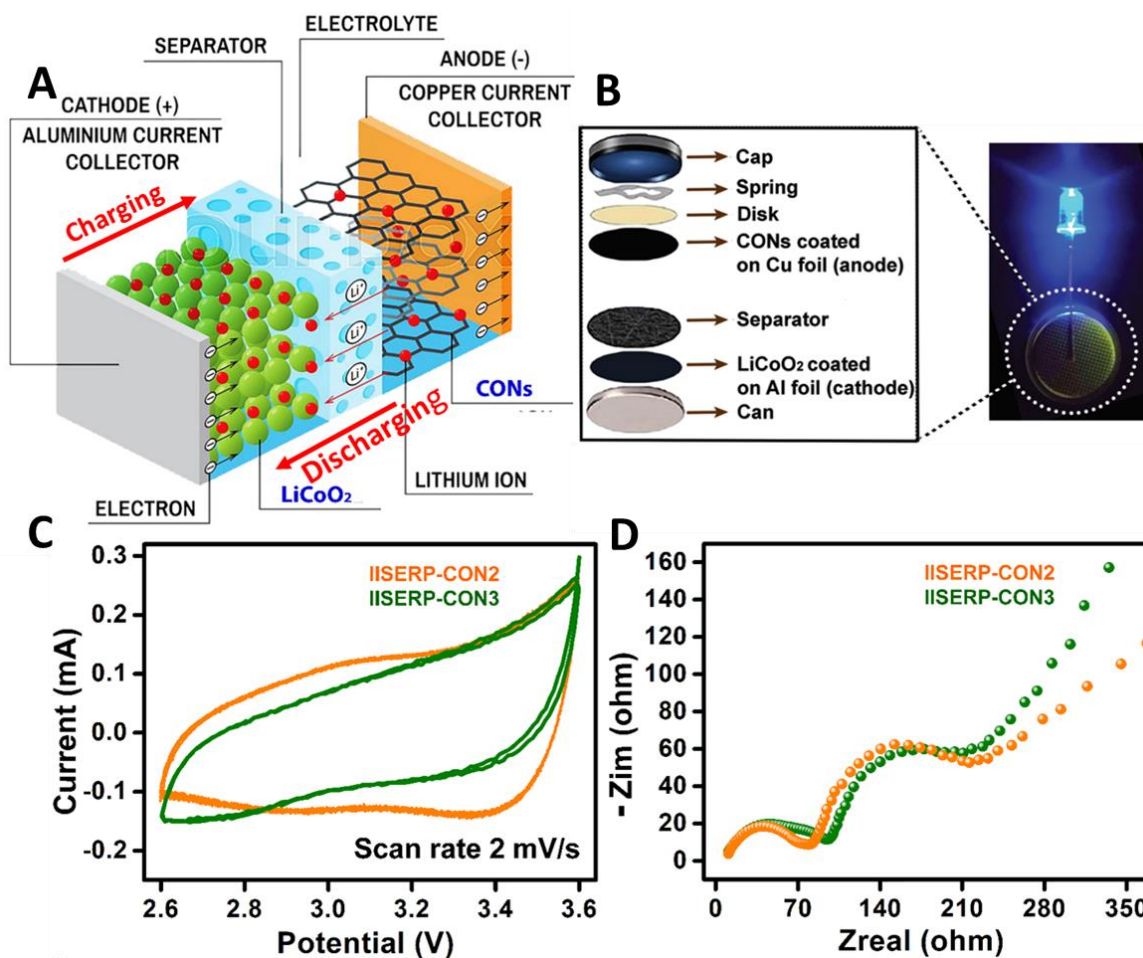


Figure 2.30. (A) A photographic scheme showing the working principle of full-cell. (B) A coin-cell assembly of the full-cell. Inset shows an LED light illuminated by the full-cell prepared using the IISERP-CON2 as anode vs. LCO cathode. (C) Comparative CV-plots of CONs measured in a full-cell configuration with a 2 mV/s scan rate. (D) Nyquist plots from the AC-impedance measurements in their full-cell configurations. Make sure the two semi circles are properly explained.

Galvanostatic charge-discharge cycling of the full-cells was performed at 100 mA/g for 200 cycles (Figure 2.31A and 2.31B). IISERP-CON2 delivered a specific capacity of 220 mAh/g with 92% capacity retention (Figure 2.31C). While the IISERP-CON3 exhibits a specific capacity of 170 mAh/g, which drops gradually with increasing cycles and about 68% capacity is retained after 200 cycles. IISERP-CON2 has a ~90% coulombic efficiency and IISERP-CON3 has ~85%. The dropping of the capacity after prolong cycling attributes to the drying of the liquid LiPF₆ electrolyte at higher potential. For better compatibility with this type of organic electrode solid electrolyte could be the possible solution.^[50-52] Although the full-cell stabilized specific capacity (220 mAh/g @100 mA/g) achieved by IISERP-CON2 is significantly higher than the capacity of the full-cell made using the commercial Graphite anodes (180 mAh/g at 100 mA/g for Battery Grade Graphite under comparable conditions; Figure A.2.22). It is higher than most other commercial anodic materials (Table 2.6). The full-cells made using IISERP-CON2 and IISERP-CON3, both exhibit an average operating potential close to 3.15 V (Figure 2.31A and 2.31B), from this the energy densities were estimated to be 364 Wh/kg for IISERP-CON2 and 286 Wh/kg for IISERP-CON3 (Table 2.6 and Table 2.7). The high energy density of the IISERP-CON2 based Li-ion full-cell is comparable to that of commercial Graphite anode-based LIB (320 Wh/kg).

Furthermore, for IISERP-CON2, only a small drop in specific capacity (22%) was observed even at current density as high as 1 A/g or in other words when the C-rate is increased to 5C (Figure 2.31D). Notably, in the commercial Graphite this drop is ~ 86% (Figure 2.31E). This superior rate-performance of the IISERP-CON2 derived full-cell LIB is remarkable, suggesting they can yield rapid charging without any appreciable capacity fading.^[27, 53-56] All these battery parameters from our evenhanded studies clearly points at the immense opportunity buried in these CON materials for the future-generation lightweight LIB.

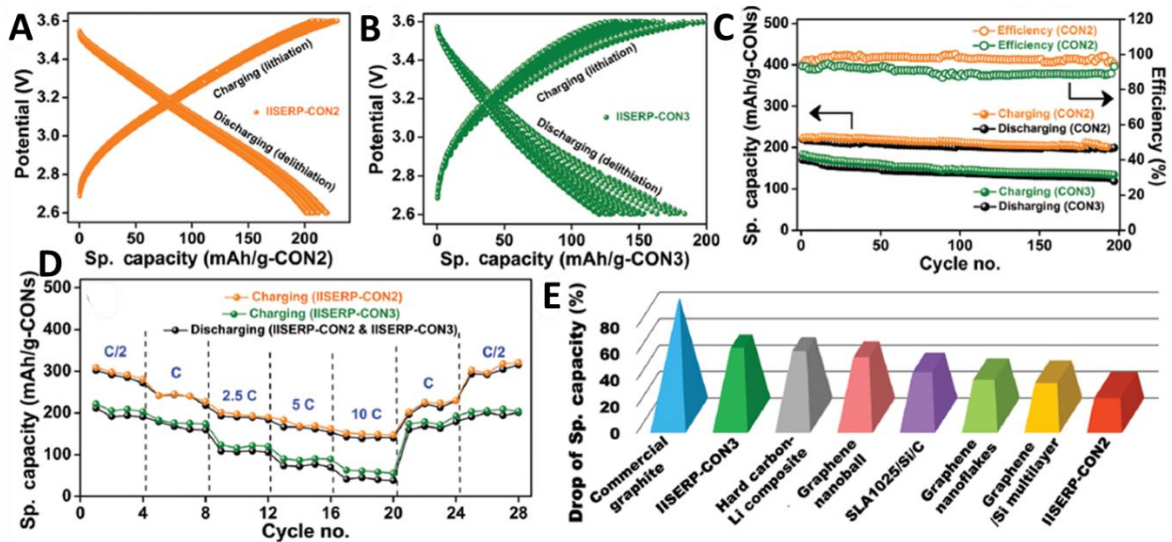


Figure 2.31. (A) and (B) Galvanostatic charge-discharge curves of the CONs up to 200 cycles at 100 mA/g current density in their full-cell configurations. Note the capacity has been expressed per gram of the anode (CON). (C) Cycling stability and battery efficiency of the full-cells made using the CONs (@ 100 mA/g). (D) C-rate performance of the CONs in their full-cell (1C = ~100 mA/g). (E) A comparative bar-chart showing the drop in specific capacity upon increasing charging rate from 1C to 10C between different high-performing/commercial materials.

Table 2.6. Comparison of the Sp. capacities of standard anode-CON materials measured in a full-cell configuration.

ANODE	CATHODE	SPECIFIC CAPACITY	CURRENT DENSITY
Hard Carbon	LCO	131 mAh/g	52 mA/g
Commercial Graphite	LCO	180 mAh/g	100 mA/g
Graphene Nanoball	NCM	151 mAh/g	5 C
SLA 1025	LCO	80 mAh/g	0.5 C
Graphene Nanoflake	LFP	165 mAh/g	1 C
Graphene Silicon Multilayer	NMC	120 mAh/g	23 mA/g
IISERP CON-2	LCO	220 mAh/g	1 C / (100 mA/g)
IISERP CON-3	LCO	170 mAh/g	1 C / (100 mA/g)

Calculation of energy density of full-cell LIB:

$$\begin{aligned}
 E \text{ (Wh/Kg)} &= \frac{1}{2} \times C \left(\frac{F}{\text{Kg}} \right) \times V^2 \text{ (Volt.)}^2 \\
 &= \frac{1}{2} \times \frac{Q}{V} \left(\frac{\text{Ah/Kg}}{\text{Volt.}} \right) \times V^2 \text{ (Volt.)}^2 \\
 &= \frac{1}{2} \times Q \left(\frac{\text{Ah}}{\text{Kg}} \right) \times V \text{ (Volt.)} \\
 &= \frac{1}{2} \times Q \times V \left(\frac{\text{Wh}}{\text{Kg}} \right)
 \end{aligned}$$

Here, E: energy density, C: capacitance, V: operating potential, Q: specific capacity or charge per unit mass

Only for final cycle the specific capacity after complete discharge and operating potential of that cycle have been considered for the energy density calculation.

Table 2.7. Energy density of electrode materials

Electrode material	Q (Ah/Kg)	V (Volt.)	E (Wh/Kg)
IISERP-CON2	230	3.17	364
IISERP-CON3	180	3.18	286
Commercial Graphite	172	3.72	320

2.2.6. Structural and chemical reasons for the CON's superior performance

The superior aspect of this particular Diels-Alder adduct based chemical exfoliation is the tendency of the exfoliated flakes not to re-aggregate. A problem that is not easy to address in case highly π -stacking materials like Graphite. Also achieving an optimal lateral-length/height ratio in such exfoliated COF is an advantage. In comparison, when Graphite is exfoliated, the later dimensions do not drop proportionally with the height reduction owing to the robust C-C bonds. This limits how far one can exfoliate the strongly-stacked Graphite layers. This is crucial in deciding the overall high surface accessibility and facile diffusion. In our experience, chemical exfoliation of COFs is a more-optimized technique compared to aggressive mechanical or soft solvent-assisted sonication methods.

Now, coming to the superior performance of the CON over Graphite, the major reason is the structure-driven chemical accessibility. For example, in Graphite, the Li intercalation leads to a LiC_6 type of compound as the theoretical limit. However, in practice, it is not straight forward for the Li-ions to access all the bulk interior of the Graphite, and especially at higher charge-discharge rates, where the Li-ions tend to have much lower residence time which becomes insufficient for forming LiC_6 at every ring. In contrast, in this exfoliated COF, IISERP-CON2, since it retains its structure without any re-aggregation, and has large pores offering complete access to the exposed functional groups (carbonyls and hydroxyls, etc.) the diffusing Li-ions, even at high C-rates, find their interaction sites efficiently. This explains the observed higher specific capacity as well as the limited drop in the capacity at high C-rates. We calculated that in IISERP-CON2 about 30 Li inserts per unit cell, which is much higher than the 1 per C_6 -ring of the Graphite. When normalized to their molecular weights, the gravimetric capacity would be 0.1 Li per mole of Graphite vs. 0.2 Li per mole of IISERP-CON2. Thus, the advantage in the IISERP-CON2 comes both from increased functionalities contributing to higher intake of Li and the facile diffusion.

To gain molecular-level insights into the Lithium interactions with the CON, we carried out simulation studies. We obtained the optimized structure of the Li@CON using simulated annealing methods (Figure 2.32A). For both CONs, the optimized structures revealed the distribution of Lithium atoms proximal to the oxygen atoms and the aromatic rings of the framework. Typical Li-O distances were 2.60 to 2.85 Å and Li- C_6 distances were at 2.6 Å, which indicates more of physical interactions and not any strong covalent interactions. This explains the facile and rapid lithiation and delithiation. Our 298K MD simulations done employing an NPT ensemble with random initial velocities reveal that Lithium is

highly diffusible within these channels (Figure 2.32A) calculations were done for a total simulation time of 5000 ps with a time step of 1.0 fs over 5000000 steps). It also conveys the stability of the Lithium loaded framework under ambient conditions (no bond-breaking or unacceptable geometries were noticed).

We have identified the most-favorable Lithium interactive sites inside the CON using GCMC simulations and tb-DFT modeling. Our findings reveal that. Most of the Lithium diffuses inside the pore of the nanosheets and is interacting with heteroatoms of the functional groups which line the CON's' nano-channels. Our MD simulations at 298K reveal that the Lithium is highly diffusible within these channels, which is expected for the reversible Li-framework interactions as observed from reversible CV and charge-discharge cycling (Figure 2.32B). It also conveys the stability of the Lithium loaded framework under ambient conditions (no unacceptable bond-breaking or geometries were noticed).

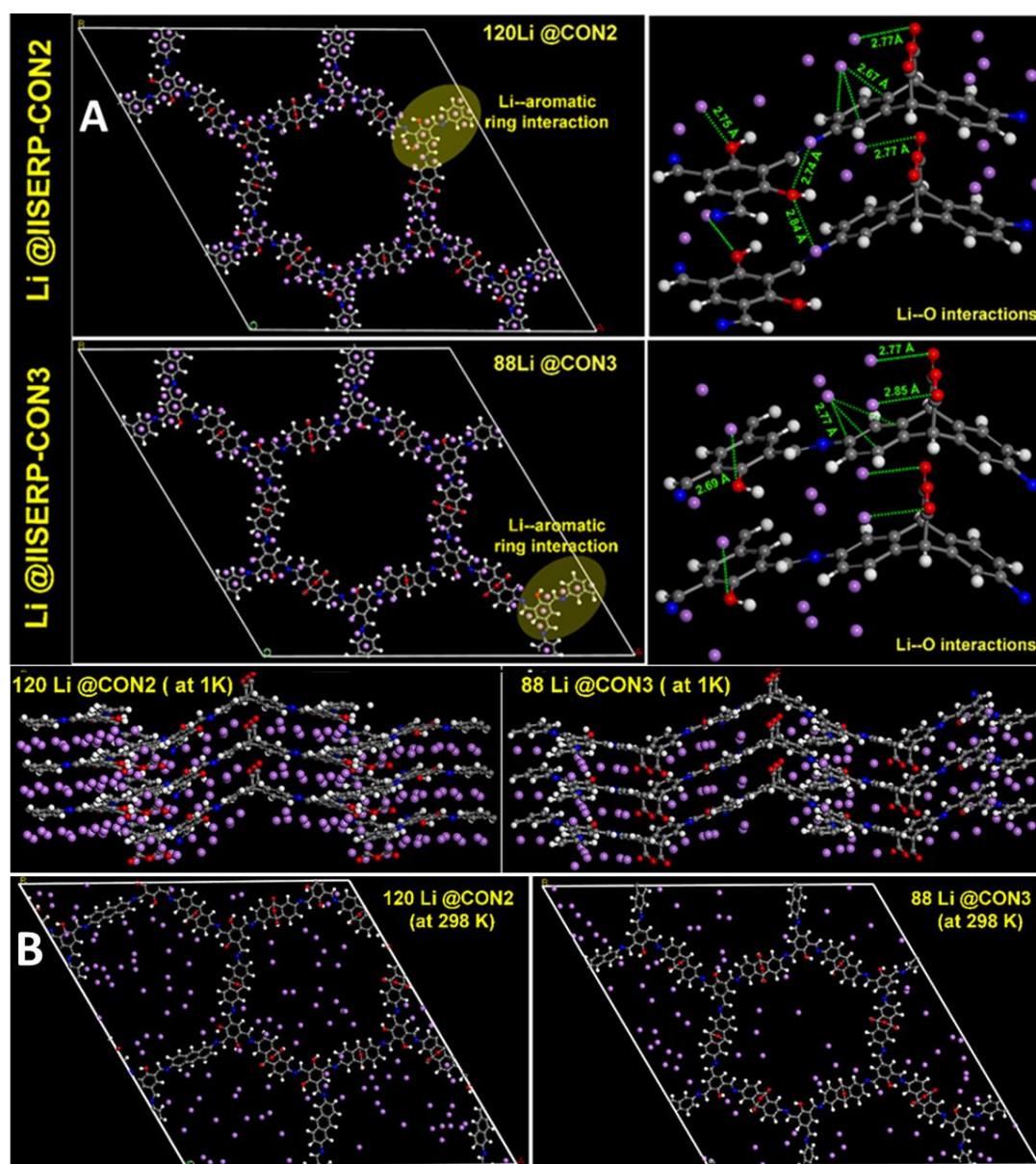


Figure 2.32. (A) Optimized structures from a Simulated Annealing routine showing the Li-framework interactions. Note that the Li-O distances and the Li-C₆ interactions are within the range of 2.65–2.85 Å, suggesting weaker interactions and the lack of any strong covalent type interactions. **(B)** A c-axis view showing the positioning of Lithium in between the layers. A

snapshot from the 298K MD simulation showing the structure with Lithium diffused into the channels. No bond-breaking or unacceptable geometries were observed.

In closing, we discuss two of the recent reports which are closely related to ours. Chen et al. described high Lithium affinity of chemically exfoliated 2D covalent organic frameworks, where the π -stacking interaction between the benzene rings has been weakened by MnO_2 nanoparticle incorporation, preventing re-stacking.^[57] A high specific capacity was achieved from this composite material of MnO_2 @CONs. Though this has a similarity to our work, there are some essential aspects where our work gains an advantage. The insertion of Lithium into the MnO_2 @COF is dominated by both the redox activity at COF and MnO_2 . Because of the incorporation of the strongly redox active 'conversion material', namely the MnO_2 , into the framework, in their case, almost a $\sim 45\%$ drop in sp. capacity was observed under high current density (1359 mAh/g-750 mAh/g @ 100 mA/g-1 A/g, respectively) vs. 35% in our IISERP-CON2. Similarly, Wang and co-workers reported an anthraquinone based COF functionalized with radical carrying strongly active redox groups.^[47] This was used as a cathode in LIB, wherein a ball-mill assisted exfoliation had resulted in enhanced diffusion of Li-ions. They achieved good stability with a specific capacity of 210 mAh/g. However, just as in the case of the MnO_2 loaded COF, here too, the strong redox activity leads to substantial fading of capacity at higher current densities. In comparison, in IISERP-CONs, we retain all the advantages of the exfoliation, but we see reversible physisorptive type interactions between the COF framework and the Lithium species. This ensures excellent rate performance, even at high current densities. Notably, the energy invested in the chemical exfoliation is lower compared to ball milling and it is easier to scale-up. Importantly, these chemically exfoliated CON, are less prone to re-aggregating or re-stacking.

From figures 2.4.D, 2.4.E and A.2.22, it is seen that the cells made using the CONs lack a flat voltage plateau compared to Graphite and need more activation cycles. This is because the lithiating sites are not as homogeneous as in Graphite. This could be a major drawback with using CON as anode materials. Nevertheless, CON-derived cells undeniably show excellent rate stability under high current density, which translates to high specific capacity even at fast charging, something that is challenging to achieve with Graphite. Hence, finding a middle ground between CON and Graphite could yield an ideal anode material.

2.3. Conclusion

The work showcases a Functionalizing Exfoliation Agent (FEA) assisted route that exfoliates COF to CON and simultaneously populates the latter with Li-interactive groups. This enables the lightweight exfoliated-COF to achieve high charge-storage despite their volumetric disadvantage. A four times enhancement in anodic performance upon exfoliation is attributed to the rapid and reversible Li-diffusion in and out of the active sites. The full-cell studies elicit the potential of the CON as a readily processable anode material against the commercially tested cathode namely the LiCoO_2 . Importantly, the full-cell is capable of delivering specific capacities surpassing the battery-grade Graphite-based LIB. The CON-derived cell retains this performance over high C-rates demonstrating excellent electrochemical stability. This structural and functional tunability opens-up the attractive possibility of using light atom rich COFs to develop lightweight batteries.

Acknowledgements

The authors thank IISER Pune for support and the funding by DST-for material for energy storage (DST/TMD/MES/2k17/103) program and the "DST-Nanomission under the Thematic Unit Program" (EMR/2016/003553). S.H. thanks DSTInspire for financial support. The authors would like to thank

SERB (EMR/2016), DST-Inspire, the MHRD-FAST, and the IUSSTF program for the necessary funding. They also thank IISER Pune for supporting the work and DST-FIST program for the AFM studies done at IISER Pune. The authors thank Dr. C. P. Vinod, NCL Pune, for the XPS and Debanjan Chakraborty, IISER Pune, for the adsorption studies. The authors thank Dr. Pramod Pillai for the access to UV-Vis spectrometer.

References

- [1] Chen, X.; Geng, K.; Liu, R.; Tan, K. T.; Gong, Y.; Li, Z.; Tao, S.; Jiang, Q.; Jiang, D., Covalent Organic Frameworks: Chemical Approaches to Designer Structures and Built-In Functions. *Angew. Chem., Int. Ed.* **2019**, doi.org/10.1002/anie.201904291
- [2] Bunck, D. N.; Dichtel, W. R., Bulk synthesis of exfoliated two-dimensional polymers using hydrazone-linked covalent organic frameworks. *J. Am. Chem. Soc.* **2013**, *135*, 14952-14955.
- [3] Das, G.; Skorjanc, T.; Sharma, S. K.; Gándara, F.; Lusi, M.; Shankar Rao, D.; Vimala, S.; Krishna Prasad, S.; Raya, J.; Han, D. S., Viologen-based conjugated covalent organic networks via Zincke reaction. *J. Am. Chem. Soc.* **2017**, *139*, 9558-9565.
- [4] Feldblyum, J. I.; McCreery, C. H.; Andrews, S. C.; Kurosawa, T.; Santos, E. J.; Duong, V.; Fang, L.; Ayzner, A. L.; Bao, Z., Few-layer, large-area, 2D covalent organic framework semiconductor thin films. *Chem. Commun.* **2015**, *51*, 13894-13897.
- [5] Mitra, S.; Sasmal, H. S.; Kundu, T.; Kandambeth, S.; Illath, K.; Diaz Diaz, D.; Banerjee, R., Targeted drug delivery in covalent organic nanosheets (CONs) via sequential postsynthetic modification. *J. Am. Chem. Soc.* **2017**, *139*, 4513-4520.
- [6] Das, G.; Biswal, B. P.; Kandambeth, S.; Venkatesh, V.; Kaur, G.; Addicoat, M.; Heine, T.; Verma, S.; Banerjee, R., Chemical sensing in two dimensional porous covalent organic nanosheets. *Chem. Sci.* **2015**, *6*, 3931-3939.
- [7] Wang, K.; Zhang, Z.; Lin, L.; Chen, J.; Hao, K.; Tian, H.; Chen, X., Covalent Organic Nanosheets Integrated Heterojunction with Two Strategies to Overcome Hypoxic-Tumor Photodynamic Therapy. *Chem. Mater.* **2019**, *32*, 3313
- [8] Sun, J.; Klechikov, A.; Moise, C.; Prodana, M.; Enachescu, M.; Talyzin, A. V., A molecular pillar approach to grow vertical covalent organic framework nanosheets on Graphene: hybrid materials for energy storage. *Angew. Chem. Int. Ed.* **2018**, *57*, 1034-1038.
- [9] Chandra, S.; Kandambeth, S.; Biswal, B. P.; Lukose, B.; Kunjir, S. M.; Chaudhary, M.; Babarao, R.; Heine, T.; Banerjee, R., Chemically stable multilayered covalent organic nanosheets from covalent organic frameworks via mechanical delamination. *J. Am. Chem. Soc.* **2013**, *135*, 17853-17861.
- [10] Lohse, M. S.; Stassin, T.; Naudin, G.; Wuttke, S.; Ameloot, R.; De Vos, D.; Medina, D. D.; Bein, T., Sequential pore wall modification in a covalent organic framework for application in lactic acid adsorption. *Chem. Mater.* **2016**, *28*, 626-631.
- [11] Xu, H.; Jiang, D., Covalent organic frameworks: crossing the channel. *Nat. Chem.* **2014**, *6*, 564.
- [12] Song, Y.; Sun, Q.; Aguila, B.; Ma, S., Opportunities of covalent organic frameworks for advanced applications. *Advanced Science* **2019**, *6*, 1801410.

- [13] Haldar, S.; Chakraborty, D.; Roy, B.; Banappanavar, G.; Rinku, K.; Mullangi, D.; Hazra, P.; Kabra, D.; Vaidhyanathan, R., Anthracene-Resorcinol Derived Covalent Organic Framework as Flexible White Light Emitter. *J. Am. Chem. Soc.* **2018**, *140*, 13367-13374.
- [14] Mukherjee, D.; Gowda Y. K, G.; Makri Nimbegondi Kotresh, H.; Sampath, S., Porous, hyper-cross-linked, three-dimensional polymer as stable, high rate capability electrode for Lithium-ion battery. *ACS Appl. Mater. Interfaces* **2016**, *9*, 19446-19454.
- [15] Bhosale, M. E.; Chae, S.; Kim, J. M.; Choi, J.-Y., Organic small molecules and polymers as an electrode material for rechargeable Lithium ion batteries. *J. Mater. Chem. A* **2018**, *6*, 19885-19911.
- [16] Xie, J.; Wang, Z.; Xu, Z. J.; Zhang, Q., Toward a High-Performance All-Plastic Full Battery with a Single Organic Polymer as Both Cathode and Anode. *Adv. Energy Mater.* **2018**, *8*, 1703509.
- [17] Lin, Z.-Q.; Xie, J.; Zhang, B.-W.; Li, J.-W.; Weng, J.; Song, R.-B.; Huang, X.; Zhang, H.; Li, H.; Liu, Y., Solution-processed nitrogen-rich Graphene-like holey conjugated polymer for efficient Lithium ion storage. *Nano energy* **2017**, *41*, 117-127.
- [18] Bai, L.; Gao, Q.; Zhao, Y., Two fully conjugated covalent organic frameworks as anode materials for Lithium ion batteries. *J. Mater. Chem. A* **2016**, *4*, 14106-14110.
- [19] Lei, Z.; Yang, Q.; Xu, Y.; Guo, S.; Sun, W.; Liu, H.; Lv, L.-P.; Zhang, Y.; Wang, Y., Boosting Lithium storage in covalent organic framework via activation of 14-electron redox chemistry. *Nat. Commun.* **2018**, *9*, 576.
- [20] Yang, H.; Zhang, S.; Han, L.; Zhang, Z.; Xue, Z.; Gao, J.; Li, Y.; Huang, C.; Yi, Y.; Liu, H., High conductive two-dimensional covalent organic framework for Lithium storage with large capacity. *ACS Appl. Mater. Interfaces* **2016**, *8*, 5366-5375.
- [21] Dahn, J.; Sleight, A.; Shi, H.; Reimers, J.; Zhong, Q.; Way, B., Dependence of the electrochemical intercalation of Lithium in carbons on the crystal structure of the carbon. *Electrochim. Acta* **1993**, *38*, 1179-1191.
- [22] Kim, M.-S.; Lee, W.-J.; Paek, S.-M.; Park, J. K., Covalent Organic Nanosheets as Effective Sodium-Ion Storage Materials. *ACS Appl. Mater. Interfaces* **2018**, *10*, 32102-32111.
- [23] Zhu, Y.; Chen, X.; Cao, Y.; Peng, W.; Li, Y.; Zhang, G.; Zhang, F.; Fan, X., Reversible intercalation and exfoliation of layered covalent triazine frameworks for enhanced Lithium ion storage. *Chem. Commun.* **2019**, *55*, 1434-1437.
- [24] Yazami, R.; Touzain, P., A reversible Graphite-Lithium negative electrode for electrochemical generators. *J. Power Sources* **1983**, *9*, 365-371.
- [25] Haldar, S.; Roy, K.; Nandi, S.; Chakraborty, D.; Puthusseri, D.; Gawli, Y.; Ogale, S.; Vaidhyanathan, R., High and Reversible Lithium Ion Storage in Self-Exfoliated Triazole-Triformyl Phloroglucinol-Based Covalent Organic Nanosheets. *Adv. Energy Mater.* **2018**, *8*, 1702170.
- [26] Lei, Z.; Chen, X.; Sun, W.; Zhang, Y.; Wang, Y., Exfoliated Triazine-Based Covalent Organic Nanosheets with Multielectron Redox for High-Performance Lithium Organic Batteries. *Adv. Energy Mater.* **2019**, *9*, 1801010.
- [27] Khomenko, V. G.; Barsukov, V. Z.; Doninger, J. E.; Barsukov, I. V., Lithium-ion batteries based on carbon-silicon-Graphite composite anodes. *J. Power Sources* **2007**, *165*, 598-608.

- [28] Shim, J.; Striebel, K. A., Cycling performance of low-cost Lithium ion batteries with natural Graphite and LiFePO₄. *J. Power Sources* **2003**, *119*, 955-958.
- [29] Hassoun, J.; Lee, K.-S.; Sun, Y.-K.; Scrosati, B., An advanced Lithium ion battery based on high performance electrode materials. *J. Am. Chem. Soc.* **2011**, *133*, 3139-3143.
- [30] Dahn, J. R.; Zheng, T.; Liu, Y.; Xue, J., Mechanisms for Lithium insertion in carbonaceous materials. *Science* **1995**, *270*, 590-593.
- [31] Levi, M. D.; Aurbach, D., Diffusion coefficients of Lithium ions during intercalation into Graphite derived from the simultaneous measurements and modeling of electrochemical impedance and potentiostatic intermittent titration characteristics of thin Graphite electrodes. *J. Phys. Chem. B* **1997**, *101*, 4641-4647.
- [32] Huang, H.; Xia, Y.; Tao, X.; Du, J.; Fang, J.; Gan, Y.; Zhang, W., Highly efficient electrolytic exfoliation of Graphite into Graphene sheets based on Li ions intercalation–expansion–microexplosion mechanism. *J. Mater. Chem.* **2012**, *22*, 10452-10456.
- [33] Toyoura, K.; Koyama, Y.; Kuwabara, A.; Oba, F.; Tanaka, I., First-principles approach to chemical diffusion of Lithium atoms in a Graphite intercalation compound. *Physical Review B* **2008**, *78*, 214303.
- [34] Luo, Z.; Liu, L.; Ning, J.; Lei, K.; Lu, Y.; Li, F.; Chen, J., A Microporous Covalent–Organic Framework with Abundant Accessible Carbonyl Groups for Lithium-Ion Batteries. *Angew. Chem. Int. Ed.* **2018**, *57*, 9443-9446.
- [35] Wu, Y.; Zeng, R.; Nan, J.; Shu, D.; Qiu, Y.; Chou, S. L., Quinone electrode materials for rechargeable Lithium/Sodium ion batteries. *Adv. Energy Mater.* **2017**, *7*, 1700278.
- [36] Häupler, B.; Wild, A.; Schubert, U. S., Carbonyls: powerful organic materials for secondary batteries. *Adv. Energy Mater.* **2015**, *5*, 1402034.
- [37] Bachmann, W. E.; Scott, L., The reaction of anthracene with maleic and fumaric acid and their derivatives and with citraconic anhydride and mesaconic acid. *J. Am. Chem. Soc.* **1948**, *70*, 1458-1461.
- [38] Durmaz, H.; Colakoglu, B.; Tunca, U.; Hizal, G., Preparation of block copolymers via Diels Alder reaction of maleimide-and anthracene-end functionalized polymers. *J. Polym. Sci., Part A: Polym. Chem.* **2006**, *44*, 1667-1675.
- [39] Grigoras, M.; Colotin, G.; Antonoaia, N. C., Synthesis and polymerization of anthracene-based itaconimides. *Polym. Int.* **2004**, *53*, 1321-1326.
- [40] Hall Jr, H.; Nogues, P.; Rhoades, J.; Sentman, R.; Detar, M., (Carbomethoxy) maleic anhydride, a highly reactive new dienophile and comonomer. *J. Org. Chem.* **1982**, *47*, 1451-1455.
- [41] Chou, T.-C.; Jiang, T.-S.; Hwang, J.-T.; Lin, K.-J.; Lin, C.-T., Laticyclic Conjugated Polyenes. Study on Diels–Alder Cycloadditions of a Facially Dissymmetric Maleic Anhydride. *J. Org. Chem.* **1999**, *64*, 4874-4883.
- [42] Khayum, M. A.; Kandambeth, S.; Mitra, S.; Nair, S. B.; Das, A.; Nagane, S. S.; Mukherjee, R.; Banerjee, R., Chemically delaminated free-standing ultrathin covalent organic nanosheets. *Angew. Chem. Int. Ed.* **2016**, *55*, 15604-15608.

- [43] Andrews, L.; Keefer, R., A Kinetic Study of the Diels-Alder Reaction of Various Anthracene and Maleic Anhydride Derivatives. *J. Am. Chem. Soc.* **1955**, *77*, 6284-6289.
- [44] Sole, C.; Drewett, N. E.; Hardwick, L. J., In situ Raman study of Lithium-ion intercalation into microcrystalline Graphite. *Faraday Discuss.* **2014**, *172*, 223-237.
- [45] Simon, P.; Gogotsi, Y.; Dunn, B., Where do batteries end and supercapacitors begin? *Science* **2014**, *343*, 1210-1211.
- [46] Yu, P.; Popov, B. N.; Ritter, J. A.; White, R. E., Determination of the Lithium ion diffusion coefficient in Graphite. *J. Electrochem. Soc.* **1999**, *146*, 8-14.
- [47] S. Wang, Q. Wang, P. Shao, Y. Han, X. Gao, L. Ma, S. Yuan, X. Ma, J. Zhou, X. Feng, *J. Am. Chem. Soc.* **2017**, *139*, 4258-4261.
- [48] Wang, S.; Wang, Q.; Shao, P.; Han, Y.; Gao, X.; Ma, L.; Yuan, S.; Ma, X.; Zhou, J.; Feng, X., Exfoliation of covalent organic frameworks into few-layer redox-active nanosheets as cathode materials for Lithium-ion batteries. *J. Am. Chem. Soc.* **2017**, *139*, 4258-4261.
- [49] Weigel, O.; Steinhoff, E., Adsorption of organic liquid vapors by chabazite. *Z. Kristallogr* **1925**, *61*, 125-154
- [50] Chen, H.; Tu, H.; Hu, C.; Liu, Y.; Dong, D.; Sun, Y.; Dai, Y.; Wang, S.; Qian, H.; Lin, Z., Cationic covalent organic framework nanosheets for fast li-ion conduction. *J. Am. Chem. Soc.* **2018**, *140*, 896-899.
- [51] Xu, Q.; Tao, S.; Jiang, Q.; Jiang, D., Ion conduction in polyelectrolyte covalent organic frameworks. *J. Am. Chem. Soc.* **2018**, *140*, 7429-7432.
- [52] Jeong, K.; Park, S.; Jung, G. Y.; Kim, S. H.; Lee, Y.-H.; Kwak, S. K.; Lee, S.-Y., Solvent-free, single Lithium-ion conducting covalent organic frameworks. *J. Am. Chem. Soc.* **2019**, *141*, 5880-5885.
- [53] Balogun, M.-S.; Qiu, W.; Luo, Y.; Meng, H.; Mai, W.; Onasanya, A.; Olaniyi, T. K.; Tong, Y., A review of the development of full cell Lithium-ion batteries: The impact of nanostructured anode materials. *Nano research* **2016**, *9*, 2823-2851.
- [54] Sun, H.; He, X.; Ren, J.; Li, J.; Jiang, C.; Wan, C., Hard carbon/Lithium composite anode materials for Li-ion batteries. *Electrochim. Acta* **2007**, *52*, 4312-4316.
- [55] Hassoun, J.; Bonaccorso, F.; Agostini, M.; Angelucci, M.; Betti, M. G.; Cingolani, R.; Gemmi, M.; Mariani, C.; Panero, S.; Pellegrini, V., An advanced Lithium-ion battery based on a Graphene anode and a Lithium iron phosphate cathode. *Nano Lett.* **2014**, *14*, 4901-4906.
- [56] Ji, L.; Zheng, H.; Ismach, A.; Tan, Z.; Xun, S.; Lin, E.; Battaglia, V.; Srinivasan, V.; Zhang, Y., Graphene/Si multilayer structure anodes for advanced half and full Lithium-ion cells. *Nano Energy* **2012**, *1*, 164-171.
- [57] Chen, X.; Li, Y.; Wang, L.; Xu, Y.; Nie, A.; Li, Q.; Wu, F.; Sun, W.; Zhang, X.; Vajtai, R., High-Lithium-Affinity Chemically Exfoliated 2D Covalent Organic Frameworks. *Adv. Mater.* **2019**, *31*, 1901640.

Chapter 3:

Tuning the Electronic Energy Level of Covalent Organic Framework for Crafting High-rate Sodium Ion Battery

3.1. Introduction:

COFs are crystalline polymers with uniform nanopores.¹⁻⁵ The out-of-plane π - π stacking of the aromatic rings between the COF layers generate hollow cylindrical channels along with the c-direction.⁶⁻¹⁰ Their pore size and shape can be tuned by choosing the monomers of desired length and geometry. Meanwhile, their organic backbone favors the stoichiometric incorporation of electrochemically active sites into the framework. This molecular-level designability gives a chance to decorate the entire wall of their cylindrical pores with redox-active functional groups. Their crystalline structure would ensure a periodic distribution of such active sites, while the sizeable nanopores ensure easy access to such sites. Also, COF's high surface area helps to store electrical charge via electrical double layer formation.¹¹⁻¹⁶ These redox-active COFs become apt electrode candidates for metal-ion batteries.¹⁷⁻²⁸ Particularly in providing the required electronic dynamo for sluggish ions like Na^+ . COF's superior anodic performance in Li-ion batteries with specific capacities surpassing commercial Graphite is recently demonstrated.^{18,20,29,30,31}

From table 3.1 it is clear that LIB technology is comparatively less challenging to build as the diameter of the Li-ion is smaller and Lithium is a lightweight metal. Hence the kinetics of the movement of the Li in back and fro direction between electrodes is very faster. Here the anodic electrode must have multiple interaction sites to enhance the charge storing ability to maintain higher energy density and the facile insertion of Lithium is needed to make the fast-charging battery to obtain maximum power density.

Now coming to the SIB technologies the main challenge is associated with the bigger size of the Sodium ion which is, of course, heavier than the Lithium. That reflects in both lower energy density and lower power density. The sluggish movement of the Sodium and very low diffusion rate restricts the commercialization of SIB technologies. But the abundance of availability of Sodium in the earth crust, chances of using the low-cost Aluminium foil as a current collector and of course the safety issue associated with the transportation possibility even in completely self-discharge rate attracts the researcher around the globe to develop the cheaper SIB technologies. For that, it is necessary to overcome all the inherent problems present in the basic working principle of SIB.

Table 3.1: Features of LIB and SIB technologies.

	Li-ion battery	Na-ion battery
Diameter of charge carrier	1.36 angstrom	1.94 angstrom
Working mechanism	Intercalation/Insertion/Conversion type	Insertion/Conversion
Fast charging	Possible, as Lithium is lighter	Quite difficult, as Sodium is heavier than Lithium
OCV	3.0 V	2.7 V
Cost	High	Low
Energy Density	High	Moderate/High
Power density	Moderate	Very low
Safety	Low	High
Materials	Scarce	Earth-abundant
Current Collector	Cu foil	Low cost Al foil
Cycling Stability	High (negligible self-discharge)	High (negligible self-discharge)
Efficiency	High (> 90%)	High (> 90%)
Temperature Range	-25 °C to 40 °C	-40 °C to 60 °C
Technological importance	Transportation restrictions at discharged state	Easy transportation even at fully discharged state

Yet, Graphite is the most used anode in commercial Li-ion batteries. It stores Li⁺ ions by inserting them into its inter-layer spaces. Unfortunately, Graphite does not show such favorability for the Na⁺ ions.³²⁻³⁴ In contrast, even the larger K⁺ ions can be inserted into the Graphite interlayers with relative ease.³⁵ The crucial problem is with the lack of thermodynamic favourability for the Na⁺ ions to reside in the interlayer spaces of Graphite.³⁶ This becomes evident from the enthalpy associated with the compounds that form during the intercalation of these different ions into Graphite. The enthalpy of formation of LiC₆ and KC₈ were found to be -16.4 and -27.5 kJ/mol, respectively. Meanwhile, NaC₆ and NaC₈ are unstable with positive enthalpies of formation (+20.8 and +19.9 kJ/mol).³⁷ This is due to the size mismatch. Interestingly, including larger solvated co-ions with Na⁺ ions, improves the latter's size-fit, but it does bring down the energy density as many sites get occupied by the "non-contributing" solvated guest.³⁸ Also, since, the Na⁺ ions are larger than Li⁺ ions, the intercalation of Na⁺ into small lattice structures (which are desirable for high-energy batteries) might be accompanied by structural and volume change. These changes, in many cases, destroy the contacts between the electrode and the current collector, leading to a prominent capacity fading during the Na-ion battery cycling. Whereas in nanostructured COFs this is an improbable problem. Thus COF could be a more suited porous host with more diversities in terms of the active sites and accommodative nano spaces.

On the kinetic front, the mere size and the associated bulk of the Na⁺ ions compared to Li⁺ ions certainly make it sluggish (Li⁺: 0.76 Å vs. Na⁺: 1.02 Å and the mass).³⁹⁻⁴¹ Hence introducing a chemical

drive to improve the ionic-mobility of Na⁺ ions would directly impact the rate-performance of the battery. In fact, with this aim hard carbon doped with heteroatoms such as B, N, S and P have been employed as anodes in Na-ion batteries with reasonable success (B doped: 278 mAh/g @0.1 A/g, N doped: 154 mAh/g @15 A/g, S doped: 182 mAh/g @3.2 A/g, P doped: 108 mAh/g @20 A/g).⁴²⁻⁴⁹ Even so, in these improved systems, the relative drop in specific capacity with increasing current density (termed as the rate-performance) is a concern. Meanwhile, hard carbons with a 3D mesoporous structure have been far more successful (>280 mAh/g @100 mA/g).^{50,51} Yet, the designed enhancement of anodic performance at high current density (236 mAh/g @10 A/g) of such hard carbons with atomic-level manipulation is primarily hampered by their amorphous structure.⁵² Also, they carry a major synthetic disadvantage as the high-temperature pyrolysis assisted doping of heteroatoms in such carbonaceous materials is a random process challenging the reproducibility and scale-up.^{42,45,48} In contrast, the COF synthesis involves stoichiometric combinations of monomers under mild synthetic conditions, which naturally circumvents this arbitrary doping and a periodic lattice with perfect positioning of active heteroatoms is possible. Recently, a carbonyl functionalized COF with enhanced performance in SIB was reported at higher current density (135 mAh/g @10 A/g).²² Independently, acid-delamination of COF layers was also shown to improve the specific capacity at lower current density in a SIB (200 mAh/g @5 A/g).²¹ But such treatments can be harsh and can disrupt the COF structure.

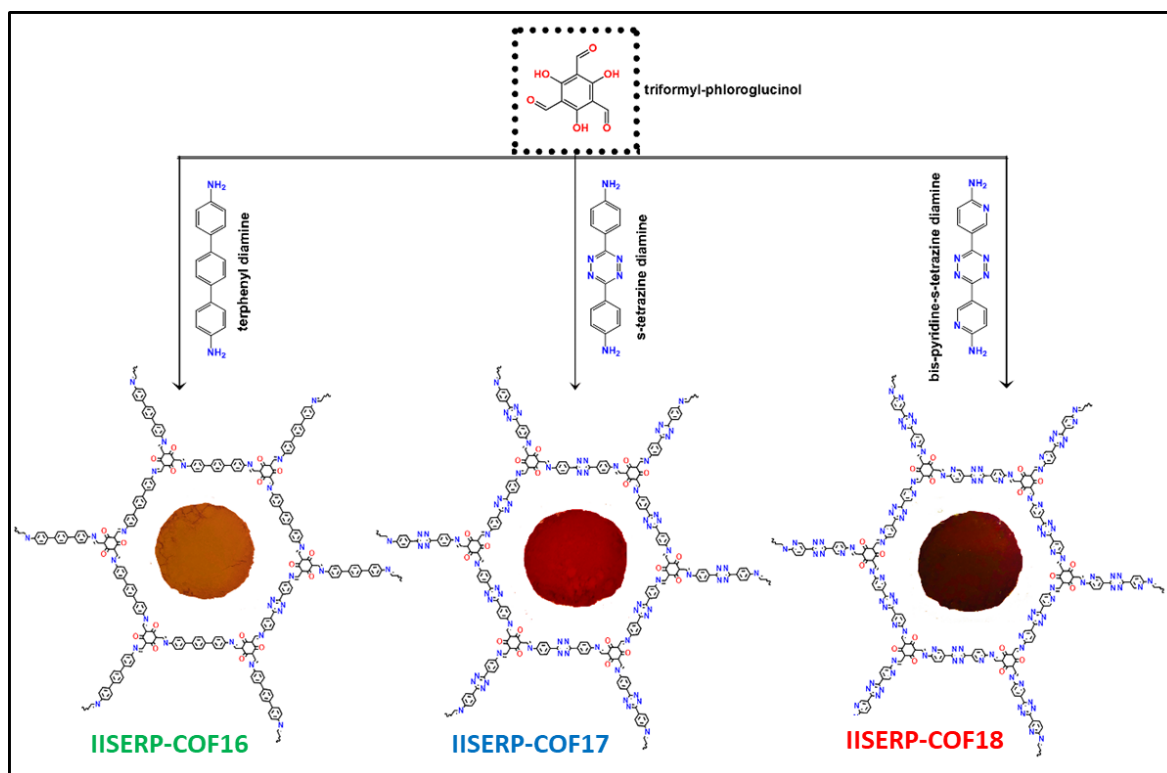
Here we have tried to develop COFs with suitably sized mesoporous structure for favourable interactions with Na⁺ ions and manipulated their chemical groups to gain electronic improvement in driving the Na⁺ ions into their pores. More specifically, we have considered three large mesoporous COFs (phenyl vs. tetrazine vs. bispyridine-tetrazine) with systematically lowered LUMO levels to gain more electron accumulation under an applied potential. This in-operation charged anode forthwith is more attractive for the heavier Na⁺ ions from the electrolyte through both pseudocapacitance and classical double layer formation. Importantly, the ordered accessible pores make the entire COF participate in the anodic action and not merely their surface. This yields a high specific capacity of 340 mAh/g @1 A/g. Its low charge transfer resistance is reflected in excellent rate-performance (only a 24% drop in specific capacity upon increasing from 0.1 to 1 A/g). Also, the favorable charge degeneracy throughout the nanowalls of the structure enhances the stability even at a very high current inputs (128 mA/g @15 A/g). It brings excellent cycling stability even up to 1400 cycles, with only 8% capacity fade. Interestingly, the phenyl analog lacking the N-heteroatom in its backbone does not show such a high performance. This notion of atomic-level tuning of the electronic energy level of the COFs for fluent Na⁺ insertion is a promising route to design next-generation anode materials for SIBs.

3.2. Results and discussion:

3.2.1. Synthesis and structural-modelling of IISERP-COF16, IISERP-COF17, IISERP-COF18:

IISERP-COF16, IISERP-COF17 and IISERP-COF18 have (3+2) frameworks formed by reacting a C₃ symmetry trialdehyde [2,4,6-trihydroxybenzene-1,3,5-tricarbaldehyde] with three different C₂ symmetry diamine containing terphenyl [(1,1':4',1''-terphenyl)-4,4''-diamine], s-tetrazine [4,4'-(1,2,4,5-tetrazine-3,6-diyl)dianiline] and s-tetrazine bispyridine [5,5'-(1,2,4,5-tetrazine-3,6-diyl)bis(pyridine-2-amine)] units (Scheme 3.1) The purity of all the monomers was confirmed from solution-state ¹H and ¹³C NMR (Figure A.3.1-A.3.6, Table A.3.1 and A.3.2). With the increase of the nitrogen contents in the framework, the color of the COFs becomes darker brown from golden yellow

(Scheme A.3.1). While IISERP-COF16 and IISERP-COF17 are known, we are reporting the bispyridine-tetrazine COF for the first time.^{53,54} These three COFs constitute a family that enables a systematic comparison of the electronic structure with the anodic performance in a SIB.



Scheme 3.1. Formation of COFs from corresponding monomers. Inset shows the photograph of the COF powders.

Synthesis of IISERP-COF16: 2,4,6-triformyl-phloroglucinol (65 mg, 0.3 mmol) and terphenyl-diamine (116 mg, 0.45 mmol) were weighed into a Pyrex tube and were dissolved in dioxane (6.0 mL) and mesitylene (3.0 mL) and stirred until a homogeneous yellow colour was observed. To this mixture, 1.0 mL of 0.6 M acetic acid was added. Then the Pyrex tube was flash frozen in a liquid nitrogen bath and sealed. The Pyrex tube along with its contents was placed in an oven at 135°C for 5 days and gradually cooled to room temperature over 12 hrs. This yielded about 140 mg of bright yellow coloured solid which was washed with hot DMF, dioxane, MeOH, acetone and THF (85%, isolated yield). This product was also subjected to a Soxhlet extraction using hot DMF/methanol/THF as solvent and filtered solid.

Synthesis of IISERP-COF17: 2,4,6-triformyl-phloroglucinol (65 mg, 0.3 mmol) and s-tetrazine-diamine (118 mg, 0.45 mmol) were weighed into a Pyrex tube and were dissolved in dioxane (6.0 mL) and mesitylene (3.0 mL) and stirred until a homogeneous red colour was observed. To this mixture, 1.0 mL of 0.6 M acetic acid was added. Then the Pyrex tube was flash frozen in a liquid nitrogen bath and sealed. The Pyrex tube along with its contents was placed in an oven at 135 °C for 5 days and gradually cooled to room temperature over 12 hrs. This yielded about 130 mg of bright yellow coloured solid which was washed with hot DMF, dioxane, MeOH, acetone and THF (70%, isolated yield). This product was also subjected to a Soxhlet extraction using hot DMF/methanol as solvent and filtered.

Synthesis of IISERP-COF18: 2,4,6-triformyl-phloroglucinol (65 mg, 0.3 mmol) and bispyridine-s-tetrazine-diamine (120 mg, 0.45 mmol) were weighed into a Pyrex tube and were dissolved in dioxane (5.0 mL) and mesitylene (3.0 mL) and stirred until a red colour was observed. To this mixture, 1.0 mL of 0.8 M acetic acid was added. Then the Pyrex tube was flash frozen in a liquid nitrogen bath and

sealed. The Pyrex tube along with its contents was placed in an oven at 135 °C for 5 days and gradually cooled to room temperature over 12 hrs. This yielded about 175 mg of bright yellow coloured solid which was washed with hot DMF, dioxane, MeOH, acetone and THF (90%, isolated yield). This product was also subjected to a Soxhlet extraction using hot DMF/methanol as solvent and filtered.

The completion of the polycondensation reactions was confirmed by ^{13}C solid-state NMR studies and IR data analysis of the COFs. The presence of appropriate peaks in the ^{13}C solid-state NMR spectra of the COFs corresponding to the keto group of β -keto enamine form (δ :185-190 ppm), pyridine (δ :143-148 ppm) and tetrazine (δ :168 ppm) reveals the functional group integrity maintained during the polycondensed polymeric structure formation (Figure 3.1).^{12,5}

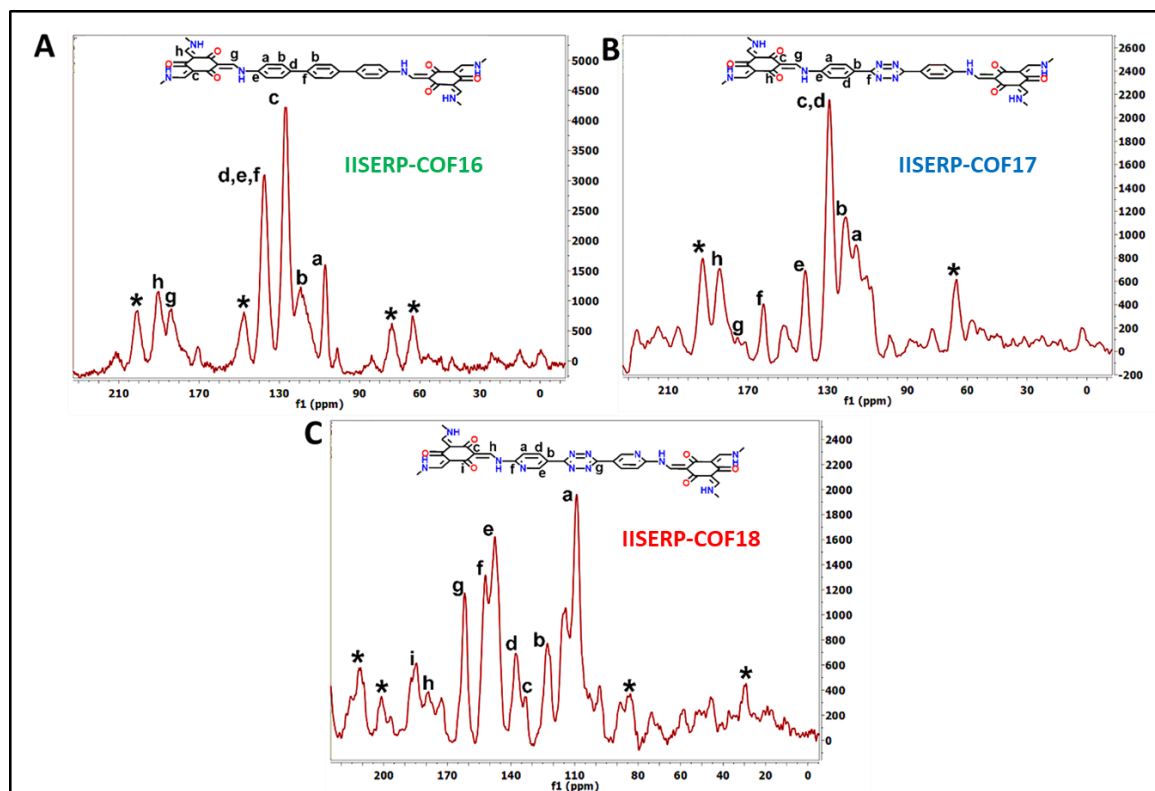


Figure 3.1. (A) CP MAS ^{13}C -NMR spectra of the IISERP-COF16 measured at 500 MHz. a, b, c, d, e, f, g and h are the corresponding peaks positions obtained from the NMR data. (*) denotes the presence of side bands. (B) CP MAS ^{13}C -NMR spectra of the IISERP-COF17 measured at 500 MHz. a, b, c, d, e, f, g and h are the corresponding peaks positions obtained from the NMR data. (*) denotes the presence of side bands. (C) CP MAS ^{13}C -NMR spectra of the IISERP-COF18 measured at 500 MHz. a, b, c, d, e, f, g, h and i are the corresponding peaks positions obtained from the NMR data. (*) denotes the presence of side bands.

The characteristic carbonyl ($\text{C}=\text{O}$) stretching frequency (1718 cm^{-1}) of the triformyl-phloroglucinol was red-shifted (1630 cm^{-1}) and the N–H stretching modes (3388 , 3317 , 3196 cm^{-1}) of the primary amine disappeared with the formation of the COFs (Figure 3.2, Table 3.2). We notice from the IR spectra that the solid powders of the as-synthesized **1** exists predominantly in β -ketoenamine form, which arises from the tautomerism between the Schiff bonds ($-\text{C}=\text{N}-$) and carbonyl ($-\text{C}=\text{O}$) units, but **2** and **3** show the presence of enolic form too.

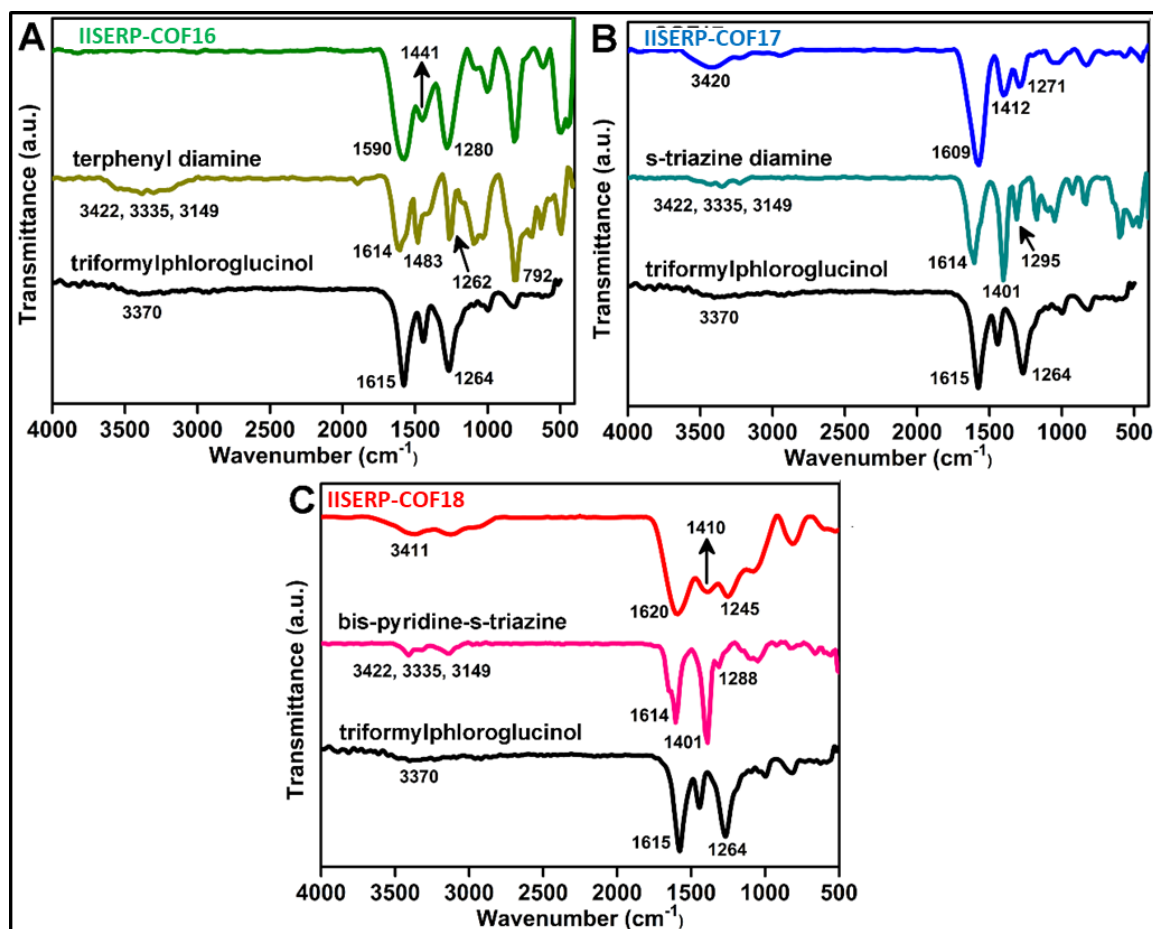


Figure 3.2. Comparison of the IR spectra of the COFs.

Table 3.2. IR data analysis of COFs

COF-Name	Enolic OH (cm ⁻¹)	carbonyl (C=O) (cm ⁻¹)	C=C bond (cm ⁻¹)	C-N bond (cm ⁻¹)
IISERP-COF16	absent	1590	1441	1280
IISERP-COF17	3420	1609	1412	1271
IISERP-COF18	3411	1620	1410	1245

Note: The enolic hydroxyl groups present in IISERP-COF17 and IISERP-COF18 are rapidly interconvertible to β -ketoenamine form.

The structural models for all three COFs were built using Materials Studio v. 6.0.⁵⁵⁻⁵⁷ An initial indexing and space group search was performed using the experimental powder X-ray diffraction (PXRD) employing the Reflex module. All three PXRD patterns indexed to a hexagonal cell. A space group search yielded P-6 and P6/m, both with a well-acceptable Figure of Merit (Figure 3.3A-3.3C). Atomic manipulations were carried out in a cell built using the higher symmetry P6/m setting to obtain an initial polymeric model of the COF with apt connectivity. The final structures were optimized with a periodic tight-binding DFT method (DFTB). Total energies were extracted from the DFTB optimizations (IISERP-COF16: eclipsed = -111080; IISERP-COF17: eclipsed = -113964; IISERP-COF18: eclipsed = -115471 kcal/mol/unit-cell). The Pawley refinements of the experimental PXRDs against their optimized models yield excellent fits for all the COFs (Figure 3.3.D). The presence of strategically positioned keto groups of the phloroglucinol units enables its strong O...H-N...intra-layer hydrogen bonds with the enamine form of the connecting Schiff bonds along *ab*-plane.⁵⁸⁻⁶⁰ The three-dimensional structure of the IISERP-COFs have π -stacked columns of resorcinol units and the columns

of benzene (for IISERP-COF16), s-tetrazine (for IISERP-COF17), bipyridine s-tetrazine rings (for **3**) covalently linked by Schiff bonds. This creates uniform one dimensional (1D) nano-channels with pores of size ~ 38 Å (factoring the van der Waals radii of the atoms) along with the c-axis. Experimental PXRD pattern shows high intensity peaks located at 2θ : 2.65° (for IISERP-COF16), 2.55° (for IISERP-COF17), 2.6° (for IISERP-COF18) for (100) reflections (Figure 3.3.D). The (001) reflections \sim along the stacking direction is observed at a $2\theta = \sim 26.5^\circ$.

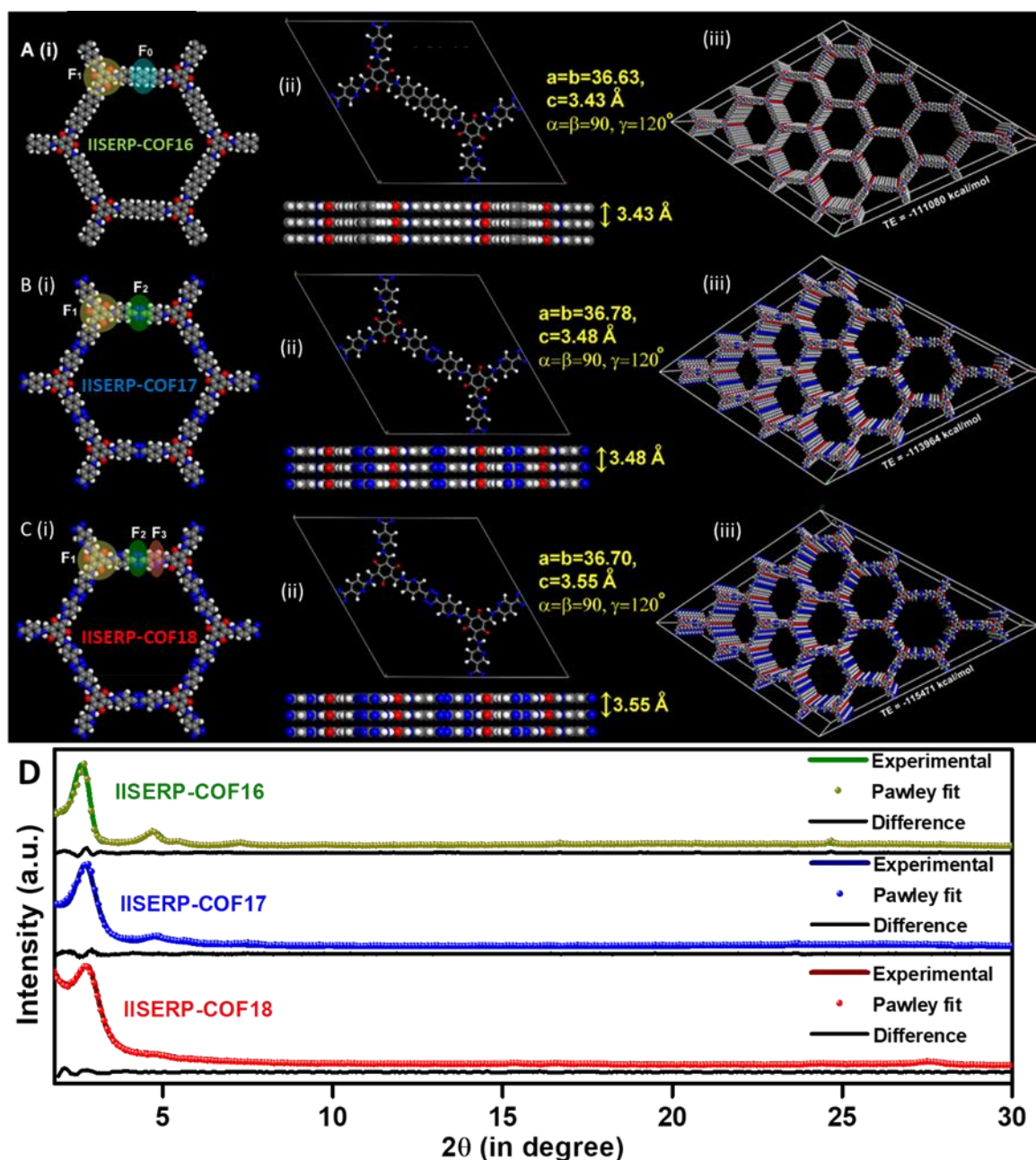


Figure 3.3. A (i), B (i) and C (i) Modeled structures of the IISERP-COF16, IISERP-COF17 and IISERP-COF18. They prefer an eclipsed configuration with an AA... stacking. F_0 , F_1 , F_2 and F_3 are the redox-active functional groups present in the IISERP-COFs. A (ii), B (ii) and C (ii) Unit cells and columnar view COFs, obtained from DFTB geometry-optimized structures. A (iii), B (iii) and C (iii) Polymeric propagation of the COFs' represented by $(4 \times 4 \times 8)$ supercells. (D) Pawley fits using the experimental PXRD patterns.

Adsorption-desorption isotherms of N₂ at 77 K, yielded a completely reversible type-2 isotherm for *all these COFs*, which approves their expected mesoporous structure (Figure 3.4-3.7, Table 3.3).⁶⁴ A Barrett-Joyner-Halenda (BJH) fit to the desorption branch reveals the presence of uniform ~36.6, 36.9 and 36.5 Å pores in IISERP-COF16,17 and 18 respectively (Figure 3.7.B). These COFs have a higher Langmuir surface area (920 m²/g for IISERP-COF16; 1452 m²/g for IISERP-COF17; 1745 m²/g for IISERP-COF18) than Brunauer-Emmett-Teller (BET) surface area (Table 3.3).^{55,57,53} All the powdered samples were subjected to Soxhlet washing using boiling THF/DMF mixture (48 hrs), to get rid of any soluble oligomers. The PXRD and porosity data reproduced well across different batches, confirming that the samples do not have any significant impurity phases.

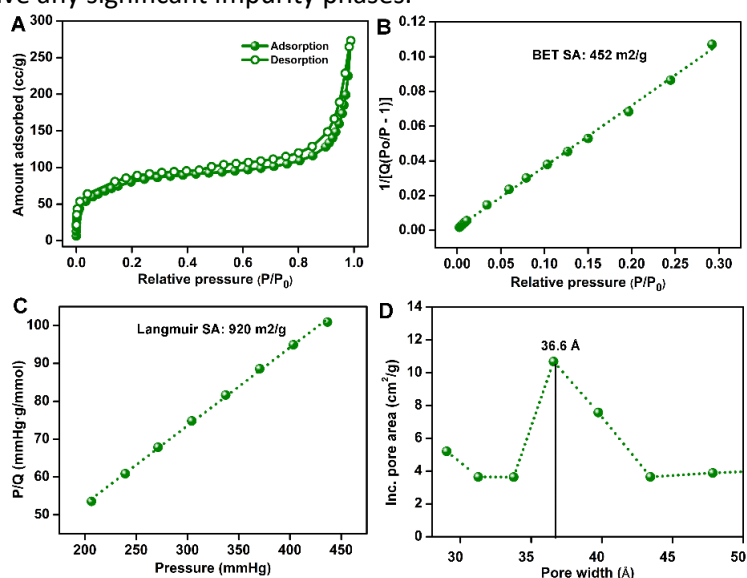


Figure 3.4. (A) N₂ adsorption-desorption isotherm of IISERP-COF16 at 77 K (B) A BET fit obtained using the low pressure region data of the N₂ adsorption isotherm. (C) A Langmuir fit obtained using the N₂ adsorption isotherm. (D) A plot of the pore width vs. incremental pore area of IISERP-COF16.

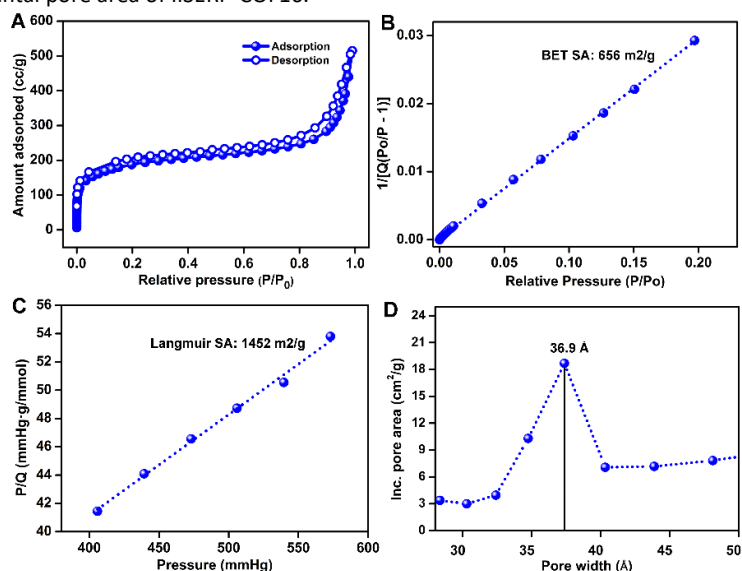


Figure 3.5. (A) N₂ adsorption-desorption isotherm of IISERP-COF17 at 77 K. (B) A BET fit obtained using the low pressure region data of the N₂ adsorption isotherm. (C) A Langmuir fit obtained using the N₂ adsorption isotherm. (D) A plot of the pore width vs. incremental pore area of IISERP-COF17.

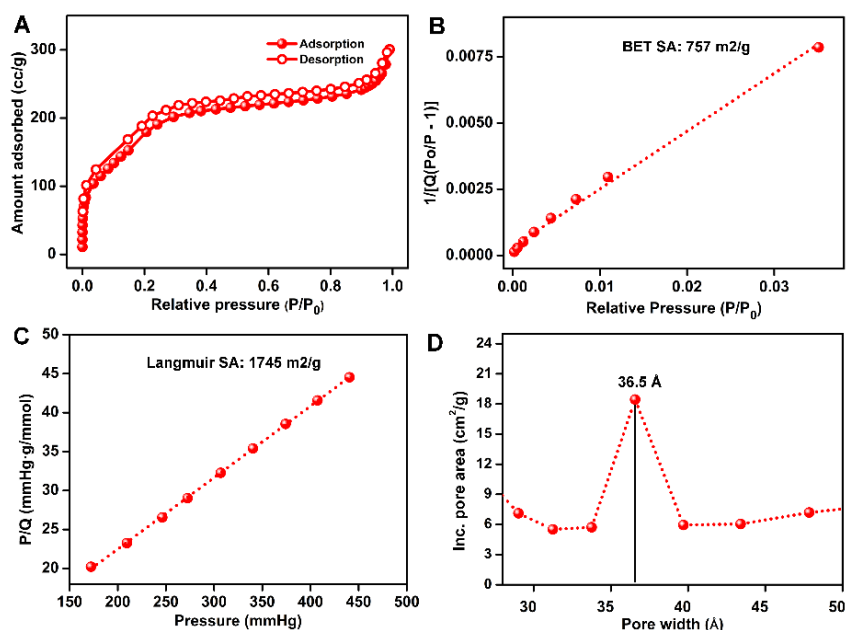


Figure 3.6. (A) N₂ adsorption-desorption isotherm of IISERP-COF18 at 77 K. (B) A BET fit obtained using the low pressure region data of the N₂ adsorption isotherm. (C) A Langmuir fit obtained using the N₂ adsorption isotherm. (D) A plot of the pore width vs. incremental pore area of IISERP-COF18.

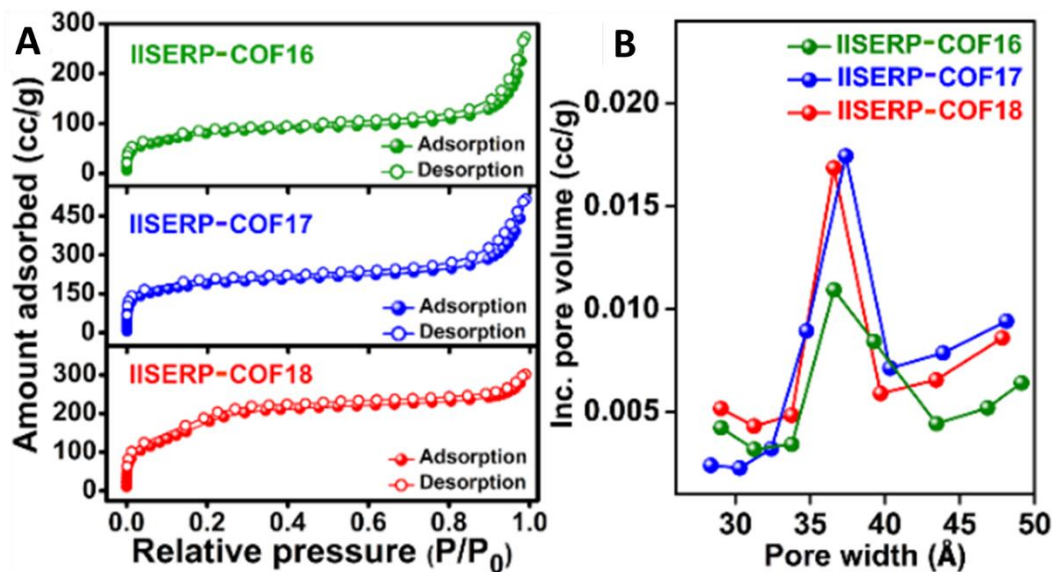


Figure 3.7. (A) Nitrogen (N₂) sorption isotherms of the COFs measured at 77 K. (B) Pore size distribution plots of the COFs obtained from BJH fit to the desorption branch.

Table 3.3. Comparison of experimental surface area (SA) with modeled surface area.

COFs	BET SA (m ² /g)	Langmuir SA (m ² /g)	Modeled SA (m ² /g)
IISERP-COF16	452	920	2601
IISERP-COF17	656	1452	2684
IISERP-COF18	757	1745	2479

Note: The calculated values are much higher than the surface area values estimated from BET or Langmuir fits. We agree that in ideal case, the surface area estimated from the fits should agree with the surface area calculated using the DFT-optimized model. In our experience, we have seen that this work quite well when it comes to ultra and microporous COFs. However, for mesoporous materials different methods such as BET, Langmuir and NLDFT used to fit the experimental isotherms all yield a much lower surface area than what is expected from the modeled structure. This makes the accurate estimation of the surface area of mesoporous material difficult. However, the lowering of surface area for COFs could certainly have contributions from the layer slipping or defects in the polymeric structure and relatively lowered degree of crystallinity as compared to other materials such as MOFs.

Under Field Emission Scanning Electron Microscope (FE-SEM), IISERP-COF16 appears as large smooth-surfaced flakes that form a stacked microstructure (Figure 3.8 and Figure A.3.7). While IISERP-COF17 has hexagonal flakes, which further aggregate into microstructures resembling petals. IISERP-COF18 has a thick fibrous morphology. In all the cases, the SEM images corroborate with the morphologies observed under the High Resolution Transmission Electron Microscope (HR-TEM) (Figure 3.8). The stacking of the layers becomes visible when viewed at the edges or the thinner portion of the sheets. High resolution images from the HR-TEM showed the presence of lattice fringes, indicating high crystallinity of these COFs (Figure A.3.8). At higher magnifications, sub-micron sized pores could be observed all across the surface of the COF flakes (Figure A.3.12).

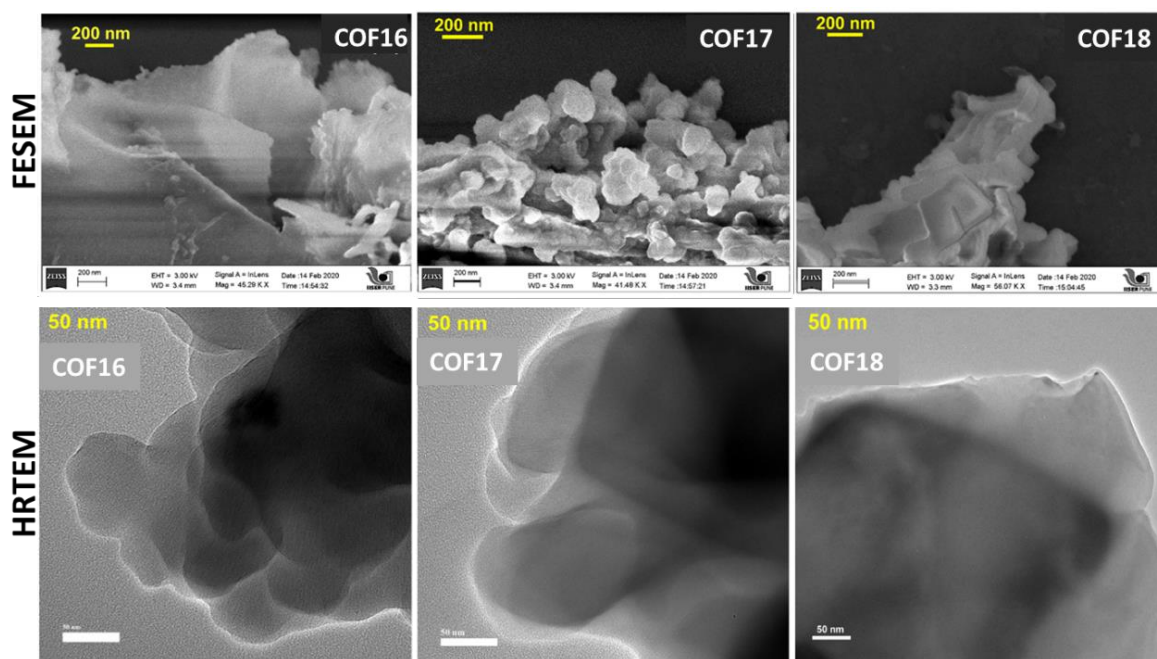


Figure 3.8. FE-SEM images of IISERP-COF16, IISERP-COF17 and IISERP-COF18 at different resolutions. At lower resolution, a fluffy cotton-like morphology can be seen. In closer view the presence of aggregated-flakes can be seen. HR-TEM images of the IISERP-COF16, IISERP-COF17 and IISERP-COF18 under different magnifications showing the aggregates formed by stacking of many sheets. Darker regions are from such multi-flake stacking. While at 10 nm resolution the uniform micropores all along the surface of the COF can be seen.

The interlayer spacing (3.3 \AA) was determined from the cross-sectional view observed for a few of the crystallites drop-casted on the TEM grid. It matched well with the layer separation distances determined from the energy and geometry optimized structure. From the Selected Area Electron Diffraction (SAED) patterns, the higher angle reflections are noticed (Figure 3.9). The SAED ring diameter ($2R$) $\sim 6 \text{ 1/nm}$ corresponds to inter-planar separation distances (3.4 \AA) of the eclipsed configuration of the refined structure (Table 3.4). This further confirms the crystallinity of this family of polycrystalline covalent organic frameworks.⁵⁹⁻⁶³ Moreover, distinct SAED patterns of COFs at 5 1/nm scale confirm the presence of diffraction of $[00l]$ planes at a higher angle. The lower angle reflections are merged in the smaller diameter range of the SAED, closer to the bright center of the SAED image.^{61-63,65}

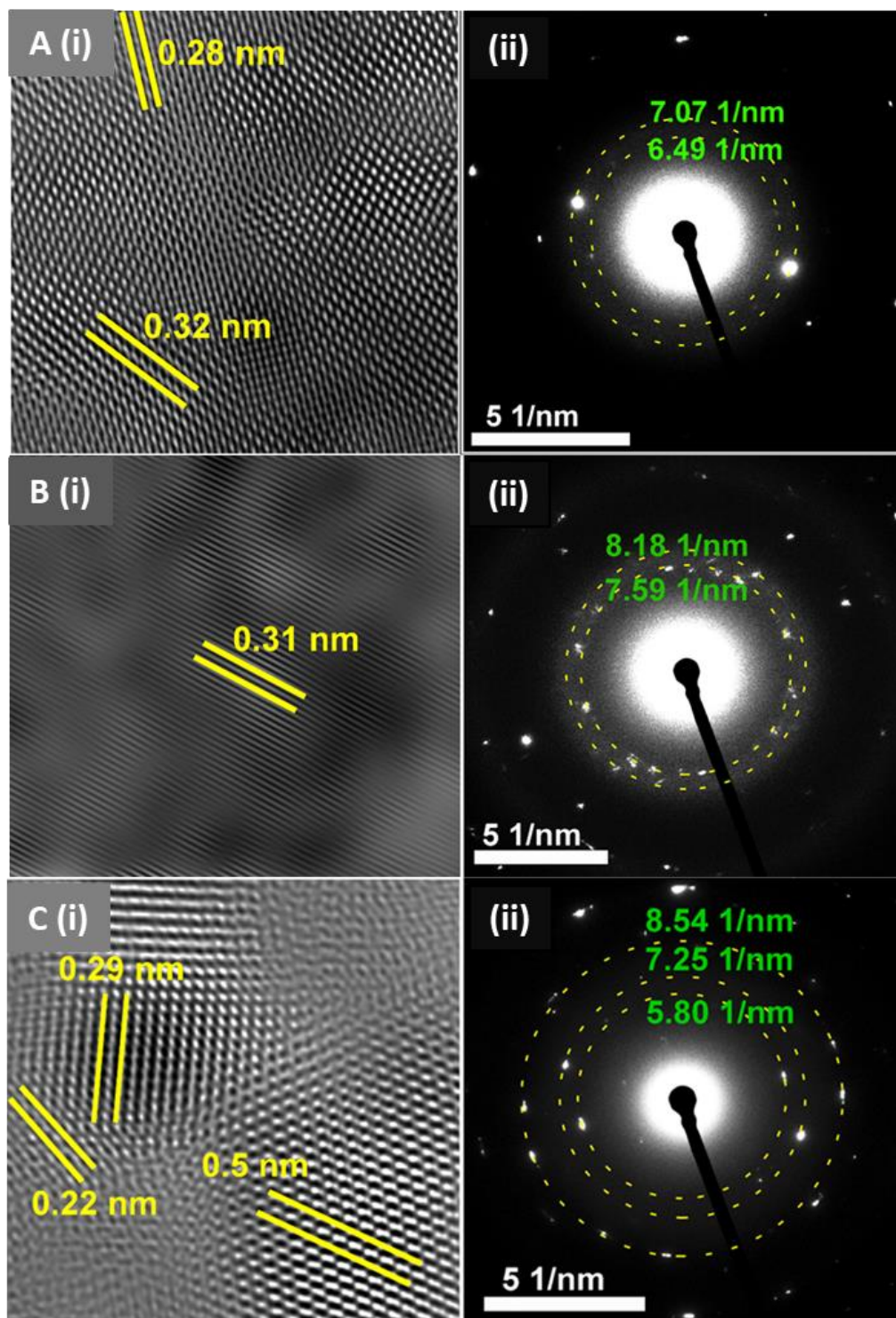


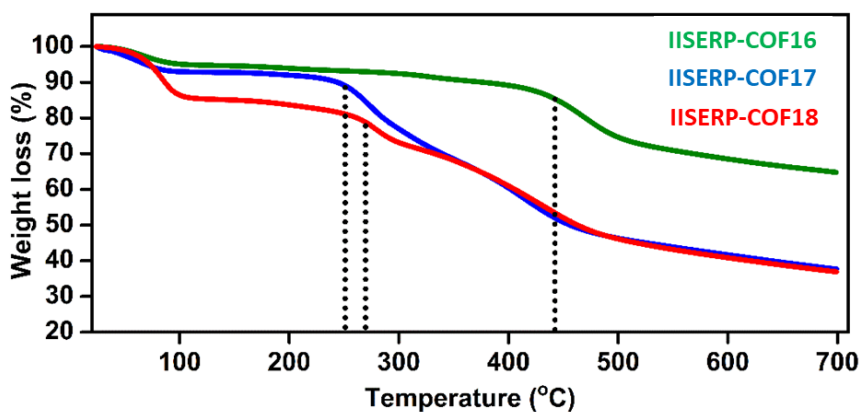
Figure 3.9. A(i), B(i), C(i) FFT pattern of the fringes area shows the d-spacing values. A(ii), B(ii), C(ii) SAED pattern of IISERP-COF16 shows the diameters of reciprocal circles. AED patterns of the COFs observed for higher angle diffraction of $00l$ planes. The units of linear distances between two bright spots of the SAED patterns are in '1/nm'.

Note: These lattice fringes could be observed across samples from different preparations and also in many regions of the drop-casted samples. The SAED pattern confirms the high degree of crystallinity in the selected flakes of the COF. Many such crystalline flakes were observed. However, the thin flakes burn under the exposure to e-beam of the HRTEM. d-spacing value calculated from the diameter (R) of the reciprocal lattice ($d=2/2R$) matches well with lattice fringes observed in FFT pattern.

Table 3.4. The diameter of the reciprocal circles in SAED pattern and calculated inter-planar spacing.

COFs	Diameter of the reciprocal circle: 2R (1/nm)	Interplanar spacing: d (nm)
IISERP-COF16	6.49	0.31
	7.07	0.29
IISERP-COF17	7.59	0.26
	8.18	0.25
IISERP-COF18	5.80	0.35
	7.25	0.28
	8.54	0.23

The strong interlayer H-bond formation of β -ketoenamine form enhances the chemical and thermal stability of IISERP-COF16 (stable up to 410 °C). However, the tetrazine containing COFs, IISERP-COF17 and IISERP-COF18, exhibit relatively lowered thermal stability (gradual weight loss on the Thermogravimetric Analysis (TGA) commences at 280 °C) (Figure 3.10.). That means the tetrazine containing COFs doesn't sustain in higher temperature. All the COFs show ample chemical stability as confirmed by the PXRD of the samples that were boiled in DMF and treated with acid and base (6M) (Figure 3.11). Probably due to mesoporous nature these COFs are unable to hold the structural integrity.

**Figure 3.10.** Thermogravimetric analysis of COFs under N₂ flow with a heating rate of 5K/min.

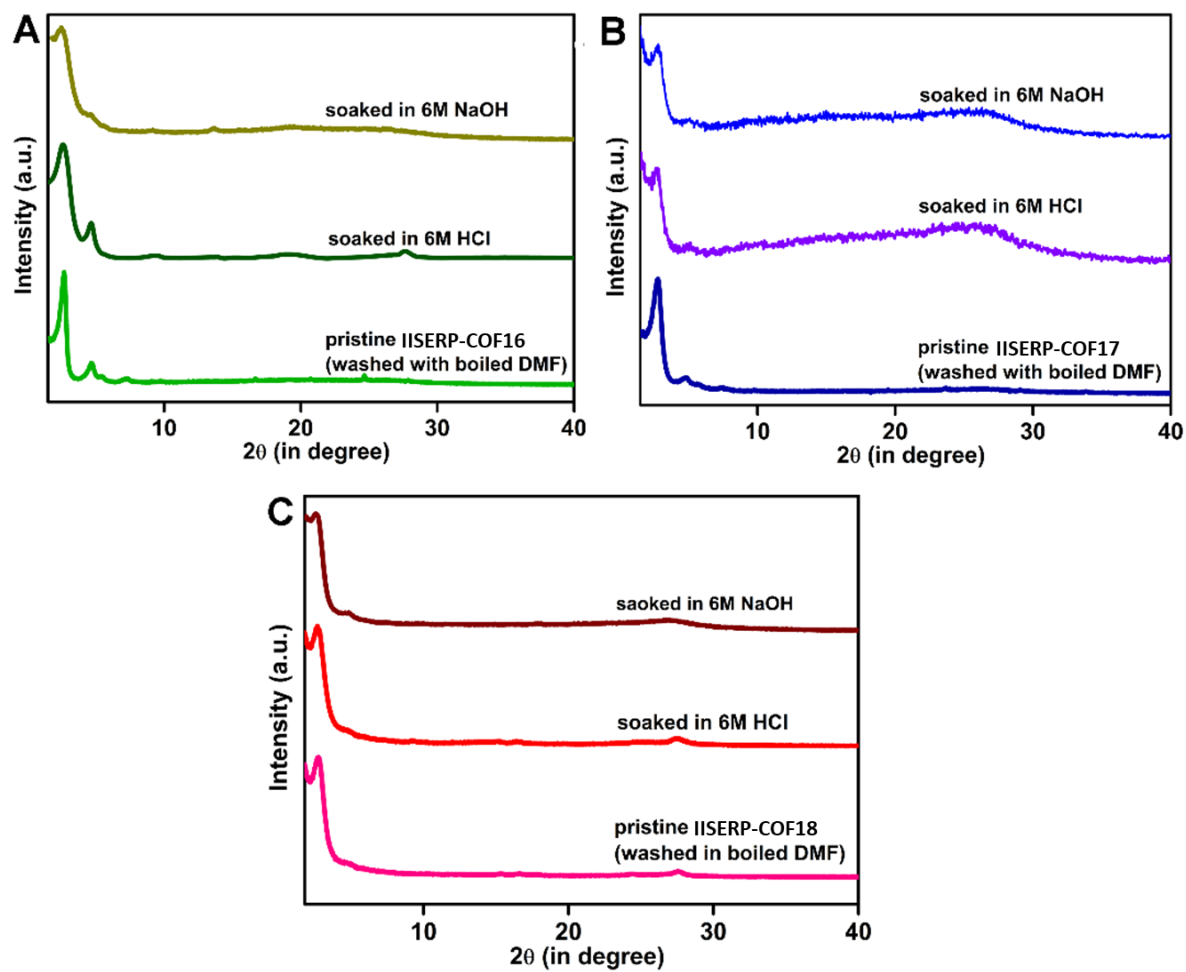


Figure 3.11. (A), (B), (C) PXRD patterns of IISERP-COF16, IISERP-COF17 and IISERP-COF18 recorded after boiled in DMF, soaked in acid and soaked in base.

3.2.2. Electronic energy levels of the COFs:

With the increase of nitrogen content in the COF backbone, the color of the isostructural COFs changes from golden yellow to brown (Figure 3.12.A and 3.12.B). Concomitantly, the Ultra Violet (UV)-visible absorption maxima shifts from lower wavelength to higher wavelength as we go from IISERP-COF16 to IISERP-COF17 (Figure 3.12.C). Each of the UV band has a long tail in the higher wavelength region, which usually contributes majorly to the color of the COFs. To gain more evidence about color change with the introduction of the nitrogenous aromatic ring, we estimated the bandgaps using Tauc plots (Figure 3.12.D).^{18,66} A continuous decrease of the bandgap from 2.75 to 2.51 to 2.20 eV has been observed with the increase of color intensity of the COFs.

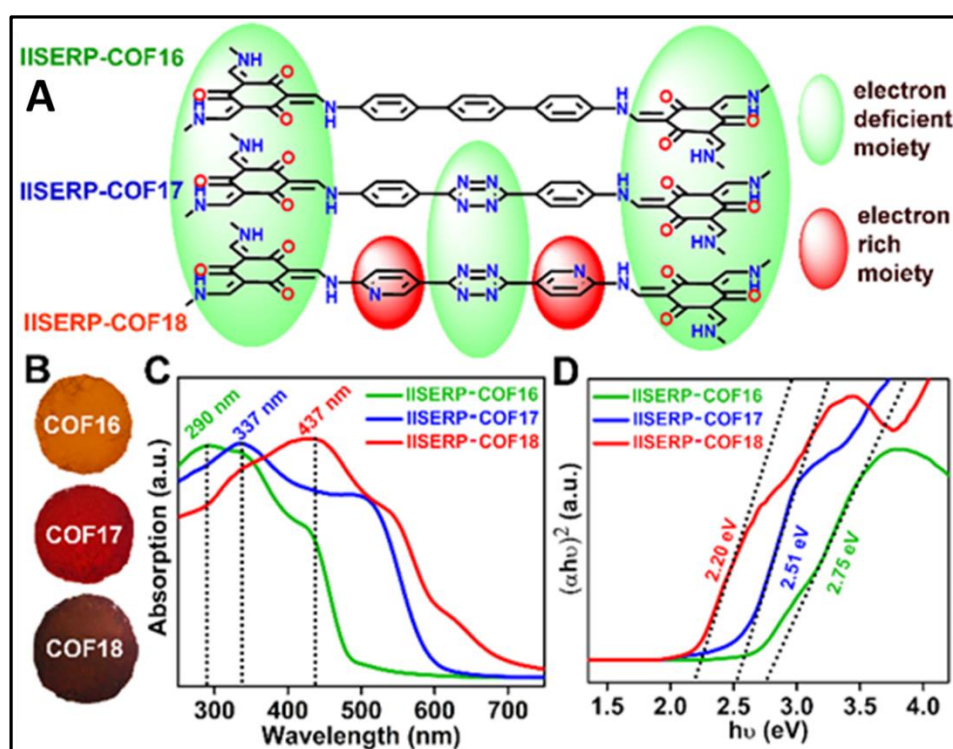


Figure 3.12. (A) Building blocks of polymeric COFs showing the presence of electron-rich and electron-deficient centers. (B) A photograph showing the color of the COFs under visible light. (C) UV-visible spectra of COFs showing the absorption maxima. (D) Bandgaps of the COFs evaluated from Tauc plot using UV-visible absorption spectra.

To add further, the band-structure/energy-levels were calculated from electrochemical methods, namely the Cyclic Voltammetry (CV) (Figure 3.13). To avoid any interference, the CV measurements were performed in a non-aqueous electrolyte medium (t-butyl-ammonium-hexafluorophosphate dissolved in acetonitrile) using a non-aqueous Ag/Ag⁺ reference and platinum flag counter electrodes (Figure 3.13.A). Slow scan rate (50 mV/s) in a potential window of -1.8 to +2.2 V was employed to scrutinize the electrochemical oxidation-reduction of the COFs. The highest oxidation potential provides the energy required to take out one electron from HOMO, whereas the lowest reduction potential corresponds to the energy needed to provide one electron to the LUMO.^{67,68} These frontier orbitals precisely define the HOMO-LUMO energy levels of the COFs with respect to NHE (Normal Hydrogen Electrode). And it is calculated by converting the potential obtained with respect to Ag-AgCl (Figure 3.13.B-3.13.D, Table 3.5). Thus, the electrochemically determined bandgaps follow the same trend as the optical bandgap with some differences in their absolute values. Interestingly, the

oxidation potentials of these COFs were nearly the same, but the reduction potentials continuously go to a more negative value with the introduction of the s-tetrazine and the bispyridine-s-tetrazine ring. Thus without many alternation of the condensed HOMO levels, the LUMO energy levels get more stabilized to lower energy levels with the inclusion of nitrogen atoms in the COF framework. Lowering of the LUMO energy levels brings out the possibility of facile reduction of the relatively electron-deficient tetrazine and pyridine moieties. In IISERP-COF18, the conjugation of the lone-pair on the pyridine ring with the tetrazine units assists the smooth electron transfer in between electron-deficient tetrazine and carbonyl units of the phloroglucinol units (Figure 3.12.A). This makes IISERP-COF18 *assume* the lowest LUMO levels among the three COFs. Importantly, the position of the pyridine nitrogen (β -position w.r.t the hydroxyl moiety) is crucial in gaining maximum conjugation advantage. The relative lowering of the LUMO energy as we move from IISERP-COF16 to IISERP-COF18 is quantitatively expressed by how far the reduction potential shifts in the negative axis of the CV (Figure 3.13.A). Thus, the IISERP-COF18, having the electron-accepting LUMO levels sitting at substantially lowered energy carries a true potential to be the anode for any ion battery.^{69,70}

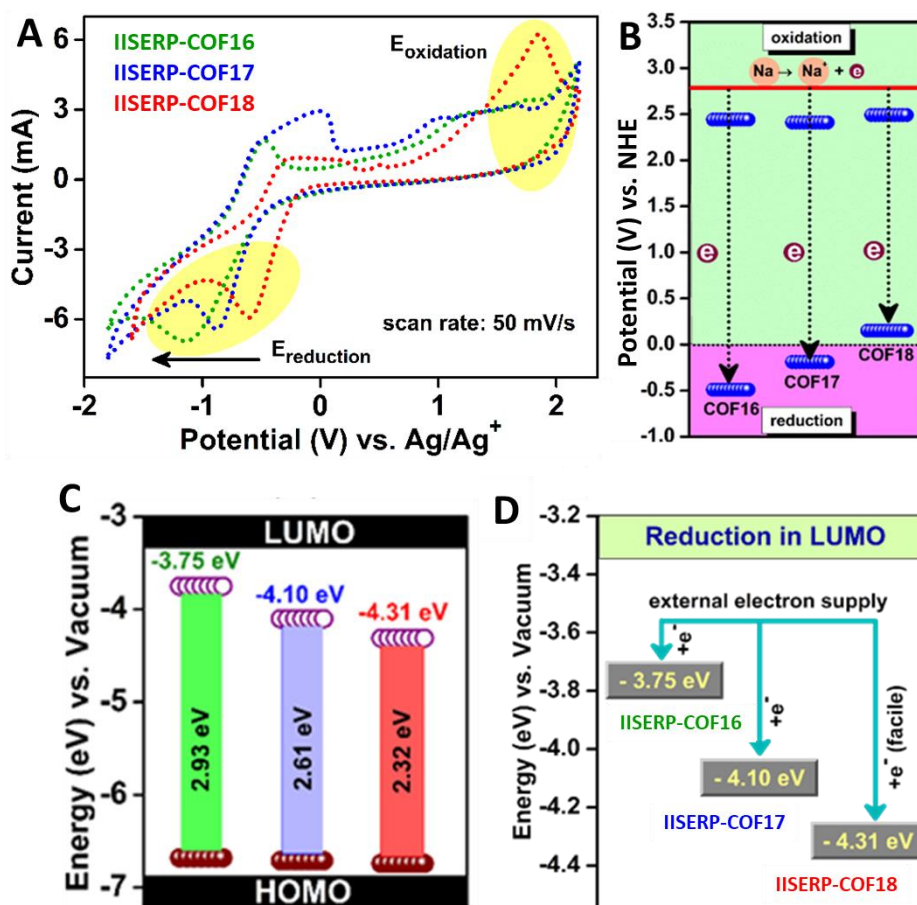


Figure 3.13. (A) Cyclic voltammograms of COFs @50 mV/s using 0.5 (M) solution of t BuNH₄PF₆/ACN (non-aqueous electrolyte system) showing the oxidation and reduction potentials. (B) Position of oxidation and reduction potential (vs. NHE) of COFs with respect to Na/Na⁺. (C) HOMO-LUMO energy levels of the COFs and their respective bandgaps evaluated from the CV measurements. (D) A graphical representation of LUMO energy levels shows the energetically favorable electrochemical reduction.

Note: Na can be easily oxidized to Na⁺ and during this oxidation process reduction of the COFs happens. The reduction affinity of COFs increases with the increase of the reduction potential of the COFs. IISERP-COF18 possess highest reduction potential among other three COFs.

. Table 3.5. Bandgap calculations using electrochemical data.

COFs	E _{Ox} vs SCE	E _{Ox} vs. NHE	E _{HOMO} (eV)	E _{Red} vs. SCE	E _{Red} vs. NHE	E _{LUMO} (eV)	E _g from CV (eV)	Optical E _g from DRS
IISERP-COF16	1.75 V	2.44 V	-6.66 eV	-1.18 V	-0.49 V	-3.75 eV	2.93 eV	2.75
IISERP-COF17	1.72 V	2.41 V	-6.63 eV	-0.889 V	-0.19 V	-4.10 eV	2.51 eV	2.51
IISERP-COF18	1.80 V	2.49 V	-6.68 eV	-0.554 V	0.150 V	-4.31 eV	2.32 eV	2.20

$E_{HOMO} = - [E_{Ox} - E_{(Fc/Fc^+)} + 4.8] \text{ eV}$
 $E_{LUMO} = - [E_{Red} - E_{(Fc/Fc^+)} + 4.8] \text{ eV}$

$E_{Ag/Ag^+ (non-aqueous)} \text{ vs. NHE: } 0.696 \text{ V and } E_{(Fc/Fc^+)} : 0.58 \text{ V}$

Where, NHE: Normal Hydrogen Electrode
SCE: Saturated Calomel Electrode
Fc/Fc⁺ : Ferrocene/Ferrocenium ion couple

3.2.3. General principle of a SIB half-cell:

In a typical SIB half-cell, the Na-metal plate is employed as a Na⁺ ion source, which gives an OCV for Na/Na⁺ of 2.75 V (Figure 3.14). When a negative potential applied to the anode it lowers the overall potential of the cell from the OCV. This potential difference favors Na → Na⁺ oxidation. Thus generated Na⁺ ions from the electrolyte combine with the electrons at the anode surface. However, the success lies in making this operation occur at a lower potential and in making the Na⁺ diffuse rapidly towards and into the anode. This can be achieved by making the anodic surface accumulate electrons rapidly and such negatively biased anode becomes a swift attractor of the incoming Na⁺ ions. This where a redox-functionalized COF could bring an advantage.

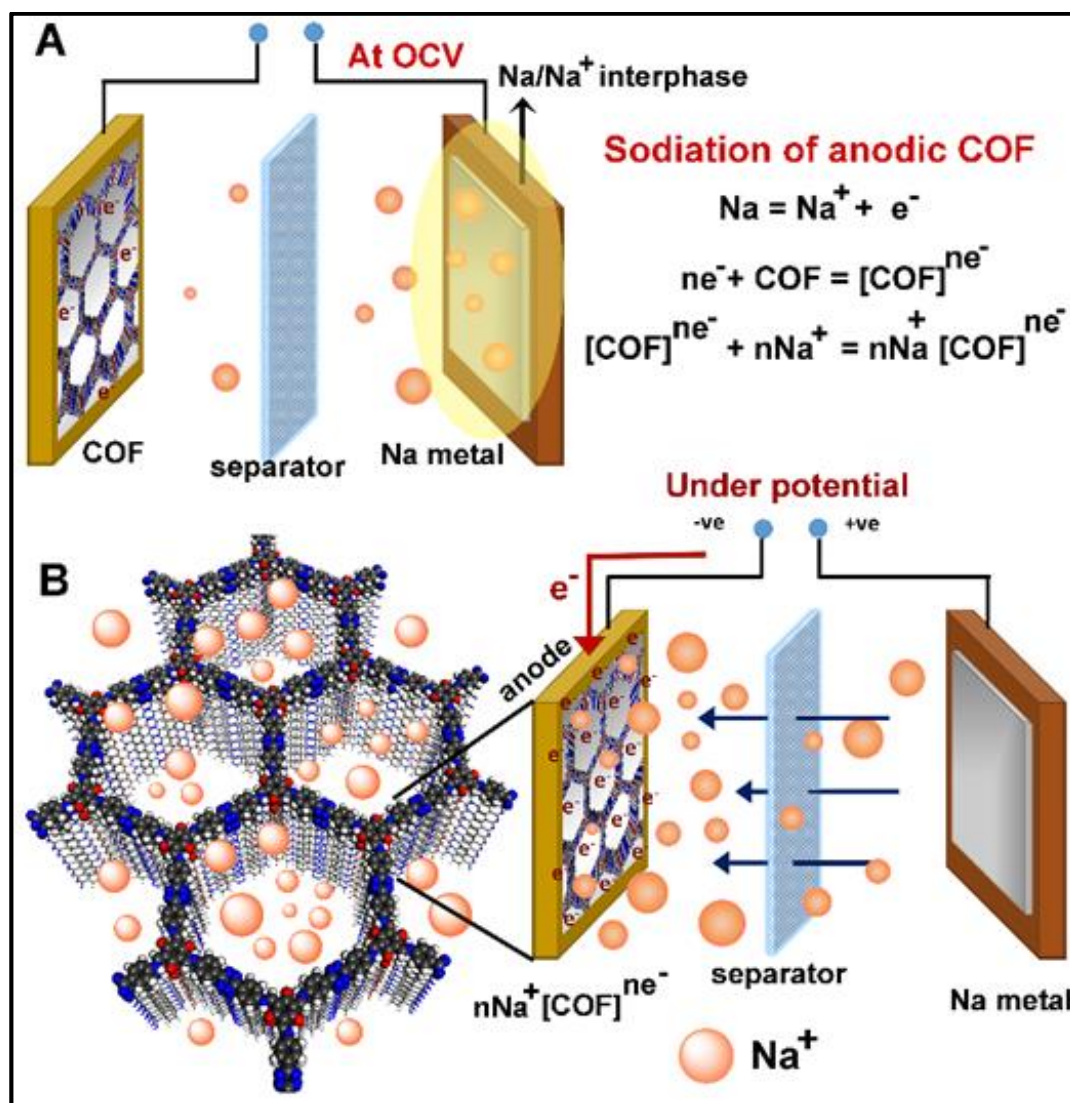


Figure 3.14. (A) A pictorial representation shows discharging or sodiation mechanism of a COF derived half-cell (SIB). The Na⁺ ions reside near the Sodium metal interphase at OCV. (B) Under applied potential, the Na⁺ ions move towards the negatively charged COF. Flow of the Na⁺ ions towards the anode induced by accumulation of externally-supplied electrons on the anode.

3.2.4. Anodic reduction and concurrent sodiation process of a SIB half-cell:

The abundance of the redox-active functional groups (keto groups, pyridine nitrogen) all along with the walls of the porous nano-channel and presence of highly electron-deficient s-tetrazine ring shows ample potential to use these COFs as an anode in half cell SIB. A slurry made by mixing 65% COFs: 25% conducting carbon: 10% polyvinylidene difluoride in N-methylpyrrolidone (NMP) solution was coated on carbon-coated aluminum foil and cut in the size of 2032 coin cell to use as the anode. The half-cell devices were fabricated using Na metal as the reference and 1 (M) NaPF₆ in 1:1 EC-DMC (2% FEC) soaked Whatman paper as the separator. The OCVs of the coin-cells came near about 2.65 V due to Na/Na⁺ interface formation on Na metal electrode.³⁹ To understand the sodiation and de-sodiation mechanisms, the CVs of the coin-cells were recorded within the potential window from 0.05 to 3 V @0.5mV/s sweep rate (Figure 3.15.A). The half-cell CVs of three different COF-derived electrodes have been compared in Figure 3.15.A. For each case, the CV of the sample subjected to 10 redox

cycles is plotted. This is to avoid the interference from the SEI formation which happens during initial cycles.⁷¹ This comparison reveals the insertion of Sodium during discharging occurring through a two-step process for IISERP-COF17 and IISERP-COF18 at 0.1 V (R_1/O_1) and 0.5 V (R_2/O_2), respectively. But IISERP-COF16 displays very little current output even at a very low potential of 0.1 V (R_1/O_1) (Figure 3.15.A). The only molecular-level functional dissimilarity of IISERP-COF16 with respect to IISERP-COF17 and IISERP-COF18 is the absence of π -stacked s-tetrazine ring throughout the nano-channel. This leaves a marked impact on the sodiation process, making the IISERP-COF16 the slowest with the most sluggish insertion of Na^+ into the nano-pores.²¹ The participation of the tetrazine rings in the redox-assisted sodiation process is evident from the CV peak at 0.5 V (R_2/O_2). During the discharge process, the anode becomes negatively charged with the applied potential; the incoming electrons are favourably accommodated by the electron-deficient s-tetrazine units of the IISERP-COF17 and IISERP-COF18. The electronic reduction of the IISERP-COF17 and IISERP-COF18 goes via a two closely spaced electron transfer steps. Thus, finally, each s-tetrazine unit accommodates $2e^-$ (Figure 3.15.B).⁷² Then two Na^+ moves from electrolyte towards the negatively charged tetrazine segment to balance the charge on the COF surface/pores.

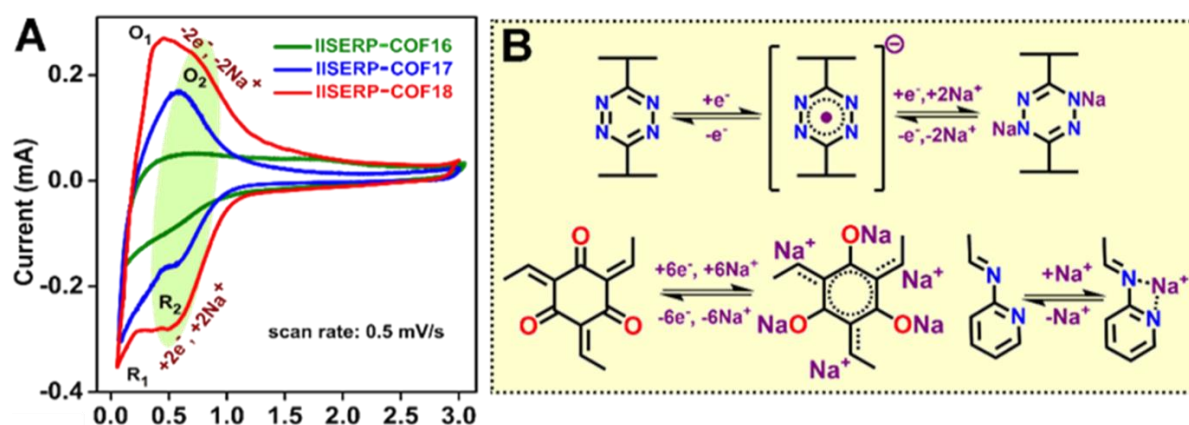


Figure 3.15. (A) CV curves from samples of IISERP-COF16, IISERP-COF17 and IISERP-COF18 subjected 10 redox cycles at 0.5 mV/s in a half-cell configuration. The comparison shows the redox-active sodiation-desodiation process (Note: The initial cycles were not considered to avoid interference from the SEI formation). (B) Mechanistic pathway of electrochemical reduction of tetrazine and phloroglucinol units followed by sodiation under a withdrawing potential. Pyridine- β -ketoenamine core provides the chelation site for Sodium.

We believe, the ease of reduction of the anodic COFs, hence the current output, depends on the stabilization of the LUMO energy level. In IISERP-COF18, since the tetrazine units are conjugated to a pyridine ring, it further lowers the electron-deficient LUMO level (Figure 3.13.D), making the electrons accumulate with extra ease. The high surface area of COF has a role in uniformly dispersing these accumulating electrons on the COF-coated anodic surface. The highest sp. capacity near about 410 mAh/g @100 mA/g was achieved by IISERP-COF18 among these three COFs. While IISERP-COF17 and IISERP-COF16 show 195 mAh/g and 90 mAh/g, respectively (Figure 3.16).

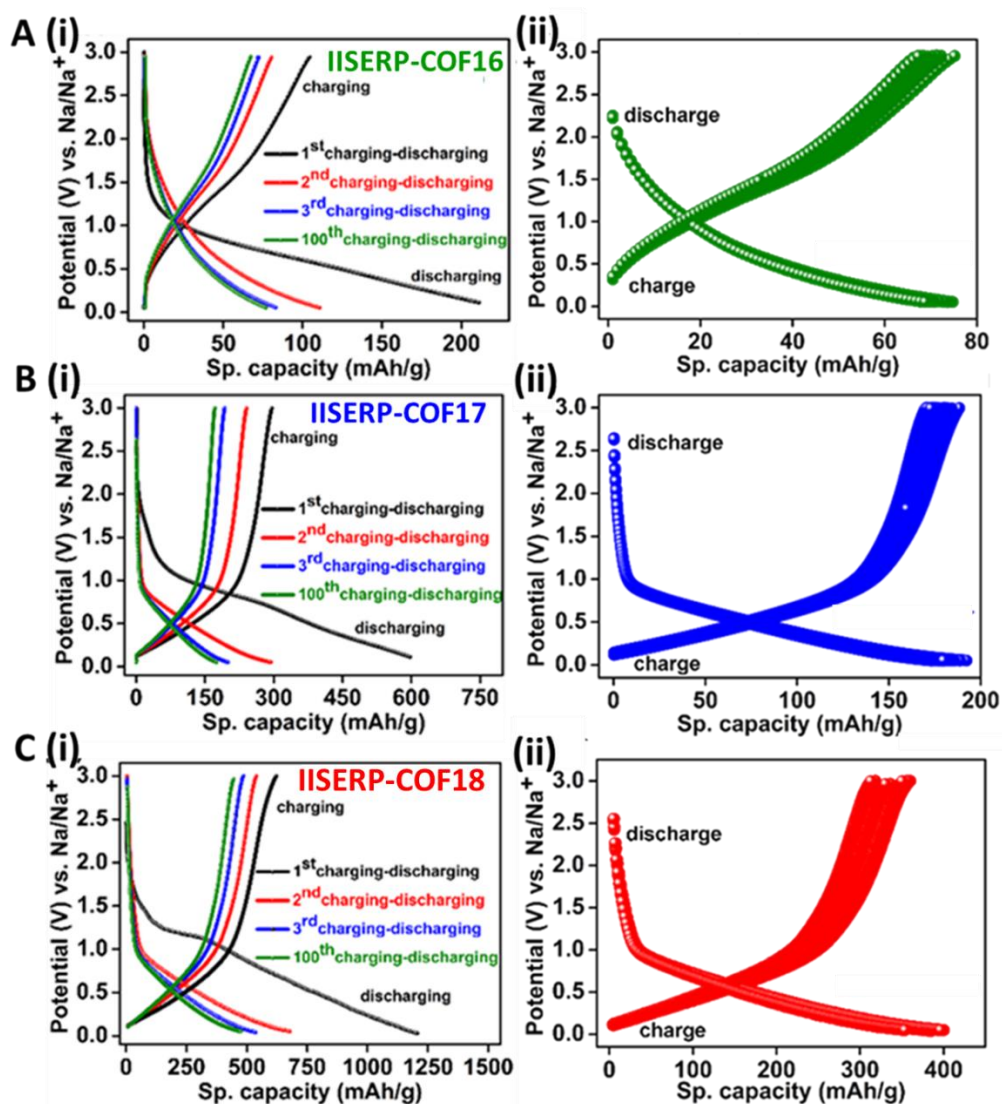


Figure 3.16 A(i), B(i) and C(i) Galvanostatic charge-discharge measurements for 1st, 2nd, 3rd and 100th cycles at the applied current density of 100 mA/g showing the sodiation-desodiation of the COFs. A(ii), B(ii) and C(ii) Charge-discharge profiles of COFs for 250 cycles @100 mA/g current density (excluding the initial SEI formations); capacity retention at high currents.

Moreover, potentiostatic charge-discharge profiles of the COFs also corroborate with the characteristic voltage plateau from 0.8 to 0.05 V observed in CVs. IISERP-COF17 and IISERP-COF18 possess a prominent reversible redox activity with comparable voltage plateau at the identical potential region, which is unlike IISERP-COF16. A perfect match of the reduction peak in CV with the sodiation capacity of the COFs helped to estimate the number of Sodium ion inserted during the sodiation process (Figure 3.17, Table 3.6). And the results come out with almost five-fold enhancement of the Sodium acceptance in IISERP-COF18 compared to IISERP-COF16 and two-fold compared to IISERP-COF17.

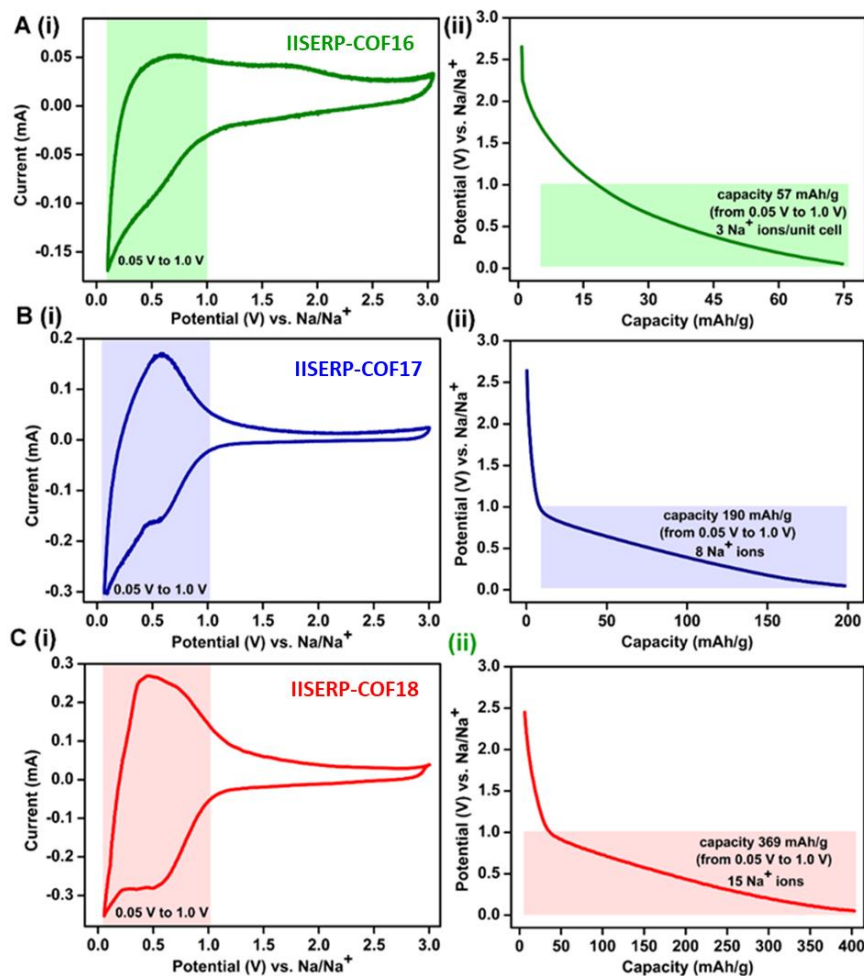


Figure 3.17. A(i), B(i) and C(i) Shown are the CVs of the three COFs subjected to 10 CV cycles at 0.5 mV/s. The highlighted region shows potential window responsible for the sodiation of the COFs. A (ii), B (ii) and C (ii) The potential vs. capacity plot of COFs at 100 mA/g current density provides the total discharging capacity and no of Sodium inserts into the framework.

Calculation: 1 mAh = 3.6 C = 2.2×10^{19} number of electron or Na⁺.

Here, for the COF based coin-cells if we observed a specific capacity of 'A' mAh/g in the potential region of 0.05 – 1 V, this would yield the number of Na⁺ ion = $A \times 2.2 \times 10^{19}$.

Thus, the specific capacity of 'A' mAh/g is realized from $A \times 2.2 \times 10^{19}$ no of Na⁺ (assuming they are the sole charge carriers).

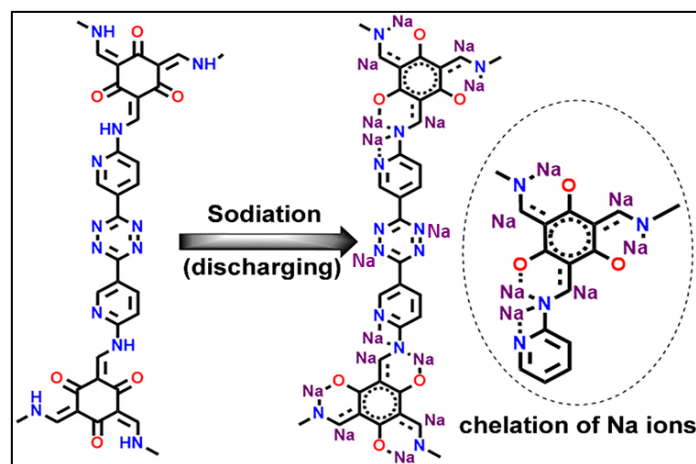
If the calculated molecular weight of the COFs is 'B' g/mol. The weight for unit cell of the COF is B / (6.023×10^{23}) g.

Considering that for 1g of the COF, the number of Na⁺ ion calculated is $A \times 2.2 \times 10^{19}$ => number of Na⁺ per unit cell = $(A \times 2.2 \times 10^{19} \times B) / (6.023 \times 10^{23})$.

Table 3.6. Calculated number of Na⁺ inserted into the framework.

COFs	Molecular weight	No of Na ⁺ inserted
IISERP-COF16	1081 g/mol	3
IISERP-COF17	1086 g/mol	8
IISERP-COF18	1093 g/mol	15

This augmentation is due to the presence of bispyridine-*s*-tetrazine backbone in the nano-channel of IISERP-COF18. The redox activity at the oxygen-rich phloroglucinol ring contributes too. In IISERP-COF18, there is the possibility of better chelation of Sodium ions in between the phloroglucinol oxygen, pyridine-nitrogen and β -keto enamine nitrogen (Scheme 3.2). This sets-up a chemically-compelled adsorptive sites in IISERP-COF18, in contrast, in IISERP-COF16 most of the Na^+ insertion is physisorptive. Also, the phloroglucinol ring could have some redox activity towards Na^+ (peak at 1.7 V) (Figure 3.17.A(i)).²¹



Scheme 3.2 A probable mechanism showing the Na^+ insertion into the functional sites of IISERP-COF18 under the applied potential. The presence of pyridine nitrogen next to the β -ketoenamine unit provides the suitable chelation sites for inserted Na^+ .

All three COFs owing to their good surface areas can also show capacitive storage, but the diffusion-controlled storage is influenced by mass transfer of Sodium. If the Sodiation happens via the redox functional groups' participation, the surface active capacitive behaviour predominates over diffusive mechanism. To compartmentalize these contributions, CVs were measured in the potential window of 0.05 - 3.0 V at different scan rates (0.1- 2.5 mV/S), and fitted to the Power law $i = av^b$ (where, v represents the scan rate and a and b are alterable parameters) to verify the capacitive behaviour. In general, when $b = 0.5$, it means that the electrode reaction is diffusion controlled and satisfies the Cottrell's equation: $i = av^{0.5}$. While the chemical interactions between the functional groups and the Na^+ occur as a surface process giving rise to values for ' b ' being close to 1. The parameter ' b ' (slope) was determined from a plot of $\log(i)$ versus $\log(v)$. (Figure 3.18-3.19).^{12,18,19} From the slope value we can interpret that most of the Na^+ insertion into the IISERP-COF16 happens via a diffusion-controlled mechanism, whereas for IISERP-COF17 and IISERP-COF18 the surface controlled capacitive Na^+ storage predominates. So, the introduction of electron deficient tetrazine ring definitely increases the surface redox activity of the COFs. IISERP-COF18 obeys the Cottrell's equation with a ' b ' value of 0.95 at 0.5V (R_2/O_2) and 0.75 at 0.1 V (R_1/O_1). This suggests that the reduction of the tetrazine ring, sodiation of the pyridine nitrogen, and phloroglucinol ring all happen via a surface-assisted pathway. Nevertheless, at a very low potential, some contribution comes from the Sodium insertion into the pores, most likely via a diffusion-controlled pathway.^{73,74}

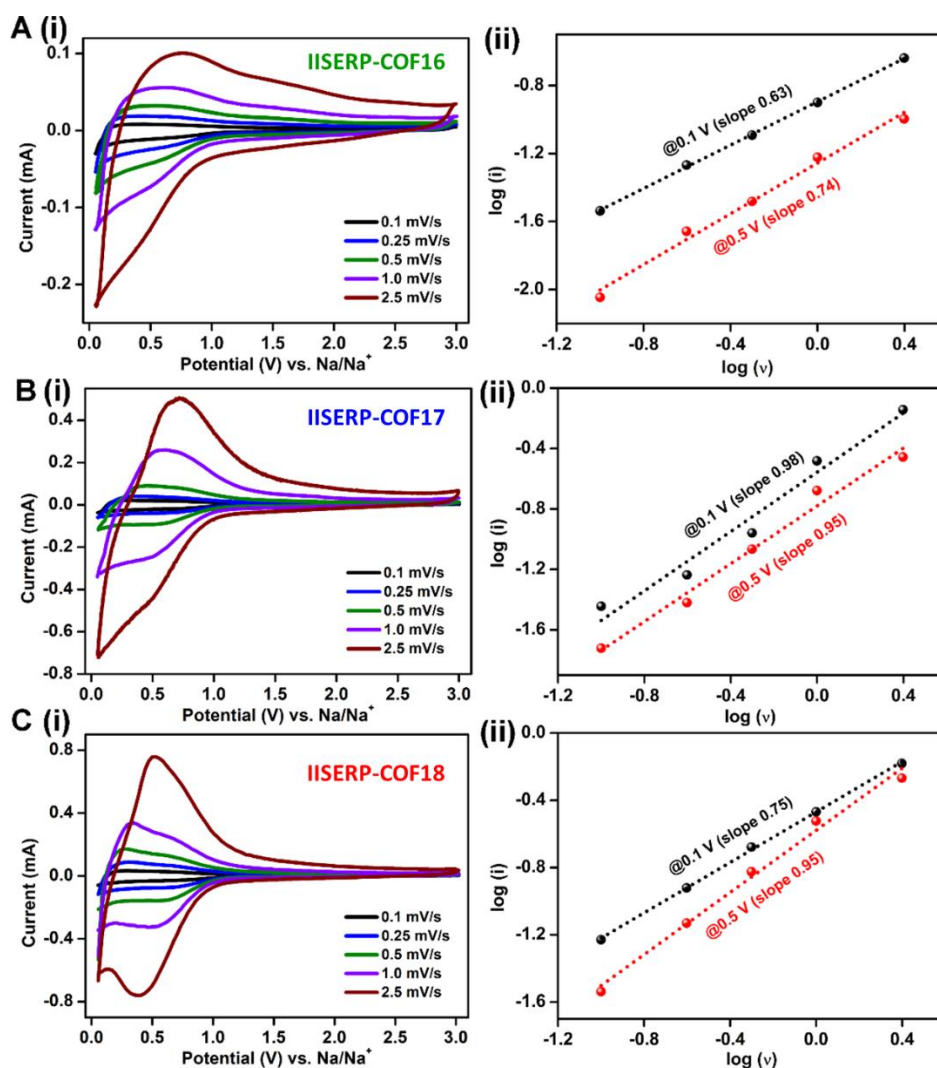


Figure 3.18. A(i), B(i) and C(i) Cyclic voltammogram plots of COFs derived coin-cell (fresh cell) measured at different scan rates. A(ii), B(ii) and C(ii) Log. of peak current intensity (anodic) vs. log. of scan rate at different potentials extracted from the CV plots.

Note: the linear increment of the peak current with the increase of current density.

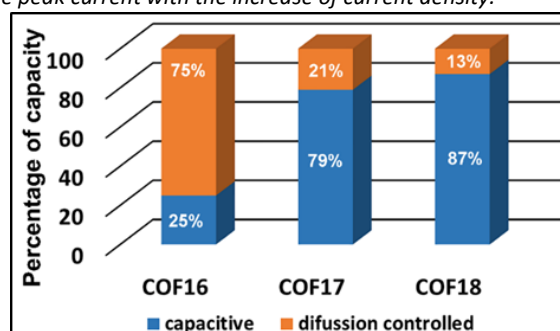


Figure 3.19. A bar plot shows the percentage of sp. capacity of COFs comes in capacitive and in diffusion controlled way.

The above-described rapid diffusion of the Na⁺ ions at the anodes helps achieve an excellent rate performance. Even at a current density of 1 A/g, the COFs (IISERP-COF17 and IISERP-COF18) retains about ~80% of the sp. capacity obtained at 100 mA/g, whereas IISERP-COF16 fails at high current inputs (Figure 3.20). Notably, IISERP-COF18 can deliver 127 mAh/g sp. capacity even at an extreme scan rate of 15 A/g (Figure 3.20 B). It is impressive to see the IISERP-COF18 stability towards high

electron accumulation and rapid redox process at these high current densities.^{21,22,73} The electrochemical cyclic stability of the IISERP-COF18 was confirmed from complete retention of its redox activity even after 250 charge-discharge cycles (@100 mA/g) without any distortion of voltage plateau and 92% retention of its capacity (340 mAh/g) even after 1400 charge-discharge cycles at 1 A/g (Figure 3.20.C). The cell with IISERP-COF18 starts with a good specific capacity, which drops from the 30th to 125th cycle and then builds up to the original value within a few cycles and stays steady. A plausible reason for this could be the good initial uptake of Na⁺ ions by the electrode (after the SEI layer formation), followed by a clogging at the pores, causing the drop. Over cycles, the accumulated Na⁺ ions, under an applied potential, disperse slowly across the electrode improving access to all the sites. This is associated with an improvement in the wetting of the electrode by the electrolyte over time.¹⁹ This is reflected even by the instability of coulombic efficiency up to 150 cycles, which stabilizes gradually to ~ 98% afterward. Such anomalous behaviour appears to be prevailing in other COF systems.²¹ Likewise, IISERP-COF17 also possess excellent stability. Meanwhile, IISERP-COF16 loses most of its sp. capacity even @500 mA/g. That suggests that the presence of the tetrazine backbone is crucial to accommodating huge electron-density in higher current input. Each of the cells has been completely discharged before being subjected to the Galvanostatic charge-discharge cycles at variable current density. This way, the capacity contribution from SEI formation will not interfere in the rate performances (Figure 3.20 C).⁷⁵⁻⁷⁷ The first cycle coulombic efficiency appears only ~50% for these COFs due to stable Solid Electrolyte Interphase (SEI) formation on the electrode surface (Table A.3.3). A lot of Sodium consumption happens irreversibly at the first discharge as the electrolytes decompose on the highly functionalized porous surface of the COFs. After a few cycles, the reversibility is achieved in sodiation-desodiation processes. This stabilizes the sp. capacities with ~98% coulombic efficiency. After a few initial cycles, the steadiness of columbic efficiency indicates the stability of the COF-derived electrodes towards multiple cycles of charge-discharge at high current densities. In comparison with other COF derived anodes for SIB, our IISERP-COF18 stands in the top in terms of very less capacity drop even at 10 and 15 A/g current density) (Figure 3.21).

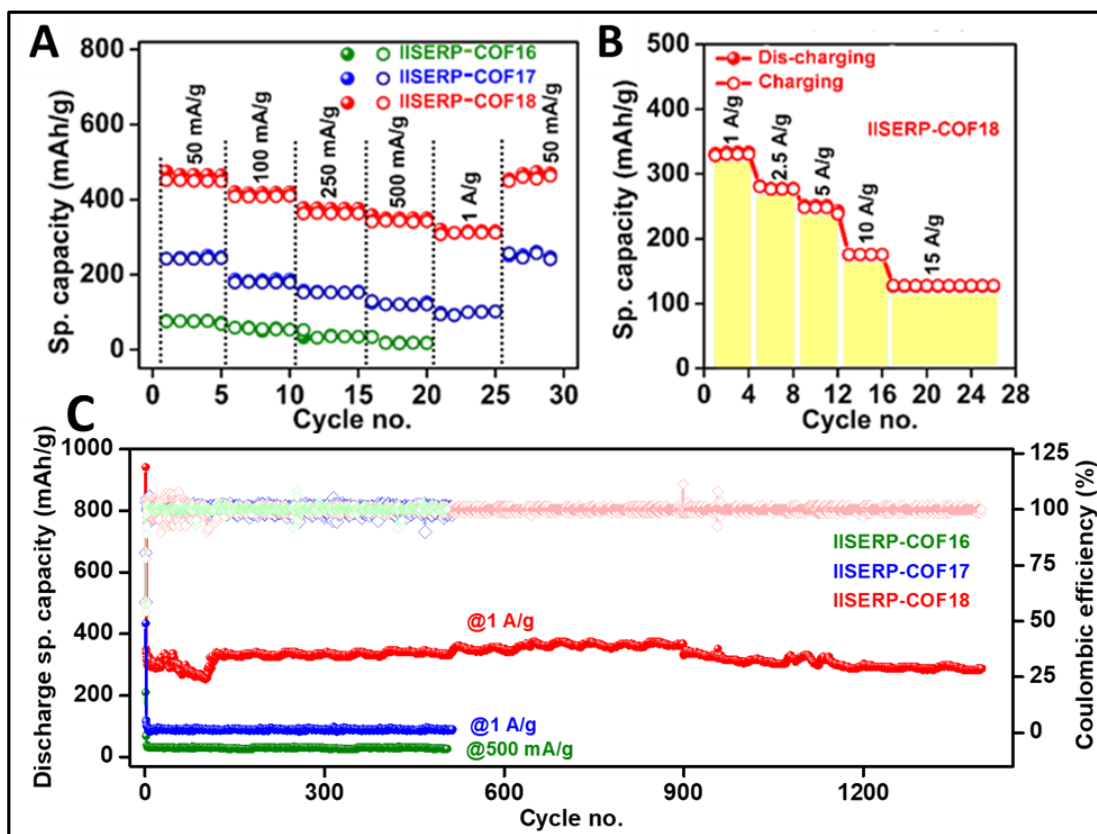


Figure 3.20. (A) Rate performance of the COFs from lower to higher current density excluding the first cycle data points (solid spheres denote discharging or sodiation, hollow spheres denote charging or desodiation) (B) Rate performance of the IISERP-COF18 at high current density (from 1 to 15 A/g). (C) Cycling stability- retention of discharge capacity @1 A/g current density (including the first cycle discharging) and coulombic efficiencies of each of the COFs. Hollow squares denotes the coulombic efficiencies of each of the COF based coin-cells. **Note:** The sp. capacity was calculated considering the mass loading of COF as reference in each of the electrode.

A comparative discussion: The very first report of COF derived anode for SIB (TFPB-TAPT COF)^{A.3.1} shows the probability of Sodium insertion in-between the interlayer space of π -stacked COF. In this COF, mainly mild redox-active Schiff base interacts with Na^+ (Figure 3.21 and Table 3.7). Following this, an acid delaminated COF (DAAQ-COF4)^{A.3.2} with exposed β -ketoenamine units undergoes sodiation under potential via α -radical formation. Easy accessibility of redox-active groups in delaminated COF helped to improve the sp. capacity. And a high-performance SIB has been fabricated with a carbonyl rich framework (TQBQ-COF),^{A.3.3} having very close proximity to the functional groups inside the Nano-channel. The rate performance was also improved significantly by the fast movement of Na^+ ions inside the highly functionalized Nano-channel. In another approach, the conductivity of COF improved by pyrolyzing the COF (NPC-2)^{A.3.4} in high temperature, that too, enhanced the rate performance of the COF. Again better diffusion of Na^+ inside thin layer COFs was well investigated in thiophene-rich covalent organic nanosheets (CON-16).^{A.5}

In our designer approach, we have optimized all the necessary factors such as the proximity of the redox-active functional groups, easy accessibility via the porous nanochannelled structure, and appreciable conductivity during Sodium insertion to improve the performance.

Moreover, the essential electronic demand for the sodiation process of the COF has been taken into account by introducing the tetrazine units. And its impact has been vindicated by a range of

experimental and modeling studies. A systematic investigation of this electronically driven enhancement of anodic property is established.

Our bispyridine-tetrazine-*tfp* COF (IISERP-COF18) shows superiority over the so far reported COF materials and organic polymeric materials^{A.3.6-A3.8} in terms of delivering high sp. capacity and ultra-high rate performance (128 mAh/g @15 A/g). Its performance is even comparable with the heteroatom-doped carbonaceous material, which is known to have much higher electronic conductivity.^{A.3.9-A3.12} In comparison, the molecular-level tuning of the COF material through design to develop high-performance anode for SIB is undoubtedly a superior approach over deriving carbonaceous material via pyrolysis of expensive COF/MOF materials.

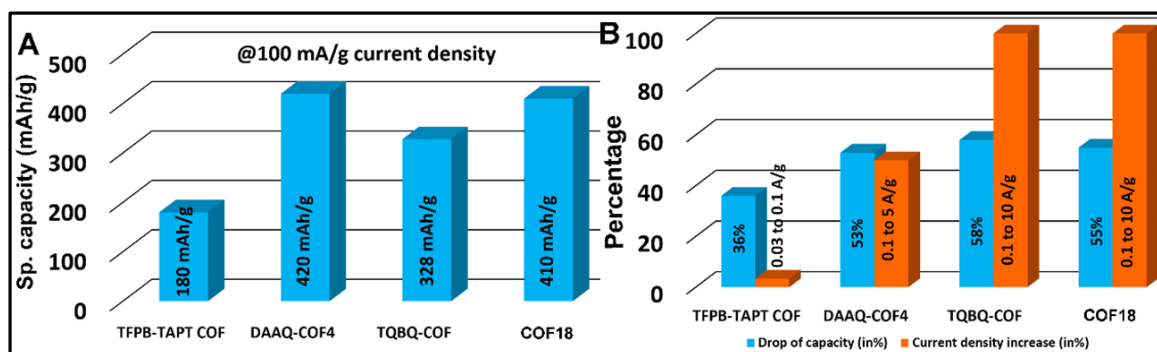


Figure 3.21. (A) Sp. capacity of the COF-derived anode material for Sodium ion battery @100 mA/g. (B) Decrease of sp. capacity of COF-derived anode material with increase of current density.

Table 3.7. Comparison table showing the electrode performance of different materials in SIB.

	Electrode materials for SIB	Sp. capacity (@0.1 A/g)	Sp. capacity (@higher current densities)
COF and COF derived materials	IISERP-COF18 ^{this work}	410 mAh/g	174 mAh/g @10 A/g, 128 mAh/g @15 A/g
	TFPB-TAPT COF ^{A.3.1}	180 mAh/g	145 mAh/g @0.2 mA/g
	DAAQ-COF4 ^{A.3.2}	420 mAh/g	198 mAh/g @5 A/g
	TQBQ-COF ^{A.3.3}	328 mAh/g	135 mAh/g @10 A/g
	NPC-2 ^{A.3.4}	229 mAh/g	127 mAh/g @2.5 A/g
	CON16 ^{A.3.5}	230 mAh/g	124 mAh/g @1 A/g
Polymeric material	ALP (Azo linked Polymer) ^{A.3.6}	170 mAh/g (@84 mA/g)	42 mAh/g @11.5 A/g
	PI-1 (NTCDA-triazine) ^{A.3.7}	331 mAh/g	103 mAh/g @5 A/g
	PI-2 (PMDA-triazine) ^{A.3.7}	210 mAh/g	70 mAh/g @5 A/g
	O-PDA-2 ^{A.3.8}	433 mAh/g	122 mAh/g @3.2 A/g
Carbonaceous material	CNS ^{A.3.9}	305 mAh/g	133 mAh/g @10 A/g, 112 mAh/g @20 A/g
	RNSC-800 ^{A.3.10} (N and S co-doped)	575 mAh/g	236 mAh/g @10 A/g
	NSC-2 ^{A.3.11} (N and S doped)	250 mAh/g	102 mAh/g @10 A/g
	NC/RGO ^{A.3.12}	395 mAh/g	211 mAh/g @10 A/g

3.2.5. Lowered resistance to charge-transfer: Confirmed from AC-impedance and DC-measurements

To evaluate the state of electronic conductivity and resistance during Na⁺ propagation within these three isostructural COFs, potentiostatic impedance was measured. An AC-sweep of 10000 to 0.10 Hz at 10 mV-rms AC amplitude was implemented on the activated coin-cells. Unlike IISERP-COF16 and IISERP-COF17, the presence of relatively electron-rich (pyridine ring) next to electron-deficient (tetrazine ring) centers increases the in-plane electronic conductivity of IISERP-COF18 via a strategic push-pull mechanism (Figure 3.22). This is verified by a three-times lowered semicircle diameters of IISERP-COF18 compared to IISERP-COF16 in the Nyquist plots (resistances of 225 for IISERP-COF18 vs. 750 for IISERP-COF16 vs. 620 Ω for IISERP-COF17 was observed at OCV itself). This is indicative of a lowered charge-transfer resistance for IISERP-COF18. The appearance of a second semi-circle (obtained in lower voltages of 0.5 V and 0.1 V) in the Nyquist plots of IISERP-COF17 and IISERP-COF18 is due to the diffusion resistivity of Na⁺ when it travels through the electrode-electrolyte interphase.⁷⁸ To further understand the advantage of having electron-deficient active sites on the anode, potentiostatic impedance of the COF derived coin-cells were measured under three different applied DC voltages i.e., @Na/Na⁺ = 2.6 V (OCV); @0.5 V (E_{red. of tetrazine}); @0.1 V (E_{insert. of Na+}) (Figure 3.22.A, 3.22.B and 3.22.C). The decrease of the intrinsic resistances of IISERP-COF17 and IISERP-COF18 with a gradual reduction of the applied potential indicates the excellent responsive charge-transfer lowering of the IISERP-COF17 and IISERP-COF18.⁷⁹ As anticipated, IISERP-COF16 became almost silent to the change of the applied potential. The abrupt decrease of resistivity of IISERP-COF18 after applying the sodiation potential, most likely arises from the easy mass transfer at the electron-rich LUMO levels confined on the tetrazine ring. The more amount of sodiation makes the structure electronically conducting with time. Moreover, among these COFs, the Warburg resistance (s) at 0.1V (after insert. of Na⁺) is the lowest for IISERP-COF18 (Figure 3.22.D, Figure 3.23 and Table 3.8). They are suggesting that the diffusion coefficient of Na⁺ (D_{Na+}) increases in conjunction with the electron acceptance capability of the COFs (following D_{Na+} ∝ 1/σ²). The diffusion coefficient of IISERP-COF18 is four fold higher than IISERP-COF17 and sixteen fold higher than IISERP-COF16. So the presence of the bispyridine-tetrazine segment makes the nano-channel of IISERP-COF18 suitable for easy Sodium transport during the electronic reduction of electron-deficient tetrazine ring.

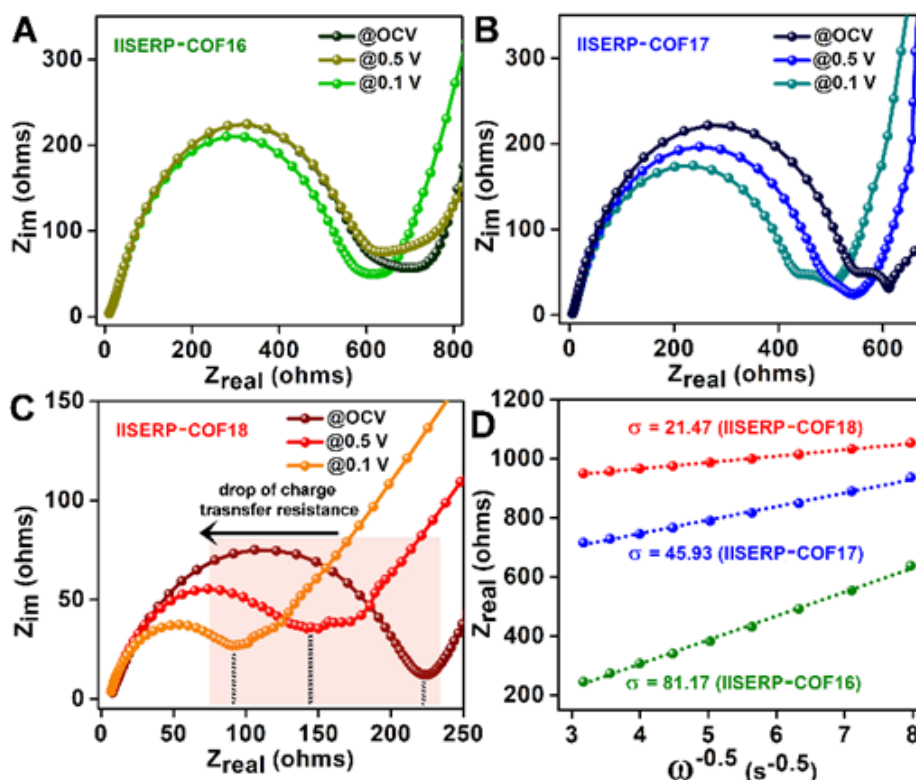


Figure 3.22. (A), (B) and (C) Nyquist plot obtained from potentiostatic impedance measurements of COFs derived half-cells @OCV, @0.5 and @0.1 V. Shaded area shows the decrease of charge transfer resistance with increase of DC bias (D) The plot of Z_{real} vs. the inverse square root of angular frequency (ω) for the COF derived coin-cells (@0.1 V DC voltage). The slopes of the fitted lines represent the Warburg coefficients (σ).

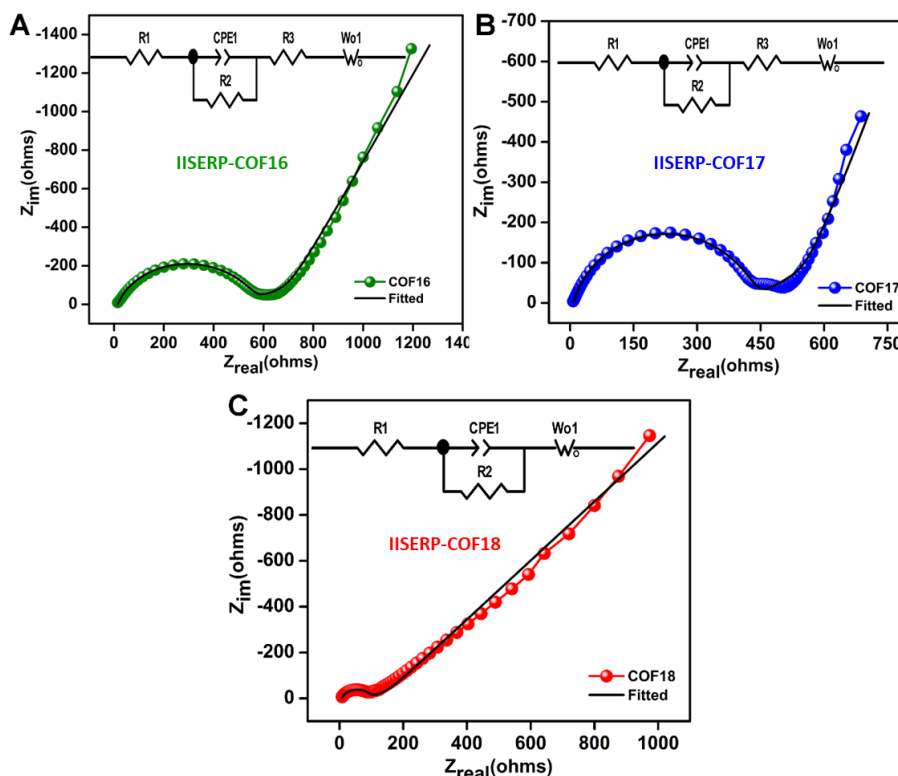


Figure 3.23. Fitted Nyquist plots of AC-impedance measurements under applied DC voltage of 0.1 V shows the decreased charge transfer resistance of the COFs.

Table 3.8. Fitting parameters of Nyquist plots using Z view software (All the parameters have the units in ohms)

IISERP-COF16	R1	CPE1-T	CPE1-P	R2	R3	Wo1-R	Wo1-T	Wo1-P
Z _{real}	1.20E+01	1.61E-05	0.83002	530	2	399	27.15	0.368
Z _{im}	1.11E-04	8.03E-01	90	5	50	3.8	0.2981	
IISERP-COF17	R1	CPE1-T	CPE1-P	R2	R3	Wo1-R	Wo1-T	Wo1-P
Z _{real}	5	3.21E-05	0.85502	420	2	340	98	0.38999
Z _{im}	0.000111	0.80276	90	5	50	3.8	0.2981	
IISERP-COF18	R1	CPE1-T	CPE1-P	R2	Wo1-R	Wo1-T	Wo1-P	
Z _{real}	4.2	1.01E-05	0.88002	80	150	3.2	0.29	
Z _{im}	0.000111	0.80276	90	5	50	3.8	0.2981	

3.2.6. Sodium-COF interactions from atomic modeling

To engage further into the Na-framework interactions, we carried out some modelling studies and simulations using the Materials Studio V.6 (Accelrys). For this, an initial configuration was obtained by dispersing 15 Sodium ions into an anionic framework of the IISERP-COF18 using a Grand canonical Monte Carlo (GCMC) algorithm^{A.3.13-A.3.15} (number of Na⁺ ions/unit cell was derived from experimentally determined values) (Figure 3.24). The resulting structure was treated as an input for a rigorous DFT optimization carried out on a 3 x 3 x 3 cell using the CASTEP routine embedded in the Materials Studio.⁸⁰ All parameters including the unit cell as well as the coordinates were relaxed. The minimization yielded a structure of the COF with Na⁺ in the pores. A 3 x 3 x 3 supercell was constructed from this structure and was subjected to a rigorous dispersion corrected DFT optimization using the CASTEP routine embedded in the Materials Studio.^(A.3.16,A.3.17) A Generalized Gradient Approximation-Perdew--Burke--Ernzerhof (GGA-*PBE*) functional was used for the exchange and correlation energy of electrons.^(A.3.18) SMART finite basis set correction was applied with a plane wave basis set cut-off of 370 eV. Electronic minimizations were done using the Density Mixing Scheme. The valence electrons were treated using the Ultrasoft pseudopotentials. The SCF tolerance was set to 1 x 10⁻⁶ eV/atom. The calculations were repeated two times to eliminate any bias from the initial configuration. Excellent convergence was achieved both the times with total energies having negligible differences (in the third decimal of the kcal/mol units).

Some of the essential findings from this DFT optimized structure of Na @COF: The distances of the Na⁺ ions from the N and O atoms of the framework fall within the range of weak coordinate-covalent bonds. The tetrazine, pyridine and the carbonyl atoms seem to be the closest sites while the Schiff nitrogens interact weakly (Figure 3.24). Also, the Na compared to Li interacts more precisely with the heteroatoms and faintly with the other C-atoms of the framework. In our earlier studies,^{18,19} the Li interacted uniformly with the framework atoms (C, N and O) and also were dispersed all along the walls of the pore. In contrast, here, the Sodium ions are confined more to the heteroatoms (Figure 3.24.C).

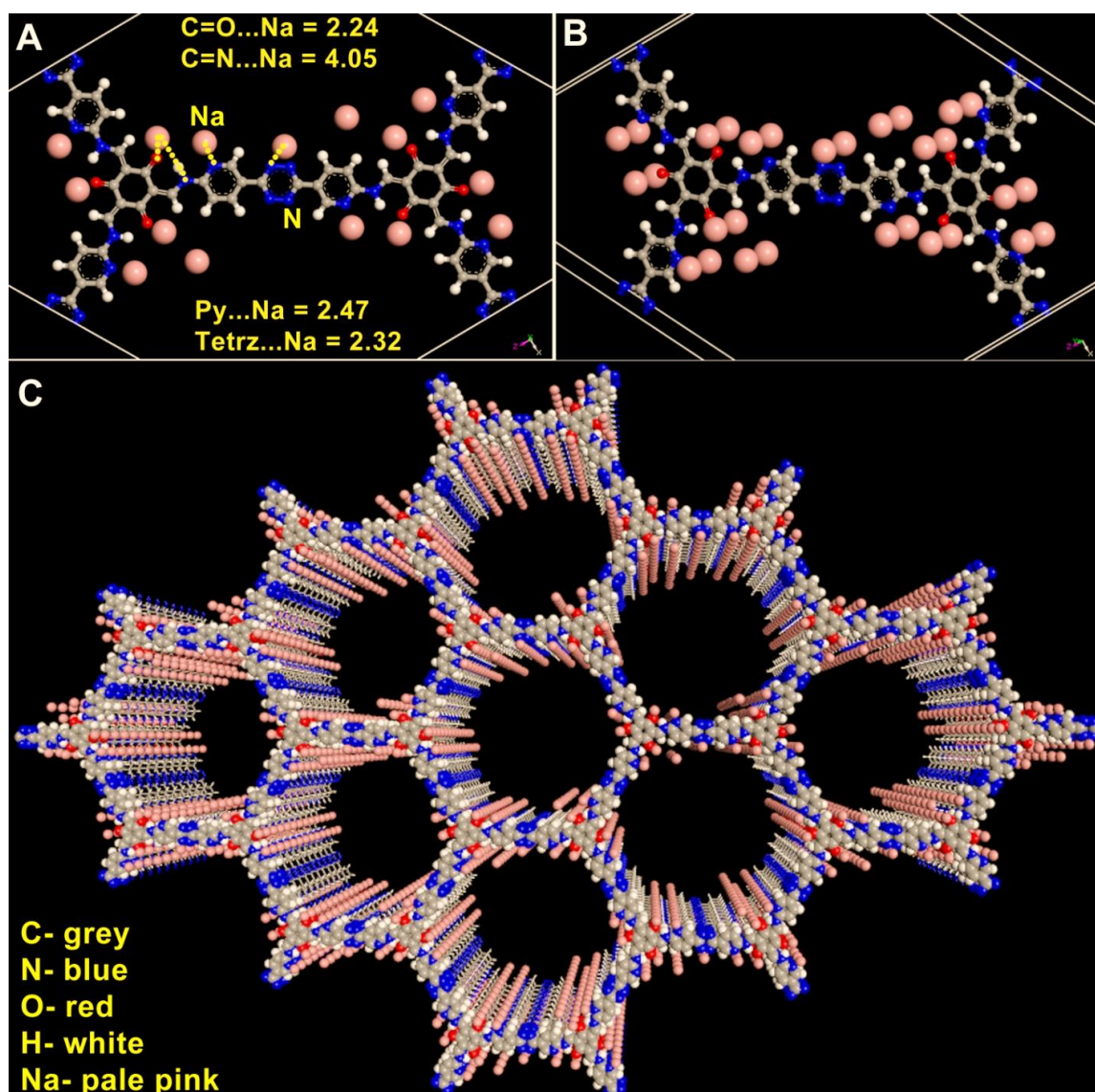


Figure 3.24. (A) DFT modeled Na @IISERP-COF18 structure shows the closest interactions between the anionic COF and the Na⁺ ions. (B) Every active site is sandwiched between two crystallographically equivalent Na⁺ sites. (C) The 3D framework showing the distribution of Na⁺ ions around the heteroatoms lining the framework.

3.3. Conclusion:

COFs knitting periodically positioned electron-rich and electron-deficient modules using conjugation serve as an excellent push-pull electronics platform. In such frameworks, the electronic activity can be tuned both at the electron-rich and -deficient centers. Keeping the electron-rich center fixed, here we have utilized tetrazine/pyridine centers as an electron-deficient node to demonstrate the effect this can bring when used as an anode in a Sodium-ion battery. The use of tetrazine/pyridine units lowers the LUMO energy level compared to a neat phenyl and this makes the former accumulate electrons with ease under an applied potential. Such e-accumulated anti-bonding LUMO levels provide the right driving force for the otherwise sluggish Na⁺ ions to run into the anode from the electrolyte. This reflects in a substantial enhancement of the specific capacity of the SIB. Importantly, thus constructed coin-cells show excellent stability even at current density as high as 15 A/g. The study establishes a clear-cut correlation between molecular-level electronic structure and battery

performance. Notably, the demonstrated approach in this family of COF is transferable to many organic systems.

Acknowledgement:

We thank IISER-Pune for support and the funding by DST-for material for energy storage (DST/TMD/MES/2k17/103) program and the SERB (EMR/2016/003553). SH thanks DST-Inspire for financial support. DK thanks SERB for NPDF (PDF/2018/000626). We thank MHRD-FAST and the IUSSTF program for the support. SBO and RV also thank DST Nanomission for funding support under the Thematic Unit program.

References

- [1] Geng, K.; He, T.; Liu, R.; Tan, K. T.; Li, Z.; Tao, S.; Gong, Y.; Jiang, Q.; Jiang, D., Covalent Organic Frameworks: Design, Synthesis, and Functions. *Chem. Rev.* **2020**. DOI: [10.1021/acs.chemrev.9b00550](https://doi.org/10.1021/acs.chemrev.9b00550).
- [2] Lohse, M. S.; Bein, T., Covalent organic frameworks: Structures, synthesis, and applications. *Adv. Funct. Mater.* **2018**, *28*, 1705553.
- [3] Bisbey, R. P.; Dichtel, W. R., Covalent organic frameworks as a platform for multidimensional polymerization. *ACS Cent. Sci.* **2017**, *3*, 533-543.
- [4] Diercks, C. S.; Yaghi, O. M., The atom, the molecule, and the covalent organic framework. *Science* **2017**, *355*, eaal1585.
- [5] Kandambeth, S.; Dey, K.; Banerjee, R., Covalent Organic Frameworks: Chemistry beyond the Structure. *J. Am. Chem. Soc.* **2019**, *141*, 1807-1822.
- [6] Gao, J.; Jiang, D., Covalent organic frameworks with spatially confined guest molecules in nanochannels and their impacts on crystalline structures. *Chem. Commun.* **2016**, *52*, 1498-1500.
- [7] Yuan, C.; Wu, X.; Gao, R.; Han, X.; Liu, Y.; Long, Y.; Cui, Y., Nanochannels of Covalent Organic Frameworks for Chiral Selective Transmembrane Transport of Amino Acids. *J. Am. Chem. Soc.* **2019**, *141*, 20187-2019.
- [8] Xu, H.; Jiang, D., Covalent organic frameworks: crossing the channel. *Nat. Chem.* **2014**, *6*, 564.
- [9] Song, Y.; Sun, Q.; Aguila, B.; Ma, S., Opportunities of covalent organic frameworks for advanced applications. *Advanced Science* **2019**, *6*, 1801410.
- [10] Xie, Z.; Wang, B.; Yang, Z.; Yang, X.; Yu, X.; Xing, G.; Zhang, Y.; Chen, L., Stable 2D Heteroporous Covalent Organic Frameworks for Efficient Ionic Conduction. *Angew. Chem.* **2019**, *131*, 15889-15893.

- [11] Wang, M.; Guo, H.; Xue, R.; Li, Q.; Liu, H.; Wu, N.; Yao, W.; Yang, W., Covalent organic frameworks: A new class of porous organic frameworks for supercapacitor electrodes. *ChemElectroChem* **2019**, *6*, 2984-2997.
- [12] Haldar, S.; Kushwaha, R.; Maity, R.; Vaidhyanathan, R., Pyridine-Rich Covalent Organic Frameworks as High-Performance Solid-State Supercapacitors. *ACS Materials Letters* **2019**, *1*, 490-497.
- [13] Li, T.; Yan, X.; Liu, Y.; Zhang, W.-D.; Fu, Q.-T.; Zhu, H.; Li, Z.; Gu, Z.-G., A 2D covalent organic framework involving strong intramolecular hydrogen bonds for advanced supercapacitors. *Polym. Chem.* **2020**, *11*, 47-52.
- [14] Khayum M, A.; Vijayakumar, V.; Karak, S.; Kandambeth, S.; Bhadra, M.; Suresh, K.; Acharambath, N.; Kurungot, S.; Banerjee, R., Convergent Covalent Organic Framework Thin Sheets as Flexible Supercapacitor Electrodes. *ACS Appl. Mater. Interfaces* **2018**, *10*, 28139-28146.
- [15] Halder, A.; Ghosh, M.; Khayum M, A.; Bera, S.; Addicoat, M.; Sasmal, H. S.; Karak, S.; Kurungot, S.; Banerjee, R., Interlayer Hydrogen-Bonded Covalent Organic Frameworks as High-Performance Supercapacitors. *J. Am. Chem. Soc.* **2018**, *140*, 10941-10945.
- [16] Wang, M.; Guo, H.; Xue, R.; Li, Q.; Liu, H.; Wu, N.; Yao, W.; Yang, W., Covalent organic frameworks: A new class of porous organic frameworks for supercapacitor electrodes. *ChemElectroChem* **2019**, *6*, 2984-2997.
- [17] Zhou, J.; Wang, B., Emerging crystalline porous materials as a multifunctional platform for electrochemical energy storage. *Chem. Soc. Rev.* **2017**, *46*, 6927-6945.
- [18] Haldar, S.; Roy, K.; Nandi, S.; Chakraborty, D.; Puthusseri, D.; Gawli, Y.; Ogale, S.; Vaidhyanathan, R., High and Reversible Lithium Ion Storage in Self-Exfoliated Triazole-Triformyl Phloroglucinol-Based Covalent Organic Nanosheets. *Adv. Energy Mater.* **2018**, *8*, 1702170.
- [19] Haldar, S.; Roy, K.; Kushwaha, R.; Ogale, S.; Vaidhyanathan, R., Chemical Exfoliation as a Controlled Route to Enhance the Anodic Performance of COF in LIB. *Adv. Energy Mater.* **2019**, *9*, 1902428.
- [20] Zhao, Z.; Chen, W.; Impeng, S.; Li, M.; Wang, R.; Liu, Y.; Zhang, L.; Dong, L.; Unruangsri, J.; Peng, C., Covalent Organic Framework-Based Ultrathin Crystalline Porous Film: Manipulating Uniformity of Fluoride Distribution for Stabilizing Lithium Metal Anode. *J. Mater. Chem. A* **2020**.

- [21] Gu, S.; Wu, S.; Cao, L.; Li, M.; Qin, N.; Zhu, J.; Wang, Z.; Li, Y.; Li, Z.; Chen, J., Tunable redox chemistry and stability of radical intermediates in 2D covalent organic frameworks for high performance Sodium ion batteries. *J. Am. Chem. Soc.* **2019**, *141*, 9623-9628.
- [22] Shi, R.; Liu, L.; Lu, Y.; Wang, C.; Li, Y.; Li, L.; Yan, Z.; Chen, J., Nitrogen-rich covalent organic frameworks with multiple carbonyls for high-performance Sodium batteries. *Nat. Commun.* **2020**, *11*, 1-10.
- [23] Li, B.-Q.; Zhang, S.-Y.; Wang, B.; Xia, Z.-J.; Tang, C.; Zhang, Q., A porphyrin covalent organic framework cathode for flexible Zn–air batteries. *Energy Environ. Sci.* **2018**, *11*, 1723-1729.
- [24] Peng, P.; Shi, L.; Huo, F.; Zhang, S.; Mi, C.; Cheng, Y.; Xiang, Z., In situ charge exfoliated soluble covalent organic framework directly used for Zn–air flow battery. *ACS nano* **2019**, *13*, 878-884.
- [25] Khayum, A.; Ghosh, M.; Vijayakumar, V.; Halder, A.; Nurhuda, M.; Kumar, S.; Addicoat, M.; Kurungot, S.; Banerjee, R., Zinc ion interactions in a two-dimensional covalent organic framework based aqueous zinc ion battery. *Chem. Sci.* **2019**, *10*, 8889-8894.
- [26] Bai, L.; Gao, Q.; Zhao, Y., Two fully conjugated covalent organic frameworks as anode materials for Lithium ion batteries. *J. Mater. Chem. A* **2016**, *4*, 14106-14110..
- [27] Yang, H.; Zhang, S.; Han, L.; Zhang, Z.; Xue, Z.; Gao, J.; Li, Y.; Huang, C.; Yi, Y.; Liu, H., High conductive two-dimensional covalent organic framework for Lithium storage with large capacity. *ACS Appl. Mater. Interfaces* **2016**, *8*, 5366-5375.
- [28] Lei, Z.; Yang, Q.; Xu, Y.; Guo, S.; Sun, W.; Liu, H.; Lv, L.-P.; Zhang, Y.; Wang, Y., Boosting Lithium storage in covalent organic framework via activation of 14-electron redox chemistry. *Nat. Commun.* **2018**, *9*, 576.
- [29] Chen, X.; Li, Y.; Wang, L.; Xu, Y.; Nie, A.; Li, Q.; Wu, F.; Sun, W.; Zhang, X.; Vajtai, R., High-Lithium-Affinity Chemically Exfoliated 2D Covalent Organic Frameworks. *Adv. Mater.* **2019**, *31*, 1901640.
- [30] Wang, S.; Wang, Q.; Shao, P.; Han, Y.; Gao, X.; Ma, L.; Yuan, S.; Ma, X.; Zhou, J.; Feng, X., Exfoliation of covalent organic frameworks into few-layer redox-active nanosheets as cathode materials for Lithium-ion batteries. *J. Am. Chem. Soc.* **2017**, *139*, 4258-4261.
- [31] Lei, Z.; Chen, X.; Sun, W.; Zhang, Y.; Wang, Y., Exfoliated Triazine-Based Covalent Organic Nanosheets with Multielectron Redox for High-Performance Lithium Organic Batteries. *Adv. Energy Mater.* **2019**, *9*, 1801010
- [32] Sawicki, M.; Shaw, L. L., Advances and challenges of Sodium ion batteries as post Lithium ion batteries. *RSC Adv.* **2015**, *5*, 53129-53154.

- [33] Seidl, L.; Bucher, N.; Chu, E.; Hartung, S.; Martens, S.; Schneider, O.; Stimming, U., Intercalation of solvated Na-ions into Graphite. *Energy Environ. Sci.* **2017**, *10*, 1631-1642.
- [34] Li, Y.; Lu, Y.; Adelhelm, P.; Titirici, M.-M.; Hu, Y.-S., Intercalation chemistry of Graphite: alkali metal ions and beyond. *Chem. Soc. Rev.* **2019**, *48*, 4655-4687.
- [35] Eftekhari, A.; Kim, D.-W., Sodium-ion batteries: new opportunities beyond energy storage by Lithium. *J. Power Sources* **2018**, *395*, 336-348
- [36] Lenchuk, O.; Adelhelm, P.; Mollenhauer, D., New insights into the origin of unstable Sodium Graphite intercalation compounds. *Phys. Chem. Chem. Phys.* **2019**, *21*, 19378-19390.
- [37] Wang, Z.; Selbach, S. M.; Grande, T., Van der Waals density functional study of the energetics of alkali metal intercalation in Graphite. *RSC Adv.* **2014**, *4*, 4069-4079.
- [38] Kim, H.; Hong, J.; Yoon, G.; Kim, H.; Park, K.-Y.; Park, M.-S.; Yoon, W.-S.; Kang, K., Sodium intercalation chemistry in Graphite. *Energy Environ. Sci.* **2015**, *8*, 2963-2969.
- [39] Hwang, J.-Y.; Myung, S.-T.; Sun, Y.-K., Sodium-ion batteries: present and future. *Chem. Soc. Rev.* **2017**, *46*, 3529-3614.
- [40] Kim, M.-S.; Lee, W.-J.; Paek, S.-M.; Park, J. K., Covalent Organic Nanosheets as Effective Sodium-Ion Storage Materials. *ACS Appl. Mater. Interfaces* **2018**, *10*, 32102-32111.
- [41] Zhang, H.; Huang, Y.; Ming, H.; Cao, G.; Zhang, W.; Ming, J.; Chen, R., Recent advances in nanostructured carbon for Sodium-ion batteries. *J. Mater. Chem. A* **2020**, *8*, 1604-1630.
- [42] Stadie, N. P.; Billeter, E.; Piveteau, L.; Kravchyk, K. V.; Döbeli, M.; Kovalenko, M. V., Direct synthesis of bulk boron-doped graphitic carbon. *Chem. Mater.* **2017**, *29*, 3211-3218.
- [43] Wang, S.; Xia, L.; Yu, L.; Zhang, L.; Wang, H.; Lou, X. W., Free-standing nitrogen-doped carbon nanofiber films: integrated electrodes for Sodium-ion batteries with ultralong cycle life and superior rate capability. *Adv. Energy Mater.* **2016**, *6*, 1502217.
- [44] Zou, G.; Wang, C.; Hou, H.; Wang, C.; Qiu, X.; Ji, X., Controllable interlayer spacing of sulfur-doped graphitic carbon Nanosheets for fast Sodium-ion batteries. *Small* **2017**, *13*, 1700762.
- [45] Hou, H.; Shao, L.; Zhang, Y.; Zou, G.; Chen, J.; Ji, X., Large-area carbon nanosheets doped with phosphorus: a high-performance anode material for Sodium-ion batteries. *Advanced science* **2017**, *4*, 1600243
- [46] Chen, W.; Wan, M.; Liu, Q.; Xiong, X.; Yu, F.; Huang, Y., Heteroatom-Doped Carbon Materials: Synthesis, Mechanism, and Application for Sodium-Ion Batteries. *Small Methods* **2019**, *3*, 1800323.

- [47] Dan, R.; Chen, W.; Xiao, Z.; Li, P.; Liu, M.; Chen, Z.; Yu, F., N-Doped Biomass Carbon/Reduced Graphene Oxide as a High-Performance Anode for Sodium-Ion Batteries. *Energy & Fuels* **2020**, *34*, 3923-3930.
- [48] Hu, M.; Zhou, H.; Gan, X.; Yang, L.; Huang, Z.-H.; Wang, D.-W.; Kang, F.; Lv, R., Ultrahigh rate Sodium ion storage with nitrogen-doped expanded Graphite oxide in ether-based electrolyte. *J. Mater. Chem. A* **2018**, *6*, 1582-1589.
- [49] Jin, Q.; Wang, K.; Feng, P.; Zhang, Z.; Cheng, S.; Jiang, K., Surface-dominated storage of heteroatoms-doping hard carbon for Sodium-ion batteries. *Energy Storage Materials* **2020**, *27*, 43-50.
- [50] Wahid, M.; Puthusseri, D.; Gawli, Y.; Sharma, N.; Ogale, S., Hard carbons for Sodium-ion battery anodes: synthetic strategies, material properties, and storage mechanisms. *ChemSusChem* **2018**, *11*, 506-526.
- [51] Liu, X.; Jiang, X.; Zeng, Z.; Ai, X.; Yang, H.; Zhong, F.; Xia, Y.; Cao, Y., High capacity and cycle-stable hard carbon anode for nonflammable Sodium-ion batteries. *ACS Appl. Mater. Interfaces* **2018**, *10*, 38141-38150.
- [52] Song, W.; Kan, J.; Wang, H.; Zhao, X.; Zheng, Y.; Zhang, H.; Tao, L.; Huang, M.; Liu, W.; Shi, J., Nitrogen and Sulfur Co-doped Mesoporous Carbon for Sodium Ion Batteries. *ACS Applied Nano Materials* **2019**, *2*, 5643-5654.
- [53] S Karak, S.; Kandambeth, S.; Biswal, B. P.; Sasmal, H. S.; Kumar, S.; Pachfule, P.; Banerjee, R., Constructing Ultraporous Covalent Organic Frameworks in Seconds via an Organic Terracotta Process. *J. Am. Chem. Soc.* **2017**, *139*, 1856-1862.
- [54] Ghosh, S.; Nakada, A.; Springer, M. A.; Kawaguchi, T.; Suzuki, K.; Kaji, H.; Baburin, I.; Kuc, A.; Heine, T.; Abe, R., Identification of Prime Factors for Efficient Photocatalytic Hydrogen Evolution of Covalent Organic Frameworks via Molecular Engineering, *ChemRxiv*, **2019**. DOI: [10.26434/chemrxiv.8957039.v2](https://doi.org/10.26434/chemrxiv.8957039.v2).
- [55] Haldar, S.; Chakraborty, D.; Roy, B.; Banappanavar, G.; Rinku, K.; Mullangi, D.; Hazra, P.; Kabra, D.; Vaidhyanathan, R., Anthracene-Resorcinol Derived Covalent Organic Framework as Flexible White Light Emitter. *J. Am. Chem. Soc.* **2018**, *140*, 13367-13374.
- [56] Chakraborty, D.; Nandi, S.; Mullangi, D.; Haldar, S.; Vinod, C. P.; Vaidhyanathan, R., Cu/Cu₂O Nanoparticles Supported on a Phenol-Pyridine COF as a Heterogeneous Catalyst for the Synthesis of Unsymmetrical Diynes via Glaser-Hay Coupling. *ACS Appl. Mater. Interfaces* **2019**, *11*, 15670-15679.

- [57] Mullangi, D.; Dhavale, V.; Shalini, S.; Nandi, S.; Collins, S.; Woo, T.; Kurungot, S.; Vaidhyanathan, R., Low-Overpotential Electrocatalytic Water Splitting with Noble-Metal-Free Nanoparticles Supported in a sp³ N-Rich Flexible COF. *Adv. Energy Mater.* **2016**, *6*, 1600110.
- [58] Zhao, X.; Pachfule, P.; Li, S.; Langenhahn, T.; Ye, M.; Schlesiger, C.; Praetz, S.; Schmidt, J.; Thomas, A., Macro/Microporous Covalent Organic Frameworks for Efficient Electrocatalysis. *J. Am. Chem. Soc.* **2019**, *141*, 6623-6630.
- [59] Kaleeswaran, D.; Vishnoi, P.; Murugavel, R., [3+ 3] Imine and β -ketoenamine tethered fluorescent covalent-organic frameworks for CO₂ uptake and nitroaromatic sensing. *J. Mater. Chem. C* **2015**, *3*, 7159-7171.
- [60] DeBlase, C. R.; Silberstein, K. E.; Truong, T.-T.; Abruña, H. D.; Dichtel, W. R., β -Ketoenamine-linked covalent organic frameworks capable of pseudocapacitive energy storage. *J. Am. Chem. Soc.* **2013**, *135*, 16821-16824.
- [61] Haase, F.; Gottschling, K.; Stegbauer, L.; Germann, L.; Gutzler, R.; Duppel, V.; Vyas, V.; Kern, K.; Dinnebier, R.; Lotsch, B., Tuning the stacking behaviour of a 2D covalent organic framework through non-covalent interactions. *Materials Chemistry Frontiers* **2017**, *1*, 1354-1361.
- [62] Zhang, L.; Zhou, Y.; Jia, M.; He, Y.; Hu, W.; Liu, Q.; Li, J.; Xu, X.; Wang, C.; Carlsson, A., Covalent Organic Framework for Efficient Two-Photon Absorption. *Matter* **2020**, *2*, 1–15.
- [63] Haase, F.; Troschke, E.; Savasci, G.; Banerjee, T.; Duppel, V.; Dörfler, S.; Grundei, M. M.; Burow, A. M.; Ochsenfeld, C.; Kaskel, S., Topochemical conversion of an imine-into a thiazole-linked covalent organic framework enabling real structure analysis. *Nat. Commun.* **2018**, *9*, 1-10.
- [64] Sotomayor, F. J.; Cychosz, K. A.; Thommes, M., Characterization of micro/mesoporous materials by physisorption: Concepts and case studies. *Acc. Mater. Surf. Res* **2018**, *3*, 34-50.
- [65] Bhat, G. A.; Haldar, S.; Verma, S.; Chakraborty, D.; Vaidhyanathan, R.; Murugavel, R., Facile Exfoliation of Single-Crystalline Copper Alkylphosphates to Single-Layer Nanosheets and Enhanced Supercapacitance. *Angew. Chem. Int. Ed.* **2019**, *58*, 16844-16849.
- [66] Nandi, S.; Singh, S. K.; Mullangi, D.; Illathvalappil, R.; George, L.; Vinod, C. P.; Kurungot, S.; Vaidhyanathan, R., Low Band Gap Benzimidazole COF Supported Ni₃N as Highly Active OER Catalyst. *Adv. Energy Mater.* **2016**, *6*, 1601189.
- [67] Jin, E.; Asada, M.; Xu, Q.; Dalapati, S.; Addicoat, M. A.; Brady, M. A.; Xu, H.; Nakamura, T.; Heine, T.; Chen, Q., Two-dimensional sp² carbon-conjugated covalent organic frameworks. *Science* **2017**, *357*, 673-676

- [68] Sick, T.; Hufnagel, A. G.; Kampmann, J.; Kondofersky, I.; Calik, M.; Rotter, J. M.; Evans, A.; Döblinger, M.; Herbert, S.; Peters, K., Oriented films of conjugated 2D covalent organic frameworks as photocathodes for water splitting. *J. Am. Chem. Soc.* **2017**, *140*, 2085-2092.
- [69] Lüder, J.; Manzhos, S., First-principle insights into molecular design for high-voltage organic electrode materials for Mg based batteries. *Frontiers in Chemistry* **2020**, *8*, 83.
- [70] Wu, S.; Wang, W.; Li, M.; Cao, L.; Lyu, F.; Yang, M.; Wang, Z.; Shi, Y.; Nan, B.; Yu, S., Highly durable organic electrode for Sodium-ion batteries via a stabilized α -C radical intermediate. *Nat. Commun.* **2016**, *7*, 1-11.
- [71] Li, K.; Zhang, J.; Lin, D.; Wang, D.-W.; Li, B.; Lv, W.; Sun, S.; He, Y.-B.; Kang, F.; Yang, Q.-H., Evolution of the electrochemical interface in Sodium ion batteries with ether electrolytes. *Nat. Commun.* **2019**, *10*, 725.
- [72] Min, D. J.; Miomandre, F.; Audebert, P.; Kwon, J. E.; Park, S. Y., s-Tetrazines as a New Electrode-Active Material for Secondary Batteries. *ChemSusChem* **2019**, *12*, 503-510.
- [73] Patra, B. C.; Das, S. K.; Ghosh, A.; Moitra, P.; Addicoat, M.; Mitra, S.; Bhaumik, A.; Bhattacharya, S.; Pradhan, A., Covalent organic framework based microspheres as an anode material for rechargeable Sodium batteries. *J. Mater. Chem. A* **2018**, *6*, 16655-16663.
- [74] Licht, S.; Douglas, A.; Ren, J.; Carter, R.; Lefler, M.; Pint, C. L., Carbon nanotubes produced from ambient carbon dioxide for environmentally sustainable Lithium-ion and Sodium-ion battery anodes. *ACS Cent. Sci.* **2016**, *2*, 162-168.
- [75] Mogensen, R.; Brandell, D.; Younesi, R., Solubility of the solid electrolyte interphase (SEI) in Sodium ion batteries. *ACS Energy Letters* **2016**, *1*, 1173-1178.
- [76] Ihsan-Ul-Haq, M.; Huang, H.; Wu, J.; Cui, J.; Yao, S.; Chong, W. G.; Huang, B.; Kim, J.-K., Thin solid electrolyte interface on chemically bonded Sb₂Te₃/CNT composite anodes for high performance Sodium ion full cells. *Nano Energy* **2020**, *71*, 104613.
- [77] Jang, J.; Kim, Y.; Chae, O. B.; Yoon, T.; Kim, S. M.; Kim, H. s.; Park, H.; Ryu, J. H.; Oh, S. M., A First-Cycle Coulombic Efficiency Higher than 100% Observed for a Li₂MO₃ (M= Mo or Ru) Electrode. *Angew. Chem. Int. Ed.* **2014**, *53*, 10654-10657.
- [78] Wang, L.; Zhao, J.; He, X.; Gao, J.; Li, J.; Wan, C.; Jiang, C., Electrochemical impedance spectroscopy (EIS) study of LiNi_{1/3}Co_{1/3}Mn_{1/3}O₂ for Li-ion batteries. *Int. J. Electrochem. Sci* **2012**, *7*, 345-353.
- [79] Roy, K.; Wahid, M.; Puthusseri, D.; Patrike, A.; Muduli, S.; Vaidhyanathan, R.; Ogale, S., High capacity, power density and cycling stability of silicon Li-ion battery anodes with a few layer black phosphorus additive. *Sustainable energy & fuels* **2019**, *3*, 245-250.

- [80] Ascherl, L.; Sick, T.; Margraf, J. T.; Lapidus, S. H.; Calik, M.; Hettstedt, C.; Karaghiosoff, K.; Döblinger, M.; Clark, T.; Chapman, K. W., Molecular docking sites designed for the generation of highly crystalline covalent organic frameworks. *Nat. Chem.* **2016**, *8*, 310-316.

Chapter 4:

Pyridine-rich Covalent Organic Frameworks as High-performance Solid-State Supercapacitors

4.1. Introduction:

COFs are crystalline polymers with uniform ordered pores.¹⁻³ Their pores can be made to be microporous or mesoporous by choosing the monomers of desired length and geometry. The organic backbone favors the stoichiometric incorporation of chemically active sites into the framework. This makes them an apt candidate for designing high-performance supercapacitors, which require large surface areas and redox active chemical groups.⁴⁻⁸ Bhaumik et al. reported a triazine COF showing good gravimetric capacitance in aqueous electrolyte.⁹ Also, one of the earliest reports includes a β -ketoenamine COF showing pseudo-capacitive behavior.¹⁰ When these different COFs and COF-derived capacitors are compared, it is evident from their cyclic voltammograms (CVs) that the neat COF does not yield a symmetrical rectangular CV expected for an ideal Electrical-Double-Layer-Capacitance (EDLC) behavior and the Galvanostatic Charge-Discharge (GCD) curves are also not symmetrical. This is a critical feature for a practical supercapacitor. Independently, COFs have been pyrolyzed to obtain high surface area microporous carbons, which have shown superior capacitor behavior.^{11,12} Alternatively, COF has been composited with electronically conducting materials such as PDOT, CNT and Graphene to gain improved electronic bustle, to retain the capacitance at high current density.¹³⁻²¹ This has a direct impact on the power density. However, in many of these, the conducting material plays a major role in the enhanced performance.

In all these capacitor materials, the EDLC formation can be enhanced by increased surface area and by introducing Faradaic Hybrid capacitors with this dual advantage of EDLC plus the pseudo-capacitance via chemical interactions.^{4,14} pseudo-capacitance are gaining interest as they can be better-integrated into a hybrid storage system, where they act as powder density provider while the batteries act as the energy density provider. An ideal hybrid capacitor can threaten the existence of conventional batteries. In such cases, which mechanism is dominant would be something to know. Recently a pyridine group containing COF was reported with supercapacitor characteristics.⁵ The logic was that the protonation ability of the pyridine group should make it exhibit capacitance in acidic electrolyte. This COF had a single pyridine group per monomer;⁵ would enriching this number of pyridine group enhance the pseudocapacitance.

Achieving high capacitance at high current densities in a solid-state capacitor remains a challenge.⁷ This is because in the COF-derived solid-state supercapacitors tried so far have the capacitance arbitrated by strong redox centers, after an initial burst, at high current densities their activity fades substantially. From all the above discussions, thus it is clear that to develop a supercapacitor from COF with high areal capacitance, one needs to optimize the surface area and implant mildly interacting redox-active centers. Hence here we have developed three COFs with pyridine lined micropores. The COF has a large number of pyridine densities per pore and we have systematically increased the number of hydroxyl

groups within the COF by using phenol, resorcinol and phloroglucinol derived trialdehydes in the construction of the COF. They all have uniform micropores (5-10 Å) giving rise to large surface areas.

4.2. Results and discussion:

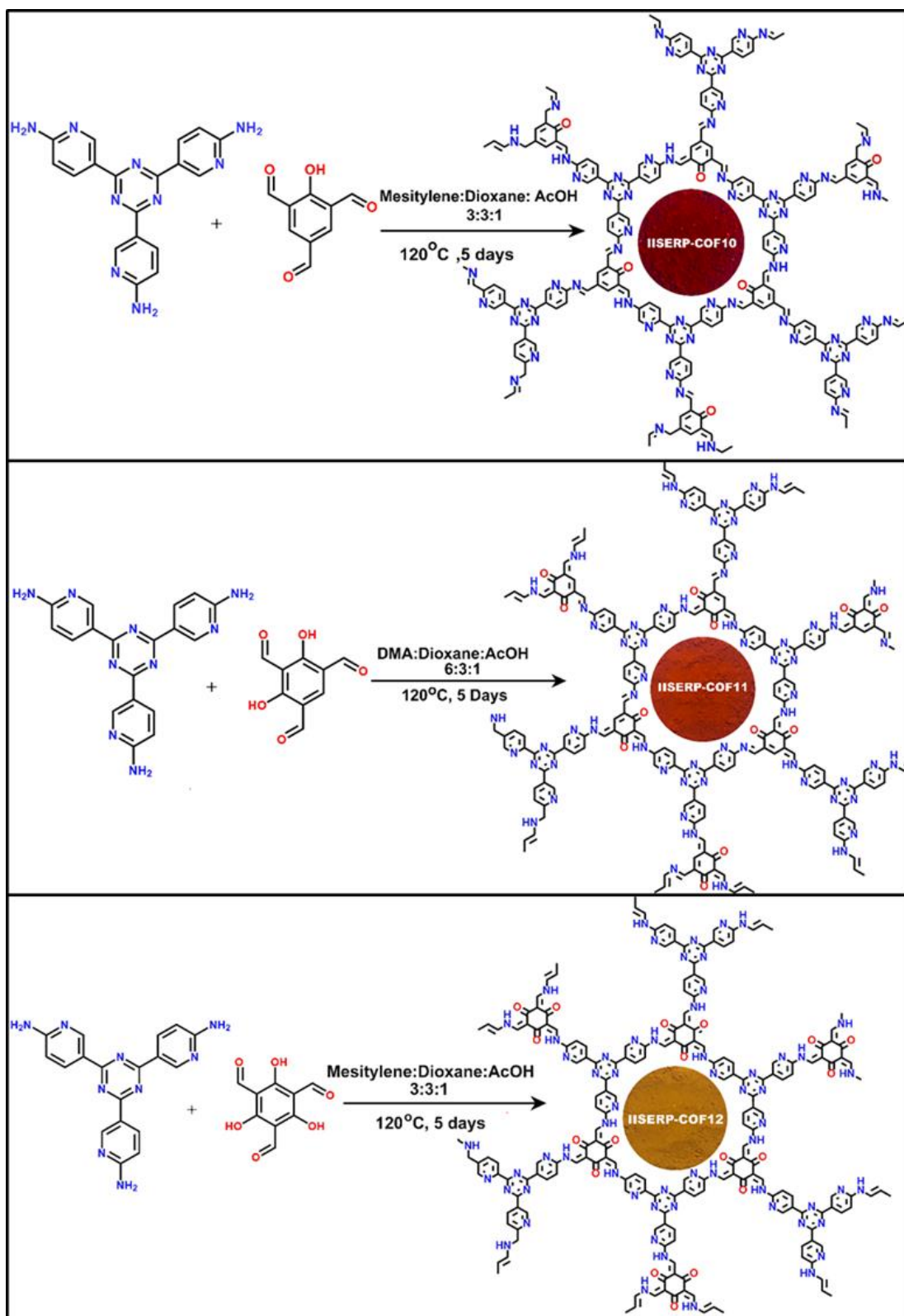
4.2.1. Synthesis and structure-modeling of IISERP-COF10, IISERP-COF11, IISERP-COF12:

IISERP-COF10, IISERP-COF11 and IISERP-COF12 have (3+3) frameworks formed by reacting a three connecting tripyridine-triazine-triamine [(5,5',5''-(1,3,5-triazine-2,4,6-triyl)tris(pyridine-2-amine))] with three different trialdehyde containing 1-/2-/IISERP-COF12 groups (2-hydroxybenzene-1,3,5-tricarbaldehyde/2,4-dihydroxybenzene-1,3,5-tricarbaldehyde/2,4,6-trihydroxybenzene-1,3,5-tricarbaldehyde) (Figure 4.1.A). All the monomers were purified via re-crystallization before use (Figure A.4.1-A.4.4, Table A.4.1-A.4.3). With the decrease of the enolic contents, the color of the COFs becomes brighter red from golden yellow (Scheme 4.1).

IISERP-COF10: 2,4,6-triformylphenol (55mg, 0.3mmol) and 5,5',5''-(1,3,5-triazine-2,4,6-triyl)tris(pyridin-2-amine (107mg, 0.3mmol) were weighed into a Pyrex tube and were dissolved in dioxane (3.0 mL) and mesitylene (3.0 mL) and stirred until a red colour was observed. To this mixture, 1.0 mL of stock acetic acid was added. Then the Pyrex tube was flash frozen in a liquid nitrogen bath and sealed. The Pyrex tube along with its contents was placed in an oven at 120°C for 5 days and gradually cooled to room temperature over 12 hrs. This yielded about 120 mg of dark-red coloured solid which was washed with hot DMF, dioxane, MeOH, acetone and THF (85%, isolated yield). This product was also subjected to a Soxhlet extraction using hot DMF/methanol as solvent and purity of filtered solid was verified by CHN analysis (Table 4.1).

IISERP-COF11: 2,4,6-triformylresorcinol (60mg, 0.3mmol) and 5,5',5''-(1,3,5-triazine-2,4,6-triyl)tris(pyridin-2-amine (107mg, 0.3mmol) were weighed into a Pyrex tube and were dissolved in dimethylacetamide (DMA) (3.0 mL) and dioxane (1.5 mL) and stirred until a red color was observed. Following this, 0.5 mL of 6M aqueous acetic acid was added. Then the Pyrex tube was flash frozen in a liquid nitrogen bath and sealed. The Pyrex tube along with its contents was placed in an oven at 120°C for 5 days and gradually cooled to room temperature over 12hrs. This yielded about 120mg of red-coloured solid which was washed with hot DMF, dioxane, MeOH, acetone and THF (90%, isolated yield). This product was subjected to a Soxhlet extraction using hot DMF/methanol as solvent and purity of filtered solid was verified by CHN analysis (Table 4.1).

IISERP-COF12: 2,4,6-triformyl Phloroglucinol (65mg, 0.3mmol) and 5,5',5''-(1,3,5-triazine-2,4,6-triyl)tris(pyridin-2-amine (107mg, 0.3mmol) were weighed into a Pyrex tube and were dissolved in dioxane (3.0 mL) and mesitylene (3.0 mL) and stirred until a yellow color was observed. Following this, 1 mL of stock acetic acid was added. Then the Pyrex tube was flash frozen in a liquid nitrogen bath and sealed. The Pyrex tube along with its contents was placed in an oven at 120°C for 5 days and gradually cooled to room temperature over 12 hrs. This yielded about 130mg of golden-yellow coloured solid which was washed with hot DMF, dioxane, MeOH, acetone and THF (90%, isolated yield). This product was also subjected to a Soxhlet extraction using DMF/methanol as solvent and purity of filtered solid was verified by CHN analysis (Table 4.1).



Scheme 4.1. Preparation of IISERP-COF10, IISERP-COF11, IISERP-COF12

Table 4.1. CHN analysis of COFs.

IISERP-COF10					
Mol. Weight (g/mol)	Formula		C	H	N
481.48	C ₂₇ N ₉ O ₁ H ₁₅	Calculated	67.35%	3.14%	26.19%
		Obtained	68.49%	3.98%	25.45%
IISERP-COF11					
Mol. Weight (g/mol)	Formula		C	H	N
994.95	C ₅₄ N ₁₈ O ₄ H ₃₀	Calculated	65.19%	3.04%	25.34%
		Obtained	67.05%	3.85%	24.12%
IISERP-COF12					
Mol. Weight (g/mol)	Formula		C	H	N
1026.95	C ₅₄ N ₁₈ O ₆ H ₃₀	Calculated	63.16%	2.94%	24.55%
		Obtained	64.92%	4.02%	22.89%

Synthesis with high dilutions, to avoid any insoluble oligomer precipitation, resulted in lower yields, but the products had exhibited comparable PXRDs. The structural models for all three COFs were built using Materials Studio v.6.0.^{22,23} An initial indexing and space group search was performed using the experimental PXRD employing the Reflex module. All three PXRD patterns indexed to a hexagonal cell, and the P-6 space group yielded well-acceptable Figure of Merit. (Figure 4.1.B, Table A.4.4) Atomic manipulations were carried out in a cell built using this setting to obtain an initial polymeric model of the COF with apt connectivities. In IISERP-COF10 and IISERP-COF11, the asymmetric substitution of the hydroxyl groups in the benzene rings of the aldehyde-derived units lowers the overall symmetry to monoclinic space group Pm, as the 6-fold inversion axis reduces to a mirror. IISERP-COF12 was modeled in P-6 setting (Figure 4.1.B). A Pawley refinements of the experimental PXRDs against their optimized models yield excellent fits for all the COFs (Figure 4.1.C). The exceptionally high crystallinity of IISERP-COF10 is worth mentioning (HKL reflection 100, 010, 1-10 @ 5.7°; 110 @ 9.9°; 2-20 @ 11.5°; 2-30 @ 15.4°; 2-21 @ 26.2° and 5-10 @ 26.5° = 2θ). Simulated vs. the experimental PXRD pattern comparisons are presented in (Figure 4.1.B). Relative energies were extracted from the DFTB optimizations (IISERP-COF10: eclipsed = -1000 kcal/mol/unit cell; IISERP-COF11: eclipsed = -5103; staggered = -7127; IISERP-COF12: eclipsed = -5802; staggered = -9412 kcal/mol/unit cell) (see table in Figure 4.1.A).

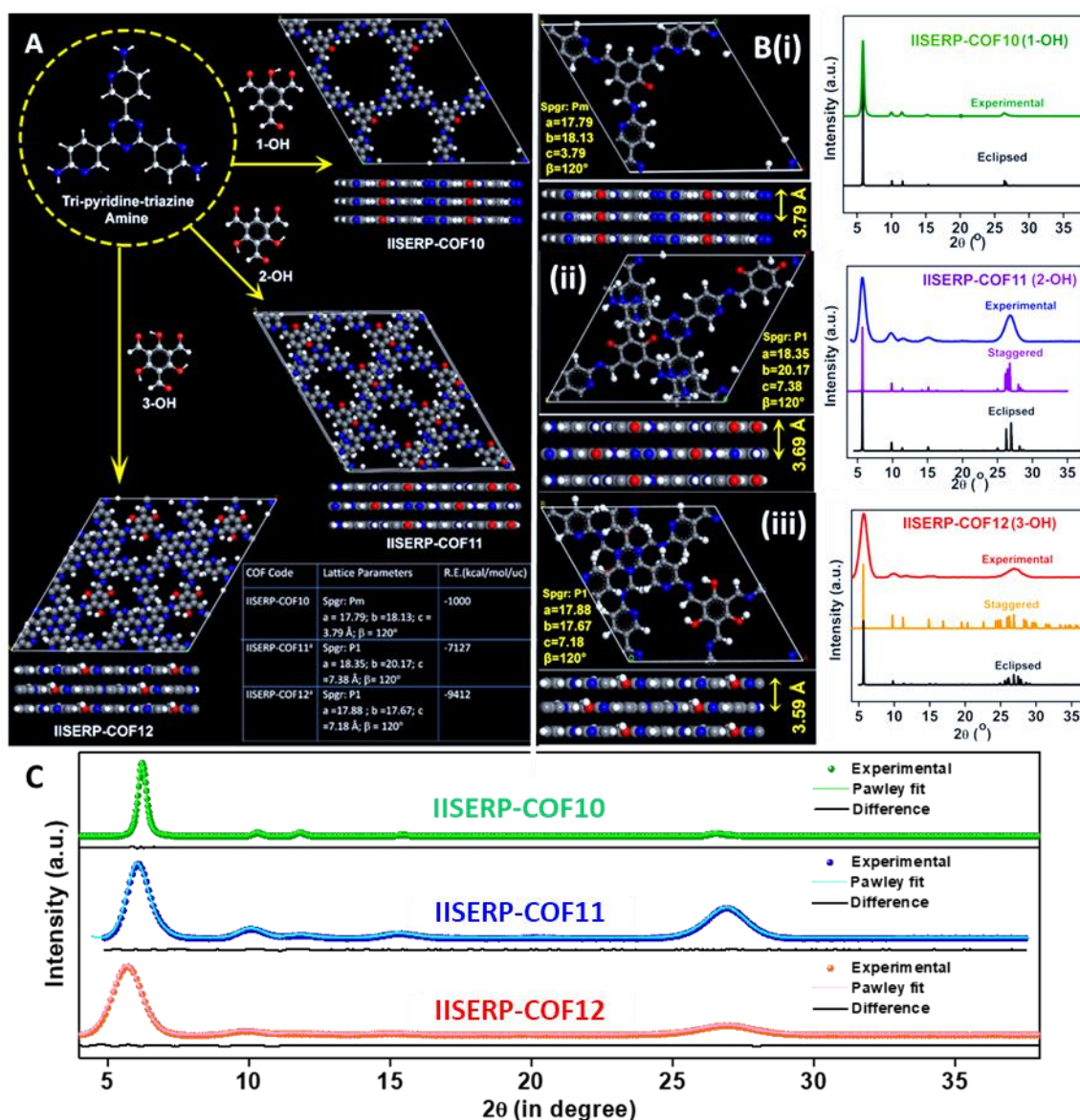


Figure 4.1. (A) Schematic representation of the tripyridine-triazine and the phenolic trialdehyde monomers. Modeled structures of the COFs formed by the reaction between these monomers. a = The IISERP-COF11 and IISERP-COF12 prefers a staggered configuration with an ABAB... stacking. (B) Unit cells and cell parameters of the COFs. A comparison of the experimental PXRD patterns of the IISERP-COF10, COF11 and COF12 with their simulated PXRD pattern for the eclipsed and the staggered configurations. From the relative intensities of these patterns, it can be seen that the eclipsed form matches the experimental pattern better for the IISERP-COF10. But the experimental PXRDs of IISERP-COF11 and COF12 fits better with the staggered model, (C) Pawley fits of the three COFs.

BET fit to the low-pressure region of the 77K N₂ adsorption branch of the IISERP-COF10 shows it has the highest surface area among all three (Figure 4.2-4.4). The pore size and pore volumes of the optimized models were correlated to the values estimated from the 77K N₂ adsorption isotherms. They matched well with the eclipsed model of IISERP-COF10 (Figure 4.1.B, Figure 4.2.A and Figure 4.5.B). However, the 2- and IISERP-COF12 had very small micropores (5.4 Å) falling into the ultra-microporous regime (Figure 4.5.D). Clearly, not supported by the eclipsed model which had much larger micropores. Hence a staggered model with an ABAB.... stacking was considered and this yields a pore size of ~5.5 Å (factoring the van der Waal radii), which matches well with the experimentally determined pore size.

All samples were synthesized multiple times and were subjected to Soxhlet washing using hot DMF (24-36 hrs), and the porosity data reproduced well across different batches.

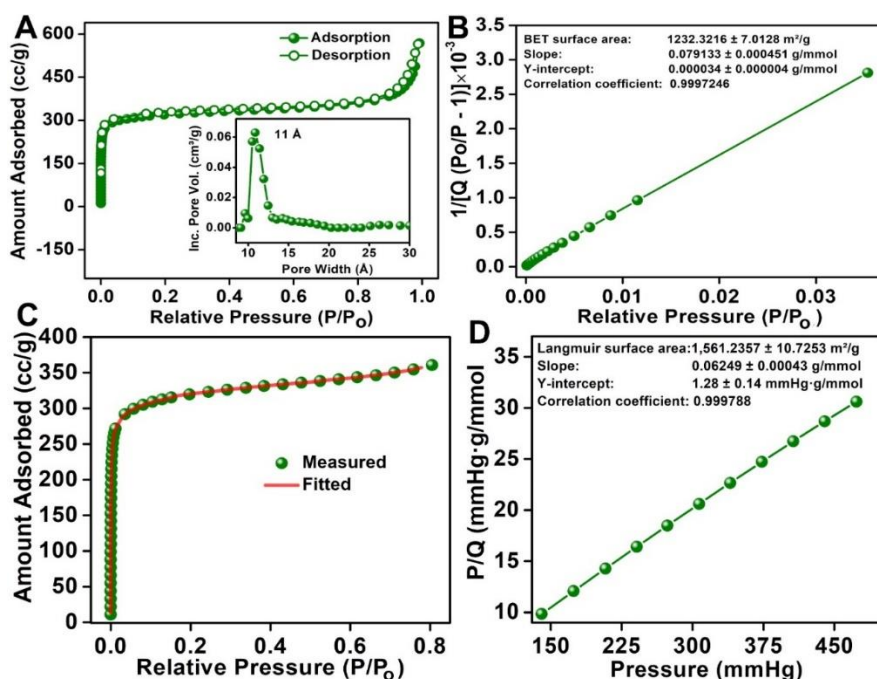


Figure 4.2. (A) N_2 adsorption-desorption isotherm of IISERP-COF10 at 77 K. Inset show a plot of the pore width vs. incremental pore volume of IISERP-COF10. (B) A BET fit obtained using the low pressure region data of the N_2 adsorption isotherm. (C) Goodness-of-fit plot of the adsorption isotherm from the DFT model (Carbon at 77K). (D) A Langmuir fit obtained using the high pressure region data of the N_2 adsorption isotherm.

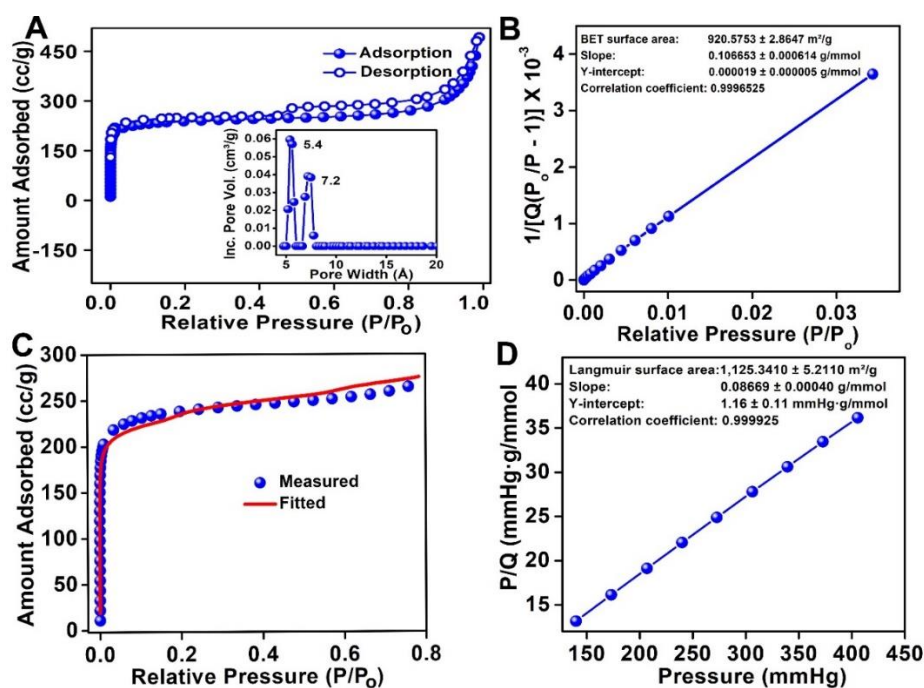


Figure 4.3. (A) N_2 adsorption-desorption isotherm of IISERP-COF11 at 77 K. Inset show a plot of the pore width vs. incremental pore volume of IISERP-COF11. (B) A BET fit obtained using the low pressure region data of the N_2 adsorption isotherm. (C) Goodness-of-fit plot of the adsorption isotherm from the DFT model (Carbon at 77K). (D) A Langmuir fit obtained using the high pressure region data of the N_2 adsorption isotherm.

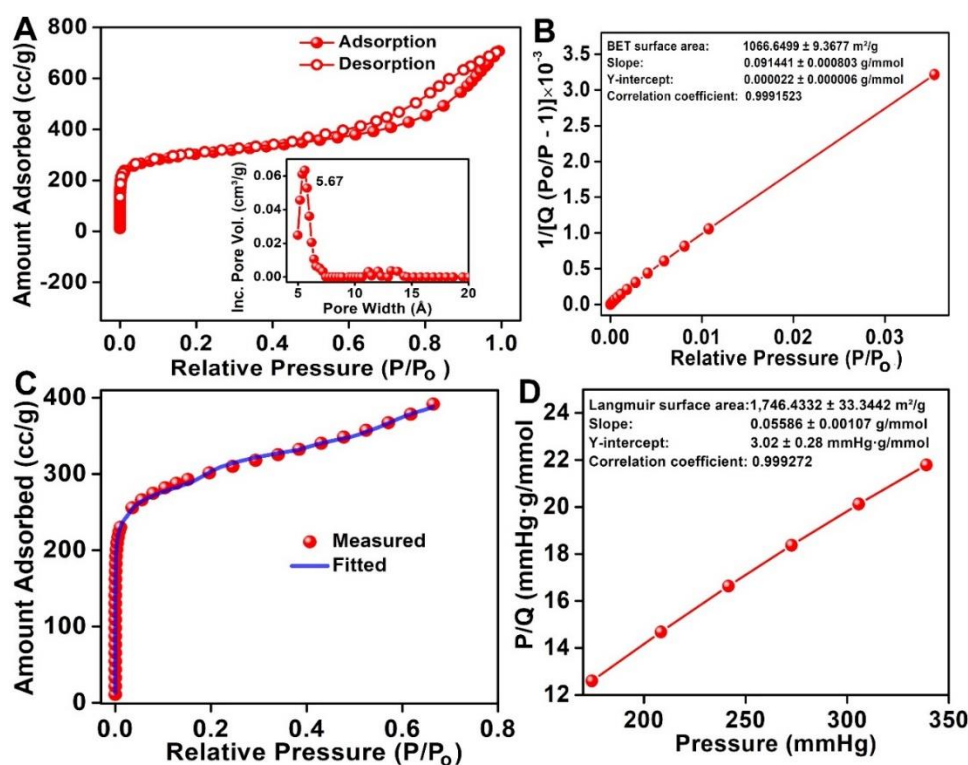


Figure 4.4. (A) N₂ adsorption-desorption isotherm of IISERP-COF12 at 77 K. Inset show a plot of the pore width vs. incremental pore volume of IISERP-COF12. (B) A BET fit obtained using the low pressure region data of the N₂ adsorption isotherm. (C) Goodness-of-fit plot of the adsorption isotherm from the DFT model (Carbon at 77K). (D) A Langmuir fit obtained using the high pressure region data of the N₂ adsorption isotherm.

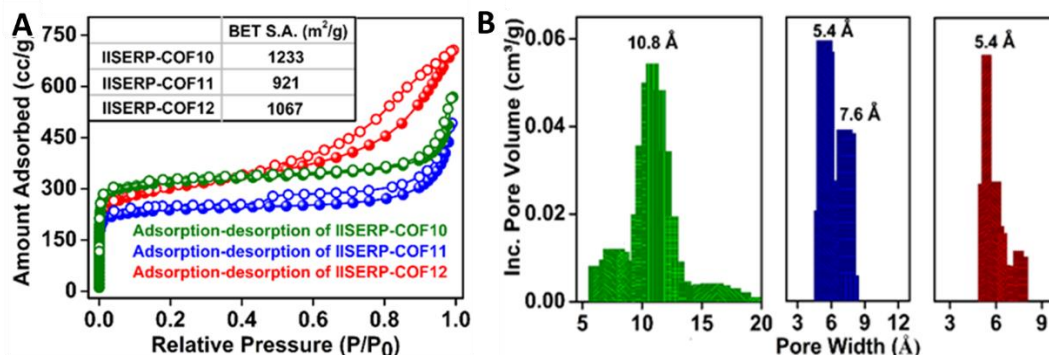


Figure 4.5. (A) Nitrogen sorption isotherms of the COFs measured at 77 K. (B) Pore size distribution plots of the COFs obtained from NLDFT fits to the 77K N₂ isotherms (Model: Carbon at 77K).

The three-dimensional structure controlled by the inter-layer arrangements can be explained by considering the hydrogen bond capabilities of the IISERP-COF10, IISERP-COF11 and the IISERP-COF12 COFs. The 3D structure of IISERP-COF10 has π -stacked columns of triazine core and phenol/resorcinol units covalently linked by Schiff bonds. This generates uniform 1D channels along the c-axis (dimension = 13.2 Å, not factoring the van der Waal radii) (Figure 4.1.B). The presence of strategically positioned hydroxyl groups of the phenol enables O•••H-N••• intra-layer hydrogen bonds with the Schiff groups. The presence of more number of hydrogen bonding -OH groups and their symmetrical positioning in IISERP-COF11 and IISERP-COF12 favors strong inter-layer hydrogen bonding making them adopt a

relatively dense *ABAB...* stacking with superior packing efficiency. This leads to the generation of the ultra-microporous structure (7.6 and 10.1 Å for IISERP-COF11; 7.4 Å for IISERP-COF12, not factoring the van der Waal radii). Thus, tuning of the number of hydroxyl-groups and their substitutional position on the benzene ring of the monomer might itself be a good design strategy for creating ultra-microporous vs. micro/mesoporous structure. Remark: The *ABCABC...* stacking with substantially improved packing and lower relative energy results in a practically non-porous structure. All these COFs possess very high Brunauer–Emmet–Teller (BET) and Langmuir surface areas (see table in Figure 4.2.B, 4.2.D, 4.3.B, 4.3.D, 4.4.B, 4.4 D and Figure 4.5.A).

^{13}C -Solid state NMR was performed at 500 MHz for all the three COFs. Characteristic peaks of pyridinal carbon (a: 149 ppm), triazine carbon (e: 166 ppm), phenolic carbon (d: 171 ppm) and carbonyl carbon (g: 182 ppm) were observed. The presence of appropriate peaks corresponding to the pyridine and triazine groups in the NMR spectra of the COFs, reveals that the monomers retain their functional group integrity during the polymerization (Figure 4.6). A details analysis of the NMR data confirms that at room temperature IISERP-COF12 is mostly present in keto form but other two COFs are present in enolic form.

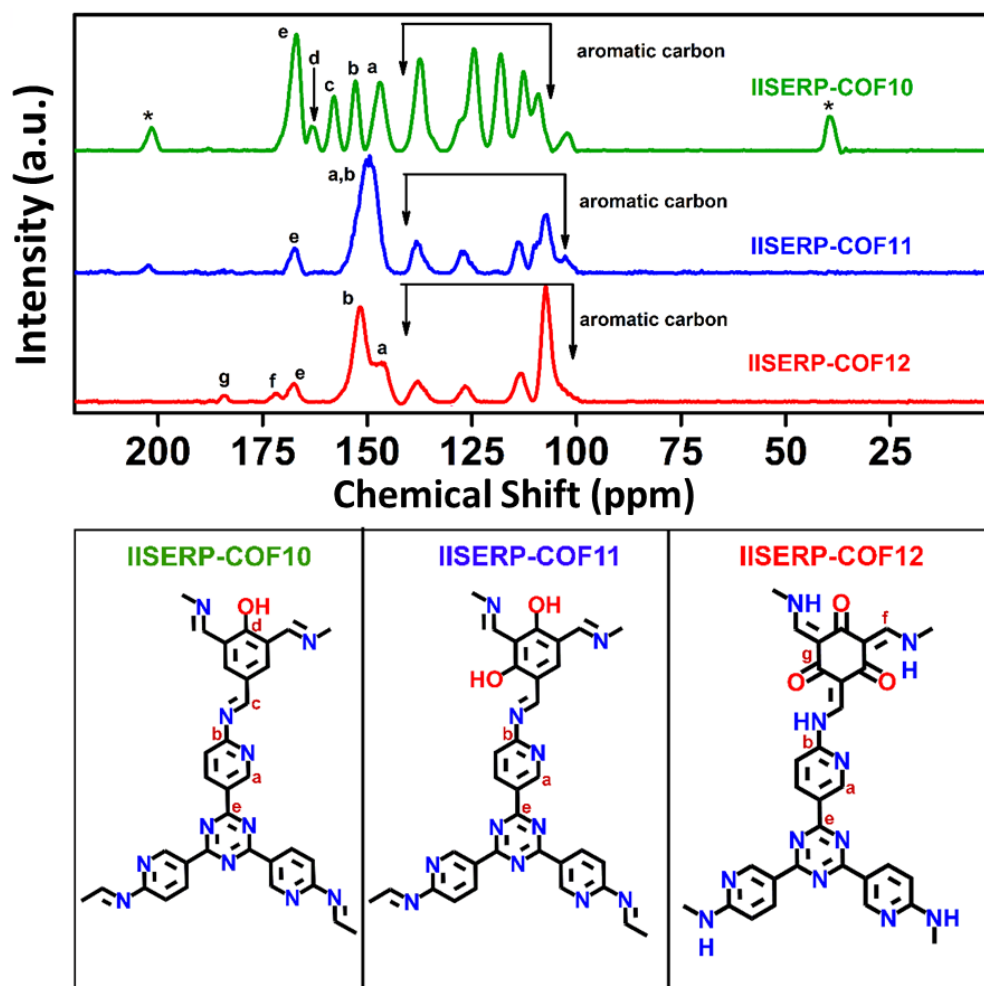


Figure 4.6. CP MAS ^{13}C -NMR spectra of the IISERP-COFs measured at 500 MHz. a,b,c,d,e,f,g,e',f' are the corresponding peaks position obtained from the NMR data.

Absence of any terminal amine or aldehyde groups in IR spectra suggests the high completeness of the polycondensation reaction (Figure 4.7, Table 4.2). We notice from the IR spectra that the as-synthesized COF at room temperature exists as β -ketoenamine, which is formed by the tautomerism between the Schiff bonds ($-C=N-$) and the β -positioned hydroxyl groups giving rise to energetically favored intra-layer H-bonding. When this sample is activated at 120°C and cooled to room temperature, the IR spectra display bands corresponding to the enol form too (Figure 4.8). We also observe this β -ketoenamine form to be chemically more stable.^{10,24}

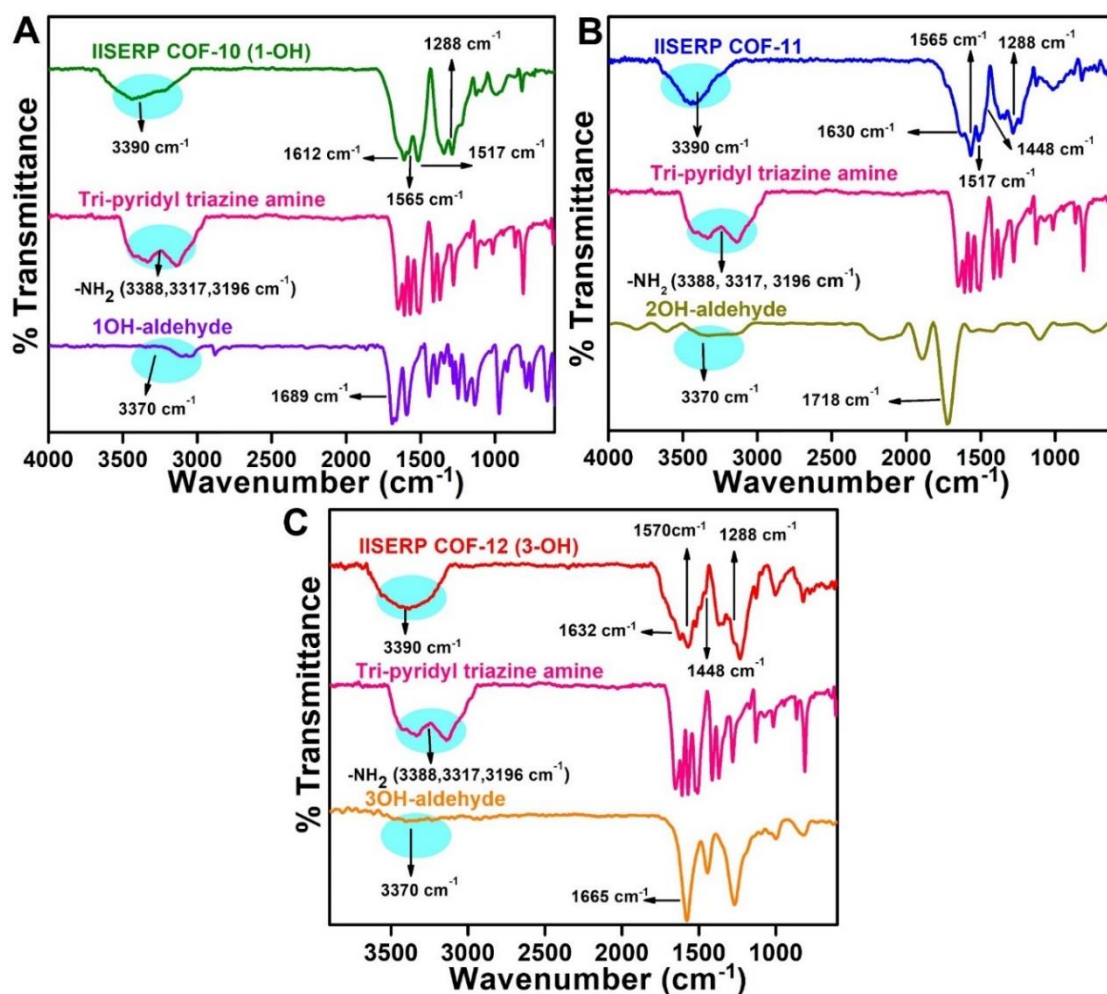


Figure 4.7. Comparison of the Fourier transform Infra-red (FT-IR) spectra.

Table 4.2. IR data analysis

COF-Name	Enolic OH (cm ⁻¹)	carbonyl (C=O) (cm ⁻¹)	C=N bond (cm ⁻¹)	C=N aromatic (cm ⁻¹)	C=C bond (cm ⁻¹)	C-N bond (cm ⁻¹)
IISERP-COF-10	3390	1612	1565	1517	1448	1288
IISERP-COF-11	3390	1630	1565	1517	1448	1288
IISERP-COF-12	3390	1632	1570	1517	1448	1288

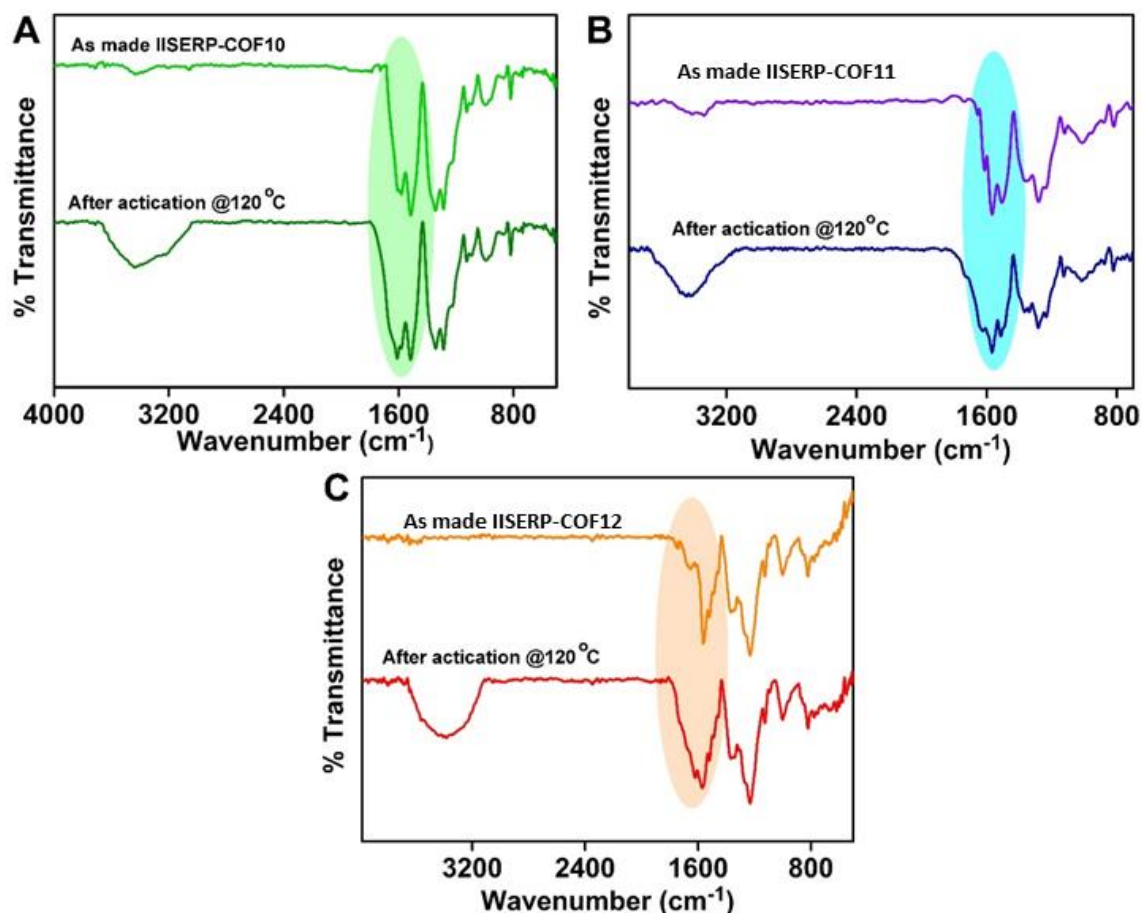


Figure 4.8. Comparison of FT-IR spectra of IISERP-COF10, IISERP-COF11, IISERP-COF12 before activation and after 120 °C activation. This shows enolic –OH peak becomes prominent upon heating at the expense of diminishing of C=O peak. This suggests in presence of moisture from air a rapid conversion from enol to keto form happens in all these COFs. The highlighted region shows the appearance/disappearance of the shoulder peaks due to the conversion from enol-to-keto and vice versa.

The variable temperature PXRD and TGA confirms that the β -ketoenamine stabilization does not show any enhanced thermal stability under the TGA (Figure 4.9). The decomposition of all these COFs starts from 350 °C. The COFs soaked in HCl (3M), H₂SO₄ (3M) and NaOH (3M) for 12hrs exhibit exceptional chemical stability, and functional group integrity (observed from IR spectra), porosity retention (adsorption isotherms) (Figure 4.10 and 4.11).

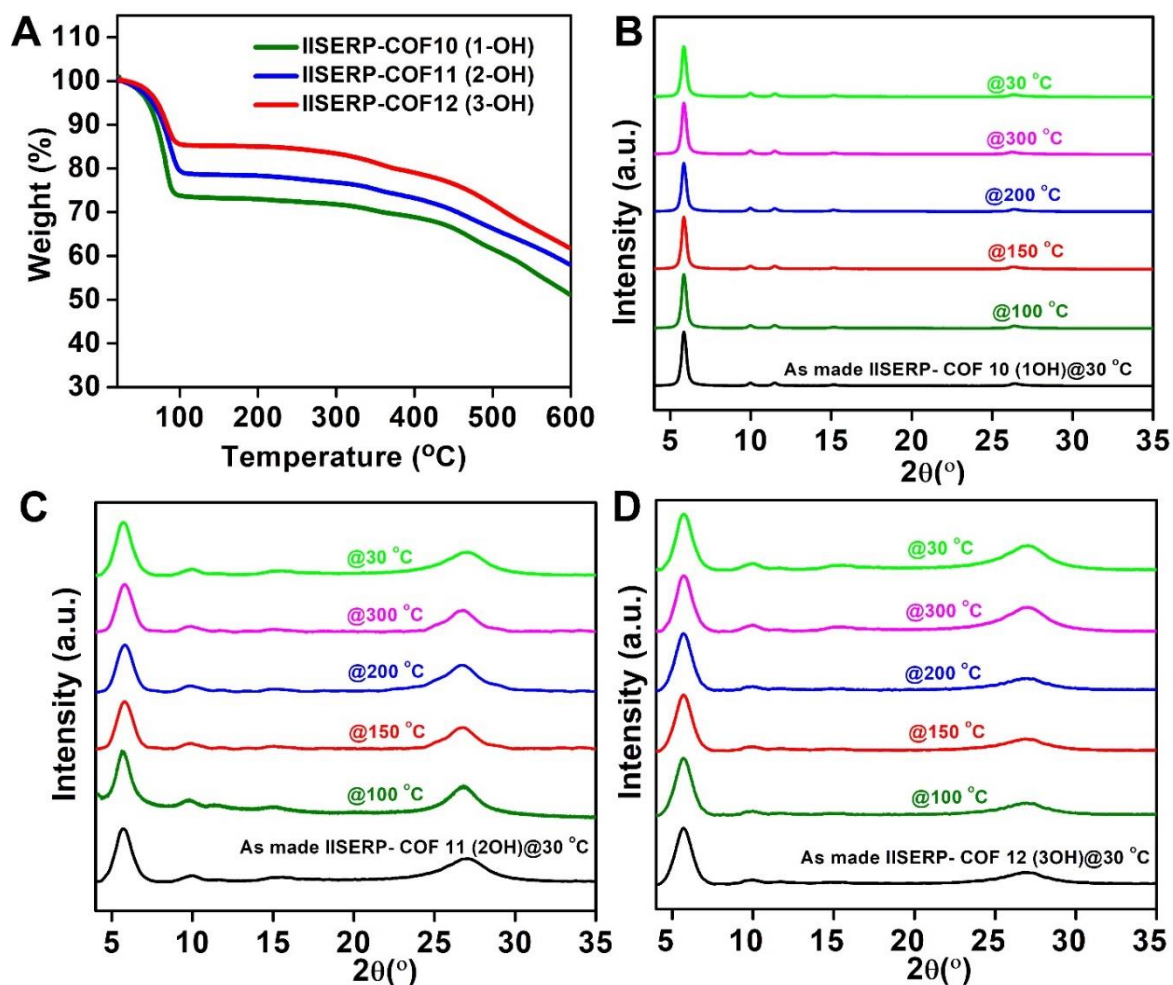


Figure 4.9. (A) Thermo gravimetric analysis of IISERP-COF 10, IISERP-COF-11 and IISERP-COF12 under N₂ flow at 5K/min rate. (B) Variable temperature PXRDs of IISERP-COF-10. (C) Variable temperature PXRDs of IISERP-COF-11. (D) Variable temperature PXRDs of IISERP-COF-12.

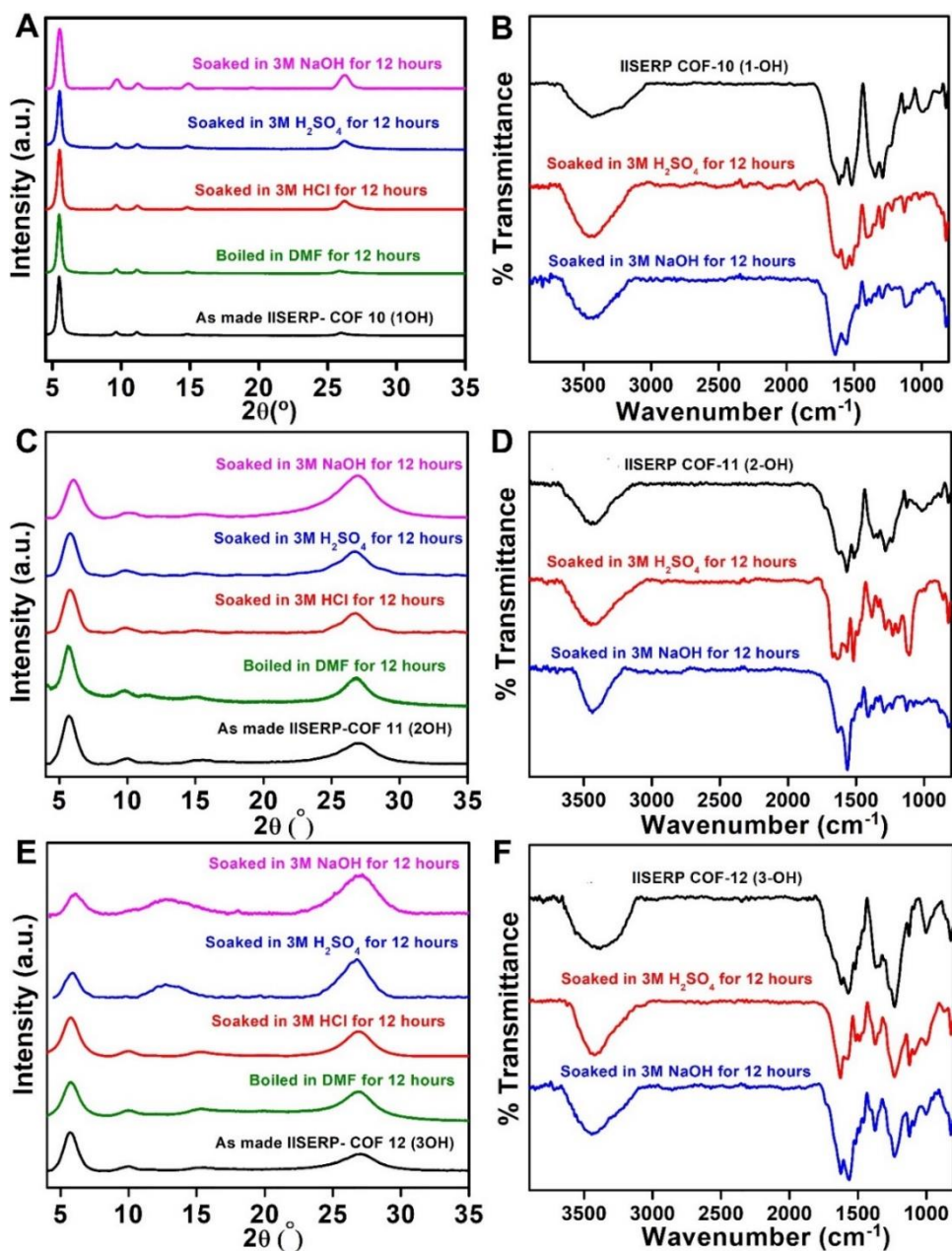


Figure 4.10. (A) PXRD and (B) IR patterns of IISERP-COF10 (IISERP-COF10) recorded after boiled in DMF, soaked in acid and soaked in base. (C) PXRD and (D) IR patterns of IISERP-COF11 (IISERP-COF11) recorded after boiled in DMF, soaked in acid and soaked in base. (E) PXRD and (F) IR patterns of IISERP-COF12 (IISERP-COF12) recorded after boiled in DMF, soaked in acid and soaked in base.

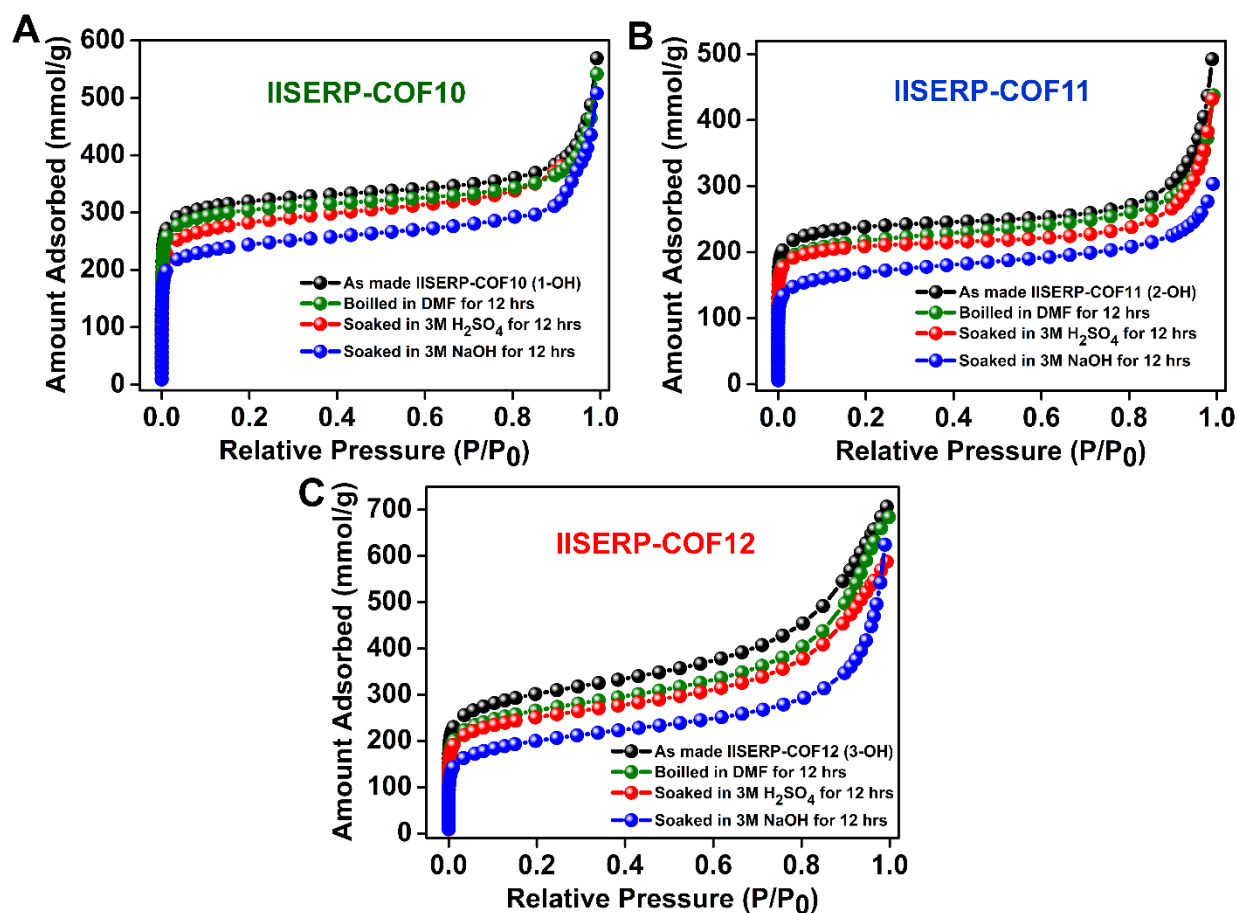


Figure 4.11. N_2 77K adsorption of IISERP-COF10, IISERP-COF11, IISERP-COF12 after boiling in DMF, after acid and base treatment.

Under FE-SEM, IISERP-COF10 and IISERP-COF11 appear as hexagonal flakes forming a stacked microstructure (Figure 4.12). At lower resolution, a fluffy cotton-like morphology can be seen. Whereas at higher resolution, the presence of aggregated-flakes is seen. These submicron-sized flakes further aggregate into structures resembling corals. However, the IISERP-COF12 has more of a thick fibrous morphology.

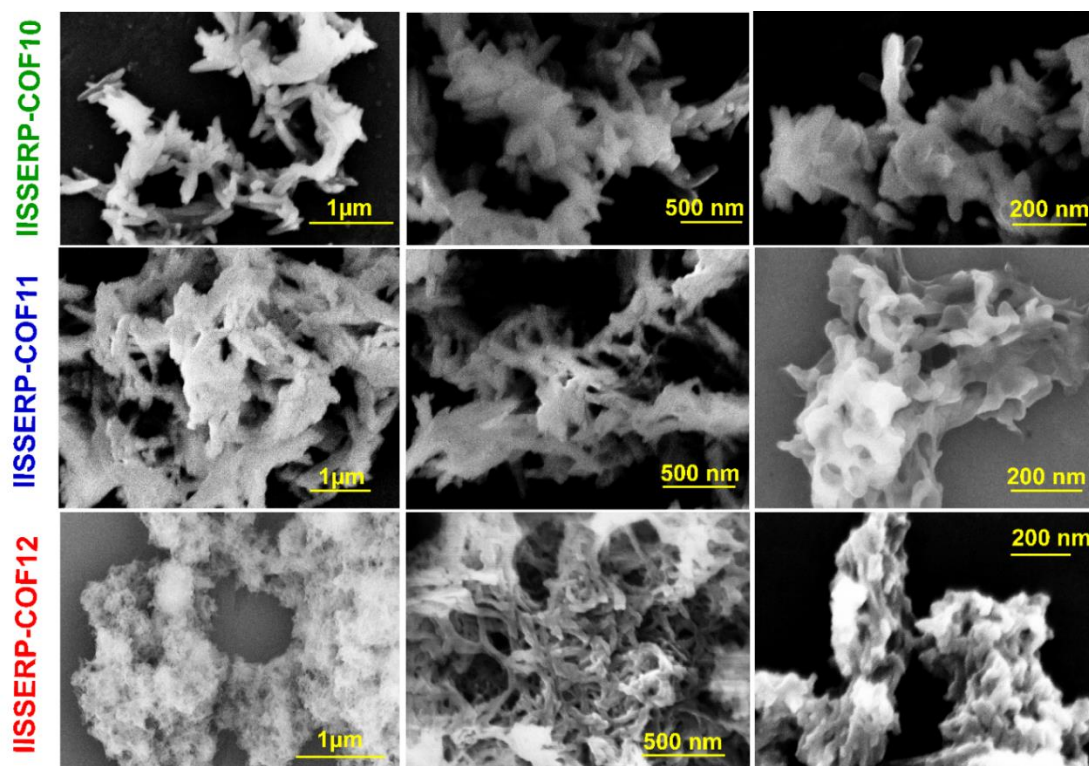


Figure 4.12. FE-SEM images of IISERP-COF10, COF11, COF12 at different resolutions. Shows flaky morphology. In all cases, the SEM images corroborate with the morphology observed under the HR-TEM.

HR-TEM images of IISERP-COF10 shows finger shaped thin flakes (Figure 4.13). Those are randomly oriented all over the places. IISERP-COF11 shows bigger size thin sheets which are stacked to each other. The morphology of IISERP-COF12 is different than other two. The flakes of this COFs are interconnected to make a net like pattern. At higher magnifications, the micropores present in the COF flakes were observed. These COFs are truly microporous having pore diameter from 5 Å to 11 Å. So that, distinguishing the angstrom level pore distribution was hardly possible even by approaching up to 5 nm magnification of the HR-TEM. However microporous nature of the COFs has been confirmed from the HR-TEM images (Figure 4.14).

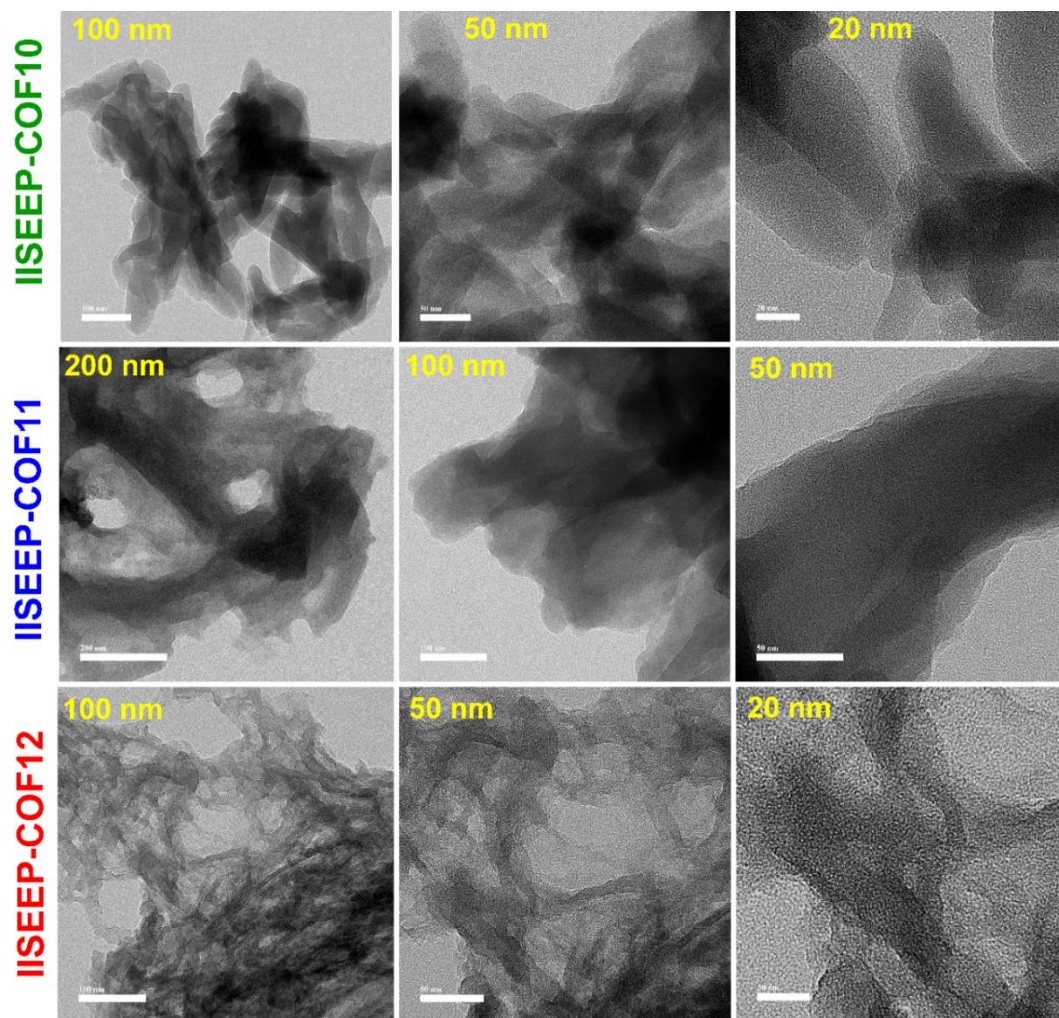


Figure 4.13. HR-TEM images of the IISERP-COF10, COF11, COF12 under different magnifications showing the aggregates formed by stacking of many sheets. Darker regions are from such multi-flake stacking.

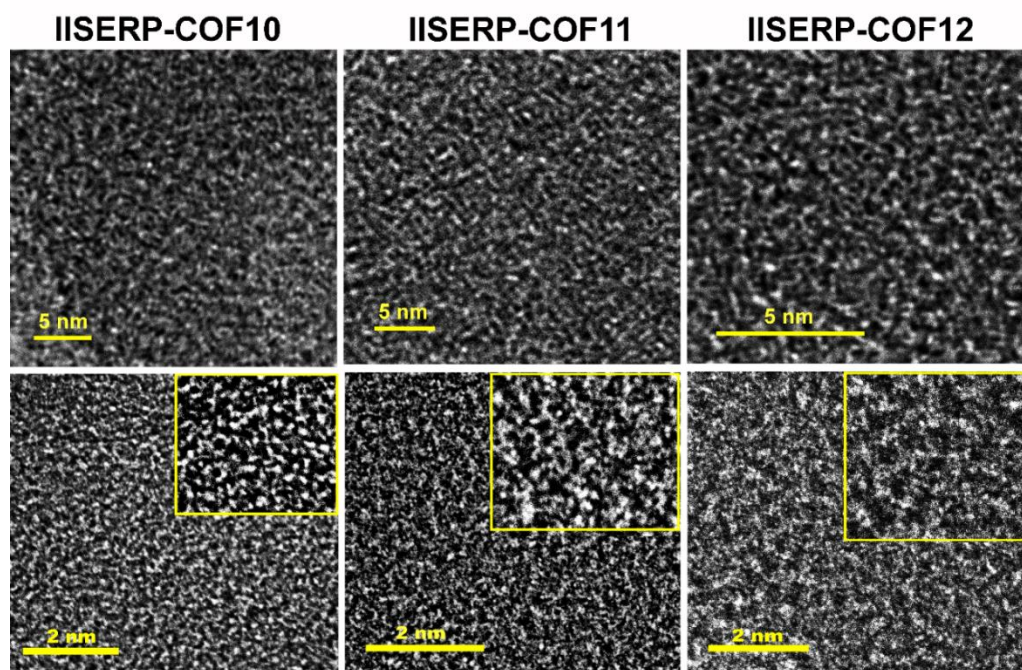


Figure 4.14. HR-TEM images of the IISERP-COF10, COF11, COF12 under higher magnifications showing microporous nature of the COFs.

4.2.2. Redox activity at pyridine groups:

The presence of pyridine-nitrogen atoms and keto-enol tautomerizable carbonyl groups in these three highly functionalized COFs motivated us to investigate their potential for charge-storage.^{5,10} For this, the electrode was fabricated by coating an ethanolic dispersion of IISERP-COF12 on carbon paper in $1 \times 1 \text{ cm}^2$ area, which was dried under vacuum for 24 hrs. Cyclic Voltammetry (CV) measurements were performed in a non-aqueous electrolyte medium (t-butyl ammonium hexafluorophosphate dissolved in acetonitrile) using a non-aqueous Ag/Ag⁺ reference and platinum flag counter electrodes. Very slow scan rates (2 mV/s) in a potential window from 0 to -3 V was employed to scrutinize the redox activity of the IISERP-COF12 (Figure 4.15). The three reversible peaks at -2.61, -1.2 and 1.65 V were assigned to electrochemical oxidation-reduction behavior of pyridine/triazine nitrogen, carbonyl-oxygen and Schiff-base nitrogen.^{10,25-28} The CV peaks due to Schiff-base nitrogen walks away at the high sweep rates (25mv/s), suggesting that their redox activity is much milder than that of C=O and pyridine. In depth, when the scan rates are low even the relatively poorly interacting Schiff-base nitrogens participate, however, when the scan rates are increased, the residence time of the electron on the COF surface gets significantly shortened, leaving little chance for the Schiff-base to interact as compared to the carbonyl and the pyridine groups (Figure 4.15.C). To substantiate this, we carried out the CV measurements on an iso-structural and iso- functional COF (TpTta COF) but deprived of pyridine groups (Figure 4.16). Interestingly, the peaks for keto and imine observed in the IISERP-COF12 under discussion were present in this control COF too, but the intense peak assigned to the pyridine group was absent (Table 4.3.). This points at the additional redox active site being available in the IISERP-COF10, IISERP-COF11 and IISERP-COF12.

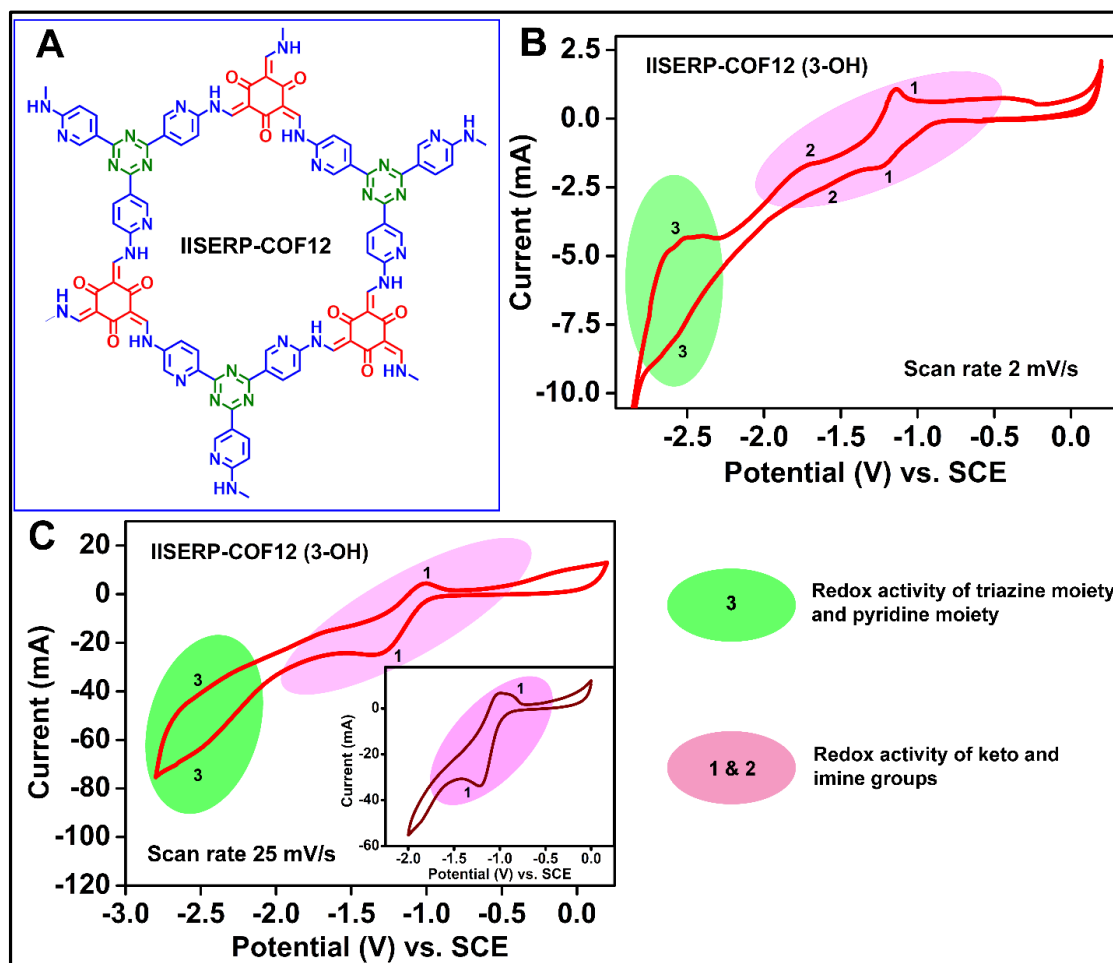


Figure 4.15. (A) A pictorial representation shows the presence of functional groups in IISERP-COF12. (B) Cyclic voltammetry measurements of IISERP-COF12 @2 mV/s using 0.5 (M) solution of $t\text{BuNH}_4\text{PF}_6/\text{ACN}$ (non aqueous electrolyte system). (C) Cyclic voltammetry measurements of IISERP-COF12 @25 mV/s in non aqueous electrolyte system. Remark: IISERP-COF12 was chosen for this study as it has the maximum number of hydroxyl units per ring.

Observation: Three distinguishable reversible peaks were observed. Pink and green shadowed area are corresponding to redox active region for keto-imine and triazine-pyridine functionality, respectively. It notifies disappearance of the CV peak due to imine bond activity at a high scan rate (25 mV/s).

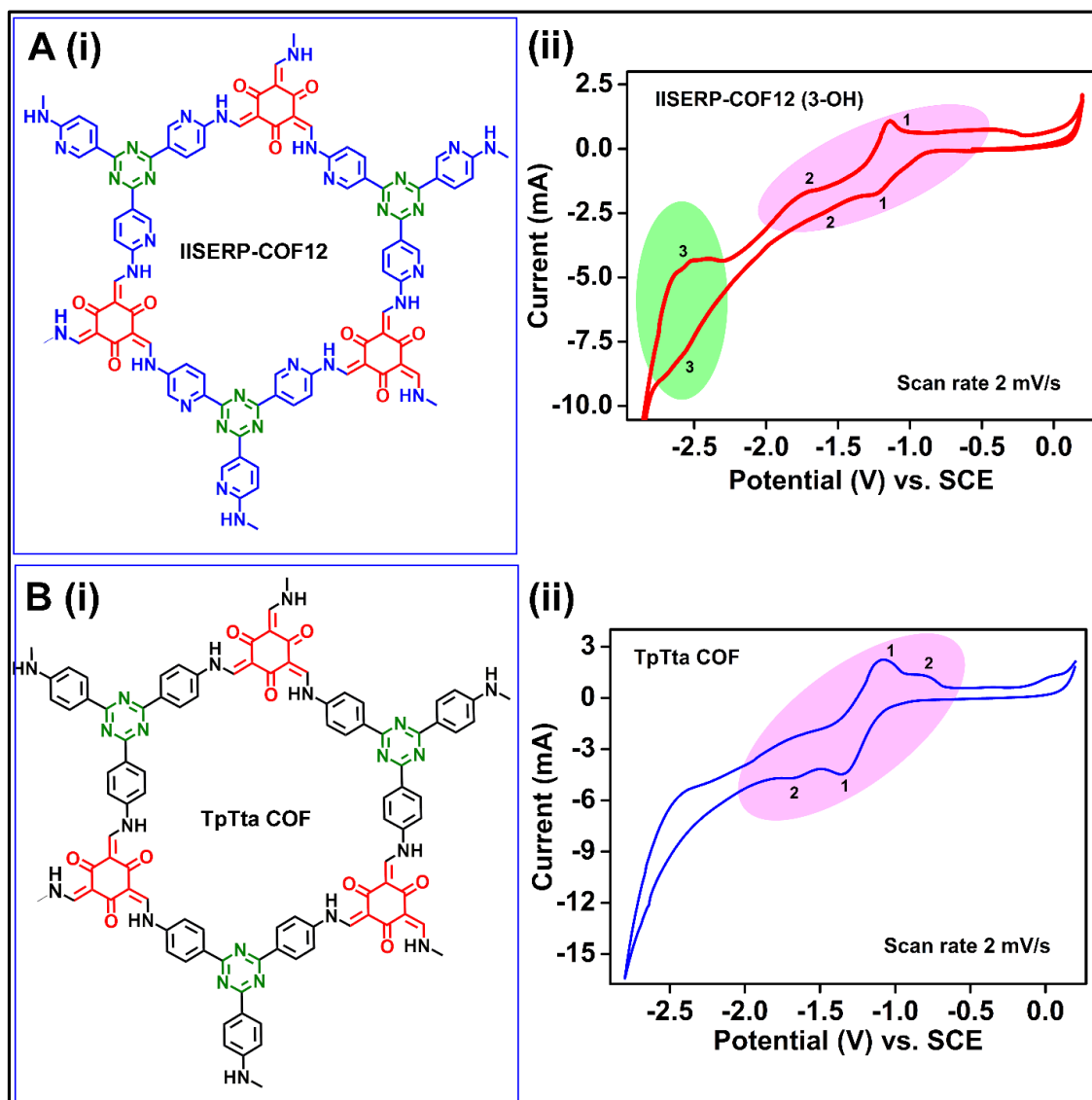


Figure 4.16. Comparison of cyclic voltammetry measurements of IISERP-COF12 and TpTta COF @2 mV/s. COF 12 shows three reversible peaks. But the TpTta COF shows only two prominent reversible peaks. The third peak arising from the activity at the triazine rings is very weak in intensity in case of the TpTta. Note: The color codes have been maintained from Figure 4.15.

Table 4.3. CV peaks for IISERP-COF12 and TpTta COF

COF codes	Pyridine groups	Triazine moiety	Keto groups	Imine groups
IISERP-COF12	-2.61 V (strong)	-2.61 V (strong)	-1.20 V	-1.65 V
TpTta COF	-	-2.45 V (weak)	-1.25 V	-1.35 V

Note. This observation clearly suggests that the redox activity of electron rich COF12 is more prominent than TpTta COF.

4.2.3. Capacitance under acidic liquid-electrolyte:

Presence of pyridine, triazine, Schiff-base nitrogens and enolizable keto groups in these COFs naturally sets up a driving force for the interaction with protons. Additionally, their porous structure can provide high diffusion space for ions,²³ with H⁺ being the smallest cation, exceptionally favorable diffusion can also be expected, but the facile diffusion of the counter anion needs to be supported. To verify this diffusion favorability, we performed CV measurements in 1M H₂SO₄ medium using a typical three-electrode system. For electrochemical measurements, glassy carbon electrode was coated with the active materials (COFs). At first, glassy carbon electrode was polished to a mirror-finish by using 0.05 micron alumina powder, thoroughly cleaned by sonicating in water for 15 min and dried in air. Thereafter, in about 1mL ethanol, COF (8 mg; 80%), carbon super P (1.5 mg; 15%) and Nafion binder (0.5 mg; 15%) were added. The solution was stirred for 10 h to make the solution homogeneous. In the next step, 1 μ l of the solution was drop-casted on the glassy carbon electrode. So the loading density of COF coated on glassy carbon electrode turns out to be 0.12 mg/cm². (considering the surface area of glassy carbon electrode 0.0707 cm²)

Finally, the electrode was dried in a hot air oven for 20 min. This was employed as the working electrode. Calomel and Platinum were used as the reference and the counter electrodes, respectively. The CV measurements were performed using 1M H₂SO₄ as the electrolyte using a typical three-electrode set-up. Archetypal rectangular shaped I-V curves were obtained and additionally, three distinct redox peaks were noticed in every case (Figure 4.3.A, Figure A.4.23). They appear reproducibly over multiple-cycles.

A comparative CV plot of these three COFs measured at 20 mV/s sweep rate has shown to indicate the difference of the redox activity of those COFs (Figure 4.17). Though a slight shift of the CV peaks happened. Two redox active peaks corresponds to phenolic-OH and pyridinal-N are still prominent. Depending on the close proximity of the the redox active functionality lined across the micropores and the energy associated with each COFs, the faradaic components may also vary. Though the profound redox activity comes here from enormous no of the pyridine moiety in each COF, but no of additional OH groups and proper positioning the OH groups near to the pyridinal nitrogen also plays a significant role for the shifting of redox active peaks here. From IISERP-COF10 to IISERP-COF12 the no of the tautomerizable OH groups increases. Moreover the chances of being present in Keto form increases with the OH group and therefore IISERP-COF12 present in keto form mainly. The affinity of Keto groups towards protonic electrolyte is higher over the enolic form. So pseudo behavior comes from tautomerizable OH groups have an obvious impact on the total capacitance.

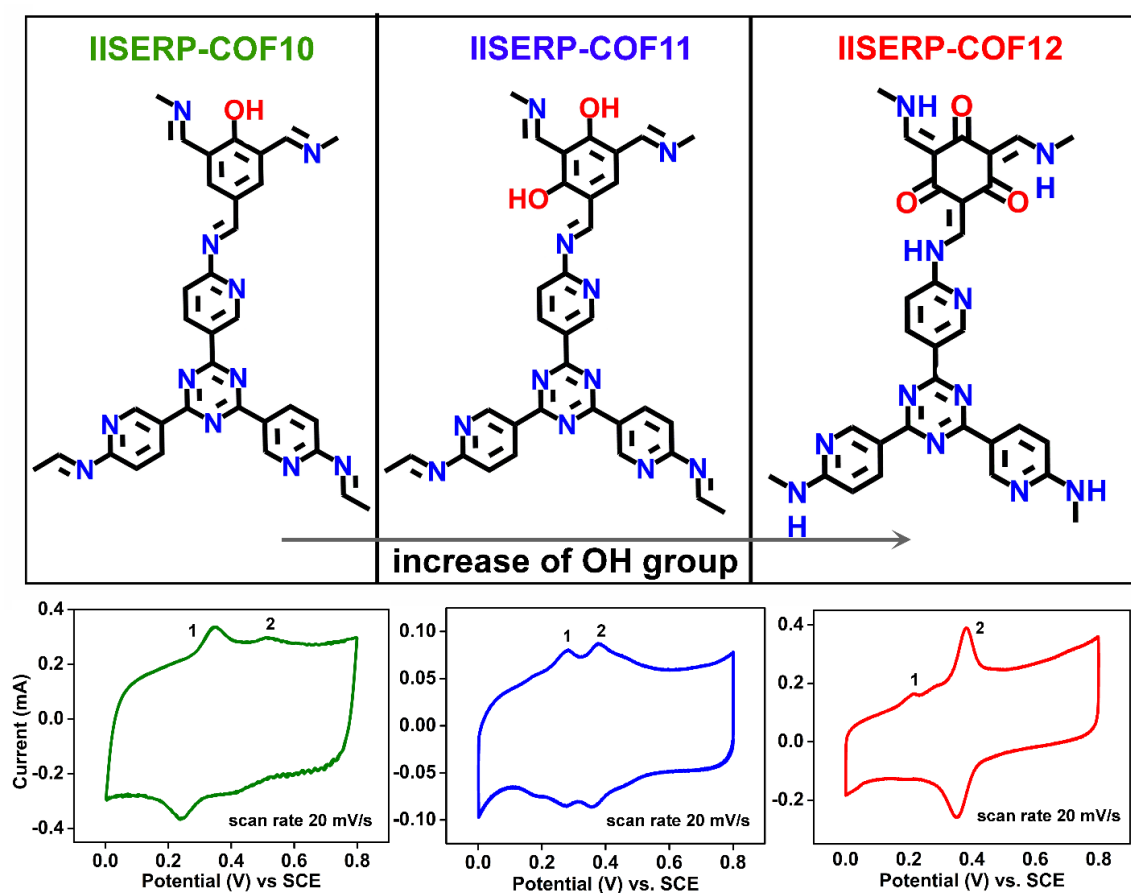


Figure 4.17. Comparison CV plots of IISERP-COFs at identical scan rate. With the increase of the no of OH functionality the redox activity changes.

As in the non-aqueous electrolyte CV experiment, here too, the control, TpTta COF, was missing the peak corresponding to the pyridine moiety. But the other two reversible peaks appeared in slightly shifted potential region (Figure 4.18). This additional peak in the CV, in case of IISERP-COF12, implies the presence of proton acceptor pyridine nitrogens. Certainly, the pyridine functionality brings a notable advantage when it comes to interacting with H^+ ions. Whereas the TpTta COF shows only the weak peaks for the interaction of proton with keto and triazine functionality. Which are also present in IISERP-COF12, but are slightly shifted. The area under the I-V curve is much higher for the IISERP-COF12 compared to the pyridine-deprived TpTta COF. This suggest that the pyridine group enhances the H^+ ion storage.

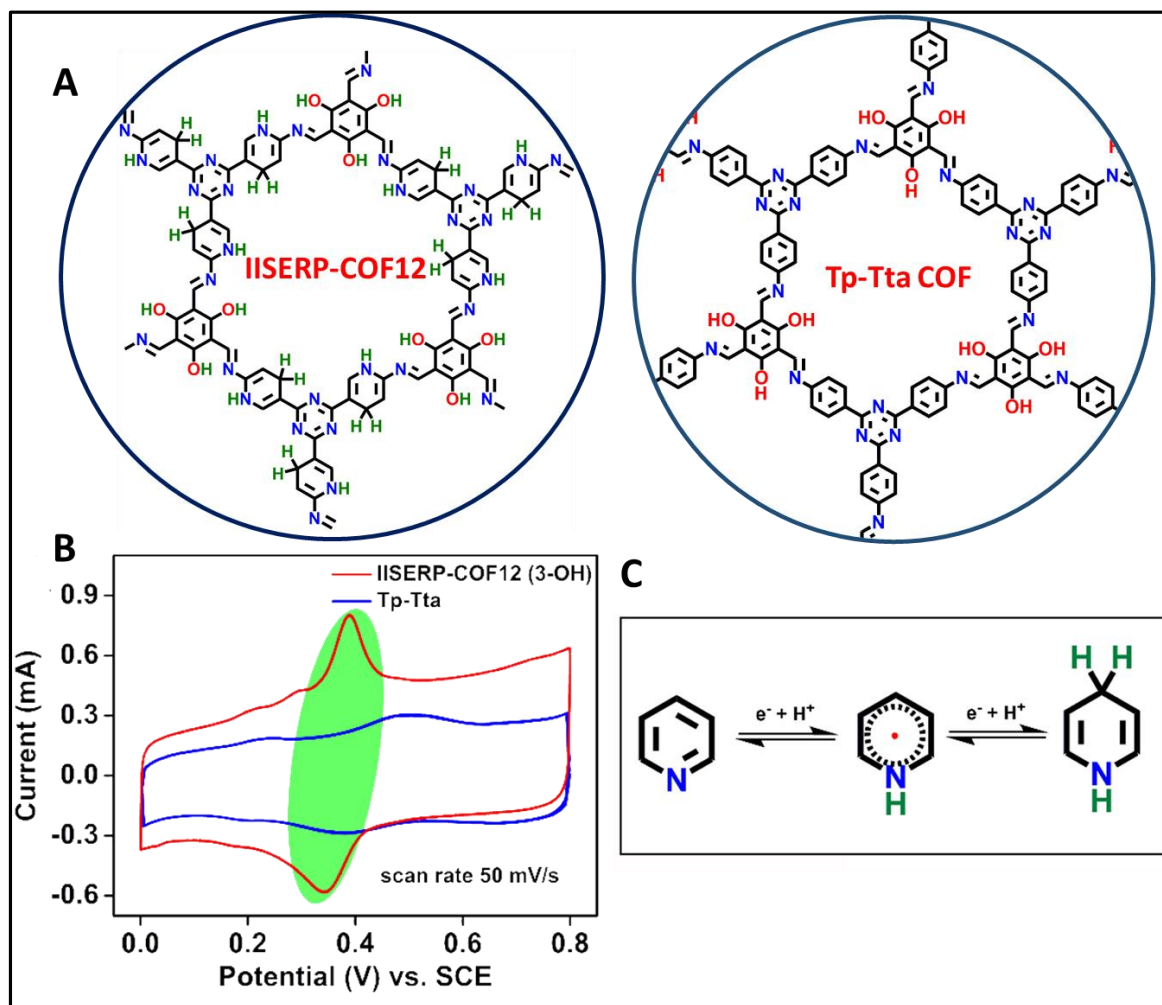


Figure 4.18. (A) A schematic showing the potential interactions of the protons (from the electrolyte) with the pyridine units of IISERP-COF12 under the electrochemical force. But Tp-Tta COF does not have such proton affinity pyridine groups. (B) Comparative CVs from a three-electrode measurement done using IISERP-COF12 and Tp-Tta COF. They were done at a current density of 50 mV/s. The CV shows the appearance of an additional sharp peak at ~ 0.3 V in the case of IISERP-COF12. The redox peaks occurring due to the protonation at the pyridine sites have been shown in green highlights. (C) Reactivity of pyridine nodes of IISERP-COFs in acidic electrolyte systems.

Scan rates were varied from 2 to 1000 mV/s in a potential window of 0-0.8 V (Figure 4.19). In general, at high scan rates, the redox peaks observed in supercapacitors disappear, leaving behind only the rectangle arising from the EDLC. This is because the diffusivity of H^+ ions in high sweep rates is very slow; this minimizes the H^+ •••Framework interaction time and chance. This is true for most other COFs reported so far^{6,29-31} and even for the N-doped Graphite, Graphene oxide and RGOs.³¹⁻³⁴ But surprisingly, here, in these COFs, the high surface area microporous structure and the pyridine-rich walls seem to provide rapid diffusion and intense affinity towards H^+ ions, which is evidenced by the complete retention of the redox peaks even at a scan rate as high as 1000 mV/s (Figure 4.19). It is well-understood that preserving the Faradaic components of the pseudo-capacitance at high scan rates along with the inherent EDLC would be advantageous, but is always a challenge in any supercapacitor. Here, undoubtedly, these COFs hold one such unique capability.

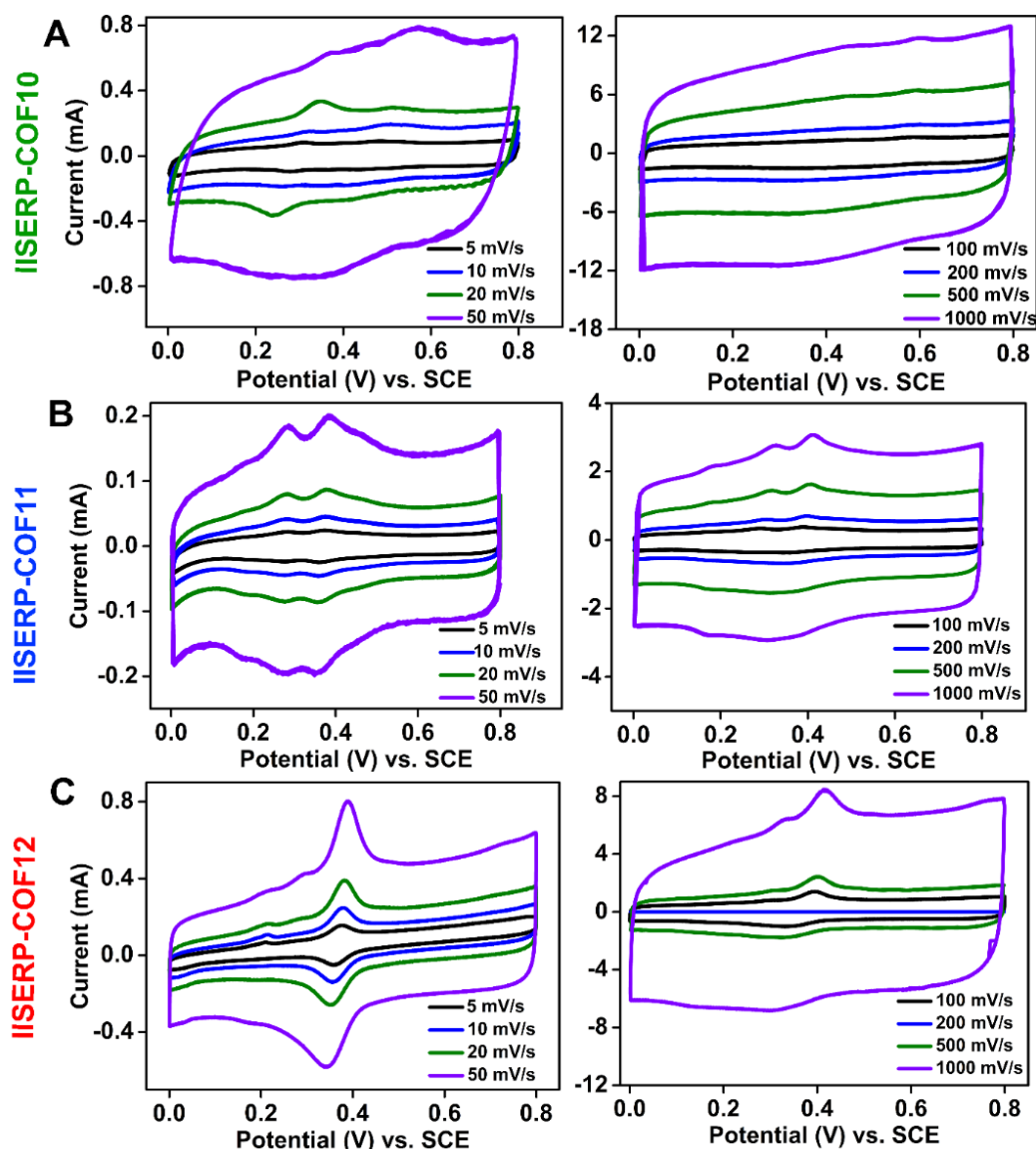


Figure 4.19. Three-electrode CV measurements using (A) IISERP-COF10, (B) IISERP-COF11 and (C) IISERP-COF12 coated working electrode at variable scan rates (from 5 mV/s to 1000 mV/s) in 1 M H₂SO₄ solution within the potential window of 0–0.8 V. All three redox peaks appeared even at high scan rates.

To differentiate between the H⁺ ion storage on the surface of the COFs (n-type mechanism)^{35,36} and easy insertion of the counter ions SO₄²⁻ (p-type mechanism)³⁷ inside the pores of the COFs, a scan rate vs. peak current plot was made (Figure 4.20.A). For all the COFs, the peak current increased uniformly with increasing scan rate yielding a perfectly linear fit. This supports a charge storage behavior originating from the formation of an electrostatic double layer between the COF surface and the H⁺ ions. A fit to the power law ($i = a\nu^b$; where i = current; ν = scan rate) furnished a 'b' value of ~ 1 for all the COFs; this further confirms the super-capacitance via EDLC formation (Figure 4.20.B). The high surface area and uniform pores of the COF is key to achieving this.

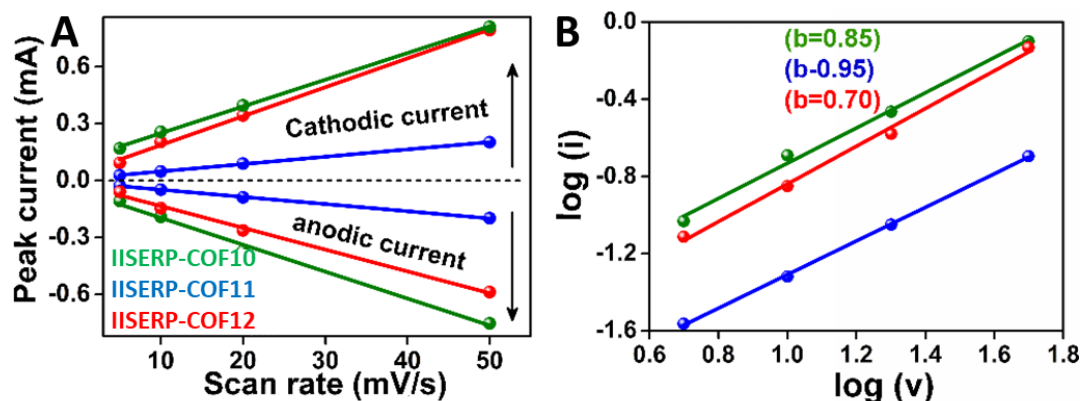


Figure 4.20. (A) Plot of the peak current vs. scan rate (5 mv to 50 mV) displaying their linear relationship. (B) A logarithmic plot of current vs. scan rate.

The gravimetric charge storage capacity of the COFs were quantified via GCD measurements. In all cases, a plot of the elapsed time vs. potential, generated by sweeping the current density from 500 to 5000 mA/g (Figure 4.21.A(ii), B(ii), C(ii)), returns a near-perfect triangular-shaped curve. This displays their ultrafast charge-storage and fast-discharging characteristics. A slight deformation of the shape occurred around 0.2 to 0.4 V attributable to minor pseudo-activity, which is also concurrent with the CV measurements. A comparison of the gravimetric capacitance of the three COFs, calculated from Eq1 and Eq2 (Figure 4.21 Table 4.4), revealed that the IISERP-COF10 delivered the highest specific capacitance (546 F/g @ 500 mA/g) among all the COFs reported so far (Figure 4.22.A).^{11,29,31,38} While the IISERP-COF11 and IISERP-COF12 store 310 and 400 F/g of charge, respectively. Interestingly, the observed capacitances do not follow the increasing number of -OH groups as we move from IISERP-COF10 to IISERP-COF12, but they correlate well with their observed BET surface area (IISERP-COF10: 1233; IISERP-COF11: 921; IISERP-COF12: 1067 m²/g).

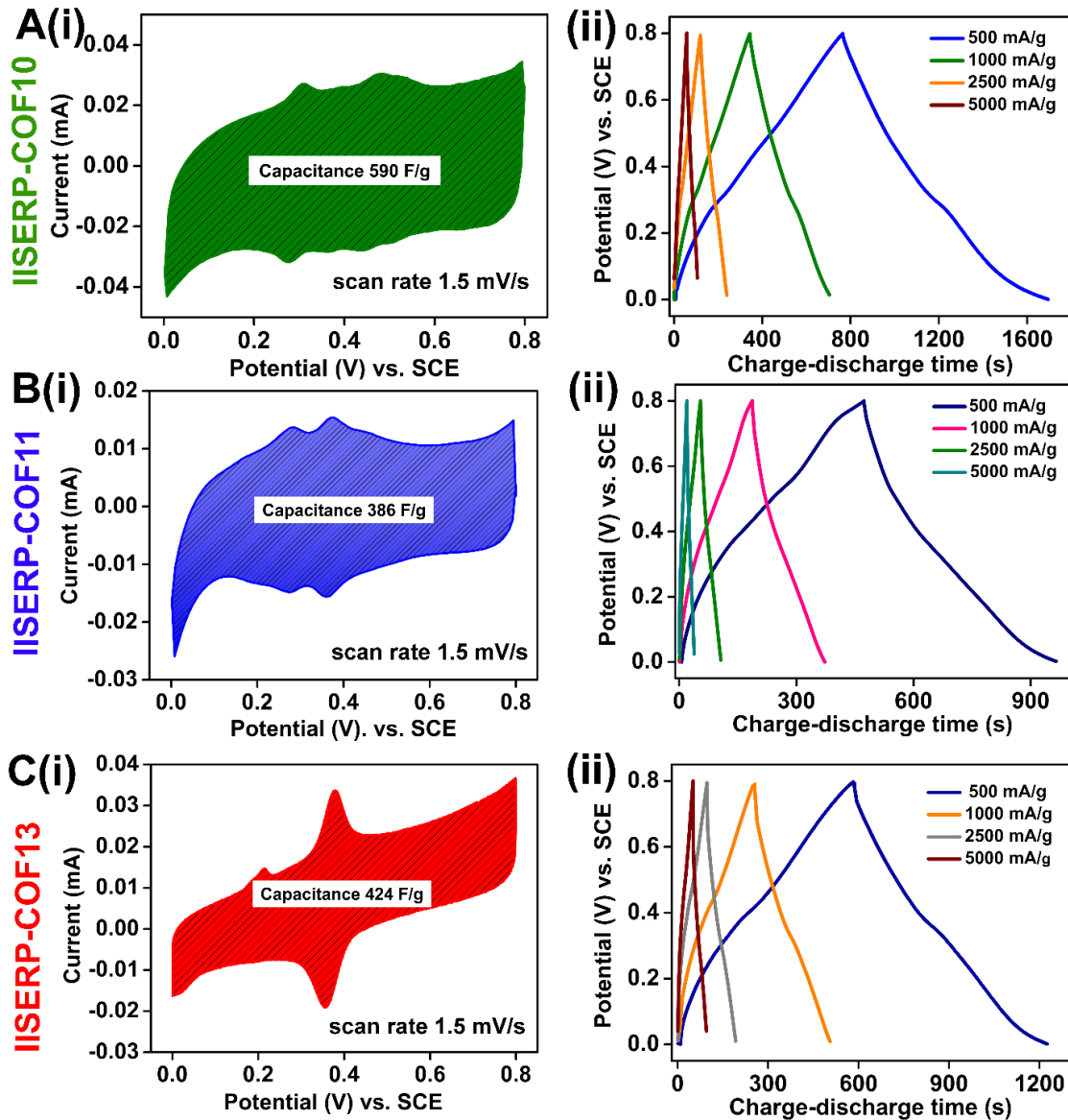


Figure 4.21. A(i), B(i) and C(i) Three-electrode CV measurements at 1.5 mV/s for the estimation of Sp. capacitance value of IISERP-COF10, COF11 and COF12 respectively. A(ii), B(ii) and C(ii) Galvanostatic charge-discharge curves for IISERP-COF10, IISERP-COF11 and IISERP-COF12 at varying current densities (from 500 mA/g to 5000 mA/g).

Note: Sp. capacitance obtained from the discharge times @500 mA/g current density are also compared with the Sp. capacitance obtained from the I-V plots derived from the CV measurements @1.5 mV/s.

The specific capacitance (C_{sp}) of the active electrode material was determined from the equation

$$C_{sp} = \frac{\int_{E_1}^{E_2} i(E) dE}{2(E_2 - E_1) \nu} \quad \text{.....Eq1 (using CV experiment)}$$

Where C_{sp} is the specific capacitance of the sample (F/g). E_1 , E_2 are the cutoff potentials in cyclic voltammetry. $i(E)$ is the instantaneous current (in Amps). $\int_{E_1}^{E_2} i(E) dE$ is the total voltammetric charge obtained by integration of positive and negative sweep in cyclic voltammograms, calculated by integrating the area under the I-V curves obtained from the CVs. $(E_2 - E_1)$ is the potential window width. m is the mass of sample (gm), ν is scan rate (V/s).

Similar to the CV experiment capacitance values are also compared using GCD curve with help of following equation

$$C_{sp} = \frac{(\int i(x) dx)}{\nu} \quad \text{.....Eq2 (using GCD curve)}$$

where C_{sp} is the specific capacitance (F/g) sample. i is the applied current density (A/g) (calculated from the coated samples' mass). t is the discharge time (s) at particular current density. V is the working potential window.

Table 4.4. Comparison of capacitance value obtained from CV and GCD

Electrode material	Capacitance calculated from CV (F/g) @1.5 mV/s	Capacitance calculation form GCD (F/g) @0.5 mA/cm ²
IISERP-COF10	590	547
IISERP-COF11	386	310
IISERP-COF12	424	400

Desirably, unlike in other COFs, the specific capacitance did not drop drastically with the increasing current density (Table 4.5). The IISERP-COF12 retains 82% (vs. 70% for IISERP-COF10; 75% for IISERP-COF11) of its capacity at 5 A/g (Figure 4.22.B). This possibly is due to the presence of an increased number of keto-enol stabilized hydroxyl groups in IISERP-COF12, which probably gives a statistical advantage to the incoming H⁺ ions when it comes to finding these active site. The ultra-micropores of 2- and IISERP-COF12 (~5.4 vs. 10.8 Å for IISERP-COF10), may also negatively impact the diffusion of the counter ions, SO₄²⁻.

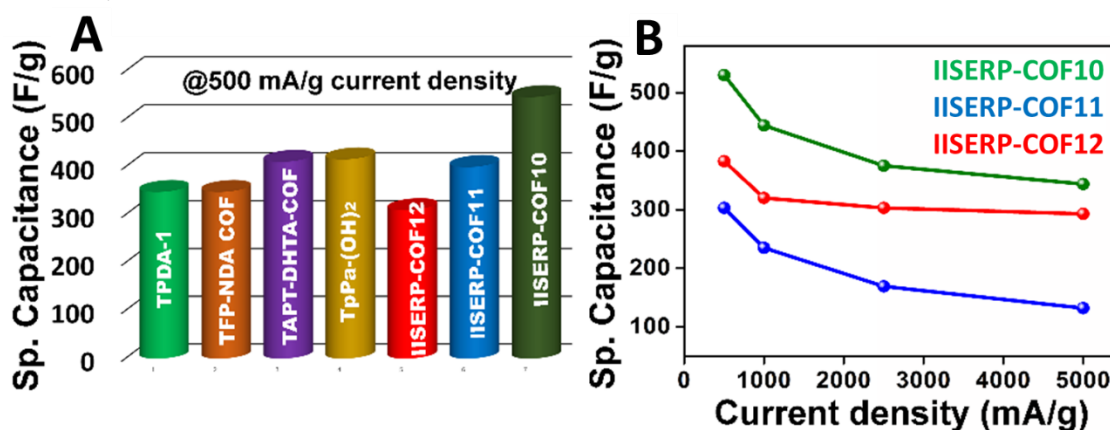


Figure 4.22. (A) A comparative bar-chart expressing the high-performance of IISERP-COF10 among all COF-derived supercapacitors. (B) Retention of the gravimetric capacitance by all the three COFs with the increase of current density from 500 mA/g to 5000 mA/g.

Table 4.5. A comparison of retention of Sp. capacitance of some high performing COF based capacitors.

COF used in the electrode	Increase of current density (A/g)	Retention of capacitance (in %)
IISERP-COF12	4.5	78
TaPa-Py COF	4.5	77.4
IISERP-COF10	4.5	73
TpPa-(OH) ₂	4.5	58
CAP - 1	9	56
IISERP-COF11	4.5	44

TpPa-COF-SWCNTs	3.8	20
DAAQ-BTA-3DG	2.5275	16.3

4.2.4. Contribution from EDLC and Faradaic Capacitance.

The high surface area of these COFs contributes mainly toward the EDLC behavior. But there can be contributions from the redox-active functional groups present in the structure. Interestingly, the redox activity remains, even at high scan rates (@1000 mV/s), suggesting that there is appreciable Faradaic activity. Taking advantage of the availability of a chemical formula for these crystalline COFs, we have partitioned the contributions from the EDLC and the pseudo-capacitance in a quantitative manner (eq 3, Figure 4.23 and Table 4.6). The graphical representation shows the systematic enhancement of the pseudo-capacitance from IISERP-COF10 COF to IISERP-COF12 COF. Notable is the difference in the potential at which this redox activity occurs in each of the COF. This can be explained by the systematic increase in the number of OH groups and their relative positioning, with respect to these pyridine groups. The latter could alter the potential at which the redox-active peaks appear as it impacts the synergy between these proximally placed functional groups. Also, the probability of existing in the keto form increases as the number of OH groups increases; hence, the IISERP-COF12 is expected to predominantly adopt the keto form. The affinity of keto groups toward protic electrolyte is higher over the enolic form. This explains the higher amount of pseudocapacitance observed for the IISERP-COF12, compared to the other two.

$I = k_1v + k_2v^{0.5}$ (power law).....Eq3.

Where I is the maximum current obtained at fixed scan rate, v is the scan rate, k₁ and k₂ are constants. The value of k₁ and k₂ have obtained by using two different equations at two different scan rates.

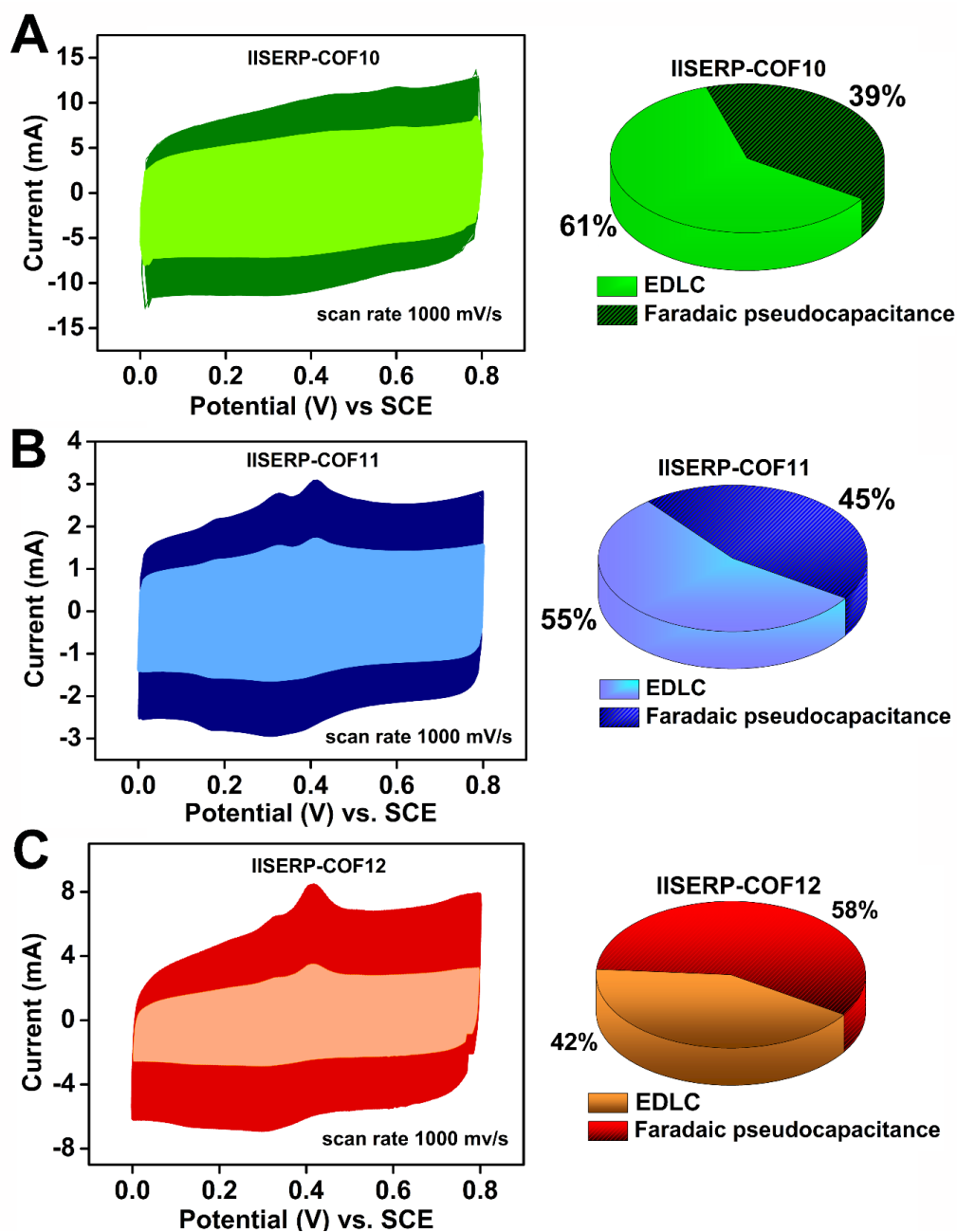


Figure 4.23. (A), (B), (C) Graphical representation of the contribution of EDLC and pseudocapacitance in each of the COFs @1000 mV/s scan rate.

Table 4.6. Capacitance contribution of each COFs coming from EDLC and pseudo activity.

Solution state three electrode system		
COFs	Contribution from EDLC (in %)	Contribution from Faradaic pseudocapacitance (in %)
IISERP-COF10	61	39
IISERP-COF11	55	45
IISERP-COF12	42	58

Also, a comparison of the capacitance values between IISERP-COF12 COF and TpTta COF, with similar BET surface areas (see Figure 4.24 and Table 4.7), and reveals that the former shows a 75% enhancement of the pseudo-activity, because of the presence of the proton-able pyridine moieties.

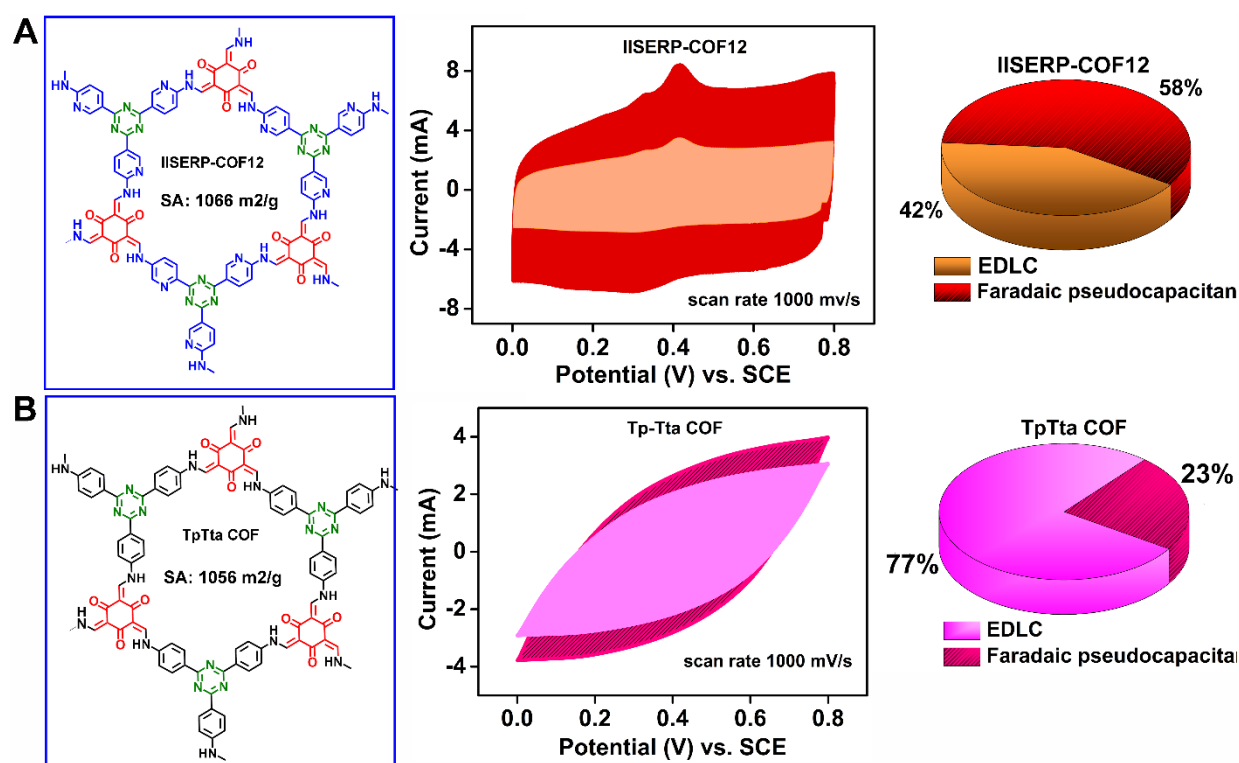


Figure 4.24. A Graphical representation of capacitance contribution from EDLC and pseudo activity of IISERP-COF12 and Tp-Tta COF.

Table 4.7. Comparison table of Sp. Capacitance of IISERP-COF12 and Tp-Tta COF.

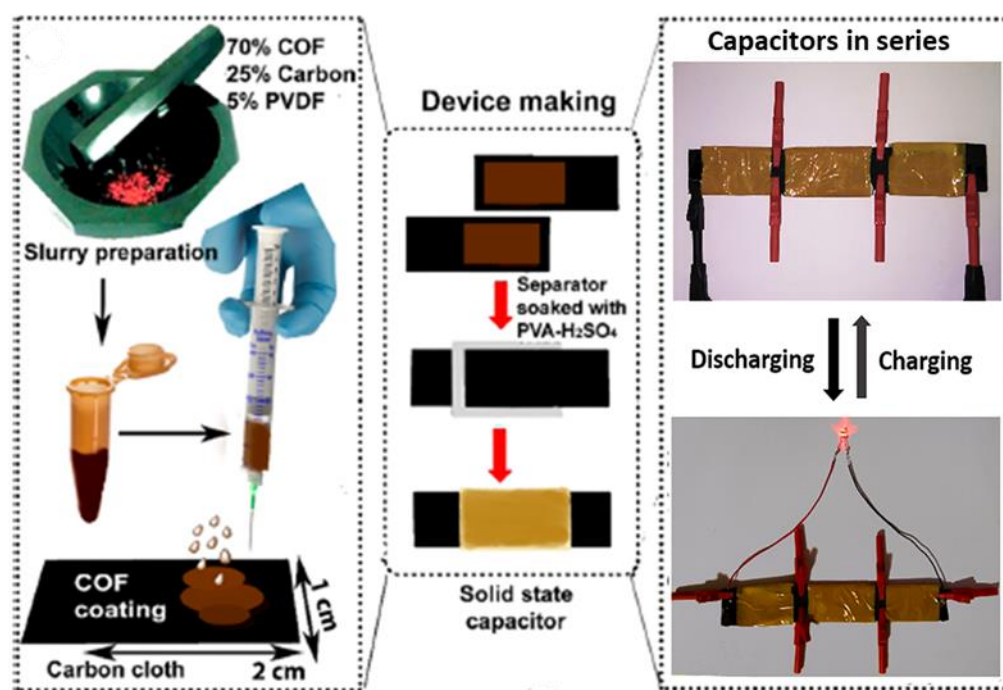
Electrode material	BET Surface area	Gravimetric capacitance calculation form GCD (F/g) @0.5 mA/cm ²	Areal Capacitance (mF/cm ²) in three electrode system @1.5 mV/s	Contribution of EDLC	Contribution of pseudocapacitance
<i>IISERP-COF12</i>	1066 m ² /g	400	50	42 %	58%
<i>Tp-Tta COF</i>	1056 m ² /g	228	24	77%	33%

4.2.5. Capacitance of the solid-state device:

The noticeable, stable, and high specific capacitance of the pyridine-enriched COFs encouraged us to assess their genuine performance in a more pragmatic solid-state device. Still, achieving high capacitance under solid-state conditions is quite challenging, compared to in the solution phase, because of decreased ionic mobility. A two-electrode solid state-capacitor device was fabricated by coating a 1 ml of the slurry made using a 70% COF (15 mg of IISERP-COF10/11/12) dispersion of N-methylpyrrolidone (NMP), 25 % of Super P carbon (4 mg) and 5% of PVDF binder (1mg) on a 1 x 2 cm² area of carbon cloth (Scheme 4.2). So the loading density of COF coated on carbon cloth turns out to be 7.5 mg/cm². The electrodes were dried at 80°C under vacuum for 48 hrs to remove the NMP. Then, one side of the electrode was allowed to wet completely by a gel electrolyte containing 1M H₂SO₄ in

polyvinyl alcohol (PVA).* Two electrodes were made by aforementioned procedure and were sandwich assembly was made by placing a Celgard separator in between.

[* **Preparation of the gel electrolyte:** To prepare the gel electrolyte, 2 g of concentrated H_2SO_4 (98%) was added to 20 mL of millipore water, 2g of PVA (polyvinyl alcohol) powders was added to it. The mixture was heated to 85 °C for about 30 minutes under continuous stirring, until the solution became clear.]



Scheme 4.2. A photographic representation of the electrode and the solid-state device preparation.

Variable scan rate (2.5 mV/s to 500 mV/s) CV measurements were conducted in the range of 0–0.8 V using these solid-state capacitors (see Figure.4.25). For all COFs, an archetypal rectangular-shaped CVs with large I–V area at both low and high scan rates revealed their high capacitance. Unlike the solution phase, here, the pseudo-capacitance feature was negligible. This is because both the working electrode and reference electrode are identical.

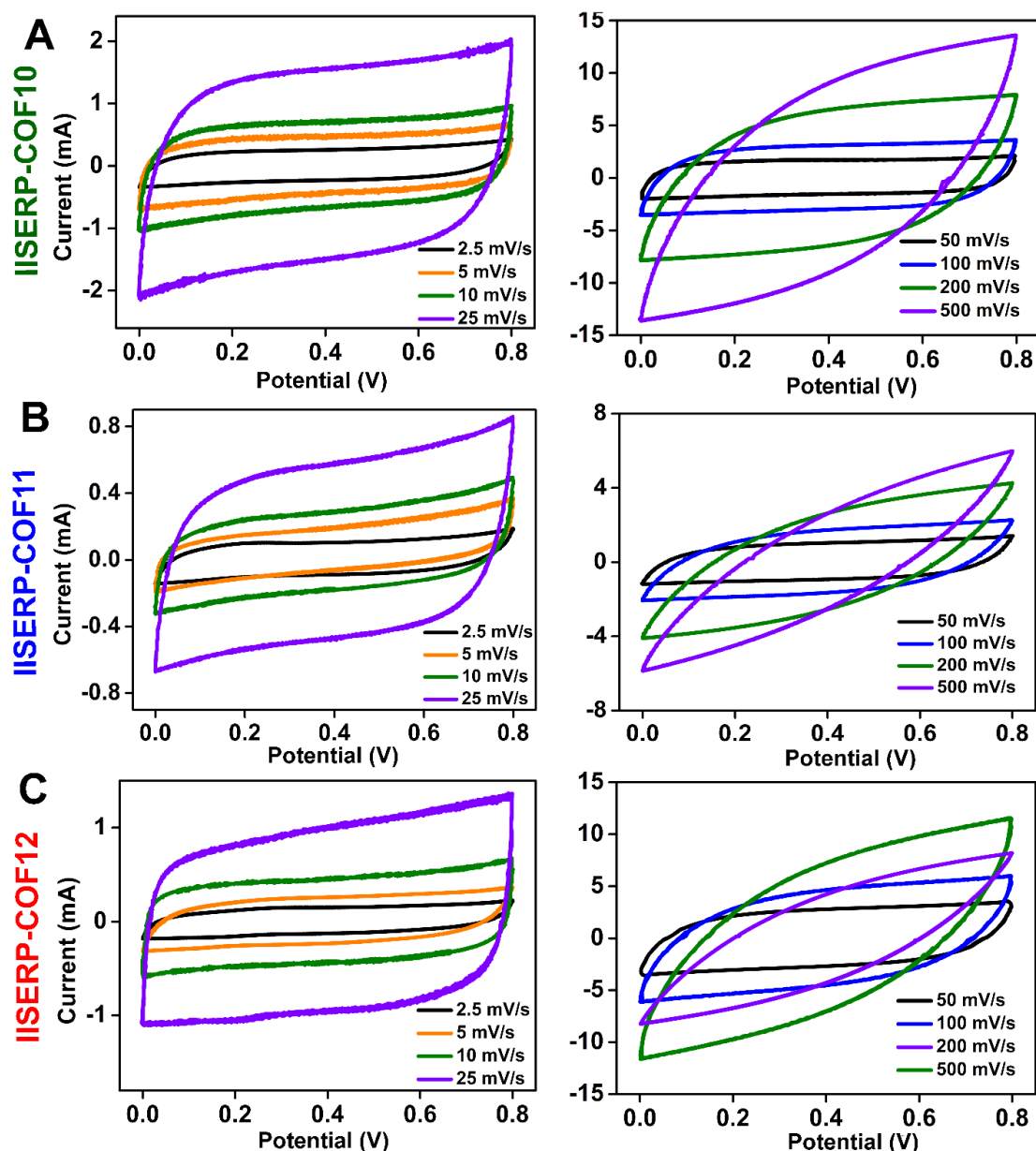


Figure 4.25. Two-electrode CV measurements using (A) IISERP-COF10, (B) IISERP-COF11 and (C) IISERP-COF12-derived solid state capacitor device at different scan rates (from 2.5 to 500 mV/s) within the potential window of 0-0.8 V. Perfect rectangular-shaped CVs were obtained at lower current densities. Notably, the area under the CV curves do not decrease abruptly even in high scan rates (50 to 500 mV/s).

Their areal capacitances estimated from the GCD (using eq 4) revealed some interesting aspects (Figure 4.26.A, 4.26.B, 4.26.C). Even under these relatively water-depleted solid-state conditions, the IISERP-COF10 delivers a specific capacitance of ~ 92 mF/cm² at 0.5 mA/cm². Meanwhile, the IISERP-COF11 and 3-OH have capacitance storage of 32 and 57 mF/cm². This facile EDLC formation confirms the sufficient wettability and high ion mobility endowed in the ordered porous structure of these COFs. Here also the trend of dropping of the sp. capacity is similar to the liquid electrolyte. IISERP-COF12 shows exceptional stability even at 5 mA/cm² current density (Figure 4.26.D). Only 18% drop of the sp. capacitance happens if we go from 0.5 mA/cm² to 5 mA/cm². Other two COFs show moderate stability with higher load of current. A comparison bar plot shows that IISERP-COF10 delivers higher areal capacitance under solid-state conditions, which is comparable to the aqueous electrolyte system. The observed areal

capacitance is higher than any other top-performing solid-state capacitors made using COF/MOF materials (see Figure 4.26.E).^{7,39-42} The cycling stability of all of these COF derived solid-state capacitors was tested over 10000 cycles (see Figure 4.26.E). IISERP-COF12 retains 95% of its initial capacity, indicating that there is no structural degradation or electrolyte drying. IISERP-COF10 and IISERP-COF11 retain 83% and 88% of their initial capacities, respectively (Figure 4.4.F). Several current collector choices were tried, but we find that the carbon cloth yields the best results, because of their ready wettability by the gel electrolyte. Critically, the solid-state device devoid of the active COF component displays no appreciable capacitance (see Figure A.4.9).

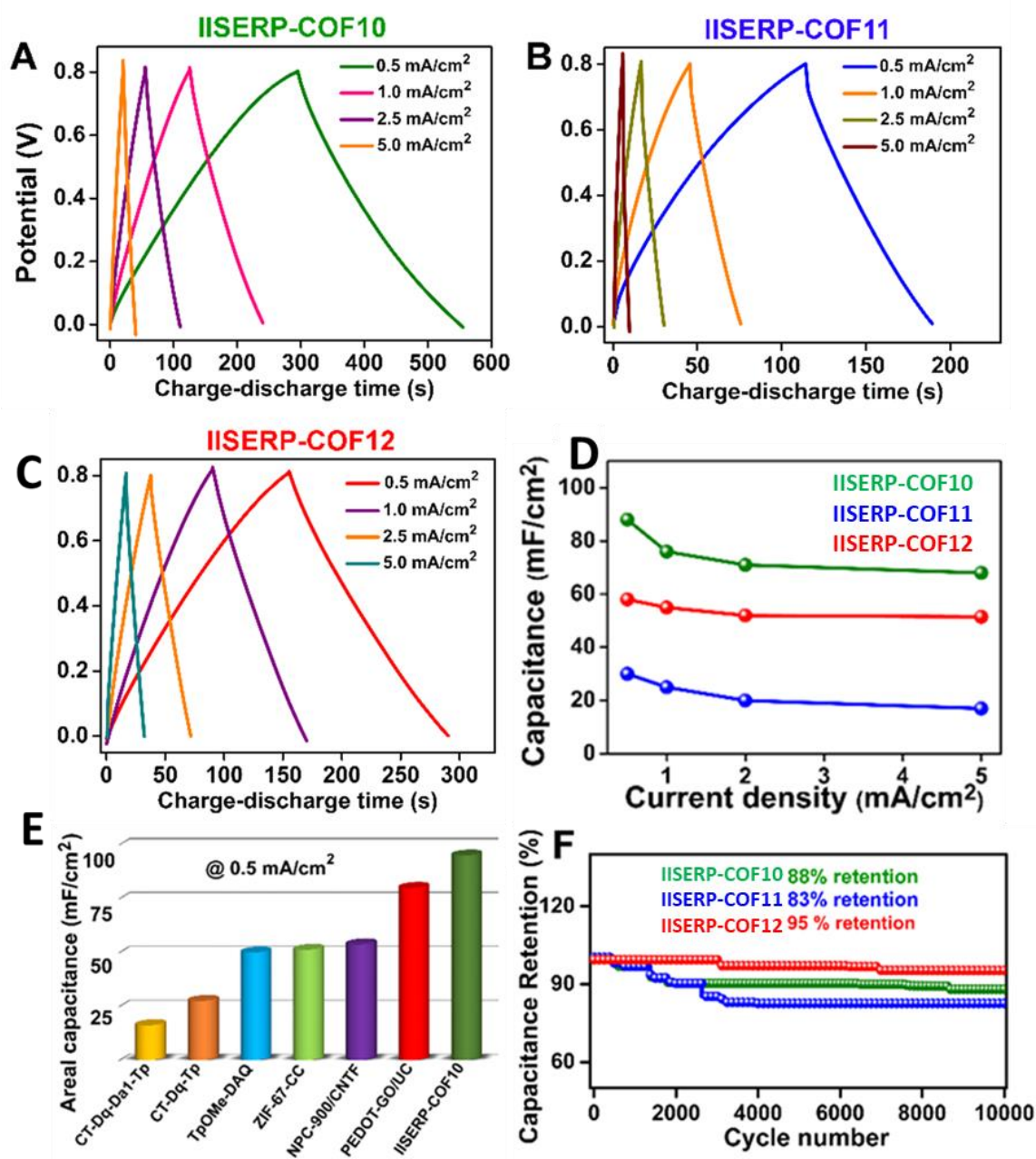


Figure 4.26. Galvanostatic charge-discharge curves of (A) IISERP-COF10 (B) IISERP-COF11 and (C) IISERP-COF12 using solid state two-electrode set-ups at variable current densities. (D) Capacitance retention at high currents (E) Comparison bar plots of areal capacitance of COF/MOF derived solid state capacitors along with IISERP-COFs. (F) Cyclic stability of the IISERP-COFs derived solid state capacitors.

Discharge time obtained from the GCD curve were used for the estimation of the areal Sp. capacitance of the COFs at different current densities. Areal capacitance was calculated using the following equation

$$C_A = (i \times t)/(V \times a) \dots \dots \dots \text{Eq4.}$$

Where C_A is the areal capacitance (mF/cm^2), 'i' is areal current density (mA/cm^2), 't' is the discharge time (sec), V is working potential window. 'a' is the geometrical area of the COF coated region on the electrode surface (cm^2)

This high solid-state areal capacitance is preserved in a wide range of current densities (from $0.5 \text{ mA}/\text{cm}^2$ to $5 \text{ mA}/\text{cm}^2$) with no perceptible decrease in capacitance. This reflects in the highest power density for IISERP-COF12 ($140 \mu\text{W}/\text{cm}^2$ at $0.5 \text{ mA}/\text{cm}^2$). Meanwhile, the IISERP-COF10 and IISERP-COF11 deliver 98 and $102 \mu\text{W}/\text{cm}^2$ (Table 4.8). The higher power density of IISERP-COF12 COFs comes from its higher electrochemical stability even at high current density. Even at $5 \text{ mA}/\text{cm}^2$ it shows negligible capacitance loss compare to other two COFs. Meanwhile IISERP-COF16 achieved higher energy density ($8.18 \mu\text{Wh}/\text{cm}^2$ at $0.5 \text{ mA}/\text{cm}^2$) as it possess higher capacitance than other two. That means a material with high surface area shows high EDLC behaviour hence high energy density.

Energy density and power density from the solid state two-electrode system were calculated using the following equation

$$E_d = \frac{C_A}{2 \times 3600} V^2 \dots \dots \dots \text{Eq5}$$

E_d is energy density (mWh/cm^2), C_A is the areal capacitance calculated (mF/cm^2) by the charge-discharge method and V is the working potential window.

$$P_d = \frac{E_d}{t} \dots \dots \dots \text{Eq6}$$

P_d power density (mW/cm^2), E_d is the energy density (mWh/cm^2), 't' is the discharge time in hour calculated from GCD curve.

Table 4.8. Energy and power densities of the COF-derived solid state capacitors

COF Code	Energy Density ($\mu\text{Wh}/\text{cm}^2$)	Power density ($\mu\text{W}/\text{cm}^2$)
IISERP-COF10	8.18	98.14
IISERP-COF11	2.84	102.384
IISERP-COF12	5.10	140.72

Three individual solid-state devices derived from IISERP-COF10 are connected in series to enhance the working potential window. After complete charging, the assembled device was able to make a light-emitting diode (LED) glow for ~ 1 min. (See Figure 4.27). The working potential window of the LED was 1.8 to 2.5 V. At low scan rate and low current densities, ample amount of charge is stored which enables lighting the LED.

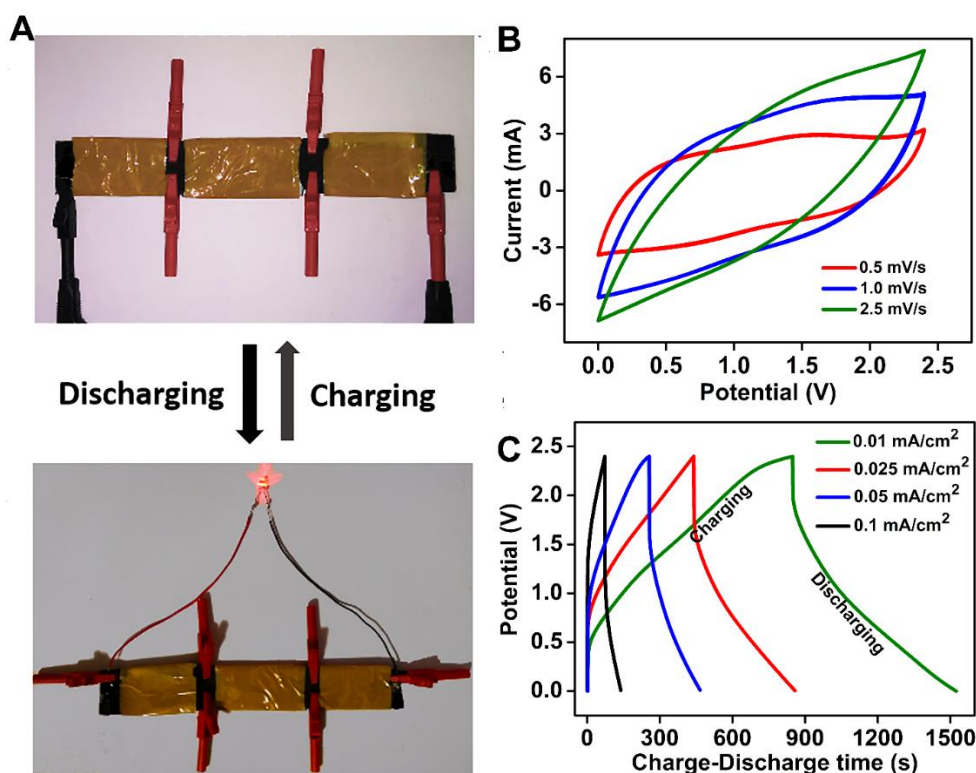


Figure 4.27. (A) Pictorial representation of glowing an LED bulb using IISERP-COF10 derived solid state capacitor device. (B) CV measurements of series connected device within the potential window of 0 V-2.4 V in different scan rates. (C) GCD curve obtained at variable current densities using the series connected device.

4.3. Conclusion:

The study of these COFs with high structural similarity and systematically varying chemical functionality reveals the ability to tune the capacitive character by atomic manipulation. High surface areas and ordered micropores give rise to significant EDLC in these COFs. Simultaneously, the interplay between the pyridine, triazine, Schiff, and hydroxyl moieties generate noticeable pseudo-capacitance from redox reactions. Interestingly, this redox activity is impacted by the concentration of hydroxyl groups and their relative positioning, with respect to other functional groups. In a broader perspective, the study accentuates the potential of pyridine functionalized COFs to deliver the high power density, rate performance, and cycle times required in rapid-power-delivery devices.

Acknowledgement

We thank IISER-Pune for support and the funding by DST for material for energy storage (No. DST/TMD/MES/2k17/103) program and the SERB (No. EMR/2016/003553). S.H. thanks DST-Inspire for financial support. We thank MHRD-FAST and the IUSSTF program for the support.

References:

- [1] Diercks, C. S.; Yaghi, O. M., The atom, the molecule, and the covalent organic framework. *Science* **2017**, 355, eaal1585.
- [2] Lohse, M. S.; Bein, T., Covalent organic frameworks: Structures, synthesis, and applications. *Adv. Funct. Mater.* **2018**, 28, 1705553.
- [3] Lyle, S. J.; Waller, P. J.; Yaghi, O. M. Covalent Organic Frameworks: Organic Chemistry Extended into Two and Three Dimensions, *Trends in Chemistry*, **2019**, 1, 172-184.
- [4] Wang, M.; Guo, H.; Xue, R.; Li, Q.; Liu, H.; Wu, N.; Yao, W.; Yang, W., Covalent organic frameworks: A new class of porous organic frameworks for supercapacitor electrodes. *ChemElectroChem.* **2019**, 6, 1–15.
- [5] Khattak, A. M.; Ghazi, Z. A.; Liang, B.; Khan, N. A.; Iqbal, A.; Li, L.; Tang, Z., A redox-active 2D covalent organic framework with pyridine moieties capable of faradaic energy storage. *J. Mater. Chem. A* **2016**, 4, 16312-16317.
- [6] DeBlase, C. R.; Hernández-Burgos, K.; Silberstein, K. E.; Rodríguez-Calero, G. G.; Bisbey, R. P.; Abruña, H. D.; Dichtel, W. R., Rapid and efficient redox processes within 2D covalent organic framework thin films. *ACS Nano* **2015**, 9, 3178-3183.
- [7] Halder, A.; Ghosh, M.; Khayum M, A.; Bera, S.; Addicoat, M.; Sasmal, H. S.; Karak, S.; Kurungot, S.; Banerjee, R., Interlayer Hydrogen-Bonded Covalent Organic Frameworks as High-Performance Supercapacitors. *J. Am. Chem. Soc.* **2018**, 140, 10941-10945.
- [8] Bhanja, P.; Bhunia, K.; Das, S. K.; Pradhan, D.; Kimura, R.; Hijikata, Y.; Irle, S.; Bhaumik, A., A New Triazine-Based Covalent Organic Framework for High-Performance Capacitive Energy Storage. *ChemSusChem* **2017**, 10, 921-929.
- [9] Patra, B. C.; Khilari, S.; Satyanarayana, L.; Pradhan, D.; Bhaumik, A., A new benzimidazole based covalent organic polymer having high energy storage capacity. *Chem. Commun.* **2016**, 52, 7592-7595.
- [10] DeBlase, C. R.; Silberstein, K. E.; Truong, T.-T.; Abruña, H. D.; Dichtel, W. R., β -Ketoenamine-linked covalent organic frameworks capable of pseudocapacitive energy storage. *J. Am. Chem. Soc.* **2013**, 135, 16821-16824.
- [11] Xu, Q.; Tang, Y.; Zhai, L.; Chen, Q.; Jiang, D., Pyrolysis of covalent organic frameworks: A general strategy for template converting conventional skeletons into conducting microporous carbons for high-performance energy storage. *Chem. Commun.* **2017**, 53, 11690-11693.

- [12] Kim, G.; Yang, J.; Nakashima, N.; Shiraki, T., Highly Microporous Nitrogen-doped Carbon Synthesized from Azine-linked Covalent Organic Framework and its Supercapacitor Function. *Chem. Eur. J.* **2017**, *23*, 17504-17510.
- [13] Wang, P.; Wu, Q.; Han, L.; Wang, S.; Fang, S.; Zhang, Z.; Sun, S., Synthesis of conjugated covalent organic frameworks/Graphene composite for supercapacitor electrodes. *RSC Adv.* **2015**, *5*, 27290-27294.
- [14] Mulzer, C. R.; Shen, L.; Bisbey, R. P.; McKone, J. R.; Zhang, N.; Abruña, H. c. D.; Dichtel, W. R., Superior charge storage and power density of a conducting polymer-modified covalent organic framework. *ACS Cent. Sci.* **2016**, *2*, 667-673.
- [15] Zha, Z.; Xu, L.; Wang, Z.; Li, X.; Pan, Q.; Hu, P.; Lei, S., 3D Graphene functionalized by covalent organic framework thin film as capacitive electrode in alkaline media. *ACS Appl. Mater. Interfaces* **2015**, *7*, 17837-17843.
- [16] Sun, B.; Liu, J.; Cao, A.; Song, W.; Wang, D., Interfacial synthesis of ordered and stable covalent organic frameworks on amino-functionalized carbon nanotubes with enhanced electrochemical performance. *Chem. Commun.* **2017**, *53*, 6303-6306.
- [17] Han, Y.; Zhang, Q.; Hu, N.; Zhang, X.; Mai, Y.; Liu, J.; Hua, X.; Wei, H., Core-shell nanostructure of single-wall carbon nanotubes and covalent organic frameworks for supercapacitors. *Chin. Chem. Lett.* **2017**, *28*, 2269-2273.
- [18] Liu, S.; Yao, L.; Lu, Y.; Hua, X.; Liu, J.; Yang, Z.; Wei, H.; Mai, Y., All-organic covalent organic framework/polyaniline composites as stable electrode for high-performance supercapacitors. *Mater. Lett.* **2019**, *236*, 354-357.
- [19] Sun, J.; Klechikov, A.; Moise, C.; Prodana, M.; Enachescu, M.; Talyzin, A. V., A molecular pillar approach to grow vertical covalent organic framework nanosheets on Graphene: hybrid materials for energy storage. *Angew. Chem. Int. Ed.* **2018**, *57*, 1034-1038.
- [20] Dogru, M.; Bein, T., On the road towards electreactive covalent organic frameworks. *Chem. Commun.* **2014**, *50*, 5531.
- [21] Li, T.; Zhu, W.; Shen, R.; Wang, H.-Y.; Chen, W.; Hao, S.-J.; Li, Y.; Gu, Z.-G.; Li, Z., Three-dimensional conductive porous organic polymers based on tetrahedral polythiophene for high-performance supercapacitors. *New J. Chem.* **2018**, *42*, 6247-6255.
- [22] Mullangi, D.; Dhavale, V.; Shalini, S.; Nandi, S.; Collins, S.; Woo, T.; Kurungot, S.; Vaidhyanathan, R., Low-Overpotential Electrocatalytic Water Splitting with Noble-Metal-Free Nanoparticles Supported in a sp^3 N-Rich Flexible COF. *Adv. Energy Mater.* **2016**, *6*.

- [23] Haldar, S.; Roy, K.; Nandi, S.; Chakraborty, D.; Puthusseri, D.; Gawli, Y.; Ogale, S.; Vaidhyanathan, R., High and Reversible Lithium Ion Storage in Self-Exfoliated Triazole-Triformyl Phloroglucinol-Based Covalent Organic Nanosheets. *Adv. Energy Mater.* **2018**, *8*, 1702170.
- [24] Daugherty, M. C.; Vitaku, E.; Li, R. L.; Evans, A. M.; Chavez, A. D.; Dichtel, W. R., Improved synthesis of β -ketoenamine-linked covalent organic frameworks via monomer exchange reactions. *Chem. Commun.* **2019**, *55*, 2680-2683.
- [25] Ahumada, G.; Oyarce, J.; Roisnel, T.; Kahlal, S.; del Valle, M. A.; Carrillo, D.; Saillard, J.-Y.; Hamon, J.-R.; Manzur, C., Synthesis, structures, electrochemical and quantum chemical investigations of Ni (II) and Cu (II) complexes with a tetradentate Schiff base derived from 1-(2-thienyl)-1, 3-butanedione. *New J. Chem.* **2018**, *42*, 19294-19304.
- [26] Karunathilake, A. A.; Thompson, C. M.; Perananthan, S.; Ferraris, J. P.; Smaldone, R. A., Electrochemically active porous organic polymers based on corannulene. *Chem. Commun.* **2016**, *52*, 12881-12884.
- [27] Seifert, S.; Schmidt, D.; Würthner, F., An ambient stable core-substituted perylene bisimide dianion: isolation and single crystal structure analysis. *Chem. Sci.* **2015**, *6*, 1663-1667.
- [28] Chakraborty, P.; Majumder, I.; Banu, K. S.; Ghosh, B.; Kara, H.; Zangrando, E.; Das, D., Mn (II) complexes of different nuclearity: synthesis, characterization and catecholase-like activity. *Dalton Trans.* **2016**, *45*, 742-752.
- [29] Chandra, S.; Chowdhury, D. R.; Addicoat, M.; Heine, T.; Paul, A.; Banerjee, R. Molecular Level Control of the Capacitance of Two-Dimensional Covalent Organic Frameworks: Role of Hydrogen Bonding in Energy Storage Materials. *Chem. Mater. Chem. Mater.* **2017**, *29*, 2074-2080.
- [30] Liu, W.; Ulaganathan, M.; Abdelwahab, I.; Luo, X.; Chen, Z.; Rong Tan, S. J.; Wang, X.; Liu, Y.; Geng, D.; Bao, Y., Two-dimensional polymer synthesized via solid-state polymerization for high-performance supercapacitors. *ACS nano* **2017**, *12*, 852-860.
- [31] Bhanja, P.; Das, S. K.; Bhunia, K.; Pradhan, D.; Hayashi, T.; Hijikata, Y.; Irle, S.; Bhaumik, A., A new porous polymer for highly efficient capacitive energy storage. *ACS Sustainable Chem. Eng.* **2017**, *6*, 202-209.
- [32] Jha, P. K.; Singh, S. K.; Kumar, V.; Rana, S.; Kurungot, S.; Ballav, N., High-level supercapacitive performance of chemically reduced Graphene oxide. *Chem* **2017**, *3*, 846-860.
- [33] Jeong, H. M.; Lee, J. W.; Shin, W. H.; Choi, Y. J.; Shin, H. J.; Kang, J. K.; Choi, J. W., Nitrogen-doped Graphene for high-performance ultracapacitors and the importance of nitrogen-doped sites at basal planes. *Nano Lett.* **2011**, *11*, 2472-2477.

- [34] Wu, Z. S.; Winter, A.; Chen, L.; Sun, Y.; Turchanin, A.; Feng, X.; Müllen, K., Three-dimensional nitrogen and boron co-doped Graphene for high-performance all-solid-state supercapacitors. *Adv. Mater.* **2012**, *24*, 5130-5135.
- [35] Kinlen, P. J.; Mbugua, J.; Kim, Y.-G.; Jung, J.-H.; Viswanathan, S., Supercapacitors using n and p-type conductive polymers exhibiting metallic conductivity. *ECS Transactions* **2010**, *25*, 157-162.
- [36] Peurifoy, S. R.; Russell, J. C.; Sisto, T. J.; Yang, Y.; Roy, X.; Nuckolls, C., Designing Three-Dimensional Architectures for High-Performance Electron Accepting Pseudocapacitors. *J. Am. Chem. Soc.* **2018**, *140*, 10960-10964.
- [37] Bai, L.; Gao, Q.; Zhao, Y., Two fully conjugated covalent organic frameworks as anode materials for Lithium ion batteries. *J. Mater. Chem. A* **2016**, *4*, 14106-14110.
- [38] Das, S. K.; Bhunia, K.; Mallick, A.; Pradhan, A.; Pradhan, D.; Bhaumik, A., A new electrochemically responsive 2D π -conjugated covalent organic framework as a high performance supercapacitor. *Microporous Mesoporous Mater.* **2018**, *266*, 109-116.
- [39] Khayum M, A.; Vijayakumar, V.; Karak, S.; Kandambeth, S.; Bhadra, M.; Suresh, K.; Acharambath, N.; Kurungot, S.; Banerjee, R., Convergent Covalent Organic Framework Thin Sheets as Flexible Supercapacitor Electrodes. *ACS Appl. Mater. Interfaces* **2018**, *10*, 28139-28146.
- [40] Wang, L.; Feng, X.; Ren, L.; Piao, Q.; Zhong, J.; Wang, Y.; Li, H.; Chen, Y.; Wang, B., Flexible solid-state supercapacitor based on a metal–organic framework interwoven by electrochemically-deposited PANI. *J. Am. Chem. Soc.* **2015**, *137*, 4920-4923.
- [41] Li, H.; Fu, D.; Zhang, X.-M., A novel adenine-based metal organic framework derived nitrogen-doped nanoporous carbon for flexible solid-state supercapacitor. *Royal Society open science* **2018**, *5*, 171028.
- [42] Fu, D.; Zhou, H.; Zhang, X. M.; Han, G.; Chang, Y.; Li, H., Flexible solid–state supercapacitor of metal–organic framework coated on carbon nanotube film interconnected by electrochemically-codeposited PEDOT-GO. *ChemistrySelect* **2016**, *1*, 285-289.

Summary

2D-redox active Covalent Organic Frameworks (COFs) offer a one-dimensional porous nano-channel through its layered structure which opens up the possibility for grafting the nano-wall with electron-rich light elements. Hereby designed way we developed the Nitrogen and Oxygen-rich 2D-COFs since these two lightweight atoms are already known to interact with electro-positive charge carriers (Li^+ , Na^+ and H^+). Whenever these atoms are introduced into the frameworks in terms of redox-active functional groups, these COFs start acting as an apt candidate for energy storage in metal-ion-battery and supercapacitors. The stability originated from the β -ketoenamine form of these COFs prohibits the degradation and dissolution of the COF derived electrodes even under applied potential. The 2D network of the COFs when decorated with multiple redox-active functional groups it resembles like heteroatom doped Graphite structure. Hence, the potential of COF derived electrode as a suitable substitute for Graphitic materials has also been properly justified in our research. We have tried to utilise the scope of synthetic development of building monomers which enhanced the number of redox centres per unit of the 2D-COFs. This opens up the jackpot to fabricate high performing electrode materials in the field of battery and supercapacitors, something which is not so straight forward in heteroatom doped Graphite. Our thorough investigations and insightful findings improved the performance of the LIB, SIB and supercapacitors very systematically when we configured the corresponding electrodes with porous COF or COF derived materials. The real-time utility of COFs to decrease the charging time of the electronic device was always the key attention of our studies. Hence either the COFs were exfoliated into nanosheets or systematically tuned in such a way that it fulfils all electronic demands to be charged rapidly via faster diffusion of the charge carriers (H^+ , Li^+ , Na^+). We also tried our best to address some obvious challenges and grey areas related to the performance of the fabricated devices which is developed from the COF based electrodes. We do agree that the insitu experiments during the charging-discharging of the device could provide strong support to establish the mechanism of the charge carriers' interactions with the framework. That is something we are focusing on our future works. The wonderful coherence of the experimental in-situ analysis with the computational modelling, along with thorough MD-simulation would draw the clear picture for the future development of the redox-active COFs as per requirement.

Appendix of The Chapters

Appendix 1

Table A.1.1. Atomic coordinates for the IISERP-CON1

Space group: P3

CELL	19.7782	19.7782	3.7839	90	90	120
C1	0.31302	0.57863	1.05911			
C2	0.2473	0.59708	1.04498			
C3	0.62353	0.56908	0.41606			
C4	0.74313	0.40332	0.00374			
C5	0.73459	0.32278	0.01485			
N6	0.55983	0.56372	0.60693			
N7	0.68067	0.64833	0.32548			
N8	0.65284	0.69569	0.46314			
C9	0.34913	0.93019	0.63161			
C10	0.67814	0.49388	0.09155			
N11	0.62562	0.49612	0.30972			
O12	0.52071	0.35133	0.00458			
C13	0.3718	0.83355	0.9622			
N14	0.32233	0.84907	0.77477			
O15	0.29699	0.4959	1.08088			
H16	0.68123	0.76059	0.43342			
H17	0.72628	0.55127	0.02628			
H18	0.46415	0.2996	0.03726			
H19	0.43474	0.88375	1.02001			
H20	0.24053	0.45488	1.18460			

Table A.1.2. Drop in surface area upon exfoliation of COF into nanosheets.

Covalent organic nanosheets (code)	BET surface area of the as-synthesized COF (in m ² /g)	BET surface area for the Exfoliated COF or nanosheets (in m ² /g)
TpTG_{Cl}	----	267
TpTG_{Br}	----	305
TpTG_I	----	298
TpPa-F₄	438	60.6
TpPa-1	535	34.6
TpPa-2	339	27.1
TpPa-NO₂	129	39.8

References:

(TpTG_{Cl}, TpTG_{Br}, TpTG_I) Chandra *et al.* *J. Am. Chem. Soc.* 2013, 135, 17853.

(TpPa-F₄, TpPa-1, TpPa-2, TpPa-NO₂) Mitra *et al.*, *J. Am. Chem. Soc.* 2016, 138, 2823.

Microscopy studies:

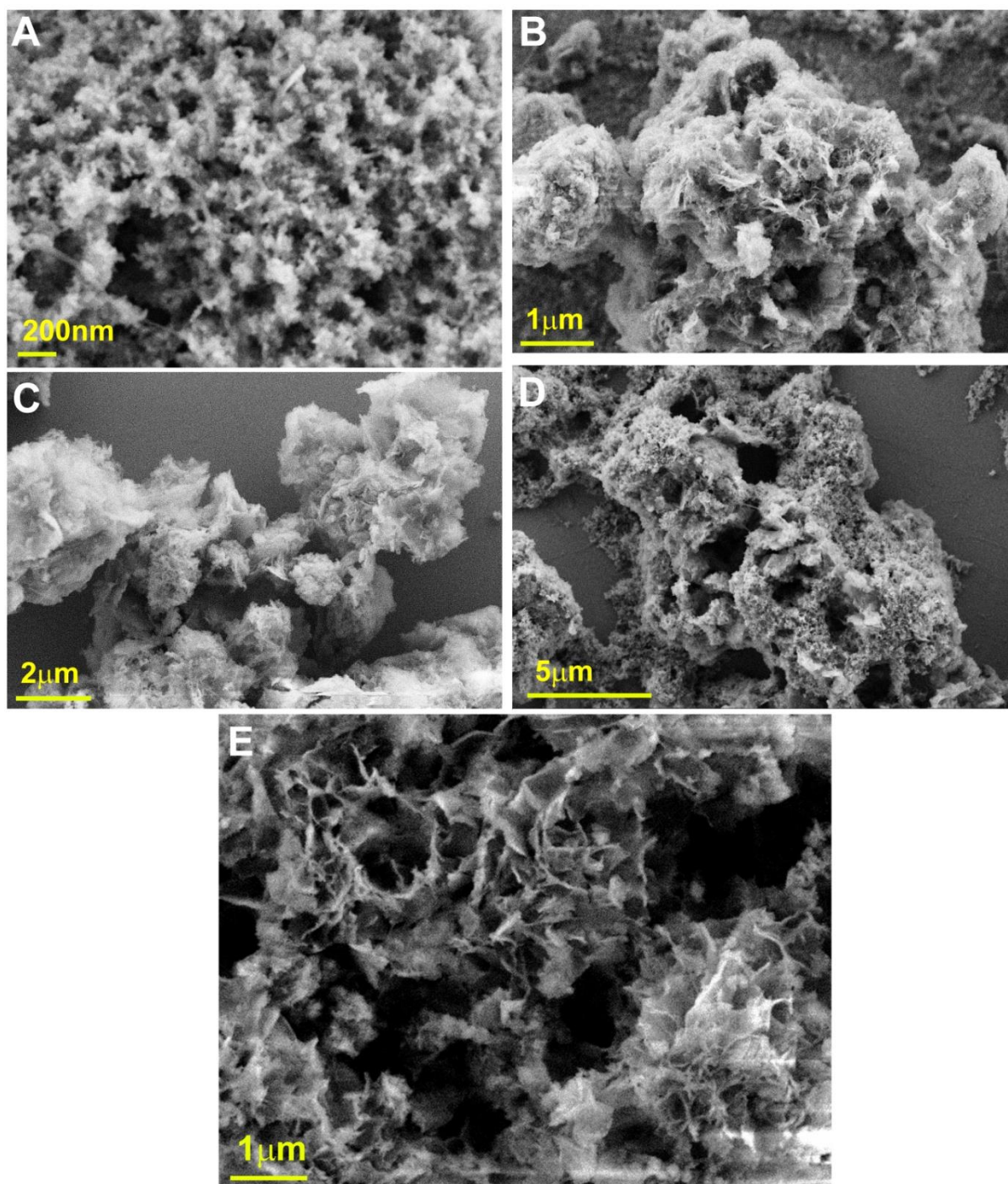


Figure A.1.1. (A)-(D) FE-SEM images at different resolutions showing the morphology of the IISERP-CON1. Nano sheet like morphology which presents in self-exfoliated form. (E) FE-SEM of the CON after 12 hrs of sonication in THF. The sample was stable to this prolonged sonication as confirmed by the PXRD and the porosity of measurements.

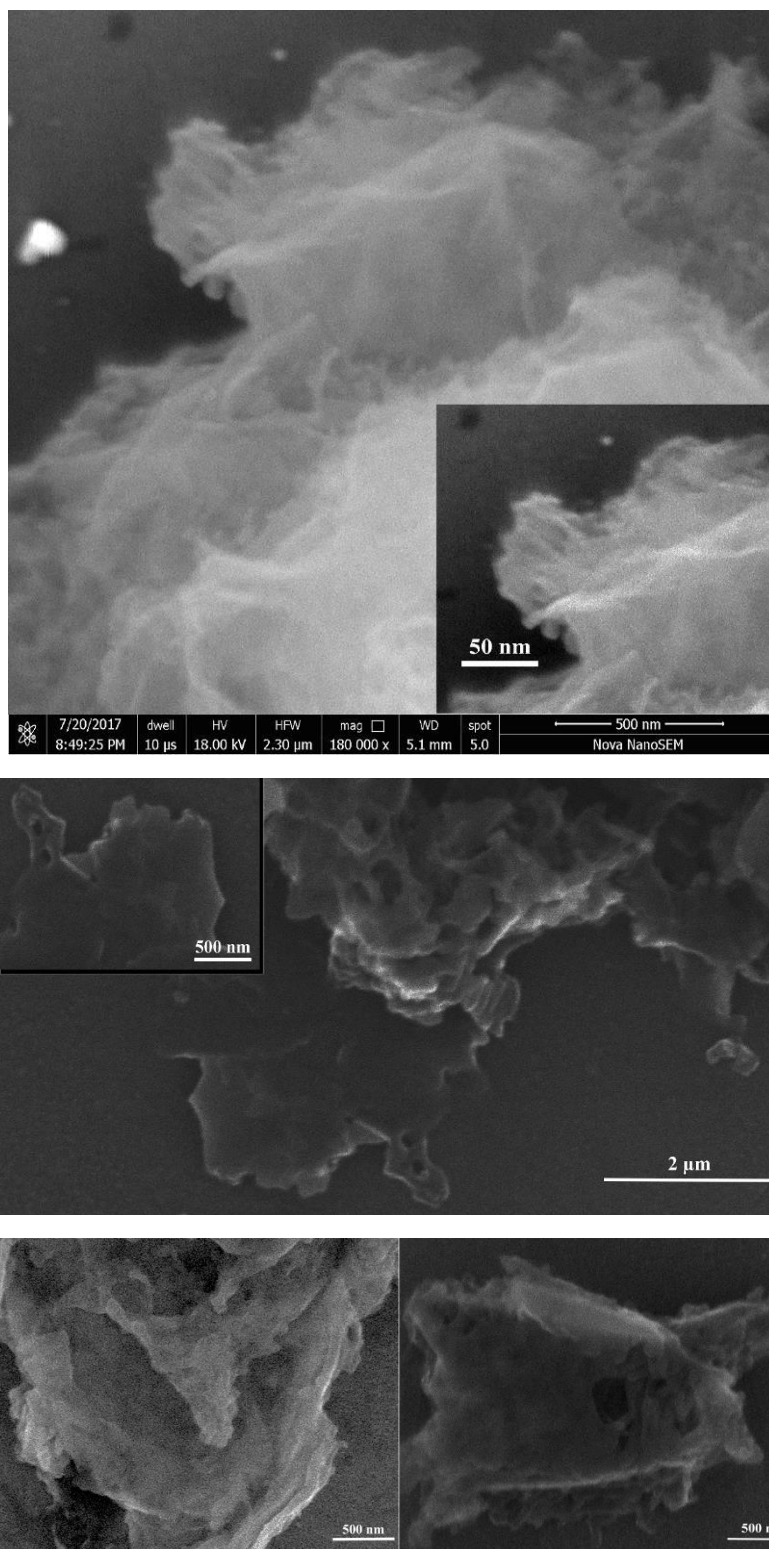


Figure A.1.2. FE-SEM images at different resolutions showing the morphology of the IISERP-CON1. Stacked flakes representing the nanosheet morphology can be observed. Dilute suspension of the samples were prepared by sonicating in MeOH (for 2hrs). The samples integrity to this treatment was confirmed by the PXRD and the porosity measurements.

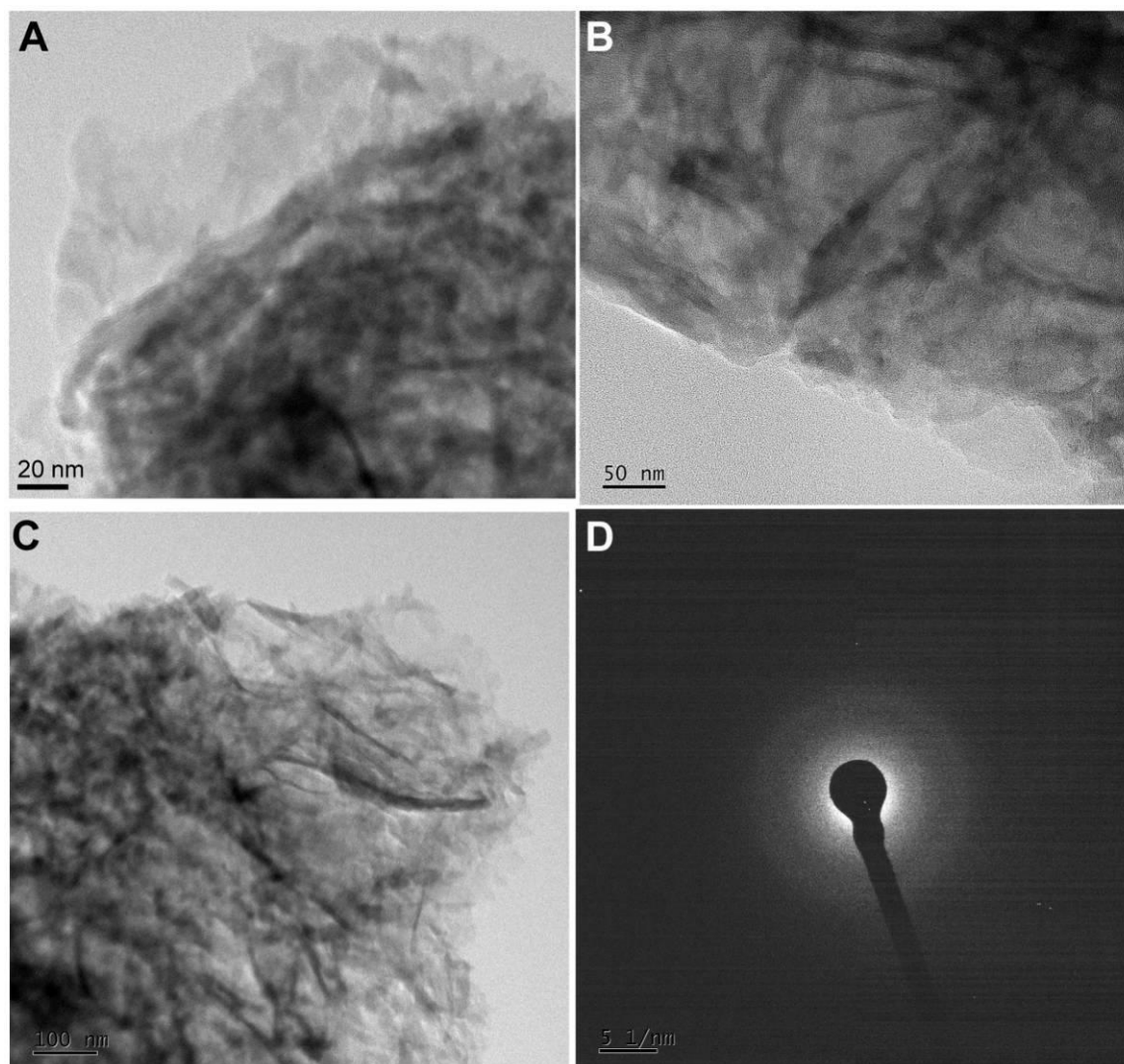
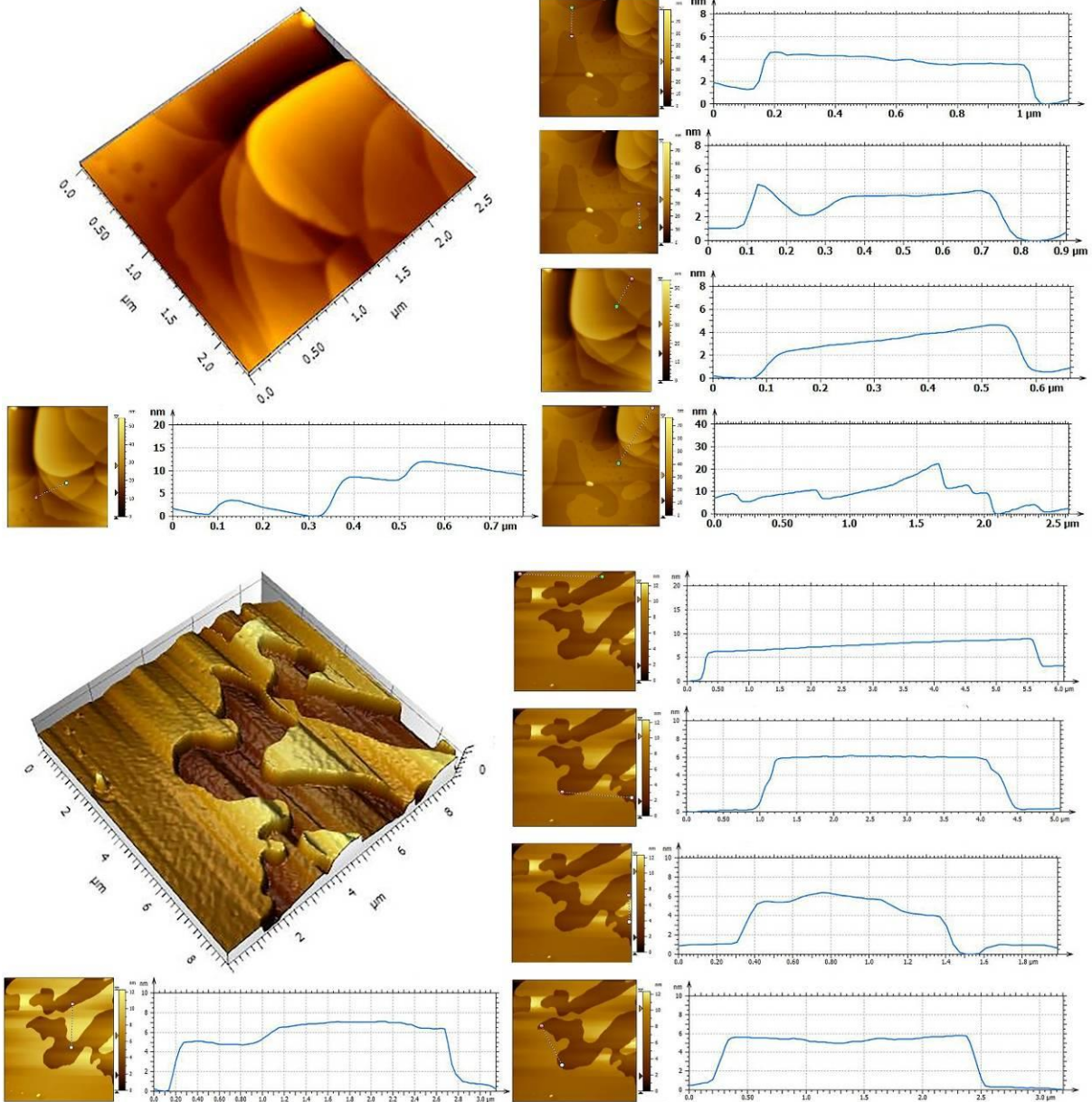


Figure A.1.3. FE-TEM image of the CON under different magnifications showing the nanosheets occurring as very thin flakes formed by stacking of few sheets. Some of these sheets wrap around the edges giving rise to the darker regions under the TEM. Other darker regions are from the inter-growing nanosheets. The SAED pattern indicates lack of high degree of crystallinity.



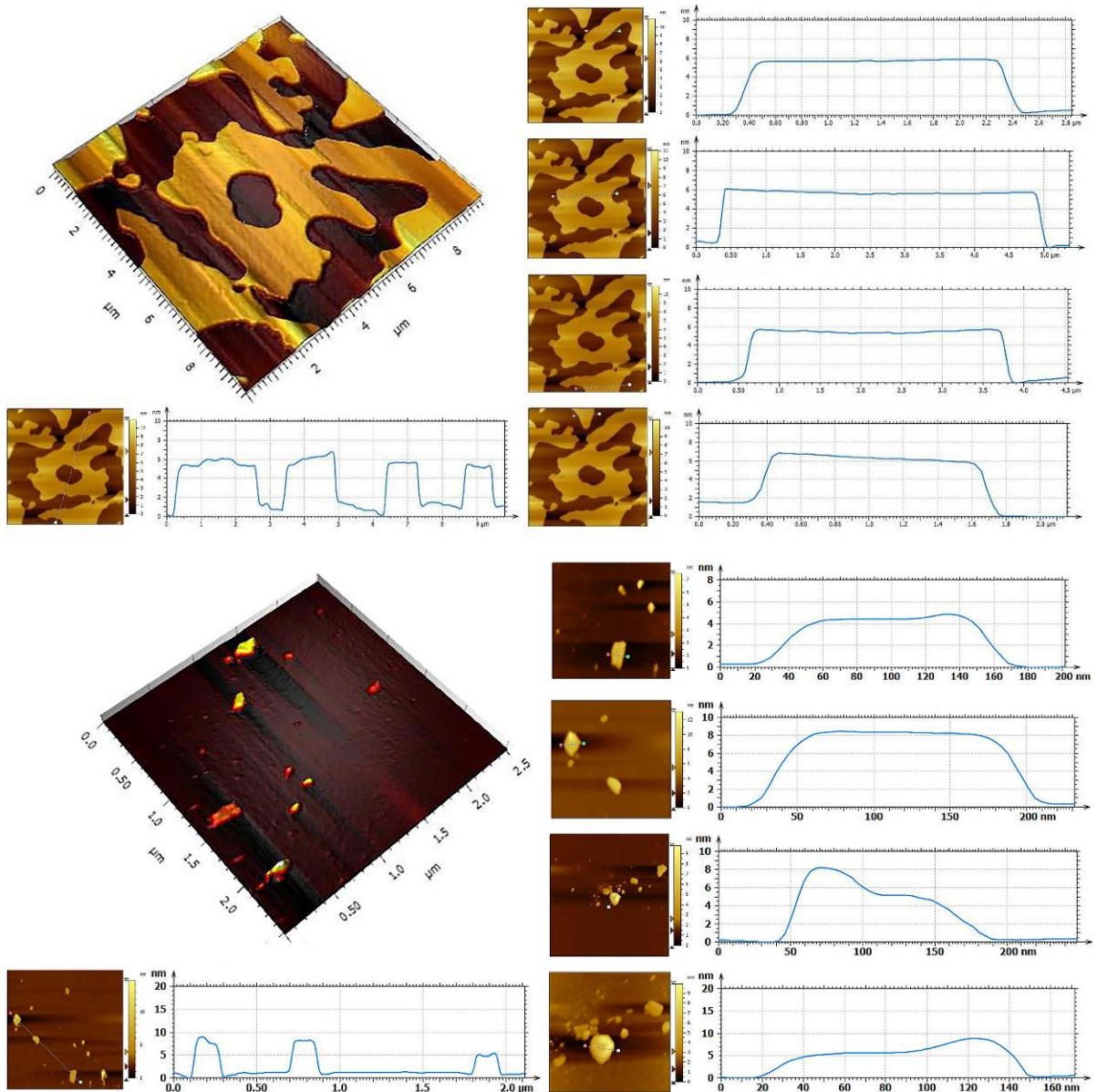


Figure A.1.4. Series of AFM images of the CON. The height profiles and 3D view from different regions of drop-casted sample prepared in MeOH. It shows an average thickness in the range of ~2 to 6nm suggesting the sample forming as uniform self-exfoliated nanosheets.

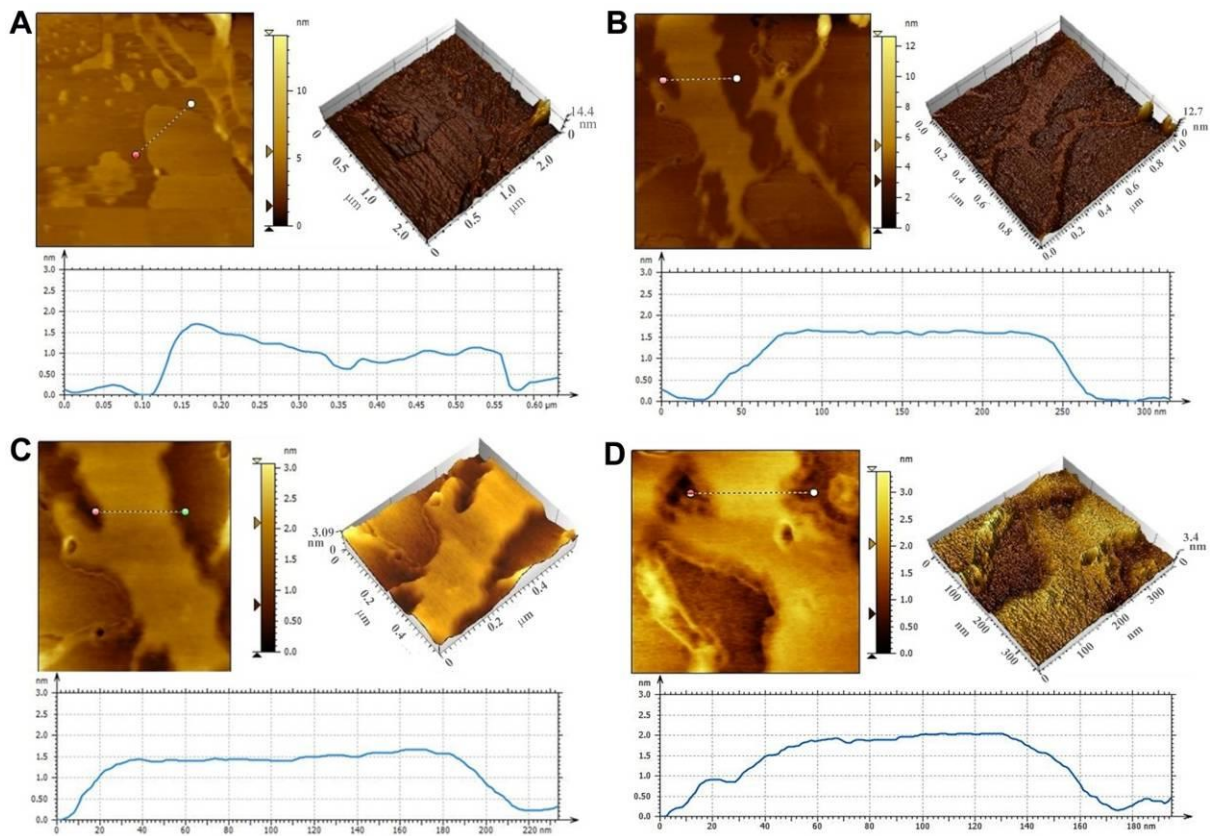
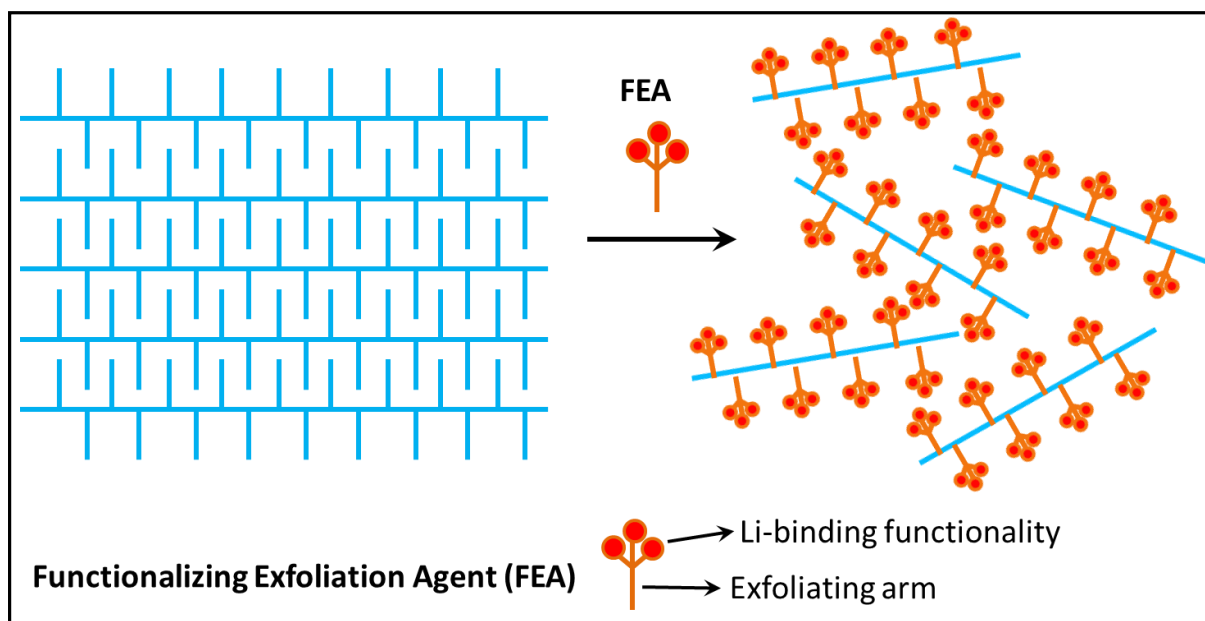


Figure A.1.5. AFM images of the CON, its height profile and 3D view from different regions of drop-casted sample prepared in THF. It shows an average thickness in the range of ~ 1.5 to 2 nm suggesting the sample forming as uniform self-exfoliated nanosheets.

Appendix 2

Concept of the Functionalizing Exfoliation Agent



Scheme A.2.1. Conceptual scheme illustrating the approach involving Functionalizing Exfoliation Agent to achieve simultaneous exfoliation and functionalization of 2D material, e.g. COF. Note: The exfoliation exposes the attached Li-binding groups which would directly impact their charge-discharge characteristics and thereby the rate-performance.

Synthesis of 2, 4, 6-Triformylresorcinol:

This compound was synthesized following previously reported method.(S1)

Synthesis of 2, 4, 6-Triformylphenol:

This compound was synthesized following previously reported method.(S2)

Synthesis of 2, 6-diaminoanthracene:

This compound was synthesized following previously reported method.(S3)

Synthesis of IISERP-COF7 and IISERP-COF8:

Table A.2.1. Atomic coordinates for IISERP-COF8.

Space Group P2/m

Lattice Parameters a = 30.951 b = 29.4946 c = 3.5457 $\alpha = 90$ $\beta = 90$ $\gamma = 120.6124$

SFAC	C	H	N	O	Occ.
C1	1	0.51578	0.55198	0.42539	1
C2	1	0.55154	0.53728	0.42549	1
C3	1	0.53759	0.48548	0.42556	1
C4	1	0.4707	0.39566	0.42559	1
C5	1	0.50586	0.38129	0.42569	1

Appendix of Chapter 2

C6	1	0.55936	0.41839	0.42572	1
C7	1	0.57323	0.47016	0.42566	1
N8	3	0.4024	0.59133	0.42517	1
C9	1	0.41158	0.63926	0.42513	1
C10	1	0.37314	0.65074	0.42511	1
C11	1	0.31863	0.61164	0.42512	1
C12	1	0.44809	0.96318	0.42545	1
C13	1	0.46331	0.01425	0.4255	1
C14	1	0.51487	0.05202	0.42552	1
C15	1	0.60424	0.07542	0.4255	1
C16	1	0.61889	0.12532	0.42555	1
C17	1	0.58214	0.14127	0.4256	1
C18	1	0.53094	0.10389	0.42558	1
N19	3	0.40721	0.80895	0.42526	1
C20	1	0.36025	0.77075	0.42523	1
C21	1	0.34822	0.71919	0.42517	1
C22	1	0.38889	0.70547	0.42508	1
C23	1	0.03697	0.4854	0.42544	1
C24	1	0.98589	0.44878	0.42548	1
C25	1	0.94798	0.46187	0.42551	1
C26	1	0.92444	0.52733	0.4255	1
C27	1	0.87453	0.49137	0.42555	1
C28	1	0.85859	0.43852	0.42559	1
C29	1	0.89604	0.42531	0.42556	1
N30	3	0.19166	0.60069	0.4253	1
C31	1	0.22888	0.59077	0.42522	1
C32	1	0.28102	0.62941	0.42517	1
C33	1	0.29741	0.68086	0.4252	1
C34	1	0.48439	0.44789	0.42551	1
C35	1	0.44864	0.46259	0.4254	1
C36	1	0.46258	0.51439	0.42534	1
C37	1	0.52948	0.60421	0.42532	1
C38	1	0.49432	0.61858	0.42524	1

Appendix of Chapter 2

C39	1	0.44082	0.58148	0.42522	1
C40	1	0.42695	0.52972	0.42526	1
N41	3	0.59778	0.40854	0.42578	1
C42	1	0.58861	0.36063	0.42582	1
C43	1	0.62705	0.34915	0.42583	1
C44	1	0.68157	0.38826	0.42581	1
C45	1	0.55209	0.03671	0.42549	1
C46	1	0.53687	0.98565	0.42544	1
C47	1	0.48531	0.94788	0.42542	1
C48	1	0.39594	0.92447	0.42541	1
C49	1	0.3813	0.87457	0.42536	1
C50	1	0.41804	0.85863	0.42533	1
C51	1	0.46924	0.89601	0.42537	1
N52	3	0.59298	0.19095	0.42567	1
C53	1	0.63994	0.22914	0.42571	1
C54	1	0.65198	0.28071	0.42577	1
C55	1	0.61131	0.29442	0.42587	1
C56	1	0.96323	0.51454	0.42548	1
C57	1	0.01432	0.55116	0.42543	1
C58	1	0.05222	0.53807	0.42541	1
C59	1	0.07577	0.4726	0.42542	1
C60	1	0.12567	0.50856	0.42538	1
C61	1	0.14161	0.56141	0.42534	1
C62	1	0.10417	0.57462	0.42537	1
N63	3	0.80855	0.39924	0.42564	1
C64	1	0.77132	0.40914	0.42571	1
C65	1	0.71918	0.37049	0.42576	1
C66	1	0.70279	0.31904	0.42574	1
O68	4	0.43436	0.73822	0.42498	1
O70	4	0.56585	0.26167	0.42599	1

Note: Atomic coordinates for IISERP-COF7 can be found in Ref.13 of the maintext.

Comparison of morphology between COFs and CONs:

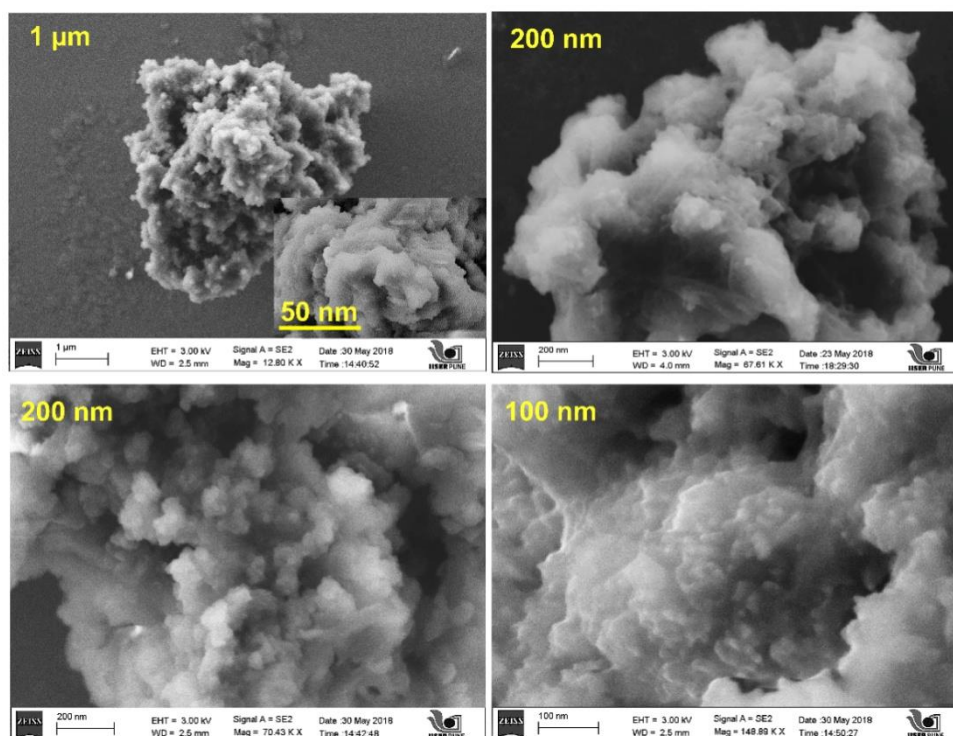


Figure A.2.1. FE-SEM images of IISERP-COF7 at different resolutions. Shows flake type morphology. At lower resolution, a fluffy cotton-like morphology was seen. Whereas at higher resolution, the presence of stacked flakes could be seen.

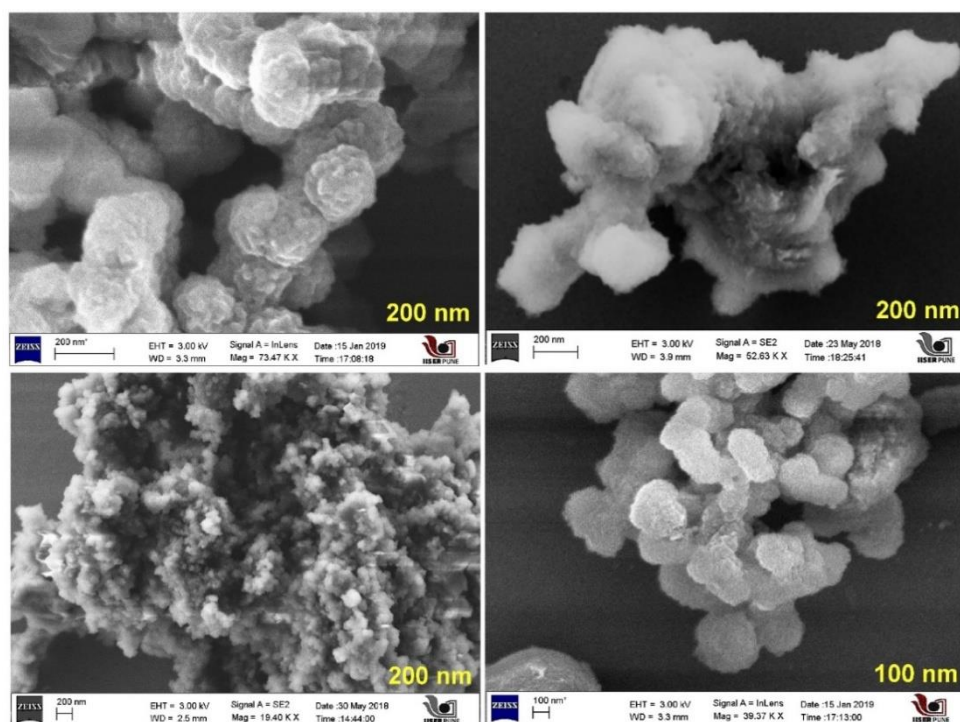


Figure A.2.2. FE-SEM images of IISERP-COF8 at different resolutions. At lower resolution, a fluffy cotton-like morphology was seen. Whereas at higher resolution, the presence of stacked flakes could be seen.

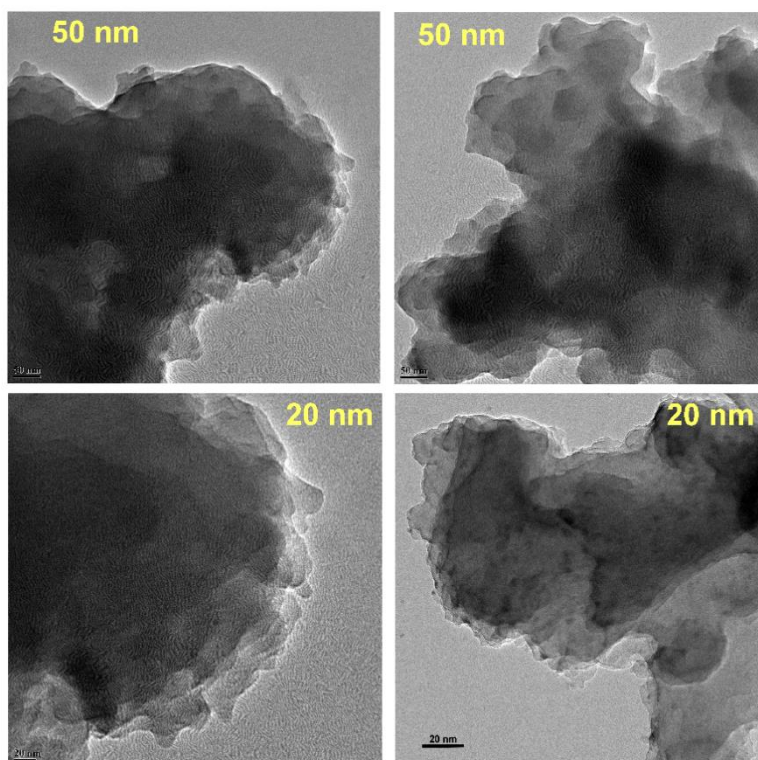


Figure A.2.3. HR-TEM images of the IISERP-COF7 under different magnifications showing the flakes formed by stacking of many sheets. Darker regions are from the stacking of many flakes.

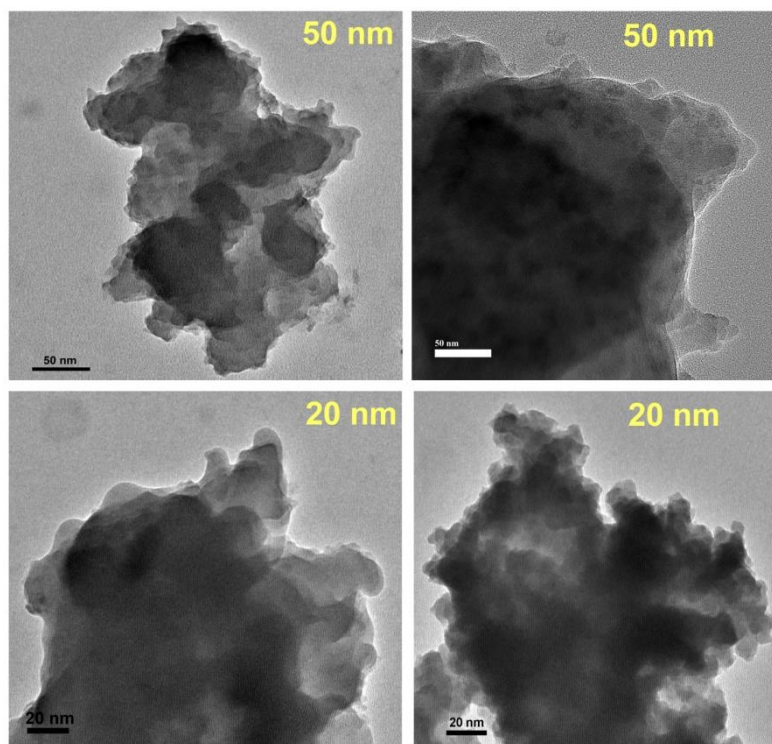


Figure A.2.4. HR-TEM images of the IISERP-COF8 under different magnifications showing the flakes formed by stacking of many sheets. Darker regions are from the stacking of many flakes.

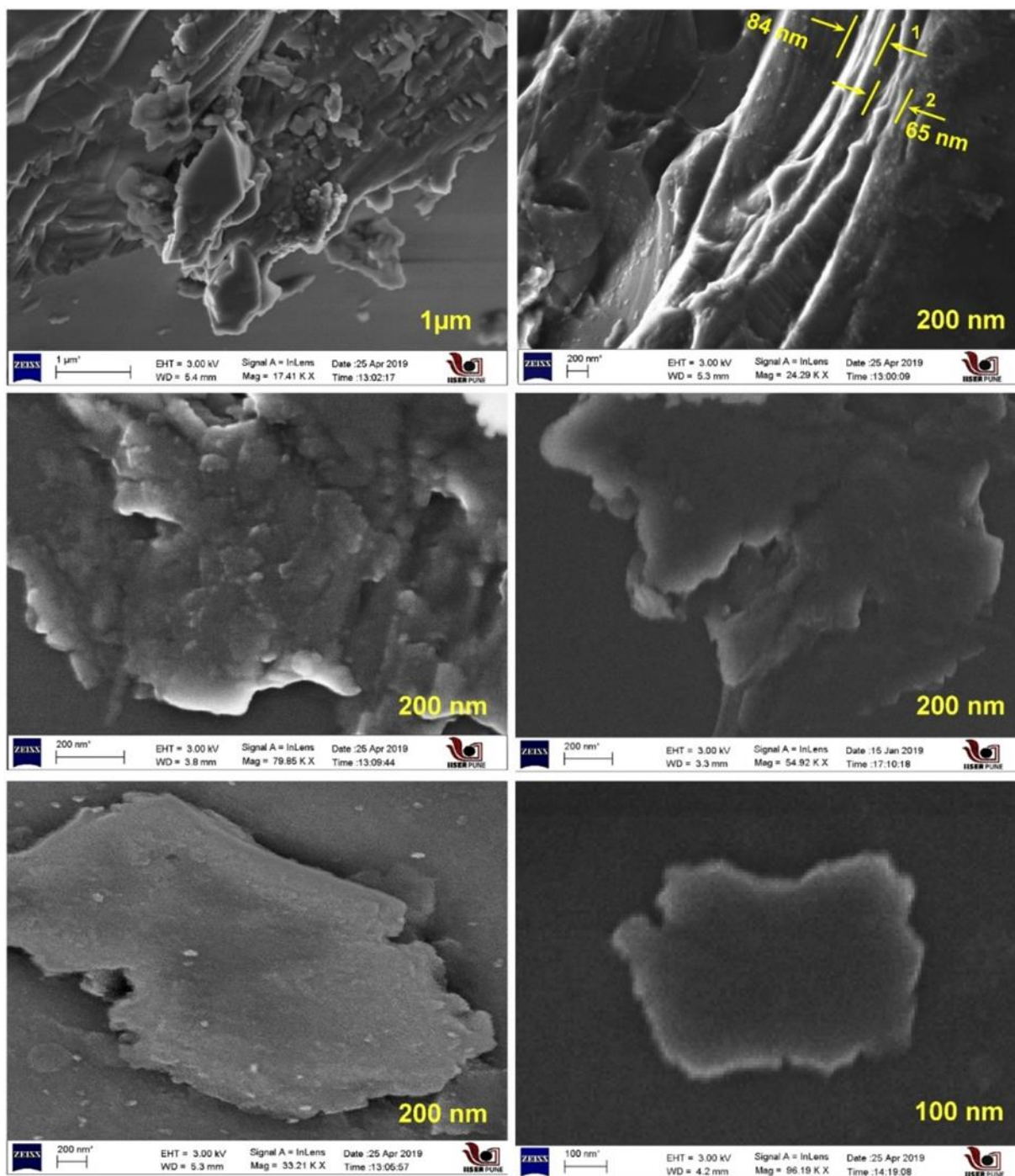


Figure A.2.5. FE-SEM images at different resolutions showing the morphology of the IISERP-CON2. Highly exposed stacked layers with 60 nm to 90 nm thickness representing the nanosheet morphology. Dilute suspension of the samples were prepared by sonicating in isopropanol (for 2hrs). The samples integrity to this treatment was confirmed by the PXRD and the porosity measurements.

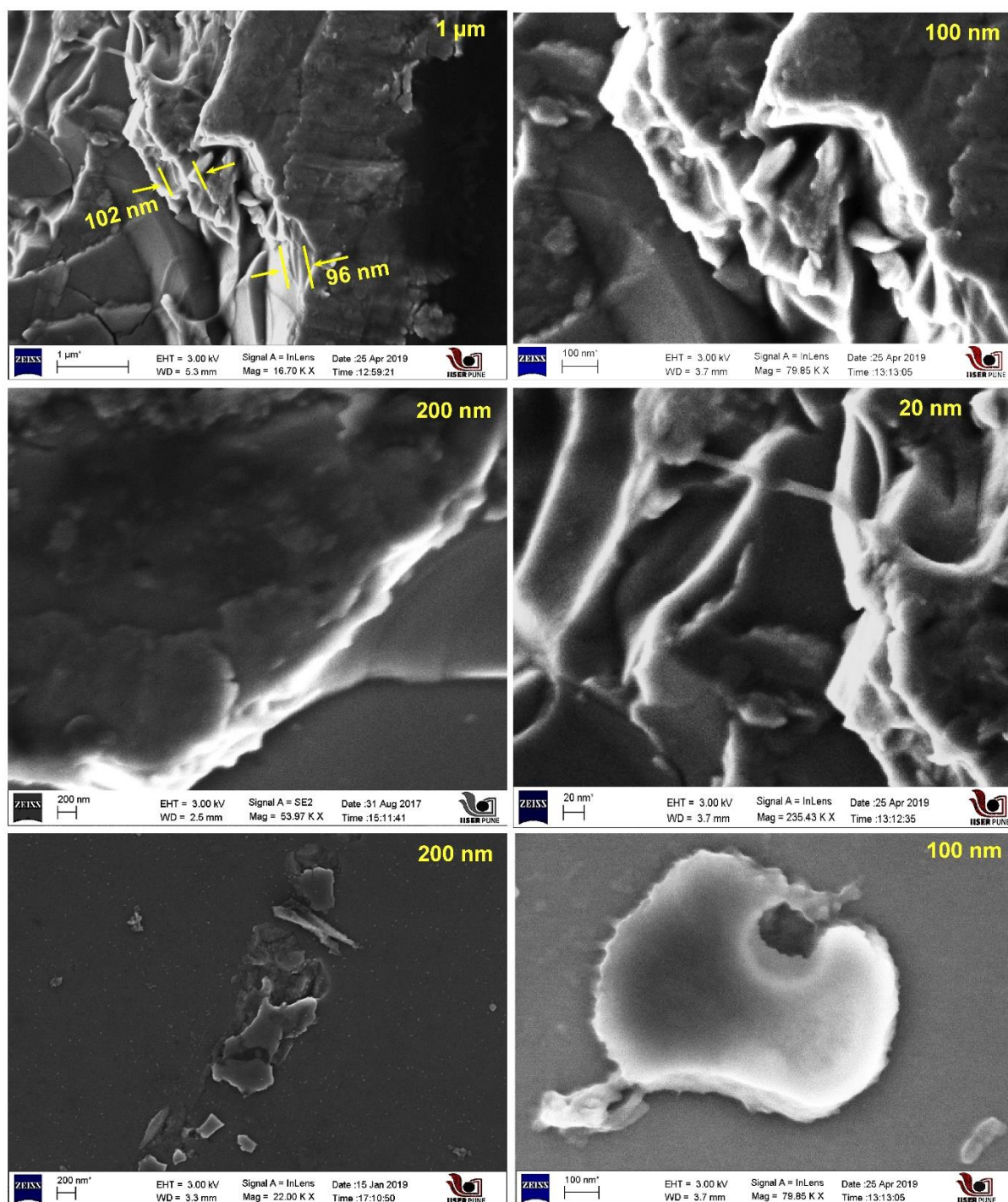


Figure A.2.6. FE-SEM images at different resolutions showing the morphology of the IISERP-CON3. Highly exposed stacked layers with 90 nm to 110 nm thickness representing the nanosheet morphology. Dilute suspension of the samples were prepared by sonicating in isopropanol (for 2hrs). The samples integrity to this treatment was confirmed by the PXRD and the porosity measurements.

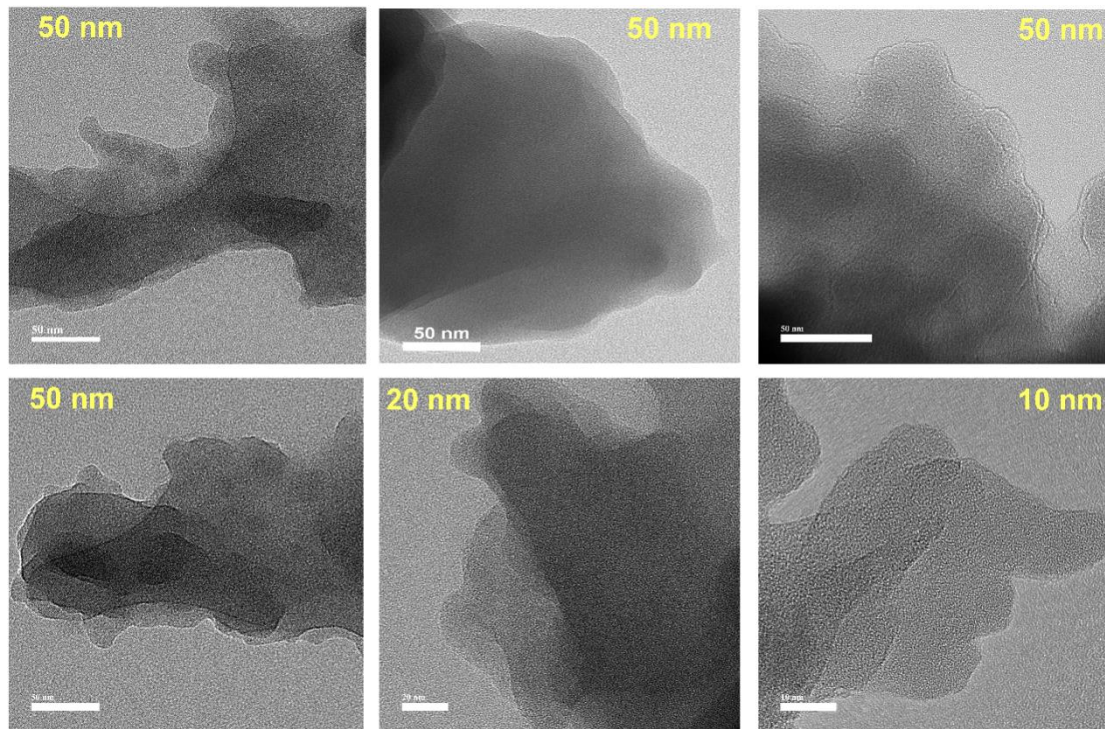


Figure A.2.7. HR-TEM image of the IISERP-CON2 under different magnifications showing the nanosheets occurring as very thin flakes formed by stacking of few sheets. Darker regions are from the thicker regions resulting from the stacking of nanosheets.

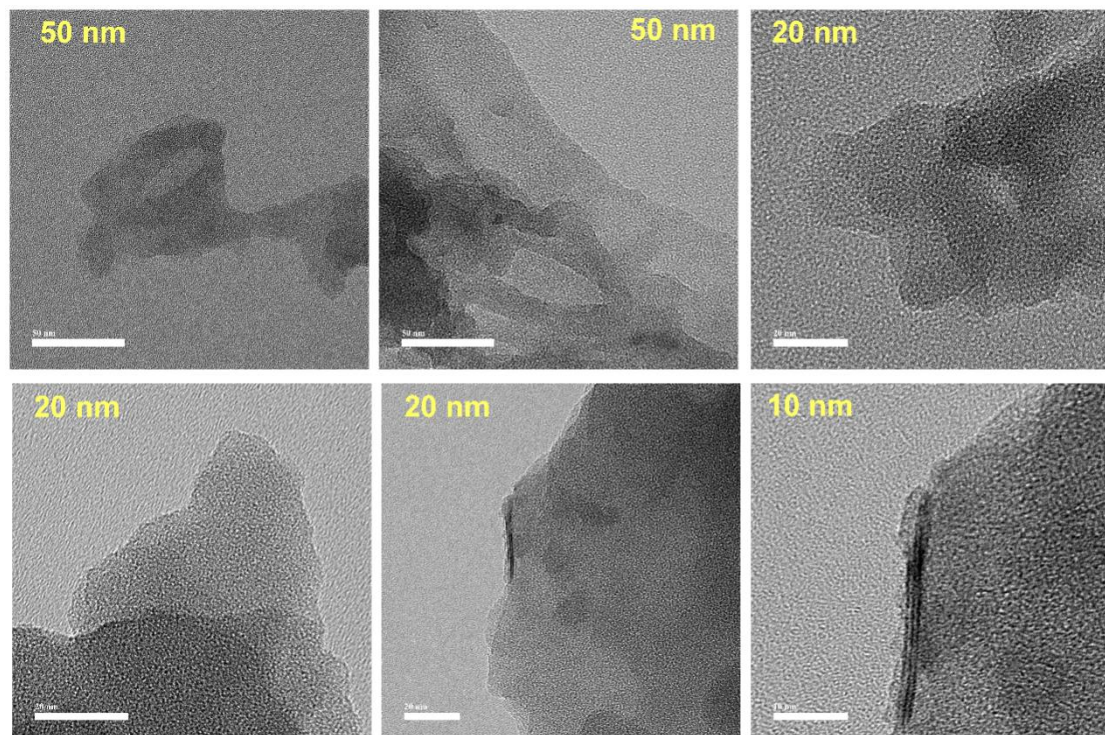


Figure A.2.8. HR-TEM image of the IISERP-CON3 under different magnifications showing the nanosheets occurring as very thin flakes formed by stacking of few sheets. Some of these sheets wrap around the edges giving rise to the darker regions under the TEM. Other darker regions are from the stacking of nanosheets.

Interlayer spacing distances of CONs:

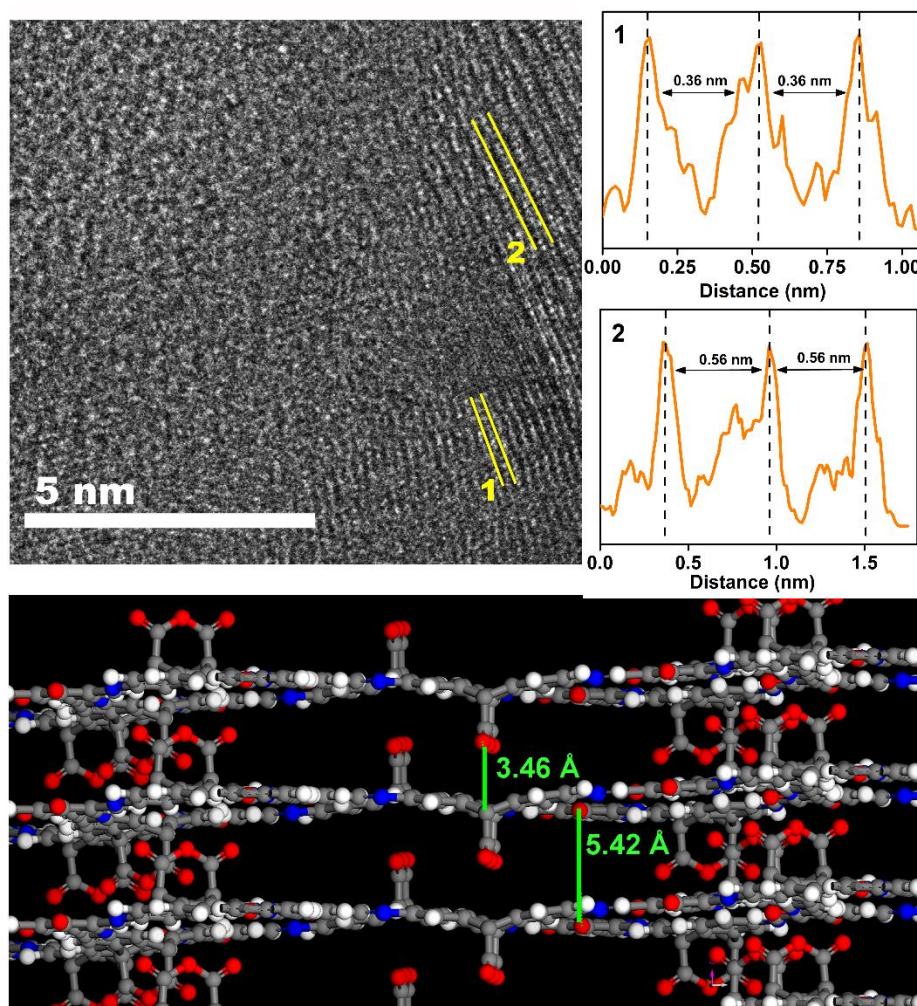


Figure A.2.9. (A) HR-TEM images of IISERP-CON2 at higher magnification showing the lattice fringes. (B) Two different d-spacing value obtained by zooming at the fringes. (C) A plot showing the distance between the layers. (D) Two distinguishable interlayer distances obtained from the model structure, where vertical positioning of the anhydride moieties give a slightly buckled structure to the layers creating shorter and longer interlayer separations compared to the parent COF with planar eclipsed structure.

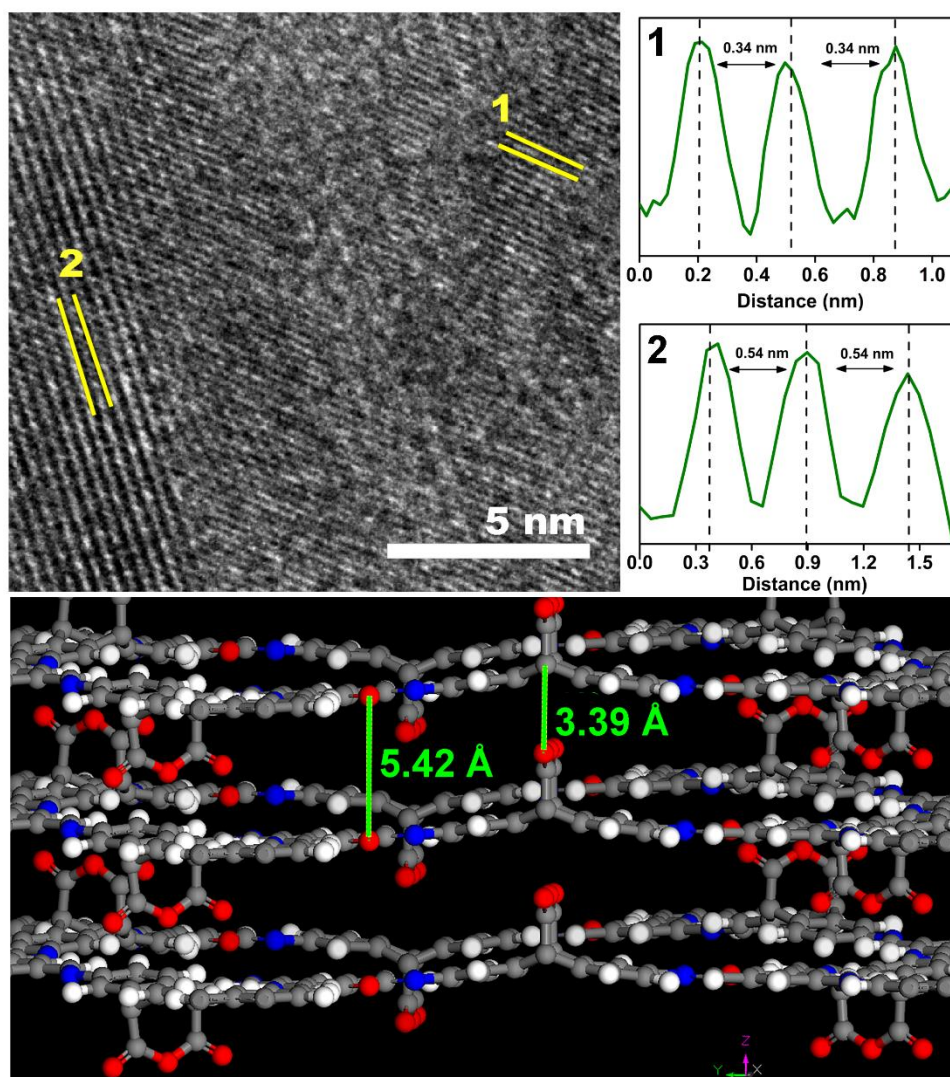


Figure A.2.10. (A) HR-TEM images of IISERP-CON3 at higher magnification showing the lattice fringes. (B) Two different d-spacing values obtained by zooming at the fringes. (C) A plot showing the distance between the layers. (D) Two distinguishable interlayer distances obtained from the model structure, where vertical positioning of the anhydride moieties give a slightly buckled structure to the layers creating shorter and longer interlayer separations compared to the parent COF with planar eclipsed structure.

Comparison between AFM images of COFs vs. CONs

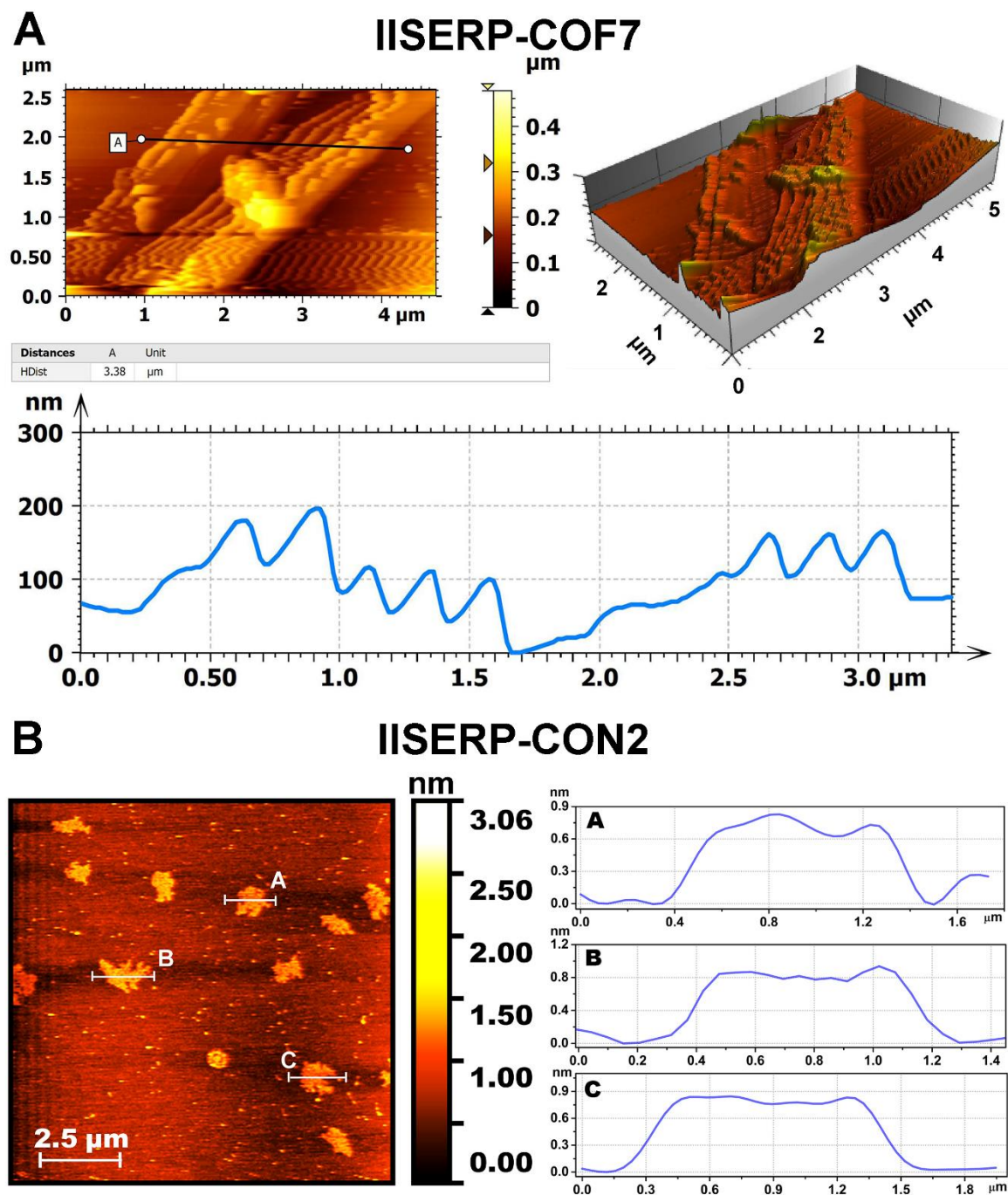


Figure A.2.11. (A) AFM images of IISERP-COF7. The height profile and corresponding 3D view of drop-casted sample prepared in isopropanol shows highly stacked layers of the COFs. It shows an average thickness of the layers of 100 nm to 300 nm. **(B)** AFM image of exfoliated COF (IISERP-CON2) and corresponding height profiles of each the discrete nanosheets. It shows an average thickness in the range of ~0.8 to 1 nm suggesting the sample forming as uniform exfoliated nanosheets.

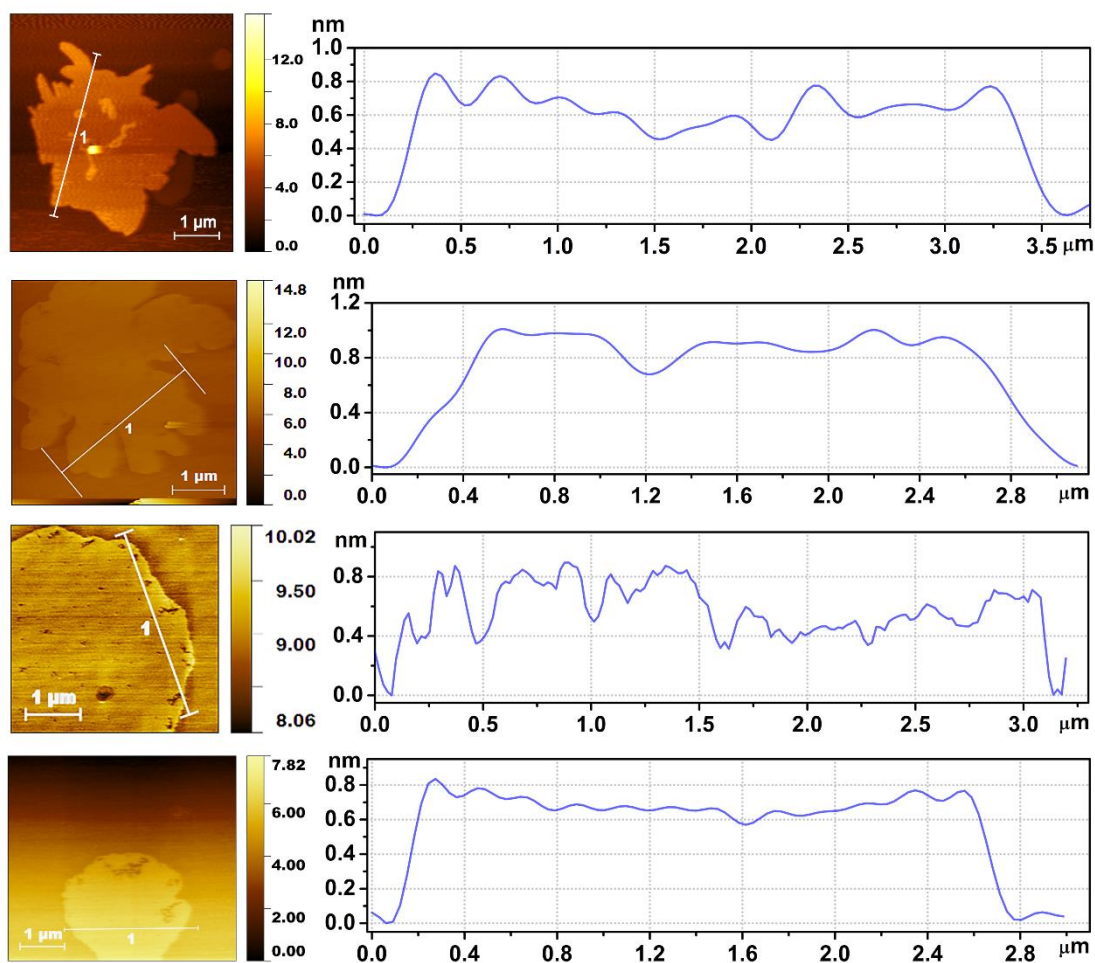


Figure A.2.12. AFM images of discrete nanosheets of IISERP-CON2 and the corresponding height profiles. It shows an average thickness in the range of ~ 0.8 to 0.9 nm suggesting the sample forming as uniform exfoliated nanosheets.

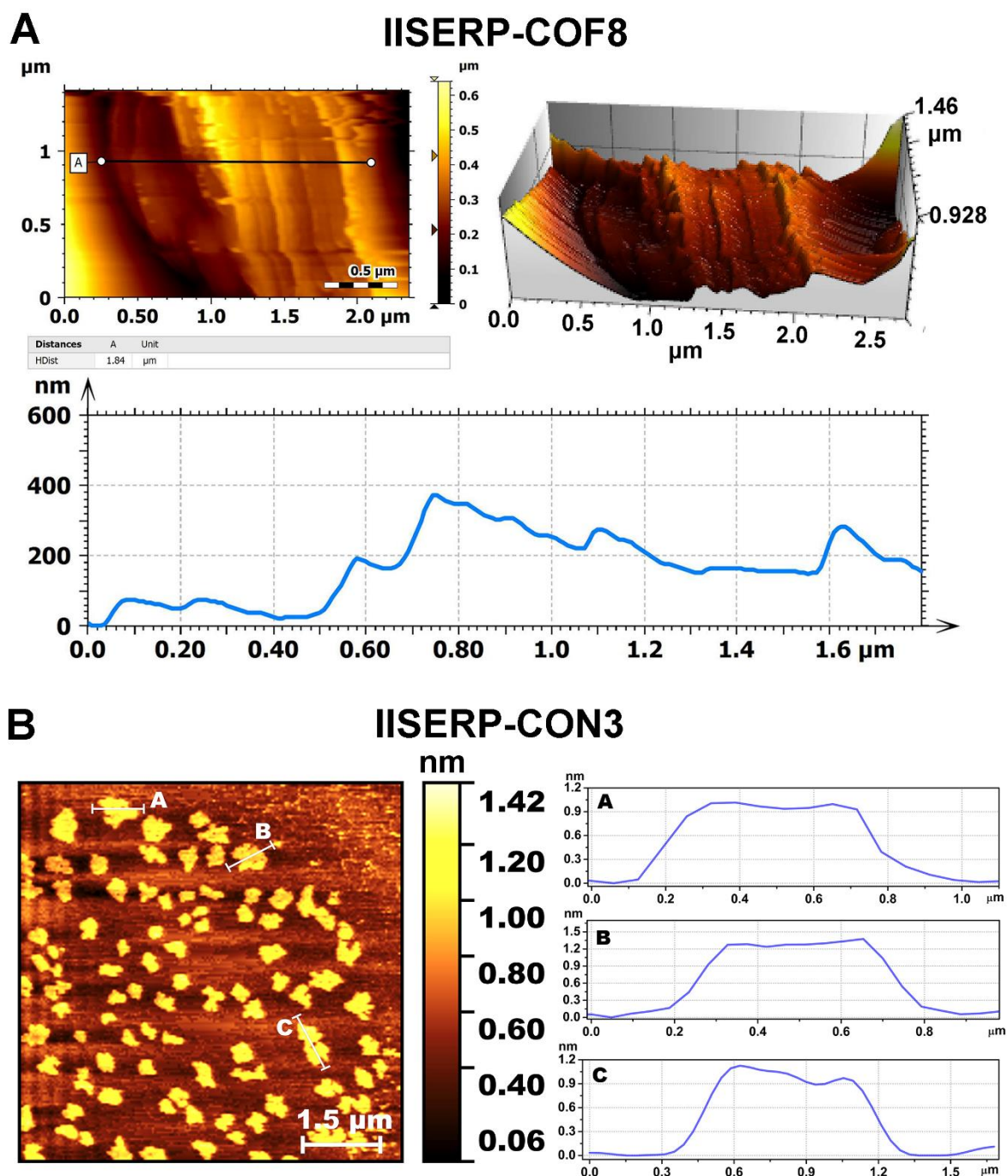


Figure A.2.13. (A) AFM image of IISERP-COF8. The height profile and corresponding 3D view of drop-casted sample prepared in isopropanol shows highly stacked layers of the COFs. It shows an average thickness of the layers of 100 nm to 400 nm. **(B)** AFM image of exfoliated COF (IISERP-CON2) and corresponding height profiles of each the discrete nanosheets. It shows an average thickness in the range of ~ 1 to 1.2 nm suggesting the sample forming as uniform exfoliated nanosheets.

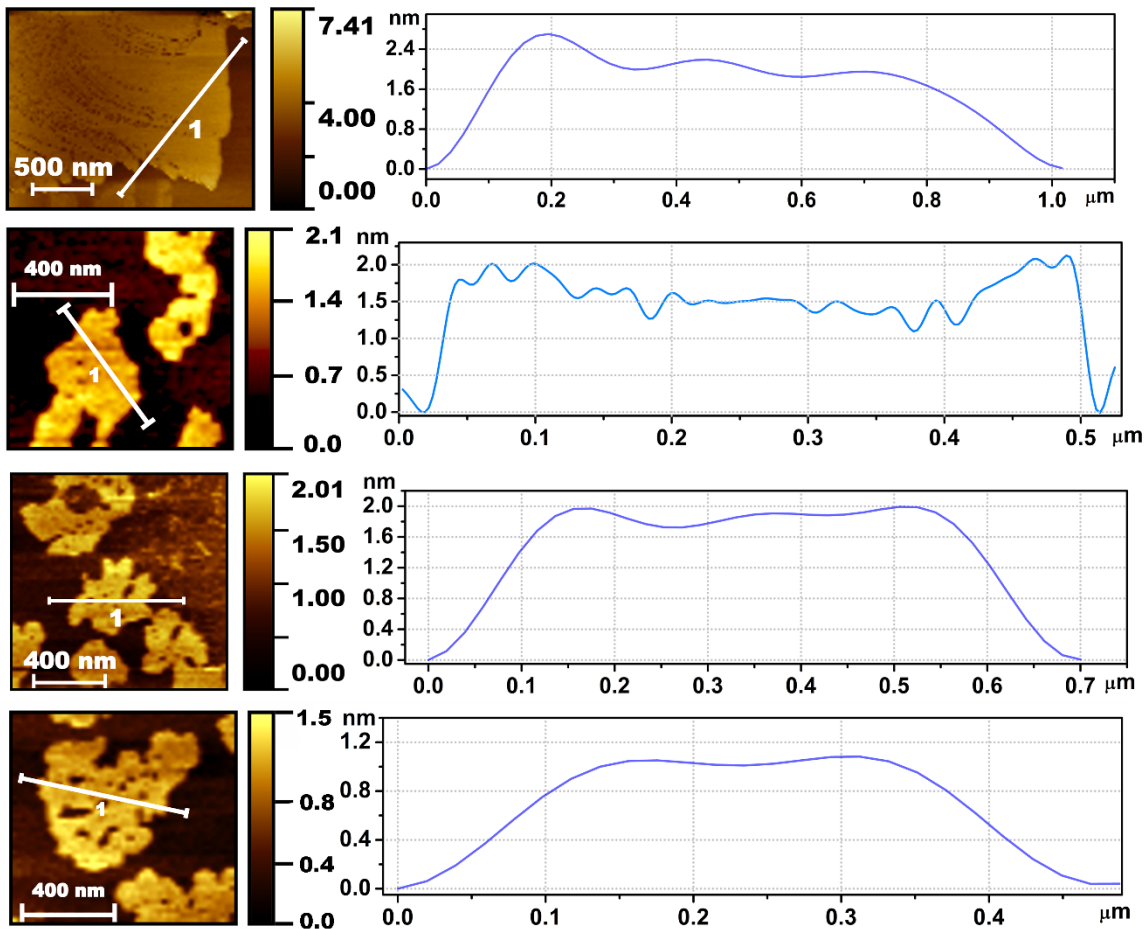


Figure A.2.14. AFM images of discrete nanosheets of IISERP-CON3 and the corresponding height profiles. It shows an average thickness in the range of ~1 to 2.5 nm suggesting the sample forming as uniform exfoliated nanosheets.

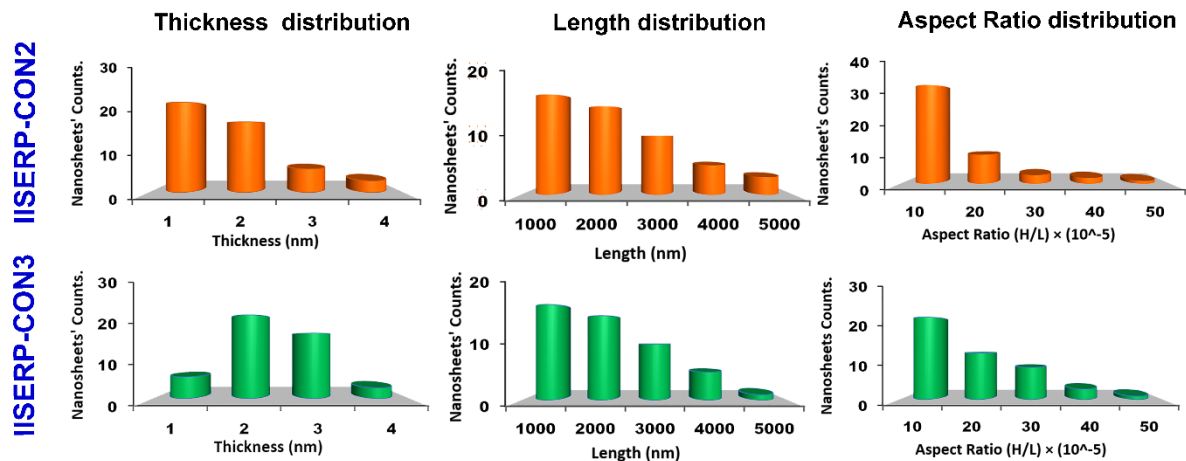


Figure A.2.15: Histogram plots of the thickness (H), lateral length (L) and the aspect ratio distribution (H/L) for IISERP-CON2 and IISERP-CON3. Most of the nanosheets' aspect ratio ranges in the order of $10^{(-5)}$. In the both cases the nanosheets are in large in lateral length but are very thin in height. These are typical dimensions observed in exfoliated nanosheets.

Adsorption data analysis of CONs:

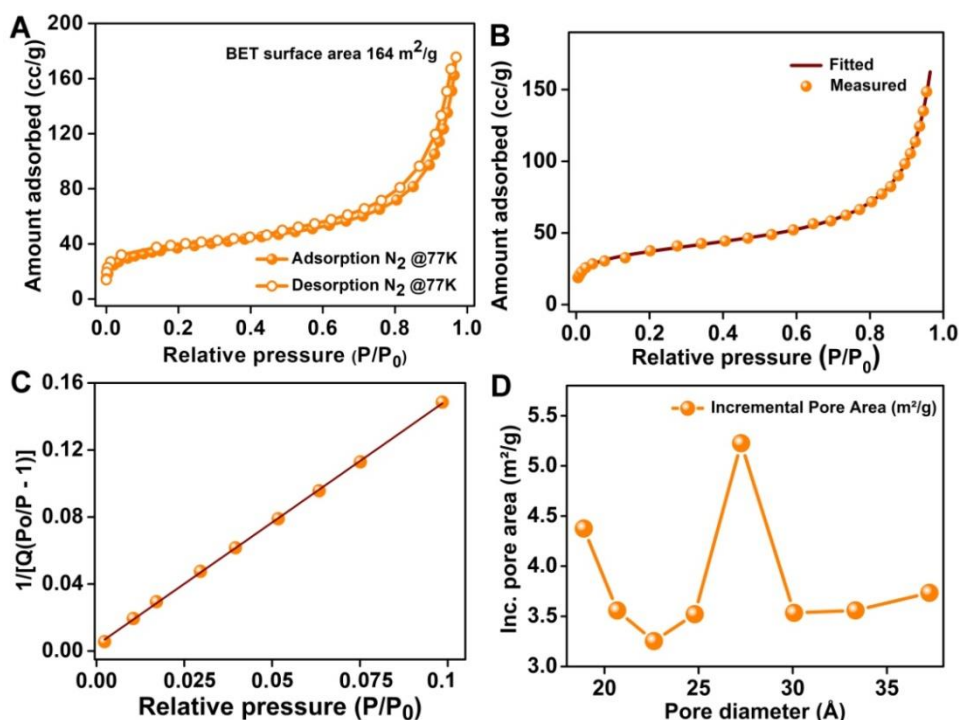


Figure A.2.16. (A) N_2 adsorption-desorption isotherms of IISERP-CON2 at 77 K. (B) Goodness-of-fit plot of the adsorption isotherm from DFT methods. (C) A BET fit obtained using the low pressure region data of the N_2 adsorption isotherm. (D) Pore width vs. incremental pore area plot of IISERP-CON2.

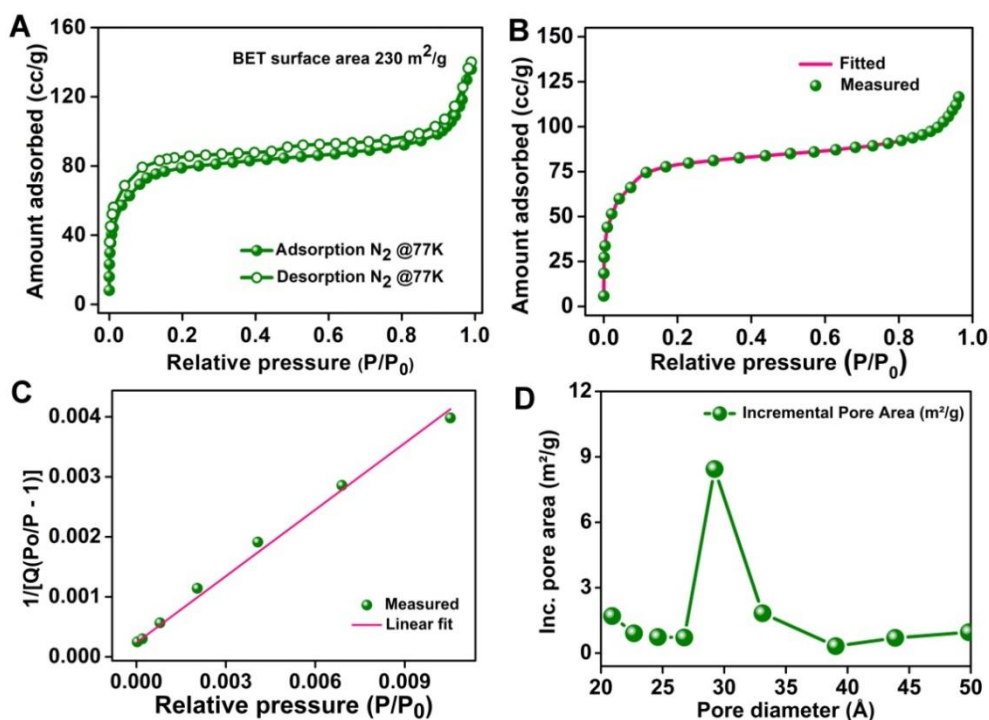


Figure A.2.17. (A) N_2 adsorption-desorption isotherms of IISERP-CON3 at 77 K. (B) Goodness-of-fit plot of the adsorption isotherm. (C) A BET fit obtained using the low pressure region of the 77K N_2 adsorption isotherm. (D) Pore width vs. incremental pore area plot of IISERP-CON3.

Electrolyte stability of the CONs:

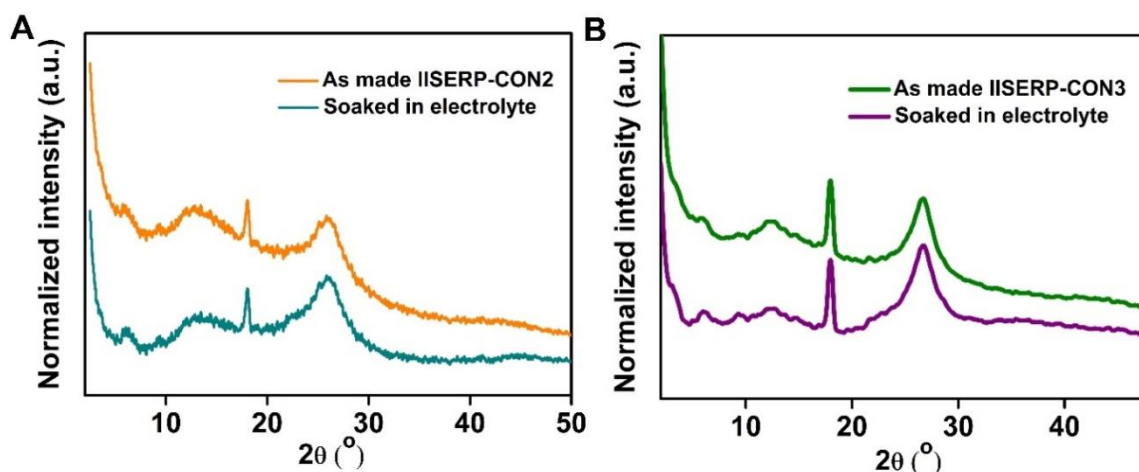


Figure A.2.18. (A) and (B) Electrolyte stability test of IISERP-CON2 and IISERP-CON3 using PXRD measurements. The CONs were soaked in the electrolyte (a solution of LiPF_6 dissolved in a mixture containing ethylenecarbonate and dimethylcarbonate) for 24hrs before being X-rayed.

XPS data analysis of Lithiated CONs:

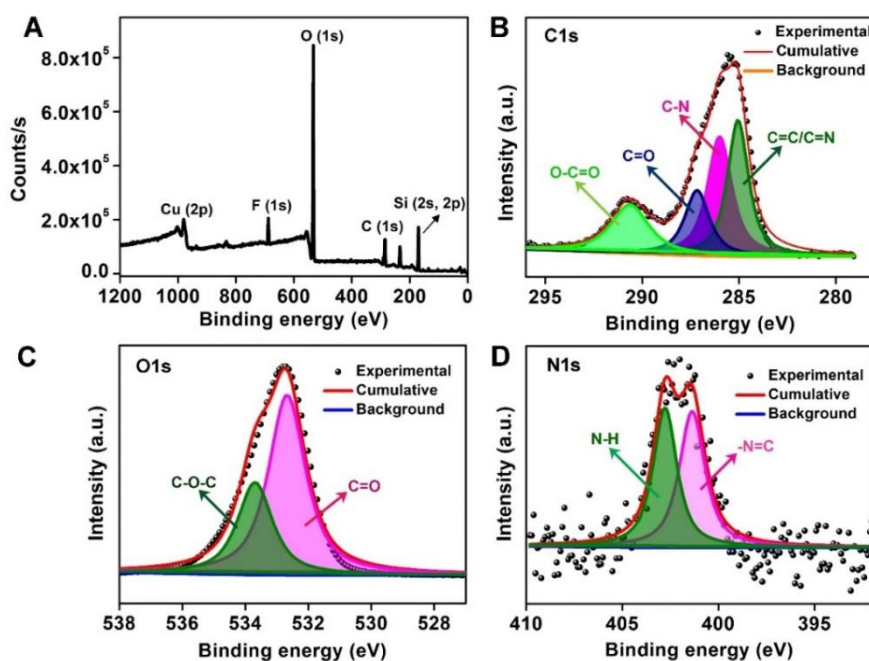


Figure A.2.19. XPS spectra of the IISERP-CON2-derived anode after completion of 100 discharge cycles. **(A)** Full range XPS spectrum after 100 discharged cycles. **(B)** C1s XPS spectra after 100 discharge cycles. **(C)** O1s XPS spectra after 100 discharge cycles. **(D)** N1s XPS spectra after 100 discharge cycles. Change in the binding energy of C=O, C-O-C confirms weak chemical interaction of Lithium with the active sites of the material. Note: N1s spectrum had very low intensity peaks and no significant change was observed in the binding energy after lithiation.

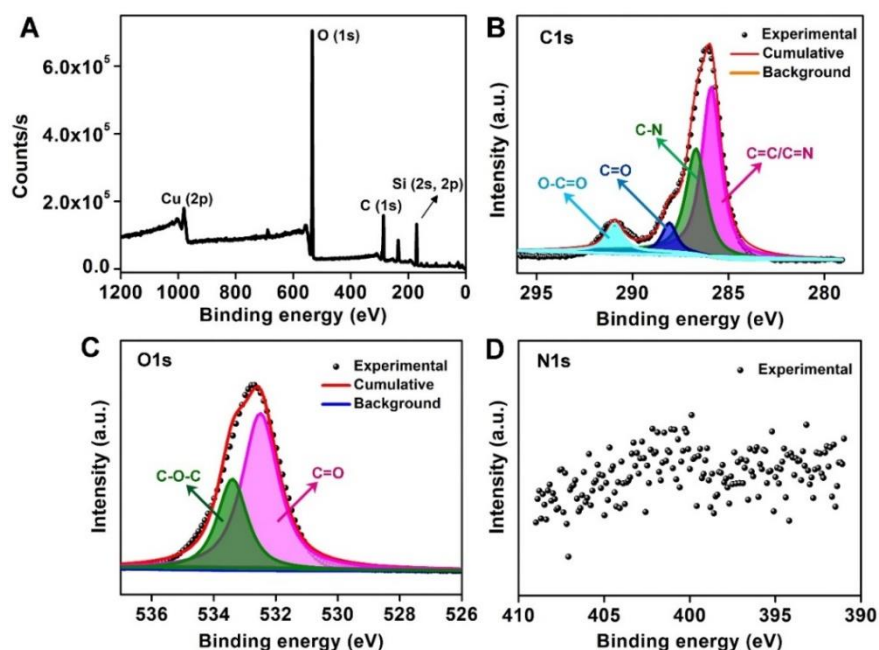


Figure A.2.20. XPS spectra of the IISERP-CON3-derived anode after completion of 100 discharge cycles. **(A)** Full range XPS spectrum after 100 discharge cycles. **(B)** C1s XPS spectra after 100 discharge cycles. **(C)** O1s XPS spectra after 100 discharge cycles. **(D)** N1s XPS spectra after 100 discharge cycles. Change in the binding energy of C=O, C-O-C confirms weak chemical interaction of Lithium with the active sites of the material. Note: There is hardly any peak for N1S in both (A) and (D).

Table A.2.2: XPS data analyses

		IISERP-CON2	IISERP-CON3
		Observed	Observed
C1s	Carbonyl C=O	287.2 eV	288.3 eV
	Anhydride O=C-O-C=O	290.8 eV	291.5 eV
		Observed	Observed
O1s	Carbonyl C=O	532.6 eV	532.3 eV
	Anhydride O=C-O-C=O	533.8 eV	533.7 eV
		Observed	Observed
N1s	Schiff bond C=N	401.1 eV	----
	Keto form's N-H	403.0 eV	----

Raman Spectra of post charged-discharged CONs:

The Raman spectrum has been recorded using the CON-derived electrodes before and after complete lithiation. For this measurement, an inert atmosphere was maintained to reduce the chances of atmospheric oxygen's interaction with the lithiated CONs. Before the Raman spectra measurements, all the electrodes' surface were subjected to thorough diethylcarbonate wash to remove the SEI layer components. The Raman spectra revealed the presence of multiple Li-O interactions (Li_2O , LiOH , Li_2O_2 , LiO_2) in a completely discharged state of the CONs (Table A.2.4, While charging of the CON-derived electrodes showed significant decrease in the intensity of those Raman peaks. From here, the

reversibility of the CONs towards the electrochemical lithiation-delithiation process has been carefully monitored.^[A.2.10-A.2.12]

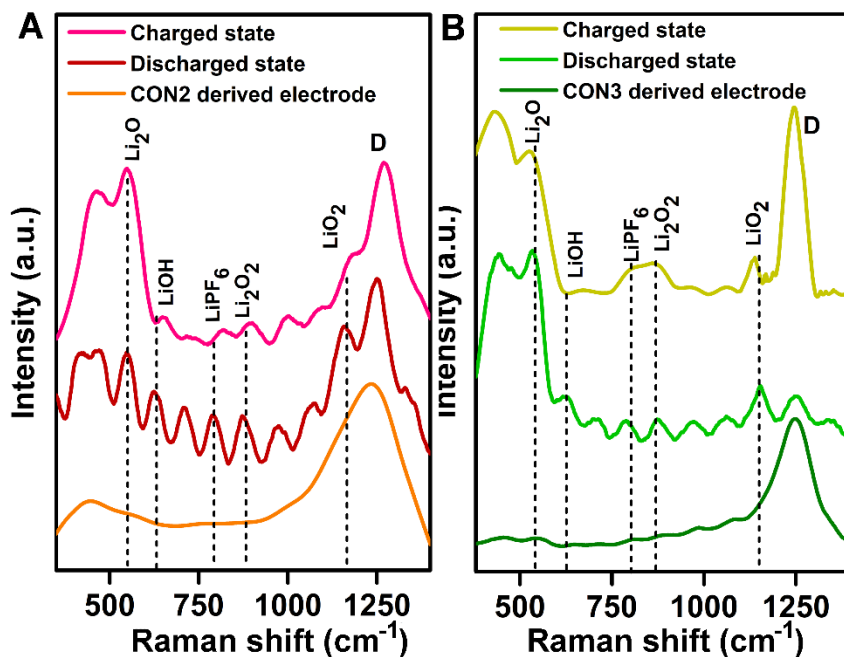


Figure A.2.21. Comparison of the Raman spectra of IISERP-CON2 and IISERP-CON3 derived electrodes with its completely discharged state and completely charged state.

Table A.2.3. Raman shift in charge-dscharged state of CONs:

Interactions	Li @CON-2	Li @CON-3
	Raman Shift (cm ⁻¹)	Raman Shift (cm ⁻¹)
	Discharged state	Discharged state
Li ₂ O	540.6	532.8
LiOH	623.7	623.2
LiPF ₆	787.2	787..2
Li ₂ O ₂	874	874.4
LiO ₂	1158.6	1154.7

Table A.2.4. Comparison of the Sp. capacities of standard anode materials measured in a half-cell configuration.

Anode materials for half-cell-LIB	Stabilized specific capacity (mAh/g)
E-TFPB-COF/MnO ₂ ^{A.2.18}	1359
COF@CNTs ^{A.2.19}	1021
E-TFPB-COF ^{A.2.18}	968
MnO ₂ /PEDOT/Graphene ^{A.2.20}	948
MnO ₂ -PPy/GF ^{A.2.21}	945
MnO ₂ -PEI-rGO ^{A.2.22}	850
IISERP-CON2^{our-work}	825
IISERP-CON2^{our-work}	720
MnO ₂ @PEDOT ^{A.2.23}	628
MnO ₂ @PPy ^{A.2.24}	620
N2-COF ^{A.2.25}	600
IISERP-CON3^{our-work}	595
N3-COF ^{A.2.25}	593
TThPP-COF ^{A.2.26}	378
Cz-COF1 ^{A.2.27}	236

Electrochemical measurements of Graphite-LCO derived full-cell:

Activated LiCoO₂ (LCO) was employed as the counter cathode and activated **Graphite** as the anode to fabricate a full-cell. At first a slurry of the cathode, LCO, and the anode, Graphite, were prepared using 70% of the active material (Graphite), 30% Super-P carbon and 10% PVDF binder. The LCO and the Graphite electrodes were electrochemically pre-activated by 200 charge-discharge cycles at 50 mA/g in a typical half-cell using Li metal as the counter. This is required to get a estimate of the truly available active sites in the Graphite to act as anode against LiCoO₂, barring the sites lost to SEI layer formation. The working potential window for this full-cell was estimated from the voltage plateau of the individual half-cells (~ 0.2 V and ~3.9 V for Graphite and LCO, respectively). This furnishes an E⁰ value for a combined full-cell of 3.7V (i.e. 3.9V-0.2V). To complete the lithiation and delithiation process in the full-cell, E⁰ ± 0.5 V i.e 3.2 to 4.2 V potential window should be applied. But to avoid the degradation of LCO cathode and the electrolyte we used highest potential was restricted up to 3.9 V.

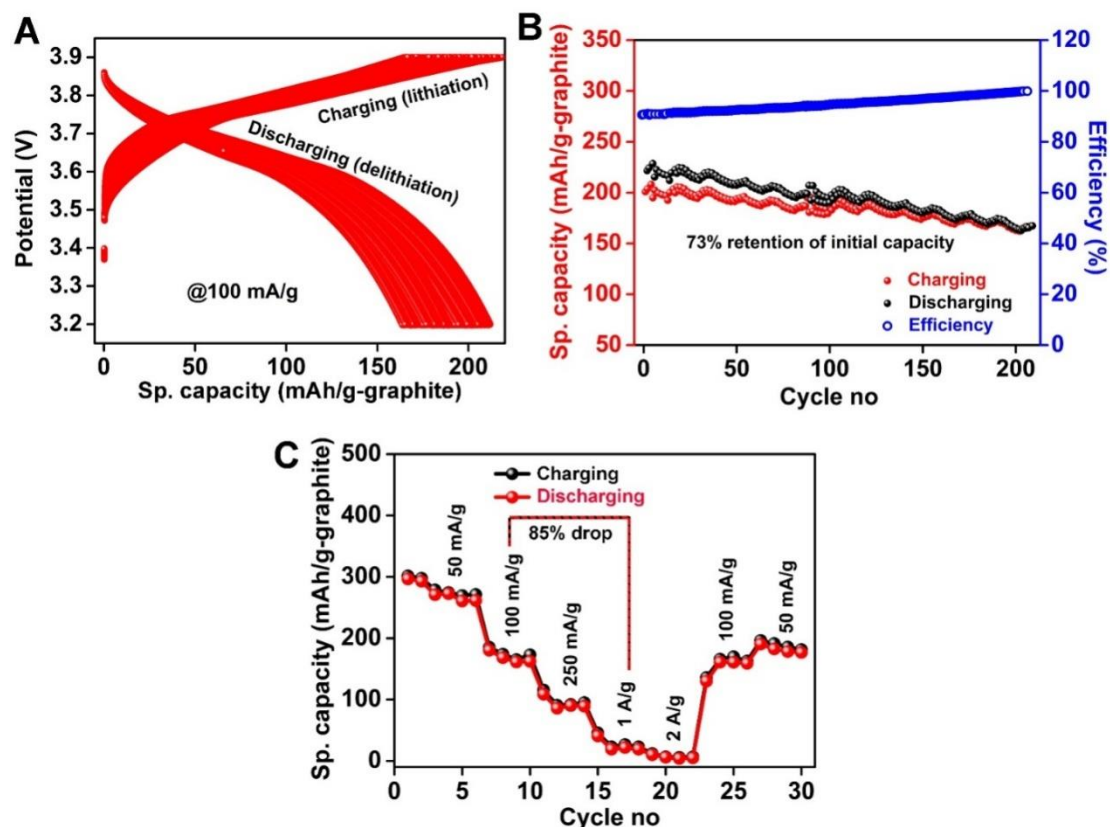


Figure A.2.22. (A) Charge-discharge curves of commercially available Graphite-LCO derived full-cell @100 mA/g current density. (B) Full-cell battery stability and efficiency established up to 200 cycles. It shows 73% retention of the initial capacity after 200th cycle. (C) Rate performance of the Graphite full-cell in a wide range of current densities (50 mA/g to 2 A/g). Note a 85% drop in specific capacity when current density is increased from 100 mA/g to 1 A/g.

Chemical stability of the post charge-discharge sample:

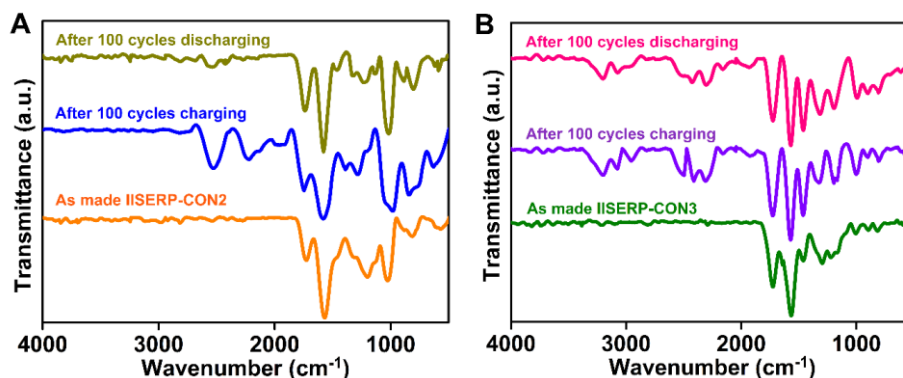


Figure A.2.23. (A) and (B) Comparison of the FT-IR spectra of IISERP-CON2 and IISERP-CON3, before charging-discharging and after 100 charging-discharging cycles. There were no significant changes observed in the spectral peaks.

References:

A.2.1: S. Haldar, K. Roy, S. Nandi, D. Chakraborty, D. Puthusseri, Y. Gawli, S. Ogale, R. Vaidhyanathan, *Adv. Energy Mater.* **2018**, *8*, 1702170.

- A.2.2:** D. Chakraborty, S. Nandi, D. Mullangi, S. Haldar, C. P. Vinod, R. Vaidhyanathan, *ACS Appl. Mater. Interfaces* **2019**, *11*, 15670-15679
- A.2.3:** M. A. Khayum, S. Kandambeth, S. Mitra, S. B. Nair, A. Das, S. S. Nagane, R. Mukherjee, R. Banerjee, *Angew. Chem. Int. Ed.* **2016**, *55*, 15604-15608.
- A.2.4:** D. Billaud, A. Naji, P. Willmann, *J. Chem. Soc., Chem. Commun.* **1995**, 1867-1868.
- A.2.5:** J. Xu, Y. Dou, Z. Wei, J. Ma, Y. Deng, Y. Li, H. Liu, S. Dou, *Advanced Science* **2017**, *4*, 1700146.
- A.2.6:** D. Mukherjee, G. Gowda Y. K, H. Makri Nimbegondi Kotresh, S. Sampath, *ACS Appl. Mater. Interfaces* **2016**, *9*, 19446-19454.
- A.2.7:** M. J. Momeni, E. Targholi, M. Mousavi-Khoshdel, *Computational Materials Science* **2016**, *124*, 166-172.
- A.2.8:** Z. Luo, L. Liu, J. Ning, K. Lei, Y. Lu, F. Li, J. Chen, *Angew. Chem. Int. Ed.* **2018**, *57*, 9443-9446.
- A.2.9:** Y. Wu, R. Zeng, J. Nan, D. Shu, Y. Qiu, S. L. Chou, *Adv. Energy Mater.* **2017**, *7*, 1700278.
- A.2.10:** L. Cabo-Fernandez, F. Mueller, S. Passerini, L. J. Hardwick, *Chem. Commun.* **2016**, *52*, 3970 - 3973.
- A.2.11:** J. Christensena, P. Albertusa, R. S. Sanchez-Carrera, T. Lohmann, B. Kozinsky, R. Liedtke, J. Ahmed, A. Kojic, *Journal of The Electrochemical Society* **2012**, *159* (2), R1-R30.
- A.2.12:** T. A. Galloway, L. Cabo-Fernandez, I. M. Aldous, F. Braga, L, J. Hardwick, *Faraday Discuss.* **2017**, *205*, 469–490.
- A.2.13:** B. Häupler, A. Wild, U. S. Schubert, *Adv. Energy Mater.* **2015**, *5*, 1402034.
- A.2.14:** Y. Wu, T. Okajima, T. Ohsaka, *Int. J. Electrochem. Sci.* **2017**, *12*, 1004-1013.(62)
- A.2.15:** Z. Zhang, J. Lu, R. S. Assary, P. Du, H.-H. Wang, Y.-K. Sun, Y. Qin, K. C. Lau, J. Greeley, P. C. Redfern, *J. Phys. Chem. C* **2011**, *115*, 25535-25542.
- A.2.16:** Wu, W. Wang, M. Li, L. Cao, F. Lyu, M. Yang, Z. Wang, Y. Shi, B. Nan, S. Yu, Z. Sun, Y. Liu, Z. Lu, *Nat Commun.* 2016, *7*, 3318.
- A.2.17:** S. Gu, S. Wu, L. Cao, M. Li, N. Qin, J. Zhu, Z. Wang, Y. Li, Z. Li, J. Chen, Z. Lu, *J. Am. Chem. Soc.* 2019, *141*, 9623–9628.
- A.2.18:** X. Chen, Y. Li, Li. Wang, Y. Xu, A. Nie, Q. Li, F. Wu, W. Sun, X. Zhang, R. Vajtai, P. M. Ajayan,* L. Chen,* and Y. Wang* *Adv. Mater.* 2019, *31*, 1901640
- A.2.19:** Z. Lei, Q. Yang, Y. Xu, S. Guo, W. Sun, H. Liu, L.-P. Lv, Y. Zhang, Y. Wang, *Nat. Commun.* 2018, *9*, 576.
- A.2.20:** C. X. Guo, M. Wang, T. Chen, X. W. Lou, C. M. Li, *Adv. Energy Mater.* 2011, *1*, 736
- A.2.21:** M. G. Akbari, S. Abouali, J. Cui, J.-K. Kim, *Mater. Chem. Front.* 2018, *2*, 1481.
- A.2.22:** C. J. Chae, K. W. Kim, Y. J. Yun, D. Lee, J. Moon, Y. M. Choi, S. S. Lee, S. Choi, S. Jeong, *ACS Appl. Mater. Interfaces* 2016, *8*, 11499.

A.2.23: X. Chen, Z. Cao, L. Xing, Y. Liao, Y. Qiu, W. Li, *Nanoscale* 2017, 9, 18467.

A.2.24: L. Feng, Y. Zhang, R. Wang, Y. Zhang, W. Bai, S. Ji, Z. Xuan, J. Yang, Z. Zheng, H. Guan, *Nanoscale Res. Lett.* 2017, 12, 518.

A.2.25: L. Bai, Q. Gao, Y. Zhao, *J. Mater. Chem. A* 2016, 4, 14106.

A.2.26: H. Yang, S. Zhang, L. Han, Z. Zhang, Z. Xue, J. Gao, Y. Li, C. Huang, Y. Yi, H. Liu, Y. Li, *ACS Appl. Mater. Interfaces* 2016, 8, 5366.

A.2.27: S. Feng, H. Xu, C. Zhang, Y. Chen, J. Zeng, D. Jiang, J.-X. Jiang, *Chem. Commun.* 2017, 53, 11334.

Appendix 3

Materials and methods for monomer synthesis:

Synthesis of 2, 4, 6-triformylphloroglucinol:

About 90 mL trifluoroacetic acid was added to dried phloroglucinol (6.014 g) and stirred for 15 mins to obtain a white suspension. Then hexamine (15.098 g) was added to the suspension. The resulting solution was heated at 100 °C for 2.5 h under N₂ atmosphere and the color of the suspension changed to dark brownish. To hydrolyse the compound 150 mL 3N HCl was added with heating at 100 °C for 1 h. The color of the dark turbid solution became clear. After cooling at room temperature, the compound was filtered through a celite flash column. The resulting filtrate was extracted using 350 mL dichloromethane and dried over magnesium-sulfate and then filtered. The solvent was evaporated by rotary evaporation, giving an off-white (yield 1.7 g) powder. The compound was recrystallized in hot DMF and characterization was done using ¹H and ¹³C NMR (Figure A.3.1), and IR studies (Figure A.3.10).

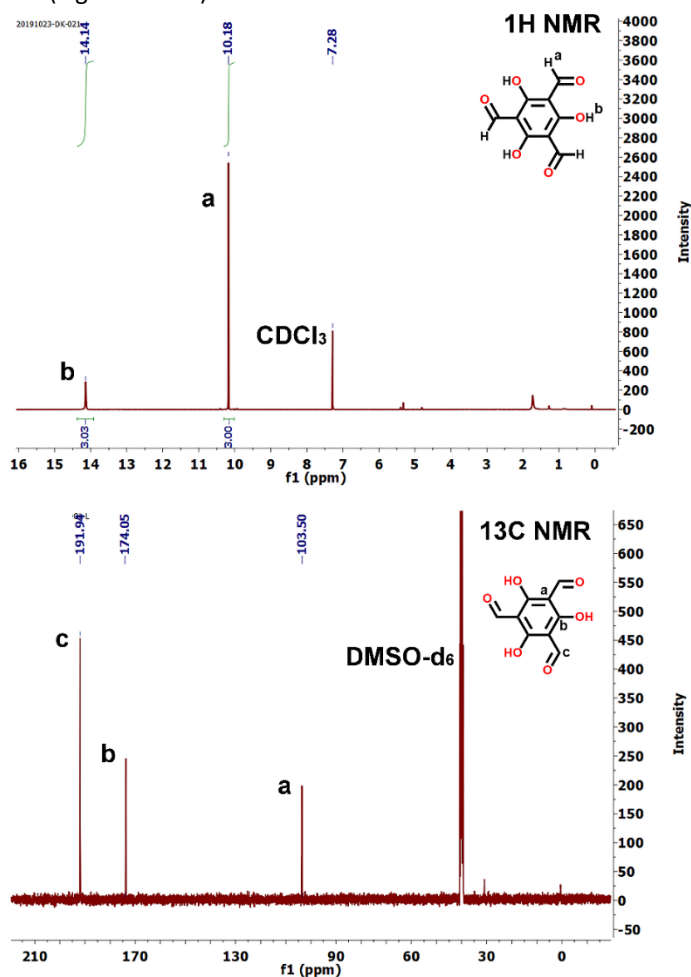
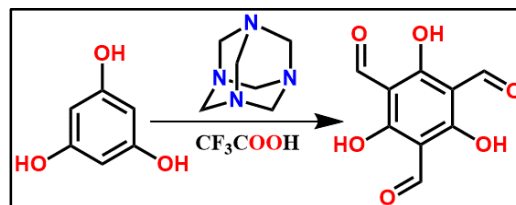


Figure A.3.1. ¹H-NMR and ¹³C-NMR of triformylphloroglucinol were recorded in deuterated chloroform and in dimethyl sulfoxide (DMSO-*d*₆), respectively, at room temperature.

Synthesis of *s*-tetrazine diamine:

Appendix of Chapter 3

In a typical synthesis, about 8 g of 4-amino-benzonitrile was dissolved in 20 ml of ethanol. 15 ml of hydrazine hydrate (con.90%) and 4 g of sulphur powder was then added to it. The solution was kept for stirring at 90 °C for 8 hrs until a bright golden yellow colored thick suspension was observed. The suspension was filtered and washed with ethanol and acetone multiple times and kept for vacuum drying overnight. The bright yellow powder was dispersed in dry DMSO by stirring and was subjected to an overnight O₂ purge. To this oxidized compound, 150 ml of distilled water was added to precipitate out a bright-red product. The filtered and dried red powder was dispersed in 5% H₂O₂ solution to oxidize fully. The bright red coloured product was isolated by centrifugation and dried in vacuum for 12 hrs. The product was washed with acetone and characterised by ¹H and ¹³C NMR (Figure A.3.2) and IR studies (Figure A.3.3).

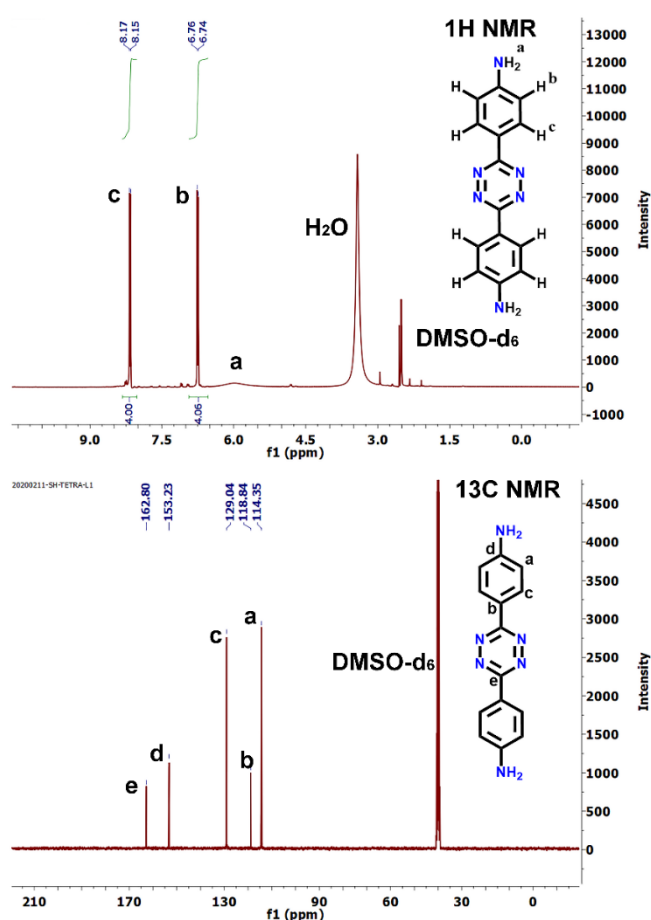
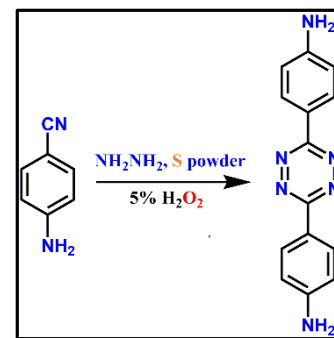


Figure A.3.2. The room temperature ¹H-NMR and ¹³C-NMR of s-tetrazine diamine were recorded in deuterated chloroform and in dimethyl sulfoxide (DMSO-*d*₆), respectively.

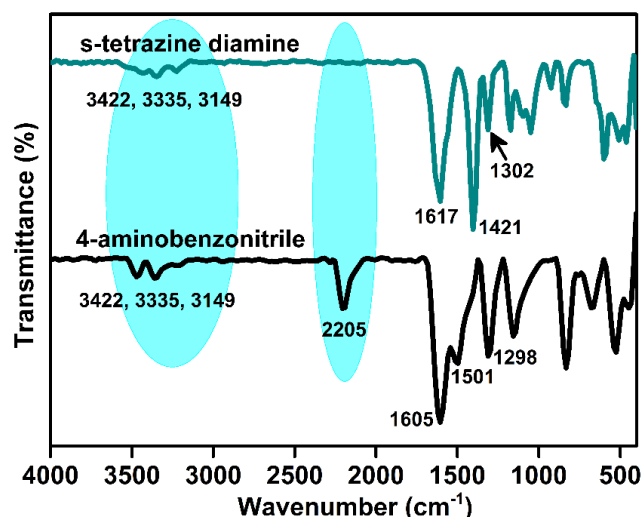


Figure A.3.3. IR spectra of 4-aminobenzonitrile and s-tetrazinediamine.

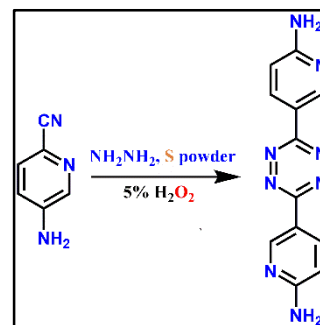
Table A.3.1. Comparison of characteristics IR frequencies.

	NH ₂ primary amine (cm ⁻¹)	C≡N Nitrile (cm ⁻¹)	N-H bend Primary amine (cm ⁻¹)	C=C bond (cm ⁻¹)	C-N bond (cm ⁻¹)
4-aminobenzonitrile	3422, 3335, 3149	2205	1605	1501	1298
s-tetrazine diamine	3422, 3335, 3149	absent	1617	1421	1302

Note: Absence of IR frequencies of nitrile groups in s-tetrazine diamine confirms the formation of tetrazine ring.

Synthesis of bispyridine-s-tetrazine diamine:

In a typical synthesis, about 8 g of 6-amino-3-pyridinecarbonitrile was dissolved in 20 ml of ethanol. 20 ml of hydrazine hydrate (con.90%) and 4 g of sulphur powder were added to it. The solution was kept for stirring at 90 °C for 8 hrs until a bright golden yellow colored thick suspension was observed. This suspension was filtered and washed with ethanol and acetone multiple times and kept for an overnight vacuum drying. The yellowish-orange powder was dispersed in dry DMSO by stirring and O₂ was purged into the dispersion overnight to oxidize the product. 150 ml of distilled water was added to it to precipitate out the red product. The filtered and dried red powder was dispersed in 5% H₂O₂ solution to oxidize fully. The dark red colored product (with yield of 70%) was isolated by centrifugation and dried in vacuum for 12 hrs. The product was washed with dimethyl-formamide and characterised by ¹H and ¹³C NMR (Figure A.3.4), IR studies (Figure A.3.5) and HRMS (Figure A.3.6).



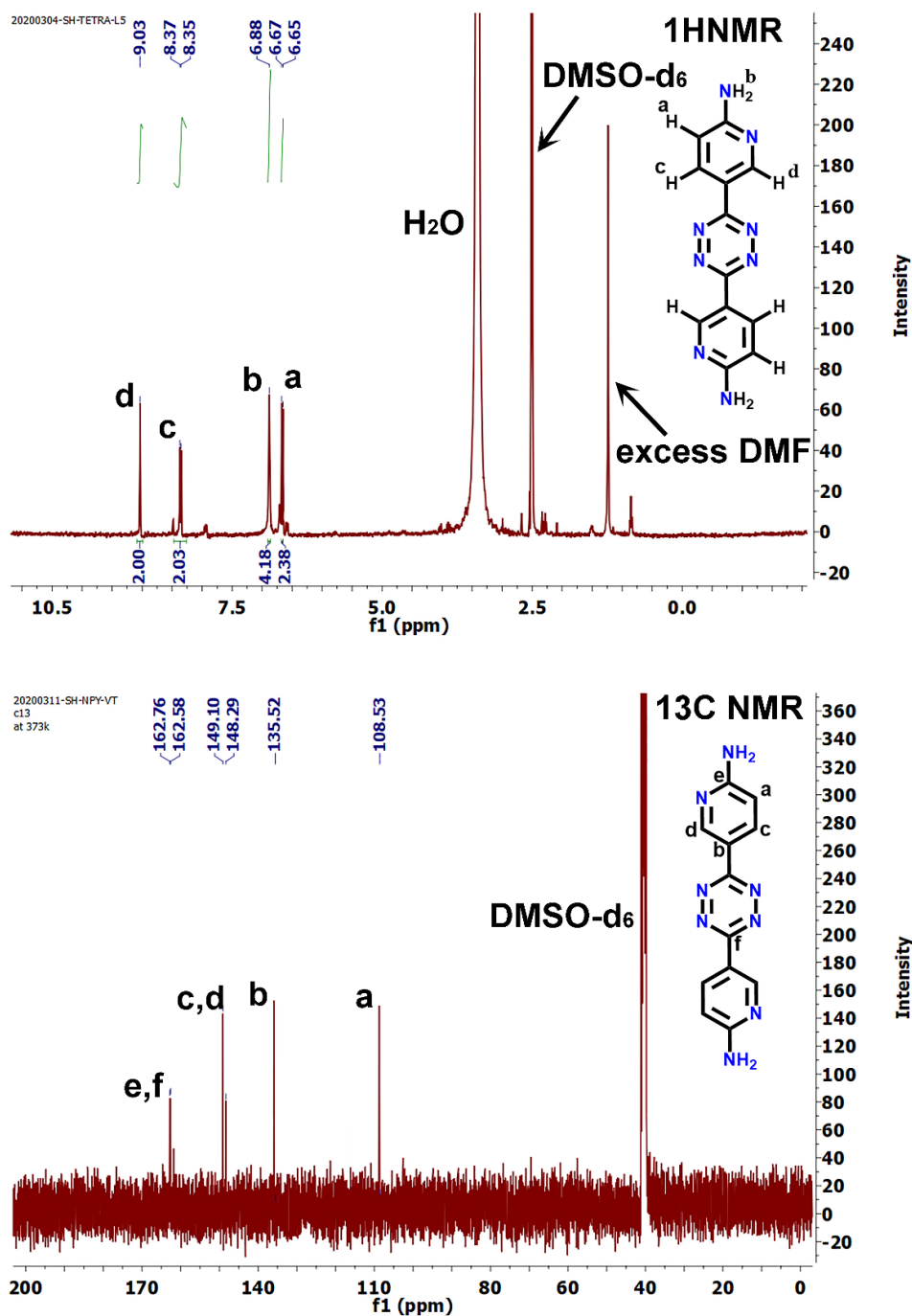


Figure A.3.4. (A): ^1H -NMR and ^{13}C -NMR of bispyridine-s-tetrazine diamine recorded in dimethyl sulfoxide (DMSO-d_6) at room temperature.

Note: The solubility of bispyridine-s-tetrazine diamine is very less in any organic solvent. But with the increase of temperature it solubilizes in (DMSO-d_6). So that, ^1H NMR data has also been taken in 373 K (Figure A.3.4. (B)).

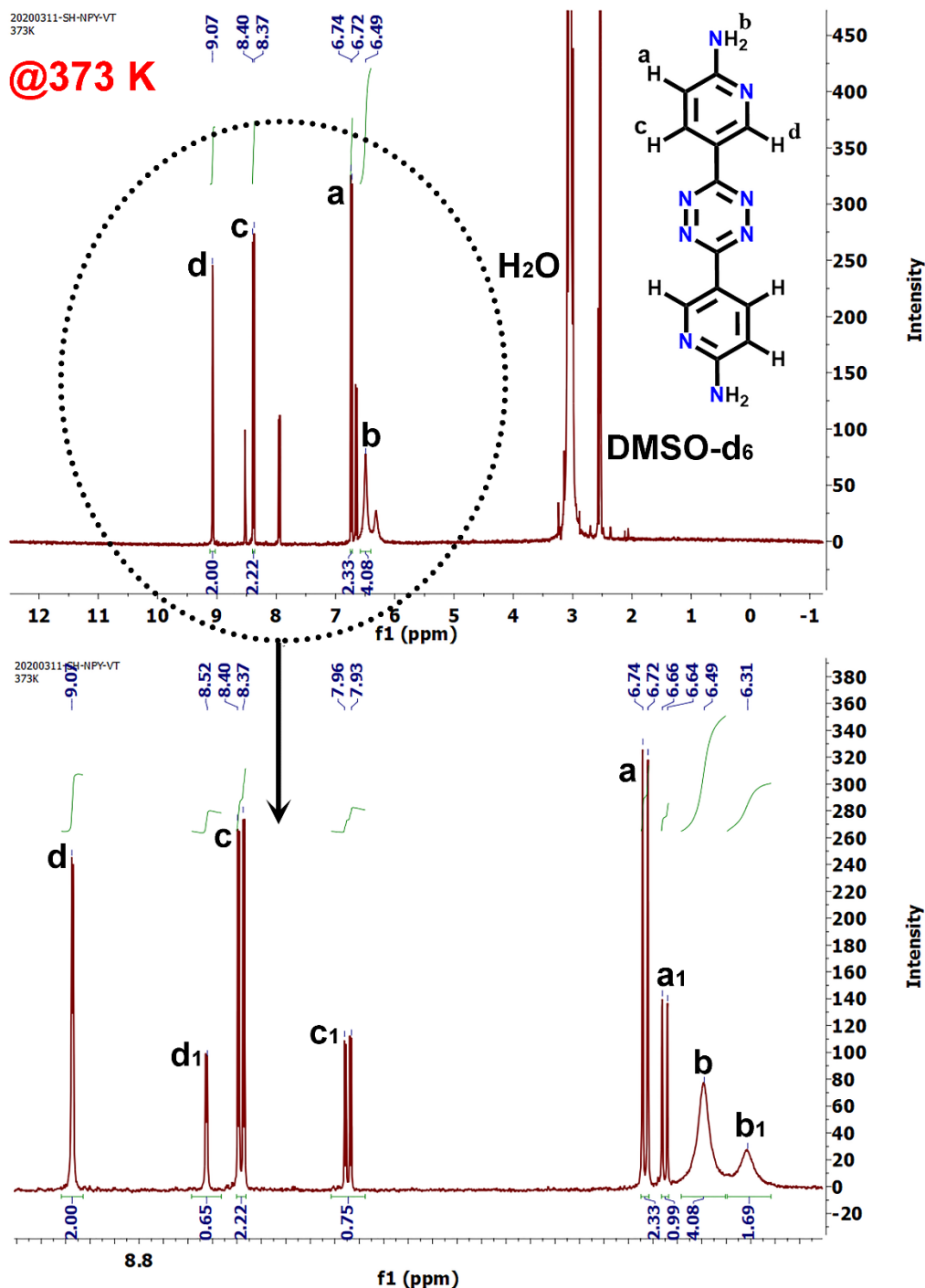


Figure A.3.4. (B): $^1\text{H-NMR}$ and $^{13}\text{C-NMR}$ of bispyridine-s-tetrazine diamine recorded in dimethyl sulfoxide (DMSO-d_6) at 373 K.

Note: Two different isomeric peaks were observed with systematic shifts. The ratio of the intensities of two sets of isomeric peaks (a, b, c, d) and (a_1, b_1, c_1, d_1) is 3:1. So the isomers coexists as a mixture with a 3:1 concentration ratio. The probability of the presence of any unreacted product was discarded as HRMS data showed a single molecular weight.

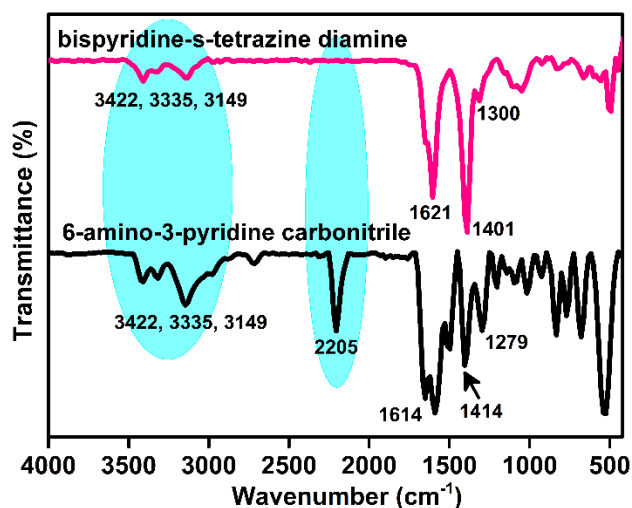


Figure A.3.5. IR spectra of 6-amino-3-pyridine carbonitrile and bis-pyridine-s-tetrazine diamine.

Table A.3.2. Comparison of characteristic IR frequencies.

	NH ₂ primary amine (cm ⁻¹)	C≡N Nitrile (cm ⁻¹)	N-H bend Primary amine (cm ⁻¹)	C=C bond (cm ⁻¹)	C-N bond (cm ⁻¹)
6-amino-3-pyridine carbonitrile	3422, 3335, 3149	2205	1614	1414	1279
bispyridine s-tetrazine diamine	3422, 3335, 3149	absent	1621	1401	1300

Note: Absence of IR frequencies of nitrile groups in bispyridine-s-tetrazine diamine confirms the formation of tetrazine ring.

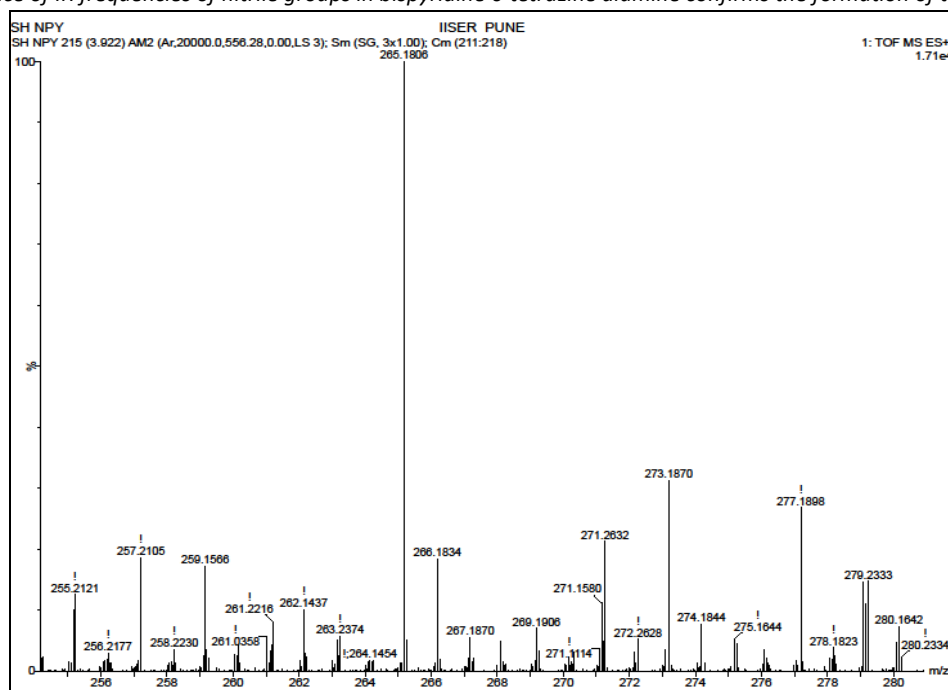


Figure A.3.6. HRMS data of bispyridine-s-tetrazine diamine shows only a single intense peak of [M+H]⁺: 265.19. The exact molecular mass of bispyridine-s-tetrazine diamine (C₁₂H₁₀N₈) is 266.10.

FE-SEM images of the COFs:

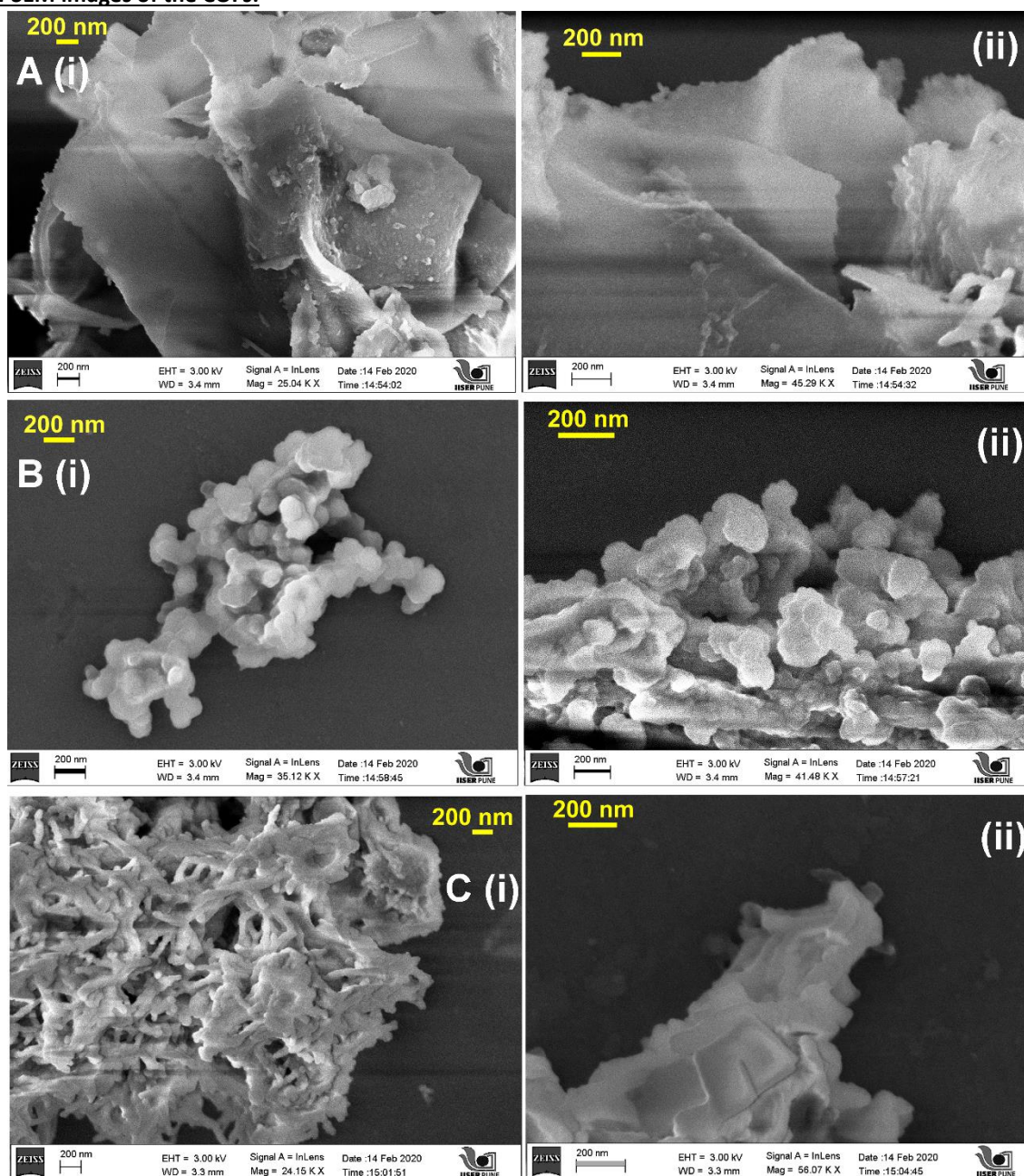


Figure A.3.7. FE-SEM images of (A) IISERP-COF16, (B) IISERP-COF17 and (C) IISERP-COF18 at different resolutions.

Note: At lower resolution, a fluffy cotton-like morphology can be seen. In closer view the presence of aggregated-flakes can be seen.

HR-TEM images of the COFs:

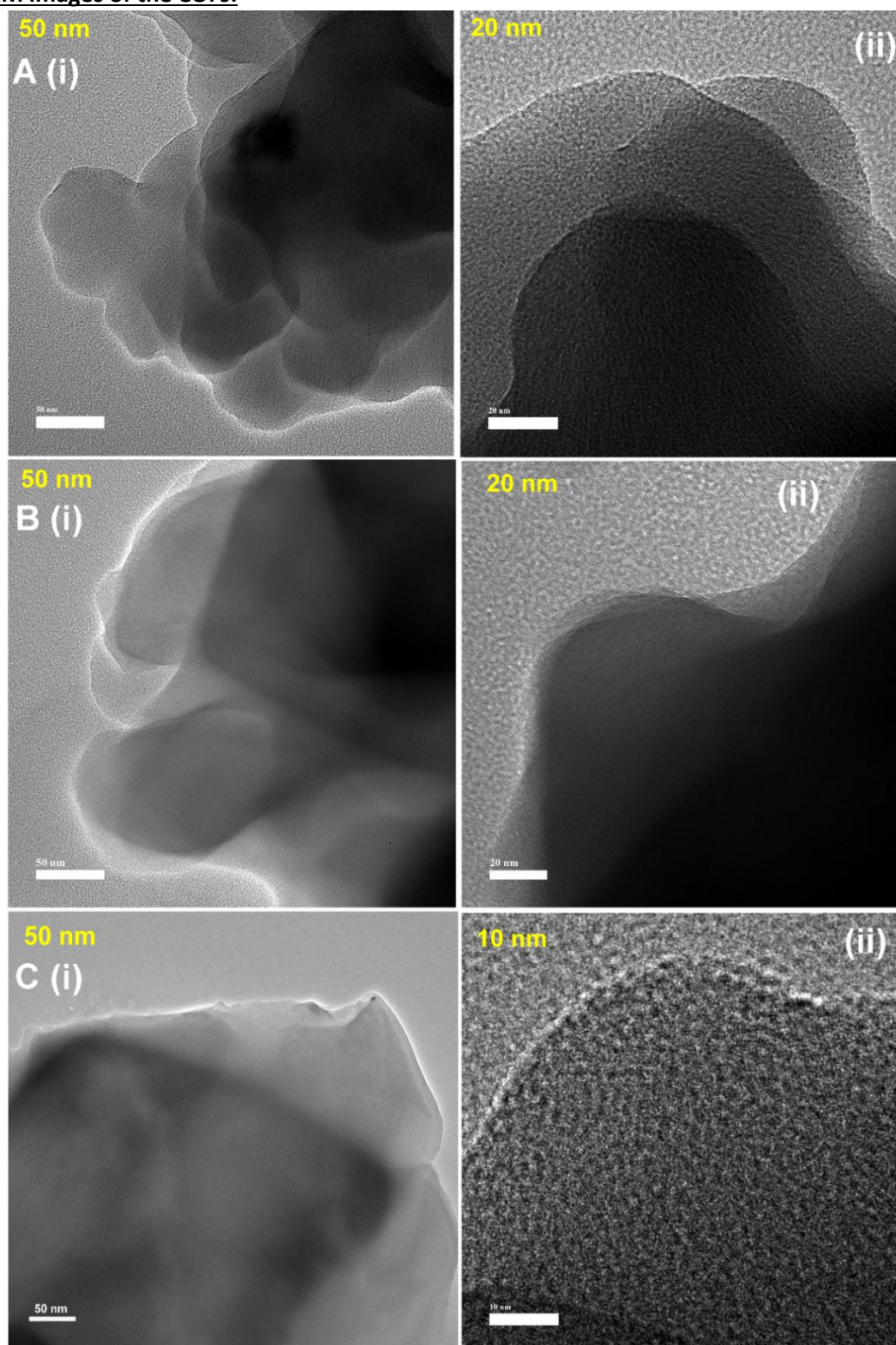


Figure A.3.8. HR-TEM images of the (A) IISERP-COF16, (B) IISERP-COF17 and (C) IISERP-COF18 under different magnifications showing the aggregates formed by stacking of many sheets. Darker regions are from such multi-flake stacking. While at 10 nm resolution the uniform micropores all along the surface of the COF can be seen.

SAED pattern of the COFs:

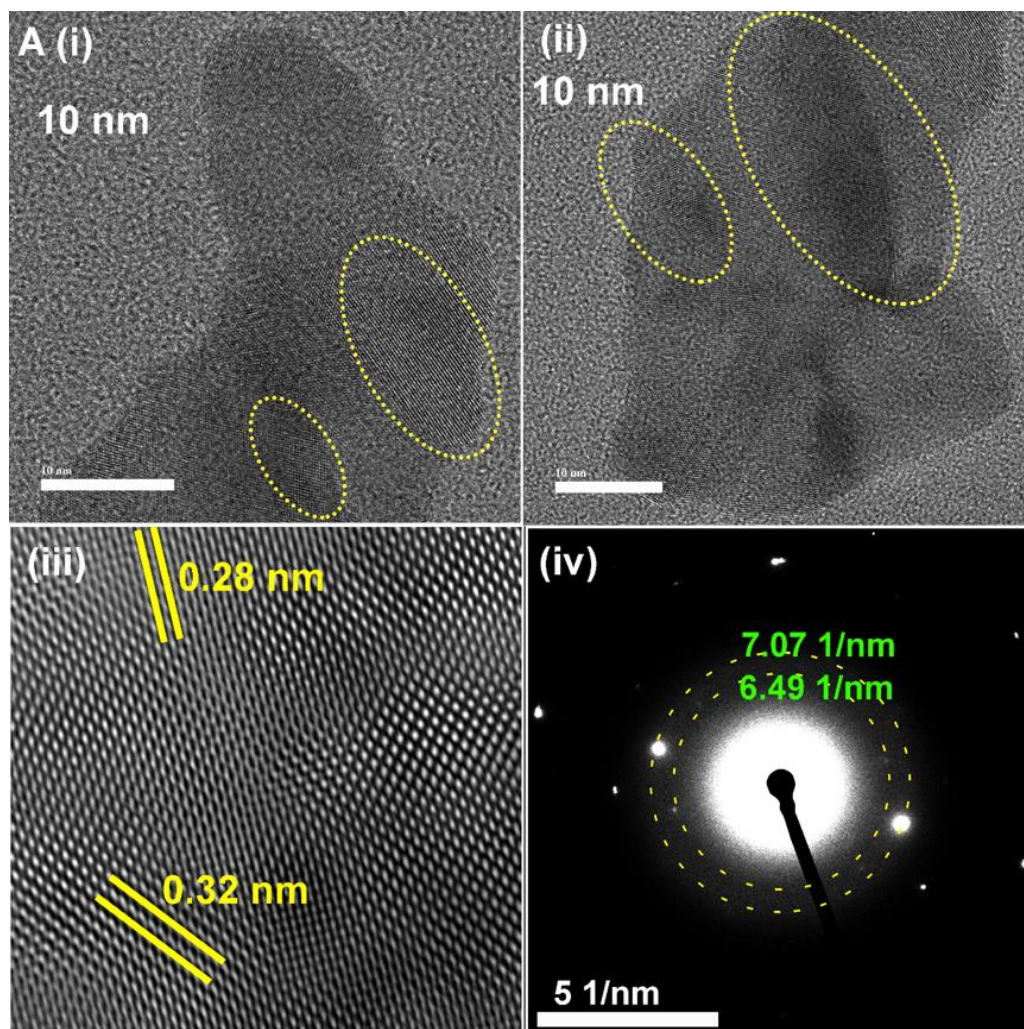


Figure A.3.9. A (i) and (ii) HR-TEM images of the IISERP-COF16 under higher magnifications showing the lattice fringes present in the COF. (iii) FFT pattern of the fringes area shows the d-spacing values. (iv) SAED pattern of IISERP-COF16 shows the diameters of reciprocal circles.

Note: These lattice fringes could be observed across samples from different preparations and also in many regions of the drop-casted samples. The SAED pattern confirms the high degree of crystallinity in the selected flakes of the COF. Many such crystalline flakes were observed. However, the thin flakes burn under the exposure to e- beam of the HRTEM.

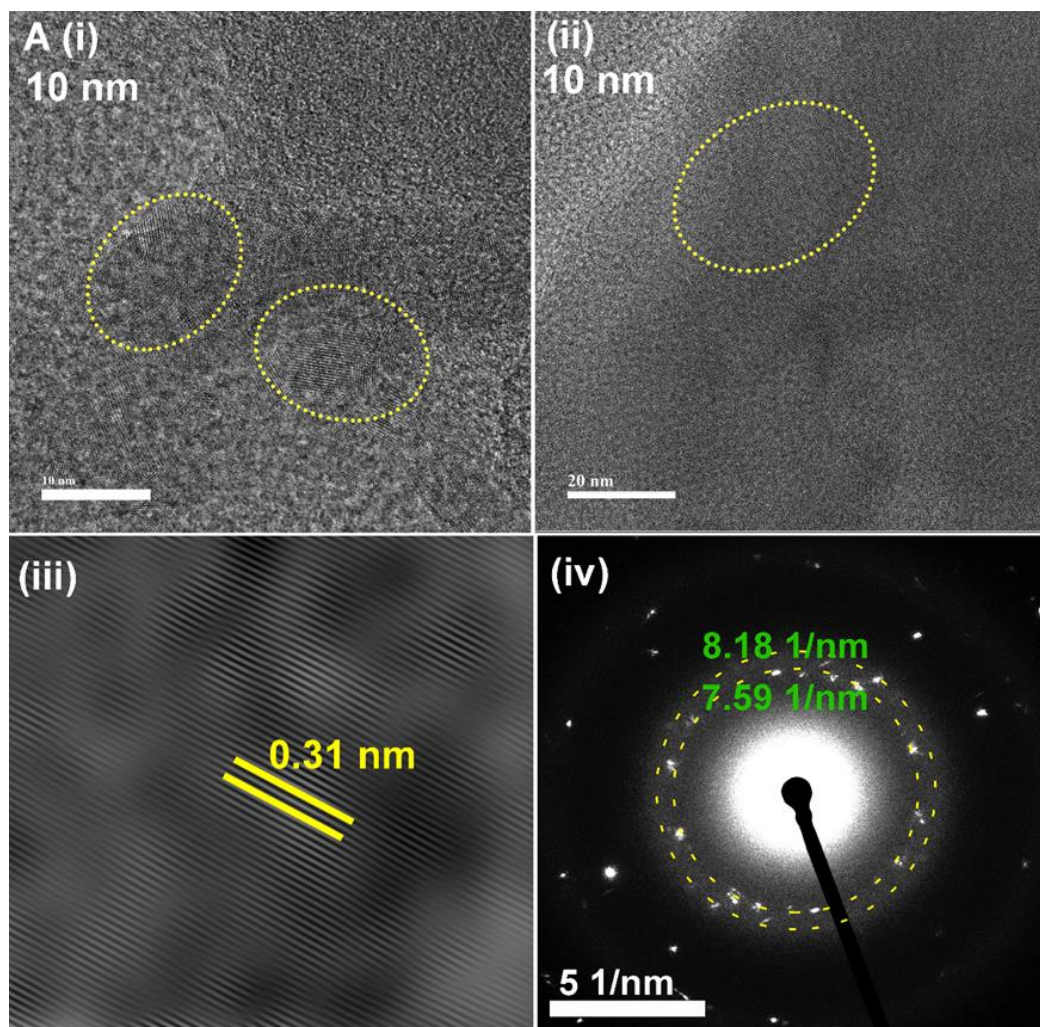


Figure A.3.10. A (i) and (ii) HR-TEM images of the IISERP-COF17 under higher magnifications showing the lattice fringes present in the COF. (iii) FFT pattern of the fringes area shows the d-spacing values. (iv) SAED pattern of IISERP-COF17 shows the diameters of reciprocal lattice.

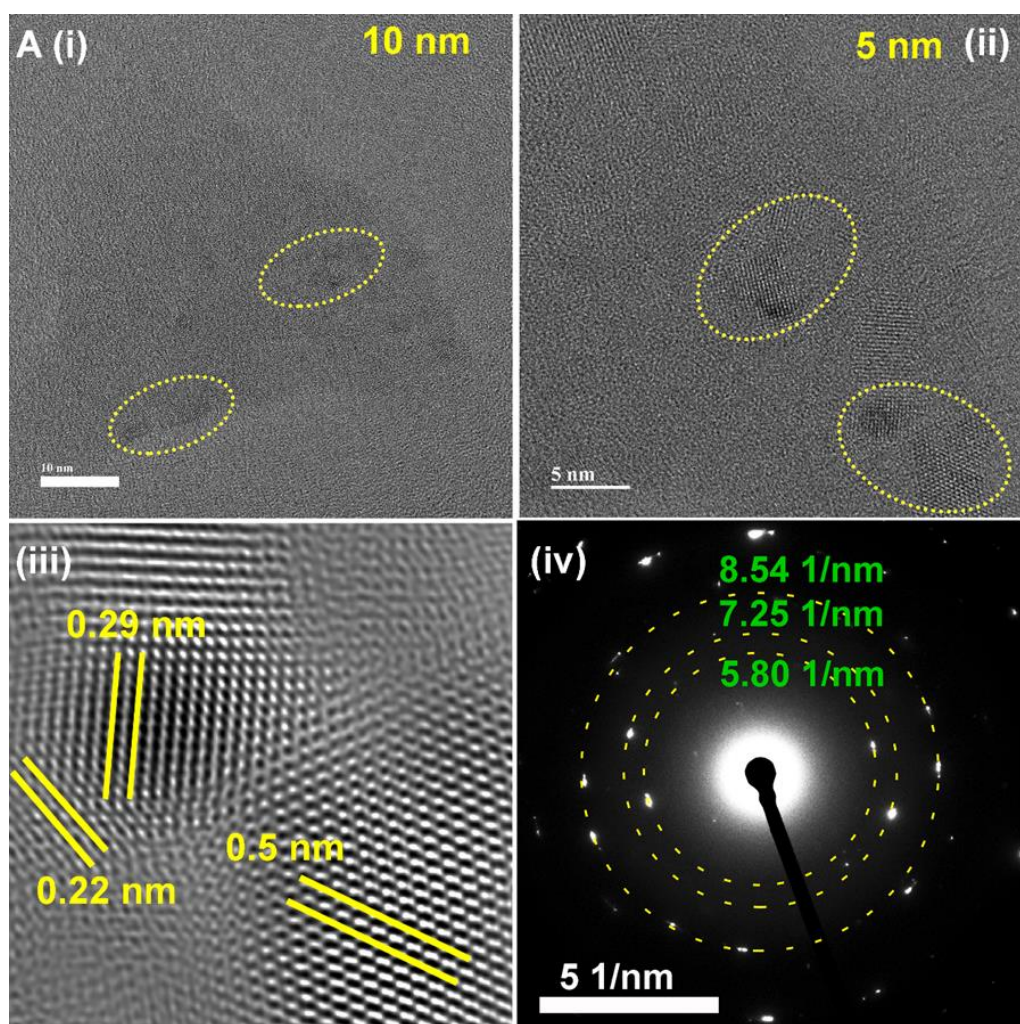


Figure A.3.11. A (i) and (ii) HR-TEM images of the IISERP-COF18 under higher magnifications showing the lattice fringes present in the COF. (iii) FFT pattern of the fringes area shows the d-spacing values. (iv) SAED pattern of IISERP-COF18 shows the diameters of reciprocal lattice.

Note: d-spacing value calculated from the diameter (R) of the reciprocal lattice ($d=2/2R$) matches well with lattice fringes observed in FFT pattern.

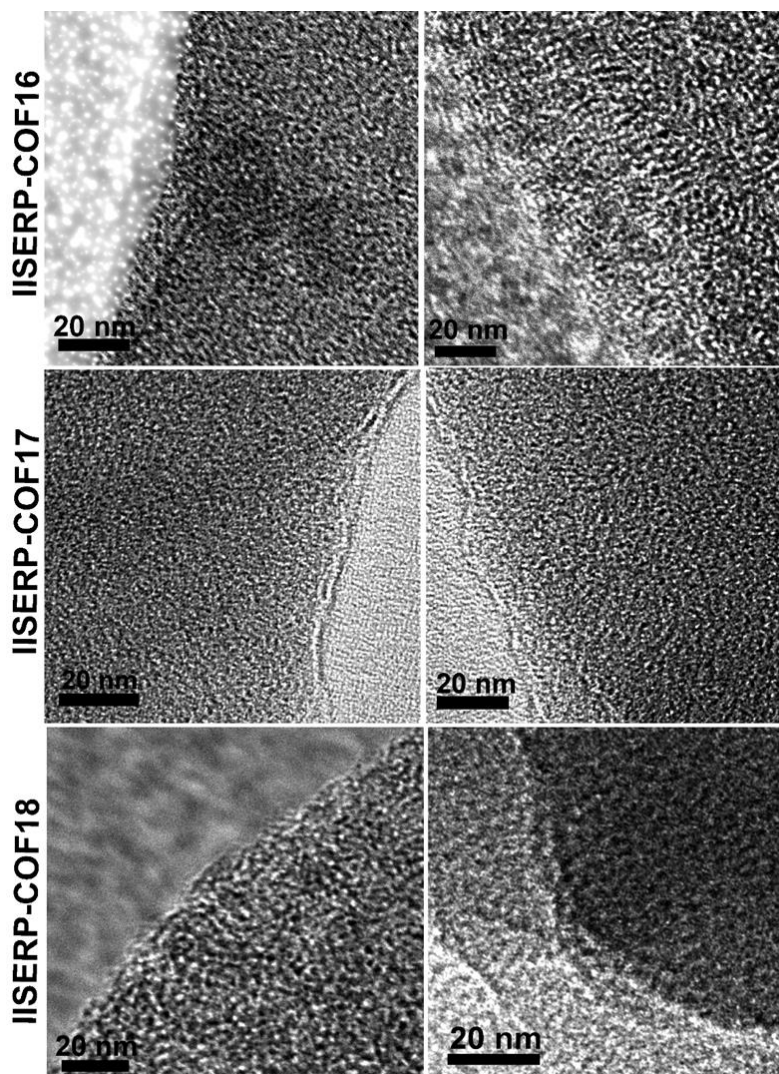


Figure A.3.12. HR-TEM images at higher contrast level showing the porous nature of the COFs at the edges of each COF flakes. The brighter region are the carbon coated Cu grid surfaces.

Cyclic voltammetry of the monomers:

Electrodes were fabricated by coating an ethanolic dispersion of the monomers on carbon paper. Coating was maintained over a $1 \times 1 \text{ cm}^2$ area. Then it was dried in vacuum for 24 hrs. The electrodes were used for the CV measurements carried out in a non-aqueous electrolyte system (*t*-butyl ammonium hexafluorophosphate dissolved in acetonitrile, $t\text{BuNH}_4\text{PF}_6/\text{ACN}$). A non-aqueous Ag/Ag^+ reference electrode and platinum flag counter electrodes were used. CV measurements were carried in 50 mV/s scan rate from -ve to +ve potential window.

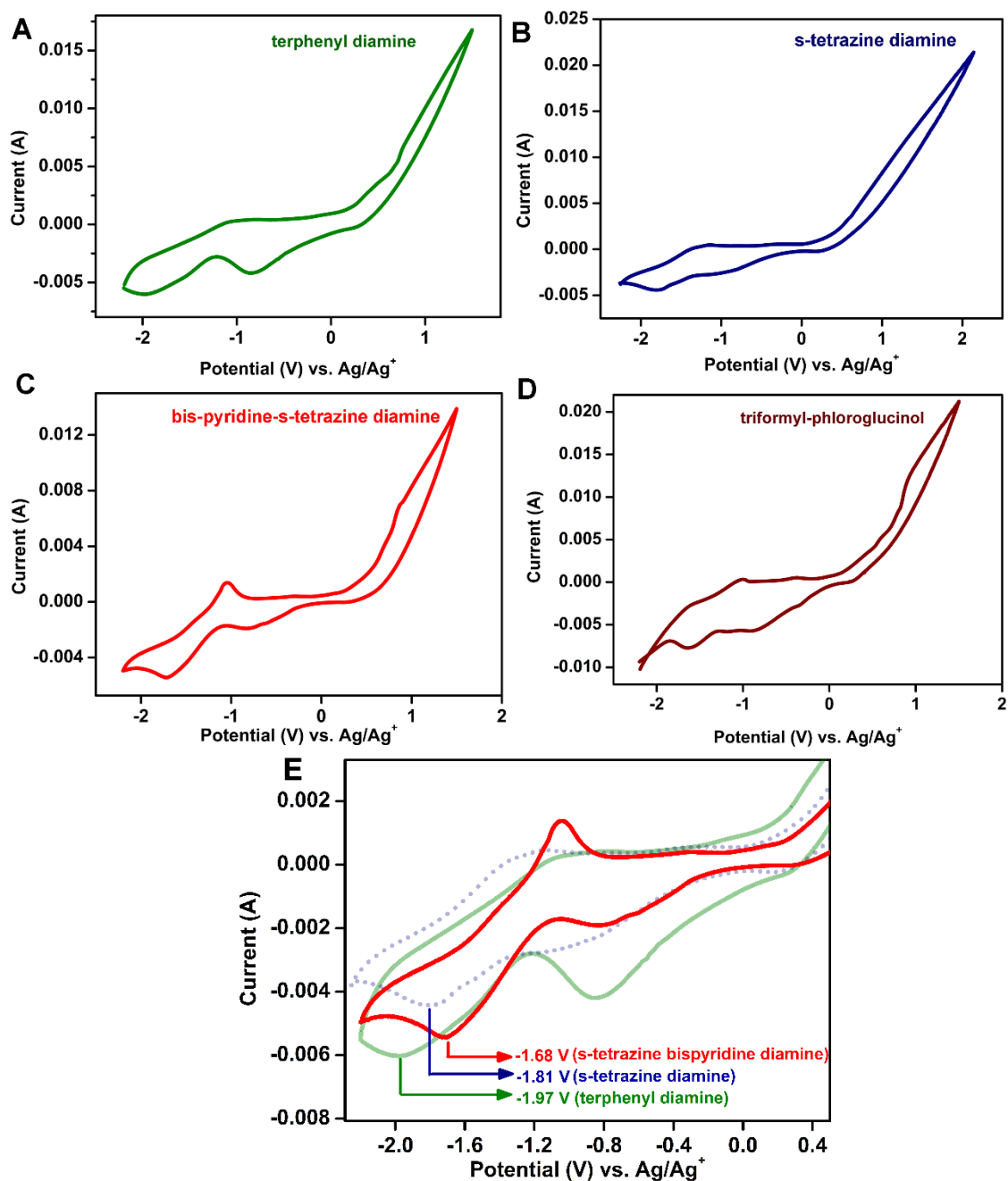


Figure A.3.13. Cyclic voltammograms of (A) terphenyl amine (B) s-tetrazine diamine (C) bispyridine-s-tetrazine diamine (D) triformylphloroglucinol @50 mV/s using 0.5 (M) solution of tBuNH₄PF₆/ACN (non-aqueous electrolyte system). (E) Position of lowest reduction potential region of the monomers.

Observation: The oxidation and reduction potential of the monomers are distinctly different in comparison with their respective COFs. A gradual shift of the lowest reduction peak is observed in the -ve quadrant as we move from terphenyl diamine to tetrazine diamine to bis-pyridine-s-tetrazine diamine. Thus the monomer itself indicates the favourability of using the bis-pyridine-tetrazine units.

Stabilization of the coulombic efficiency:

We carried out the OCV studies using the COF-derived coin-cells. The OCV gradually decreases with time (Figure A.3.27). This indicates the self-discharge process of the battery without the influence of an external potential. This could also be contributing to the initial drop in coulombic efficiency along with the SEI layer formation. The first cycle coulombic efficiency appears only ~50% for these COFs due to stable Solid Electrolyte Interphase (SEI) formation on the COF derived electrode surface. A lot of Sodium consumption happens irreversibly at the first discharge itself as the electrolytes decompose on the highly functionalized porous surface of the COFs. After a few cycles, the reversibility achieved in the sodiation-desodiation process. That stabilizes the sp. capacities with ~98% coulombic efficiency (Figure A.3.28, Table A.3.8). The steadiness of coulombic efficiency well after the initial cycles indicates the stability of the COF-derived electrodes over multiple cycles of charge-discharge at high current densities.

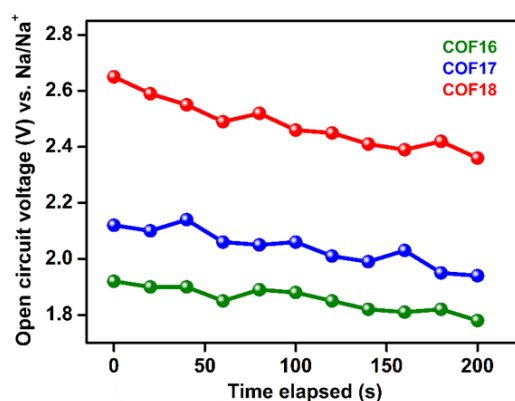


Figure A.3.14. Self-discharge process of the COF-derived half-cells as a function of time.

Table A.3.3. First cycle coulombic efficiency of COF derived anodes estimated from galvanostatic charge-discharge at 100 mA/ current density.

COFs	Discharge sp. capacity (mAh/g) @100 mA/g	Charge sp. capacity (mAh/g) @100 mA/g	Coulombic Efficiency (%)
IISERP-COF16	210	120	57.0
IISERP-COF17	590	310	53.2
IISERP-COF18	1220	605	49.6

References:

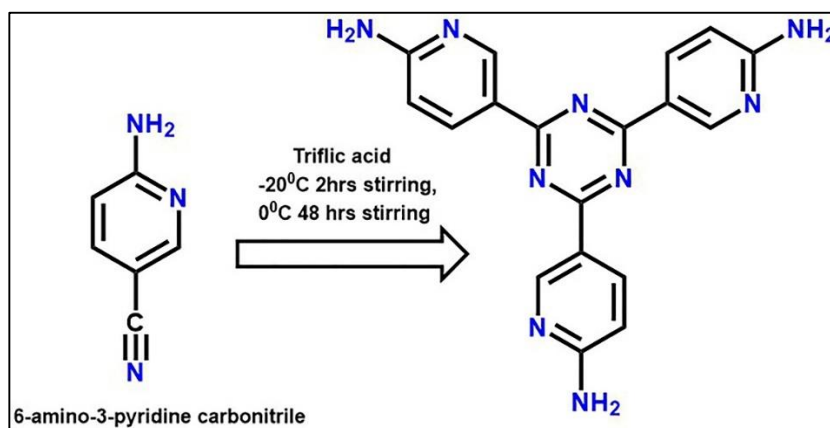
- A.3.1.** B. C. Patra, S. K. Das, A. Ghosh, P. Moitra, M. Addicoat, S. Mitra, A. Bhaumik, S. Bhattacharya and A. Pradhan, *J. Mater. Chem. A*, 2018, **6**, 16655-16663.
- A.3.2.** S. Gu, S. Wu, L. Cao, M. Li, N. Qin, J. Zhu, Z. Wang, Y. Li, Z. Li and J. Chen, *J. Am. Chem. Soc.*, 2019, **141**, 9623-9628.
- A3.3.** R. Shi, L. Liu, Y. Lu, C. Wang, Y. Li, L. Li, Z. Yan and J. Chen, *Nat. Commun.*, 2020, **11**, 1-10.
- A.3.4.** X. Zhang, G. Zhu, M. Wang, J. Li, T. Lu, L. Pan, *Carbon*, 2017, **116**, 686-694.
- A.3.5.** M.-S. Kim, W.-J. Lee, S.-M. Paek and J. K. Park, *ACS Appl. Mater. Interfaces*, 2018, **10**, 32102-32111.
- A.3.6.** K. S. Weeraratne, A. A. Alzharani, and H. M. El-Kaderi, *ACS Appl. Mater. Interfaces*, 2019, **11**, 23520-23526.
- A.3.7.** Z. Li, J. Zhou, R. Xu, S. Liu, Y. Wang, P. Li, W. Wu, M. Wu, *Chemical Engineering Journal*, 2016, **287**, 516-522.
- A.3.8.** T. Sun, Z.-j. Li, H.-J. Wang, D. Bao, F.-L. Meng, and X.-B. Zhang, *Angew. Chem. Int. Ed.*, 2016, **55**, 1-6.
- A.3.9.** Y. Chen, L. Shi, S. Guo, Q. Yuan, X. Chen, J. Zhou and H. Song, *J. Mater. Chem. A*, 2017, **5**, 19866-19874.

- A.3.10.** W. Song, J. Kan, H. Wang, X. Zhao, Y. Zheng, H. Zhang, L. Tao, M. Huang, W. Liu and J. Shi, *ACS Appl. Nano Mater.*, 2019, **2**, 5643-5654.
- A.3.11.** Q. Jin, K. Wang, P. Feng, Z. Zhang, S. Cheng and K. Jiang, *Energy Storage Mater.*, 2020, **27**, 43-50.
- A.3.12.** R. Dan, W. Chen, Z. Xiao, P. Li, M. Liu, Z. Chen and F. Yu, *Energy Fuels*, 2020, **34**, 3923-3930.
- A.3.13.** F.-X. Coudert, A. H. Fuchs, *Coordination Chemistry Reviews*, 2016, **15**, 211-236.
- A.3.14.** C. Abrioux, B. Coasne, G. Maurin, F. Henn, A. Boutin, A. Di Lella, C. Nieto-Draghi and A. H. Fuchs, *Adsorption*, 2008, **14**, 743-754.
- A.3.15.** S. Buttefey, A. Boutin, C. Mellot-Draznieks, A. Fuchs, *J. Phys. Chem. B*, 2001, **105**, 9569-9575.
- A.3.16.** First principles methods using CASTEP, S. J. Clark et al., *Z. Kristallogr.*, 2005, **220**, 567-570.
- A.3.17.** L. Ascherl, T. Sick, J. T. Margra, S. H. Lapidus, M. Calik, C. Hettstedt, K. Karaghiosoff, M. Döblinger, T. Clark, K. W. Chapman, F. Auras and T. Bein, *Nature Chemistry*, 2016, **8**, 310-316.
- A.3.18.** J. P. Perdew, K. Burke and M. Ernzerhof, *Phys. Rev. Lett.*, 1996, **77**, 3865-3868.

Appendix 4:

Materials and methods for COF synthesis:

Synthesis of 5,5',5''-(1,3,5-triazine-2,4,6-triyl)tris(pyridin-2-amine):



Scheme A.4.1. Preparation of 5,5',5''-(1,3,5-triazine-2,4,6-triyl)tris(pyridin-2-amine).

In a typical synthesis, 1.544 g (13.076 mmol) 6-Amino-3-pyridinecarbonitrile was taken in a round bottom flask at -20 °C. Then 8 mL (88.8 mmol) CF₃SO₃H was added dropwise for 20 minutes. The resulting mixture was stirred for 24 h at room temperature in an inert atmosphere. Subsequently, the reaction mixture was quenched with distilled water and was neutralized by adding 2M NaOH solution until the pH was 7. At this pH, a pale yellow precipitate was observed which with further increase in pH it turns white. This white precipitate was filtered off and washed several times with distilled water. The purified product was characterized by ¹H and ¹³C NMR (Figure A.4.1). This ligand was again re-crystallized from hot DMF (Figure A.4.2). Remark: This ligand is being reported for the first time.

Solution state NMR studies:

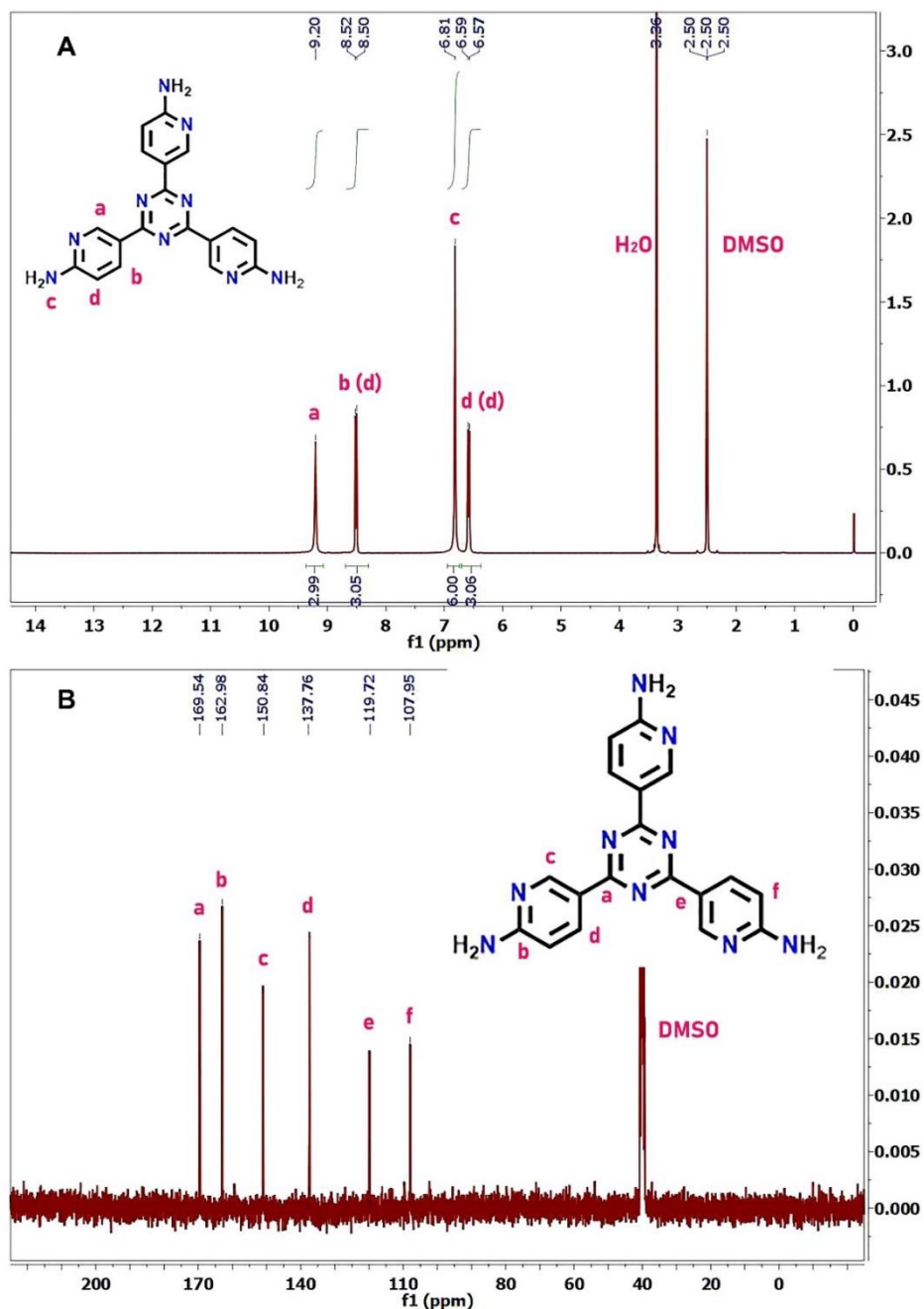


Figure A.4.1. ^1H -NMR and ^{13}C -NMR of 5,5',5''-(1,3,5-triazine-2,4,6-triyl)tris(pyridin-2-amine) were recorded in deuterated dimethyl sulfoxide (DMSO- d_6) at room temperature.

Single crystal structure of tri-pyridine-triazine amine :

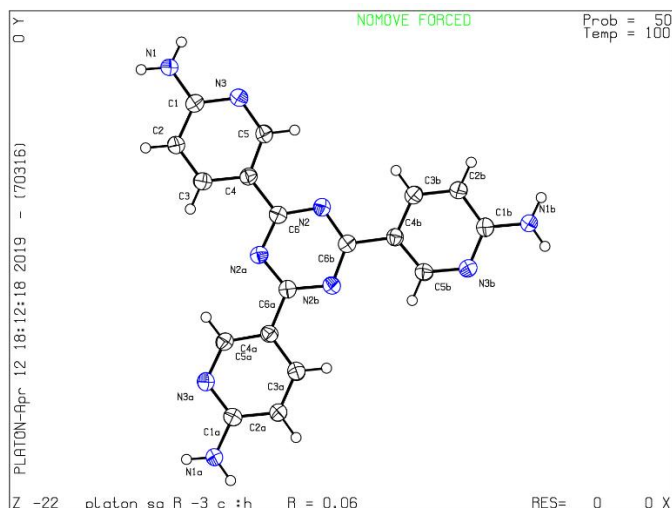


Figure A.4.2. ORTEP model (at 50% probability); Carbon (black), Nitrogen (blue), Hydrogen (white).

Table A.4.1. Single crystal X-ray diffraction parameters

C-C = 0.0034 Å			Wavelength=1.54178
Bond precision:			
Cell:	a=24.203(3)	b=24.203(3)	c=13.343(2)
	alpha=90	beta=90	gamma=120
Temperature: 100 K			
	Calculated	Reported	
Volume	6769(2)	6769(2)	
Space group	R -3 c	R -3 c :h	
Hall group	-R 3 2" c	-R 3 2" c	
Moiety formula	C18 H15 N9 [+ solvent]	C18 H15 N9	
Sum formula	C18 H15 N9 [+ solvent]	C18 H15 N9	
Mr	357.39	357.39	
Dx, g cm-3	1.052	1.052	
Z	12	12	
Mu (mm-1)	0.565	0.565	
F000	2232.0	2232.0	
F000'	2238.51		
h,k,lmax	29,29,16	29,29,15	
Nref	1504	1464	
Tmin,Tmax	0.748,0.798	0.748,0.798	
Data completeness (%)	97.3		
Theta(max)	72.698		
R1 = 0.0581		wR2 = 0.1563	
GOF = 1.094			
Abs. Correction method= Multi-scan; T Limits: Tmin=0.748 Tmax=0.798			

Synthesis of 2, 4, 6-triformylphenol:

This compound was synthesized following previously reported method[#]. This ligand was recrystallized by dissolving in hot DMF (Figure A.4.3, Table A.4.2).

[#] Xu et al. *Chem. Commun.*, **2015**, *51*, 10868

Single crystal structure of 2-hydroxybenzene-1,3,5-tricarbaldehyde :

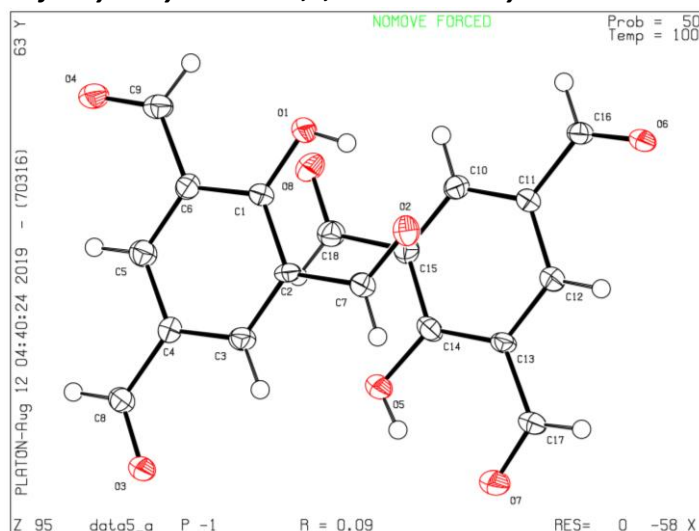


Figure A.4.3. ORTEP model of triformyl phenol (at 50% probability); Carbon (black), Oxygen (red), Hydrogen (white).

Table A.4.2. Single crystal X-ray diffraction parameters

C-C = 0.0054 Å		Wavelength=1.54178
Bond precision:		
Cell:	a= 7.8800(11) b= 8.7364(13) c= 11.1502(17)	
	alpha= 98.233(9) beta= 91.784(8) gamma=100.958(9)	
Temperature: 100 K		
	Calculated	Reported
Volume	744.50(19)	744.50(19)
Space group	P -1	P -1
Hall group	-P 1	-P 1
Moiety formula	C9 H6 O4	C9 H6 O4
Sum formula	C9 H6 O4	C9 H6 O4
Mr	178.14	178.14
Dx, g cm⁻³	1.589	1.589
Z	4	4
Mu (mm⁻¹)	1.090	1.090
F000	368.0	368.0
F000'	369.40	
h,k,lmax	9,10,13	9, 10, 13
Nref	2944	2849
Tmin,Tmax	0.546,0.647	0.546, 0.647
Data completeness (%)	96.8	
Theta(max)	0.647	
R1 = 0.0900		
GOF = 1.058		
Abs. Correction method= Multi-scan; T Limits: Tmin=0.546,Tmax=0.647		

Synthesis of 2, 4, 6-triformylresorcinol:

This compound was synthesized following previously reported method[#]. This ligand was recrystallized by dissolving in hot DMF (Figure A.4.4, Table A.4.3).

[#] Haldar et al. *J. Am. Chem. Soc.* **2018**, *140*, 13367–13374

Single crystal structure of 2,4-dihydroxybenzene-1,3,5-tricarbaldehyde

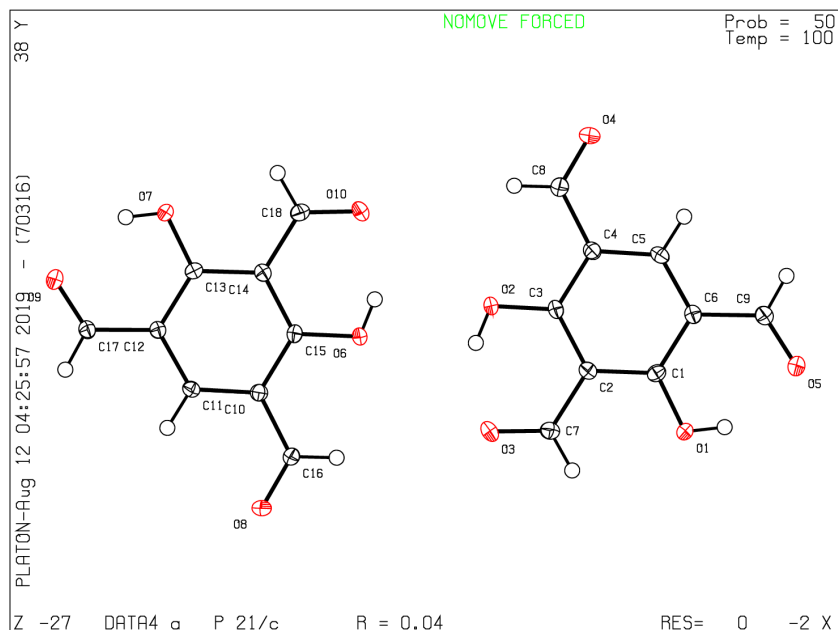


Figure A.4.4. ORTEP model of triformyl resorcinol (at 50% probability); Carbon (black), Oxygen (red), Hydrogen (white).

Table A.4.3. Single crystal X-ray diffraction parameters

Bond precision: C-C = 0.0020 Å		Wavelength=1.54178
Cell:	a= 10.3543(12) b= 8.7806(10) c= 17.1264(19)	
	alpha= 90 beta= 96.824(5) gamma=90	
Temperature: 100 K		
	Calculated	Reported
Volume	1546.1(3)	1546.0(3)
Space group	P 21/c	P 21/c
Hall group	-P 2ybc	-P 2ybc
Moiety formula	C9 H6 O5	C9 H6 O5
Sum formula	C9 H6 O5	C9 H6 O5
Mr	194.14	194.14
Dx, g cm ⁻³	1.668	1.668
Z	8	8
Mu (mm ⁻¹)	1.207	1.207
F000	800.0	800.0
F000'	803.19	
h,k,lmax	12,10,21	12,10,21
Nref	3057	3049
Tmin,Tmax	0.749,0.886	0.749,0.886
Data completeness (%)	99.7	
Theta(max)	72.534	
R1 = 0.0443(2572)		
GOF = 1.033		
Abs. Correction method= Multi-scan; T Limits: Tmin=0.749,Tmax=0.886		

Synthesis of 1, 3, 5-triformylphloroglucinol:

1, 3, 5-Triformylphloroglucinol was synthesized following previously reported methods#. This ligand was recrystallized by dissolving in CHCl₃.

Chong et al. *Org. Lett.* **2003**, *5*, 3823-3826

***Single crystal structure of 2,4,6-trihydroxybenzene-1,3,5-tricarbaldehyde has already been provided in the previous report.**

Table A.4.4. Atomic coordinates for IISERP-COF10
Space group: Pm, Monoclinic.
Lattice Parameters: a = 17.79; b = 18.13; c = 3.79 Å; β = 120°

Atom	x	y	z	Occ.
C1	0.25909	0.48728	0.02714	1
N2	0.17893	0.43465	0.02723	1
C3	0.65338	0.80366	0.02744	1
C4	0.28162	0.70249	0.02728	1
C5	0.36845	0.75131	0.0271	1
N6	0.19646	0.31336	0.02707	1
C7	0.16055	0.22961	0.02707	1
C8	0.07502	0.17473	0.02724	1
C9	0.02508	0.2111	0.02737	1
C10	0.06012	0.29602	0.02734	1
C11	0.03684	0.08292	0.02725	1
N12	0.08575	0.04805	0.02713	1
C13	0.51023	0.77442	0.02706	1
N14	0.56707	0.75314	0.02735	1
C15	0.20008	0.85167	0.02694	1
C16	0.29432	0.5775	0.02718	1
C17	0.24623	0.61582	0.02739	1
N18	0.68895	0.88758	0.0274	1
C19	0.77281	0.93339	0.02744	1
C20	0.82582	0.9005	0.02748	1
C21	0.78733	0.81399	0.02761	1
C22	0.70221	0.76612	0.02761	1
C23	0.91769	0.95298	0.02738	1
N24	0.95262	0.03674	0.02737	1
C25	0.22654	0.73787	0.02738	1
N26	0.25428	0.81807	0.02688	1
C27	0.14626	0.34702	0.0272	1
C28	0.42065	0.71731	0.02704	1
C29	0.38168	0.62966	0.027	1
N30	0.1161	0.80236	0.02725	1
C31	0.06917	0.83926	0.02727	1
C32	0.10075	0.92497	0.02703	1

C33	0.18716	0.97401	0.02666	1
C34	0.23615	0.93794	0.02659	1
C35	0.04761	0.96375	0.02715	1
N36	0.96381	0.91482	0.02727	1
O37	0.4301	0.59219	0.02674	1

Characterization of Tp-Tta COF:

A details of the characterization data and adsorption studies have been provided and compared with the previous report as well.

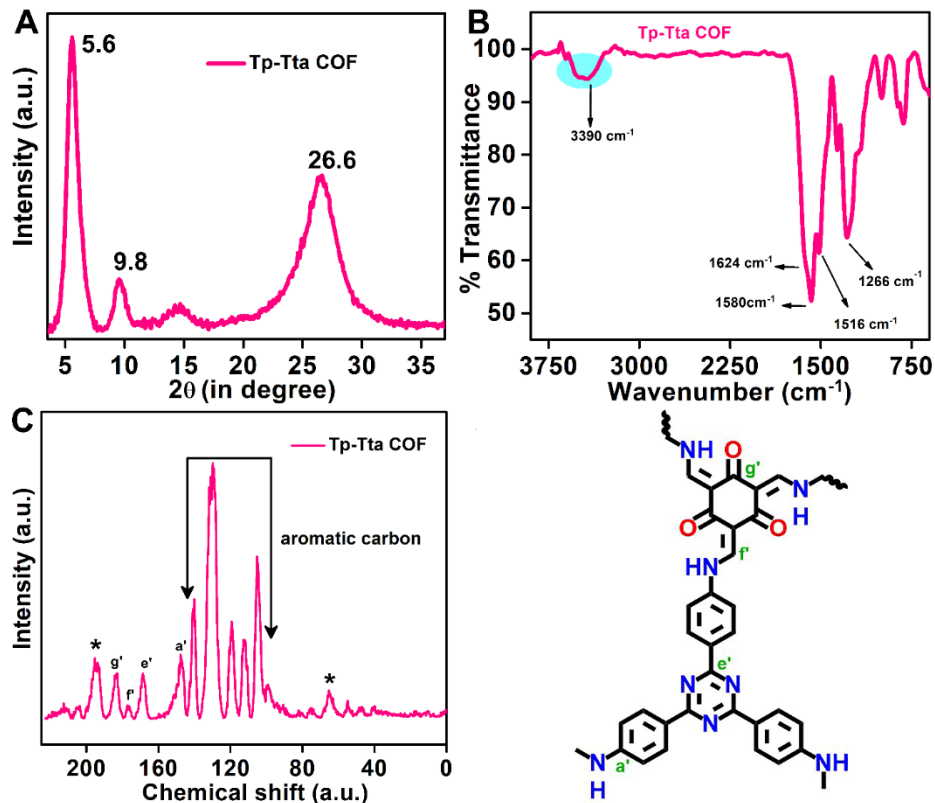


Figure A.4.5. (A) Powder diffraction pattern of TpTta COF. (B) FT-IR spectrum of the activated COF (C) CP MAS ^{13}C -NMR spectra of the COF measured at 500 MHz.

Table A.4.5. A. PXRD data comparison.

COF-Name	2 θ ($^\circ$) corresponds to (100) Plane	2 θ ($^\circ$) corresponds to (110) Plane	2 θ ($^\circ$) corresponds to (001) Plane Broad peak
TP-Tta COF (Reported)	5.6	9.9	26.5
This work (Reproduced)	5.6	9.8	26.6

B. IR data comparison:

COF-Name	Enolic OH (cm^{-1})	carbonyl (C=O) (cm^{-1})	C=N aromatic (cm^{-1})	C=C bond (cm^{-1})	C-N bond (cm^{-1})
TP-Tta COF (Reported)	-	1622	-	1445	1256
This work (Reproduced)	3390	1624	1516	1448	1266

C. Solid state NMR data comparison.

COF-Name	Aromatic carbon atoms (ppm)	carbonyl Carbon (ppm)	C-N (ppm)	Triazine Core (ppm)
TP-Tta COF (Reported)	105 to 137	183	150	167
This work (Reproduced)	110 to 140	184	151	168

Adsorption data analysis of TpTta COF:

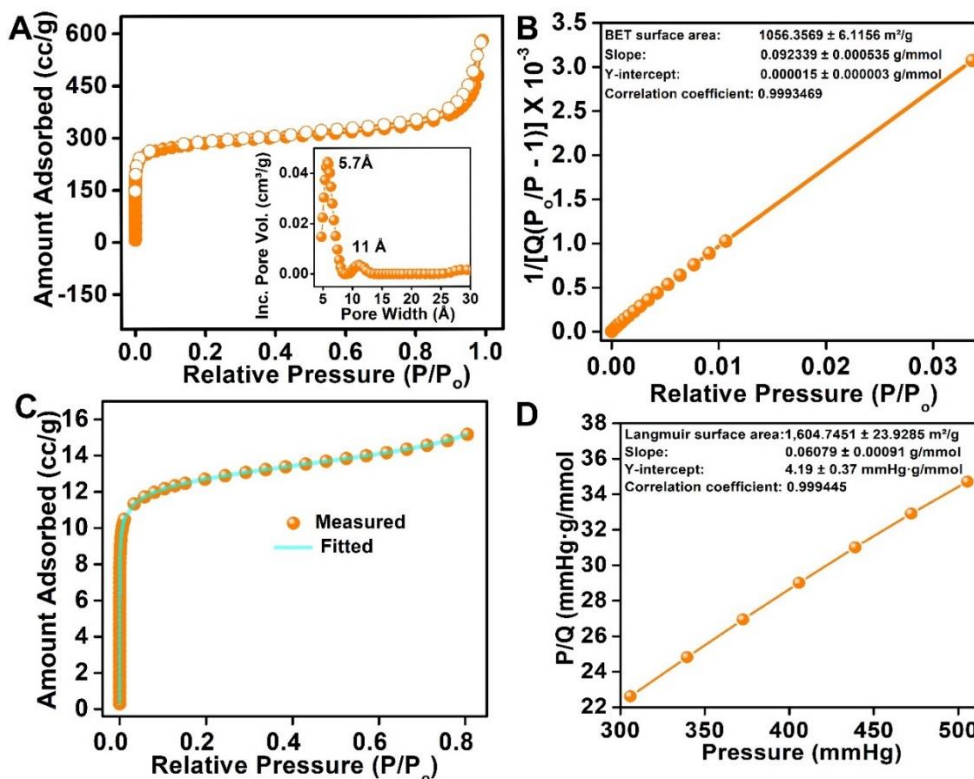


Figure A.4.6. (A) N₂ adsorption-desorption isotherm of TpTta-COF at 77 K. Inset show a plot of the pore width vs. incremental pore volume of TpTta-COF. (B) A BET fit obtained using the low pressure region data of the N₂ adsorption isotherm. (C) Goodness-of-fit plot of the adsorption isotherm from the DFT model (Carbon at 77K). (D) A Langmuir fit obtained using the high pressure region data of the N₂ adsorption isotherm.

Table A.4.6. Comparison table of sp. capacitance using COF and COF derived electrode materials

Electrode materials	Electrolytes	Working Voltage (V)	Current density (A·g ⁻¹)	Specific capacitance (F·g ⁻¹)
TPDA-1 ^{A.4.1}	1 M H ₂ SO ₄	0 to 1	0.5	348
TFP-NDA-COF ^{A.4.2}	1 M H ₂ SO ₄	0 to 1	0.5	348
TpPa-(OH) ₂ ^{A.4.3}	1M phosphate buffer	-0.2 to 0.5	0.5	416
TAPT-DHTA-COF0.1@PP ^{A.4.4}	6M KOH	- 1 to 0	0.5	411
TpPa-COF-SWCNTs ^{A.4.5}	1 M H ₂ SO ₄	-0.2 to 0.75	0.5	153
carbonized ACOF1 ^{A.4.6}	6M KOH	- 1 to 0	1	234
carbonized COF1 ^{A.4.6}	6M KOH	- 1 to 0	1	191
COFs/NH ₂ -Rgo ^{A.4.7}	1M Na ₂ SO ₄	0 to 0.5	0.2	533
s-HPC ^{A.4.8}	1-ethyl-3-methylimidazolium tetrafluoroborate (EMIMBF ₄)	0 to 3	0.5	171
m-HPC ^{A.4.8}	1-ethyl-3-methylimidazolium tetrafluoroborate (EMIMBF ₄)	0 to 3	0.5	163
L-HPC ^{A.4.8}	1-ethyl-3-methylimidazolium tetrafluoroborate (EMIMBF ₄)	0 to 3	0.5	162
XL-HPC ^{A.4.8}	1-ethyl-3-methylimidazolium tetrafluoroborate (EMIMBF ₄)	0 to 3	0.5	192
IISERPCOF-10	1 M H ₂ SO ₄	0 to 0.8	0.5	546
IISERPCOF-11	1 M H ₂ SO ₄	0 to 0.8	0.5	310
IISERPCOF-12	1 M H ₂ SO ₄	0 to 0.8	0.5	400

Control studies using only glassy carbon electrode:

A thorough electrochemical measurements has been carried out using bare glassy carbon electrode. The gravimetric capacitance calculation for bare glassy carbon electrode is not possible. Because the weight of the electroactive part is not known. So that areal capacitance has been compared by GCD measurements at 0.5 mA/cm^2 and by CV measurements at 1.5 mV/s (Table A.4.7). The capacitance contribution from the glassy carbon electrode is negligible.

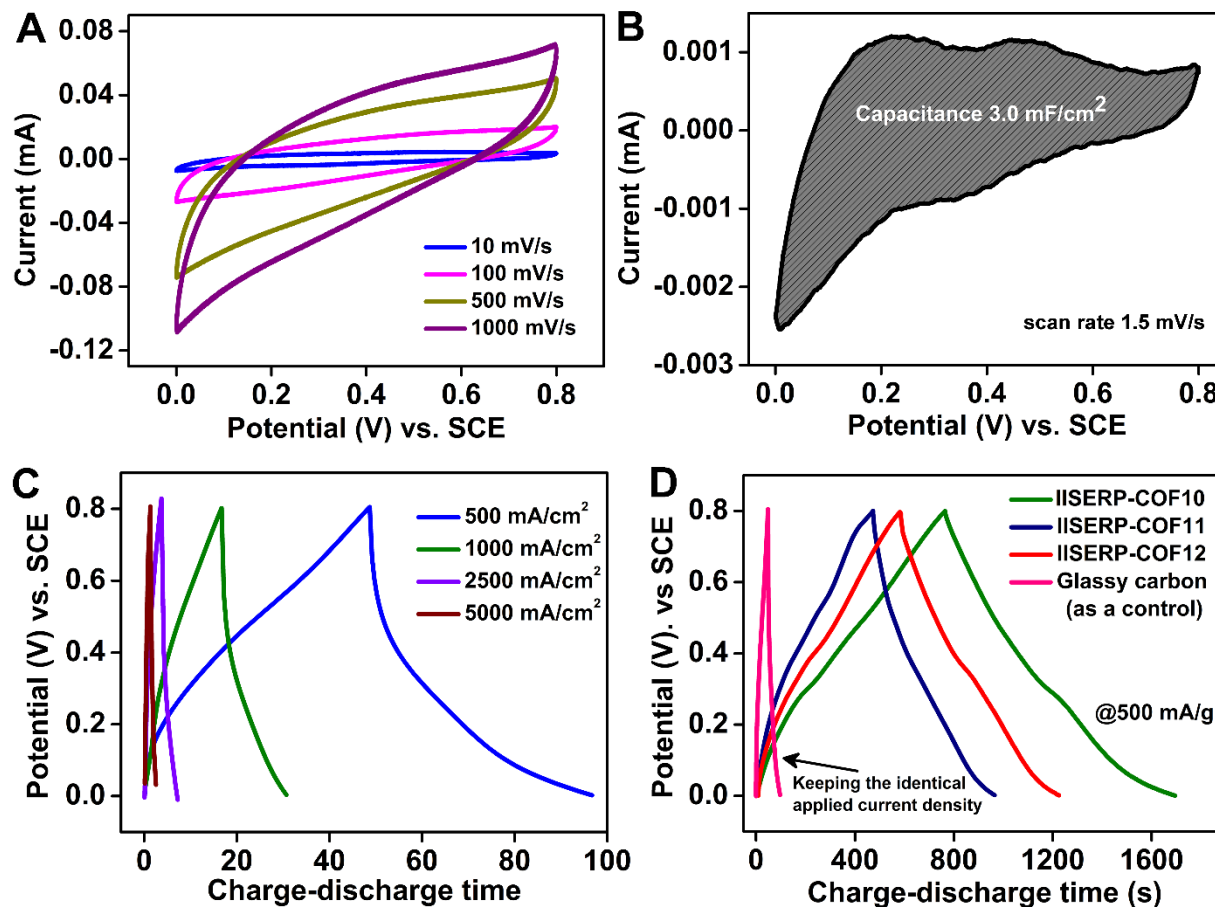


Figure A.4.7. (A) Three-electrode CV measurements using bare glassy carbon working electrode at variable scan rates (from 10 mV/s to 1000 mV/s) in $1 \text{ M H}_2\text{SO}_4$ solution within the potential window of $0\text{-}0.8 \text{ V}$. (B) Three-electrode CV measurement at 1.5 mV/s for the estimation of S_p capacitance value of glassy carbon electrode. (C) Galvanostatic charge-discharge curves for glassy carbon at varying current densities (from 500 mA/g to 5000 mA/g). (D) A comparison of Galvanostatic charge-discharge curves of IISERP-COFs and glassy carbon electrode at identical applied current density. This control experimental was carried out on glassy carbon electrode by removing the COF coating from the glassy carbon surface and by keeping the applied current density same. Which shows contribution in discharging time from glassy carbon electrode is negligible.

Table A.4.7. Comparison of areal capacitance value of COFs with glassy carbon electrode.

COF used in the electrode	Areal capacitance of COFs in three electrode system (mF/cm ²)	Areal capacitance of Glassy carbon electrode (mF/cm ²)	Areal capacitance of only COFs (mF/cm ²)
IISERP-COF10	65	3.0	62
IISERP-COF11	41		38
IISERP-COF12	50		47
Tp-Tta COF	27		24

This table shows that the areal capacitance of bare glassy carbon electrode is only 3 F/cm². During the capacitance measurement of the COFs that glassy carbon electrode surface was coated with active COF material. So the surface of glassy carbon electrode was not exposed much to the electrolyte solution for storing charge under applied potential.

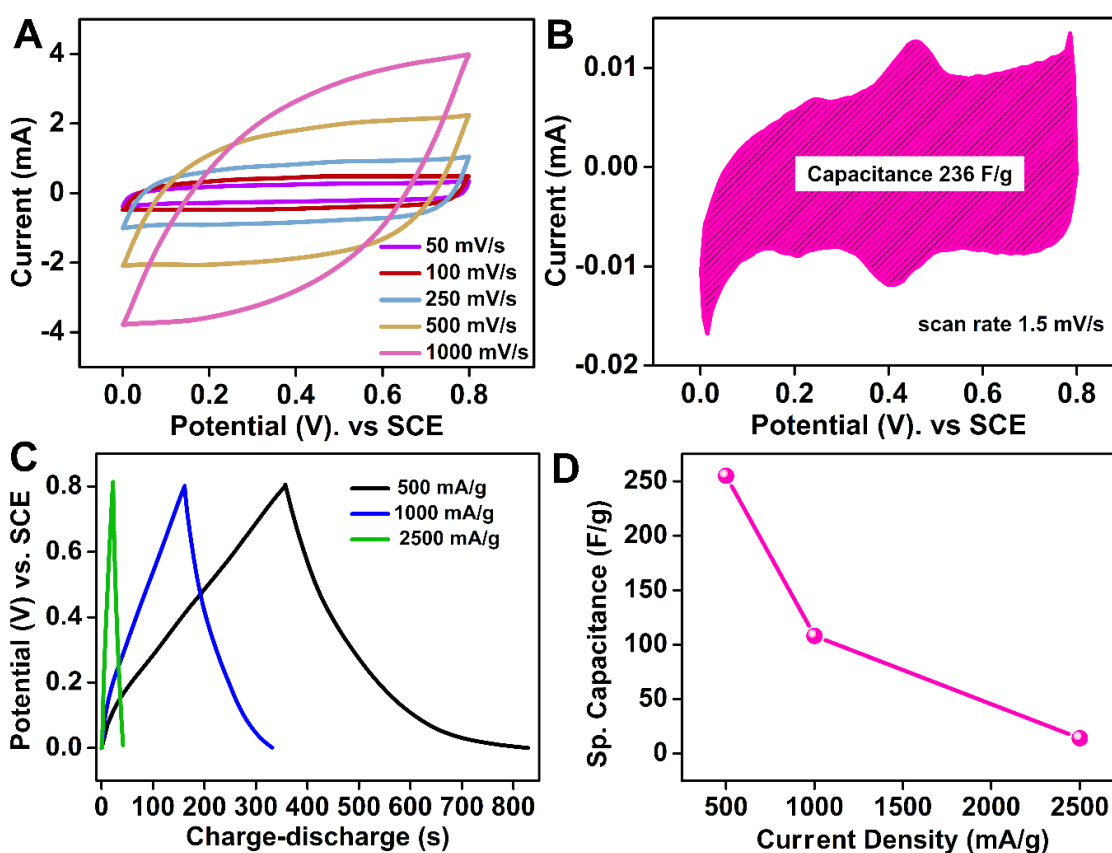


Figure A.4.8. (A) Three-electrode CV measurements of Tp-Tta derived electrode at variable scan rates (from 50 mV/s to 1000 mV/s) in 1 M H₂SO₄ solution within the potential window of 0-0.8 V. (B) Three-electrode CV measurement at 1.5 mV/s for the estimation of Sp. capacitance value of Tp-Tta COF. (C) Galvanostatic charge-discharge curves for glassy carbon at varying current densities (from 500 mA/g to 2500 mA/g). (D) Retention of the gravimetric capacitance of Tp-Tta COF with the increase of current density from 500 mA/g to 2500 mA/g.

Control studies:

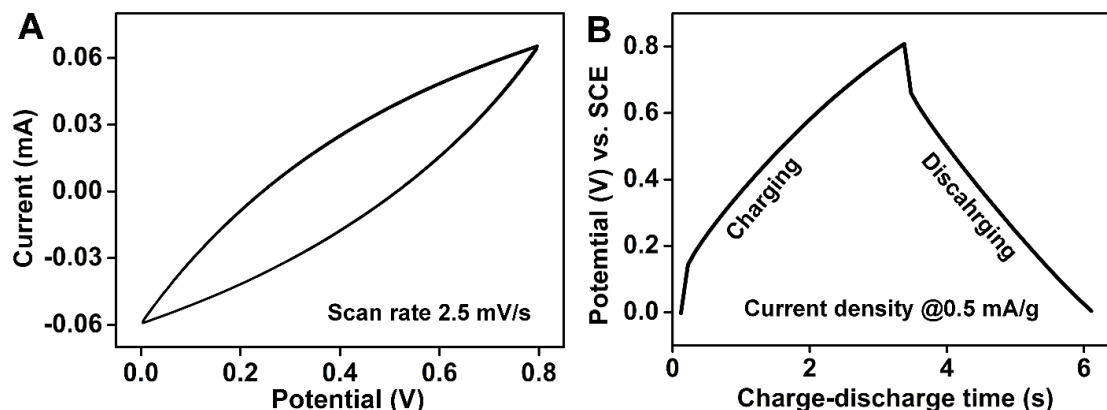


Figure A.4.9. (A) CV measurements @2.5 mV/s using only carbon cloth derived solid state capacitors (without the active material, COF). (B) GCD curve obtained @0.5 mA/g current density using carbon cloth-derived solid state capacitor. Note that the charge-discharge times are several orders lower compared to when the COF was used as the active material => extremely low specific capacitance.

Impedance analysis of the COF-derived solid state capacitor:

Impedance analysis were performed with the solid state device made of IISERP-COF10, IISERP-11, IISERP-12. The frequency was varied from 1 MHz to 10 mHz at a constant open-circuit potential with an amplitude of 10 mV. As can be seen from the Figure A.4.10, a very low charge-transfer resistance is observed in the high frequency region, this directly reflects the observed high capacitance.

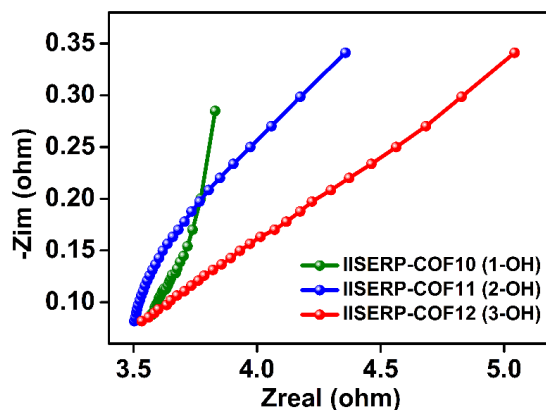



Figure A.4.10: Nyquist plots from the AC-impedance measurements of the IISERP-COF10, IISERP-COF11 and IISERP-COF12 using solid state two-electrode assembly.

References:


- A.4.1. Bhanja, P.; Das, S. K.; Bhunia, K.; Pradhan, D.; Hayashi, T.; Hijikata, Y.; Irle, S.; Bhaumik, A., A new porous polymer for highly efficient capacitive energy storage. *ACS Sustainable Chem. Eng.* **2017**, *6*, 202-209.
- A.4.2. Das, S. K.; Bhunia, K.; Mallick, A.; Pradhan, A.; Pradhan, D.; Bhaumik, A., A new electrochemically responsive 2D π -conjugated covalent organic framework as a high performance supercapacitor. *Microporous Mesoporous Mater.* **2018**, *266*, 109-116.
- A.4.3. Chandra, S.; Chowdhury, D. R.; Addicoat, M.; Heine, T.; Paul, A.; Banerjee, R. Molecular Level Control of the Capacitance of Two-Dimensional Covalent Organic Frameworks: Role of Hydrogen Bonding in Energy Storage Materials. *Chem. Mater.* **2017**, *29*, 2074–2080.
- A.4.4. Xu, Q.; Tang, Y.; Zhai, L.; Chen, Q.; Jiang, D., Pyrolysis of covalent organic frameworks: A general strategy for template converting conventional skeletons into conducting microporous carbons for high-performance energy storage. *Chem. Commun.* **2017**, *53*, 11690-11693.
- A.4.5. Han, Y.; Zhang, Q.; Hu, N.; Zhang, X.; Mai, Y.; Liu, J.; Hua, X.; Wei, H.; Core-shell nanostructure of single-wall carbon nanotubes and covalent organic frameworks for supercapacitors. *Chin. Chem. Lett.* **2017**, *28*, 2269–2273.
- A.4.6. Kim, G.; Yang, J.; Nakashima, N.; Shiraki, T., Highly Microporous Nitrogen-doped Carbon Synthesized from Azine-linked Covalent Organic Framework and its Supercapacitor Function. *Chem. Eur. J.* **2017**, *23*, 17504-17510.
- A.4.7. Wang, P.; Wu, Q.; Han, L.; Wang, S.; Fang, S.; Zhang, Z.; Sun, S., Synthesis of conjugated covalent organic frameworks/Graphene composite for supercapacitor electrodes. *RSC Adv.* **2015**, *5*, 27290–27294.
- A.4.8. Baumann, D.; Lee, C.; Wan, C.; Sun, H.; Duan, X., Hierarchical Porous Carbon Derived from Covalent Triazine Frameworks for High Mass Loading Supercapacitors. *ACS Materials Lett.* **2019**, *1*, 320–326.

Copyrights

 Sattwick Haldar <haldar@students.iiserpune.ac.in>

Thank you for your order with RightsLink / John Wiley and Sons

no-reply@copyright.com <no-reply@copyright.com> 9 January 2020 at 18:05
To: sattwick.haldar@students.iiserpune.ac.in



Thank you for your order!

Dear Mr. SATTWICK HALDAR,

Thank you for placing your order through Copyright Clearance Center's RightsLink® service.


Order Summary


Licensee: IISER Pune
Order Date: Jan 9, 2020
Order Number: 4744750326472
Publication: Advanced Energy Materials
Title: High and Reversible Lithium Ion Storage in Self-Exfoliated Triazole-Trimethyl Phloroglucinol-Based Covalent Organic Nanosheets
Type of Use: Dissertation/Thesis
Order Total: 0.00 USD

View or print complete details of your order and the publisher's terms and conditions.

Sincerely,
Copyright Clearance Center


Tel: +1-855-239-3415 / +1-878-646-2777
customerservice@copyright.com
https://myaccount.copyright.com



 Sattwick Haldar <haldar@students.iiserpune.ac.in>

Thank you for your order with RightsLink / John Wiley and Sons

no-reply@copyright.com <no-reply@copyright.com> 9 January 2020 at 18:05
To: sattwick.haldar@students.iiserpune.ac.in



Thank you for your order!

Dear Mr. SATTWICK HALDAR,

Thank you for placing your order through Copyright Clearance Center's RightsLink® service.


Order Summary


Licensee: IISER Pune
Order Date: Jan 9, 2020
Order Number: 4744750326472
Publication: Advanced Energy Materials
Title: Chemical Exfoliation as a Controlled Route to Enhance the Anodic Performance of COF in LIB
Type of Use: Dissertation/Thesis
Order Total: 0.00 USD

View or print complete details of your order and the publisher's terms and conditions.

Sincerely,
Copyright Clearance Center

Tel: +1-855-239-3415 / +1-878-646-2777
customerservice@copyright.com
https://myaccount.copyright.com




 Sattwick Haldar <haldar@students.iiserpune.ac.in>

RESPONSE REQUIRED for Your Request to Royal Society of Chemistry

1 message

no-reply@copyright.com <no-reply@copyright.com> 23 July 2020 at 11:42
To: sattwick.haldar@students.iiserpune.ac.in



Dear Mr. SATTWICK HALDAR,

Royal Society of Chemistry has approved your recent request. Before you can use this content, you must accept the license fee and terms set by the publisher.

Use this link to accept (or decline) the publisher's fee and terms for this order.


Request Summary:
Submit date: 22-Jul-2020
Request ID: 802019454
Publication: Nanoscale Horizons
Title: Tuning the electronic energy level of covalent organic frameworks for crafting high-rate Na-ion battery anode.
Type of Use: Republish in a thesis/dissertation

Please do not reply to this message.

To speak with a Customer Service Representative, call +1-855-239-3415 toll free or +1-978-646-2600 (24 hours a day), or email your questions and comments to support@copyright.com.

Sincerely,
Copyright Clearance Center

Tel: +1-855-239-3415 / +1-878-646-2600
support@copyright.com
Manage Account



 Pyridine-Rich Covalent Organic Frameworks as High-Performance Solid-State Supercapacitors

Author: Sattwick Haldar, Rinku Kushwaha, Rahul Malty, et al
Publication: ACS Materials Letters
Publisher: American Chemical Society
Date: Oct 1, 2019
Copyright © 2019, American Chemical Society

PERMISSION/LICENSE IS GRANTED FOR YOUR ORDER AT NO CHARGE

This type of permission/license, instead of the standard Terms & Conditions, is sent to you because no fee is being charged for your order. Please note the following:

- Permission is granted for your request in both print and electronic formats, and translations.
- If figures and/or tables were requested, they may be adapted or used in part.
- Please print this page for your records and send a copy of it to your publisher/graduate school.
- Appropriate credit for the requested material should be given as follows: "Reprinted (adapted) with permission from (COMPLETE REFERENCE CITATION). Copyright (YEAR) American Chemical Society." Insert appropriate information in place of the capitalized words.
- One-time permission is granted only for the use specified in your request. No additional uses are granted (such as derivative works or other editions). For any other uses, please submit a new request.

 Boosting lithium storage in covalent organic framework via activation of 14-electron redox chemistry

Author: Zhendong Lei et al
Publication: Nature Communications
Publisher: Springer Nature
Date: Feb 6, 2018
Copyright © 2018, Springer Nature

Creative Commons

This is an open access article distributed under the terms of the Creative Commons CC BY license, which permits unrestricted use, distribution, and reproduction in any medium, provided the original work is properly cited.

You are not required to obtain permission to reuse this article.
To request permission for a type of use not listed, please contact Springer Nature

Nitrogen-rich covalent organic frameworks with multiple carbonyls for high-performance sodium batteries

Author: Ruijuan Shi et al
Publication: Nature Communications
Publisher: Springer Nature
Date: Jan 10, 2020
Copyright © 2020, Springer Nature

SPRINGER NATURE

Creative Commons
This is an open access article distributed under the terms of the Creative Commons CC BY license, which permits unrestricted use, distribution, and reproduction in any medium, provided the original work is properly cited.
You are not required to obtain permission to reuse this article.
To request permission for a type of use not listed, please contact Springer Nature

Interlayer Hydrogen-Bonded Covalent Organic Frameworks as High-Performance Supercapacitors

Author: Arjun Halder, Meena Ghosh, Abdul Khayum M, et al
Publication: Journal of the American Chemical Society
Publisher: American Chemical Society
Date: Sep 1, 2018
Copyright © 2018, American Chemical Society

ACS Publications
Most Trusted. Most Cited. Most Read.

PERMISSION/LICENSE IS GRANTED FOR YOUR ORDER AT NO CHARGE
This type of permission/license, instead of the standard Terms & Conditions, is sent to you because no fee is being charged for your order. Please note the following:

- Permission is granted for your request in both print and electronic formats, and translations.
- If figures and/or tables were requested, they may be adapted or used in part.
- Please print this page for your records and send a copy of it to your publisher/graduate school.
- Appropriate credit for the requested material should be given as follows: "Reprinted (adapted) with permission from (COMPLETE REFERENCE CITATION). Copyright (YEAR) American Chemical Society." Insert appropriate information in place of the capitalized words.
- One-time permission is granted only for the use specified in your request. No additional uses are granted (such as derivative works or other editions). For any other uses, please submit a new request.

If credit is given to another source for the material you requested, permission must be obtained from that source.

Covalent Organic Frameworks: Design, Synthesis, and Functions

Author: Keyu Geng, Ting He, Ruoyang Liu, et al
Publication: Chemical Reviews
Publisher: American Chemical Society
Date: Jan 1, 2020
Copyright © 2020, American Chemical Society

ACS Publications
Most Trusted. Most Cited. Most Read.

PERMISSION/LICENSE IS GRANTED FOR YOUR ORDER AT NO CHARGE
This type of permission/license, instead of the standard Terms & Conditions, is sent to you because no fee is being charged for your order. Please note the following:

- Permission is granted for your request in both print and electronic formats, and translations.
- If figures and/or tables were requested, they may be adapted or used in part.
- Please print this page for your records and send a copy of it to your publisher/graduate school.
- Appropriate credit for the requested material should be given as follows: "Reprinted (adapted) with permission from (COMPLETE REFERENCE CITATION). Copyright (YEAR) American Chemical Society." Insert appropriate information in place of the capitalized words.
- One-time permission is granted only for the use specified in your request. No additional uses are granted (such as derivative works or other editions). For any other uses, please submit a new request.

If credit is given to another source for the material you requested, permission must be obtained from that source.

List of Publications

Included in Thesis:

Corresponding Author:

11. Chemical Exfoliation as a Controlled Route to Enhance the Anodic Performance of COF in LIB

Sattwick Haldar,* Kingshuk Roy, Rinku Kushwaha, Satishchandra Ogale* and Ramanathan Vaidhyanathan*

Advanced Energy Materials, 2019, 9, 1902428 (Impact factor: 25.245)

First Author:

10. High and Reversible Lithium Ion Storage in Self-Exfoliated Triazole-Triformyl Phloroglucinol-Based Covalent Organic Nanosheets

Sattwick Haldar, Kingshuk Roy, Shyamapada Nandi, Debanjan Chakraborty, Dhanya Puthusseri, Yogesh Gawli, Satishchandra Ogale* and Ramanathan Vaidhyanathan*

Advanced Energy Materials, 2018, 8, 1702170 (Impact factor: 25.245)

9. Pyridine-rich Covalent Organic Frameworks as High performance Solid State Supercapacitors

Sattwick Haldar, Rinku Kushwaha, Rahul Maity and Ramanathan Vaidhyanathan*

ACS Materials Letters, 2019, 1, 490 (Impact factor: Pending)

8. Tuning the Electronic Energy Level of Covalent Organic Framework for Crafting High-rate Na-ion Battery Anode

Sattwick Haldar, Kaleeswaran D, Deepak Rase, Kingshuk Roy, Satishchandra Ogale and Ramanathan Vaidhyanathana*

Nanoscale Horizons, 2020, Advance Article, DOI: 10.1039/D0NH00187B (Impact factor: 9.927)

Not included in thesis:

First Author:

7. Anthracene-Resorcinol Derived Covalent Organic Framework as Flexible White Light Emitter

Sattwick Haldar, Debanjan Chakraborty, Bibhisn Roy, Gangadhar Banappanavar, Kushwaha Rinku, Dinesh Mullangi, Partha Hazra, Dinesh Kabra* and Ramanathan Vaidhyanathan*

Journal of the American Chemical Society, 2018, 41, 13367 (Impact factor: 14.612)

6. Facile Exfoliation of Single-Crystalline Copper Alkylphosphates to Single-Layer Nanosheets and Enhanced Supercapacitance

Gulzar A. Bhat,⁺ **Sattwick Haldar**,⁺ (**Equal first author**) Sonam Verma, Debanjan Chakraborty Ramanathan Vaidhyanathan* and Ramaswamy Murugavel*

Angewandte Chemie International Edition, 2019, 58, 16844 (Impact factor: 12.959)

Co-Author:

5. Strategically Designed Azolyl-Carboxylate MOFs for Potential Humid CO₂ Capture

Shyamapada Nandi, **Sattwick Haldar**, Debanjan Chakraborty and Ramanathan Vaidhyanathan*

Journal of Materials Chemistry A, 2017, 5, 535

4. Cu/Cu₂O Nanoparticles Supported on a Phenol–Pyridine COF as a Heterogeneous Catalyst for the Synthesis of Unsymmetrical Dienes via Glaser–Hay Coupling

Debanjan Chakraborty, Shyamapada Nandi, Dinesh Mullangi, **Sattwick Haldar**, Chathakudath P. Vinod and Ramanathan Vaidhyanathan*

ACS Applied Materials and Interfaces, 2019, 11, 17, 15670

3. Fe₃SnC: A 3D Antiperovskite Intermetallic Carbide System as a New Robust High Capacity Li-ion Battery Anode

Kingshuk Roy, Vinila Chavan, Sk Mujaffar Hossain, **Sattwick Haldar**, Ramanathan Vaidhyanathan*, Prasenjit Ghosh* and Satishchandra Ogale*

Chem Sus Chem, 2019, 12, 1

2. Carbon Derived from Soft Pyrolysis of COF as a Support for Small-Sized RuO₂ Showing Exceptionally Low-Overpotential for OER

Debanjan Chakraborty, Shyamapada Nandi, Rajith Illathvalappil, Dinesh Mullangi, Rahul Maity, Santosh K. Singh, **Sattwick Haldar**, Chathakudath P. Vinod, Sreekumar Kurungot* and Ramanathan Vaidhyanathan*

ACS Omega, 2019, 4, 13465

1. Nanoporous Covalent Organic Framework Embedded with Fe/Fe₃O₄ Nanoparticles as Air-Stable Low-Density Nanomagnets

Rinku Kushwaha, Dhananjayan Kaleeswaran, Sattwick Haldar, Debanjan Chakraborty, Dinesh Mullangi, Aditya Borah, Chathakudath P. Vinod, Ramaswamy Murugavel, and Ramanathan Vaidhyanathan

ACS Appl. Nano Mater, 2020, 3, 9088

List of Patents

1. Self-Exfoliated Triazole-Triformyl Phloroglucinol Based Covalent Organic Nanosheets For High And Reversible Lithium-Ion Storage (*US Patent No: US 2020/0123169 A1*)

Inventor: **Haldar Sattwick**, Roy Kingshuk, Nandi Shyamapada, Vaidhyanathan Ramanathan.

2. Covalent Organic Framework As Flexible White Light Emitter (*IN Patent No:201821028796*)

Inventor: **Sattwick Haldar**, Debanjan Chakraborty, Bibhisan Roy, Gangadhar Banappanavar, Kushwaha Rinku, Dinesh Mullangi, Partha Hazra, Dinesh Kabra and Ramanathan Vaidhyanathan.

Anthracene-Resorcinol Derived Covalent Organic Framework as Flexible White Light Emitter

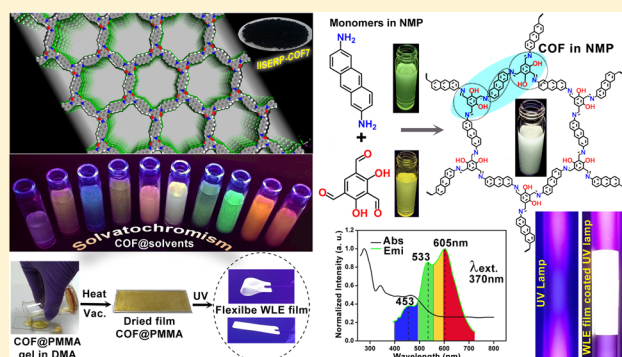
Sattwick Haldar,^{†,‡,⊥} Debanjan Chakraborty,^{†,‡,⊥} Bibhisan Roy,^{†,||} Gangadhar Banappanavar,^{§,||} Kushwaha Rinku,^{†,‡} Dinesh Mullangi,^{†,‡} Partha Hazra,[†] Dinesh Kabra,^{*,§} and Ramanathan Vaidyanathan^{*,†,‡,⊥}

[†]Department of Chemistry and [‡]Centre for Energy Science, Indian Institute of Science Education and Research, Pune, 411008 India

[§]Department of Physics, Indian Institute of Technology, Mumbai, 400076 India

Supporting Information

ABSTRACT: The ordered modular structure of a covalent organic framework (COF) facilitates the selective incorporation of electronically active segments that can be tuned to function cooperatively. This designability inspires developing COF-based single-source white light emitters, required in next-generation solid-state lighting. Here, we present a new anthracene-resorcinol-based COF exhibiting white light emission. The keto–enol tautomers present in the COF give rise to dual emission, which can be tuned by the O-donor and N-donor solvents. Importantly, when suspended in a solid polymer matrix, this dual emission is retained as both tautomers coexist. A mere 0.32 wt % loading of the COF in poly(methyl methacrylate) (PMMA) gives a solvent-free film with intense white light emission (CIE coordinates (0.35, 0.36)). From steady-state and time-resolved studies, the mechanism of the white light emission has been unambiguously assigned to fluorescence, with the blue emission originating from the π -stacked columns of anthracene, and the mixture of red and green from the keto–enol tautomerized resorcinol units. The study introduces the COF as a new class of readily processable, single-source white light emitter.



INTRODUCTION

COFs are crystalline organic polymers.^{1–3} Their modular structure enables facile incorporation of specific functional units in their construction and thereby provides an opportunity for extending such functional units into an extended periodic lattice, which can amplify their properties.^{1–9} Reports on the potential of COFs and their composites in diverse applications are surging.^{10–34} Exploiting their structural tunability, e-rich fluorophoric modules have been incorporated into COFs to gain intrinsic photoluminescence.^{35–41} However, the utilization of highly luminescent building units in the COF construction does not always guarantee photoluminescence. This is because many π -electron-rich molecular stacks tend to self-quench via aggregation.⁴² The structural topology and conjugation pathway have a key role to play in controlling the energy flow and thereby the photoluminescence. For example, hydroxyl-functionalized aromatics, as donors, have been combined with diimides, serving as acceptors.^{43,44} The photoinduced electron transfer and charge separation dynamics are cardinal to these systems. Similarly, by assembling multiple π -electron-rich cores (tetraphenylethene-benzenetrol) into a kagome lattice or by combining phenolic cores with pyrene, excellent blue light emission was achieved.^{45,46} Many of these photoluminescent COFs belong to the boronate ester

family and a few to the more accessible Schiff-bonded ones.^{47–49} Of these, the most relevant to the present study is the anthracene-based boronate ester COF reported by Jiang and co-workers.⁵⁰ In this COF, the anthracene units have shown photoresponsive ($4\pi + 4\pi$) dimerization, which suppresses the excimer formation transforming the blue luminescent COF into a nonluminescent one.

Developing white light emitters from single-source fluorophores can contribute immensely to solid-state lighting devices and displays. Current literature indicates that white light emission can be obtained from small conjugated organic molecules,^{51–53} from composite heterostructures such as hybrid GaN/organic-small-molecule via aggregation-induced emission, from inorganic–organic compounds such as lead halide perovskites,^{54–60} and from simple metal–organic complexes,^{61,62} and more pertinently, from amorphous organic polymers via donor–acceptor assemblies,⁶³ by encapsulating optically active quantum dots,^{64,65} by mixing blue–green–red light-emitting organic polymers,^{66–68} and by implanting organic dyes into porous matrices.⁶⁹ The recently reported

Received: August 3, 2018

Published: September 26, 2018

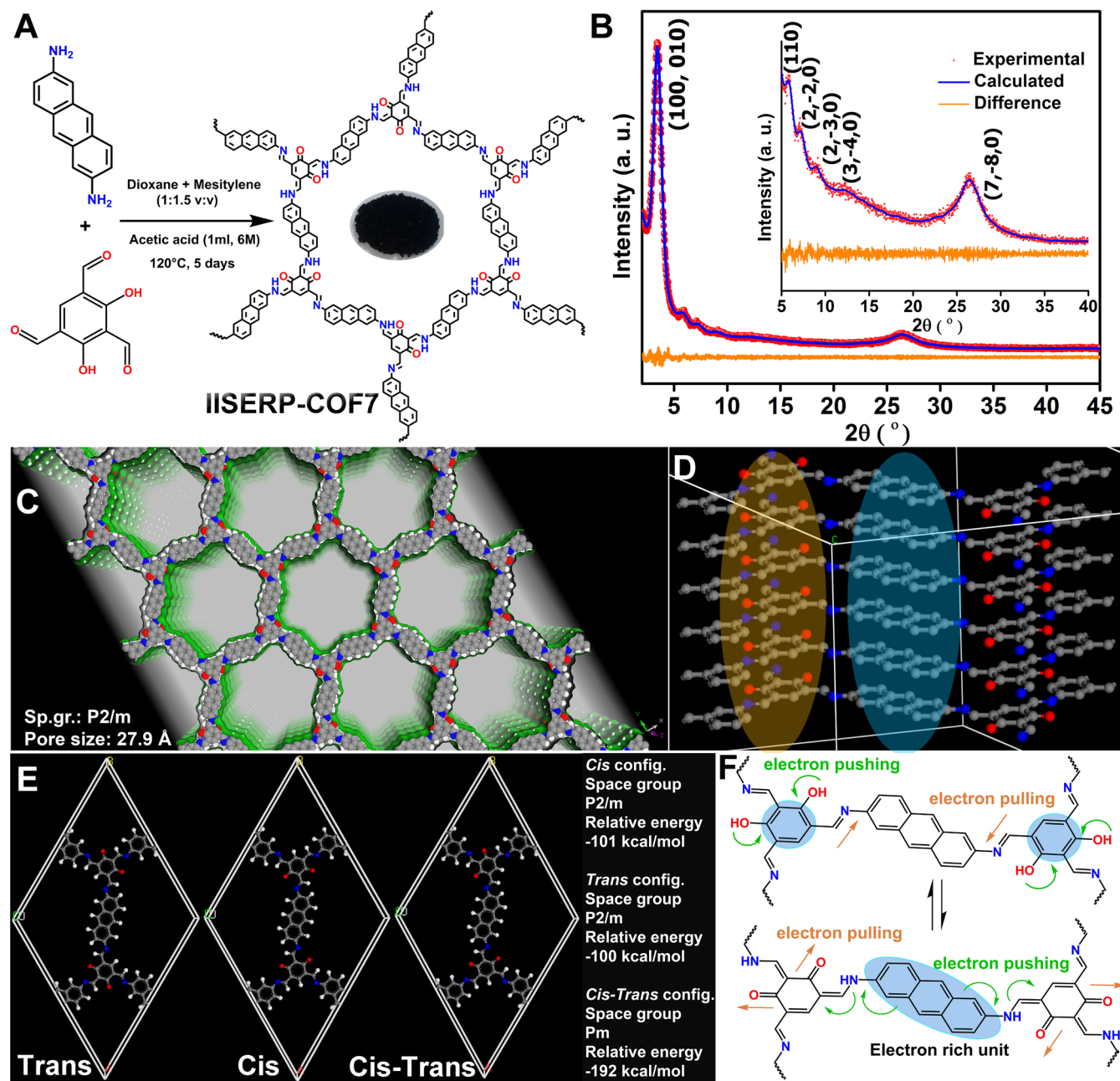


Figure 1. (A) Schematic representation of IISERP-COF7 synthesis. (B) Pawley refinement fit for the trans-configuration of the IISERP-COF7 obtained in the monoclinic $P2/m$ space group. (C) Structure of **1** with the Connolly surface representation (probe radius = 1.4 Å) showing uniform 1D channels (~27.9 Å, not factoring the van der Waals radii) in the eclipsed configuration. (D) Interplanar view showing the columnar π -stacks formed by the anthracene and the resorcinol units (interlayer separation = 3.473 Å). (E) Unit cells of the three different configurations of the COF formed by the different geometric conformations of the resorcinol units. All their structures have been geometry optimized using DFTB methods, and their relative energies are presented here. (F) Schematic of the push–pull electronic mobility in the COF framework.

COF-based near-white light emitter is limited by inadequacies in engineering them into membranes.⁷⁰

The above-referenced studies on photoluminescent COFs suggest the potential for generating white light emission via a molecular design approach.^{35,40–44} To this aim, we have combined a simple and readily available anthracene diamine with trimethylresorcinol into a COF via Schiff bonds, IISERP-COF7 (Figure 1A). These building units have the potential to introduce push–pull electronics, proton transfer, and π -stack assisted aggregation-enhanced luminescence.⁵⁰ Typically, most photophysical studies in COFs have been carried out in the solution phase. The utilization of the COF in an application

such as white light emission requires retaining emissive properties in the solid state. Rendering them as flexible organic films is a windfall.⁶⁵

Here the anthracene-resorcinol COF forms as a fine black powder (absorbs all the colors of the spectrum), which when dispersed in small concentrations into suitable solvents displays white light emission. Interestingly, a flexible white light emitting film could be prepared by dispersing tiny amounts of the COF into a nonphotoluminescent processable polymer. Through elaborate steady-state and time-resolved studies, we have related the origin of blue, green, and red emissions to the different organic modules in the COF.

RESULTS AND DISCUSSION

IISERP-COF7, **1**, is a 3 + 2 framework formed by a 3-connecting phenolic aldehyde (2,4-dihydroxybenzene-1,3,5-tricarbaldehyde) and a linear diamine (anthracene-2,6-diamine) (Figure 1A). The presence of resorcinol units in the COF gives rise to cis, trans, and cis–trans configurations. The structure in its cis- and trans-forms were refined using Pawley methods. Excellent fits were obtained for both configurations in the $P2/m$ space group (Figure 1B, Table S2). Also, geometry optimization was carried out using the dispersion-corrected periodic tight binding density functional theory (DFTB).

The lowest energy configurations of both the cis- and trans-forms adopt a planar eclipsed structure (Figure 1C). The 3D structure of the COF has π -stacked columns of anthracene and resorcinol units covalently linked by Schiff bonds (Figure 1D). This results in uniform 1D channels along the c -axis (dimension = 27.9 Å, not factoring the van der Waal radii). The presence of strategically positioned hydroxyl groups of the resorcinol enables its O...H–N... intralayer hydrogen bonds with the Schiff groups. The cis- and trans-forms have comparable relative energies. Meanwhile, the eclipsed form has a lower relative energy compared to the staggered form (–182 (eclipsed, trans) vs –100 kcal/mol (staggered, trans)). A comparison of the simulated powder X-ray diffraction (PXRD) pattern of the eclipsed and the staggered models with the experimental PXRD showed that the relative intensities of the second and third most intense peaks, (110) and (2–20), fitted the experimentally observed relative intensities much better (Figure S1). Also, the pore size estimated using the eclipsed model matches the experimentally determined one better. In addition to the cis- and trans-configurations, there are two other unique cis–trans configurations possible (Scheme S1). These were solved in the Pm space group with comparable energies. The energies of the cis–trans-forms were lower than the trans/cis-forms by ~92 kcal/mol (Figure 1E). The variation in the relative energies arises from the differences in the orientation and separation of the hydroxyl groups of the adjacent layers. The linking of these monomers through Schiff bonds can give rise to a push–pull electronic flow within the framework as shown in Figure 1F, and the electronic activity is evidenced from the CV measurements (Figure S2).

The bulk purity of **1** was established from the match between the experimental powder X-ray diffraction pattern and the simulated pattern (Figures 1B). Thermogravimetric analysis (TGA) measurement and the variable-temperature PXRD (VT-PXRD) of IISERP-COF7 display its exceptional thermal stability up to temperatures as high as 300 °C. Adsorption–desorption of N₂ on **1**, at 77 K, yielded a completely reversible type-1 isotherm, with a small hysteresis characteristic of a mesoporous structure.⁴¹ A model-independent BJH fit to the desorption branch reveals the presence of uniform ~27 Å pores. The pore volume was estimated to be 0.645 cm³/g. **1** has a Brunauer–Emmet–Teller (BET) surface area of 657 m²/g (Figures S3–S7).

Under the field emission scanning electron microscope (FE-SEM), the COF appears as aggregated submicrometer-sized flaky crystallites. Field emission transmission electron microscopy (FE-TEM) and atomic force microscopy (AFM) reveal the COF forming as sheets that are stacked into aggregates (Figure S8). The solid-state ¹³C NMR (500 MHz) spectrum shows the presence of both keto (δ = 184 ppm) and enol

forms (δ = 174 ppm). Importantly, the model compound formed by combining the trialdehyde with monoamine had only the enol form (Figures S9 and S10, Table S3). This corroborates well with the functional groups fingerprinted from the Fourier transform infrared (FTIR) spectra (Figure S11). The characteristic carbonyl (C=O) stretching frequency (1718 cm⁻¹) of the triformylresorcinol was red-shifted (1630 cm⁻¹) and the N–H stretching modes (3388, 3317, 3196 cm⁻¹) of the primary amine disappeared with the formation of the COF. Enolic OH (3390 cm⁻¹), imine C=N (1565 cm⁻¹), and the C=O (1630 cm⁻¹) and C=C (1448 cm⁻¹) stretching bands from the β -ketoenamine were observed, which confirms the coexistence of both enol and keto forms in the solid phase. Although FTIR spectra of the model compound demonstrated similarity in the peak pattern with the COF, the presence of only the enolic –OH (3504 cm⁻¹), imine C–H (2925 cm⁻¹), and C=N (1590 cm⁻¹) stretching bands suggests that the model compound adopts only the enolic form (Figure S11). Thus, the extended polymeric framework of the COF is crucial to stabilizing both the tautomers. The strategic positioning of the hydroxyl groups (β -position with respect to the –C=N–bond) stabilizes the framework via keto–enol tautomerism. Notably, there are only two such centers in this COF as compared to the three in other phloroglucinol-derived frameworks,^{17,18} yet high chemical stability is observed. As proof, the COF is stable to boiling in highly polar solvents such as dimethylformamide (DMF), *N*-methylpyrrolidone (NMP), and water and even to soaking in acid (3M HCl) and base (3M NaOH) (Figures S12–S16). This can be crucial when it comes to applying these COFs for solution processing.

Raman spectroscopy was performed using a Horiba LabRAM HR Evolution spectrometer coupled with an Olympus MPLN 100× microscope objective. In parallel to detecting the Raman response, the microscope also collects luminescence from the sample. The powdered COF sample was dispersed in methanol solution and drop cast on a Si wafer for the experiment. Excitation of the COF at 785 nm leads to a broad emission centered at ~820 nm (Figure S17), which increases in intensity with laser power. Several sharp peaks at 1158, 1414, 1618, and 2878 cm⁻¹ were observed on top of the broad luminescence background. All these features remain consistent in frequency with slight variations in intensity for different positions on the sample. The broad peak centered at 820 nm (Figure S17) confirms that the COF photoluminesces over a broad spectral range in the near IR. On the basis of the structure of the COF and its precursors, we attribute the Raman peaks at 1158, 1414, 1618, and 2878 cm⁻¹ to =C–H in-plane deformation, C=C in-plane vibration, C=N stretch, C=C stretch, and imine C–H stretch, respectively.

Photoluminescence Studies. The IISERP-COF7 forms as a fluffy black powder (see inset in Figure 1A). Typically, such a dark color would indicate that the material can absorb in the entire UV–vis spectrum. To probe this, **1** was dispersed in viscous solvents such as *N*-methylpyrrolidone, dimethylformamide, and dimethylacetamide (DMA) (5 mg of COF in 20 mL of solvent), and the UV–vis spectra were recorded. In all solvents, the spectra showed three absorption maxima (Figure S18). As a representative, the absorption spectra of **1** in NMP is shown in Figure 2.

Prompted by this observation, all these solvent dispersions were checked under UV light (365 nm), and remarkably, **1** exhibits solvatochromism with the emitted colors covering the entire visible spectrum (Figures 2 and S19),⁷¹ rightly matching

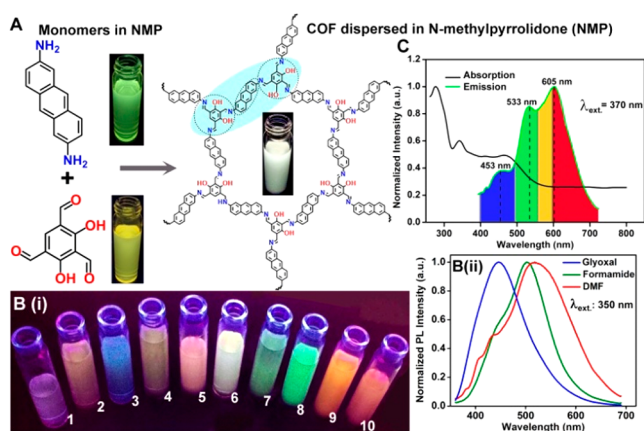


Figure 2. (A) Dispersions of the monomers and the COF suspended in NMP pictured under a UV lamp. (B(i)) COF dispersion in different solvents placed under a UV lamp. Codes: 1, THF; 2, dioxane; 3, glyoxal; 4, pyridine; 5, DMA; 6, NMP; 7, ethanol; 8, formamide; 9, picoline; 10, DMF. (B(ii)) Emission spectra obtained for the COF dispersion in three different solvents showing the red, green, and blue bands. (C) Absorption (black) and emission (green) spectra of the COF dispersion in NMP. The three characteristic RGB bands have been highlighted.

the color map and not just the blue emission expected for anthracene (Figure S20).^{50,61} Notably, the emission from the NMP dispersion was bright white (Figure 2A inset). However, the bulk COF powder when placed under UV did not show any white emission. Here we suspect a particle aggregation

induced self-quenching.⁷² Interestingly, the UV–vis absorbance spectra recorded using the solid black powder also had three absorption maxima around the same region as observed for the solvent dispersions (Figure S21). Following this, the NMP dispersion, giving the brightest white emission, was excited at a $\lambda_{\text{max}} = 340$ nm, and the emission spectrum exhibited three distinct bands corresponding to the blue, green, and red (Figure 2C). Similar excitation experiments were carried out on DMF and DMA dispersions, and they too showed RGB emission bands but with varying intensities and slight changes in emission maxima (Figure S22).

Origin of White Light Emission. These preliminary observations motivated us to prod further into the potential mechanism of the observed emission. For this, we decided to compartmentalize the structural components in the COF responsible for the blue, green, and red emission. As a control to track the effects of anthracene units in the COF, we recorded the UV–vis spectrum for the anthracene diamine in NMP. This yielded a green emission (Figure 2A and Figure S23), while we observed a yellow emission for the resorcinol-trialdehyde (Figure 2A). Also, a dispersion formed by mixing the diamine and the aldehyde in NMP in equimolar quantities gave a relatively dull orange color emission under a UV lamp (Figure S23). This conveys that the mixture of the individual components cannot give rise to white light emission, emphasizing the role of the polymeric stacked structure of the COF in the generation of RGB-derived white light.

Blue Emission from Anthracene Stacks. From the fact that anthracene molecules in NMP give a blue light emission

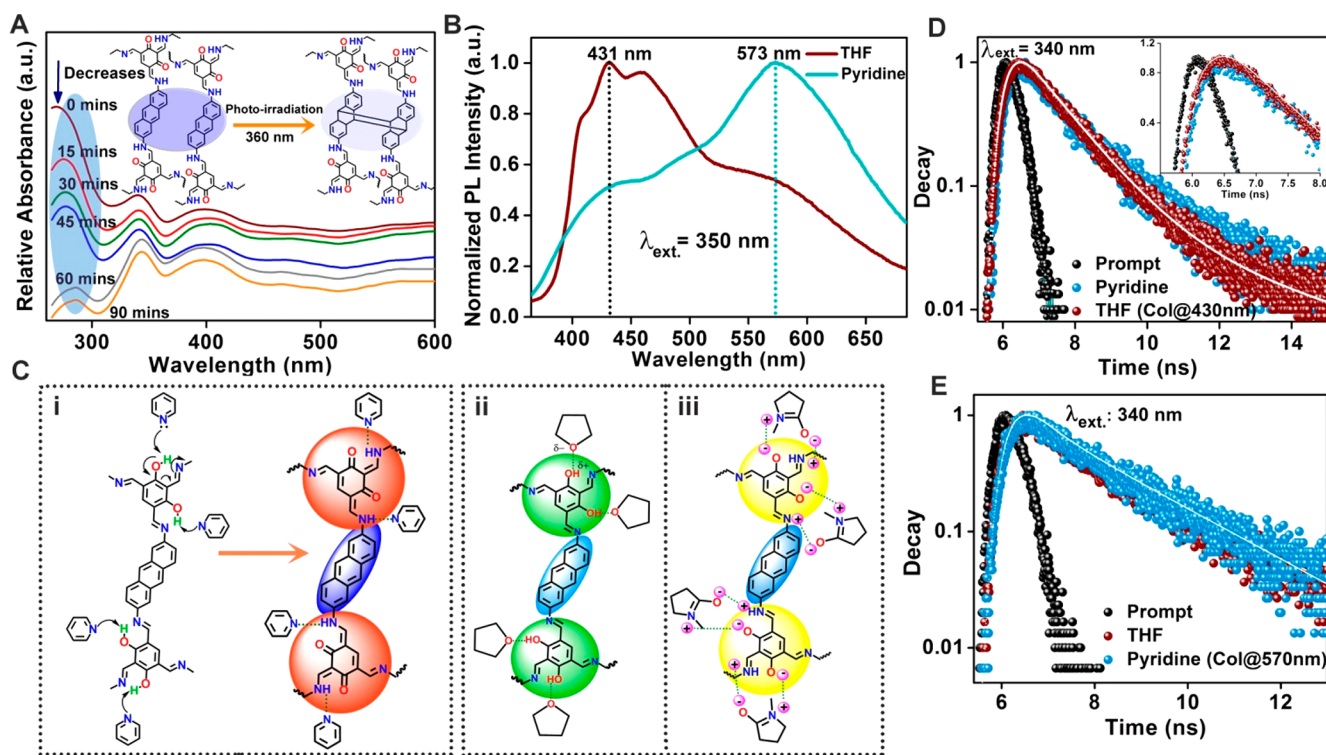


Figure 3. (A) Absorption spectra from a photoirradiation of the COF dispersion in DMF measured as a function of time. Inset: Schematic representation of the dimerization of the anthracene units causing the gradual disappearance of the blue band. (B) Comparison of the emission spectra of the COF dispersed in a N-donor solvent (pyridine) and an O-donor (THF). (C) (i) Proton abstraction mechanism in pyridine that stabilizes the keto-form; (ii) hydrogen bonding by THF stabilizes the enol-form; (iii) polarized NMP stabilizing the intermediate keto–enol form. (D, E) Comparison of fluorescence lifetime decay between the COF dispersions in THF vs pyridine. Note that they are collected at different wavelengths.

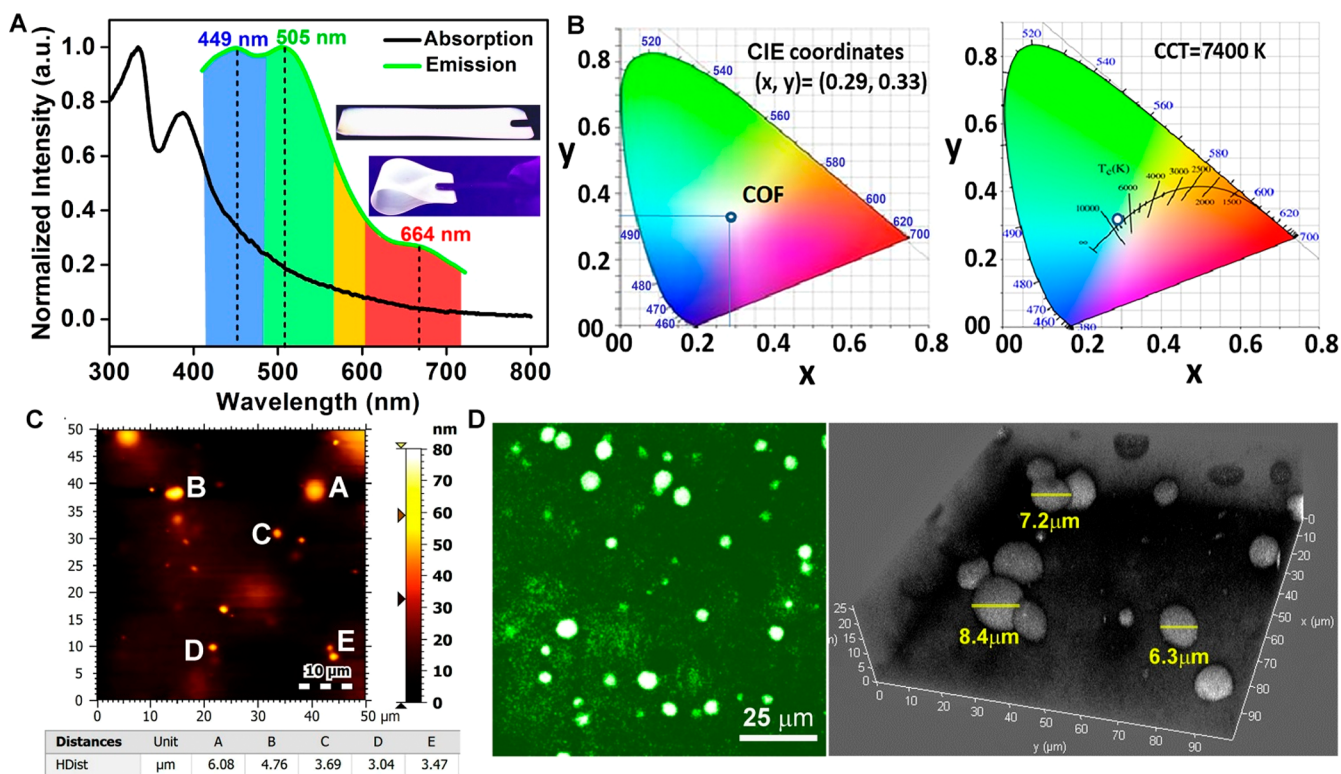


Figure 4. (A) Solid-state absorption and emission spectra of COF@PMMA (excitation wavelength: 420 nm). The inset shows the COF@PMMA film under a UV lamp. (B) CIE coordinate and the CCT diagram for the film of thickness 2 mm. (C) AFM image of the COF@PMMA. The bright regions are the COF particles dispersed in the PMMA matrix (dark). The table at the bottom shows the thickness corresponding to the labeled particles. (D, E) Confocal microscopy images of the COF@PMMA showing the COF particles as bright regions against the dark PMMA matrix measured at 405 nm. The 3D image shows the particle size of the COF in the dispersion. From AFM and confocal images, it can be seen that the particles closer to the surface and the ones that are buried in the polymer both have comparable sizes.

(Figure S20), we suspected that the COF's blue emission could have its origin in the anthracene stacks. To corroborate this, the COF was kept under a 360 nm laser excitation, which is known to promote its dimerization via $4\pi + 4\pi$ cycloaddition (inset of Figure 3A). Such a cycloaddition is known to happen both in isolated anthracene units⁷³ and in COF structures containing anthracene stacks.⁵⁰ Importantly, the dimerization weakens the conjugation. If a complete dimerization occurs, it shifts the blue emission band to much higher energy,⁵⁰ or when a partial dimerization results, it typically causes quenching of the blue emission band.⁵⁰ De facto, the absorbance spectrum of **1** exposed to this 360 nm laser recorded at regular intervals showed a systematic drop in the intensity of the first peak (~ 280 nm), while the intensity of the higher wavelength peaks remains almost the same (Figure S24). It is to be noted that the excitation in the wavelength range 280–350 nm gave rise to the blue emission in NMP (400–500 nm, Figures S25 and S26). This matches with the anthracene emission band in NMP (Figure S20), which unambiguously suggests that the blue emission has most of its origin at the anthracene units of the COF. The columnar π -stacking of these units within the COF gives rise to aggregation-enhanced luminescence when dispersed in NMP.³⁰ At the same time, in bulk, the particles aggregate, resulting in aggregation-induced self-quenching, making the solid powder appear nonluminescent under UV.⁷²

Red–Green Emission from the Tautomeric Resorcinol Units. As mentioned earlier, the resorcinol-trialdehyde emits yellow color under UV. From the color map, yellow resides

right in between green and red. It implies that the resorcinol-trialdehyde is potentially a source of green and red in the COF. Eminently, in the COF, this unit is linked to the anthracene core via the Schiff bond. And from the geometry/orientation of these functional groups strong keto–enol tautomerism is expected between the resorcinol units and the $-\text{CH}=\text{N}-$ (Figure S25). In the ground state, in the absence of stimuli, the tautomers are expected to be in equilibrium having both keto and enol forms, as evident from the presence of peaks corresponding to both these forms in the ^{13}C -SSNMR and IR (Figures S10 and S11). This equilibrium can be shifted toward one side by the solvent effects. From such a biased state, we decided to determine the contributions of the keto and enol forms to the green and red emissions. Put differently, the UV–vis spectra were recorded under conditions that majorly favor one or the other of these forms. We screened the absorption and emission properties of the COF dispersions in a range of polar N-donor (pyridine, picoline, and acetonitrile) and O-donor (THF, dioxane, ethanol, and methanol) solvents (Figure S26). We expected that the N-donor solvents due to their basicity could help in the transfer of protons from the enol to the Schiff nitrogens and thereby enhance the population of the keto form (Figure 3B(i)).⁷⁴ Similarly, we anticipated the O-containing solvents to stabilize the enol form via hydrogen bonding, wherein the phenolic hydrogen gets sandwiched between the oxygen from the phenol group and the oxygen of the solvent (Figure 3B(ii)). As expected, the N-donor solvents increase the relative intensity of the yellowish-orange band, while the oxygen-containing solvents enhance the relative

intensity of the blue-green band (Figure 3C). This was further investigated using the fluorescence lifetime decay. The green emission decays faster compared to the red, in pyridine, while the red emission decays faster in THF (Figure 3D and E)), confirming the pyridine stabilizes the keto form (red-shifted) and that THF stabilizes the enol form (blue-shifted).

NMP with Syn-Oriented N- and O-Donor Functionalities Assisting White Light Emission. Conjointly, the keto–enol tautomers can have a transition state where the proton is equally shared by the $\text{C}=\text{NH}$ – and the $\text{R}-\text{O}^-$ units (Figure 3B(iii)). In such an idealized transition state, one can expect the keto–enol tautomers to be present in a $\sim 50\%:50\%$ ratio. Now, the NMP represents a single molecule carrying an oxygen center and a basic nitrogen center. Hence, it should be able to promote the above-mentioned stabilization of the enol form via hydrogen bonding and simultaneously the basic nitrogen should facilitate the keto form via proton transfer (Figure 3B(iii)). This is due to the ability of NMP to provide a proper syn orientation of N and O atoms with respect to the polarizable centers of the tautomers. Thus, NMP is a unique solvent, which can simultaneously stabilize keto and enol forms in a near 50:50 ratio. Hypothesizing that enol and keto forms have the same quantum efficiency of emission, a high quantum yield can be expected. In fact, in NMP a quantum yield of 64% ($\pm 15\%$) was observed. However, we found that the emission band for the red was notably stronger than the blue and green, and this can be explained by the solvation dynamics effect.⁷⁵ The solvation of the polarized transition state by the surrounding NMP lowers its excited-state energy. This would enhance the fluorescence lifetime of the red band, which was confirmed by the lifetime decay (Figure 3D and E, Table S4). A comparison of the emission spectra from the different solvents containing both N- and O-donor groups has been made in the Supporting Information. As can be seen from Figure S19, the DMA and DMF do not give a white emission as prominently as the NMP; however, all these solvents enhance the red band in the emission spectra (Figures S22 and S26). Also, the possibility of a proton exchange between the Schiff groups and the phenol ($\text{R}-\text{OH}$) via an excited-state intermolecular (between the COF and solvent) or intramolecular proton transfer (within the COF, Figure S27) was examined. The existence of an excited-state intramolecular proton transfer was evidenced (Figure S27C, see Supporting Information).

Flexible Solid-State White Light Emitting Films from COF–Polymer Dispersions. The COF forms as a black powder, and the white light emission (WLE) is perceived from their dilute solvent dispersions. The utilization of these materials in illuminating devices can benefit significantly if such WLE can be accomplished in a solid state particularly in the form of flexible films. This requires a solution processing method for this COF. About 0.32 wt % of the COF was dispersed with PMMA in a solution containing either DMA, DMF, or NMP (Figure S29). This results in a transparent pale-yellow-colored thick gel. This gel remains stable even after 2 months without any notable precipitation (Figure S29). The gel was directly coated on a glass surface and was dried in a vacuum oven for about 2 h. This results in a film that gives a discernible WLE under a UV lamp (inset of Figure 4A) and showed the characteristic RGB emission. All three bands were slightly red-shifted compared to the corresponding bands observed for the solvent suspensions.⁷⁶ Notably, there is no visible change in the emission when the films are made to

bend. The CIE coordinates for the film of thickness 2 mm with a COF loading of 0.30 wt % were estimated to be (0.29, 0.33) and found to be a cold emission (CCT = 7400 K, Figure 4B). Interestingly these coordinates could be adjusted to (0.35, 0.36), resulting in neutral white light emission (CCT = 4480 K) by varying the doping concentration of COFs in the PMMA matrix (Figure S30, Table S5). To verify if there is a role of the trapped solvent in the emission, we evacuated the film under high vacuum (10^{-4} – 10^{-5} Torr) at 120 °C for 48 h, after which the film remained entirely intact without any visible cracks and showed WLE comparable to the as-made film (Figure S29).

The dispersivity of the COF in the film was investigated using AFM and confocal optical microscopy (Figure 4C–E), which confirmed the COF being well-dispersed. The COF particles in the film were about 3–8 μm in size, as verified from these microscopy images (see Figures 4C,D and S31 and S32). Importantly, the COF particles arrested within the hydrophobic polymer exist as isolated spheres, compared with the platy aggregates found in the bulk powder (Figure S8). This could be crucial to deriving the white luminescence in this otherwise aggregated black powder. As a control, we prepared the neat film without the COF (PMMA in DMA). The colorless transparent film did not give any notable emission under the UV lamp (Figure S33). The film was stable in water, methanol, ethanol, THF, and dioxane, but dissolved in DMF, DMA, and NMP. Interestingly, films soaked in 6 M NaOH and 6 M HCl solutions for 48 h still retained their white light luminescence (Figure S34).

Further photophysical properties of the film were gathered using steady-state and time-resolved measurements. The fluorescence lifetime spectra of the film brought out some interesting observations. While the lifetime of the green emission from the film was precisely comparable to the NMP suspensions, the blue and red emission decayed faster in the case of the film (2.5 and 3 times faster for green and red, respectively, Figure 5A). This is because the film does not have the benefit of the stabilization via solvation. A low-temperature PL spectrum and fluence-dependent measurements were done from 10 to 300 K to determine the activation energy using a JANIS cryostat and a highly sensitive gated ICCD

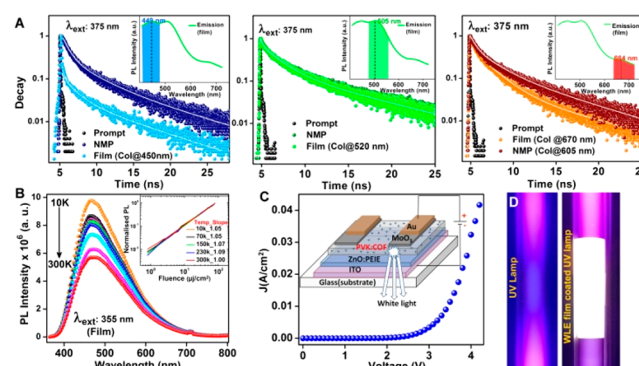


Figure 5. (A) Comparison of the fluorescence lifetime decay plot of the NMP dispersion vs the film collected in the blue region, the green region, and the red region. The inset shows the corresponding emission band for the film. (B) Variable-temperature PL measurements on the film (excitation wavelength: 355 nm). (C) J – V plot from a LED device made using IISERP-COF7. Inset is a schematic of the device construction. (D) Comparison of a normal UV lamp vs the COF@PMMA film coated one showing WLE.

spectrometer (Andor i-star) employing a pulsed laser (Innolas Picolo) at 355 nm excitation. The film shows a decrease in PL intensity with increasing temperature (Figures 5B and S35, Table S6). The linearity observed in the fluence data in the entire temperature range suggests the fluorescence to be the dominant process. This is attributable to increased classic temperature-activated nonradiative phonon-assisted channels.⁷⁷ The data are well-fitted with the Arrhenius equation,⁷⁸ and the activation energy is found to be 59.2 meV (see inset of Figure 5B). The studies confirm the lack of any E-delayed fluorescence or phosphorescence. An intense white light emission from a UV lamp coated with the film can be seen from Figure 5D. Absolute solid-state quantum yield measurements using an integrating sphere and the relative quantum yield using a reference suggested a QY of <10% for the COF@PMMA (see Supporting Information).⁷⁹

To explore the electroluminescence potential of the COF, we fabricated a light-emitting diode using the IISERP-COF7 (COFLED). The thin-layer nanocomposite of the COF with the poly(9-vinylcarbazole) (PVK)⁸⁰ was integrated into a device with the following construct: ITO/ZnO/PEIE/COFs:PVK (0.3 wt %)/MoO₃/Au (Figure 5C). A pristine PVK-based LED was employed as the reference to assess the intrinsic efficiency of the COF. The electroluminescence (EL) spectrum from the COFLED is shown in Figure S36. It matches with the PL spectrum of this composite layer (PVK:COF), but with a small red-shift in the emission peak, which can be attributed to injected carrier relaxation kinetics, as observed in other systems too.⁸¹ Under electrical excitation, the majority of the EL comes from the COF with a minor contribution from the host. The *J*-*V* plot of the COFLED displays its diode characteristics (Figure 5C). The injection currents in these COFLEDs are on the lower side compared to the recently reported MOF-based LED.⁸² However, we note that these are not optimized devices, and there is significant room for improvement via compositional/device engineering. Nevertheless, to the best of our knowledge, a successful electrically driven COF-LED is being reported for the first time with strikingly broad emission; this highlights the potential of COFs for white light LED applications.

CONCLUSION

The work demonstrates the potential of a COF to serve as a single-source white light emitter and showcases its facile solution processability, and even the prospect of using it as an electroluminescent material in optical devices. However, they need to be tuned further to obtain favorable HOMO-LUMO gaps and more pronounced electronic delocalization/mobility. Such engineering is possible either by exploiting the porosity of the COF to introduce more complex functionality or by choosing the right modules in the COF construction.

ASSOCIATED CONTENT

Supporting Information

The Supporting Information is available free of charge on the ACS Publications website at DOI: 10.1021/jacs.8b08312.

Materials and methods, calculation details, and photo-physical measurement details (PDF)

AUTHOR INFORMATION

Corresponding Authors

*vaidhya@iiserpune.ac.in

*dkabra@phy.iitb.ac.in

ORCID

Partha Hazra: 0000-0003-0422-1399

Ramanathan Vaidhyanathan: 0000-0003-4490-4397

Author Contributions

[†]S. Haldat and D. Chakraborty are shared first authors.

Author Contributions

[‡]B. Roy and G. Banappanavar are shared second authors.

Notes

The authors declare no competing financial interest.

ACKNOWLEDGMENTS

We thank Ms. Bijoya Mandal, Mr. D. V. S. Datta, and Prof. Eric Borguet from Temple University, Philadelphia, PA, USA, for their help with the Raman spectroscopy. We thank Dr. Pramod Pillai (IISER Pune) for the UV-vis spectrometer. We thank DST-nano mission, SERB, DST-Inspire, and the MHRD-FAST program for the necessary funding.

REFERENCES

- (1) Ma, T.; Kapustin, E. A.; Yin, S. X.; Liang, L.; Zhou, Z.; Jing Niu, J.; Li, L.-H.; Wang, Y.; Su, J.; Li, J.; Wang, X.; Wang, W. D.; Wang, W.; Sun, J.; Yaghi, O. M. *Science* **2018**, *361*, 48–52.
- (2) Diercks, C. S.; Yaghi, O. M. *Science* **2017**, *355*, 1585.
- (3) Waller, P. J.; Gándara, F.; Yaghi, O. M. *Acc. Chem. Res.* **2015**, *48*, 3053–3063.
- (4) Segura, J. L.; Mancheno, M. J.; Zamora, F. *Chem. Soc. Rev.* **2016**, *45*, 5635–5671.
- (5) Feng, X.; Ding, X.; Jiang, D. *Chem. Soc. Rev.* **2012**, *41*, 6010.
- (6) Huang, N.; Wang, P.; Jiang, D. *Nat. Rev. Mater.* **2016**, *1*, 16068.
- (7) Rogge, S. M. J.; Bavykina, A.; Hajek, J.; Garcia, H.; Olivios-Suarez, A. I.; Sepúlveda-Escribano, A.; Vimont, A.; Clet, G.; Bazin, P.; Kapteijn, F.; Daturi, M.; Ramos-Fernandez, E. V.; Llabrés i Xamena, F. X.; Speybroeck, V. V.; Gascon, J. *Chem. Soc. Rev.* **2017**, *46*, 3134–3184.
- (8) Ding, S. Y.; Wang, W. *Chem. Soc. Rev.* **2013**, *42*, 548.
- (9) Wang, T.; Xue, R.; Wang, Y. W. M.; Guo, H.; Yang, W. *Prog. Chem.* **2018**, *30*, 753–764.
- (10) Ding, S. Y.; Gao, J.; Wang, Q.; Zhang, Y.; Song, W. G.; Su, C. Y.; Wang, W. *J. Am. Chem. Soc.* **2011**, *133*, 19816–19822.
- (11) Sun, Q.; Aguila, B.; Earl, L. D.; Abney, C. W.; Wojtas, L.; Thallapally, P. K.; Ma, S. *Adv. Mater.* **2018**, *30*, 1705479.
- (12) Sun, Q.; Aguila, B.; Perman, J.; Butts, T.; Xiao, F.-S.; Ma, S. *Chem.* **2018**, *4*, 1726–1739.
- (13) Mullangi, D.; Dhavale, V.; Shalini, S.; Nandi, S.; Collins, S.; Woo, T.; Kurungot, S.; Vaidhyanathan, R. *Adv. Energy Mater.* **2016**, *6*, 1600110.
- (14) (a) Biswal, B. P.; Chandra, S.; Kandambeth, S.; Lukose, B.; Heine, T.; Banerjee, R. *J. Am. Chem. Soc.* **2013**, *135*, 5328–5331. (b) Suvendu Karak, S.; Sushil Kumar, S.; Pradip Pachfule, P.; Rahul Banerjee, R. *J. Am. Chem. Soc.* **2018**, *140*, 5138–5145.
- (15) Du, Z.-L.; Dang, Q.-Q.; Zhang, X.-M. *Ind. Eng. Chem. Res.* **2017**, *56*, 4275–4280.
- (16) Shi, X.; Yao, Y.; Xu, Y.; Liu, K.; Zhu, G.; Chi, L.; Lu, G. *ACS Appl. Mater. Interfaces* **2017**, *9*, 7481–7488.
- (17) Haldar, S.; Roy, K.; Nandi, S.; Chakraborty, D.; Puthusseri, D.; Gawli, Y.; Ogale, S.; Vaidhyanathan, R. *Adv. Energy Mater.* **2018**, *7*, 1702170.
- (18) Nandi, S.; Singh, S. K.; Mullangi, D.; Illathvalappil, R.; George, L.; Vinod, C. P.; Kurungot, S.; Vaidhyanathan, R. *Adv. Energy Mater.* **2016**, *6*, 1601189.
- (19) Côté, A. P.; Benin, A. I.; Ockwig, N. W.; O’Keeffe, M.; Matzger, A. J.; Yaghi, O. M. *Science* **2005**, *310*, 1166.
- (20) Huang, N.; Zhai, L.; Couprie, D. E.; Addicoat, M. A.; Okushita, K.; Nishimura, K.; Heine, T.; Jiang, D. *Nat. Commun.* **2016**, *7*, 12325.

- (21) Nagai, A.; Chen, X.; Feng, X.; Ding, X.; Guo, Z.; Jiang, D. *Angew. Chem., Int. Ed.* **2013**, *52*, 3770.
- (22) Dalapati, S.; Addicoat, M.; Jin, S.; Sakurai, T.; Gao, J.; Xu, H.; Irle, S.; Seki, S.; Jiang, D. *Nat. Commun.* **2015**, *6*, 7786.
- (23) Du, Y.; Yang, H.; Whiteley, J. M.; Wan, S.; Jin, Y.; Lee, S. H.; Zhang, W. *Angew. Chem., Int. Ed.* **2016**, *55*, 1737.
- (24) Colson, J. W.; Dichtel, W. R. *Nat. Chem.* **2013**, *5*, 453.
- (25) Uribe-Romo, F. J.; Doonan, C. J.; Furukawa, H.; Oisaki, K.; Yaghi, O. M. *J. Am. Chem. Soc.* **2011**, *133*, 11478.
- (26) Colson, J. W.; Woll, A. R.; Mukherjee, A.; Levendorf, M. P.; Spittler, E. L.; Shields, A. B.; Spencer, M. G.; Park, J.; Dichtel, W. R. *Science* **2011**, *332*, 228.
- (27) Gomes, R.; Bhanja, P.; Bhaumik, A. *Chem. Commun.* **2015**, *51*, 10050–10053.
- (28) Fang, Q.; Zhuang, Z.; Gu, S.; Kaspar, R. B.; Zheng, J.; Wang, J.; Qiu, S.; Yan, Y. *Nat. Commun.* **2014**, *5*, 4503.
- (29) Duhović, S.; Dinč, M. *Chem. Mater.* **2015**, *27*, 5487.
- (30) Xiang, Z.; Cao, D. *J. Mater. Chem. A* **2013**, *1*, 2691.
- (31) Dogru, M.; Bein, T. *Nat. Nanotechnol.* **2011**, *6*, 333.
- (32) Bertrand, G. H.; Michaelis, V. K.; Ong, T. C.; Griffin, R. G.; Dinca, M. *Proc. Natl. Acad. Sci. U. S. A.* **2013**, *110*, 4923.
- (33) Guo, J.; Xu, Y.; Jin, S.; Chen, L.; Kaji, T.; Honsho, Y.; Addicoat, M. A.; Kim, J.; Saeki, A.; Ihee, H.; Seki, S.; Irle, S.; Hiramoto, M.; Gao, J.; Jiang, D. *Nat. Commun.* **2013**, *4*, 2736.
- (34) DeBlase, C. R.; Silberstein, K. E.; Truong, T. T.; Abruña, H. D.; Dichtel, W. R. *J. Am. Chem. Soc.* **2013**, *135*, 16821.
- (35) Crowe, J. W.; Baldwin, L. A.; McGrier, P. L. *J. Am. Chem. Soc.* **2016**, *138*, 10120–10123.
- (36) Bhunia, A.; Esquivel, D.; Dey, S.; Fernández-Teñan, R.; Goto, Y.; Inagaki, S.; Voorta, P. V. D.; Janiak, C. *J. Mater. Chem. A* **2016**, *4*, 13450.
- (37) Zhou, T.-Y.; Xu, S.-Q.; Wen, Q.; Pang, Z.-F.; Zhao, X. J. *J. Am. Chem. Soc.* **2014**, *136*, 15885–15888.
- (38) Auras, F.; Ascherl, L.; Hakimoun, A. H.; Margraf, J. T.; Hanusch, F. C.; Reuter, S.; Bessinger, D.; Döblinger, M.; Hettstedt, C.; Karaghiosoff, K.; Herbert, S.; Knochel, P.; Clark, T.; Bein, T. *J. Am. Chem. Soc.* **2016**, *138*, 16703–16710.
- (39) Jin, S.; Supur, M.; Addicoat, M.; Furukawa, K.; Chen, L.; Nakamura, T.; Fukuzumi, S.; Irle, S.; Jiang, D. *J. Am. Chem. Soc.* **2015**, *137*, 7817–7827.
- (40) Jin, S.; Furukawa, K.; Addicoat, M.; Chen, L.; Takahashi, S.; Irle, S.; Nakamura, T.; Jiang, D. *Chem. Sci.* **2013**, *4*, 4505–4511.
- (41) Chen, L.; Furukawa, K.; Gao, J.; Nagai, A.; Nakamura, T.; Dong, Y.; Jiang, D. *J. Am. Chem. Soc.* **2014**, *136*, 9806–980.
- (42) Pratt, A. C. *Chem. Soc. Rev.* **1977**, *6*, 63–81.
- (43) Jin, S.; Ding, X.; Feng, X.; Supur, M.; Furukawa, K.; Takahashi, S.; Addicoat, M.; El-Khouly, M. E.; Nakamura, T.; Irle, S.; Fukuzumi, S.; Nagai, A.; Jiang, D. *Angew. Chem., Int. Ed.* **2013**, *52*, 2017.
- (44) Feng, X.; Chen, L.; Honsho, Y.; Saengsawang, O.; Liu, L.; Wang, L.; Saeki, A.; Irle, S.; Seki, S.; Dong, Y.; Jiang, D. *Adv. Mater.* **2012**, *24*, 3026.
- (45) Dalapati, S.; Jin, E.; Addicoat, M.; Heine, T.; Jiang, D. *J. Am. Chem. Soc.* **2016**, *138*, 5797–5800.
- (46) Wan, S.; Guo, J.; Kim, J.; Ihee, H.; Jiang, D. *Angew. Chem., Int. Ed.* **2008**, *47*, 8826–8830.
- (47) Gao, Q.; Li, X.; Ning, G.-H.; Leng, K.; Tian, B.; Liu, C.; Tang, W.; Xu, H.-S.; Loh, K. P. *Chem. Commun.* **2018**, *54*, 2349–2352.
- (48) Das, P.; Mandal, S. K. *J. Mater. Chem. A* **2018**, *6*, 16246–16256.
- (49) Lin, G.; Ding, H.; Yuan, D.; Wang, B.; Wang, C. *J. Am. Chem. Soc.* **2016**, *138*, 3302–3305.
- (50) Huang, N.; Ding, X.; Kim, J.; Ihee, H.; Jiang, D. *Angew. Chem., Int. Ed.* **2015**, *54*, 8704–8707.
- (51) Yang, Y.; Lowry, M.; Schowalter, C. M.; Fakayode, S. O.; Escobedo, J. O.; Xu, X.; Zhang, H.; Jensen, T. J.; Fronczek, F. R.; Warner, I. M.; Strongin, R. M. *J. Am. Chem. Soc.* **2006**, *128*, 14081–14092.
- (52) Wang, L.; Duan, L.; Lei, G.; Qiu, Y. *Jpn. J. Appl. Phys.* **2004**, *43*, L560–L562.
- (53) Guan, Y.; Niu, L. *J. Phys.: Conf. Ser.* **2009**, *152*, 012049.
- (54) Dohner, E. R.; Hoke, E. T.; Karunadasa, H. I. *J. Am. Chem. Soc.* **2014**, *136*, 1718–1721.
- (55) (a) Mahmoudi, G.; Gurbanov, A. V.; Rodríguez-Hermida, S.; Carballo, R.; Amini, M.; Bacchi, A.; Mitoraj, M. P.; Sagan, F.; Kukulka, M.; Safin, D. A. *Inorg. Chem.* **2017**, *56*, 9698–9709. (b) Shen, X.; Sun, C.; Bai, X.; Zhang, X.; Wang, Y.; Wang, Y.; Song, H.; Yu, W. W. *ACS Appl. Mater. Interfaces* **2018**, *10*, 16768–16775.
- (56) Mao, L.; Wu, Y.; Stoumpos, C. C.; Wasielewski, M. R.; Kanatzidis, M. G. *J. Am. Chem. Soc.* **2017**, *139*, 5210–5215.
- (57) Bansode, U.; Naphade, R.; Game, O.; Agarkar, S.; Ogale, S. J. *Phys. Chem. C* **2015**, *119*, 9177–9185.
- (58) Kumawat, N. K.; Gupta, D.; Kabra, D. *Energy Technol.* **2017**, *5*, 1734–1749.
- (59) Draguta, S.; Sharia, O.; Yoon, S. J.; Brennan, M. C.; Morozov, Y. V.; Manser, J. S.; Kamat, P. V.; Schneider, W. F.; Kuno, M. *Nat. Commun.* **2017**, *8*, 200.
- (60) Rao, K. V.; Datta, K. K.; Eswaramoorthy, M.; George, S. J. *Adv. Mater.* **2013**, *25*, 1713–1718.
- (61) Lee, K. H.; Park, J. K.; Seo, J. H.; Park, S. W.; Kim, Y. S.; Kim, Y. K.; Yoon, S. S. *J. Mater. Chem.* **2011**, *21*, 13640–13648.
- (62) Hamada, Y.; Sano, T.; Fujii, H.; Nishio, Y.; Takahashi, H.; Shibata, K. *Jpn. J. Appl. Phys.* **1996**, *35*, 1339.
- (63) Tang, C.; Liu, X.-D.; Liu, F.; Wang, X.-L.; Xu, H.; Huang, W. *Macromol. Chem. Phys.* **2013**, *214*, 314–342.
- (64) Tu, M.-L.; Su, Y.-K.; Chen, R.-T. *Nanoscale Res. Lett.* **2014**, *9*, 611.
- (65) Lin, H.-Y.; Sher, C.-W.; Lin, C.-H.; Tu, H.-H.; Chen, X. Y.; Lai, Y.-C.; Lin, C.-C.; Chen, H.-M.; Yu, P.; Meng, H.-F.; Chi, G.-C.; Honjo, K.; Chen, T.-M.; Kuo, H.-C. *ACS Appl. Mater. Interfaces* **2017**, *9*, 35279–35286.
- (66) Deng, X.-Y. *Int. J. Mol. Sci.* **2011**, *12*, 1575–1594.
- (67) AlSalhi, M. S.; Alam, J.; Dass, L. A.; Raja, M. *Int. J. Mol. Sci.* **2011**, *12*, 2036–2054.
- (68) Ananthkrishnan, S. J.; Varathan, E.; Subramanian, V.; Somanathan, N.; Mandal, A. B. *J. Phys. Chem. C* **2014**, *118*, 28084–28094.
- (69) Pallavi, P.; Bandyopadhyay, S.; Louis, J.; Deshmukh, A.; Patra, A. *Chem. Commun.* **2017**, *53*, 1257.
- (70) Li, X.; Gao, Q.; Wang, J.; Chen, Y.; Chen, Z.-H.; Xu, H.-S.; Tang, W.; Leng, K.; Ning, G.-H.; Wu, J.; Xu, Q.-H.; Quek, S. Y.; Lu, Y.; Loh, K. P. *Nat. Commun.* **2018**, *9*, 2335.
- (71) (a) Chen, G.; Li, W.; Zhou, T.; Peng, Q.; Zhai, D.; Li, H.; Yuan, W. Z.; Zhang, Y.; Tang, B. Z. T. *Adv. Mater.* **2015**, *27*, 4496–4501. (b) Roy, B.; Reddy, M. C.; Hazra, P. *Chem. Sci.* **2018**, *9*, 3592.
- (72) Zhou, D.; Li, D.; Jing, P.; Zhai, Y.; Shen, D.; Qu, S.; Rogach, A. L. *Chem. Mater.* **2017**, *29*, 1779–1787.
- (73) O'donnell, M. *Nature* **1968**, *218*, 460–461.
- (74) Matwijczuk, A.; Karcz, D.; Walkowiak, R.; Furso, J.; Gladyszewska, B.; Wybraniec, S.; Niewiadomy, A.; Karwasz, G. P.; Gagos, M. *J. Phys. Chem. A* **2017**, *121*, 1402–1411.
- (75) Dopfer, O.; Fujii, M. *Chem. Rev.* **2016**, *116*, 5432–5463.
- (76) Sek, D.; Siwy, M.; Bijak, K.; Grucela-Zajac, M.; Malecki, G.; Smolarek, K.; Bujak, L.; Mackowski, S.; Schab-Balcerzak, E. *J. Phys. Chem. A* **2013**, *117*, 10320–10332.
- (77) Tombe, S.; Adam, G.; Heilbrunner, H.; Apaydin, D. H.; Ulbricht, C.; Sariciftci, N. S.; Arendse, C. J.; Iwuoha, E.; Scharber, M. C. *J. Mater. Chem. C* **2017**, *5*, 1714–1723.
- (78) Fang, Y.; Wang, L.; Sun, Q.; Lu, T.; Deng, Z.; Ma, Z.; Jiang, Y.; Jia, H.; Wang, W.; Zhou, J.; Chen, H. *Sci. Rep.* **2015**, *5*, 1038.
- (79) Dey, A.; Rao, A.; Kabra, D. *Adv. Opt. Mater.* **2017**, *5*, 1600678.
- (80) Brandt, J. R.; Wang, X.; Yang, Y.; Campbell, A. J.; Fuchter, M. J. *J. Am. Chem. Soc.* **2016**, *138*, 9743–9746.
- (81) Kumawat, N. K.; Dey, A.; Narasimhan, K. L.; Kabra, D.; ACS *Photonics* **2015**, *2*, 349.
- (82) Haider, G.; Usman, M.; Chen, T.-P.; Perumal, P.; Lu, K.-L.; Chen, Y.-F. *ACS Nano* **2016**, *10*, 8366–8375.

High and Reversible Lithium Ion Storage in Self-Exfoliated Triazole-Triformyl Phloroglucinol-Based Covalent Organic Nanosheets

Sattwick Haldar, Kingshuk Roy, Shyamapada Nandi, Debanjan Chakraborty, Dhanya Puthusseri, Yogesh Gawli, Satishchandra Ogale,* and Ramanathan Vaidhyanathan*

Covalent organic framework (COF) can grow into self-exfoliated nanosheets. Their graphene/graphite resembling microtexture and nanostructure suits electrochemical applications. Here, covalent organic nanosheets (CON) with nanopores lined with triazole and phloroglucinol units, neither of which binds lithium strongly, and its potential as an anode in Li-ion battery are presented. Their fibrous texture enables facile amalgamation as a coin-cell anode, which exhibits exceptionally high specific capacity of $\approx 720 \text{ mA h g}^{-1}$ ($@ 100 \text{ mA g}^{-1}$). Its capacity is retained even after 1000 cycles. Increasing the current density from 100 mA g^{-1} to 1 A g^{-1} causes the specific capacity to drop only by 20%, which is the lowest among all high-performing anodic COFs. The majority of the lithium insertion follows an ultrafast diffusion-controlled intercalation (diffusion coefficient, $D_{\text{Li}^+} = 5.48 \times 10^{-11} \text{ cm}^2 \text{ s}^{-1}$). The absence of strong Li-framework bonds in the density functional theory (DFT) optimized structure supports this reversible intercalation. The discrete monomer of the CON shows a specific capacity of only 140 mA h g^{-1} $@ 50 \text{ mA g}^{-1}$ and no sign of lithium intercalation reveals the crucial role played by the polymeric structure of the CON in this intercalation-assisted conductivity. The potentials mapped using DFT suggest a substantial electronic driving-force for the lithium intercalation. The findings underscore the potential of the designer CON as anode material for Li-ion batteries.

aromatic groups, which via columnar π - π stacking order into a periodic 3D structure (Scheme S1, Supporting Information). Their modular construct and ordered porosity makes them find use in diverse applications^[1–27] Here we are seeking application of 2D COFs in metal-ion batteries, which are typically made of electrodes with layered structures, for example, graphite as anode and LiCoO_2 as cathode. Owing to their graphite resembling structure, COF can serve as anode. Since their initial discovery, many 2D materials with comparable layered structures have been explored as lithium insertion–deinsertion materials.^[28–39] Some of the highly desirable characteristics of a superior anode material include moderate to high surface accessibility to ensure maximum charge storage per unit area, and the other is the hierarchical porosity for favorable kinetics. Exfoliation enhances surface accessibility and active site creation in such 2D materials.^[40–48] In this regard, COFs could have much more to offer.^[49–51]

Exfoliation in any 2D material is largely dependent on the interlayer forces holding them. Typically, the COF layers are held together by interlayer π - π interactions or in some cases via additional hydrogen bonding.^[52,53] However, unlike graphite, the layers of COF are not built from fused aromatic rings. In their optimized

1. Introduction


Covalent organic framework (COF) is a crystalline organic polymer. Many 2D COFs have layers built from crosslinking

S. Haldar, K. Roy, S. Nandi, D. Chakraborty, Dr. D. Puthusseri, Dr. R. Vaidhyanathan
Department of Chemistry
Institute of Science Education and Research
Dr. Homi Bhabha Road, Pashan, Pune 411008, India
E-mail: vaidhya@iiserpune.ac.in

Dr. Y. Gawli
Physical and Materials Chemistry Division
National Chemical Laboratory (CSIR-NCL)
Pashan, Pune 411008, India

Prof. S. Ogale
Department of Physics
Institute of Science Education and Research
Dr. Homi Bhabha Road, Pashan, Pune 411008, India
E-mail: satishogale@gmail.com

Prof. S. Ogale, Dr. R. Vaidhyanathan
Centre for Energy Science
Indian Institute of Science Education and Research
Dr. Homi Bhabha Road, Pashan, Pune 411008, India

 The ORCID identification number(s) for the author(s) of this article can be found under <https://doi.org/10.1002/aenm.201702170>.

DOI: 10.1002/aenm.201702170

structure, the layers are held together by relatively fewer π - π interactions at interlayer separations of 3.4–4.5 Å (Scheme S1, Supporting Information), which can enable facile exfoliation into nanosheets without losing the overall structure.^[54–57] Nanosheets are known to perform well as ion storage materials because of their high active site access and shortened diffusion path length for the guests.^[41,58,59] The covalent organic nanosheets (CON) can be considered as a few-layers-thick disordered derivative of a COF. Many carbon-based materials with disordered structures exhibit much higher practical capacities for ion storage than the theoretical value of graphite.^[60] This is because in their disordered form they possess more number of Li-C₆ rings interactions.^[60] Also, presence of electronegative atoms in such C₆ rings promotes such interactions as the lone pairs from the heteroatom can stabilize the positive charge created on the ring during its interaction with the lithium. The modular construction of a COF enables the stoichiometric introduction of such hetero atoms and also the chemical nature of the heteroatom can be tuned to control the interactions with the extra-framework species (e.g., nitrogen: pyridyl vs triazine vs Schiff can be customized).^[2–6] Crucially, such electrochemically driven lithium addition onto the heteroatom sites is reversible.^[60]

Compared to inorganic materials and graphite,^[28–48] less is known about the utilization of COF for Li-ion storage.^[61–70] As an effective approach, Li co-workers^[61] developed a thiophene-based conjugated COF as anode with high specific capacity (666 mA h g⁻¹), but this capacity drops significantly with increasing current density. Similarly, Fe₂O₃ supported on nanosheets of graphene shows high anode activity arising from the redox reactivity at the iron center (1355 and 982 mA h g⁻¹ for charge and discharge cycles, respectively).^[71] However, over multiple cycles, these redox active systems tend to drop in performance owing to some irreversible reactions between the lithium and the active material.^[71–73] At high current densities, such undesirable irreversible reactions become more frequent and lower the coulombic efficiency. This is true also for the other transition metal-based anodic materials.^[72,73] So, use of relatively less reactive (milder Lewis base/acid) neutral groups or moieties as active sites could promise longer cycle life.

Here we report a new COF wherein, for the first time, we have incorporated triazole moiety as a means to introduce flexibility into the framework. This COF, even during synthesis, grows into self-exfoliated CON. The short triazole linkers (a 120° linker)^[74,75] generate uniform micropores with walls lined by optimally spaced –OH and N-atoms, giving rise to favorable lithium interacting pockets. These groups, phenols and triazoles, being weak acids (pK_a, phenol = 10.3; 1,2,4-triazole = 9.3) are expected to interact mildly with lithium. A Li-ion coin-cell comprising this CON-derived anode exhibits high specific capacity ≈720 mA h g⁻¹ at 100 mA g⁻¹, which is among the highest reported capacities for self-standing nongraphenic organic materials. Importantly, the cell retains this high specific capacity even after 100 cycles and shows only a small drop (≈150 mA h g⁻¹) in specific capacity even at a current density as high as 1 A g⁻¹. It retains a high specific capacity of 460 mA h g⁻¹ even at 2 A g⁻¹. Simulations using density functional theory (DFT), coupled with analytical studies, help us identify the lowest energy configuration of the lithium loaded

CON (Li@CON), which has a structure with optimal Li-framework interactions. In addition, the electronic driving force for the insertion–deinsertion of lithium is evident from the lowering of bandgap and from the difference in electron-density/potential maps.

2. Results

2.1. Synthesis and Structural Solution

The Indian Institute of Science Education and Research Pune (IISERP)-CON1, prepared from a reaction between a trialdehyde and 3,5-diaminotriazole under mild solvothermal conditions (Figure S1, Supporting Information), grows as a homogeneous fluffy reddish-brown powder. From a Pawley refinement, the structure was modeled in P-6 space group. This model has a 2D structure where hexagonal layers are held together in an eclipsed arrangement by π -stacking phloroglucinol and triazole rings (Figure S2, Supporting Information). To obtain the lowest energy configuration, we optimized the geometry of the 2D hexagonal model using periodic tight-binding DFT method. A fully cell and motion group relaxed optimization resulted in a solution in P3 space group, which had 140 kcal mol⁻¹ lower relative energy (Figure 1A,B). In this lowest energy structure, the layer flexes around the triazole ring “pivot” to form a wavy 2D stack (Figure 1C,D). The triazole rings now buckle out-of-plane and crosslink (120° linker) the phloroglucinol in the *ab*-plane.^[74] The phloroglucinols from the adjacent layers π -stack at distance of 3.47 Å, while the triazole units stack at a distance of 3.26 Å. The nanosheets in this self-exfoliated form do not contain sufficient layers to give rise to strong intensity peaks in the powder X-ray diffraction (PXRD) pattern (Figure 1E and Figure S3, Supporting Information). This agrees well with the observations made by Banerjee and co-workers.^[76] Furthermore, the formation of the CON was confirmed from solid state nuclear magnetic resonance (SSNMR) and IR spectroscopy (Figure 1F and Figures S5 and S8, Supporting Information). Other experimental supports for this covalent organic nanosheet structure as the most probable one come from the porosity measurements (Figure 1G), the field emission-scanning electron microscopy (FE-SEM, Figure 2A,B), the field emission-transmission electron microscopy (FE-TEM, Figure 2C), and the atomic force microscopy (AFM) studies (Figure 2E).

2.2. Characterization: Porosity and Morphology

The IISERP-CON1 shows good N₂ uptake at 77 K (≈220 cc g⁻¹ in the *P/P*₀ range of 0–0.8 and a characteristic pore condensation at higher *P/P*₀ region). Such high uptakes confirm its behavior resembling COF-derived nanosheets.^[54–57,76] The pore size distribution was estimated from the 77 K N₂ isotherms using a DFT fit. The majority of the micropores are concentrated around 13 and 17 Å (Figures S9 and S10, Supporting Information). Few hierarchical mesopores are also present (Figure 1G). If the material had adopted a perfectly planar hexagonal sheet structure, there should have been uniform 1D channels of 21 Å (Figure S2, Supporting Information), which was not the

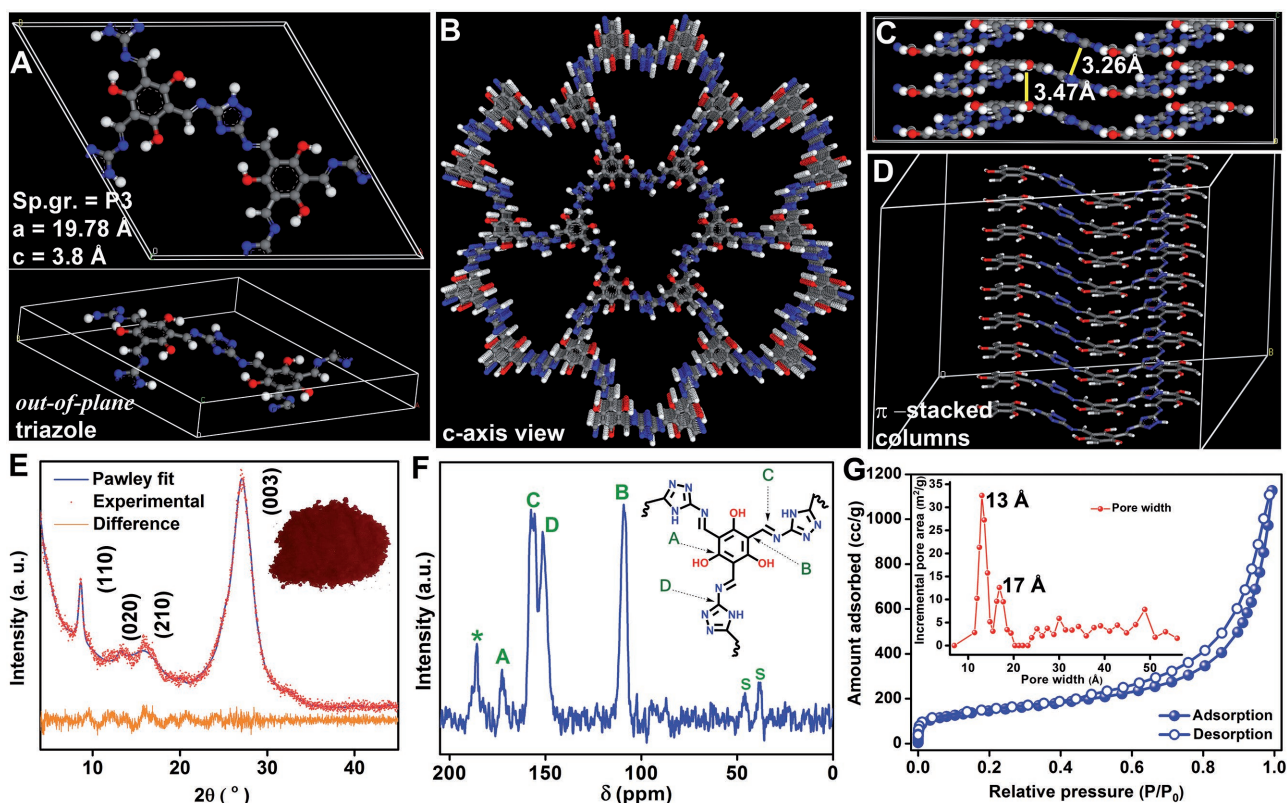


Figure 1. A) Unit cell of IISERP-CON1 showing the phloroglucinol units placed in different planes crosslinked by the triazole unit. C—gray; N—blue; O—red; H—white. B) Framework structure showing the triangular pores along C-axis with dimensions of 13 (shortest noncovalent atom-to-atom distance) and 16 Å (longest atom-to-atom). C) Buckled layers of IISERP-CON1. D) Uniform columnar π -stack of phloroglucinol units and the triazole units. E) Pawley fit to the experimental PXRD. Refinement parameters: $R_p = 4.45\%$; $wR_p = 5.80\%$. F) Atom assigned ^{13}C -SSNMR. *—terminal unreacted aldehyde; s—solvents. G) Nitrogen adsorption isotherm at 77 K. Inset shows the pore size distribution from a DFT fit.

case. It exhibits a Brunauer–Emmett–Teller (BET) surface area of $507 \text{ m}^2 \text{ g}^{-1}$ (Figure S11, Supporting Information) and a pore volume of 0.37 cc g^{-1} (from nonlocalized density functional theory, carbon @ 77 K, spherical model). The BET surface area of this CON is notably higher than what has been reported for other exfoliated COFs.^[55,56] However, it is much lower than the theoretically estimated Connolly surface area ($2070 \text{ m}^2 \text{ g}^{-1}$; pore volume = 0.57 cc g^{-1} ; Figure S4, Supporting Information). This significant drop in surface area is most likely due to the exfoliated nature of the CON. Typically, exfoliation of COF is known to decrease its surface area to a large extent (Table S2, Supporting Information). The material is practically insoluble in any of the common organic solvents even under boiling conditions, which excludes it from being a mere organic cage or oligomer. The IISERP-CON1 shows good thermal and chemical stability toward different solvents, electrolytes, and acidic media (Figure 2 and Figures S12 and S13, Supporting Information).

Under the FE-SEM, the CON shows a flaky morphology reminiscent of commercially available high surface area graphenes (Figure 2A and Figures S14 and S15, Supporting Information).^[77] Furthermore, the FE-TEM images of the CON shows a morphology archetypical of exfoliated COF—thin layers rolled up appearing as wavy flakes resembling high resolution-transmission electron microscopy (HR-TEM) images of graphenes (Figure S16, Supporting Information).^[78] In a higher resolution FE-TEM image

(5 nm), the fine porous surface of the nanosheets could be observed (Figure 2C). Another strong evidence for the presence of few-layers-thick nanosheets comes from the AFM. The height profile and the dimensions extracted from the AFM images of a drop-cast sample showed thicknesses of $\approx 2\text{--}6 \text{ nm}$ and aspect ratio (height/lateral length) of < 0.1 (Figure 2E and Figures S17–S19, Supporting Information). Also, the contact angles between the nanosheets and the substrate fall in the range of $< 1^\circ$, suggesting that the surface of the nanosheets is almost flat having no curvature (Figure S20, Supporting Information). These features are consistent with previous observations on exfoliated nanosheets.^[76,79,80] A dispersion of the CON in methanol exhibited Tyndall effect even after standing for 24 h supporting the nanodimensional morphology of the COF (Figure S22, Supporting Information).

2.3. Electrochemistry: Coin-Cell-Cyclic Voltammetry and Galvanostatic Charge–Discharge Cycling

Having obtained the porous structure with multiple organic functionalities ($-\text{OH}$, $-\text{C}=\text{N}-$, triazole rings and aromatic carbons) that can interact with inorganic cations and considering its exfoliated-carbon-like morphology, we investigated the potential of this material as an anode in Li-ion battery. A coin-cell battery assembly was fabricated in an argon-filled glove box using a

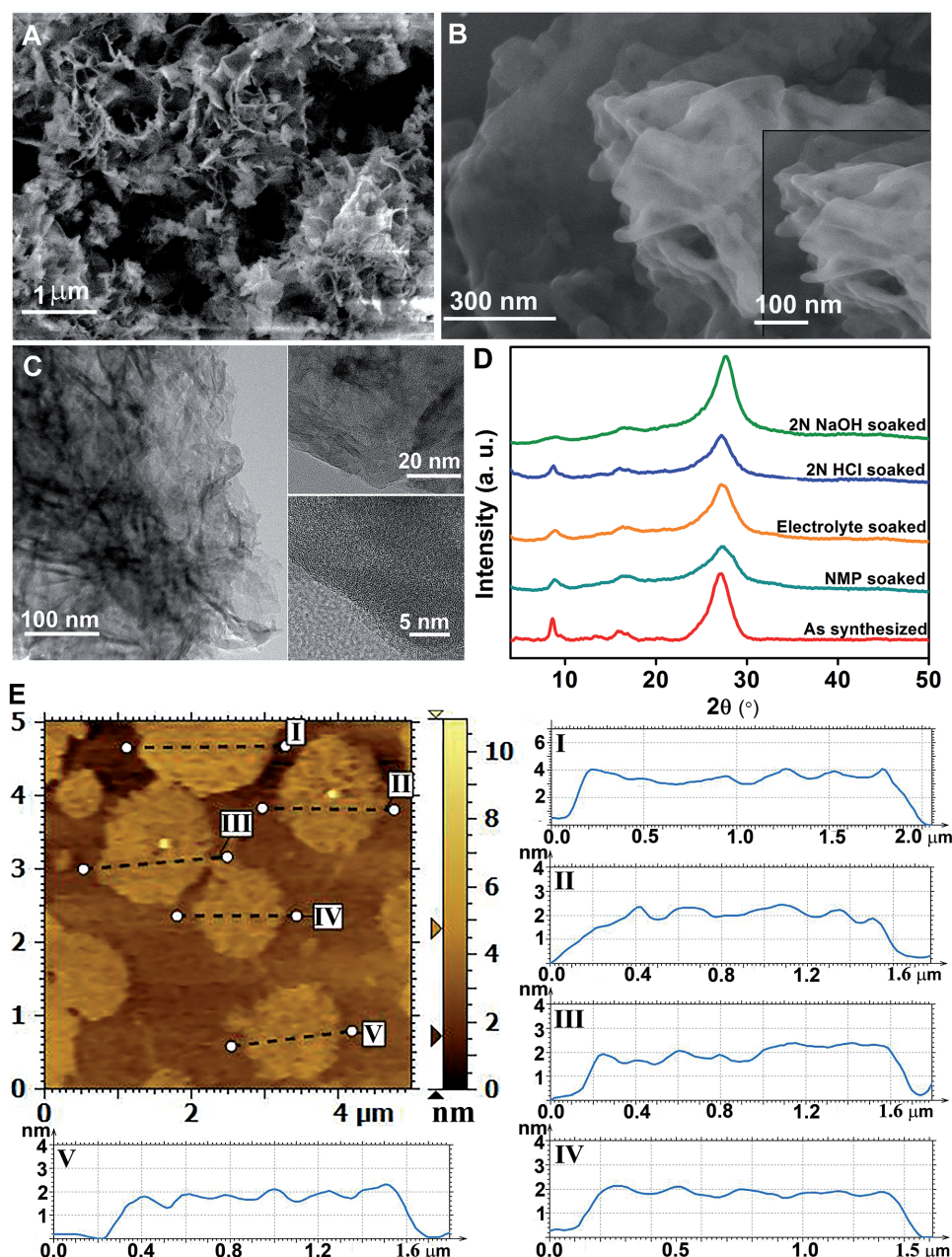


Figure 2. A) FE-SEM image of IISERP-CON1 showing the flaky morphology. B) Higher resolution FE-SEM showing stacking of very thin nanosheets. C) FE-TEM image showing the thin layers of the nanosheets with inundated or wrinkled surface and at higher resolution the sub-nanopores on the surface of the nanosheets can be seen. D) Chemical stability of the CON from PXRD. E) The AFM image showing the thickness of the drop-casted sample. The height profile plot quantifies it to be in the range of $\approx 2\text{--}4$ nm (see the Supporting Information for more images).

slurry made by mixing 75% CON: 20% conducting carbon: 5% polytetrafluoroethylene (PTFE) binder in *N*-methylpyrrolidone (NMP) (Figure S23, Supporting Information). To investigate the lithium insertion–deinsertion characteristics of the CON, we engaged a coin-cell (2032) assembly connected to a charge–discharge unit. A cyclic voltammogram (CV) was measured using a 0.2 mV s^{-1} sweep-rate in the potential window of 0.01–3 V (Figure 3A and Figure S24, Supporting Information). In its 1st cycle, the CV showed a prominent peak at 0.48 V corresponding to the formation of solid electrolyte interphase (SEI) layer and the corresponding current is

-0.36 mA .^[81,82] From the 2nd cycle onward, the peak due to the SEI layer formation diminished leaving a stable CV. The sharp peak at very low potential (≈ 0.02 V) suggests effortless intercalation of lithium into the nanosheets. The second significant peak at 1.0 V appears as a broad feature. Importantly, this peak arising from chemical interactions is notably weaker compared to what is reported for other COFs and organic materials which form true covalent bonds with lithium.^[61,64,83]

To verify, if there was any capacitive mechanism involved in the lithium loading and to confirm that the broad peak at 1.0 V

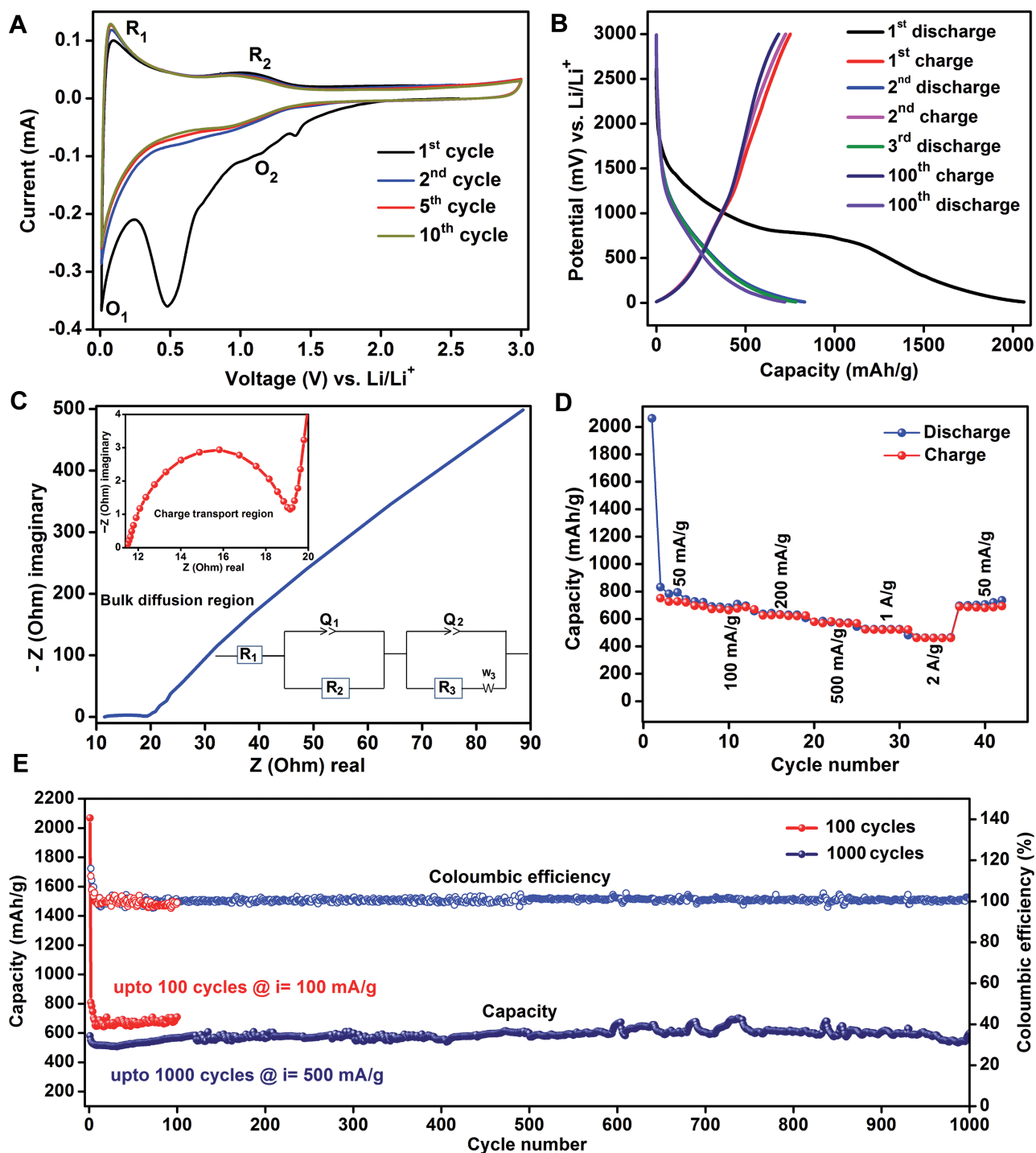


Figure 3. A) CV curve showing the presence of two redox peaks due to the intercalation (0.02 V) and weak binding (≈ 1 V) of lithium into the CON. B) Galvanostatic charge–discharge cycling measurements showing the high cyclability. C) AC-impedance plot of IISERP-CON1 showing its low resistivity. Inset shows the fitted equivalent circuit. $R_1 = Q_2/R_2 + Q_3/(R_3 + W_3)$; series resistance, $R_1 = 11.46$; charge transfer resistance, $R_2 = 8.13$; $R_3 = 96.46 \Omega$. D) Rate performance plots for IISERP-CON1. E) Capacity retention and 100% columbic efficiency over 100/1000 cycles.

is not merely due to a poor resolution from faster scan rate, a variable scan rate CV was performed (0.1–10 mV s^{-1} ; potential window: 0.01–3 V) (Figure S25, Supporting Information). The peak profiles remained the same. A fit to the power law, $i = a\nu^b$ (i = current; ν = scan rate), resulted in $b = 0.5$ @0.02 V

which obeys Cottrell's equation suggesting that the lithium loading operated mostly via a diffusion-controlled intercalation mechanism (Figure S26, Supporting Information).^[84,85] While the “ b ” values (Table S3, Supporting Information) of 0.93 @1 V and 0.86 @2.5 V suggest only a little contribution from the

surface-controlled charge storage behavior (capacitive). Also, both the anodic and cathodic peak currents vary linearly with the square root of the scan rate suggesting that the process is mostly mass transfer controlled (Figure S27, Supporting Information).^[86] This would mean that the high specific capacity depends significantly on the mobility of the lithium ions within the bulk of the CON. To establish this, the Warburg coefficient was calculated from the ac-impedance measurements and was fitted into the standard ionic diffusion expression (Figures S28 and S29, Supporting Information). The lithium diffusion coefficient (Figure S30, Supporting Information) is calculated to be D_{Li^+} of $5.48 \times 10^{-11} \text{ cm}^2 \text{ s}^{-1}$, which is quite comparable to those found in other graphitic as well as 2D inorganic materials with large lithium mobility.^[87–94]

Galvanostatic charge–discharge sweeps at a constant current density of 100 mA g^{-1} corroborate well with the I – V features in the CV curves (Figure 3B). A peak centered at 0.48 V in the CV (Figure 3A) denotes the formation of SEI layer in the first discharge cycle, which corresponds to the very high initial discharge capacity of 2060 mA h g^{-1} (Figure 3B). In the 2nd cycle, the capacity drops to 835 mA h g^{-1} as the SEI layer formation walks away. Following this, over 100 charge–discharge cycles were carried out. The cell maintains high and stable discharge capacity of 720 mA h g^{-1} ($@100 \text{ mA g}^{-1}$) during this prolonged cycling, which essentially confirms the potential of our material to act as a stable Li-ion battery anode. Also, the CON-derived Li-ion cell desirably has a low resistivity. AC-impedance measurements revealed that the cell carries a series resistance as low as 11.46Ω and a charge transfer resistance of 8.13Ω (Figure 3C). Furthermore, only a small drop in specific capacity (150 mA h g^{-1}) is observed even at current density as high as 1 A g^{-1} (Figure 3D). The charging capacity in the corresponding cycles is compatible with the discharge capacities leaving a coulombic efficiency almost of 100% in every cycle (Figure 3E). In comparison, other nanostructured materials with high specific capacities for Li-ion battery show significant drop in capacity with both increasing current density and prolonged cycling.^[61,71,81,83,95–98] And, this has been explained by the formation of some highly energetic redox species which bind irreversibly with the lithium during the battery cycling.^[71] The exfoliated-COF structure and hierarchical pores most probably assist this faster lithium diffusion into shortened paths compared to a highly stacked COF, where the slower kinetics would increase the contact time with the active sites leading to unwelcome irreversible chemical binding. However, it is essential to have the covalently bound extended framework structure to realize the observed intercalation assisted lithium charge–discharge. For instance, when we carried out the charge–discharge cycles and the CV using the monomer formed by reacting the trialdehyde involved in the construction of IISERP-CON1 with 3-amino-1,2,4-triazole, the capacity was only 140 mA h g^{-1} (Figures S31 and S32, Supporting Information). Moreover, in the CV, the intercalation peak expected at 0.02 V was missing while the other peaks due to chemical interaction, observed for the IISERP-CON1, could be seen (Figure S32, Supporting Information). Interestingly, the lithium insertion into the monomer is completely reversible with 100% coulombic efficiency. Meaning, the triazole units coupled with the phenolic triformyl units and its C_6 rings form modules capable of providing reversible chemical

interactions with lithium. This capability is retained in the CON constructed from these modules. The presence of these weak interactions between the enolic monomer and the lithium is confirmed from $^1\text{H-NMR}$ (Figure S33, Supporting Information).

2.4. Cycling Stability

The electrochemical cyclic stability of the CON was confirmed from complete retention of its redox activity (from CV) even after 100 charge–discharge cycles ($@100 \text{ mA g}^{-1}$) (Figure S34, Supporting Information) and 98% retention of its capacity even after 1000 galvanostatic charge–discharge cycles ($@500 \text{ mA g}^{-1}$) (Figure 3E). AC-impedance measurements indicated no change in resistance of the cycled cell (Bulk resistance: $R = 19 \Omega$ (before); 18.5Ω (after)), which suggests the lack of any ohmic loss or material degradation (Figure S35, Supporting Information).^[87] To further substantiate the integrity of the CON under the applied electrochemical stress, an electrode with neat CON in NMP, without using any conducting carbon, was subjected to 100 charge–discharge cycles. From PXRD, IR and FE-SEM measurements (Figures S36–S38, Supporting Information), we confirmed that the postcycling material retains crystallinity and its chemical structure. In the IR, a few new peaks appear at lower wave numbers, which can be attributed to the weak Li-framework interactions (Figure S37, Supporting Information). This stability is true for the monomer too.

2.5. Computational Studies

2.5.1. Simulated Structure of Li@CON: Li-Framework Interactions from Model and X-Ray Photoelectron Spectroscopy (XPS)

To shed light into the CON's structural contributions toward this high and reversible lithium storage capacity, we employed simulations.^[11,12,22,23,99] From the observed capacity 720 mA h g^{-1} , the number of lithium ions stored per formula unit of the CON was calculated to be 16 (Figures S39 and S40, Supporting Information). Using this as a starting composition, we generated a $2 \times 2 \times 2$ cell of the IISERP-CON1, and the lithium ions were allowed to find the best probable positions using simulated annealing methods (Materials Studio V6). The most probable positions were further DFT-optimized for geometry using the Cambridge Serial Total Energy Package (CASTEP). In the final structure (relative energy: -127 eV), the lithium ions occupy positions close to the framework walls and reside in the interlayer space (Figure 4A). This is significantly different from their top-on positioning found in graphenic substrates.^[100,101] A short contact analysis reveals some meaningful findings vis-à-vis the lithium positions around the ring nitrogens of the triazole and the hydroxyl oxygens of the phloroglucinol. Two different lithium containing chains form, one is via the interaction of the lithium with the $-\text{N}$ and the $-\text{OH}$ of these groups, respectively (Figure 4B), and the other from the interaction with only the nitrogens of the triazole (Figure 4C). In these chains, the Li-N/Li-O separations are in the range of 2.69 – 2.80 \AA , which is much longer than the Li-N/Li-O distances found in the covalently bound lithium (≈ 1.8 – 2.0 \AA).

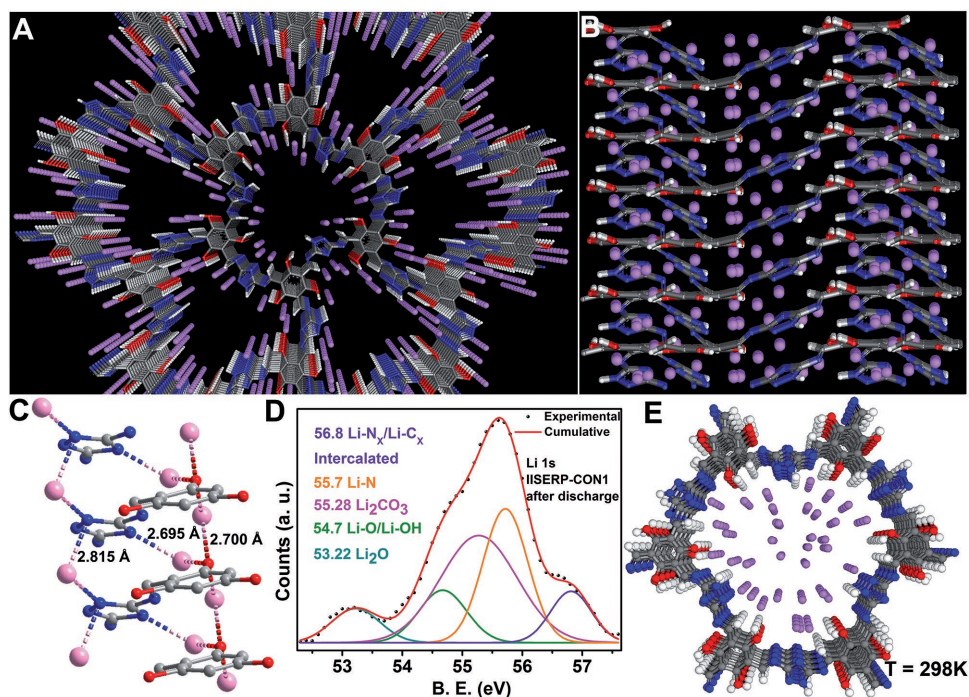


Figure 4. A) A perspective view of the simulated 3D structure of the lithiated CON. Li—magenta; C—gray; N—blue; O—red; H—white. B) shows the Li occupying the interlamellar spaces in the CON. C) shows the columns of lithium that form via its interaction with phloroglucinol and triazole moieties. D) Li 1s XPS spectra of the postcharge–discharge electrode (after 100 cycles). E) Room temperature structure of the Li@CON from MD simulations. Note the lithiums are more dispersed.

Interestingly, owing to the geometry of these layers the more reactive Schiff bond nitrogens are not accessible for any interaction (Figure 4A). This perhaps explains the lack of strong interactions which could lead to irreversible lithium loading. To

further verify this, we carried out an experiment wherein we reacted the CON with $\text{Li}(\text{OH})_2$ via both mechanical grinding and solution assisted process. The resulting products were analyzed using inductively coupled plasma. The analysis revealed

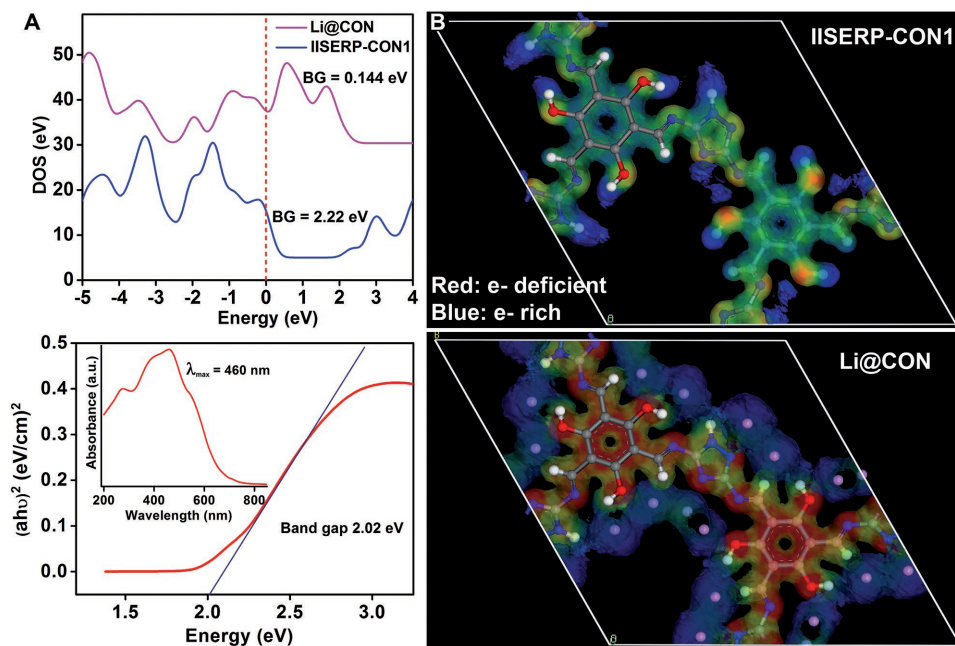


Figure 5. A) Comparison of the band gaps of the as-made CON, the Li@CON calculated using DFT methods and the optical band gap of the as-made CON estimated from the solid-state UV–vis spectrum. B) Comparison of the electron density and potential map of CON and the Li@CON. DOS—density of states.

that there was only about <2% loading of lithium in both cases, which is considerably lower than the amount estimated from the measured specific capacity (16–18%). Thus, the bulk of the high specific capacity observed under the applied potential stems from intercalation involving weaker forces. However, since the lithium loading was carried out without any electrochemical force, this cannot entirely exclude the formation of reactive species on the CON surface. In molecular compounds with fused aromatic rings, under an applied potential, lithium is known to form strong interactions which are reversible.^[68–70] To establish this, we analyzed the postdischarge sample sealed under an argon atmosphere using XPS. XPS showed peaks corresponding to Li–N, Li–N_x and Li–O/Li–OH interactions. In addition, the peaks due to Li₂CO₃, occurring from the electrolyte contributions, were also observed (Figure 4D and Figures S41 and S42, Supporting Information).

A molecular dynamics simulation was carried out to establish the room temperature stability of the Li@CON. The relative total energy was higher by 459 kcal mol⁻¹ compared to the 0 K configuration. Importantly, the final averaged structure adopted a P1 symmetry and in this structure the framework was more buckled and the lithium ions were randomly positioned, yet the framework maintains the overall symmetry (Figure 4E and Figure S43, Supporting Information).

2.5.2. Bandgap and Electrostatic Potentials— Electronic Contributions

To gain evidence for the electronic driving force for the lithiation, we have calculated the bandgap changes between the pristine CON and its lithiated form. The dispersion corrected DFT calculation employing a plane wave basis cutoff of 500 eV yielded a bandgap of 2.2 eV for this nonconjugated IISERP-CON1, which matches well with the experimentally determined optical bandgap (2.02 eV, Figure 5A and Figure S44, Supporting Information).^[12] This agrees well with the lack of appreciable electronic conductivity in the four-probe measurements. However, upon lithiation, the computed bandgap lowers to 0.144 eV. Such lowering of the bandgap, in the minimized configuration of the Li@CON, suggests the likelihood of a strong electronic driving force.^[12] This is well substantiated by the observed electron density and potential map, calculated using the DMol³ package of the Materials Studio. A comparison of the electrostatic potential of the pristine CON and the lithium adsorbed CON shows a marked change in the electron distribution upon the lithium insertion (Figure 5B).

Noticeably, due to the electrostatic interactions of the lithium ions, the charge difference on the nearby carbon and nitrogen atoms has become less pronounced and the CON becomes highly activated and deplete of electrons. Clearly, the C₆ rings seem to participate by transferring significant electron density toward the lithium ions.^[68–70] In our opinion, the calculation could be displaying the best case scenario by overestimating the electrostatics. Nonetheless, it is pointing in the right direction.

3. Discussion

Stable performance over a wide current density window is imperative for any competing anode material. In this regard,

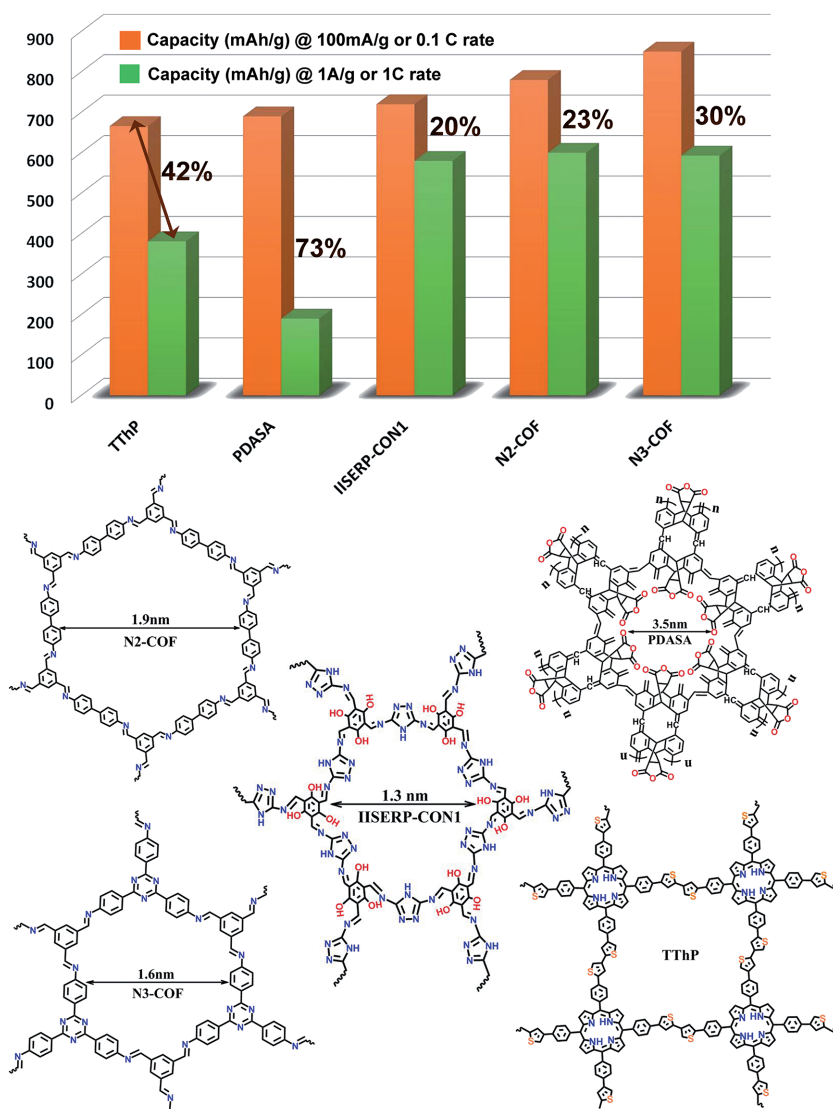


Figure 6. Top: A bar chart showing the drop in specific capacity when the current density is increased from 100 mA g⁻¹ to 1 A g⁻¹ in different organic framework materials with anodic character. Bottom: A schematic representation of the structure of these organic frameworks showing the high and compact packing of functional groups in IISERP-CON1 giving rise to highly favorable pockets for Li interaction. Note the compound codes have been adopted from the original literature.

a worthy observation from our lithium insertion–deinsertion study comes from a comparison of the specific capacities of IISERP-CON1 at the low (0.1 A g^{-1}) and the high (1 A g^{-1}) current densities with other organic materials.^[61,64,83,97,98] As can be seen from the bar chart in **Figure 6**, the drop in specific capacity with increasing the current density from 0.1 to 1 A g^{-1} is about 20% in IISERP-CON1, which is the lowest among all the organic framework materials reported so far. We attribute this to the optimal interaction between the CON and the lithium and more importantly to the lack of any undesirable irreversible redox activity. Figure 6 shows the structures of some of the recently reported self-standing organic frameworks with high capacities for lithium storage. A comparison of their structures with that of the IISERP-CON1, evidently, brings some of its distinctive structural features. In IISERP-CON1 the electron-rich phloroglucinol nodes are linked by the short 120° linkers derived from 3,5-diaminotriazole. This short linker not only generates nanospaces with a high density of functional groups but favors cooperativity between the different functionalities in assembling the lithium species (Figure 4C). In comparison, the relatively longer linkers in the other frameworks (N2-COF, N3-COF, and TThP) further far space the heteroatoms that serve as the active sites. On the other hand, in poly(dihydroanthracene succinic anhydride) (PDASA),^[83] the pores are large and the anhydride functionalities are even more proximal than the functional groups in IISERP-CON1 and this reflects in its higher specific capacity (1050 mA h g^{-1} @ 0.05 A g^{-1}). However, this high capacity drops by 73%, which is substantially higher in comparison to the 20% drop in the case of IISERP-CON1. This lowered stability of PDASA could be due to the presence of relatively stronger and potentially irreversible Li–COO bonds. Moreover, despite being short linkers, the triazoles generate large enough pores in the framework which are crucial to realizing smooth mass and charge transport. Meanwhile, the flexibility at the triazole enables the buckling of the layers which assists the formation of π -stacking columnar motifs within its packing, which in turn ensures the necessary stability required under the electrolyte solutions and the applied potential.

4. Conclusions

Here, we have developed “by-design” a flexible covalent organic framework, which self-exfoliate into nanosheets under the solvothermal conditions. Presence of nanopores lined by mildly interacting triazole and phloroglucinol units in their framework enables these nanosheets to reversibly insert–deinsert lithium ions. The short diffusion path lengths provided by the nanosheet structure favor ultrafast kinetics for the lithium insertion. DFT-optimized structure of the lithiated CON displays no strong Li-framework binding, which explains the reversibility and the cyclic stability. Importantly, the high capacity (720 mA h g^{-1}) and ability to maintain the capacity over a wide current density window is distinct to this material (<20% drop with increase in current density from 100 mA g^{-1} to 1 A g^{-1} , lowest among all self-standing nongraphenic organic frameworks). Thus covalent organic frameworks functionalized with mildly binding groups can serve as highly active anodes

in Li-ion battery. In their exfoliated form, they become highly suited for ion-intercalation. Our findings reveal the remarkable ability of these highly designable COF-derived nanostructures to act as electrode materials and prompt further studies.

Supporting Information

Supporting Information is available from the Wiley Online Library or from the author.

Acknowledgements

S.H. and K.R. contributed equally to this work. The authors thank Prof. Marimuthu Krishnan (International Institute of Information Technology (IIIT), Hyderabad) for the valuable discussions on the computational aspects. The authors acknowledge the IISER, Pune and the Ministry of Human Resource Development (MHRD), India for funding of our research through the Frontier Areas of Science and Technology (FAST) program. The authors thank “Funding by Department of Science and Technology (DST)-Nanomission under the Thematic Unit Program” and the Science and Engineering Research Board (SERB) (EMR/2016/003553) for the support. The authors thank Enovex Corp., Canada and DST-Clean Energy Research Initiative (CERI) for support. S.H. thanks DST-Inspire for financial support. The authors thank “Central Surface Analytical Facility of IIT Bombay” for the XPS and Centre for Materials for Electronics Technology (CMET), Pune for the TEM.

Conflict of Interest

The authors declare no conflict of interest.

Keywords

anodic COF, covalent organic nanosheets, lithium storage, self-exfoliated COF

Received: August 8, 2017
Revised: September 19, 2017
Published online: November 24, 2017

- [1] A. P. Côté, A. I. Benin, N. W. Ockwig, M. O’Keeffe, A. J. Matzger, O. M. Yaghi, *Science* **2005**, *310*, 1166.
- [2] P. J. Waller, F. Gándara, O. M. Yaghi, *Acc. Chem. Res.* **2015**, *48*, 3053.
- [3] X. Feng, X. Ding, D. Jiang, *Chem. Soc. Rev.* **2012**, *41*, 6010.
- [4] N. Huang, L. Zhai, D. E. Coupry, M. A. Addicoat, K. Okushita, K. Nishimura, T. Heine, D. Jiang, *Nat. Commun.* **2016**, *7*, 12325.
- [5] N. Huang, P. Wang, D. Jiang, *Nat. Rev. Mater.* **2016**, *1*, 16068.
- [6] S. M. J. Rogge, A. Bavykina, J. Hajek, H. Garcia, A. I. Olivos-Suarez, A. Sepúlveda-Escribano, A. Vimont, G. Clet, P. Bazin, F. Kapteijn, M. Datur, *Chem. Soc. Rev.* **2017**, *46*, 3134.
- [7] J. W. Colson, W. R. Dichtel, *Nat. Chem.* **2013**, *5*, 453.
- [8] S. B. Alahakoon, C. M. Thompson, G. Occhialini, R. A. Smaldone, *ChemSusChem* **2017**, *10*, 1.
- [9] S. Y. Dinga, W. Wang, *Chem. Soc. Rev.* **2013**, *42*, 548.
- [10] Z. Xiang, D. Cao, *J. Mater. Chem. A* **2013**, *1*, 2691.

- [11] D. Mullangi, V. Dhavale, S. Shalini, S. Nandi, S. Collins, T. Woo, S. Kurungot, R. Vaidhyanathan, *Adv. Energy Mater.* **2016**, *6*, 1600110.
- [12] S. Nandi, S. K. Singh, D. Mullangi, R. Illathvalappil, L. George, C. P. Vinod, S. Kurungot, R. Vaidhyanathan, *Adv. Energy Mater.* **2016**, *6*, 1601189.
- [13] H. Furukawa, O. M. Yaghi, *J. Am. Chem. Soc.* **2009**, *131*, 8875.
- [14] Z. Li, Y. Zhi, X. Feng, X. Ding, Y. Zou, X. Liu, Y. Mu, *Chemistry* **2015**, *21*, 12079.
- [15] V. S. Vyas, F. Haase, L. Stegbauer, G. Savasci, F. Podjaski, C. Ochsenfeld, B. V. Lotsch, *Nat. Commun.* **2015**, *6*, 9508.
- [16] H. Xu, S. Tao, D. Jiang, *Nat. Mater.* **2016**, *15*, 722.
- [17] H. Ma, B. Liu, B. Li, L. Zhang, Y.-G. Li, H.-Q. Tan, H.-Y. Zang, G. Zhu, *J. Am. Chem. Soc.* **2016**, *138*, 5897.
- [18] Y. Peng, G. Xu, Z. Hu, Y. Cheng, C. Chi, D. Yuan, H. Cheng, D. Zhao, *ACS Appl. Mater. Interfaces* **2016**, *8*, 18505.
- [19] H. Oh, S. B. Kalidindi, Y. Um, S. Bureekaew, R. Schmid, R. A. Fischer, M. A. Hirscher, *Angew. Chem., Int. Ed.* **2013**, *52*, 13219.
- [20] R. S. Sprick, J.-X. Jiang, B. Bonillo, S. Ren, T. Ratvijitvech, P. Guiglion, M. A. Zwijnenburg, D. J. Adams, A. I. Cooper, *J. Am. Chem. Soc.* **2015**, *137*, 3265.
- [21] X. Ding, J. Guo, X. Feng, Y. Honsho, J. G. Seki, P. Maitarad, A. Saeki, S. Nagase, D. Jiang, *Angew. Chem., Int. Ed.* **2011**, *50*, 1289.
- [22] S.-Y. Ding, J. Gao, Q. Wang, Y. Zhang, W.-G. Song, C.-Y. Su, W. Wang, *J. Am. Chem. Soc.* **2011**, *133*, 19816.
- [23] D. Mullangi, S. Nandi, S. Shalini, S. Sreedhala, C. P. Vinod, R. Vaidhyanathan, *Sci. Rep.* **2015**, *5*, 10876.
- [24] D. Mullangi, S. Shalini, S. Nandi, B. Chokxia, R. Vaidhyanathan, *J. Mater. Chem. A* **2017**, *5*, 8376.
- [25] J. Guo, Y. Xu, S. Jin, L. Chen, T. Kaji, Y. Honsho, M. A. Addicoat, J. Kim, A. Saeki, H. Ihee, S. Seki, S. Irle, M. Hiramoto, J. Gao, D. Jiang, *Nat. Commun.* **2013**, *4*, 3736.
- [26] G. H. V. Bertrand, V. K. Michaelis, T.-C. Ong, R. G. Griffin, M. Dinca, *Proc. Natl. Acad. Sci. USA* **2013**, *110*, 4923.
- [27] S. Wan, F. Gándara, A. Asano, H. Furukawa, A. Saeki, S. K. Dey, L. Liao, M. W. Ambrogio, Y. Y. Botros, X. Duan, S. Seki, J. F. Stoddart, O. M. Yaghi, *Chem. Mater.* **2011**, *23*, 4094.
- [28] J. N. Coleman, M. Lotya, A. O'Neill, S. D. Bergin, P. J. King, U. Khan, K. Young, A. Gaucher, S. De, R. J. Smith, I. V. Shvets, S. K. Arora, G. Stanton, H.-Y. Kim, K. Lee, G. T. Kim, G. S. Duesberg, T. Hallam, J. J. Boland, J. J. Wang, J. F. Donegan, J. C. Grunlan, G. Moriarty, A. Shmeliov, R. J. Nicholls, J. M. Perkins, E. M. Grievson, K. Theuwissen, D. W. McComb, P. D. Nellist, V. Nicolosi, *Science* **2011**, *331*, 568.
- [29] C. Tan, X. Cao, X.-J. Wu, Q. He, J. Yang, X. Zhang, J. Chen, W. Zhao, S. Han, G.-H. Nam, M. Sindoro, H. Zhang, *Chem. Rev.* **2017**, *117*, 6225.
- [30] X. Zhang, L. Hou, A. Ciesielski, P. Samori, *Adv. Energy Mater.* **2016**, *6*, 1600671.
- [31] L. Peng, Y. Zhu, C. Dahong, R. S. Ruoff, G. Yu, *Adv. Energy Mater.* **2016**, *6*, 1600025.
- [32] L. Shia, T. Zhao, *J. Mater. Chem. A* **2017**, *5*, 3735.
- [33] M. R. Lukatskaya, O. Mashtalir, C. E. Ren, Y. Dall'Agnese, P. Rozier, P. L. Taberna, M. Naguib, P. Simon, M. W. Barsoum, Y. Gogotsi, *Science* **2013**, *341*, 1502.
- [34] L. Peng, X. Peng, B. Liu, C. Wu, Yi. Xie, Y. Guihua, *Nano Lett.* **2013**, *13*, 2151.
- [35] S. Jin, G. Yang, H. Song, H. Cui, C. Wang, *ACS Appl. Mater. Interfaces* **2015**, *7*, 24932.
- [36] Q.-F. Li, C.-G. Duan, X. G. Wan, J.-L. Kuo, *J. Phys. Chem. C* **2015**, *119*, 8662.
- [37] U. K. Sen, S. Mitra, *ACS Appl. Mater. Interfaces* **2013**, *5*, 1240.
- [38] Y. F. Huang, W. H. Ruan, D. L. Lin, M. Q. Zhang, *ACS Appl. Mater. Interfaces* **2017**, *9*, 909.
- [39] C. Liu, F. Li, L.-P. Ma, H.-M. Cheng, *Adv. Mater.* **2010**, *22*, E28.
- [40] K. Sakaushi, M. Antonietti, *Acc. Chem. Res.* **2015**, *48*, 1591.
- [41] M. Agostini, S. Brutti, J. Hassoun, *ACS Appl. Mater. Interfaces* **2016**, *8*, 10850.
- [42] S. Stankovich, D. A. Dikin, R. D. Piner, K. A. Kohlhaas, A. Kleinhammes, Y. Jia, Y. Wu, S. T. Nguyen, R. S. Ruoff, *Carbon* **2007**, *45*, 1558.
- [43] T. S. Sahu, S. Mitra, *Sci. Rep.* **2015**, *5*, 12571.
- [44] J. Xiao, D. Choi, L. Cosimbescu, P. Koeh, J. Liu, J. P. Lemmon, *Chem. Mater.* **2010**, *22*, 4522.
- [45] M. Xu, H. Sun, C. Shen, S. Yang, W. Que, Y. Zhang, X. Song, *Nano Res.* **2015**, *8*, 801.
- [46] G. Ananya, S. Raghu, S. Ramaprabhu, *J. Mater. Chem. A* **2017**, *5*, 2784.
- [47] V. Aravindan, Y.-S. Lee, S. Madhavi, *Adv. Energy Mater.* **2015**, *5*, 1402225.
- [48] B. Qiu, M. Zhang, Y. Xia, Z. Liu, Y. S. Meng, *Chem. Mater.* **2017**, *29*, 908.
- [49] D. N. Bunck, W. R. Dichtel, *J. Am. Chem. Soc.* **2013**, *135*, 1495.
- [50] A. B. Marco, D. Cortizo-Lacalle, I. Perez-Miqueo, G. Valenti, A. Boni, J. Plas, K. Strutycki, S. D. Feyter, F. Paolucci, M. Montes, A. N. Khlobystov, M. Melle-Franco, A. Mateo-Alonso, *Angew. Chem., Int. Ed.* **2017**, *56*, 1.
- [51] Y. Ishijima, M. Okaniwa, Y. Oaki, H. Imai, *Chem. Sci.* **2017**, *8*, 647.
- [52] X. Chen, M. Addicoat, E. Jin, L. Zhai, H. Xu, N. Huang, Z. Guo, L. Liu, S. Irle, D. Jiang, *J. Am. Chem. Soc.* **2015**, *137*, 32417.
- [53] Y.-P. Mo, X.-H. Liu, B. Sun, H.-J. Yan, D. Wang, L.-J. Wan, *Phys. Chem. Chem. Phys.* **2017**, *19*, 539.
- [54] M. A. Khayum, S. Kandambeth, S. Mitra, M. A. Nair, A. Das, S. S. Nagane, R. Mukherjee, R. Banerjee, *Angew. Chem., Int. Ed.* **2016**, *55*, 15604.
- [55] S. Mitra, H. S. Sasmal, T. Kundu, S. Kandambeth, K. Illath, D. D. Díaz, R. Banerjee, *J. Am. Chem. Soc.* **2017**, *139*, 4513.
- [56] S. Chandra, S. Kandambeth, B. P. Biswal, B. Lukose, S. M. Kunjir, M. Chaudhary, R. Babarao, T. Heine, R. Banerjee, *J. Am. Chem. Soc.* **2013**, *135*, 17853.
- [57] B. J. Smith, L. R. Parent, A. C. Overholts, P. A. Beauce, R. P. Bisbey, A. D. Chavez, N. Hwang, C. Park, A. M. Evans, N. C. Gianneschi, W. R. Dichtel, *ACS Cent. Sci.* **2017**, *3*, 58.
- [58] S. Wang, L. Wang, K. Zhang, Z. Zhu, Z. Tao, J. Chen, *Nano Lett.* **2013**, *13*, 4404.
- [59] O. A. Vargas, C. A. Caballero, J. Morales, *Nanoscale* **2012**, *4*, 2083.
- [60] X. Han, G. Qing, J. Sun, T. Sun, *Angew. Chem., Int. Engl. Ed.* **2012**, *57*, 5147.
- [61] H. Yang, S. Zhang, L. Han, Z. Zhang, Z. Xue, J. Gao, Y. Li, C. Huang, Y. Yi, H. Liu, Y. Li, *ACS Appl. Mater. Interfaces* **2016**, *8*, 5366.
- [62] S. Wang, Q. Wang, P. Shao, Y. Han, X. Gao, L. Ma, S. Yuan, X. Ma, J. Zhou, X. Feng, B. Wang, *J. Am. Chem. Soc.* **2017**, *139*, 4258.
- [63] D. A. Vazquez-Molina, G. S. Mohammad-Pour, C. Lee, M. W. Logan, X. Duan, J. K. Harper, F. J. Uribe-Romo, *J. Am. Chem. Soc.* **2016**, *138*, 9767.
- [64] L. Bai, Q. Gao, Y. Zhao, *J. Mater. Chem. A* **2016**, *4*, 14106.
- [65] F. Xu, S. Jin, H. Zhong, D. Wu, X. Yang, X. Chen, H. Wei, R. Fu, D. Jiang, *Sci. Rep.* **2015**, *5*, 8225.
- [66] C. R. Mulzer, L. Shen, R. P. Bisbey, J. R. McKone, N. Zhang, H. D. Abruña, W. R. Dichtel, *ACS Cent. Sci.* **2016**, *2*, 667.
- [67] D.-H. Yang, Z.-Q. Yao, D. Wu, Y.-H. Zhang, Z. Zhou, X.-H. Bu, *J. Mater. Chem. A* **2016**, *4*, 18621.
- [68] D. Cao, J. Lan, W. Wang, B. Smit, *Angew. Chem., Int. Ed.* **2009**, *48*, 4730.
- [69] E. Tylianakis, E. Klontzas, G. E. Froudakis, *Nanoscale* **2011**, *3*, 856.

- [70] D. J. Kim, S. H. Je, S. Sampath, J. W. Choi, A. Coskun, *RSC Adv.* **2012**, *2*, 7968.
- [71] X. Zhu, Y. Zhu, S. Murali, M. D. Stoller, R. S. Ruoff, *ACS Nano* **2011**, *5*, 3333.
- [72] L. Zhang, H. B. Wu, X. W. D. Lou, *Adv. Energy Mater.* **2014**, *4*, 1300958.
- [73] S. Goriparti, E. Miele, F. De Angelis, E. Di Fabrizio, R. P. Zaccaria, C. Capiglia, *J. Power Sources* **2014**, *257*, 421e443.
- [74] E. O. R. Beake, M. T. Dove, A. E. Phillips, D. A. Keen, M. G. Tucker, A. L. Goodwin, T. D. Bennett, A. K. Cheetham, *J. Phys.: Condens. Matter* **2013**, *25*, 395403.
- [75] J.-Y. Yue, Y.-P. Mo, S.-Y. Li, W.-L. Dong, T. Chen, D. Wang, *Chem. Sci.* **2017**, *8*, 2169.
- [76] S. Mitra, S. Kandambeth, B. P. Biswal, M. A. Khayum, C. K. Choudhury, M. Mehta, G. Kaur, S. Banerjee, A. Prabhune, S. Verma, S. Roy, U. K. Kharul, R. Banerjee, *J. Am. Chem. Soc.* **2016**, *138*, 2823.
- [77] FE-SEM Image of a Commercially Sold Special Graphene Sheet, <http://www.simbatt.com/en/XIE.html>.
- [78] D. Geng, Y. Chen, Y. Chen, Y. Li, Y. Li, X. Sun, S. Ye, S. Knights, *Energy Environ. Sci.* **2011**, *4*, 760.
- [79] J. A. Foster, S. Henke, A. Schneemann, R. A. Fischer, A. K. Cheetham, *Chem. Commun.* **2016**, *52*, 10474.
- [80] I. Berlanga, M. L. Ruiz-González, J. M. González-Calbet, J. L. G. Fierro, R. Mas-Ballesté, F. Zamora, *Small* **2011**, *7*, 1207.
- [81] Z. Xing, Z. Ju, Y. Zhao, J. Wan, Y. Zhu, Y. Qiang, Y. Qian, *Sci. Rep.* **2016**, *6*, 26146.
- [82] A. P. Cohn, L. Oakes, R. Carter, S. Chatterjee, A. S. Westover, K. Share, C. L. Pint, *Nanoscale* **2014**, *6*, 4669.
- [83] D. Mukherjee, Y. K. G. Gowda, H. M. N. Kotresh, S. Sampath, *ACS Appl. Mater. Interfaces* **2017**, *9*, 19446.
- [84] V. Augustyn, P. Simon, B. Dunn, *Energy Environ. Sci.* **2014**, *7*, 1597.
- [85] P. Simon, Y. Gogotsi, B. Dunn, *Science* **2014**, *343*, 1210.
- [86] T. Nokami, T. Matsuo, Y. Inatomi, N. Hojo, T. Tsukagoshi, H. Yoshizawa, A. Shimizu, H. Kuramoto, K. Komae, H. Tsuyama, J.-I. Yoshida, *J. Am. Chem. Soc.* **2012**, *134*, 19694.
- [87] H. Liu, Q. Cao, L. J. Fu, C. Li, Y. P. Wu, H. Q. Wu, *Electrochem. Commun.* **2006**, *8*, 1553.
- [88] X. H. Rui, N. Ding, J. Liu, C. Li, C. H. Chen, *Electrochimica Acta* **2010**, *55*, 2384.
- [89] Y.-Q. Wang, L. Gu, Y.-G. Guo, H. Li, X.-Q. He, S. Tsukimoto, Y. Ikuhara, L.-J. Wan, *J. Am. Chem. Soc.* **2012**, *134*, 7874.
- [90] H. Wu, Y. Meng, K. Lu, Z. Wei, *J. Mater. Chem. A* **2013**, *1*, 6366.
- [91] G. X. Wang, L. Yang, Y. Chen, J. Z. Wang, S. Bewlay, H. K. Liu, *Electrochim. Acta* **2005**, *50*, 4649.
- [92] C. Ho, I. D. Raistrick, R. A. J. Huggins, *Electrochem. Soc.* **1980**, *127*, 343.
- [93] Y. Cui, X. Zhao, R. Guo, *Electrochim. Acta* **2010**, *55*, 922.
- [94] Z. Ma, Y. Peng, G. Wang, Y. Fan, J. Song, T. Liu, X. Qin, G. Shao, *Electrochim. Acta* **2015**, *156*, 77.
- [95] C. Luo, R. Huang, R. Kevorkyants, M. Pavanello, H. He, C. Wang, *Nano Lett.* **2014**, *14*, 1596.
- [96] J. Xie, X. Rui, P. Gu, J. Wu, Z. J. Xu, Q. Yan, Q. Zhang, *ACS Appl. Mater. Interfaces* **2016**, *8*, 16932.
- [97] J. Wu, X. Rui, C. Wang, W.-B. Pei, R. Lau, Q. Yan, Q. Zhang, *Adv. Energy Mater.* **2015**, *5*, 1402189.
- [98] J. Wu, X. Rui, G. Long, W. Chen, Q. Yan, Q. Zhang, *Angew. Chem., Int. Engl. Ed.* **2015**, *54*, 7354.
- [99] Y. S. Menga, M. E. Arroyo-de Dompablo, *Energy Environ. Sci.* **2009**, *2*, 589.
- [100] M. Hankel, D. Ye, L. Wang, D. J. Searles, *J. Phys. Chem. C* **2015**, *119*, 21921.
- [101] D. Chen, A.-J. Avestro, Z. Chen, J. Sun, S. Wang, M. Xiao, Z. Erno, M. M. Algaradah, M. S. Nassar, K. Amine, Y. Meng, J. F. Stoddart, *Adv. Mater.* **2015**, *27*, 2907.

Chemical Exfoliation as a Controlled Route to Enhance the Anodic Performance of COF in LIB

Sattwick Haldar,* Kingshuk Roy, Rinku Kushwaha, Satishchandra Ogale,* and Ramanathan Vaidhyathan*

Dedicated to Prof. Akira Yoshino, Prof. M. Stanley Whittingham and Prof. John B. Goodenough to congratulate them for their wonderful contribution to Li-ion battery research

A covalent organic framework (COF), built from light atoms with a graphitic structure, could be an excellent anodic candidate for lightweight batteries, which can be of use in portable devices. But to replace the commercial graphite anode, they need more Li-interactive sites/unit-cell and all such sites should be made to participate. The compromise made in the volumetric density to gain the gravimetric advantage should be minimal. Exfoliation enhances surface/functional group accessibility yielding high capacity and rapid charge storage. A chemical strategy for simultaneous exfoliation and increase of Li-loving active-pockets can deliver a lightweight Li-ion battery (LIB). Here, anthracene-based COFs are chemically exfoliated into few-layer-thick nanosheets using maleic anhydride as a functionalizing exfoliation agent. It not only exfoliates but also introduces multiple Li-interactive carbonyl groups, leading to a loading of 30 Li/unit-cell (vs one Li per C_6). The exfoliation enhances the specific capacity by ≈ 4 times ($200\text{--}790\text{ mAh g}^{-1}$ @ 100 mA g^{-1}). A realistic full-cell, made using the exfoliated COF against a LiCoO_2 cathode, delivers a specific capacity of 220 mAh g^{-1} over 200 cycles. The observed capacity stands highest among all organic polymers. For the first report of a COF derived full-cell LIB, this is a windfall.

can be of use in portable devices, such as solar lanterns, aviation systems, and other automotives. However, to replace the volumetrically advantageous battery-grade graphite as an anode, they need to have more number of Li-interactive sites per unit cell and all such sites should be made to participate. In short, the compromise made in the volumetric density to gain the gravimetric advantage should be minimal. COF's organic framework can be functionalized with Li-binding heteroatoms. Now, if a chemical strategy can be devised to achieve simultaneous exfoliation and increase of Li-loving active pockets, it could open up the possibility of an anodic material which is lightweight and yet can accomplish substantial lithium loading when coupled with a practical cathode like LiCoO_2 . Another structural advantage of COF as for exfoliation is the presence of in-layer pores, because of which their layers are held together by relatively less number of π - π interactions per specific area compared to graphite. This makes

COFs easily exfoliatable.^[2–13] If it can be achieved via a chemical route, it can fetch high tunability.^[2–8]

Several new organic polymers with 2D structures are being considered as anodes in LIB. Some display substantial specific capacities; for example, the best-performing amorphous polymers have capacities in the range of $\approx 400\text{--}670\text{ mAh g}^{-1}$ @ 100 mA g^{-1} .^[14–17] More specifically, the covalent organic frameworks, with a crystalline structure, exhibit capacities of 593, 600, 666 mAh g^{-1} .^[18–20] Lei et al. reported a COF@CNTs composite with a half-cell capacity of 952 mAh g^{-1} , but with moderate rate stability.^[19] In all these graphite-resembling layered anodic COFs, the insertion/intercalation mechanism is dominant.^[21–24] In them, the concentration and the accessibility of the Li-interactive sites largely control the overall specific capacity of the anode, and the ion-diffusion rates control the charge-discharge speeds.^[25,26] Both can be positively impacted by exfoliation.

A common feature among all these studies is that most investigations have been on half-cell configuration wherein the anodic material is tested against lithium metal (cathode). This

1. Introduction

Covalent organic framework (COF) can be a potential anodic material in lithium ion battery (LIB).^[1] Since they are built from lighter atoms and with a porous structure, they can be an excellent anodic candidate in developing lightweight batteries, which

S. Haldar, K. Roy, R. Kushwaha, Dr. R. Vaidhyathan
Department of Chemistry and Centre for Energy Science
Indian Institute of Science Education and Research
Dr. Homi Bhabha Road, Pashan, Pune 411008, India
E-mail: sattwick.haldar@students.iiserpune.ac.in; vaidhya@iiserpune.ac.in
Prof. S. Ogale
Department of Physics
Indian Institute of Science Education and Research
Dr. Homi Bhabha Road, Pashan, Pune 411008, India
E-mail: satishogale@iiserpune.ac.in

 The ORCID identification number(s) for the author(s) of this article can be found under <https://doi.org/10.1002/aenm.201902428>.

DOI: 10.1002/aenm.201902428

presents the best-case scenario, as it is quite easy to pull the lithium out of Li-metal at very low potentials (0.02–0.08 V) and these lithium can occupy the anodes. Thus the electrochemical stability of the material being tested is not fully challenged. This is why the good performance of an anodic material in the half-cell does not necessarily translate to their full-cell.^[27–29] In contrast, in a full-cell, for example, one made using LiCoO₂, much higher potential is required to pull out the Li-ions from the cathode (≈ 3.8 V).^[27] Which means the anode should withstand it. Also, the Li-insertion into the anode needs to continue as the potential drops and this typically yields a smooth and gradual curve in the Galvanostatic charge–discharge measurements.^[30–33] To date, there are no reports of COF performing under such challenging full-cell conditions.

Recently, we demonstrated a COF, which forms as covalent organic nanosheets (CON) even during synthesis shows remarkable anodic performance in an LIB half-cell.^[25] Concomitantly, reports have appeared wherein COF (nonexfoliated) or its composite with highly conducting or anodic carbons have been shown to have appreciable performance in a Li-ion half-cell.^[18–20,33–36] However, a systematic study showing the enhancement of a COF's anodic performance upon exfoliation to CON is not available. Thus, our objective was to design a versatile exfoliation strategy involving a functionalizing exfoliation agent (FEA) (Scheme S1, Supporting Information) and to see the performance of the COF versus CON as an anode material in an LIB. Here, we describe two anthracene-rich COFs which are readily exfoliated into few-layer-thick nanosheets using maleic anhydride as the FEA. It provides a means to concentrate more Li-interactive carbonyl oxygens into the framework with improved active site access.^[14,34–36] These CONs in a practical full-cell LIB, give a stable specific capacity of 220 mAh g⁻¹@100 mA g⁻¹ (vs 184 mAh g⁻¹@100 mA g⁻¹ for graphite). It carries an energy density of 364 Wh kg⁻¹ (vs 320 Wh kg⁻¹ for graphite) over 200 cycles. The observed full-cell capacity is the highest among all organic-polymers operating with lithium insertion or intercalation type phenomenon. For the first report of a full-cell performance of a COF-derived LIB, this is remarkable.

2. Results and Discussion

A detailed description of the synthesis, characterization, and structure solution of the anthracene COFs (IISERP-COF7 (1) and IISERP-COF8 (2)) are presented in Figures S1–S4 and Tables S1 and S2 (Supporting Information).

2.1. Chemical Exfoliation of COFs to CONs (IISERP-CON2 (3) and IISERP-CON3 (4))

Anthracene moieties are known to react with anhydrides via an [4 + 2] addition mechanism.^[37–42] This breaks the conjugation at the anthracene sites, which can be monitored using UV–vis and NMR studies.^[37–39] When this chemical reaction is carried out on systems containing stacks of anthracene, the associated structural changes can be followed.^[13] This prompted us to consider the anthracene functionalized COFs for this exfoliation

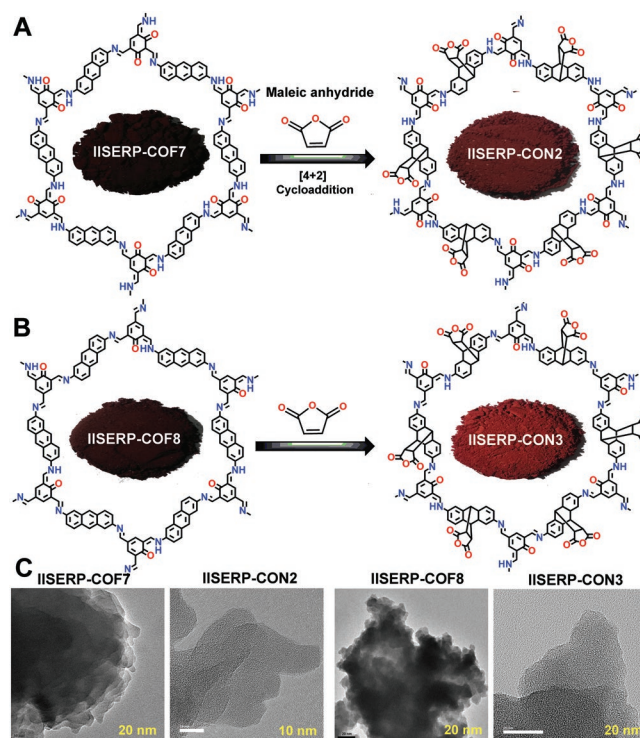


Figure 1. A) Diels–Alder cycloaddition of maleic anhydride to the anthracene rings of the COFs. Inset shows the photographic images of the COF and the CONs. B, C) Comparative HRTEM images of the COFs and CONs. The chemical exfoliation of the COF to few-layer thick CON via the cycloaddition is evident. Presence of micro pores in the CONs can be seen from the HRTEM images.

study. To this strategy, the IISERP-COF7 and IISERP-COF8 were subjected to a thermal Diels–Alder reaction with maleic anhydride (48 h with 1 M maleic anhydride solution prepared in a mesitylene + tetrahydrofuran mixture; the reaction was carried out under nitrogen) (Figure 1A; and Scheme S2, Supporting Information). We propose the maleic anhydride to be a FEA.

This besides aiding the exfoliation adds carbonyl groups into the polymeric framework through the anhydride functionality, such groups are known to interact with lithium (Figure 1A).^[15]

The adduct formation causes a noticeable color change from black to brownish-red color. Visualizable morphological changes were also seen. Also, the Diels–Alder adduct formation between the COF's anthracene rings and the maleic anhydride follows second-order reaction kinetics as monitored from the disappearance of the anthracene's absorption peak in the UV–vis spectra (Figure S5, Supporting Information).^[43] A dispersion of this exfoliated COF showed the characteristic Tyndall effect (Figure S6, Supporting Information).

Under the field emission scanning electron microscope (FE-SEM) and higher resolution transmission electron microscope (HR-TEM), the as-synthesized COFs appear as aggregated submicrometer-sized flaky crystallites (Figures S7–S10, Supporting Information). These crystallites have a hexagonal sheet morphology with prominent stacking and the lattice fringes could be observed and they correspond to a distance of 3.4 Å matching the interlayer distance expected from the modeled structure (Figure S11, Supporting Information). Meanwhile, the

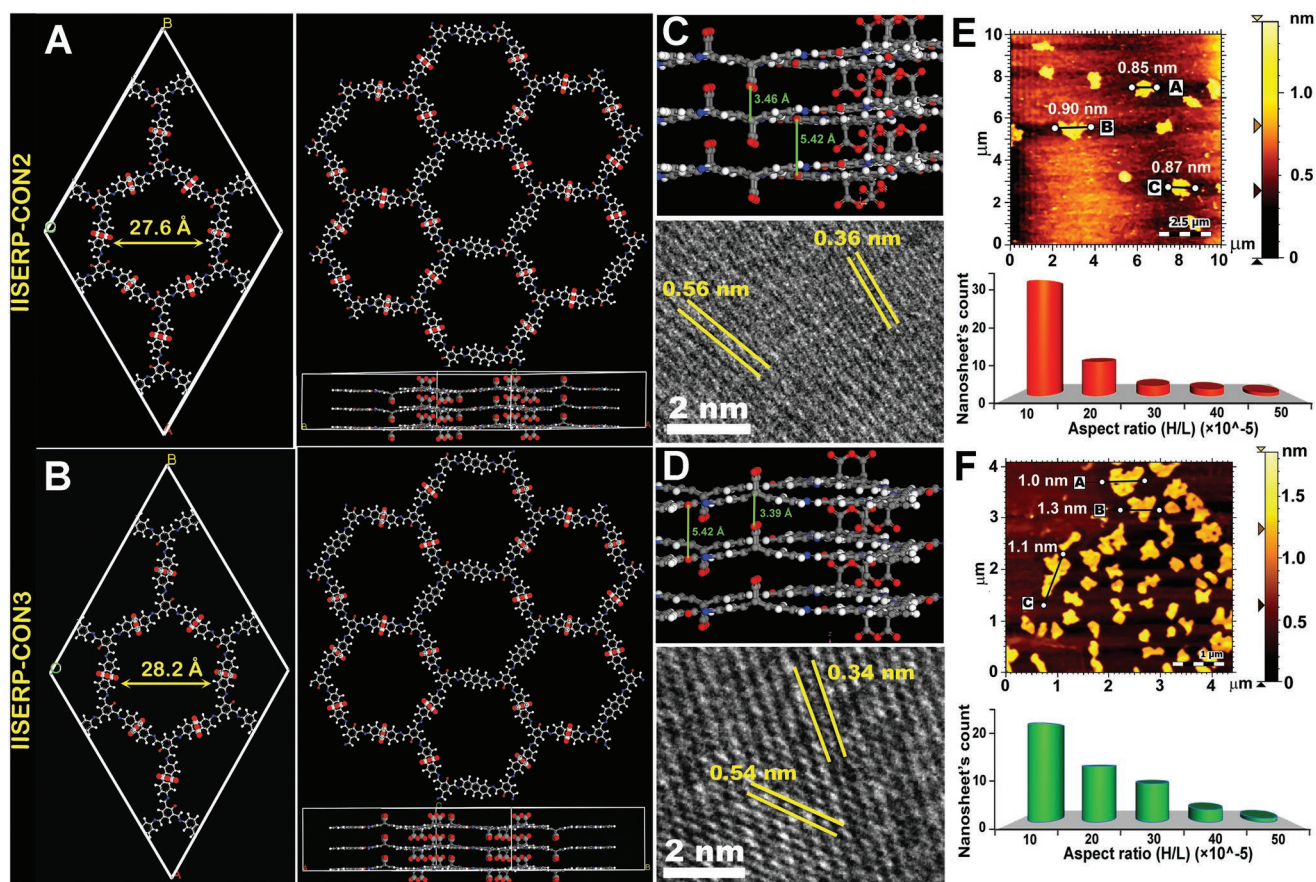


Figure 2. A,B) Structure of the Diels–Alder cyclo-added CONs modeled using DFT methods (Relative energy for up-down anhydride configuration, IISERP-CON2 = $-100 \text{ kcal mol}^{-1}$; IISERP-CON3 = $-95 \text{ kcal mol}^{-1}$). The lowest energy conformer having the maleic anhydride groups positioned up-and-down the COF layers is shown. C,D) Comparison of the interlayer separation of the model with those obtained from the HRTEM images. E,F) Representative AFM images showing the thickness distribution (lateral width (L) and height (H)) of the CON flakes obtained from the chemical exfoliation. The statistical plots of the aspect ratio (H/L) are obtained from 65 independent AFM images.

C–C bond addition via the Diels–Alder reaction exfoliated the stacked COF into covalent organic nanosheets with substantially lowered aggregation and appeared with more exposed sheet-type structure as observed from the FE-SEM and HR-TEM images (Figure 1B,C; and Figures S12–S15, Supporting Information). Such discrete sheets with flat surfaces distribute homogeneously. Now, there are two possibilities for the final structure of the CONs: i) all the cycloaddition could have occurred on one face of the anthracene units of the COF layer (all-up); ii) the cycloaddition could be happening at either faces of the anthracene units, giving rise to the anhydride group running above and below the plane of the layers (up-down) (Figure S16, Supporting Information). Though the structure with the up-down arrangement has lower relative energy ($-29\,401 \text{ kcal mol}^{-1}$), the packing efficiency quantified by a packing fraction turns out to be $\approx 45\%$ for both the configurations.

The ordered packing is evident from the observation of lattice fringes for these CONs under the HR-TEM. Lattice fringes with two different separations, 3.4 and 5.4 Å, were observed, which agrees well with the modeled structure of the CON (Figure 2C,D; and Figures S17 and S18, Supporting Information). The larger interplanar separation in the CON could also aid the facile insertion.

Firm evidence for the exfoliation into CONs comes from the atomic force microscopy (AFM). In comparison to the COFs (100–200 nm thick), these exfoliated nanosheets are very thin with only 1 and 1.5 nm thickness on average, which correspond to only 2–5 layers (Figure 2E; and Figures S19–S22, Supporting Information). Thickness and aspect-ratio were calculated with the help of AFM data analysis for both the products. From ≈ 65 images of each sample, the statistical distribution plots were made. Majority of the 3's flakes have a thickness in the range of 0.8–1.5 nm (Figure 2F; and Figure S23, Supporting Information). The 4's thickness ranged from 1–3 nm. To the best knowledge, this is the lowest thickness values achieved for any exfoliated COFs. The lateral length of the nanosheets ranged from 1000 to 3000 nm. This yields extremely low aspect ratio (height/length) of $\approx 1 \times 10^{-6}$ – 2×10^{-6} (Figure 2F; and Figure S23, Supporting Information). Notably, the lateral dimensions of the flakes obtained from this chemical exfoliation route are much larger compared to the earlier reported self-exfoliated IISERP-CON1,^[25] but it is comparable to the dimensions observed in the solvent exfoliated COF reported by Dichtel and co-workers.^[2]

The NMR comparisons also revealed the COFs coexisting in keto and enol tautomeric forms, but the CONs, in their

solid-state, exist predominantly in the keto form (Figure S24, Supporting Information). This has implications on the interactions with the incoming lithium species during the cell operation. When the CONs were exposed to acidic (6N HCl) or basic (6N NaOH) environments they remained in their keto form which was confirmed from the lack of any phenolic $-OH$ groups in the IR spectra, which is in contrast to the COFs (Figures S25 and S26, Supporting Information).^[13] Thus the exfoliation alters the host's chemical structure. The formation of the disordered nanosheets from the highly π -stacked COFs was monitored by comparing the Bragg reflections of the powder X-ray diffraction (PXRD) patterns and the adsorption data of the pre- and postchemically exfoliated phases (Figure 3A,B). For this purpose, the reaction mixtures were quenched after 12 h and the insoluble solid products were isolated. In the PXRD, the intensity of the $(100/010)$ reflections appearing at the lowest 2θ drops significantly, while the intensity of the $00l$ reflections increases as the exfoliation is achieved (Figure 3B). For both CONs, a prominent peak appears at 17.5° and the peak at 26.5° becomes more intense after the completion of the exfoliation (after 48 h of reaction) (Figures S27 and S28, Supporting Information). Importantly, the former peak indexes to the 001 reflection, while the higher angle peak to the 002 reflection from the optimized simulated structure. However, the peak at 17.5° is relatively sharper, and we suspect this could be due to some preferred orientation effects and not due to any oligomeric species forming as an impurity. This is because the powder pattern shown in Figure S26 (Supporting Information) was obtained very reproducibly from multiple batches of samples.

These changes in the PXRD pattern can be explained by considering the change in the ratio between the ab-plane atoms exposed to the X-ray to the c-direction planes that get exposed when the highly π -stacked COF converts to a few-layer thick disordered CON (Figure 3C). Also, the appearance of the peak at $\approx 17.5^\circ$ in the PXRD pattern of the CONs is because of the introduction of the anhydride functionality (Dienophile), which orients along the c-direction. Hence the $00l$ reflections get altered. Notably, in the simulated PXRD pattern of the CONs, the peak at $\approx 17.5^\circ$ is prominent and this appears when we introduce the maleic anhydride appendages into the modeled structure. This peak indexes to the 001 reflection in the tight-binding density functional theory optimized structure (Figure S27, Supporting Information).

The appearance of this prominent peak at $2\theta = 17.5^\circ$ (001 reflection) in the CON is further supported by the presence of lattice fringes in the HRTEM images with a spacing of ≈ 0.56 nm, which corresponds to a $2\theta = 17.5^\circ$ (from Bragg's Equation) (Figure S28, Supporting Information). So, in the CON's PXRD, both the increase in the contribution from the atomic planes in the c-direction due to disorderliness as well as the increase of the number of atoms along the c-direction due to the insertion of the maleic anhydride units appears to increase the intensity of these $00l$ reflections.

The porosity data further supports with a noticeable drop in Brunauer–Emmett–Teller surface area (from 657 to 164 m^2 g^{-1} and 725 to 230 m^2 g^{-1}) with the increase of the reaction time (Figure 3D; and Figures S29 and S30, Supporting Information). This is because CONs do not form channels/tunnels as deep as

COF in the c-direction. Nevertheless, the pore widths for 3 and 4 after 12 and 48 h reaction remain almost the same compared to the pristine COFs (Figure S31, Supporting Information). This advocates that the layer-by-layer exfoliation of the COF sheets did not destroy the orientation of the functional groups along the nanopores. Besides, in this exfoliated configuration, achieved by the insertion of the anhydride groups, many surface-exposed $C=O$ groups become available for chemical interactions with lithium as perceived from X-ray photoelectron spectroscopy (XPS) and Raman studies (Scheme S3, Figures S33–S35, and Tables S3 and S4, Supporting Information).

2.2. Rapid Li-Ion Diffusion in Exfoliated COF

The lithium diffusion coefficients were determined from half-cell measurements with CON-LiPF₆-Li metal coin-cell configurations. The coin-cells with an open circuit voltage of around 2.85 V were connected to a charge–discharge cyclor and cyclic voltammogram (CV) were recorded at a scan rate of 2 mV s^{-1} . An anodic potential window of 0.01–3 V was swept. Notably, the reversible peaks due to the insertion–deinsertion of lithium were observed in both COF and CON with similar-looking CV profiles (Figure S36A(i) and B(i), Supporting Information). Also, the CV shows an increased current associated with the (R1/O1) and the (R2/O2) peaks of the CON as compared to the COF. We believe, this is due to the carbonyl oxygens being more exposed for interaction with the incoming Li-ions in the exfoliated structure of the CONs compared to the COFs, where they are more buried (Scheme S2, Supporting Information). In both CONs, unlike the COFs, the capacity started to increase steadily up to ≈ 280 cycles, stabilizing at 790 mAh g^{-1} for 3 and 580 mAh g^{-1} for 4. These high capacities remain intact even after 1000 cycles retaining their 100% Columbic efficiency (Figure S36C, Supporting Information). Even after increasing the current density only 34% and 42% capacity drop were observed for 3 and 4, respectively (Figure S37, Supporting Information). Multiple CV cycles measured using the same CON-derived electrodes showed excellent reversibility (Figures S38, Supporting Information). With the increase of the number of cycles, the insertion of lithium under very low potential (0.03 V) enhances, which reflects in the higher current contribution in low potential with the cycling of the half-cell battery. Moreover, the reversible peak in higher potential (1.6 V) becomes more prominent, thus contributes more amount of current than the initial cycles.

The lithium insertion into the CONs occurring at very low potential could be diffusion or surface controlled process.^[44–46] To verify this, the CVs were performed with a variable scan rate (from 1 to 50 mV) using fresh cells. A linear fit to the power-law $i = av^b$ (i = current; v = scan rate) resulted in $b = 0.61$ @0.03 V for 3 (Figures S39 and S40 and Scheme S4, Supporting Information) obeys the Cottrell's equation and advocates a diffusion-controlled insertion mechanism as being the dominant process at the low potentials. At higher potentials, the “b” values of 0.63 @1 V and 0.80 @1.6 V means surface-controlled charge storage arising from the chemical reactivity of CONs' functional groups with Li⁺. Also, with the increase of the cycle number, the functional groups become more activated toward

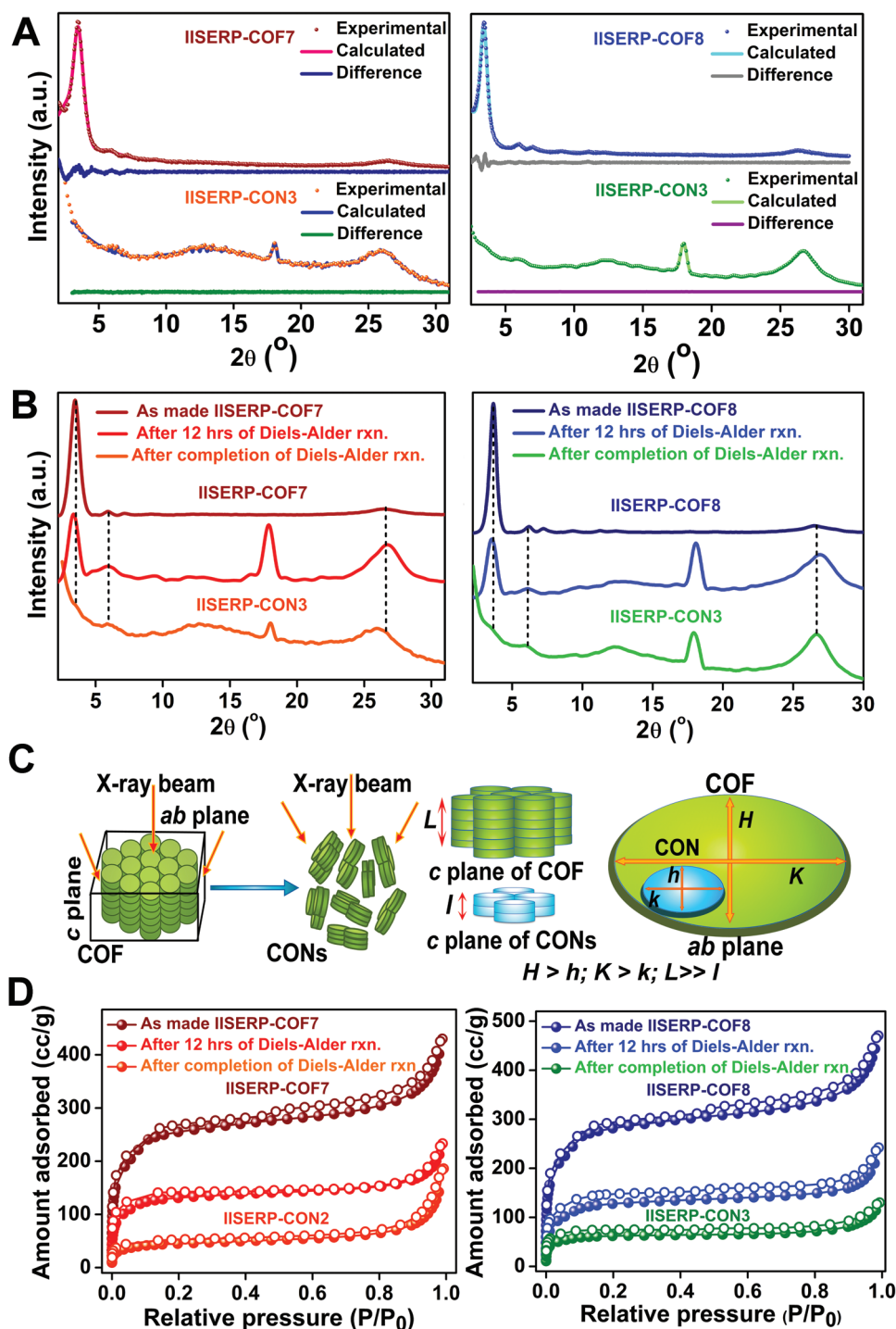


Figure 3. A) Pawley fits of the COF and the CONs refined using Materials Studio. B) The experimental PXRD of the COF compared with the PXRD of the extracts isolated at different time intervals during the cycloaddition reaction. C) A schematic illustrating the reason for the relative intensity variations in the PXRD of the COF versus CON. COF exposes more of ab -plane atoms, while the CON with increased height/lateral-length ratio exposes more atoms along the c -direction. COF planes are indicated with HKL; CON planes are indicated with hkl. D) N_2 adsorption-desorption isotherms of the COF and the CONs collected at 77 K. The Diels-Alder adduct formation completes in 48 h.

the lithium insertion, which is reflected again in the higher surface controlled behavior after 1000 charge-discharge cycles. This signifies the presence of mildly interacting oxygen-rich functional moiety in the skeleton of the CONs also contributes

toward the lithium affinity. For easy grasping, a diagram has been provided to denote the change of mechanism from diffusion-dominated kinetics to the surface-controlled kinetics of CON derived electrodes, which also results in the decreased resistance of

ionic/charge-transfer and increased reversible capacities during the repetitive lithiation and delithiation process (Figures S41 and S42, Supporting Information). However, this contribution to the overall specific capacity is much lesser compared to the contribution from the insertion occurring at the lower potentials. This suggests that the lithium insertion into the pores of the nanosheets becomes more and more effortless with many cycling. Such capacity enhancement with cycling should typically reflect in improved Li-ion diffusion coefficient. Also, for structural reasons (Figure S36D, Supporting Information), it should be more prominent in the CON compared to the parent COF. To verify this, AC-impedance analyses were performed with the COF and CON derived half-cells. The diffusion coefficient calculated from the Warburg tail for the COF and the CON were compared using freshly pressed coin-cells and the coin-cells, which had already been subjected to 1000 charge–discharge cycles (Figure S43, Supporting Information). It yielded diffusion coefficients, D_{Li^+} of $\approx 3.69 \times 10^{-11} \text{ cm}^2 \text{ s}^{-1}$ for 3 and 3.62×10^{-11} for 4, which are almost three times higher than the D_{Li^+} values obtained for the COFs (i.e., 1.26×10^{-11} for 1 and 2.26×10^{-11} for 2, respectively, Table S7, Supporting Information).^[25,47,48] Combining the observations from the CV and the XPS and Raman, carried out on a completely discharged (Li-loaded CON) samples, we propose a mechanism for the lithium loading, which displays the change from diffusion-dominated kinetics to surface-controlled kinetics at the CON-derived electrodes (Figures S33–S35, Supporting Information). This results in the decreased resistance for the ion/electron transfers and increases the reversible capacities during the repetitive lithiation and delithiation process.

2.3. Exfoliated-COFs Performance Under High Potentials of a Full-Cell LIB

The noticeable stable and high specific capacities of the CONs encouraged us to assess their actual performance as an anode in a practical LIB. A full-cell brings the maximum energy density that can be derived from a specific anode–electrolyte–cathode combination. Thus, measuring the anodic performance of the 3 against well-standardized commercial cathode and electrolyte would explicitly display its practical capacity. Here, activated LiCoO_2 (LCO) was employed as the counter cathode and activated 3/4 as the anode to fabricate a full-cell. At first, a slurry of the cathode, LCO, and the anode, CON, was prepared using 70% of the active material, 30% Super-P carbon and 10% polyvinylidene difluoride binder. The LCO and the CONs electrodes were electrochemically preactivated by 200 charge–discharge cycles at 50 mA g^{-1} in a typical half-cell using Li metal as the counter. This is required to get an estimate of the truly available active sites in the CON to act as anode against LiCoO_2 , barring the sites lost to solid electrolyte interface layer formation.

It is essential to recognize that the CONs could retain their activity and structure even after this pretreatment step. The half-cell having the LCO pressed against the lithium electrode, after 200 cycles, stabilized to a specific capacity of 198 mAh g^{-1} (Figure S44, Supporting Information). Meanwhile, the half-cells having the 3/4 pressed against the lithium metal yielded

three and four times higher specific capacities compared to the LiCoO_2 , respectively. Therefore, to achieve maximum capacity in the CON-LCO full-cell, a CON to LCO weight ratio of 1:4 was employed.

A full-cell was fabricated integrating the completely charged CONs as anode and completely discharged LCO as the cathode. About $200 \mu\text{L}$ of 1 M LiPF_6 dissolved in a 1:1 ethylenecarbonate:dimethylcarbonate solvent mixture along with 5% fluoroethylenecarbonate was used as the electrolyte (Figure 4A). To ensure complete lithiation and delithiation in the full-cell, $E^0 \pm 0.5 \text{ V}$, i.e., 2.6–3.6 V was employed as the potential window (see the similar calculation for graphite derived full-cell in the Supporting Information). CVs were recorded for 5 cycles at 2 mV s^{-1} scan rate for both the full-cells in a working potential window of 2.6–3.6 V (Figure 4B). Looking at the CV, one can see a large area under the curve in the potential window of 3.2–3.6 V, rendering a high current \times voltage value. This is the potential where the Li-ions are stripped-off from the LCO cathode and the same is spontaneously inserted into the CON anode. This larger current at this high potential is realized due to the facile insertion of Li into the CON. Impedance measurements on the full-cells show two distinct charge transfer resistances in the high-frequency region (Figure 4C). Such Cole–Cole plots with two semicircles are known. The higher frequency semicircle can be assigned as the surface film resistance (R_{sf}) which is due to the formation of electrode–electrolyte interphase layer and the lower frequency semicircle can be assigned as the charge transfer resistance (R_{ct}).^[49] Galvanostatic charge–discharge cycling of the full-cells was performed at 100 mA g^{-1} for 200 cycles (Figure 4D,E). 3 delivered a specific capacity of 220 mAh g^{-1} with 92% capacity retention (Figure 4F). While the 4 exhibits a specific capacity of 170 mAh g^{-1} , which drops gradually with increasing cycles and about 68% capacity is retained after 200 cycles. 3 has a $\approx 90\%$ Columbic efficiency and 4 has $\approx 85\%$. The capacity drop after prolong cycling is due to the drying of the liquid LiPF_6 electrolyte at the higher potentials. Employing better compatible solid electrolytes could offer a plausible solution.^[50–52] The full-cell stabilized specific capacity (220 mAh g^{-1} @ 100 mA g^{-1}) achieved by 3 is significantly higher than the capacity of the full-cell made using the commercial graphite anodes (180 mAh g^{-1} at 100 mA g^{-1} for Battery Grade Graphite under comparable conditions, Figure S45, Supporting Information). It is higher than most other commercial anodic materials (Table S8, Supporting Information). The full-cells made using 3 and 4, both exhibit an average operating potential close to 3.15 V (Figure 4D,E), from this the energy densities were estimated to be 364 Wh kg^{-1} for 3 and 286 Wh kg^{-1} for 4 (Table S9, Supporting Information). The high energy density of the 3 based Li-ion full-cell is comparable to that of commercial graphite anode-based LIB (320 Wh kg^{-1}). Furthermore, for 3, only a small drop in specific capacity (22%) was observed even at current density as high as 1 A g^{-1} or in other words when the C-rate is increased to 5C (Figure 4G). Notably, in the commercial graphite this drop is $\approx 86\%$ (Figure 4H). This superior rate-performance of the 3 derived full-cell LIB is remarkable, suggesting they can yield rapid charging without any appreciable capacity fading.^[27,53–56] All these battery parameters from our evenhanded studies clearly points at the immense opportunity buried in these CON materials for the future-generation lightweight LIB.

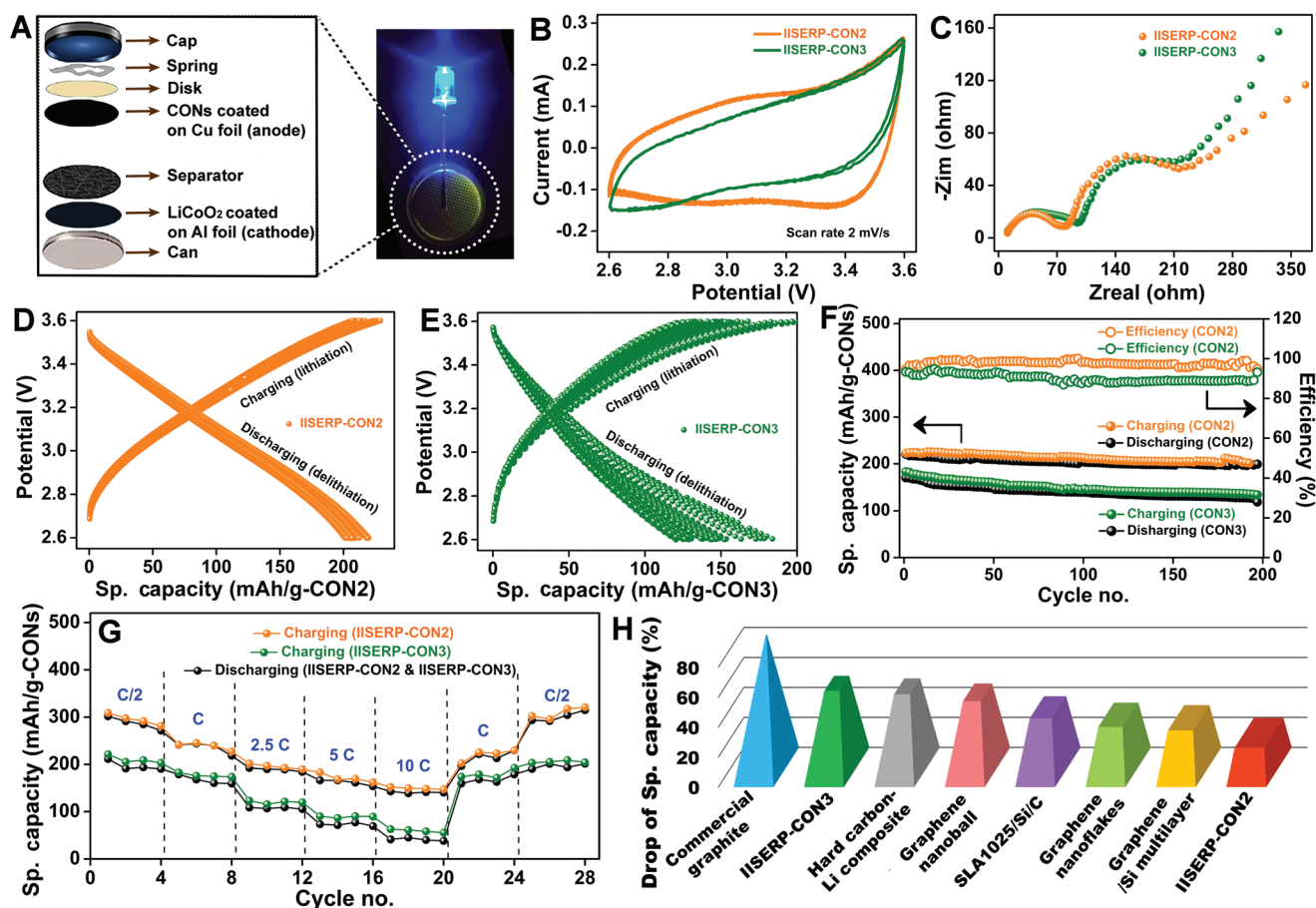


Figure 4. A) A photographic scheme showing the coin-cell assembly of the full-cell. Inset shows an LED light illuminated by the full-cell prepared using the IISERP-CON2 as anode versus LCO cathode. B) Comparative CV-plots measured in a full-cell configuration with a 2 mV s⁻¹ scan rate. C) Cole-cole plots from the AC-impedance measurements in their full-cell configurations. D,E) Galvanostatic charge–discharge curves of the CONs up to 200 cycles at 100 mA g⁻¹ current density in their full-cell configurations. Note the capacity has been expressed per gram of the anode (CON). F) Cycling stability and battery efficiency of the full-cells made using the CONs (@100 mA g⁻¹). G) C-rate performance of the CONs in their full-cell (1C = ≈100 mA g⁻¹). H) A comparative bar-chart showing the drop in specific capacity upon increasing charging rate from 1C to 10C between different high-performing/commercial materials.

2.4. Structural and Chemical Reasons for the CON's Superior Performance

The superior aspect of this particular Diels–Alder adduct-based chemical exfoliation is the tendency of the exfoliated flakes not to reaggregate. A problem that is not easy to address in case highly π -stacking materials like graphite. Also achieving an optimal lateral-length/height ratio in such exfoliated COF is an advantage (Figure 2E,F; and Figure S23, Supporting Information). In comparison, when graphite is exfoliated, the later dimensions do not drop proportionally with the height reduction owing to the robust C–C bonds. This limits how far one can exfoliate the strongly stacked graphite layers. This is crucial in deciding the overall high surface accessibility and facile diffusion. In our experience, chemical exfoliation of COFs is a more-optimized technique compared to aggressive mechanical or soft solvent-assisted sonication methods.

Now, coming to the superior performance of the CON over graphite, the major reason is the structure-driven chemical

accessibility. For example, in graphite, the Li intercalation leads to a LiC₆ type of compound as the theoretical limit. However, in practice, it is not straightforward for the Li-ions to access all the bulk interior of the graphite, and especially at higher charge–discharge rates, where the Li-ions tend to have much lower residence time which becomes insufficient for forming LiC₆ at every ring. In contrast, in this exfoliated COF, IISERP-CON2, since it retains its structure without any reaggregation, and has large pores offering complete access to the exposed functional groups (carbonyls and hydroxyls, etc.) the diffusing Li-ions, even at high C-rates, find their interaction sites efficiently. This explains the observed higher specific capacity as well as the limited drop in the capacity at high C-rates. We calculated that in IISERP-CON2 about 30 Li inserts per unit cell, which is much higher than the 1 per C₆-ring of the graphite. When normalized to their molecular weights, the gravimetric capacity would be 0.1 Li per mole of Graphite versus 0.2 Li per mole of IISERP-CON2. Thus, the advantage in the IISERP-CON2

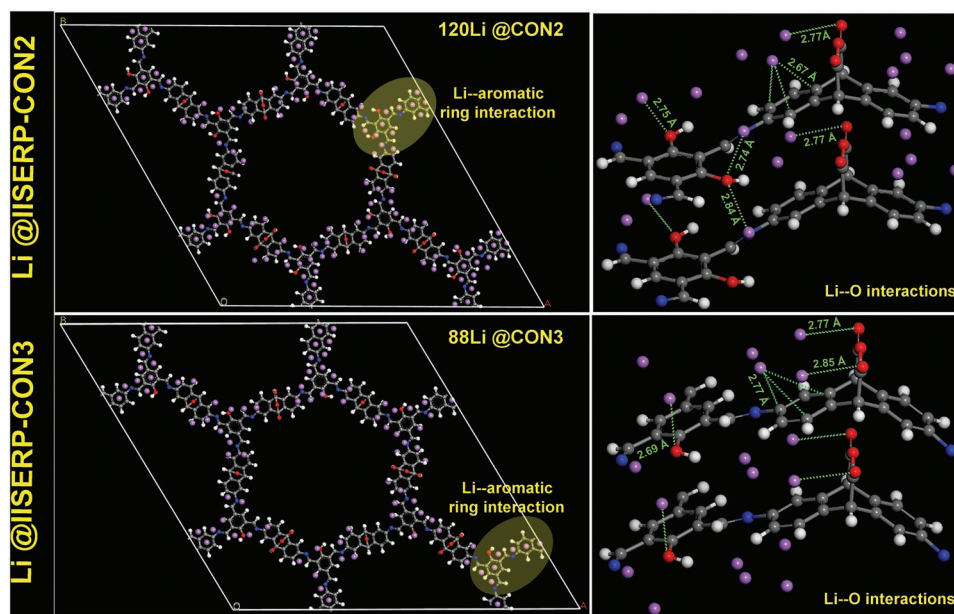


Figure 5. Optimized structures from a Simulated Annealing routine showing the Li-framework interactions. Note that the Li-O distances and the Li-C₆ interactions are within the range of 2.65–2.85 Å, suggesting weaker interactions and the lack of any strong covalent type interactions.

comes both from increased functionalities contributing to higher in-take of lithium and its facile diffusion.

To gain molecular-level insights into the lithium interactions with the CON, we carried out simulation studies. We obtained the optimized structure of the Li@CON using simulated annealing methods (Figure 5A; and Figure S46, Supporting Information). For both CONs, the optimized structures revealed the distribution of lithium atoms proximal to the oxygen atoms and the aromatic rings of the framework. Typical Li-O distances were 2.60–2.85 Å and Li-C₆ distances were at 2.6 Å, which indicates more of physical interactions and not any strong covalent interactions. This explains the facile and rapid lithiation and delithiation. Our 298K MD simulations done employing an NPT ensemble with random initial velocities reveal that lithium is highly diffusible within these channels (Figure S47, Supporting Information). It also conveys the stability of the lithium loaded framework under ambient conditions (no bond-breaking or unacceptable geometries were noticed).

In closing, we discuss two of the recent reports which are closely related to ours. Chen et al. described high lithium affinity of chemically exfoliated 2D covalent organic frameworks, where the π -stacking interaction between the benzene rings has been weakened by MnO₂ nanoparticle incorporation, preventing restacking.^[57] A high specific capacity was achieved from this composite material of MnO₂@CONs. Though this has a similarity to our work, there are some essential aspects where our work gains an advantage. The insertion of lithium into the MnO₂@COF is dominated by both the redox activity at COF and MnO₂. Because of the incorporation of the strongly redox active “conversion material,” namely the MnO₂, into the framework, in their case, almost a \approx 45% drop in sp. capacity was observed under high current density (1359–750 mAh g⁻¹ @ 100 mA g⁻¹ A g⁻¹, respectively) versus 35% in our IISERP-CON2. Similarly, Wang and co-workers

reported an anthraquinone-based COF functionalized with radical carrying strongly active redox groups.^[47] This was used as a cathode in LIB, wherein a ball-mill assisted exfoliation had resulted in enhanced diffusion of Li-ions. They achieved good stability with a specific capacity of 210 mAh g⁻¹. However, just as in the case of the MnO₂ loaded COF.^[57] Here too, the strong redox activity leads to substantial fading of capacity at higher current densities. In comparison, in IISERP-CONs, we retain all the advantages of the exfoliation, but we see reversible physiosorptive type interactions between the COF framework and the lithium species. This ensures excellent rate performance, even at high current densities. Notably, the energy invested in the chemical exfoliation is lower compared to ball milling and it is easier to scale-up. Importantly, these chemically exfoliated CON, are less prone to reaggregating or restacking.

From Figure 4D,E; and Figure S36 (Supporting Information), it is seen that the cells made using the CONs lack a flat voltage plateau compared to graphite and need more activation cycles. This is because the lithiating sites are not as homogeneous as in graphite. This could be a major drawback with using CON as anode materials. Nevertheless, CON-derived cells undeniably show excellent rate stability under high current density, which translates to high specific capacity even at fast charging, something that is challenging to achieve with graphite. Hence, finding a middle ground between CON and graphite could yield an ideal anode material.

3. Conclusion

The work showcases an FEA assisted route that exfoliates COF to CON and simultaneously populates the latter with Li-interactive groups. This enables the lightweight exfoliated-COF to achieve high charge-storage despite their volumetric

disadvantage. A four times enhancement in anodic performance upon exfoliation is attributed to the rapid and reversible Li-diffusion in and out of the active sites. The full-cell studies elicit the potential of the CON as a readily processable anode material against the commercially tested cathode namely the LiCoO₂. Importantly, the full-cell is capable of delivering specific capacities surpassing the battery-grade graphite-based LIB. The CON-derived cell retains this performance over high C-rates demonstrating excellent electrochemical stability. This structural and functional tunability opens-up the attractive possibility of using light atom rich COFs to develop lightweight batteries.

Supporting Information

Supporting Information is available from the Wiley Online Library or from the author.

Acknowledgements

S.H. and K.R. contributed equally to this work. The authors thank IISER-Pune for support and the funding by DST-for material for energy storage (DST/TMD/MES/2k17/103) program and the “DST-Nanomission under the Thematic Unit Program” (EMR/2016/003553). S.H. thanks DST-Inspire for financial support. The authors would like to thank SERB (EMR/2016), DST-Inspire, the MHRD-FAST, and the IUSSTF program for the necessary funding. They also thank IISER Pune for supporting the work and DST-FIST program for the AFM studies done at IISER Pune. The authors thank Dr. C. P. Vinod, NCL Pune, for the XPS and Debanjan Chakraborty, IISER Pune, for the adsorption studies. The authors thank Dr. Pramod Pillai for the access to UV-Vis spectrometer.

Conflict of Interest

The authors declare no conflict of interest.

Keywords

anodic covalent organic nanosheets, chemical exfoliation, full cell lithium ion batteries, functionalizing exfoliation agents, lithium storage

Received: July 25, 2019

Revised: October 12, 2019

Published online: November 14, 2019

- [1] X. Chen, K. Geng, R. Liu, K. T. Tan, Y. Gong, Z. Li, S. Tao, Q. Jiang, D. Jiang, *Angew. Chem., Int. Ed.* **2019**, <https://doi.org/10.1002/anie.201904291>.
- [2] D. N. Bunck, W. R. Dichtel, *J. Am. Chem. Soc.* **2013**, *135*, 14952.
- [3] G. Das, T. Skorjanc, S. K. Sharma, F. Gándara, M. Lusi, D. Shankar Rao, S. Vimala, S. Krishna Prasad, J. Raya, D. S. Han, *J. Am. Chem. Soc.* **2017**, *139*, 9558.
- [4] J. I. Feldblyum, C. H. McCreery, S. C. Andrews, T. Kurosawa, E. J. Santos, V. Duong, L. Fang, A. L. Ayzner, Z. Bao, *Chem. Commun.* **2015**, *51*, 13894.
- [5] S. Mitra, H. S. Sasmal, T. Kundu, S. Kandambeth, K. Illath, D. Díaz Díaz, R. Banerjee, *J. Am. Chem. Soc.* **2017**, *139*, 4513.
- [6] G. Das, F. Benyettou, S. K. Sharama, T. Prakasam, F. Gándara, A. Victor, N. I. Saleh, R. Pasricha, R. Jagannathan, M. A. Olson, A. Trabolsi, *Chem. Sci.* **2018**, *9*, 8382.
- [7] K. Wang, Z. Zhang, L. Lin, J. Chen, K. Hao, H. Tian, X. Chen, *Chem. Mater.* **2019**, *31*, 3313.
- [8] J. Sun, A. Klechikov, C. Moise, M. Prodana, M. Enachescu, A. V. Talyzin, *Angew. Chem., Int. Ed.* **2018**, *57*, 1034.
- [9] S. Chandra, S. Kandambeth, B. P. Biswal, B. Lukose, S. M. Kunjir, M. Chaudhary, R. Babarao, T. Heine, R. Banerjee, *J. Am. Chem. Soc.* **2013**, *135*, 17853.
- [10] M. S. Lohse, T. Stassin, G. Naudin, S. Wuttke, R. Ameloot, D. De Vos, D. D. Medina, T. Bein, *Chem. Mater.* **2016**, *28*, 626.
- [11] H. Xu, D. Jiang, *Nat. Chem.* **2014**, *6*, 564.
- [12] Y. Song, Q. Sun, B. Aguila, S. Ma, *Adv. Sci.* **2019**, *6*, 1801410.
- [13] S. Halder, D. Chakraborty, B. Roy, G. Banappanavar, K. Rinku, D. Mullangi, P. Hazra, D. Kabra, R. Vaidhyanathan, *J. Am. Chem. Soc.* **2018**, *140*, 13367.
- [14] D. Mukherjee, G. Gowda Y. K, H. Makri Nimbegondi Kotresh, S. Sampath, *ACS Appl. Mater. Interfaces* **2017**, *9*, 19446.
- [15] M. E. Bhosale, S. Chae, J. M. Kim, J.-Y. Choi, *J. Mater. Chem. A* **2018**, *6*, 19885.
- [16] J. Xie, Z. Wang, Z. J. Xu, Q. Zhang, *Adv. Energy Mater.* **2018**, *8*, 1703509.
- [17] Z.-Q. Lin, J. Xie, B.-W. Zhang, J.-W. Li, J. Weng, R.-B. Song, X. Huang, H. Zhang, H. Li, Y. Liu, *Nano Energy* **2017**, *41*, 117.
- [18] L. Bai, Q. Gao, Y. Zhao, *J. Mater. Chem. A* **2016**, *4*, 14106.
- [19] Z. Lei, Q. Yang, Y. Xu, S. Guo, W. Sun, H. Liu, L.-P. Lv, Y. Zhang, Y. Wang, *Nat. Commun.* **2018**, *9*, 576.
- [20] H. Yang, S. Zhang, L. Han, Z. Zhang, Z. Xue, J. Gao, Y. Li, C. Huang, Y. Yi, H. Liu, *ACS Appl. Mater. Interfaces* **2016**, *8*, 5366.
- [21] J. Dahn, A. Sleight, H. Shi, J. Reimers, Q. Zhong, B. Way, *Electrochim. Acta* **1993**, *38*, 1179.
- [22] M.-S. Kim, W.-J. Lee, S.-M. Paek, J. K. Park, *ACS Appl. Mater. Interfaces* **2018**, *10*, 32102.
- [23] Y. Zhu, X. Chen, Y. Cao, W. Peng, Y. Li, G. Zhang, F. Zhang, X. Fan, *Chem. Commun.* **2019**, *55*, 1434.
- [24] R. Yazami, P. Touzain, *J. Power Sources* **1983**, *9*, 365.
- [25] S. Halder, K. Roy, S. Nandi, D. Chakraborty, D. Puthusseri, Y. Gawli, S. Ogale, R. Vaidhyanathan, *Adv. Energy Mater.* **2018**, *8*, 1702170.
- [26] Z. Lei, X. Chen, W. Sun, Y. Zhang, Y. Wang, *Adv. Energy Mater.* **2019**, *9*, 1801010.
- [27] V. G. Khomenko, V. Z. Barsukov, J. E. Doninger, I. V. Barsukov, *J. Power Sources* **2007**, *165*, 598.
- [28] J. Shim, K. A. Striebel, *J. Power Sources* **2003**, *119–121*, 955.
- [29] J. Hassoun, K.-S. Lee, Y.-K. Sun, B. Scrosati, *J. Am. Chem. Soc.* **2011**, *133*, 3139.
- [30] J. R. Dahn, T. Zheng, Y. Liu, J. Xue, *Science* **1995**, *270*, 590.
- [31] M. D. Levi, D. Aurbach, *J. Phys. Chem. B* **1997**, *101*, 4641.
- [32] H. Huang, Y. Xia, X. Tao, J. Du, J. Fang, Y. Gan, W. Zhang, *J. Mater. Chem.* **2012**, *22*, 10452.
- [33] K. Toyoura, Y. Koyama, A. Kuwabara, F. Oba, I. Tanaka, *Phys. Rev. B* **2008**, *78*, 214303.
- [34] Z. Luo, L. Liu, J. Ning, K. Lei, Y. Lu, F. Li, J. Chen, *Angew. Chem., Int. Ed.* **2018**, *57*, 9443.
- [35] Y. Wu, R. Zeng, J. Nan, D. Shu, Y. Qiu, S. L. Chou, *Adv. Energy Mater.* **2017**, *7*, 1700278.
- [36] B. Häupler, A. Wild, U. S. Schubert, *Adv. Energy Mater.* **2015**, *5*, 1402034.
- [37] W. E. Bachmann, L. Scott, *J. Am. Chem. Soc.* **1948**, *70*, 1458.
- [38] H. Durmaz, B. Colakoglu, U. Tunca, G. Hizal, *J. Polym. Sci., Part A: Polym. Chem.* **2006**, *44*, 1667.
- [39] M. Grigoros, G. Colotin, N. C. Antonoia, *Polym. Int.* **2004**, *53*, 1321.
- [40] H. Hall Jr., P. Nogue, J. Rhoades, R. Sentman, M. Detar, *J. Org. Chem.* **1982**, *47*, 1451.

- [41] T.-C. Chou, T.-S. Jiang, J.-T. Hwang, K.-J. Lin, C.-T. Lin, *J. Org. Chem.* **1999**, *64*, 4874.
- [42] M. A. Khayum, S. Kandambeth, S. Mitra, S. B. Nair, A. Das, S. S. Nagane, R. Mukherjee, R. Banerjee, *Angew. Chem., Int. Ed.* **2016**, *55*, 15604.
- [43] L. J. Andrews, R. M. Keefer, *J. Am. Chem. Soc.* **1955**, *77*, 6284.
- [44] C. Sole, N. E. Drewett, L. J. Hardwick, *Faraday Discuss.* **2014**, *172*, 223.
- [45] P. Simon, Y. Gogotsi, B. Dunn, *Science* **2014**, *343*, 1210.
- [46] P. Yu, B. N. Popov, J. A. Ritter, R. E. White, *J. Electrochem. Soc.* **1999**, *146*, 8.
- [47] S. Wang, Q. Wang, P. Shao, Y. Han, X. Gao, L. Ma, S. Yuan, X. Ma, J. Zhou, X. Feng, *J. Am. Chem. Soc.* **2017**, *139*, 4258.
- [48] S. Yang, B. Yan, J. Wu, L. Lu, K. Zeng, *ACS Appl. Mater. Interfaces* **2017**, *9*, 13999.
- [49] T. Weigel, F. Schipper, E. M. Erickson, F. A. Susai, B. Markovsky, D. Aurbach, *ACS Energy Lett.* **2019**, *4*, 508.
- [50] H. Chen, H. Tu, C. Hu, Y. Liu, D. Dong, Y. Sun, Y. Dai, S. Wang, H. Qian, Z. Lin, L. Chen, *J. Am. Chem. Soc.* **2018**, *140*, 896.
- [51] Q. Xu, S. Tao, Q. Jiang, D. Jiang, *J. Am. Chem. Soc.* **2018**, *140*, 7429.
- [52] K. Jeong, S. Park, G. Y. Jung, S. H. Kim, Y. H. Lee, S. K. Kwak, S. Y. Lee, *J. Am. Chem. Soc.* **2019**, *141*, 5880.
- [53] M.-S. Balogun, W. Qiu, Y. Luo, H. Meng, W. Mai, A. Onasanya, T. K. Olaniyi, Y. Tong, *Nano Res.* **2016**, *9*, 2823.
- [54] H. Sun, X. He, J. Ren, J. Li, C. Jiang, C. Wan, *Electrochim. Acta* **2007**, *52*, 4312.
- [55] J. Hassoun, F. Bonaccorso, M. Agostini, M. Angelucci, M. G. Betti, R. Cingolani, M. Gemmi, C. Mariani, S. Panero, V. Pellegrini, *Nano Lett.* **2014**, *14*, 4901.
- [56] L. Ji, H. Zheng, A. Ismach, Z. Tan, S. Xun, E. Lin, V. Battaglia, V. Srinivasan, Y. Zhang, *Nano Energy* **2012**, *1*, 164.
- [57] X. Chen, Y. Li, L. Wang, Y. Xu, A. Nie, Q. Li, F. Wu, W. Sun, X. Zhang, R. Vajtai, P. M. Ajayan, L. Chen, Y. Wang, *Adv. Mater.* **2019**, *31*, 1901640.